UNDERGROUND POTASH MINE DESIGN BASED ON ROCK MECHANICS PRINCIPLES AND MEASUREMENTS

A THESIS

SUBMITTED FOR THE DEGREE OF DOCTOR OF PHILOSOPHY

in the

UNIVERSITY OF NEWCASTLE UPON TYNE

by

B.K. HEBBLEWHITE, B.E., (New South Wales)

October 1977

Underground Potash Mine Design Based on Rock Mechanics Principles and Measurements

B. K. Hebblewhite

Ph.D. Thesis October, 1977

ABSTRACT

The design criteria for an underground potash mine are established on the basis of rock mechanics principles and measurements taken at the Cleveland Potash Limited Boulby mine in North Yorkshire, England.

The requirements of the mine design are that a maximum and efficient extraction ratio is achieved, stable and safe working conditions exist within the mine, and no damaging subsidence occurs on the surface. In particular, the workings at Boulby are at a depth of 1100 metres below the surface and are overlain by water-bearing Bunter sandstone strata, 120 metres above the potash horizon. Consequently, the major problem of the mine design concerns minimizing the subsidence-induced strains at the base of the Bunter sandstone in order to prevent a possible water inrush into the mine.

The various design parameters to meet these requirements are established on the basis of theoretical, laboratory and 'in-situ' analyses. A study of Canadian potash mining practice is included to provide valuable design information.

The theoretical work consists of both face element and finite element numerical techniques. These are initially elastic solutions to provide comparisons of initial stress conditions around different mine panel geometries. A face element technique is developed to analyse mining panels where the length is considerably greater than the panel width.

Large scale underground instrumentation provides detailed information on stress conditions, time-dependent deformations around mine roadways and strain distributions within pillars. This information, together with surface subsidence measurements and laboratory determined rheological properties, is used to provide more realistic boundary conditions for the numerical modelling of the mining layouts.

The combination of the theoretical analyses and the measured data provide a set of design criteria for an optimum mining layout which satisfies the above requirements.

LIST OF CONTENTS

			Page No.
CHAPTER	1.	INTRODUCTION	1
	1.1	The North Yorkshire Evaporite Deposits	2
	1.1.1	The Nature and Origin of Potash Deposits	3
	1.1.2	Boulby Geology	7
	1.2	Boulby Mine	11
	1.3	Rock Mechanics Research Project	13
	1.3.1	Project Objectives	13
	1.3.2	Previous Research	14
	1.3.3	Current Research	16
CHAPTER	2.	COMPUTER TECHNIQUES FOR THEORETICAL AND DATA ANALYSES	18
	2.1	Numerical Modelling	18
	2.1.1	Suitable Elastic Models	20
	2.1.2	Comparison of Face Element and Finite Element Techniques	22
	2.1.3	FEMITPLT - 2D Finite Element Program	24
	2.1.4	Face Element Method	31
	2.1.5	Numerical Model for Long Panels	33
	2.1.6	Face Element Solution by Perturbation	40
	2.1.7	Comparison of Face Element and Analogue Solutions	45
	2.1.8	Panel Simulation - Types of Boundary Conditions and Models	46
	2.1.9	Subsidence Analysis	48
	2.2	Data Analysis	50

		Page No.
2.3	Auxiliary Programs	57
CHAPTER 3.	FACE ELEMENT ANALYSES OF LOW EXTRACTION PANELS	59
3.1	Material Properties and Seam Parameters	60
3.2	Pillar Strength Safety Factor	61
3.3	Results	64
3.3.1	Layout 1 - 5 Entries, 60m Square Pillars	65
3.3.2	Layout 2 - 5 Entries, 40m Square Pillars	69
3.3.3	Layout 3 - 7 Entries, 40m Square Pillars	71
3.3.4	Layout 4 - 7 Entries, 30m, 45m, 60m by 60m Pillars	74
3.3.5	Layout 5 - 11 Entries, 30m Square Pillars	77
3.3.6	Layout 6 - 11 Entries, 30m Herringbone Pillars	80
3.3.7	Layout 7 - 9 Entries, 24m Square Pillars	86
3.3.8	Layout 8 - 7 Entries, 15m by 45m Herringbone Pillars	88
3.4	Comparison of Results	94
3.4.1	Panel Pillar Stability	94
3.4.2	Barrier Pillar Stability	102
3.4.3	Above Seam Stability	108
3.5	Summary of Conclusions	110
CHAPTER 4.	FACE ELEMENT AND FINITE ELEMENT ANALYSES OF HIGH EXTRACTION PANELS	114
4.1	Yield Pillar Technique	114
4.2	Face Element Analyses	116
4.2.1	Above Seam Results	117

		Page No.
4.2.2	Barrier Pillar Results	121
4.3	Finite Element Analyses	129
4.3.1	Finite Element Results	133
4.4	Summary of Conclusions	146
CHAPTER 5.	MECHANICAL PROPERTIES OF NEAR-SEAM STRATA	149
5.1	Triaxial Compression Tests	151
5.1.1	Triaxial Compression - Potash Results	153
5.1.2	Triaxial Compression - Shale Results	158
5.1.3	Triaxial Compression - Carnallite Marl Results	162
5.1.4	Comparison of Results	166
5.2	Middle Halite - Elastic Properties	169
5.3	Summary of Near-Seam Mechanical Properties	170
5.4	Anhydrite Tensile Strength and Modulus	171
5.5	Summary of Conclusions	173
CHAPTER 6.	COMPLETE STRESS-STRAIN BEHAVIOUR OF MODEL POTASH PILLARS AND ADJACENT ROCK TYPES	175
6.1	Importance of Post-Failure Characteristics	175
6.2	Equipment and Test Program	179
6.2.1	Platen Effects	182
6.2.2	Strain Rate	183
6.3	Results	184
6.3.1	Width:Height Ratio Tests	187
6.3.2	Volumetric Strain	194
6.3.3	Strain Rate Effect	195
6.3.4	Size Effect	197

		Page No.
6.3.5	Shape Effect	199
6.3.6	Creep in Relation to Stress-Strain Curves	200
6.3.7	Shale v. Potash Results	204
6.3.8	Shale v. Halite v. Potash Results	205
6.4	Pillar Stability in Relation to Roof Stiffness	205
6.5	Summary of Conclusions	208
CHAPTER 7.	MEASUREMENT OF THE STRESS FIELD ABOVE THE MINING HORIZON	210
7.1	Estimated In-Situ Stress	210
7.2	Stress Measurement by Overcoring Technique	212
7.2.1	The Talbott Mark II Strain Cell	213
7.2.2	The Principle of Overcoring	216
7.3	Site of Overcoring Operation	218
7.3.1	Equipment and Initial Drilling	220
7.4	Discussion of Results	223
7.4.1	Cell 1	223
7.4.2	Cell 2	226
7.4.3	Cell 3	230
7.4.4	Cell 4	236
7.4.5	Cell 5	243
7.5	Comparison of Results and Summary of Conclusions	244
CHAPTER 8.	ANALYSIS OF IN-SITU INSTRUMENTATION RESULTS	248
8.1	Instrumentation	248
8.2	Shaft Pillar Results	252

		Page No.
8.3	No. 1 Panel Results	273
8.3.1	Site 1P1	273
8.3.2	Site 1P2	286
8.3.3	Comparison of 1P1 and 1P2 Results	290
8.3.4	Site 1P4	294
8.3.5	Sites 1P7, 1P8, 1P9	301
8.4	No. 2 Panel Results	311
8.5	South Development Results	315
8.6	East Panel Results	321
8.7	Comparison of 25m, 40m and 60m Pillars	326
8.8	Comparison of Roadway Closure Rates	330
8.9	Surface Subsidence	334
8.9.1	Angle of Draw	340
8.9.2	Time Lag	341
8.9.3	Summary of Angle of Draw and Time Lag Conclusions	342
8.9.4	Lateral Strains	343
8.10	Summary of Conclusions	346
CHAPTER 9.	SUMMARY OF OTHER RELEVANT EVAPORITE MINING OPERATIONS	349
9.1	Rock Salt Mines	349
9.2	European Potash Mines	350
9.3	Canadian Potash Mines	352
9.4	Application of Canadian Methcd to Boulby	360

		Page No.
CHAPTER 10.	CONCLUSIONS	362
10.1	Panel and Barrier Dimensions	362
10.2	Pillar Dimensions	364
10.3	Roadway Stability	365
10.4	Subsidence	366
10.5	Other Conclusions	367
10.6	Recommendations for Future Work	368
CHAPTER 11.	APPENDICES	370
	A. Computer Program Control Data and Listings	370
	B. Table B1 - Extensometer Anchor Depths	401
	Shaft Pillar Site Layouts	405
	Shaft Pillar Site Geology	409
	Extensometer Results	414
	Convergence, Roof Sag, Floor Heave Results	429
	C. No. 2 Shaft Extensometer Results	447
REFERENCES		450

LIST OF FIGURES

Fig. No.		Page No.
1-1	Location of Mine Site and Lease Area	2
1-2	Evaporite Deposition in a Restricted Basin Similar to the Zechstein Sea (after Patchet)	5
1-3	Strata Sequence (from Borehole S20)	8
1-4	Near-Seam Strata Sequence	9
1-5	Plan of Mine Workings (early 1977)	12
2-1	Stress-Strain Options in 'Minbump'	21
2-2	Virgin and Relief Loads	27
2-3	Mesh Used for 'Kirsch' Problem	29
2-4	'Kirsch' Problem Results	29
2-5	Room and Pillar Layout with Barriers	33
2-6	3D Face Element Mesh for Panel Layout	35
2-7	Stresses in Y-Direction Along Panel	36
2-8	Statically Equivalent Trains of Stress	37
2-9	2D Face Element Mesh	39
2-10	Subroutine Flowchart for Program 'Dataplot'	52
3-1	Triaxial Strength Safety Factor	63
3-2	Layout 1 3D Mesh (not to scale)	66
3-3	Layout 1 In-Seam Normal Stresses	66
3-4	Subsidence and Strain 200m Above Layout 1	68
3-5	Layout 2 3D Mesh (not to scale)	70
3-6	Layout 2 In-Seam Normal Stresses	70
3-7	Subsidence and Strain 200m Above Layout 2	71

Fig. No.		Page No.
3-8	Layout 3 3D Mesh (not to scale)	73
3-9	Layout 3 In-Seam Normal Stresses	73
3-10	Subsidence and Strain 200m Above Layout 3	74
3-11	Layout 4 3D Mesh (not to scale)	75
3-12	Layout 4 In-Seam Normal Stresses	75
3-13	Subsidence and Strain 200m Above Layout 4	77
3-14	Layout 5 3D Mesh (not to scale)	78
3-15	Layout 5 In-Seam Normal Stresses	78
3-16	Subsidence and Strain 200m Above Layout 5	80
3-17	Layout 6 3D Mesh (not to scale)	81
3-18	Layout 6 In-Seam Normal Stresses	81
3-19	Subsidence and Strain 200m Above Layout 6	85
3-20	Layout 7 3D Mesh (not to scale)	87
3-21	Layout 7 In-Seam Normal Stresses	87
3-22	Layout 8 3D Mesh (not to scale)	89
3-23	Layout 8 In-Seam Normal Stresses	89
3-24	Stress Distribution Across Pillars	91
3-25	Subsidence and Strain 120m Above Layout 8	93
3-26	Strength Safety Factor (F_s) v. Width:Height Ratio	96
3-27	Average Pillar Deviator Stress ($\sigma_{DEV.}$) v. W:H Ratio	98
3-28	F_T v. Deviator Stress	100
3-29	Time-Dependent Safety Factor (F_T) v. Width:Height Ratio	101
3-30	'K' Factor v. Panel Extraction Ratio (e)	105
3-31	Lateral Strain 120m Above 240m Panels	109
3-32	Lateral Strain Safety Factor Curves	111

Fig. No.		Page No.
4-1	120m Above Seam $\varepsilon_{max.}$, $S_{max.}$ v. (Block Width x e)	119
4-2	1100m Above Seam $S_{max.}$ v. (Block Width x e)	119
4-3	Lateral Strain Safety Factor Curves	120
4-4	Lateral Strain Profile 120m Above 4 x 60m Panel Block Mined 1, 2, 3, 4	122
4-5	Lateral Strain Profile 120m Above 4 x 60m Panel Block Mined 1, 4, 3, 2	123
4-6	Stress Distribution Between 50m Panels	124
4-7	$\sigma_{Dev.}$ v. Barrier Width	125
4-8	σ_N / σ_V v. Barrier Width	125
4-9	Basic Layout for Production Blocks	130
4-10	Finite Element Mesh	131
4-11	Principal Compressive Stress Distribution Around 5-Entry Panel with Stiff Pillars	134
4-12	Principal Compressive Stress Distribution Around 5-Entry Panel with Yielding Pillars	135
4-13	Induced Compressive Stress Distribution Around 5-Entry Panel with Yielding Pillars	137
4-14	Induced Tensile Stress Distribution Around 5-Entry Panel with Yielding Pillars	138
4-15	Warping Ratio v. Pillar Yield	140
4-16	Roof Shear Stress v. Pillar Yield	140
4-17	Roof Sag v. Height Above Seam	141
4-18	Lateral Strain v. Yield	141
4-19	Maximum Deviator Stress v. Pillar Yield	144
4-20	Closure v. Time for Stable and Unstable Panels	145

Fig. No.		Page No.
5-1	Cross-Section of Triaxial Cell (after Buzdar)	152
5-2	Relationship Between Mohr Envelope and Specimen Failure Mechanism	154
5-3	Effect of Confinement on Stress-Strain Curve for Potash	155
5-4	Potash Triaxial Compression Specimens (photograph)	156
5-5	Mohr Envelope for Potash	157
5-6	Effect of Confinement on Stress-Strain Curve for Shale	159
5-7	Shale and Marl Triaxial Compression Specimens (photograph)	160
5-8	Mohr Envelope for Shale	161
5-9	Effect of Confinement on Stress-Strain Curve for Carnallite Marl	164
5-10	Mohr Envelope for Carnallite Marl	165
5-11	Failure Strain v. Confinement	167
5-12	Relative Strength Ratio v. Confinement	167
5-13	Strength v. Confinement	168
5-14	Young's Modulus and Poisson's Ratio for Middle Halite	169
6-1	Stress-Strain Path for Yield Pillar	176
6-2	A Closed Loop System for Servo-Controlled Testing Machines	178
6-3	Servo-Controlled Testing Machine (photograph)	180
6-4	Effect of Width:Height Ratio on Potash Model Pillars	188

Fig. No.		Page No.
6-5	Model Pillars PPMP3 and PPMP4 (photograph)	190
6-6	Model Pillar PPMP5 (photograph)	191
6-7	Distortion of 1cm Square Grid on Base of PPMP2	192
6-8	Lateral Strain Across X and Y Diameters of PPMP2	192
6-9	Effect of Strain Rate on Potash Model Pillars	196
6-10	Strain Rate Effect	197
6-11	Progressive Failure of Model Pillar PPMP7 (photograph)	198
6-12	Effect of Size on Potash Model Pillars	199
6-13	Effect of Shape on Potash Model Pillars	200
6-14	Creep of Model Pillar PPMP15	202
6-15	Relationship between Creep and Stress-Strain Behaviour	203
6-16	Shale v. Potash Model Pillar Results	204
6-17	Shale, Potash, Middle Halite Results	206
6-18	Roof Stiffness v. Pillar Unloading Stiffness	208
7-1	Mark II Talbott Strain Cell (photograph)	214
7-2	Overcoring Site Location	218
7-3	Geology and Cell Location	219
7-4	Drill Site (photograph)	221
7-5	Core Recovered (photograph)	221
7-6	Cell Reference Axes	223
7-7	Cell 1 Results	225
7-8	Cell 2 Results	227
7-9	Cell 2 Stress Orientations	230

Fig. No.		Page No.
7-10	Cell 3 Results	232
7-11	Cell 3 Strain v. Distance	233
7-12	Cell 3 Stress Orientations	236
7-13	Cell 4 Results	237
7-14	Cell 4 Strain v. Distance	238
7-15	Cell 4 Gauge Corrections	240
7-16	Cell 4 Laboratory Modulus Testing	242
7-17	Cell 4 Stress Orientations	243
7-18	Cells 1, 3, 4 (photograph)	245
8-1	Extensometer Installation and Reading (photograph)	250
8-2	Shaft Pillar Development	253
8-3	Borehole 4 Strain v. Depth	255
8-4	Site N.U.06 Roof Displacement	256
8-5	Roof Support (photograph)	259
8-6	Roof Failure (photograph)	260
8-7	Roof Failure (photograph)	261
8-8	Borehole 19 Strain v. Depth	264
8-9	Shaft Pillar Potash Road Closure Rates	265
8-10	60m Pillar Strain Rates v. Depth	267
8-11	Borehole 28 Strain Rates v. Depth	267
8-12	Borehole 28 $\ln$ Strain Rate v. Time	267
8-13	$(\dot{d}/\dot{o})$ v. Time	269
8-14	$\dot{\varepsilon}_c$ v. Time	269
8-15	Layout of Experimental Roadways	274
8-16	Site 1P1 Layout	275

Fig. No.		Page No.
8–17	Geological Sections Through G and 3X/C – Site 1P1	276
8–18	Total Closure at Site 1P1 During Junction Development	278
8–19	Vertical Section Along 3X/C	280
8–20	Floor Closure Rate v. Time – Site 1P1	281
8–21	Strain v. Depth – Boreholes 3, 7 – Site 1P1	283
8–22	Site 1P1 Roof Sag	284
8–23	Site 1P1 Roof Sag Rate	285
8–24	Site 1P2 Layout	287
8–25	Geological Sections Through K and 3X/C – Site 1P2	288
8–26	Floor Closure Rate v. Time – Site 1P2	289
8–27	Strain v. Depth – Borehole 11 – Site 1P2	291
8–28	Sites 1P1, 1P2 Convergence	292
8–29	Subsidence v. Depth Above Mine Openings	293
8–30	C – D Pillar Splitting Experiment	295
8–31	Relative Sequence of Mining Past Plane of Instrumentation	296
8–32	Floor and Roof Closure Rates v. Time – Site 1P4	298
8–33	Borehole 23 Bay Strain	299
8–34	1P4 Lateral Strain Rates	300
8–35	Condition of Road C (photograph)	302
8–36	Shale Roof (photograph)	303
8–37	Road D and No. 2X/C (photograph)	304
8–38	Layout of 1P7, 1P8, 1P9	305
8–39	1P7 Results	307
8–40	1P8 Results	308
8–41	1P9 Results	309

Fig. No.		Page No.
8-42	Layout of 2P1, 2P2	312
8-43	2P1, 2P2 Results	313
8-44	South Development Layout	316
8-45	South Development Results	317
8-46	J - H Pillar Strain Rates	318
8-47	$\ln \dot{\varepsilon}_{40}$ v. Time	319
8-48	East Panel Layout	322
8-49	East Panel Results	323
8-50	Strain Rate v. Depth - 25m pillars	324
8-51	$\ln \dot{\varepsilon}_{25}$ v. Time	325
8-52	Pillar Strain Rates v. Depth	327
8-53	Pillar Deformation Relative to Sidewall	327
8-54	Average Vertical Pillar Strain and Deformation v. Time	329
8-55	Roadway Closure Rates	331
8-56	Position of Subsidence Monitoring Lines Relative to Underground Workings	336
8-57	Underground Face Positions Between Oct. 1975 and Sept. 1976	337
8-58	Surface Subsidence - Line 1	338
8-59	Surface Subsidence - Line 2	339
8-60	Lateral Strains - Line 1	344
8-61	Lateral Strains - Line 2	345
9-1	Sylvite Mine (photograph)	354
9-2	Canadian Stress Relief System	356

Fig. No.		Page No.
9-3	Noranda Mine (photograph)	358
9-4	Cominco Mine (photograph)	359

LIST OF TABLES

Table No.		Page No.
1-1	World Potash Production (after Freeman (5))	4
1-2	Common Potash Minerals	6
2-1	Details of Analog Comparison Panel (after Oravecz)	45
2-2	Ratio of Pillar Stresses to Tributary Area Stress	46
3-1	Panel Layout Geometries	62
3-2	Layout 1 In-Seam Stress Results	67
3-3	Layout 1 Above Seam Results for 200m Horizon	68
3-4	Layout 2 In-Seam Stress Results	69
3-5	Layout 2 Above Seam Results for 200m Horizon	71
3-6	Layout 3 In-Seam Stress Results	72
3-7	Layout 3 Above Seam Results for 200m Horizon	72
3-8	Layout 4 In-Seam Stress Results	76
3-9	Layout 4 Above Seam Results for 200m Horizon	76
3-10	Layout 5 In-Seam Stress Results	79
3-11	Layout 5 Above Seam Results for 200m Horizon	80
3-12	Layout 6 In-Seam Stress Results	84
3-13	Layout 6 Above Seam Results for 200m Horizon	84
3-14	Layout 7 In-Seam Stress Results	88
3-15	Layout 8 In-Seam Stress Results	90
3-16	Average Pillar Stresses for Long Pillar Panels	92
3-17	Layout 8 Above Seam Results for 120m Horizon	93
3-18	Time-Dependent Safety Factors	100
3-19	Barrier Loading Factor	104

Table No.		Page No.
4-1	Maximum Subsidence Above a Four Panel Block	118
4-2	Material Types and Properties for Finite Element Model	132
5-1	Mean Values for Mechanical Properties of Potash and Shale (after Wiggett (9))	150
5-2	Triaxial Compression Results - Potash	154
5-3	Triaxial Compression Results - Shale	158
5-4	Triaxial Compression Results - Carnallite Marl	163
5-5	Summary of Near-Seam Mechanical Properties	171
5-6	Tensile Strength of Upper Anhydrite	172
5-7	Tensile Elastic Modulus of Upper Anhydrite	173
6-1	Model Pillars - Specimen Details and Results	185
6-2	Model Pillar Volumetric Strain	194
7-1	Specific Gravity and Thickness of Geological Sequence	211
7-2	Cell 2 Overcoring - Elastic Strain Recovery	228
7-3	Cell 2 Principal Stresses and Directions	229
7-4	Cell 3 Overcoring - Elastic Strain Recovery	234
7-5	Cell 3 Principal Stresses and Directions	235
7-6	Cell 4 Overcoring - Elastic Strain Recovery	241
7-7	Cell 4 Principal Stresses and Directions	243

Table No.		Page No.
8-1	Site N.U.06 - 50 day Anchor Displacements	256
8-2	60m Pillar Closure and Strain Rates	270
8-3	Roof - Floor Closure Rates (mm/day)	332

ACKNOWLEDGEMENTS

I would like to thank:

- Professor E.L.J. Potts for providing the opportunity and facilities for carrying out this work and directing the project.

- Cleveland Potash Limited for financing the project. Thanks are due to various mine personnel for their assistance and co-operation, and in particular, to Mr. D.M. Beadnall for continued support throughout the investigation.

- Dr. R.K. Dunham and Mr. H.D.S. Miller for their help and supervision of the project.

- Mr. T. Pollock and his technical staff for their help in the laboratory and for the manufacture and installation of much of the instrumentation.

- Present and former staff and students of the Department of Mining Engineering, especially Dr. M. Thompson, Mr. A. Price, Mr. D.J. Maconochie and Mr. S.T. Horseman for a great deal of useful advice.

- My wife, for typing the manuscript, and for her patience and constant encouragement.

CHAPTER 1

INTRODUCTION

1. INTRODUCTION

The study of rock mechanics as a mining science has developed rapidly during the last twenty years. The application of the science of rock mechanics to the practical problems of mining engineering has been an even more recent development. Previously the constraints on mining which rock mechanics defines had been established purely by accident - roof collapses, pillar collapses, rock bursts, floor heave, subsidence, etc. Many of these potential problems and the constraints they lead to can now be predicted initially by means of a fundamental rock mechanics investigation and subsequently by regular monitoring of mine stability in both experimental and production mining areas.

The mining engineer's decisions related to mine stability, however, must be made in relation to his main objective which is to maintain production at an economically viable level. The general increase in mining depth and decrease in grade of ore reserves currently being developed throughout the world necessitates far greater efficiency in the methods and level of extraction. This presents a more complex problem to the rock mechanics engineer. He now has to determine maximum levels of extraction which will continue to provide stability underground throughout the workings together with acceptable levels of surface subsidence. This balance between an economically viable extraction ratio and overall stability is becoming more and more critical.

The research work undertaken in this investigation is part of a long term project to study the rock mechanics problems associated

with the development and operation of a potash mine beneath the North Yorkshire Moors at Boulby, near Staithes.

1.1 The North Yorkshire Evaporite Deposits

The potash seam which is mined at Boulby forms part of a series of evapcrite strata which were discovered while drilling for oil near Whitby in 1938-39. The potash seam was encountered at depths in excess of 1250m but due to lack of technology at the time, further development with a view to mining was deferred. During the 1960's I.C.I. carried out further exploration in the Staithes area and encountered a potash seam at shallower depths, up to 1050m. This potash deposit was substantiated by some fifteen boreholes which indicated that the deposit existed over a large area extending out beneath the North Sea.

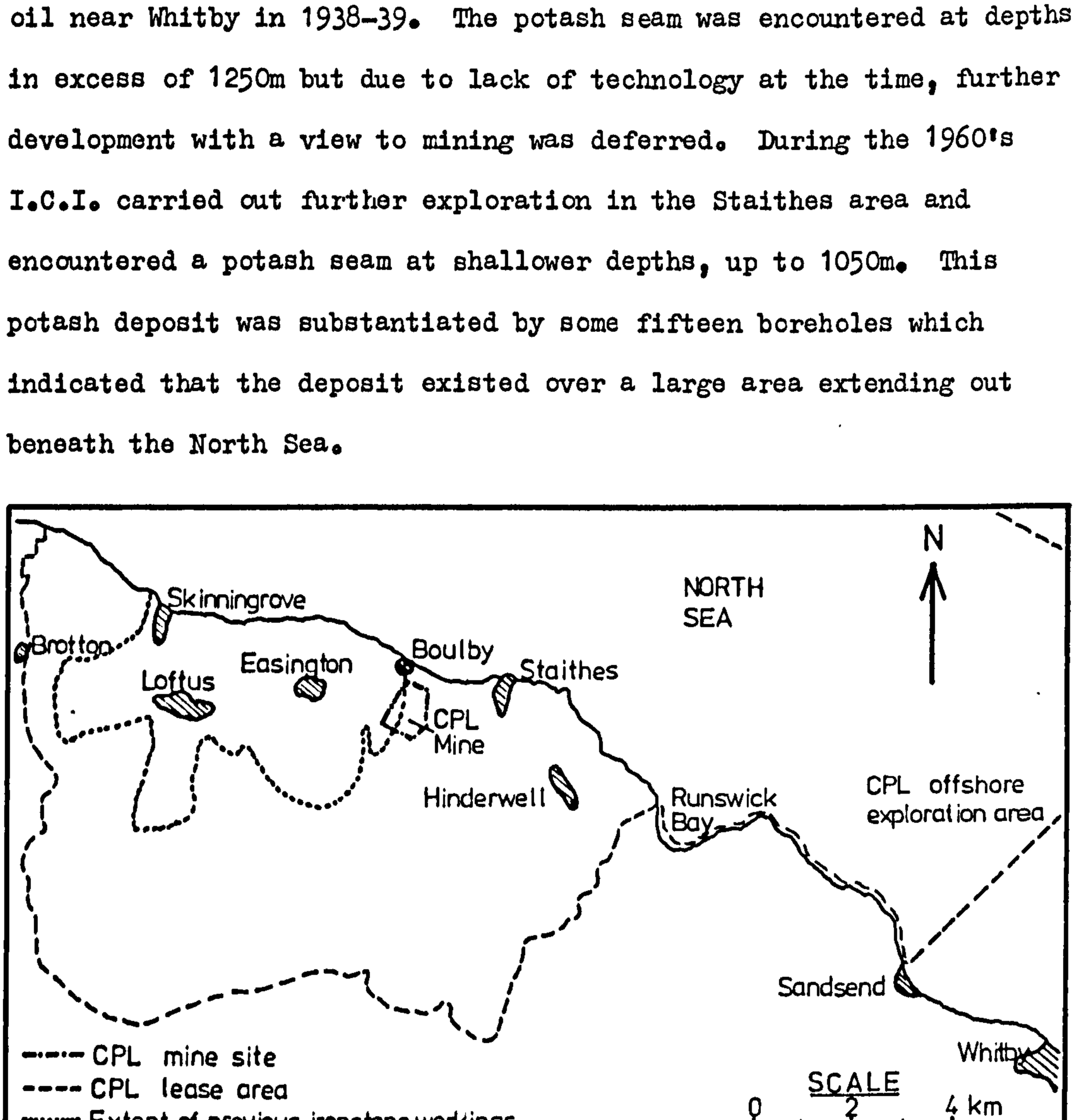

FIG. 1-1 LOCATION OF MINE SITE AND LEASE AREA

I.C.I., in partnership with Charter Consolidated Ltd., formed a subsidiary operating company, Cleveland Potash Ltd., in 1967 and planning permission was granted in 1968 for a 1.5m tonnes per year conventional potash mining operation at Boulby (1). Fig. 1-1 shows the location of the mine site and the extent of the Cleveland Potash leases.

1.1.1 The Nature and Origin of Pctash Deposits

Potash is the term commonly used to describe any salt containing potassium. Potassium occurs naturally in a wide variety of rocks but the content rarely exceeds 5% K_2O equivalent and the extraction and refining of such material to a usable product is difficult and expensive. Practically all the present world supplies of potash are obtained from the evaporation of naturally concentrated brines or from fossil deposits. The use of potash is primarily as a fertilizer and demand for the mineral is increasing rapidly with major agricultural expansion requiring greater productivity from limited land resources throughout the world.

The major producer of potash in the western world is Canada where the vast deposits of the Middle Devonian age Prairie Evaporites in Saskatchewan are being exploited by nine major mining operations (2). Other major potash producing areas are found in U.S.A., Europe and the Communist countries. The Department of Mining Engineering at Newcastle University has been involved in research projects concerning pctash mining in France and Spain (3, 4). Table 1-1 lists the latest available production figures from the major potash producing countries.

Table 1-1 World Potash Production (after Freeman (5))

Country	Production ('000 tonnes K_2O equivalent)		
	1974	1975	1976 (*)
U.S.S.R.	6,586	7,944	8,250
Canada	5,480	5,436	4,998
G.D.R.	2,864	3,019	3,160
U.S.A.	2,326	2,294	2,205
F.R.G.	2,620	2,222	2,036
France	2,083	1,920	1,603
Israel	607	716	700
Spain	396	459	535
Congo	285	286	254
Italy	151	141	140
U.K.	11	15	45
Total	23,410	24,453	23,926

* Preliminary figures only

The deposition of the Yorkshire evaporites took place during the Permian age in a formation known as the Zechstein Sea. This marine basin covered the whole area of what is now north-east England, the North Sea and a large part of Europe. Three series of evaporite strata were deposited, the Boulby potash being part of the Middle Evaporites. The sequence of deposition is illustrated in Fig. 1-2, the evaporites being formed by crystallization from a saturated brine solution. The order of deposition is limestone-dolomite

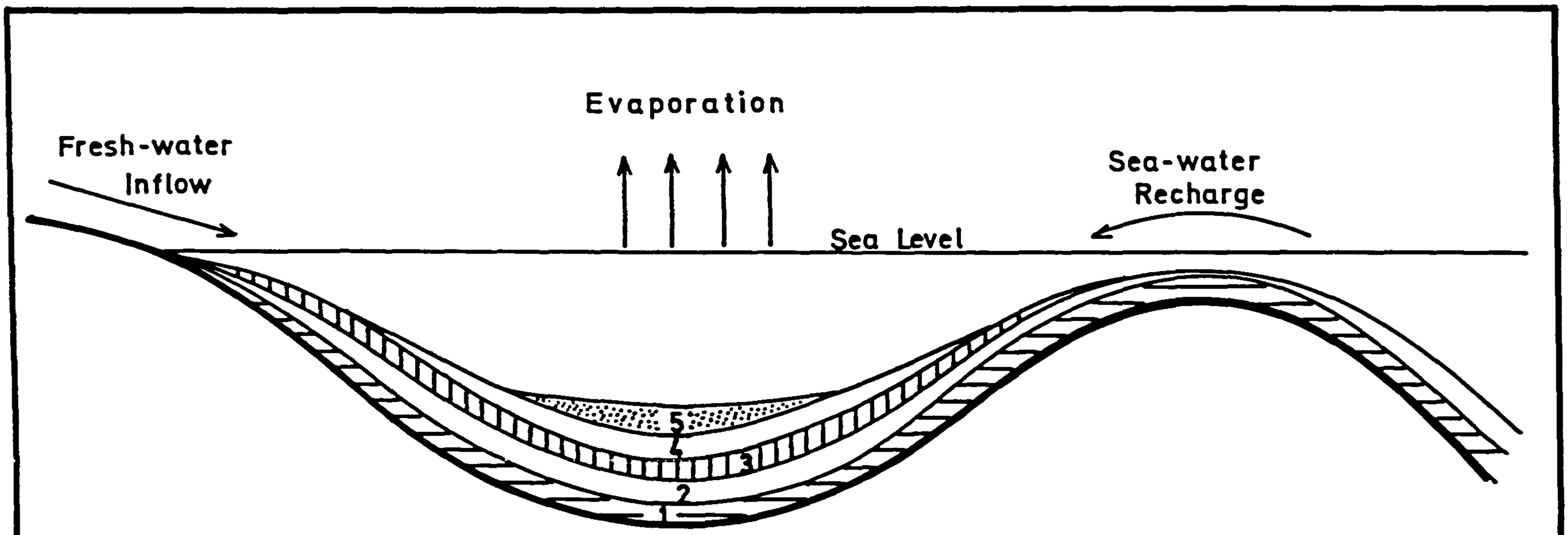

FIG. 1-2 EVAPORITE DEPOSITION IN A RESTRICTED BASIN SIMILAR TO THE ZECHSTEIN SEA (after Patchet)

SC. V6 / 31

($CaCO_3$ and $MgCO_3$) first, being the least soluble, followed by anhydrite ($CaSO_4$) and gypsum ($CaSO_4 - 2H_2O$), halite (NaCl), then the most soluble, the potassium and magnesium salts. This cycle is obviously very susceptible to changes due to fresh or salt water inflows, climatic changes and other geographical influences. Consequently the evaporite sequence is often irregular and can be infiltrated by insoluble strata.

Table 1-2 lists the most common potash minerals deposited in this final stage of brine crystallization.

Table 1-2 Common Potash Minerals

Mineral Name	Composition	Equivalent K_2O Content (%)
Sylvite	KCl	63.1
Carnallite	$KCl.MgCl_2.6H_2O$	17.0
Kainite	$KCl.MgSO_4.3H_2O$	18.9
Polyhalite	$K_2SO_4.MgSO_4.2CaSO_4.2H_2O$	15.5
Langbeinite	$K_2SO_4.MgSO_4$	22.6

Obviously sylvite is the most desirable potash mineral based on its high K_2O content and it is sylvite which occurs predominently in the potash deposits of North Yorkshire. The sylvite occurs most commonly in the form of sylvinite, the name given to the mechanical mixture of sylvite, halite, anhydrite and possibly some other minor evaporites and impurities. The grade of ore which is mined at Boulby varies between about 15% and 30% K_2O equivalent.

1.1.2 Boulby Geology

The geology overlying the potash seam at Boulby is a mixture of marine sediments and evaporites. Fig. 1-3 shows the general sequence of strata based on the information obtained from the S20 shaft borehole (6). Fig. 1-4 shows the detailed geology in the vicinity of the seam. The strata are generally flat and fairly regular in composition although the thickness of various beds varies considerably within the area of the C.P.L. lease. Details of the geology have been described previously (7, 8) and only details of specific interest to rock mechanics will be described here.

Much of the area surrounding the immediate mine site at Boulby has been mined previously for ironstone which occurs as a number of seams in the Middle Lias, about 40m below the surface. The extent of these workings is indicated on Fig. 1-1. Obviously, in terms of surface subsidence due to mining the potash at 1100m depth, consideration must be given to the presence of the ironstone workings, many areas of which were mined on a high extraction room and pillar system.

Apart from the near-surface estuarine deposits, the only water-bearing strata in the sequence is the massive Bunter Sandstone. This is 300m thick on average and consists of fine grained, red sandstones grading into mudstones. The sandstone contains a semi-saturated brine solution, movement of which is restricted by the low permeability of the strata, but is under high hydrostatic pressure. During shaft-sinking there was evidence of fissures containing water from the sandstone occurring in the Upper Permian Marl which is below the Bunter Sandstone and can approach to within 75m above the seam.

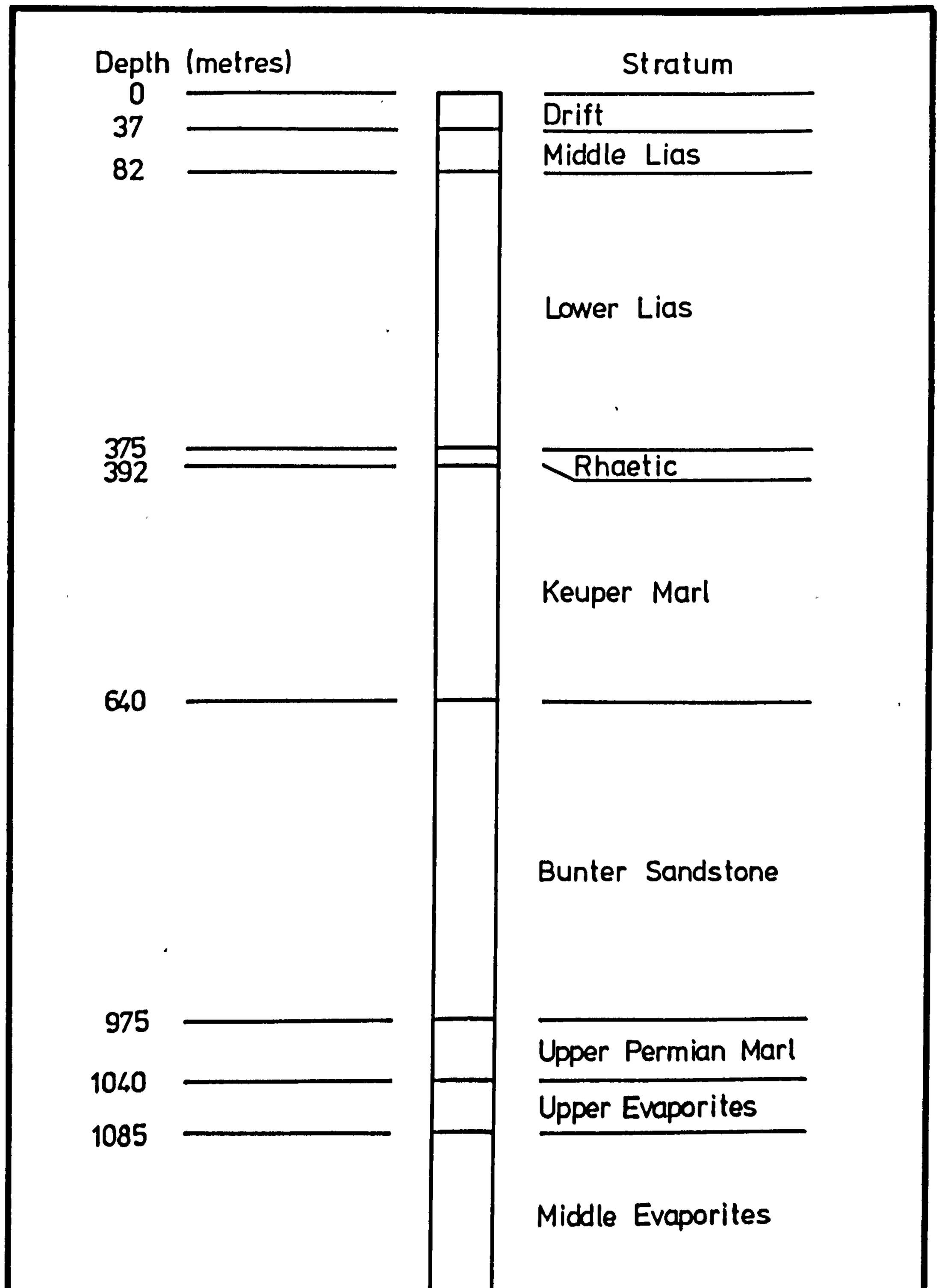

FIG. 1-3 STRATA SEQUENCE (from Borehole S20)

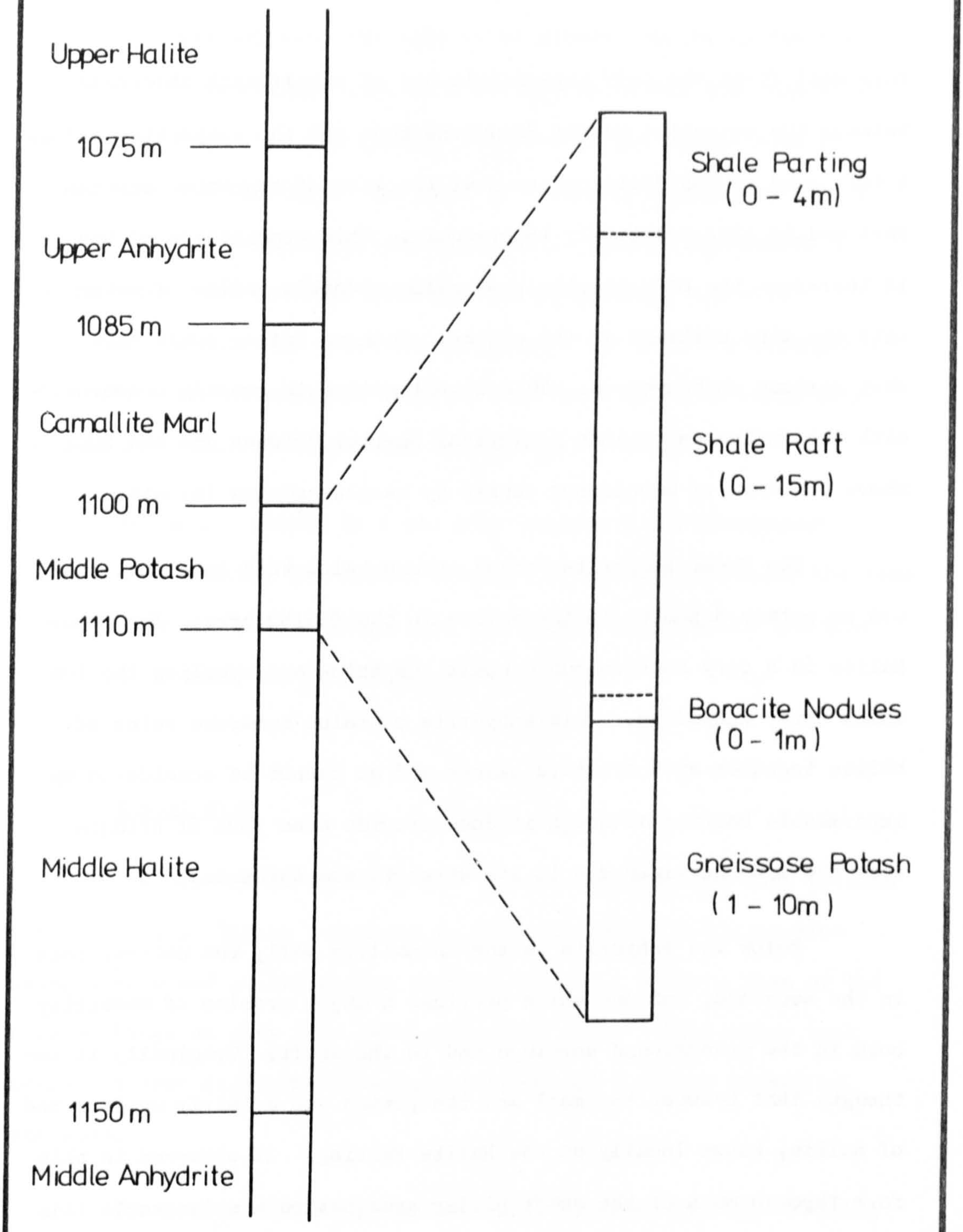

FIG. 1-4 NEAR - SEAM STRATA SEQUENCE

This marl forms the cnly impermeable bed of significant thickness between the saturated Bunter Sandstone beds and the evaporites below. A thin band of anhydrite occurs near the base of the Upper Permian Marl and is also relatively impermeable. This combination of beds is therefore the main barrier preventing possible inflow of water into the mine workings in the potash. Such an inflow could have very serious consequences. This investigation is greatly concerned with the influence on this geological barrier between 75m and 200m above the seam of subsidence caused by various mining layouts.

The Upper Evaporite series occurs below this level but there are no potash deposits in the series in the Boulby area. The Upper Halite is a very homogeneous deposit 35m thick and overlies the 10m thick Upper Anhydrite. This anhydrite contains numerous veins of halite together with fracture planes and so cannot be considered an impermeable barrier although it does provide some form of bridging over the mine workings due to its strength and thickness.

Below the anhydrite is the Carnallite Marl, the weakest rock in the sequence, and one which provides a major problem of stability both in the underground workings and in the shaft. Originally it was thought that between the marl and the potash was a fairly uniform bed of halite, known locally as the Halite Parting. It occurred in this form through much of the shaft pillar area but on a wider scale this bed, together with the potash seam, has been redefined as shown in Fig. 1-4. The Gneissose potash forms what is now known as primary ore while the remainder of various shale types is known as secondary ore, due to the frequently high grade sylvite content. The shale also contains varying amounts of halite, anhydrite and boracite (9).

The primary ore, referred to as potash, varies in thickness from 0 to 10m averaging about 3m while the secondary ore (shale) can be anything from 0 to 16m thick. The base of the potash seam is fairly flat but the top of the seam is extremely undulating making control of roof conditions very difficult. This is aggravated by the fact that the shale is interspersed by randomly oriented slickenside planes and veins of sylvinite. The very low strength of the shale material combined with the weak marl above it cause very serious roof control conditions throughout the mine.

Below the potash is a far more competent and homogenous thick bed of halite, the Middle Halite. It extends 40m below the seam and overlies the Middle Anhydrite, the Magnesian Limestone and then the third or Lower series of evaporites.

1.2 Boulby Mine

The mine is serviced by two 5.5m diameter shafts sunk between 1969 and 1974. Mining commenced in 1973 in the shaft pillar area using a room and pillar mining system. Fig. 1-5 shows a plan of the mine workings as they have developed up to 1977. Sites where rock mechanics investigations have been carried out are also marked on the plan.

The method of mining was initially by undercutting, drilling and blasting, with mucking out to a conveyor system by means of Eimco load-haul-dump vehicles (10). Due to the presence of various hydrocarbon gases in the secondary ore all equipment and explosives used underground have to be approved as intrinsically safe. Late in

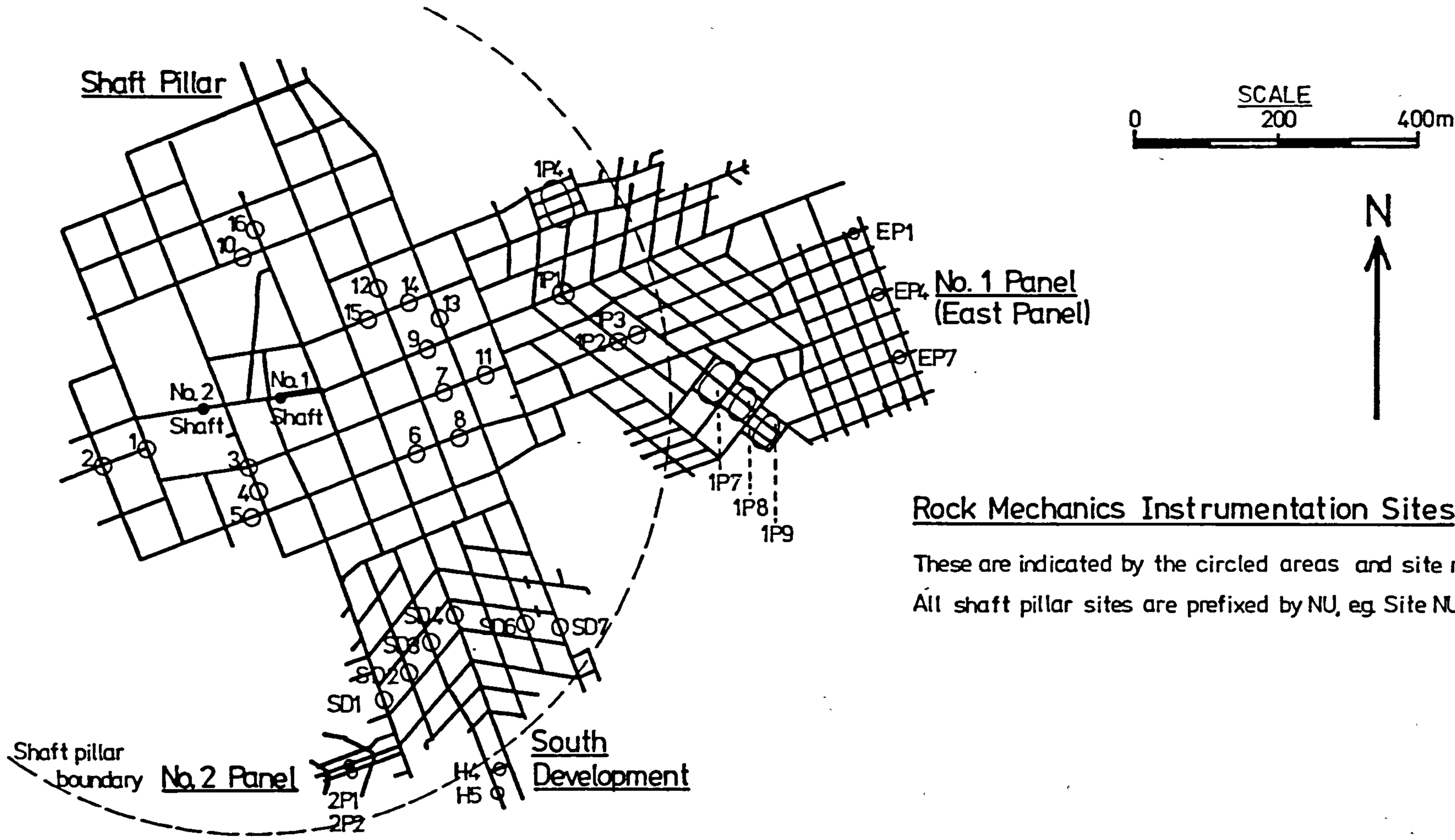

Rock Mechanics Instrumentation Sites

These are indicated by the circled areas and site numbers

All shaft pillar sites are prefixed by NU, eg. Site NU06.

FIG. 1-5 PLAN OF MINE WORKINGS (EARLY 1977)

1976 two continuous mining machines were introduced. A Marietta full face, two rotor borer and a Jeffreys Heliminer. A second Heliminer is now in operation and each of the continuous machines are using shuttle cars for ore haulage to the conveyors. Roadways are excavated with a rectangular profile (with the exception of the Marietta which mines an ellipse profile) and the mining height is currently between 3m and 3.5m. Roadway widths vary between 4.5m and 8m.

1.3 Rock Mechanics Research Project

The Department of Mining Engineering at the University of Newcastle upon Tyne has been involved with the rock mechanics investigations for Boulby Mine from the initial exploration stages up to the present time. The initial work consisted of fundamental research into the mechanical and rheological properties of rock core obtained from exploration boreholes. On the basis of these properties, interpretations were made related to design constraints for the underground excavations including both shaft and mine excavations. These were followed by laboratory modelling and in-situ measurements which have continued to monitor ground conditions in the mine and provide more realistic estimates for the parameters associated with the mine design.

1.3.1 Project Objectives

The initial objectives of the research project have been broadened considerably as specific problems have arisen during the development and operational phases of the mine. However, the basic

terms of reference remain the same as those defined by Patchet (7) when he stated that the project should define:

"1. The specific extraction ratio which yields the optimum underground and surface conditions and the likelihood of achieving the minimum economic extraction ratio.

2. The underground stability problems likely to be encountered.

3. Which strata are likely to prove troublesome to short duration operations such as sinking shafts or to the long term life of the mine such as potential water inflows.

4. The best mine structure design parameters with regard to long term underground stability, surface subsidence, machinery operating requirements and extraction ratio."

1.3.2 Previous Research

The laboratory work was initiated by Buzdar (11) and carried on by Patchet (7). Patchet studied the mechanical properties and strengths of the complete geological succession at Boulby. He initiated uniaxial creep testing of the near-seam strata and also Cheshire rocksalt which was used as a substitute material for potash in early model testing in the laboratory. This work consisted of a series of model pillar creep tests in 1000 tonne creep rigs under loading conditions anticipated in the mine. A 2000 tonne creep rig was also built for further physical modelling of mine excavations.

One of the basic conclusions from Patchet's work was that for long term stability of pillared mine workings it was essential for a triaxially confined core of rock to exist within the pillar and remain confined, even though slightly diminished with time. It was found that for such a situation to exist under an assumed vertical virgin stress of up to -27.6 MN/m^2 the width:height ratio of the pillar should not fall below 10:1.

Cook (8) carried on the research project with particular emphasis being placed on the stability of the shaft excavations through the Upper Evaporite strata. Cook extended the laboratory testing program to triaxial creep testing in order to analyse the rheological properties of the evaporites. He modelled the shaft excavation in halite in the laboratory and then instrumented the No. 2 shaft as it was sunk through the Upper Halite. On the basis of his laboratory testing a 0.46m gap was left between the rock and the concrete shaft lining through the Upper Halite to allow for time-dependent closure of the excavation. This has proved quite adequate and the closure is still being monitored. Cook also initiated the installation of the first rock mechanics sites in the mine workings for monitoring roadway closures and strata deformations.

The problem of roof support by rock bolting has been investigated by Dunham (12), Tonkin (13) and Wiggett (9). Wiggett also carried out laboratory testing to define the mechanical properties of the secondary ore encountered underground.

1.3.3 Current Research

The program of research which forms the subject matter of this investigation has been an attempt to relate large quantities of underground data to some form of model which can be used as a basis for mine design. The other data for such a model have come from further laboratory testing of samples from the mine including model pillars of potash; comparative theoretical analyses of panel layouts; and a study of other potash mining operations.

A considerable amount of time has been spent on developing suitable techniques for numerical modelling of the underground layouts by both face element and finite element methods. The analysis of data recorded from the underground instrumentation has also required the development of a series of computer data processing techniques together with a number of peripheral programs.

The laboratory work has not been a major section of the research for two reasons. Firstly, the ready access to the mine itself has enabled a great deal of effort to be put into underground monitoring and experimentation rather than physical modelling in the laboratory. Secondly, it has been very difficult to obtain suitable specimens of rock from the mine for testing work. This has ruled out any large scale creep testing program which had been envisaged originally. Consequently, it has not been possible to establish a sophisticated numerical model for mine design based on the rheological properties of the evaporites.

The in-situ investigations have proved to be the major source of data. This has led to the development of an empirical model, based

on actual experimentation and measurement in the mine. Initial shaft pillar instrumentation sites were set up to relate room and pillar stability to geological variation. Later sites involved areas of experimental pillar dimensions and roadway configurations.

An overcoring operation was carried out to measure the in-situ virgin stress field. All of these results have been used in conjunction with information from the theoretical and laboratory work in order to define suitable panel geometries. The basic criteria for these geometries have already been outlined, i.e. room and pillar stability together with minimal subsidence-induced effects at the base of the Bunter Sandstone and on the surface. Some preliminary surface subsidence data has been analysed and correlated with the geometry of the mine workings and the design parameters.

CHAPTER 2

COMPUTER TECHNIQUES FOR THEORETICAL AND DATA ANALYSES

2. COMPUTER TECHNIQUES FOR THEORETICAL AND DATA ANALYSES

There have been two areas of work on this project which have required computer facilities and techniques of analysis. The first of these concerns numerical modelling of mining layouts and excavations. The second area is that of data processing from the vast number of measuring stations underground as well as laboratory data analysis. Each of these areas has required either modifications of existing computer programs or development of new programs to handle the specific problems concerned. Consequently, a considerable amount of time has been spent on computing throughout the investigations carrying out initial program development as well as continued modification of programs for both the numerical modelling and data analysis. All computer programs used are in Fortran language and are compatible with IBM Fortran. They have all been run on IBM 360/168 and 370 machines.

Many of the techniques and programs described in this chapter have been developed during the course of the project and so some of the initial work has not been investigated fully by programs developed at a later stage.

2.1 Numerical Modelling

This work has been concerned with modelling complete panel layouts as well as individual roadway excavations. The ideal model for simulating this type of mining operation would be a numerical technique incorporating time-dependent properties of all the strata concerned. There are such programs available, generally finite element

programs, but only very few of them are general purpcse programs applicable to mining situations and these are expensive and difficult to obtain. Even with a suitable program it is still essential to have a knowledge of the particular rheological behaviour of the strata to be analysed. This knowledge cannot be obtained from measurements underground since none of the variables concerned - stress, strain, time - are controllable. It is necessary to conduct a major laboratory testing program where either the stress conditions, or the strain-time relationship is controlled and known.

Due to reasons mentioned in Chapter 1 such a testing program was not possible during this investigation and so it was decided to develop an 'empirical' model based on the 'gross' behaviour of various geometries of rock and excavations in the mine. Data from this source has been abundant from numerous variations of geology and geometry. However, this data has all been from within the seam or on the surface whereas one of the primary objectives of this project concerns the above-seam strata behaviour. Therefore it has still been necessary to supplement the mine measurements with some basic theoretical work even if it lacks the sophistication of the ideal rheological model.

It was decided that an elastic model could be used to provide a series of comparisons of initial conditions for various geometries of excavation. Such a model has limitations in that the magnitudes of deformations and strains due to creep are in excess of elastic magnitudes and also time-dependent. However, it was felt that an elastic solution could approximate initial stress conditions and indicate areas of potential failure on a comparative basis, e.g. one layout geometry is more likely to produce critical lateral strains above the seam than

another. The effect of creep is to cause migration away from and relaxation of stress concentrations around the excavation. This fact must be borne in mind when interpreting results from this model. Later work on the high extraction panels took account of the large creep strains within the seam by modifying the boundary conditions of the elastic model to incorporate pillar yield. Similar models for both coal and salt have provided good correlation with underground measurements by assuming that yield and creep is confined to pillars while the surrounding strata is modelled elastically (14, 15).

2.1.1 Suitable Elastic Models

A number of numerical elastic models were considered for use with this problem. The first model was MINSIM (Mining Simulator), developed by the South African Chamber of Mines for the deep level gold mining industry (16). This program was available and had been run successfully for a number of problems.

One of the great advantages of MINSIM was the ease of simulating advancing headings and observing changes in stress conditions and closures. There were two major drawbacks however. The first was that the plane of analysis consisted of a square block containing a discrete number of squares which represented the mining layout (60 by 60). Beyond the block it was assumed that no mining had taken place. Therefore if a detailed analysis of a large pillared panel was required the simulation was unrealistic since the panel was surrounded by inadequate boundary conditions on all four sides. It was not possible to simulate a long panel in any great detail. The second and more significant

drawback was that MINSIM was developed for hard rock mining and so it made the assumption that the seam material was incompressible. This is obviously not the case in softer material such as coal or potash. On this basis it was considered unsuitable for analysis of the Boulby situation.

A second method considered was developed by Crouch & Fairhurst (14) for predicting coal mine bumps in the United States. Basically, it consisted of a numerical analysis using harmonic, or potential functions - a digital equivalent to the electrical resistance analogue developed in South Africa and applied to high compressibility coal seams (17, 18). Although suffering from the same drawbacks as MINSIM due to the discrete block size of the plane of analysis, this method, referred to as MINBUMP, had one significant advantage. This was that it incorporated up to four different yield criteria for the seam material other than the purely elastic condition. Fig. 2-1 illustrates the five possible stress-strain relationships. Each criterion was defined

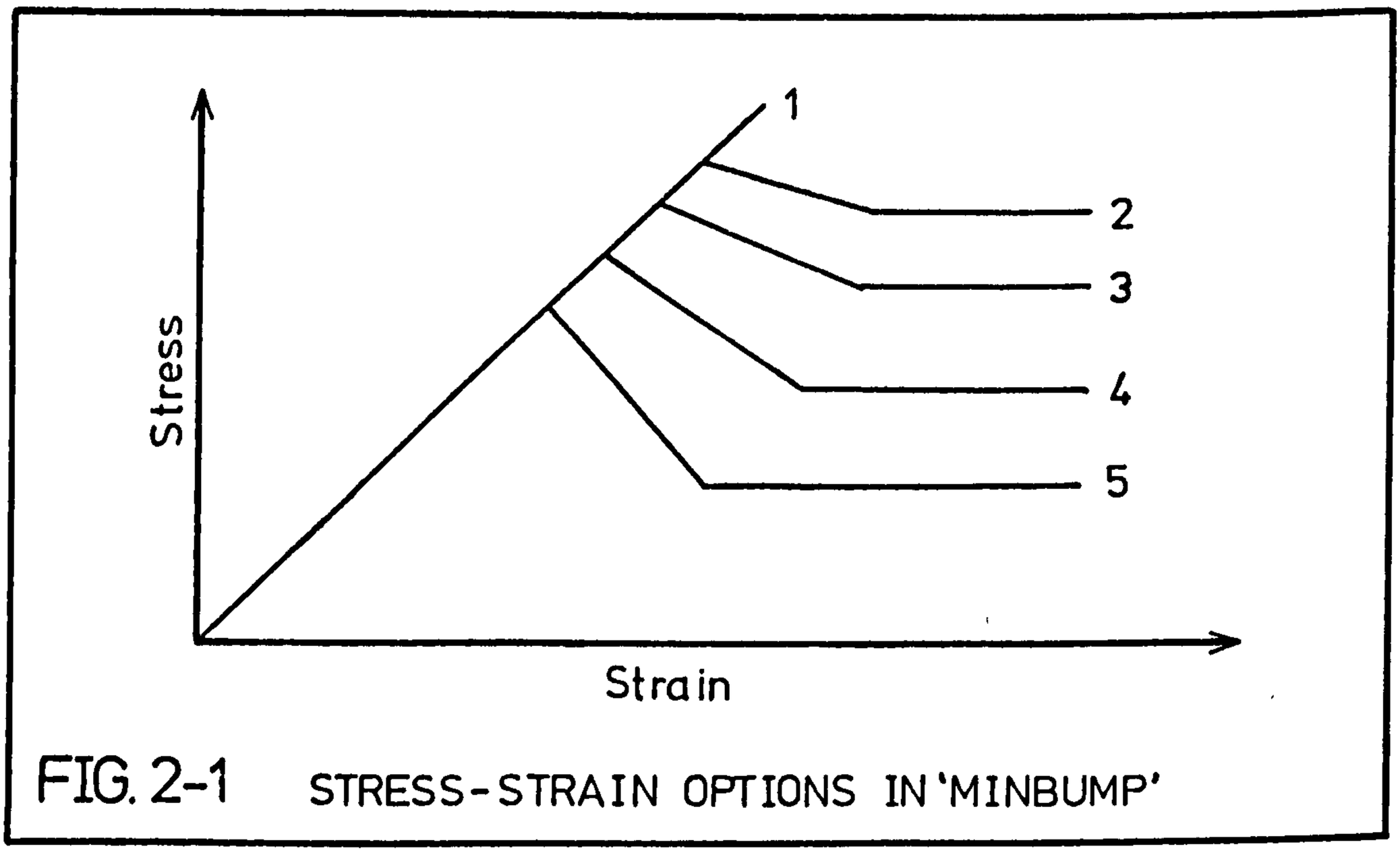

FIG. 2-1 STRESS-STRAIN OPTIONS IN 'MINBUMP'

by an elastic modulus, peak strength, peak strain, residual strength and residual strain beyond which plastic yield occurred. The different yield criteria could be assigned to the squares of the block on the basis of distance from the excavation, representing different residual stiffnesses within the seam. This provided a useful model for analysis of seam conditions but there was no facility for analysing the influence of the excavations above the seam horizon. The main reason that MINBUMP was nct used even for seam analyses was that the program as listed in the report (14) contained a number of programming errors. Even when the simple errors were debugged the program would not run satisfactorily and so it was abandoned.

2.1.2 Comparison of Face Element and Finite Element Techniques

The finite element technique has been widely used in many fields of engineering including rock mechanics. On the other hand the face element technique is a more recent development of the potential function theory applied to rock mechanics in the first instance by Salamon (20). There have been various programs written based on this theory and the face element method is the name given by Thompson (19) to his technique for two and three dimensional solutions of elastostatic problems.

Both techniques have numerous applications in rock mechanics in both underground and surface simulation. One of the basic differences is in the modelling of the problem using a mesh of discrete ncdal points which are connected to form elements. The finite element nethcd requires that the complete problem be modelled by a mesh of

elements for which a stiffness matrix is formed based on individual element stiffnesses. Therefore individual elements may be assigned different mechanical properties enabling composite materials to be modelled. The face element method purely defines the boundary of the system with a mesh of elements. Within that boundary the material is assumed to be homogenous, isotropic and in the case of Thompson's programs, linearly elastic. This obviously restricts the use of the method since only one type of material can be modelled within the boundary but there are great advantages in this.

The differences between the two techniques and their inherent advantages and disadvantages can be summarized as follows:

i) The finite element method offers far more versatility in that it can model a system made up of numerous different materials. The face element method assumes only one set of material properties within the boundary of elements although boundary conditions can be modified to represent interaction between different materials.

ii) The mesh required for the face element method is much smaller and simpler to prepare than that for the finite element method. This represents great time savings and also means greatly reduced requirements of computer storage enabling far more complicated geometries to be analysed using the face element method.

iii) The face element method provides a more precise solution away from the boundary elements. The finite element solution accuracy is very dependent on mesh geometry and

represents an approximation based on the nodal density.

iv) The face element method does not require a finite boundary within the material but assumes an infinite continuum away from the excavation. Therefore it does not lose accuracy through boundary condition approximations within the material.

Both of these methods have particular applications for which they are best suited. The two programs available initially give elastic solutions but can be modified to enable non-linear and time-dependent properties to be taken into account. However, it must be realised that with either method the solution obtained is only as accurate as the material properties and boundary conditions used. For this reason there is no point in using complex solutions if the realistic boundary conditions are not known or cannot be modelled.

2.1.3 FEMITPLT - 2D Finite Element Program

This program is a two-dimensional, isotropic, elastic, finite element solution based on plane strain, i.e. the stress perpendicular to the plane of the mesh is non-zero but the strain in that direction is considered as zero. The basic method of solution can be summarized by the following equations.

i) The displacement function (f) is a vector defined by

$$(f) = [N] (\delta)^e \qquad (2.1)$$

for each element, e, where (δ) represents the displacements of the element nodes. In this program only triangular elements are permitted.

$[N]$ is a matrix of functions defining the nodal positions, known as shape functions.

ii) Strains at any point within the element are defined by the matrix $[B]$ such that

$$(\varepsilon) = [B](\delta)^e \qquad (2.2)$$

iii) These strains are now related to stresses using the basic elastic constitutive relationship,

$$(\sigma) = [D]^e\left((\varepsilon) - (\varepsilon_o)\right) + (\sigma_o) \qquad (2.3)$$

where (ε_o) and (σ_o) refer to initial strains and initial residual stresses and the components of $[D]$ for plane strain are

$$[D] = \frac{E(1-\nu)}{(1+\nu)(1-2\nu)}\begin{bmatrix} 1 & \nu/(1-\nu) & 0 \\ \nu/(1-\nu) & 1 & 0 \\ 0 & 0 & \frac{(1-2\nu)}{2(1-\nu)} \end{bmatrix} \qquad (2.4)$$

iv) The stiffness matrix $[k]^e$ is now defined by the relationship,

$$[k]^e = \int [B]^T [D] [B] \, d(\text{vol.}) \qquad (2.5)$$

using the principle of virtual work where the element represents a volume of unit thickness.

v) Nodal forces developed by the element are therefore defined by this stiffness matrix as

$$(F)^e = [k](\delta)^e \qquad (2.6)$$

The initial strains and stresses can also be defined similarly.

vi) System force equilibrium must now be established by normal structural means of analysis. The overall stiffness matrix for the system $[K]$ is made up of a simple summation of the individual elemental stiffness $[k]^e$. Therefore the equilibrium of forces for the entire system is defined as,

$$(R) = [K](\delta) + (F)_{\varepsilon_o} + (F)_{\sigma_o} \qquad (2.7)$$

where (R) represents all the external nodal forces.

The program FEMITPLT, is based on the subroutines developed by Zienkiewicz (21). The basic solution of simultaneous equations is carried out using the Gauss-Seidel iterative process (21) which gives a progressive approximation to the solution of equations. The stiffness matrix is formed in a compacted state having removed all zero terms and a pointer matrix is used to indicate the correct location of each term of the stiffness matrix. This system results in a great saving of storage space and, due to the reduced bandwidth, a saving in time also.

The program consists of a main control program plus 12 subroutines many of which are additional to or have been modified from the original Zienkiewicz subroutines (21). In its present form FEMITPLT has a mesh capacity of 1100 elements and 600 nodes. The maximum compacted semi-bandwidth is 45 and up to 50 different material types can be incorporated. The main modifications to the program have concerned loading conditions and graphical output. The loading options have been designed specifically for mining applications although there is one option for which no gravitational forces are applied. The gravitational or virgin stress field is calculated in

subroutine VIRESS. The stress at each element centroid is calculated in X and Y directions due to the initial stress conditions prescribed.

Subroutine RELOAD then calculates the load normal to each side of each element due to the virgin stresses. This virgin load is exerted equally and opposite across each element boundary hence equilibrium exists. Once an excavation is created the virgin load on one side of the boundary is removed resulting in the opposite load, now termed a 'relief' load, causing displacement towards the excavation. Fig. 2-2 illustrates this concept. By nominating which

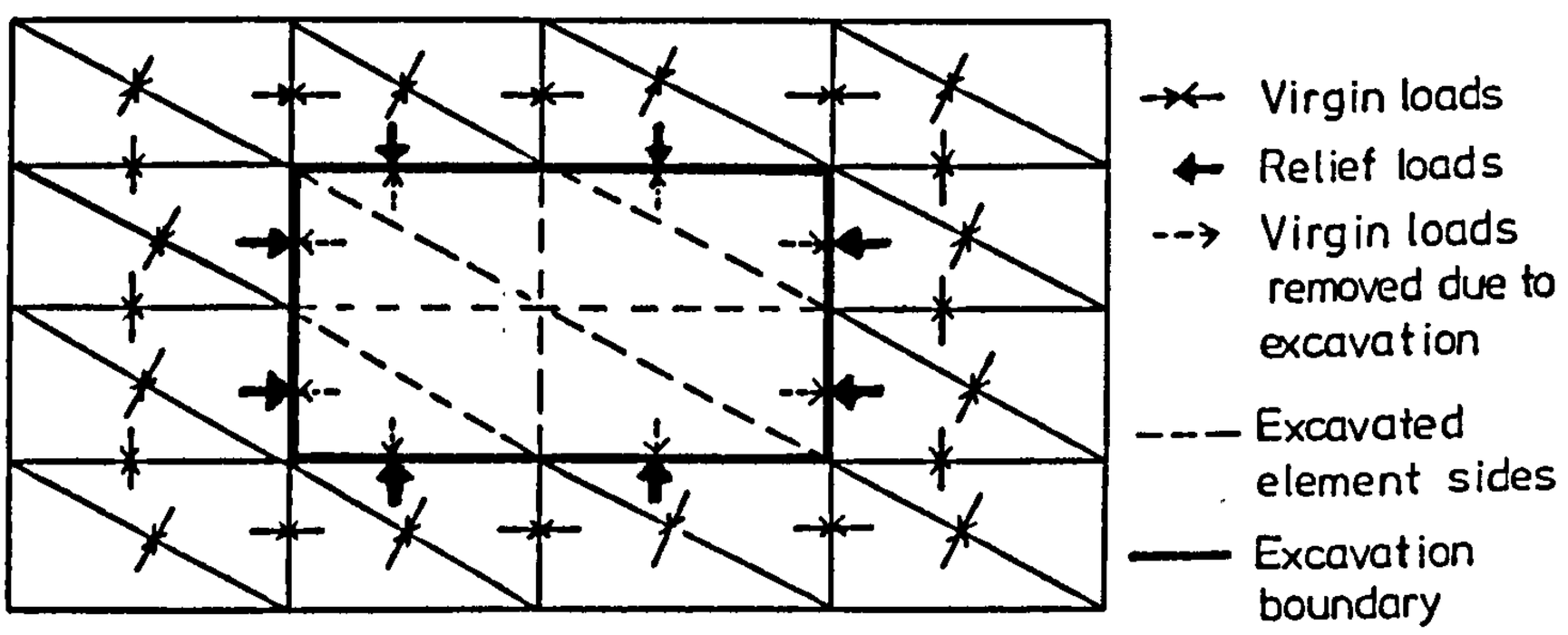

FIG. 2-2 VIRGIN AND RELIEF LOADS

element forms the excavation boundary the program automatically generates these relief loads as X and Y components at each of the two nodes on the boundary.

Other loading options include virgin stresses with relief loads applied manually; or virgin stresses with automatic relief loads generated and additional loads applied manually (e.g. pre-tensioned rock bolts or any other such load exerted by a support

system).

There are four plotting subroutines included in FEMITPLT. The first collects and organises the stress and displacement results, DISPL plots displacements as vectors from each node position within the mesh boundary while STRECN and STRETN plot the principal compressive and tensile stresses as vectors through the element centroid positions.

In order to check the accuracy of FEMITPLT a mesh was drawn up as shown in Fig. 2-3 to simulate the problem of a circular hole in a homogenous elastic plate. The exact solution to this problem was found by Kirsch in 1898. The equations derived by Kirsch are as follows (in polar co-ordinates, r and θ).

$$\sigma_r = \frac{1}{2}(\sigma_x+\sigma_y)(1-R^2) + \frac{1}{2}(\sigma_x-\sigma_y)(1+3R^4-4R^2)\cos 2\theta \qquad (2.8)$$

$$\sigma_\theta = \frac{1}{2}(\sigma_x+\sigma_y)(1+R^2) - \frac{1}{2}(\sigma_x-\sigma_y)(1+3R^4)\cos 2\theta \qquad (2.9)$$

$$\tau_{r\theta} = -\frac{1}{2}(\sigma_x-\sigma_y)(1-3R^4+2R^2)\sin 2\theta \qquad (2.10)$$

where σ_r is the radial stress

σ_θ is the tangential stress

$\tau_{r\theta}$ is the shear stress

σ_x, σ_y are the stresses applied to the plate boundary

R is the ratio of hole radius to the radial distance to the point (r, θ).

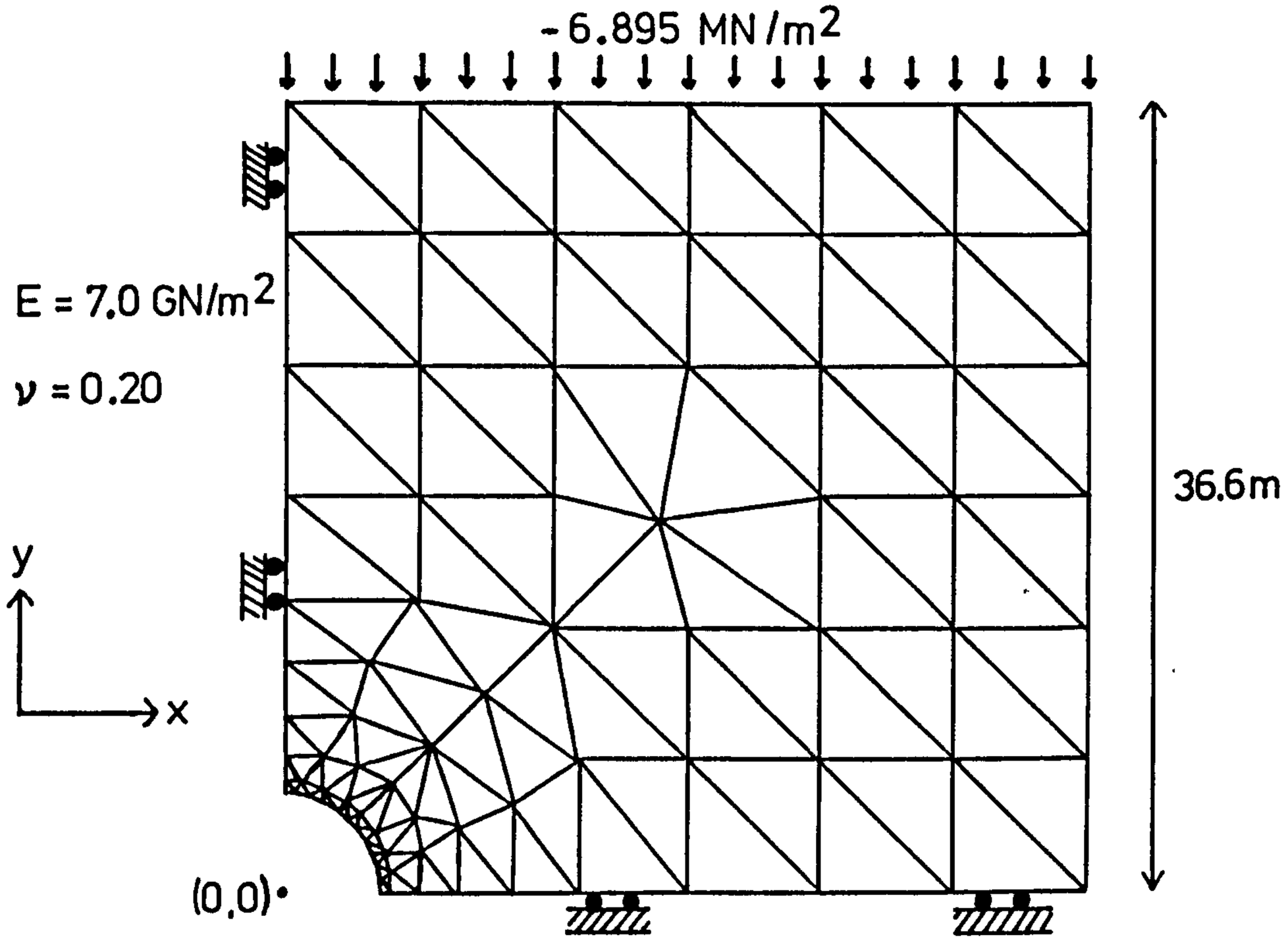

FIG. 2-3 MESH USED FOR 'KIRSCH' PROBLEM

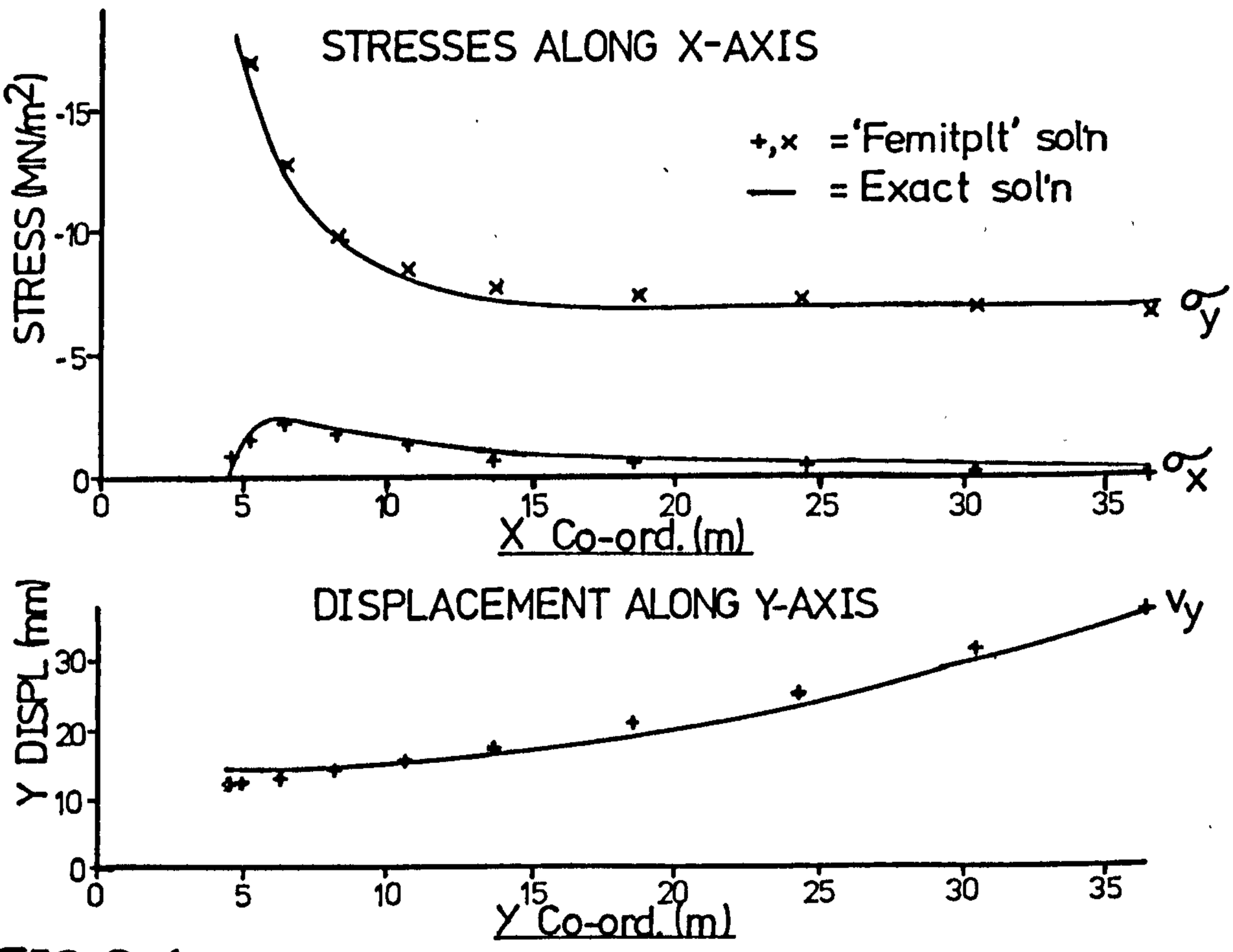

FIG. 2-4 'KIRSCH' PROBLEM RESULTS

For plane strain the displacement equations become

$$u_r = C_1\left[\tfrac{1}{2}(\sigma_x+\sigma_y)(r+Ra) + \tfrac{1}{2}(\sigma_x-\sigma_y)(r-R^3a+4Ra)(\cos 2\theta)\right]$$
$$-C_2\left[\tfrac{1}{2}(\sigma_x+\sigma_y)(r-Ra) - \tfrac{1}{2}(\sigma_x-\sigma_y)(r-R^3a)(\cos 2\theta)\right] \qquad (2.11)$$

$$v_\theta = C_1\left[-\tfrac{1}{2}(\sigma_x-\sigma_y)(r+2Ra+R^3a)(\sin 2\theta)\right]$$
$$-C_2\left[\tfrac{1}{2}(\sigma_x-\sigma_y)(r-2Ra+R^3a)(\sin 2\theta)\right] \qquad (2.12)$$

where u_r is the radial displacement

v_θ is the tangential displacement

a is the hole radius

and $$C_1 = (1-\nu^2)/E \qquad (2.13)$$

$$C_2 = (\nu(1+\nu))/E \qquad (2.14)$$

where ν is Poisson's Ratio

E is Young's Modulus

A program called KIRSCH was written to use the mesh data from the FEMITPLT mesh to calculate the exact solution of stresses and displacements. These values were converted in the program to the same orthogonal co-ordinate system with stresses calculated at element centroids and nodes, and displacements at nodes. In order to compare the FEMITPLT stress solution (resolved for element centroids only) with the KIRSCH solution for the X and Y axes of the problem the method reccmmended by Zienkiewicz (21) was used, i.e. averaging the stresses from each element which connects to a node and applying the average stress to that node position.

Fig. 2-4 shows the various plots of stresses and displacements along the two axes obtained from the exact (KIRSCH) solution and the FEMITPLT solution. In general, the correlation is very good. The main deviation from the exact solution appears to be caused by the courseness of the finite element mesh and its limited extent. This is apparent from the deviation of the two solutions at the mesh boundary where the boundary conditions imposed on the FEMITPLT mesh have altered the solution. However, apart from the restrictions of the mesh the correlation of the two solutions appears to be quite acceptable.

Program listings and users manual for FEMITPLT and KIRSCH are contained in an unpublished report (22). The report also contains details of a simplified version of FEMITPLT and a mesh plotting program, MESHPLOT.

2.1.4 Face Element Method

The fundamental equation describing displacements in terms of potential functions ϕ_i (either two or three depending on the dimensions of the boundary) which is used in face element theory is,

$$u_j = 2(1-\nu)\frac{\partial \phi_j}{\partial x_3} - (1-2\nu)\frac{\partial \phi_3}{\partial x_j} + (1-2\nu)\partial_{j3}\frac{\partial \phi_k}{\partial x_k} - x_3\frac{\partial^2 \phi_k}{\partial x_j \partial x_k} \quad (2.15)$$

with summation implied over k and $\nabla^2 \phi_j = 0$

The system to be considered is divided into a set of either line or area elements around its boundary each of which is considered to have a set of pctential functions. These element potentials are a function

of the distance between the element centroid and some point within the body of the system. For a two dimensional problem the element potential is proportional to log r where r is the distance referred to above, whereas in three dimensions the element potential is proportional to 1/r. There is a unique constant of proportionality C_j^k for each element such that the element potentials, $\psi_j^k(r)$ are defined for the element k as,

$$\psi_j^k(r) = C_j^k \log r \qquad (j = 1, 2) \qquad (2.16)$$

for two dimensions, and

$$\psi_j^k(r) = C_j^k(1/r) \qquad (j = 1, 2, 3) \qquad (2.17)$$

for three dimensions.

The individual element potentials are then summed to obtain the system potential functions ϕ_j with the constants C_j^k as the only unknowns. The prescribed boundary conditions are then equated to those induced by the potential functions ϕ_j and this enables a set of simultaneous equations in C_j^k to be solved. The complete stress and displacement conditions around the boundary can now be determined for each element and for any point within the body of the system defined by a bench mark set of co-ordinates.

Thompson (19) carried out a number of checks on the validity of face element solutions obtained using his two and three dimensional programs (FACEL2D and FACEL3D). These correlated well with known solutions, provided that certain constraints on element sizes and bench mark positions were observed.

2.1.5 Numerical Model for Long Panels

The problem of modelling a panel of rectangular pillars where the panel length could be considered infinite relative to the width presented a number of problems. It was a three dimensional problem but obviously beyond the capabilities of a finite element program due to the very large number of elements required in the mesh for such a simulation. Deist and Oravecz (23) proposed a method of superpcsition of orthogonal, two dimensional, finite element solutions across and along a panel layout. This produced a solution to the problem but appeared to be a very tedious way of solving it.

Salamon (24) devised a method using pctential theory and a two dimensional finite element solution. Fig. 2-5 shows the panel layout considered. The total load bearing width of the panel is $4c_1$ made up of a row of four pillars, symmetrical about the panel centre.

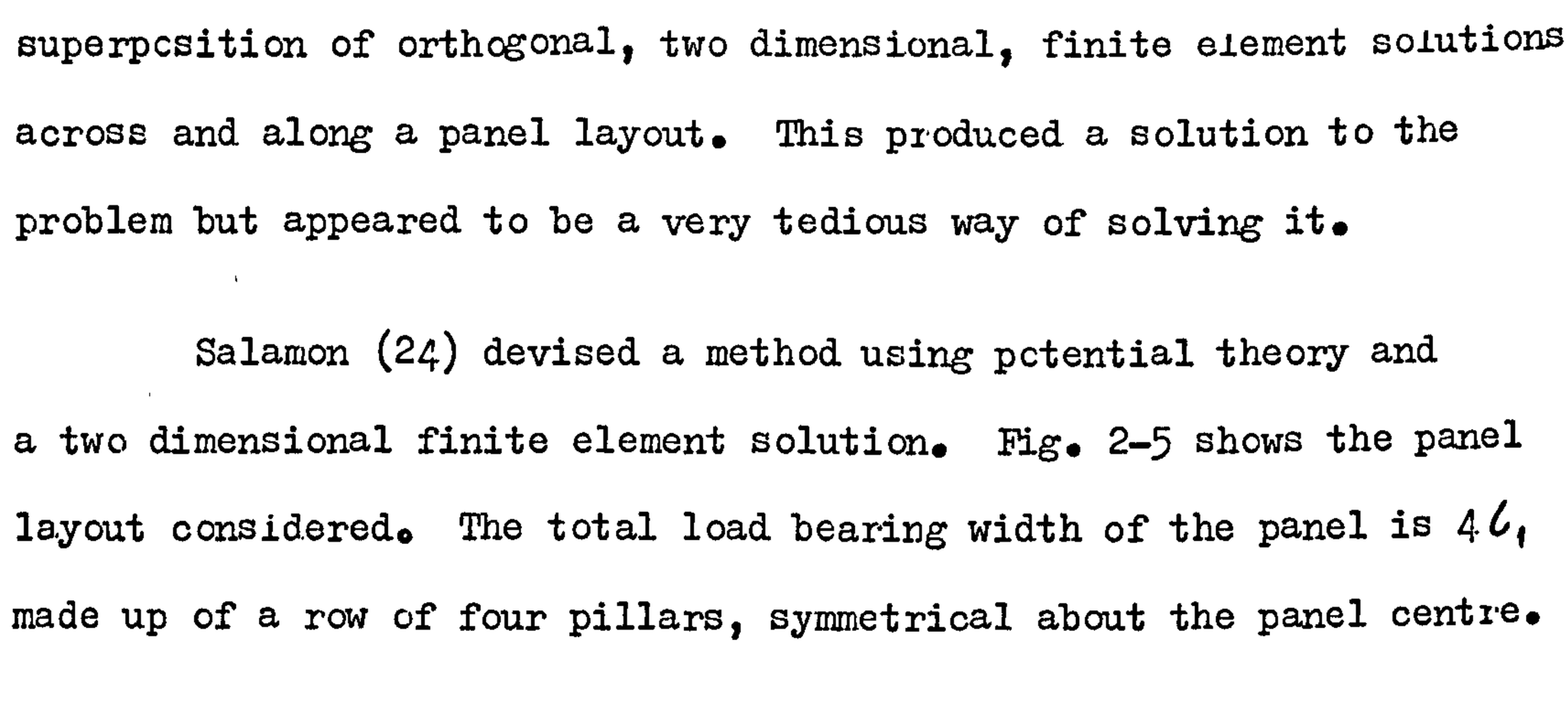

FIG. 2-5 ROOM AND PILLAR LAYOUT WITH BARRIERS

He defined the repetitive stress distribution in the y direction over a width of $2c_1$ by a Fourier series,

$$p(y) = \sum_{m=0}^{\infty} a_m \cos(\alpha_m y) \qquad (2.18)$$

where

$$\alpha_m = \frac{m\pi}{L_2} \quad , \qquad (2.19)$$

$$a_0 = \frac{P}{4 \ell_1 L_2} \quad , \quad a_m = \frac{P \sin m\mu_2}{2 m \pi \ell_1 \ell_2} \qquad (2.20)$$

and

$$\mu_1 = \frac{\pi \ell_1}{L_2} \quad , \quad \mu_2 = \frac{\pi \ell_2}{L_2} \qquad (2.21)$$

where P is the total compressive load on each row cf four pillars across the panel width. The term a_0 in (2.20) represents the intensity of load across the width $2\ell_1$ if $p(y)$ were distributed normally. Salamon establishes the stress distribution due to this component by a plane strain finite element solution since it is independent of the y co-ordinate.

An alternative to this method, avoiding the Fourier series solution and using both two dimensional and three dimensional face element methods, was developed by the author in conjunction with Thompson (19).

Fig. 2-6 shows how the panel and barriers to be considered are subdivided into a plane of elements. The induced normal stress distribution which would exist over such a panel is represented by

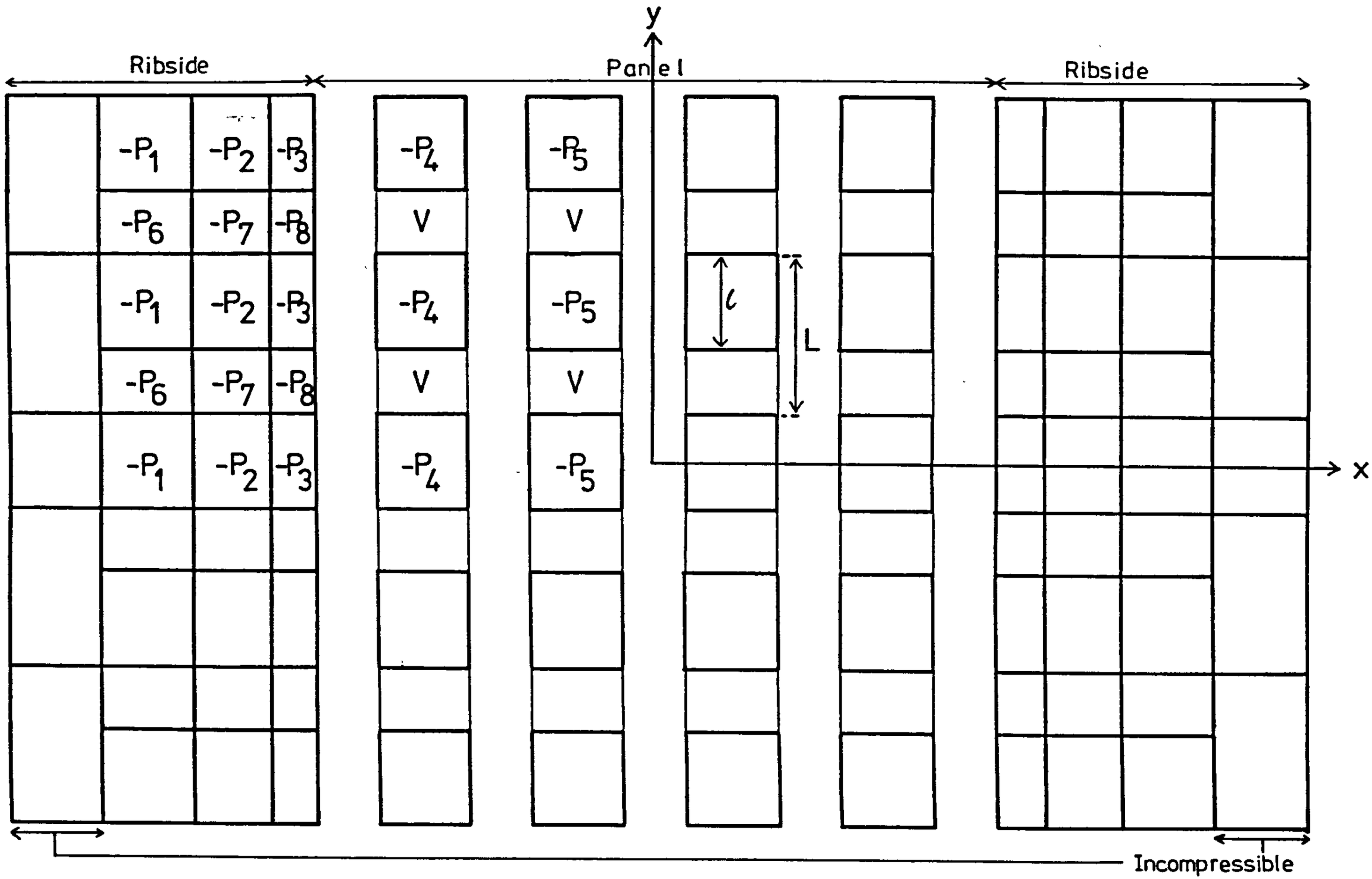

FIG. 2-6 3D FACE ELEMENT MESH FOR PANEL LAYOUT

the unknown compressive stresses, $-P_1$ to $-P_8$ (symmetrical in four quadrants) and the relief stresses, V, equal and opposite to the assumed virgin stress conditions. The outermost column of elements within each barrier is assumed to be incompressible and so the elements are specified with zero displacement conditions.

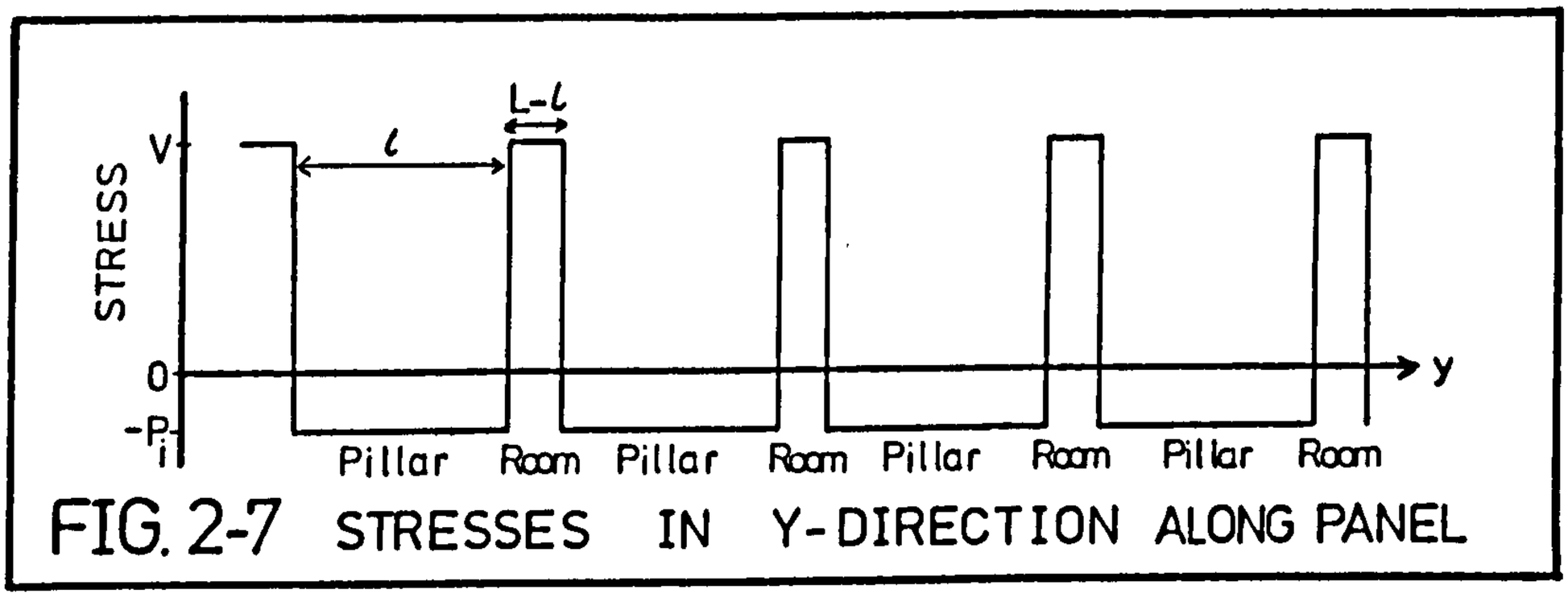

FIG. 2-7 STRESSES IN Y-DIRECTION ALONG PANEL

Fig. 2-7 shows the induced stress distribution in the y direction which continues indefinitely along the line of the panel for any particular column of pillars and rooms, i.e. This train of stresses can be replaced by two statically equivalent trains of stress shown in Fig. 2-8.

The pillar stresses are equivalent in terms of load equilibrium to a mean stress of $(-P_i \frac{l}{L})$ with a variation of $(P_i \frac{l}{L})$ over the rooms and $(-P_i(1 - \frac{l}{L}))$ over the pillars (Fig. 2-8(a)). The room stresses are equivalent to a mean stress of $(V(1 - \frac{l}{L}))$ plus balancing stresses of $(V\frac{l}{L})$ over the rooms and $(-V(1 - \frac{l}{L}))$ over the pillars (Fig. 2-8(b)).

By recombining these two stress trains, an overall mean $p^i(y)$ is obtained which is constant in the y direction.

$$p^i(y)_{mean} = -P_i \frac{l}{L} + V(1 - \frac{l}{L}) \qquad (2.22)$$

with a variation over pillars and rooms of

$$p^i(y)_{pillar} = -P_i(1 - \frac{l}{L}) - V(1 - \frac{l}{L}) \qquad (2.23)$$

and $$p^i(y)_{room} = P_i\frac{l}{L} + V\frac{l}{L} \qquad (2.24)$$

On the basis of these three equations, a solution can be obtained by applying the principle of St Venant. This states that if a system of forces acting on one portion of the boundary is replaced by a statically equivalent system of forces on the same portion of the boundary then the stresses in the region removed from the portion concerned remain the same. Consider the forces due to the stress variations described by equations (2.23) and (2.24). Since the statically equivalent set of forces equals zero over each pair of pillars and rooms then the influence of such a loading system is extremely localised.

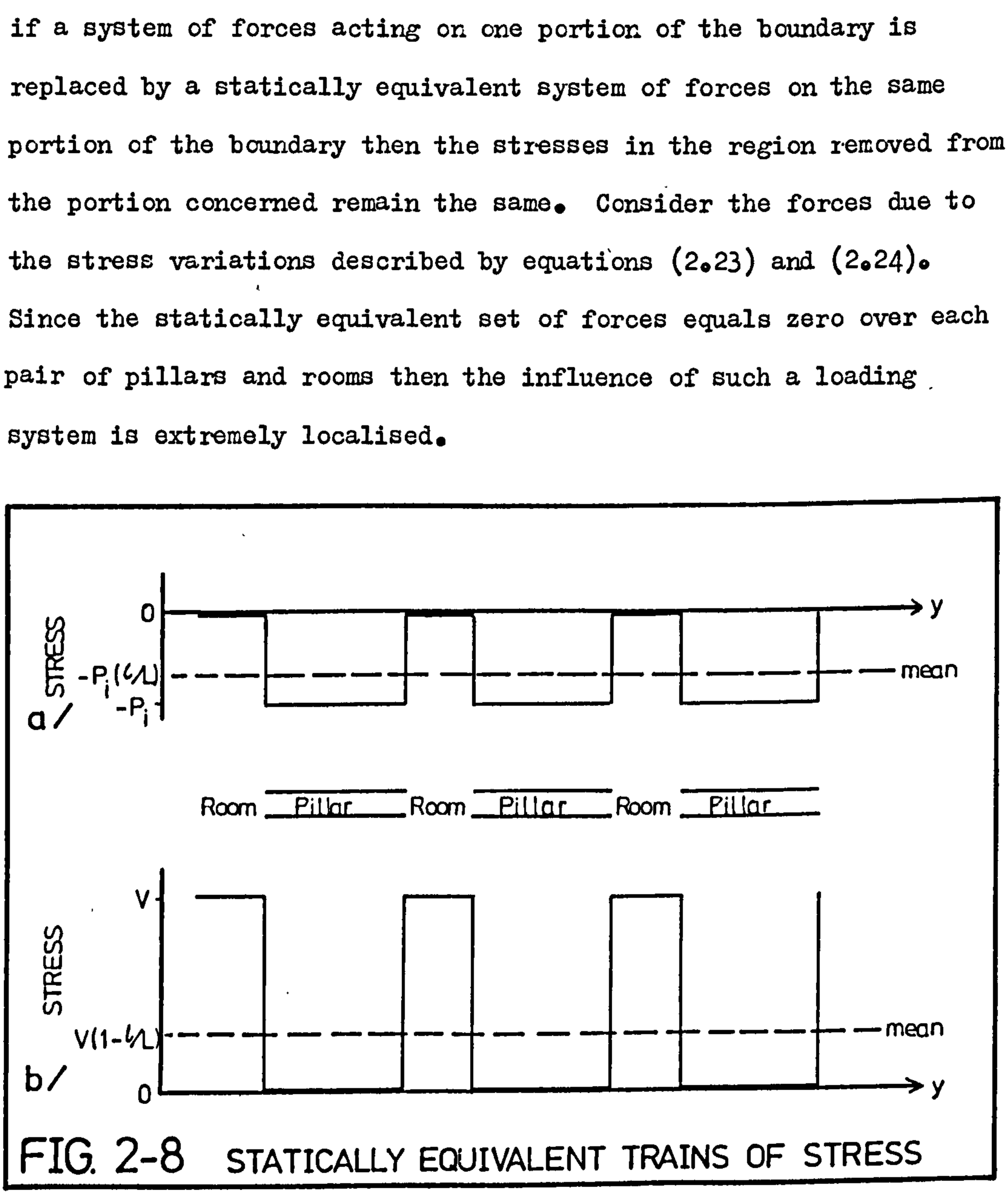

FIG. 2-8 STATICALLY EQUIVALENT TRAINS OF STRESS

This problem can now be solved using the twc and three dimensional face element programs as follows. Firstly, both programs automatically subtract the compressive virgin stress magnitude (-V) from all boundary stress values to obtain induced stresses only. Therefore, the input stresses should be total stresses, i.e. the stresses described by equations (2.22), (2.23) and (2.24) should have the virgin stress (-V) added to them. The resulting equations are,

$$p^i(y)_{mean} = -P_i^* \frac{l}{L} \qquad (2.25)$$

$$p^i(y)_{pillar} = -P_i^* (1 - \frac{l}{L}) \qquad (2.26)$$

$$p^i(y)_{room} = P_i^* \frac{l}{L} \qquad (2.27)$$

where $-P_i^*$ is the total stress $(-P_i - V)$ acting on the i'th column of pillars.

A similar train of stresses exists in the ribside such as the alternating sequence of $-P_3$ and $-P_8$ in Fig. 2-6. The equivalent set of equations for a ribside situation may be derived from equations (2.22) - (2.24) by replacing P_i by P_{i1} and V by $-P_{i2}$ and then adding (-V) to all equations. P_{i1} represents the ribside stress for the element in line with pillars in the x direction while P_{i2} corresponds to the element in line with rooms in the x direction. P_{i1}^*, P_{i2}^* are the alternating total stresses in the i'th column of the ribside which define the ribside train of stresses, $p_r^i(y)$, as

$$p_r^i(y)_{mean} = -P_{i1}^* \frac{1}{L} - P_{i2}^* (1 - \frac{1}{L}) \qquad (2.28)$$

$$p_r^i(y)_{pillar} = (-P_{i1}^* + P_{i2}^*) (1 - \frac{1}{L}) \qquad (2.29)$$

$$p_r^i(y)_{room} = (-P_{i1}^* + P_{i2}) \frac{1}{L} \qquad (2.30)$$

Using these equations, the mean values for the ribside and panel trains of stress can be represented by a two dimensional plane strain face element solution, since they are independent of the y axis. The solution is based on the assumption that the only boundary conditions are the stresses normal to the seam. Each pillar is represented by a single element and so the average shear stress is taken to be zero cver the whole of the element.

The two dimensional solution therefore only requires a single line mesh made up of one element for each pillar and room and one for each ribside element. The 2D mesh which would be used in conjunction with the problem in Fig. 2-6 is shown in Fig. 2-9.

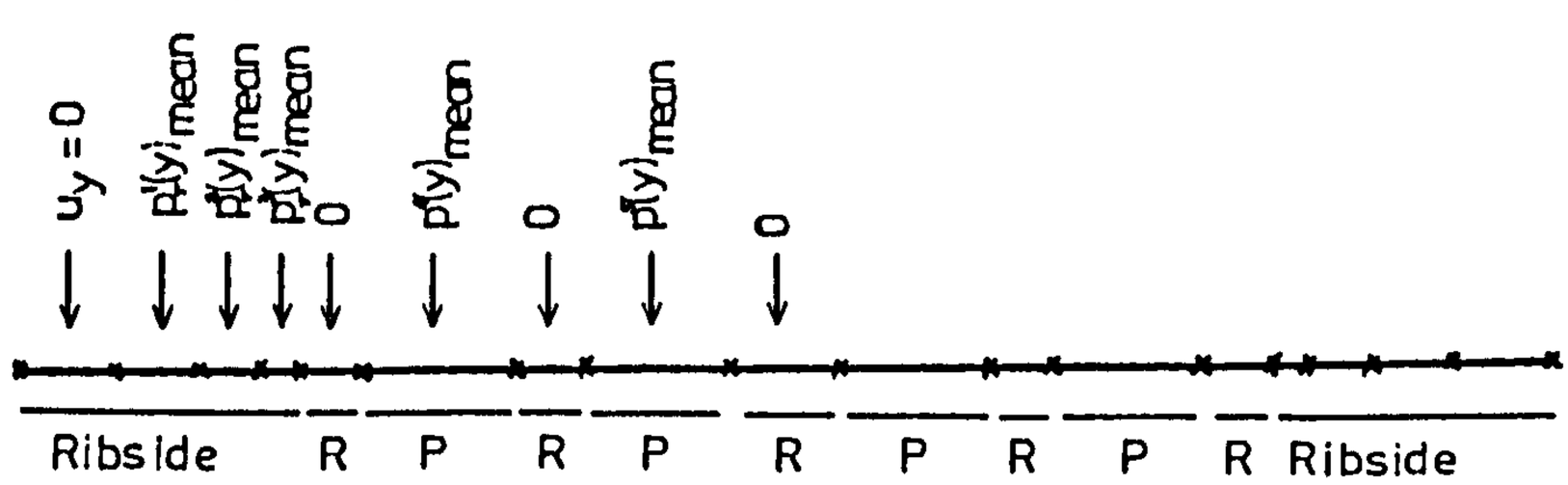

FIG. 2-9 2D FACE ELEMENT MESH

The boundary stresses for such a mesh are based on equations (2.25) and (2.28). Approximate values are used initially for P_i^*, P_{i1}^* and P_{i2}^* and the values obtained for $p^i(y)_{mean}$ and $p_r^i(y)_{mean}$ are applied to the line of elements with zero stress applied to the room elements. The solution is very fast due to the extremely simple mesh.

The three dimensional solution makes use of St Venant's principle by only requiring two rows of rooms and pillars either side of the central pillar row to simulate a panel of infinite length. The boundary stress system is obtained from equations (2.26), (2.27), (2.29) and (2.30), i.e. the equivalent stress trains variant from the mean stress, and each pair of these is equivalent to a zero load system in the y direction. Therefore the influence of pillars more than two rows away from the central row is insignificant to the three dimensional section of the solution. Hence only five rows of pillars are required, as shown in Fig. 2-6, to represent a panel of infinite length using this method.

The actual technique for obtaining the final solution using this method is described in the next section.

2.1.6 Face Element Solution by Perturbation

This technique was developed for the problem described above. However, it is equally applicable to any face element problem where the plane of the mined seam is taken as the boundary, with unknown pillar stresses normal to the plane as the variables, and unknown convergences within the seam. The method allows for seam properties

to differ from those of the horizon within the boundary. Details of the technique are as follows.

For a set of n unknown boundary variables (either pillar or ribside stresses) let the stresses be termed Q_i (i = 1, n). Within the program, using the properties of the horizon material a displacement u_i is calculated for each element where a boundary stress has been applied. These displacements correspond to a deformation of the boundary of the half space either above or below the plane of the seam. Assuming roof and floor to behave identically, the deformation of the seam will be double that of the boundary. The seam deformation is then converted to a resultant stress R_i on the basis of the seam modulus and height, i.e.,

$$Q_i \xrightarrow{\text{Horizon properties}} u_i \xrightarrow{\text{Seam properties}} R_i$$

The aim of the perturbation technique is to satisfy the equation

$$R_i - Q_i = 0 \quad (\text{for } i = 1, n) \tag{2.31}$$

Firstly, apply an estimate of the boundary stresses, Q_i° to the model and obtain a resultant stress R_i°. Next, perturb each stress in turn by an amount δQ_i. This requires n re-runs of the program until all the boundary stresses have new values $Q_i^{\circ} + \delta Q_i$. From each perturbation the influence of the element whose stress variable is being changed may be calculated on all the other variable elements. i.e. the influence of the i'th element on the j'th may be described as

$$\delta Q_i \longrightarrow \delta u_{ij} \longrightarrow \delta R_{ij}.$$

From this relationship an influence factor, k_{ij}, may be defined as,

$$k_{ij} = \frac{\delta R_{ij}}{\delta Q_i} \tag{2.32}$$

which represents the ratio of stress change induced on the j'th element by a change of stress on the i'th element to the latter stress change. For any element, say j, the value of the stress variable will be affected by changes of all the other variables to the extent

$$\Delta Q_j = \sum_{i=1}^{n} \left(\delta Q_i . k_{ij} \right) \tag{2.33}$$

From the n perturbation runs an influence matrix $[K]$ is obtained, made up of the k_{ij} influence factors.

For the case of an isotropic elastic medium the set of equations of the form (2.33) can be assembled into a set of n linear simultaneous equations which satisfy equation (2.31). These are of the form

$$Q_j^o + \delta Q_j = R_j^o + \sum_{i=1}^{n} \left(\delta Q_i . k_{ij} \right) \tag{2.34}$$

for j equal to each of the variable elements, with the stress changes δQ_i as the n unknown variables.

This equation can be rearranged to give

$$\left(\sum_{i=1}^{n} \left(\delta Q_i \cdot k_{ij} \right) \right) - \delta Q_j = Q_j^o - R_j^o \qquad (2.35)$$

which can be written in matrix form as

$$[M](Q) = (Q^o - R^o) \qquad (2.36)$$

where

$$[M] = [K]^T - [I] \qquad (2.37)$$

$[K]$ is the n by n influence matrix

$[I]$ is an n by n identity matrix

(δQ) is a column vector of the n unknown stress changes

$(Q^o - R^o)$ is a column vector of the n differences between initial estimate and resultant stresses.

The final set of resultant stresses is simply

$$(R) = (Q^o) + (\delta Q) \qquad (2.38)$$

This method has been incorporated into a program called FACSOLVE which is listed in Appendix A together with the control commands for running the face element programs. FACSOLVE uses a NAG (Nottingham Alogorithms Group) subroutine, FO4AEF, to solve the linear simultaneous equations using Crout's method. As with all NAG routines, double precision variables are required as input to the subroutine.

FACSOLVE has been written primarily for the combined use of two and three dimensional programs on long panel analyses. In order to use it just for single program solutions, zero values should

be input for the second set of boundary displacements. The program requires modulus and thickness of the seam, number of perturbed and non-perturbed stress values, the stresses themselves with the changed values and the complete set of variable element displacements for the initial and perturbation runs. The facility for not perturbing some stresses is used in the ribside where the variation in the y direction is considered negligible. The element stress is treated as an unknown value and is perturbed in the two dimensional solution but is a constant zero stress and non-perturbed in the three dimensional case.

Therefore to obtain the complete solution to the long panel problem, the two meshes, linear (2D) and planar (3D), are drawn up. Initial total stresses are estimated and the boundary stresses based on equations (2.25) to (2.30) are applied. The estimated stresses are then perturbed. The solution is independent of the magnitude of perturbation but the latter should be large enough to avoid computer accuracy affecting results. The matrix $[K]$ is very susceptible to computer 'round-off' error with small displacements so perturbation should be of the order of 50% of initial stress estimates. The complete set of stresses and displacements for the boundary variables is then input to FACSOLVE together with the seam properties and the solution is obtained.

Up to 20 variables can be handled by FACSOLVE with present dimensions but this could easily be enlarged. The limiting factor is the time taken running the three dimensional solutions. The solution for stresses and displacements above the seam can be obtained using bench marks in the two dimensional mesh loaded on the basis of the obtained stresses. This is because the equilibrium

loading on the three dimensional mesh, by St Venant's principle, has little influence on stresses or displacements away from the seam. This was verified using three dimensional bench marks in some early runs with balanced numbers of rows of rooms and pillars.

2.1.7 Comparison of Face Element and Analogue Solutions

Investigations into pillar loading in bord and pillar coal workings were carried out by Oravecz (17). He studied the load distributions across numerous panel geometries using an electrical resistance analogue model. In order to check the validity of a face element solution using the long panel and perturbation techniques, one of Oravecz's panels was modelled. Details of the panel layout are summarised in Table 2-1. The two dimensional

Table 2-1 Details of Analog Comparison Panel (after Oravecz)

No. 2 Seam Workings - Colliery 3 - Secondary Extraction	
Average depth to mid-seam	66.68m
Height of workings	5.49m
Bord centre distance	19.81m
Pillar width	13.71m
Bord width	6.10m
Areal extraction	52.07%
No. of pillars in panel	7
Panel width	144.78m
Seam elastic modulus	3.92 GN/m^2
Horizon elastic modulus	6.27 GN/m^2
Horizon Poisson's ratio	0.15
Virgin Stress level at seam	1.667 MN/m^2
Tributary Area Pillar Stress	3.751 MN/m^2

mesh comprised 21 elements (22 nodes) while the three dimensional mesh had 93 elements (188 nodes). The ribside was modelled by an outer row cf incompressible elements and then twc rows of compressible elements. The stress variation within the ribside along the direction of the panel was neglected.

The results of the comparison are listed in Table 2-2 for the average pillar stresses. The values are listed as a ratio of the tributary area stress quoted in Table 2-1. The pillars are numbered increasingly towards the panel centre from the ribside.

Table 2-2 Ratio of Pillar Stresses to Tributary Area Stress

	Analogue Stress Ratio (after Oravecz)	Face Element Stress Ratio	Stress Deviation (% of Analogue Stress)
Pillar 1	0.7846	0.8279	+5.52
Pillar 2	0.9008	0.8615	-4.36
Pillar 3	0.9262	0.8716	-5.60
Pillar 4	0.9343	0.8751	-6.34

From Table 2-2 it can be seen that the maximum deviation of solution is just over 6%, the face element solution under-estimating the average pillar stresses towards the panel centre relative to the analogue solution. However, the two methods show quite acceptable correlation for this type of simulation.

2.1.8 Panel Simulation - Types of Boundary Conditions and Models

One of the problems encountered with the panel simulations

was in establishing the correct boundary conditions at the edges of the problem. Within the ribside it was initially thought that imposing a zero displacement condition was restricting the behaviour of the ribside in the proximity of the panel.

An attempt was made to use zero normal stress as the boundary restraint rather than displacement. Using this boundary condition it was found that the resultant solution stresses would not converge to the imput stresses, i.e. it was not possible to satisfy equation (2.31). It appeared that this was due to a lack of any fixed displacement condition along the mesh resulting in any number of different divergent solutions.

It was decided to return to the zero displacement criterion but the problem of restricting ribside movement was overcome by making the first ribside element very narrow (less than 5m) then one or two compressible elements before the zero displacement elements.

This technique was used for a comparative study of the low extraction, conventional room and pillar panels (see Chapter 3). In order to model the higher extraction, yield pillar panels, an alternative method was chosen. Since the concept of yield pillars (discussed in Chapter 4) requires that the pillars only provide support to the immediate roof strata, a realistic elastic model should not allow for any load-bearing capacity to be provided by the yield pillars within the panel.

A two dimensional face element vertical plane strain solution was chosen to model this type of panel with the entire panel being

represented by a single, wide excavation. Such a model should more closely represent the conditions of time-dependent yield of the panel pillars to the extent where the barriers between panels provide the major support capacity for the upper strata. A model such as this requires simple zero normal stress conditions around the boundary of the panel excavation.

The final type of model used, again for the high extraction panels, was a vertical plane strain finite element solution using FEMITPLT. This was used to study a single panel with the pillars included in order to quantify the amount of pillar yield required for stress redistribution above the panel. Yield was simulated by changing the pillar moduli. This model was also used to investigate the effects of the different strata on subsidence above the seam.

2.1.9 Subsidence Analysis

The results of bench mark displacements above the seam from the face element programs predict a subsidence profile on the assumption of isotropic elastic homogeneity of the strata. However, due to the differences in stratum properties and possible discontinuities between the strata, it was felt that the subsidence strains predicted by the face element solution would be under-estimated. The opposite extreme would be if the interface concerned behaved as a free, unrestrained surface.

The actual interface conditions in the level of strata below the Bunter Sandstone are not known. However, it is reasonable

to assume that there are some shear zones and joints in the Upper Permian Marl and the anhydrite band and so the interface conditions within this material would lie somewhere between the twc extremes described above.

Therefore, a method was developed whereby the vertical displacements from the face element results which defined the subsidence profile were accepted. However the lateral strains associated with this profile were calculated in two ways. The first was using the slope displacements predicted by the face element program. The second method was to use the National Coal Board's curvature method (25) on the assumption that the interface behaved as a free surface. The strains predicted from the two methods were averaged and this mean strain was used as the best estimate of sub-surface, subsidence-induced lateral strains.

This method is similar to one developed by Dejean and Martin (26) for the French coal measures where they attempted to predict subsidence effects on some old workings above the present extraction area. They found that by calculating the subsidence profile itself by the two methods above, the amplitude and shape of the profiles were very similar. However, the critical radius, which is most significant in the tensile strain zone, was different with each method. An average of the two methods gave close correlation with measured data.

A program, UGSUB, was written to be used with a version of the face element program which output all the bench mark data onto a separate file. UGSUB simply carries out the two strain analyses

described above and produces an average for each bench mark, on as many horizons as specified.

2.2 Data Analysis

As already outlined, this investigation has been very largely directed towards analysis and interpretation of in-situ data. By the end of 1976 over 600 measuring stations in the form of either extensometer anchors or convergence points had been installed in the mine. These were being monitored with a frequency of up to once a day, and on average, once a week. Consequently the quantity of data to be handled necessitated the use of as much computer processing as possible.

Due to the variety in the types of data recorded it was necessary to develop a fairly versatile program to handle the variation in input and produce a standard output. This was considered more suitable than using a large number of individual programs for each type of data input. The program which was developed was also structured to be able to handle laboratory data produced from various sources such as strain gauges, dial gauges, LVDT's etc., with time as the independent variable.

The program developed, DATAPLOT, has been written specifically for this investigation although it incorporates a greatly modified section of a program by Patchet (7), called ANALYSER, as part of subroutine READIN. A listing of DATAPLOT is included in Appendix A which includes specific instructions concerning data input. The program consists of a main control program plus four subroutines.

Fig. 2-10 shows the arrangement of the subroutines and a generalised flowchart for the program.

The control program, MAIN, receives input concerning the number of data sets to be analysed, types of data and the type of plotting output required, if any. Subroutine READIN reads all the sets of data and carries out all the basic numerical analysis procedures, in turn, for each data set. These results are printed and are also stored in separate files as sets of paired results (e.g. time-deformation, time-strain rate etc.) if any other program analysis is required. Subroutine PLOT calculates the scaling for each plot which has been requested. Scaling is either automatic, where suitable scales are chosen so that the data curves use the maximum amount of the A4 page, or else increment sizes can be specified manually for each plot. Subroutine AXES is called from PLOT to draw the appropriate axes and label and number them. PLOT then carries out all the plotting and writes the headings.

For use with extensometer data, subroutine BAYSTN calculates the bay strains between anchors up to a maximum of 10 anchors excluding the mouth or reference anchor. BAYSTN plots the strains independently, on axes prepared by AXES, but if bay strain rates are required, the bay strains are re-organised and input to READIN at a separate point, ENTRY READ2. BAYSTN then directs these bay strain rate data to PLOT and AXES if plotting is required.

The types of data which can be analysed by DATAPLOT are as follows:

i Extensometer data - multiple anchor borehole data in

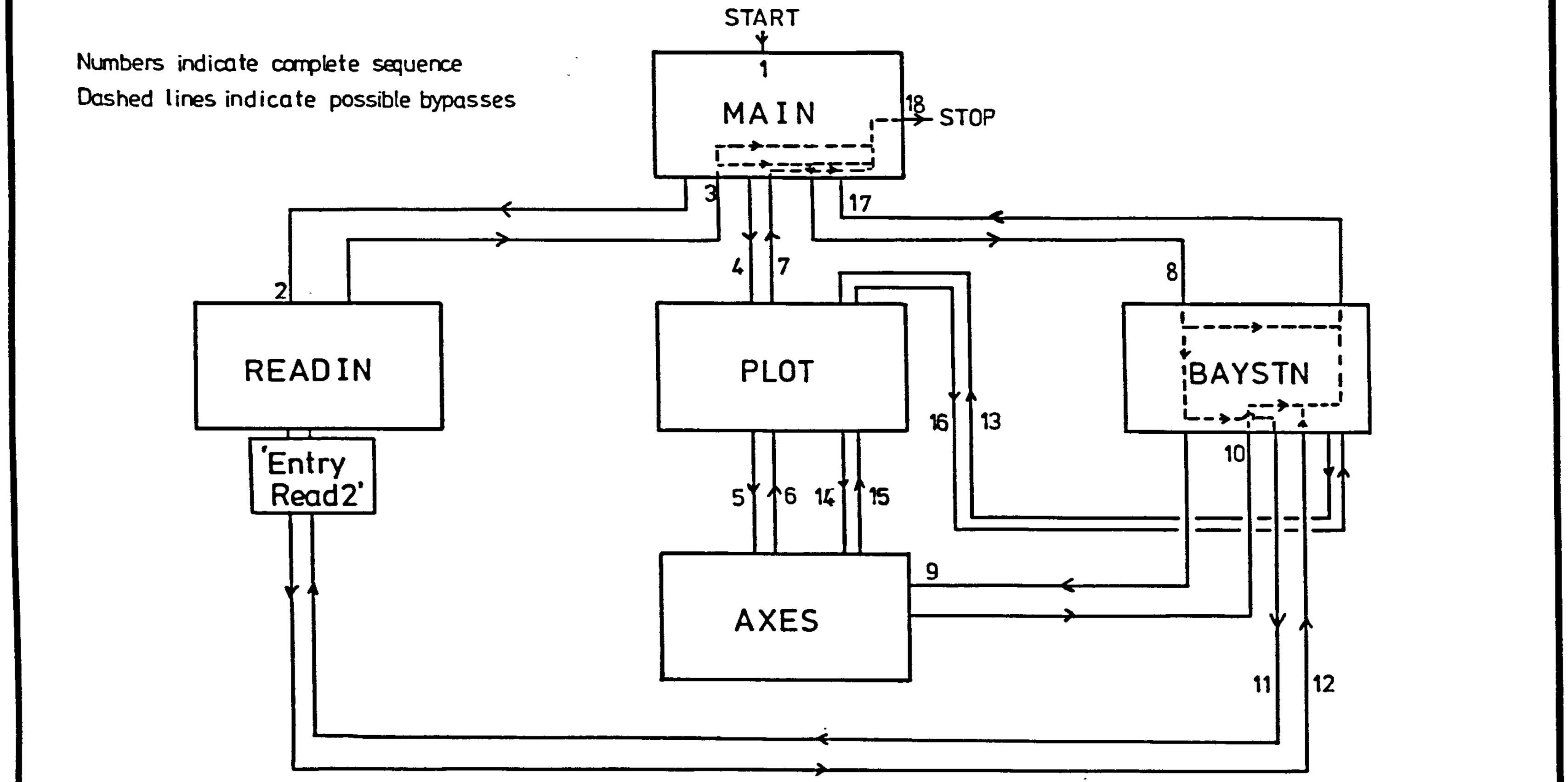

FIG. 2-10 SUBROUTINE FLOWCHART FOR PROGRAM 'DATAPLOT'

the form of either imperial or metric deformations, relative to the extensometer mouth station.

ii Convergence data - using a Newcastle Mark 1 extensometer for convergence monitoring by steel tapes - readings from micrometer and changes in tape hole position (referred to as old data format in program).

iii Convergence data - direct tape or levelling measurements of changes in level of any point (roof, floor, wall, etc.) with respect to a stable bench mark.

iv Laboratory data - dial gauge, strain gauge or LVDT readings for laboratory specimens. Data as either deformation, strain or microstrain.

v Talbott Strain Cell data - Strain gauge data from a cell used for monitoring or overcoring. Drilling depths can be input together with times for overcoring penetration rate plots. Resolved stresses can be plotted relative to time.

In each of these data types, the time can be specified as elapsed time in days from the start of readings or as direct time - hours, minutes - plus date as day, month and year. All readings are reduced to deformations or strains and times relative to the value of the first reading. Up to six readings can be supplied with each time value and these are averaged to a mean value for subsequent analysis.

A number of options can be controlled by the time value in the middle of a data set. These include the base reference value of

deformation or strain, bay length for extensometer data, instrument adjustment, imperial to metric input.

The following are the forms of plotted output available:

(i) Deformation v. Time

(ii) Strain v. Time

(iii) Strain Rate v. Time

(iv) Smoothed Strain v. Time

(v) Smoothed Strain Rate v. Time

(vi) Bay Strain v. Time

(vii) Bay Strain Rate v. Time

(viii) Smoothed Bay Strain v. Time

(ix) Smoothed Bay Strain Rate v. Time

(x) Bay Strain v. Borehole Depth

(xi) Bay Strain Rate v. Borehole Depth

(xii) Smoothed Bay Strain Rate v. Borehole Depth

(xiii) Convergence v. Time

(xiv) Convergence Rate v. Time

(xv) Smoothed Convergence Rate v. Time

(xvi) Stress v. Time (for overcoring)

(xvii) Strain v. Drilling Distance (for overcoring)

The borehole depth plots for extensometer data are for specified elapsed times. Bay strains and rates are plotted at the mid-point between the two anchor depths which form the bay, for each time specified. All plotted rate curves are plots of the exponential logarithm of the rate. Any negative values of rates are bypassed.

The actual analysis process produces data under the following headings:

Time	Date	Elapsed Days	Mean Reading
Deformation	Strain	Smoothed Strain	Residual (S.S. - Poly)
Log_e Sm. Strain	Strain Rate	Sm. Strain Rate	Log_e Sm. Strain Rate

Times, deformations and strains are calculated using standard procedures. Strains are either in terms of percentage or microstrain. Strain rates are calculated over the previous time interval for each point.

The smoothed values listed in the output are obtained by means of a running, least-squares polynomial smoothing technique. Let the pairs of co-ordinates such as time, strain be called (t_i, y_i) where there are m such pairs and y is a function of t. The smoothing process looks at five such pairs in each step, say

$$f(t_{i-2}),\ f(t_{i-1}),\ f(t_i),\ f(t_{i+1}),\ f(t_{i+2})$$

The values of these functions and the five time values are input to a least-squares orthogonal polynomial subroutine. This subroutine is one of the NAG routines, E02ABF, and it calculates a weighted polynomial approximation to the supplied data points using Forsythe's method. The polynomial, p(t) is in this case specified as third order and its coefficients, P_0, P_1, P_2, P_3, are computed such that they minimise the expression

$$\sum_{j=1}^{5} W_j \left(p(t_j) - f(t_j)\right)^2$$

where W_j is the weight assigned to each function.

For each set of five pairs, the value of the smoothed polynomial is assigned to the middle pair, i.e.

$$y^s_i = p(t_i) \tag{2.39}$$

Since p(t) is of the form

$$p(t) = P_0 + P_1 t + P_2 t^2 + P_3 t^3 \tag{2.40}$$

then the derivative is easily defined,

$$p'(t) = P_1 + 2P_2 t + 3P_3 t^2 \tag{2.41}$$

Therefore the smoothed strain rates are calculated as being the derivative of the smoothed strain polynomial for the middle pair of each set of five pairs of co-ordinates.

After five pairs are fitted the value of i is increased by one and the next set of five pairs is considered. Thus the smoothed function value is obtained for each successive pair of co-ordinates. For the cases where i = 3 and i = m-2, the values of smoothed strains and smoothed strain rates are also evaluated for the initial twc and final two pairs of data points respectively. This provides an estimate of initial strain rates at the starting point of each data set which can be very useful.

The weighting factors, W_j, referred to earlier are all assigned a value of 1.0 except for the initial value which is given a weighting of 100.0 to ensure the correct starting point for the initial value of each complete smoothed curve.

A further section of subroutine READIN performs a polynomial fit to the entire data set of time-smoothed strain values. The same routine, E02ABF is used but the polynomial is allowed to be anything up to fourth order. The column of values for Residuals in the outputs represents the difference between the smoothed strain value at a point of time and the fitted polynomial for that point. The coefficients of the polynomial of best fit are listed below each set of output.

The program is stored in compiled form in file DPOBJ. It is capable of handling as many blocks of data as time permits, up to 10 sets of data per block and up to 150 pairs of data points within each set. The limit of the polynomial fitting subroutine is 200 sets of functions and so for large data sets (up to 300) a version of DATAPLOT which bypasses the curve fitting section is compiled in file DPLARGE. The version in DPOBJ causes an x to be marked on the plots at the location of each point. If this is not desired, another version of the program compiled in DPOBJ2 should be used. All the plotting subroutines called are part of the N.U.M.A.C. (Northumbrian Universities Multiple Access Computer) *PLOTLIB library.

2.3 Auxiliary Programs

A number of short programs have been written to handle specific types of data or to link up with the main programs already discussed. The principal ones of these are mentioned here.

SURFSUB is a data handling program to process surface subsidence data from levelling results. The plotted subsidence

profiles produced by C.P.L. are scanned on a D-Mac table to produce punched card data containing pairs of co-ordinates which define the subsidence curves. This data is the input for SURFSUB which calculates the lateral strains associated with this subsidence on the basis of the N.C.B. curvature method referred to previously. Output is in the form of printout of subsidence and strains which is also stored on file for plotting by the program, XYPLOT.

XYPLOT is a very general purpose plotting program for handling sets of X and Y co-ordinates. Up to ten curves can be plotted on each picture and automatic or manual scaling is available. All titles must be supplied.

STRAINPLOT is simply a data organisation program. It converts Talbott cell data from the format required for the stress analysis programs (27) into the required format for strain analysis and plotting with DATAPLOT.

FACEPLOT is a program for plotting the planar three dimensional face element meshes. It is a modification of the two dimensional finite element plotting program, MESHPLOT, referred to earlier but is compatible with the face element data format.

Listings of these programs are not included in this thesis but the basic controls for using them are described in Appendix A.

CHAPTER 3

FACE ELEMENT ANALYSES OF LOW EXTRACTION PANELS

3. FACE ELEMENT ANALYSES OF LOW EXTRACTION PANELS

This chapter presents the results of a number of theoretical analyses of different panel layouts. The layouts are analysed in the order in which they were drawn up by the mine staff at C.P.L. and according to the panel geometries specified by them.

The term 'low extraction panels' is used as a general description of the types of layouts which have been intended to provide long term stability over a large area of the panel and are therefore inherently of low extraction. In this context long term refers to at least several years. This stability is a result of the panel pillars containing a confined core of material capable of carrying the full 'cover load' based on tributary area theory. A more detailed discussion of this is contained in later sections.

The panel layouts considered here are all repeatable in the direction of the panel line. The method of analysis is therefore that described in Chapter 2 using the combined two and three dimensional face element analyses and the long panel solution. This solution provides a measure of the stress distribution across any row of pillars and the subsidence strains above any section of the panel except in the vicinity of the advancing panel faceline.

The solution of stresses is in terms of average pillar stresses normal and tangential to the seam and as described previously the analysis assumes isotropic, homogeneous elasticity. The results therefore provide comparative measures of stress and subsidence only.

3.1 Material Properties and Seam Parameters

The analyses described in this chapter all use the original figures and estimates for mechanical properties. The same properties have been assumed for the seam as for the horizon above the seam, formed predominantly of similar evaporites. These analyses were initiated prior to detailed testing of the near seam strata and for comparative purposes the same figures have been used throughout. These are:

Young's Modulus (E) - 7.00 GN/m^2

Poisson's Ratio (ν) - 0.25

The vertical pre-mining or virgin stress level was assumed to be based on the standard rule of $-22.6\ kN/m^2$ per metre depth for stress gradient with horizontal stress defined by the elasticity relationship based on Poisson's ratio. This gave a ratio of one third for horizontal to vertical virgin stress. On the basis of the depth to seam being 1097m the virgin stress levels at the seam were taken as,

$$\sigma_V = -24.8\ MN/m^2$$

$$\sigma_H = -8.3\ MN/m^2$$

The strata interfaces above the seam which are of interest in terms of subsidence are located between 75m and 200m above the seam. These heights vary considerably over different areas of the seam and so subsidence results have been considered at a number of different heights although a standard of 120m was established for the later analyses. This corresponds to a position where the Upper Permian Marls grade into the mudstones at the base of the Bunter Sandstone.

It was at this level in the shaft excavations where water was known tc have penetrated significantly from the sandstone.

All roadways have been assumed to have a rectangular cross-section, 6m wide and 3m high and the seam has been assumed to lie in a horizontal plane. Panel extraction ratios are calculated on an area basis between the edges of each ribside.

Table 3-1 lists the basic dimensions for each of the panel layouts analysed. Pillars are numbered towards the centre of the panel, pillar 1 being adjacent to the ribside.

3.2 Pillar Strength Safety Factor

In order to assess the relative stability of the pillars within each panel on the basis of strength a relative safety factor can be calculated. Due to the great depth at Boulby the resultant stress levels are in excess of the uniaxial strength of the material and so pillars rely on triaxial confinement of a central core to provide stability. The safety factor must therefore be based on the triaxial strength of the pillar material.

Such a safety factor has been established on the basis of the Mohr envelope for potash obtained by Patchet (7). This is shown in Fig. 3-1 where σ_1 and σ_3 represent a pair of principal stresses, normal and tangential to the seam respectively. The safety factor is defined for a particular value of σ_3 as

$$F_s = \sigma_{1(fail)} / \sigma_1 \qquad (3.1)$$

Table 3.1 Panel Layout Geometries

Panel Variables	1	2	3	4	5	6	7	8
No. of roads (in direction of panel)	5	5	7	7	11	11	9	7
Pillar widths (m) (across panel direction)	60	40	40	30* 45 60	30	30 40**	24	15
Pillar lengths (m) (in direction of panel)	60	40	40	60	30	34	24	45
Angle (^{o}) between panel roads and cross-cuts	90	90	90	90	90	60	90	60
Width:Height ratio of pillars	20:1	13.3:1	13.3:1	10:1 15:1 20:1	10:1	10:1	8:1	5:1
Total panel width (m)	270	190	282	312	366	376	246	132
Panel extraction ratio %	19.2	26.8	26.0	21.3	31.7	29.9	37.6	36.0
Comments	* Widths are for pillars 1, 2, 3 numbered from the ribside. ** Pillar 3, on one side only, is 40m wide.							

for a given σ_3, where $\sigma_{1(fail)}$ is the major principal stress which, in conjunction with σ_3, forms a Mchr's circle in contact with the Mohr envelope for potash.

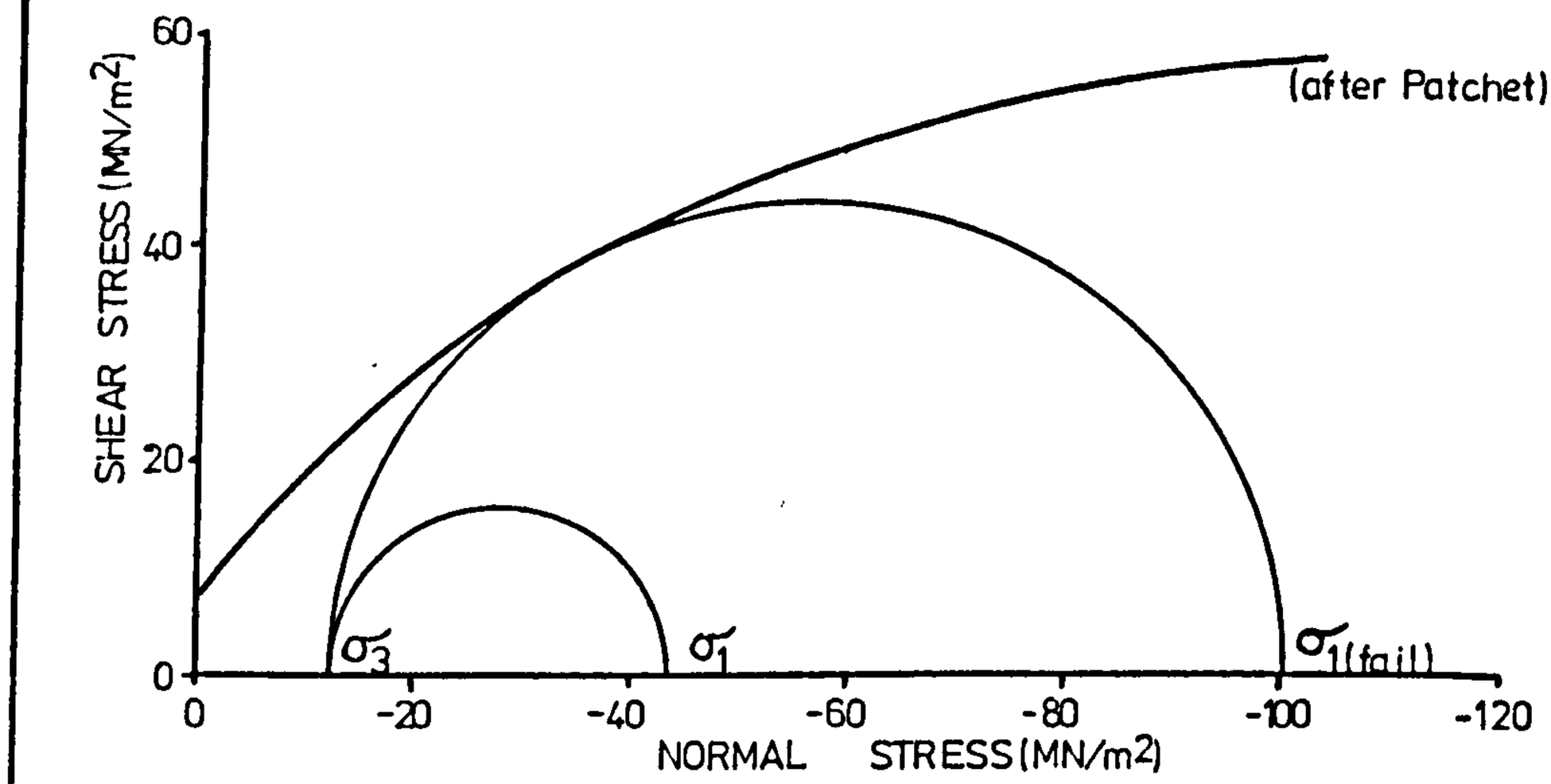

FIG. 3-1 TRIAXIAL STRENGTH SAFETY FACTOR

This safety factor describes the relative stability of a section of material in terms of strength under instantaneous loading (i.e. stability due to initial loading conditions only). In a later section a safety factor is introduced to take into account the time-dependent behaviour of the material. The distinction between these two factors can be emphasised by example. A pillar with a strength factor of 1.0 is likely to fail (exhibit excessive yield) immediately once the full load has been applied to it. A pillar with a time-dependent factor of 1.0 could have a strength factor in excess of 2.0 or more but due to a high rate of creep it will eventually have no central confined core and so it will yield excessively. Such a pillar cannot be classified as having long term stability.

3.3 Results

The results of each layout analysis are presented in this section both for the in-seam stresses and the above-seam subsidence. The three dimensional mesh configuration is shown for each layout. The analysis for the early layouts was not as comprehensive as for later ones but the essential results are included.

It should be noted that although the ribside element in each mesh has been made narrow to prevent distortion of adjacent element results, its own results are not necessarily accurate. This is particularly the case with the tangential stress value. The fact that the three dimensional element is very long with respect to its width and that the tangential stress is averaged for the horizontal plane in both directions gives a misleading result. This is because the horizontal stress along the panel approaches a peak at the ribside whereas the stress across the panel approaches zero and so the average figure for the plane incorporating both directions is somewhat meaningless for narrow elements adjacent tc an excavation.

The term deviator stress, $\sigma_{Dev.}$, used in the results refers to the difference between major and minor principal stresses, $\sigma_N - \sigma_{Tang.}$. Another term used for comparison of results is the tributary area stress, $\sigma_{T.A.}$. This is simply the stress that would exist on each pillar of the panel, assuming that extraction within the panel caused uniform distribution of stress on all the panel pillars. In other words, if the tributary area stress existed on each pillar then there would be no extra stress

thrown onto the adjacent barriers. This stress is defined as,

$$\sigma_{T.A.} = \frac{\sigma_v}{1-e} \qquad (3.2)$$

where σ_v is the assumed vertical virgin stress and

e is the panel extraction ratio.

Once the resolved normal stress for the pillar, σ_i, in the i'th column is obtained, a stress reduction factor, K_i, can be defined for each pillar where

$$K_i = 1 - \frac{\sigma_i}{\sigma_{T.A.}} \qquad (3.3)$$

This factor is a measure of the protection afforded to the panel pillars by load bearing ribsides on either side of the panel.

3.3.1 Layout 1 - 5 Entries, 60m Square Pillars

This layout was analysed using two zones of compressible material in the ribside, 5m and 15m wide, with a massive block of zero displacement material adjacent to them. The stress variation in the panel direction on both ribside zones was obtained. Fig. 3-2 shows the layout represented by the planar mesh used. The results of the normal stresses (σ_N) obtained across the line AA are shown in Fig. 3-3 with the ribside variation across the line BB marked with dashed lines.

For this panel layout, the value of $\sigma_{T.A.}$ is -30.7 MN/m^2. Table 3-2 contains the full set of in-seam stress analysis results.

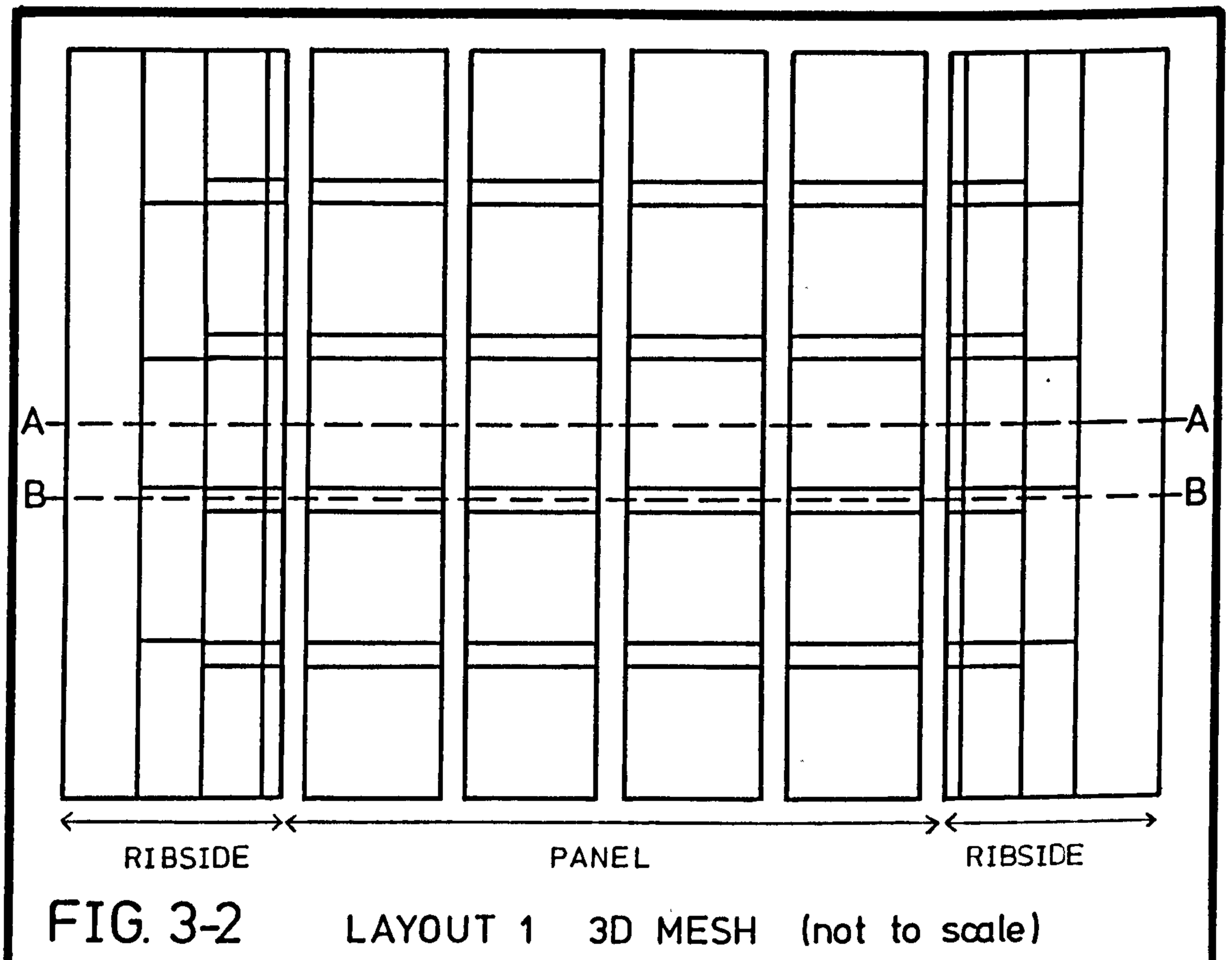

FIG. 3-2 LAYOUT 1 3D MESH (not to scale)

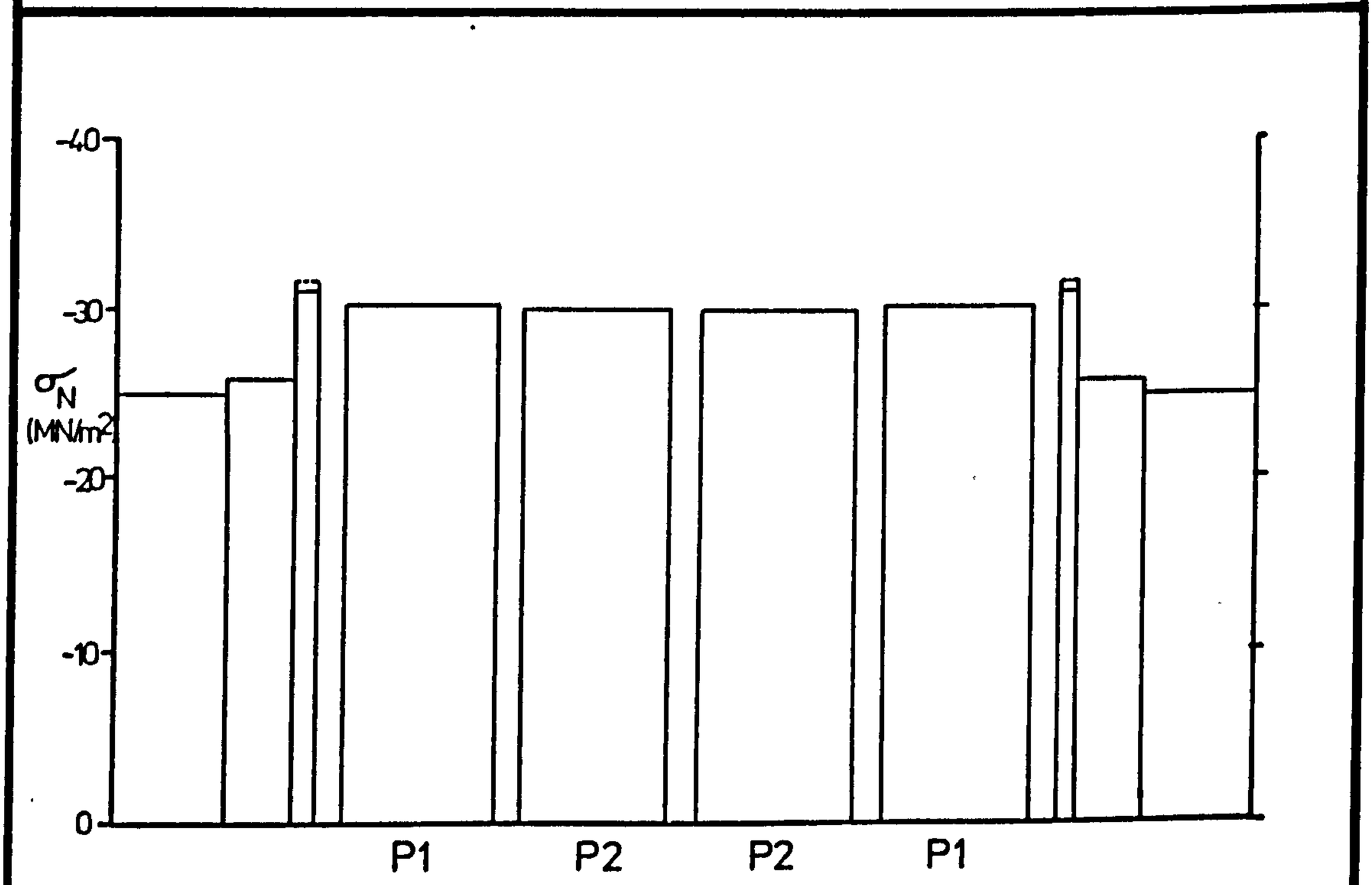

FIG. 3-3 LAYOUT 1 IN-SEAM NORMAL STRESSES

Table 3-2 Layout 1 In-Seam Stress Results

Panel Zone (AA and BB refer to Fig. 3-2)	σ_N (MN/m^2)	$\sigma_{Tang.}$ (MN/m^2)	$\sigma_{Dev.}$ (MN/m^2)	F_ε	K (%)
1st Compr. Zone (AA)	-25.8	- 9.4	-16.4	3.29	
1st Compr. Zone (BB)	-25.8	- 9.4	-16.4	3.29	
Ribside Zone (AA)	-31.1	-14.6	-16.5	3.32	
Ribside Zone (BB)	-31.6	-14.7	-16.9	3.29	
Pillar 1	-30.2	-11.9	-18.3	3.12	1.6
Pillar 2	-30.0	-11.6	-18.4	3.12	2.3

The results of the above seam analysis are presented in Table 3-3. For this layout the only horizon considered was 200m above the seam. The lateral strains have been calculated using the surface curvature method, i.e. assuming that the horizon deforms as an unrestrained surface. The locations of various pcints are defined in terms of a co-ordinate system with origin at the ribside and negative x axis heading perpendicularly into the ribside. Fig. 3-4 shows the subsidence and lateral strain profiles superimposed on each other. The position of maximum strains is accurate to ±20m based on the spacing of bench marks used in this and later layout analyses.

Table 3-3 Layout 1 Above Seam Results for 200m Horizon

	$S_{max.}$ (mm)	$S_{rib.}$ (mm)	S_{50} (mm)	S_{10} (mm)	$\varepsilon_{max.}$
Parameter	1.02	0.86	0.56	0.10	0.000020
X Co-ord. (m)	135	0	-88	-332	-140

where $S_{max.}$ is maximum subsidence

$S_{rib.}$ is subsidence above the ribside

S_{50} is 50% subsidence

S_{10} is 10% subsidence

$\varepsilon_{max.}$ is maximum lateral tensile strain.

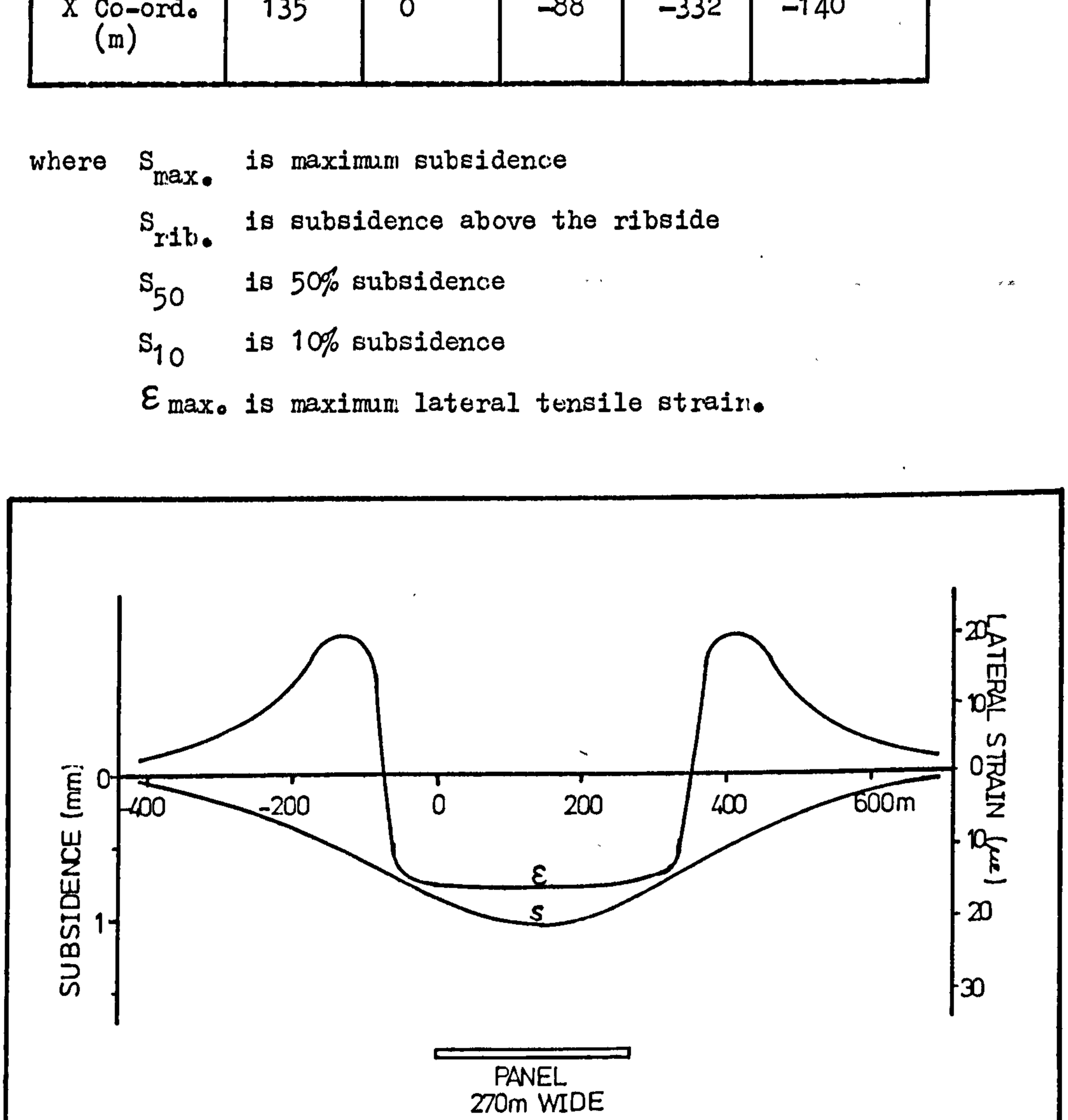

FIG. 3-4 SUBSIDENCE AND STRAIN 200m ABOVE LAYOUT 1

3.3.2 Layout 2 - 5 Entries, 40m Square Pillars

Once again two compressible ribside zones were used, 5m and 15m wide. Stress variation in the panel direction was calculated for both zones. Fig. 3-5 shows the planar mesh used while Fig. 3-6 shows the normal stress distribution using the same convention for lines AA and BB as in layout 1.

The value of $\sigma_{T.A.}$ for this panel geometry is -33.9 MN/m^2. Table 3-4 contains the in-seam stress analysis results.

Table 3-4 Layout 2 In-Seam Stress Results

Panel Zone (AA and BB refer to Fig. 3-5)	σ_N (MN/m^2)	$\sigma_{Tang.}$ (MN/m^2)	$\sigma_{Dev.}$ (MN/m^2)	F_s	K (%)
1st Ccmpr. Zone (AA)	-26.2	- 9.7	-16.5	3.28	
1st Compr. Zone (BB)	-26.2	- 9.7	-16.5	3.28	
Ribside Zone (AA)	-31.5	-15.1	-16.4	3.34	
Ribside Zone (BB)	-32.1	-15.3	-16.8	3.30	
Pillar 1	-32.6	-13.3	-19.3	3.04	3.8
Pillar 2	-32.5	-13.1	-19.4	3.03	4.1

The above seam results for layout 2 are again for a horizon 200m above the seam and are presented in Table 3-5.

Fig. 3-7 shows the subsidence and lateral strain curves for layout 2 using the same co-ordinate reference as for layout 1.

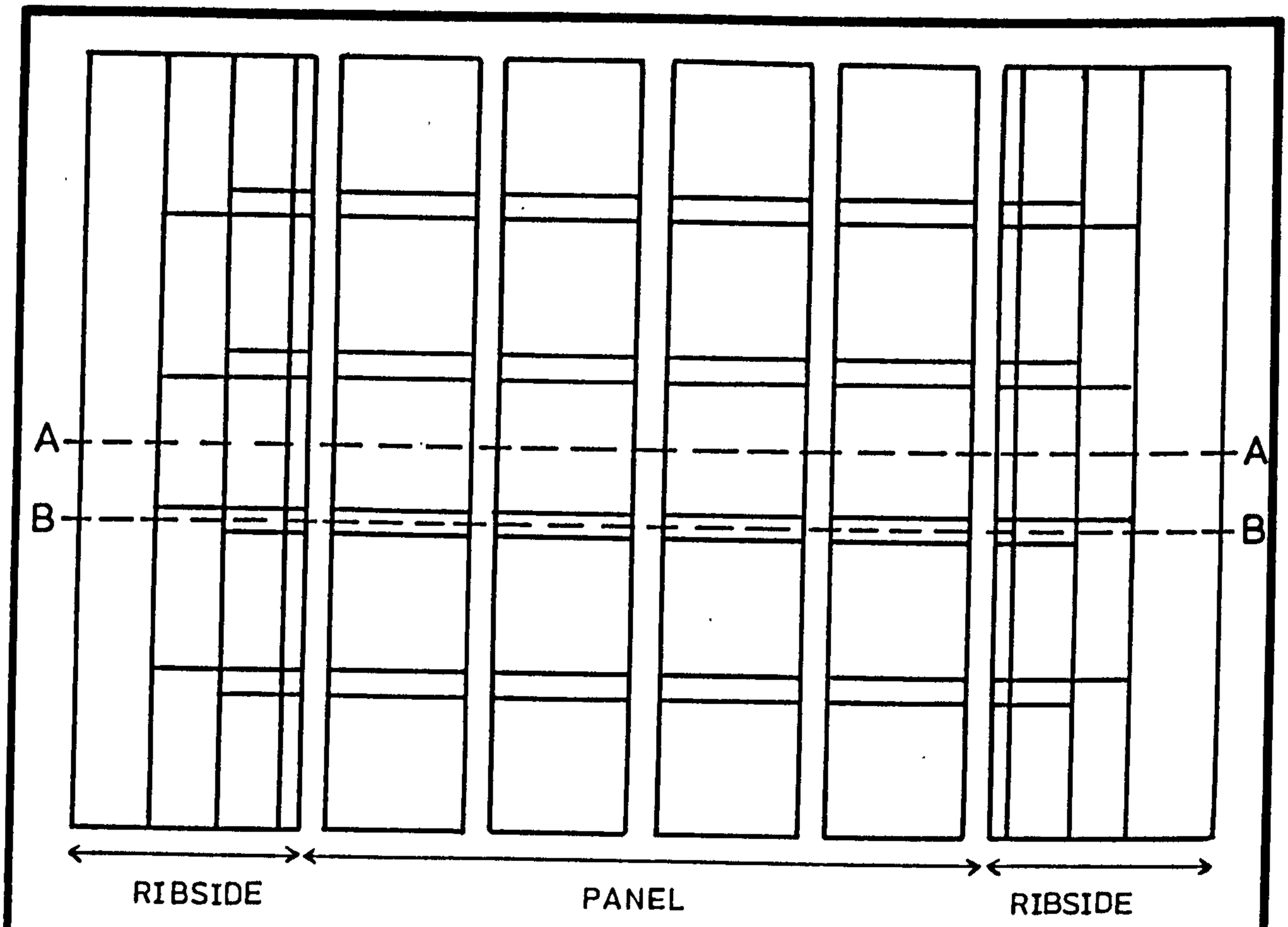

FIG. 3-5 LAYOUT 2 3D MESH (not to scale)

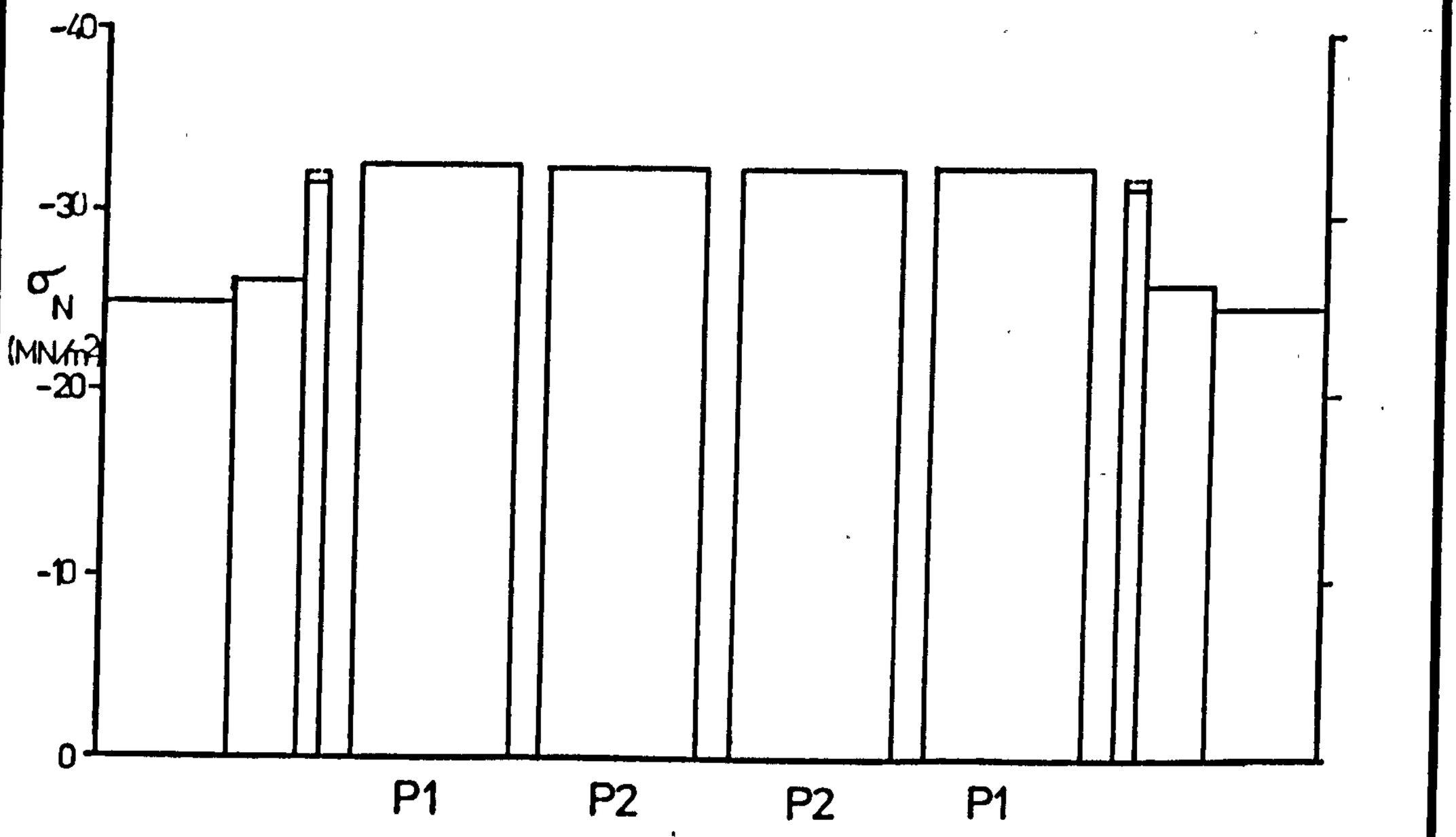

FIG. 3-6 LAYOUT 2 IN-SEAM NORMAL STRESSES

Table 3-5 Laycut 2 Above Seam Results for 200m Horizon

	$S_{max.}$ (mm)	$S_{rib.}$ (mm)	S_{50} (mm)	S_{10} (mm)	$\varepsilon_{max.}$
Parameter	4.12	3.28	2.06	0.41	0.000046
X Cc-ord. (m)	95	0	-84	-326	-140

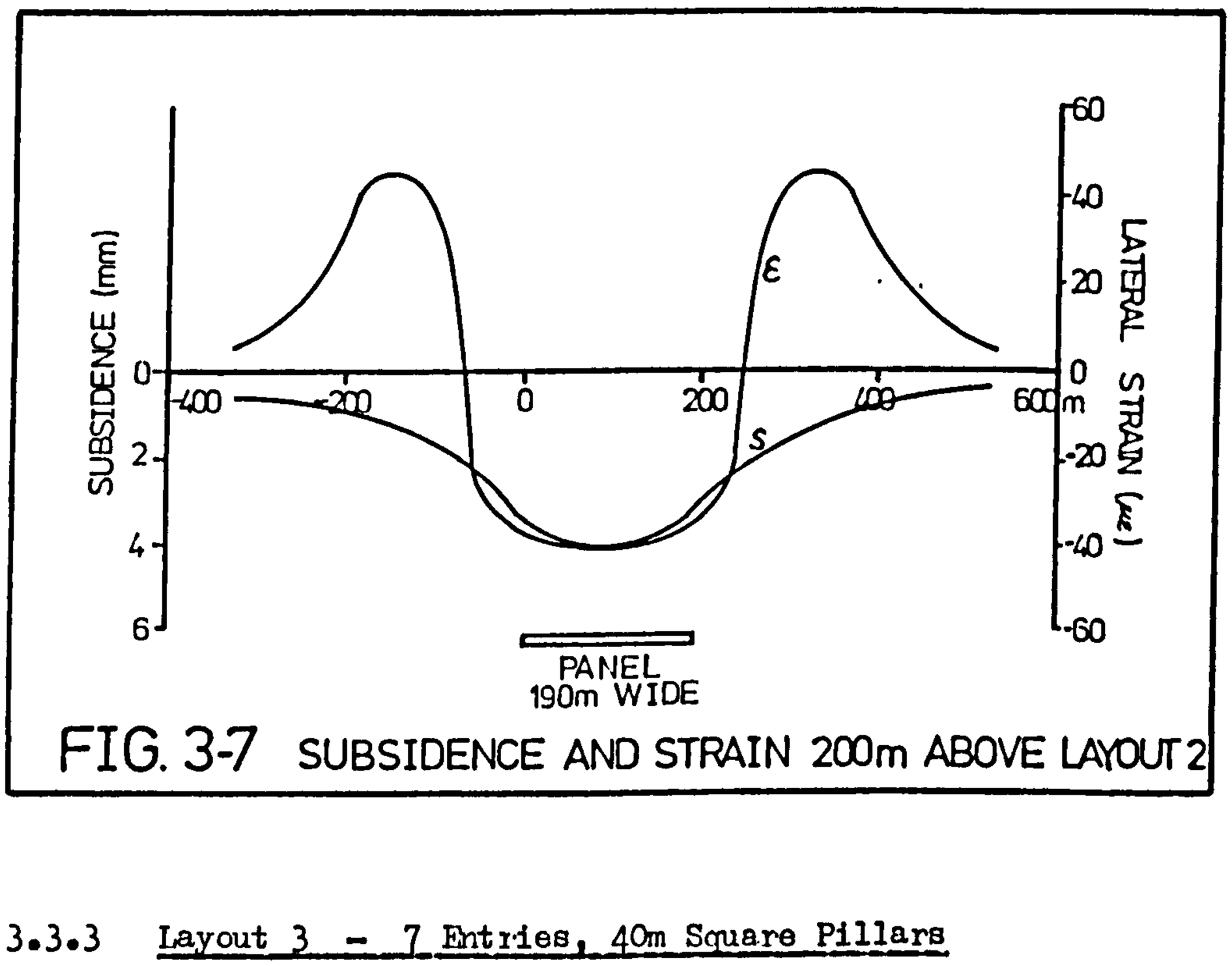

FIG. 3-7 SUBSIDENCE AND STRAIN 200m ABOVE LAYOUT 2

3.3.3 Layout 3 - 7 Entries, 40m Square Pillars

For this layout the ribside was modelled using three compressible zones since it appeared from earlier results that the zero displacement criterion could be inhibiting stress variation in the adjacent zone. The zone widths here were 5m, 10m and 25m.

Fig. 3-8 shows the mesh configuration while Fig. 3-9 shows the normal stress distribution.

The value of $\sigma_{T.A.}$ for this layout is -33.5 MN/m^2. Table 3-6 contains the in-seam stress analysis results.

Table 3-6 Layout 3 In-Seam Stress Results

Panel Zone (AA and BB refer to Fig. 3-8)	σ_N (MN/m^2)	$\sigma_{Tang.}$ (MN/m^2)	$\sigma_{Dev.}$ (MN/m^2)	F_s	K (%)
1st Compr. Zone (AA)	-25.5	- 9.0	-16.5	3.27	
1st Compr. Zone (BB)	-25.5	- 9.0	-16.5	3.27	
2nd Compr. Zone (AA)	-26.0	- 9.6	-16.4	3.29	
2nd Compr. Zone (BB)	-26.0	- 9.6	-16.4	3.29	
Ribside Zone (AA)	-31.0	-14.6	-16.4	3.33	
Ribside Zone (BB)	-31.5	-14.8	-16.7	3.32	
Pillar 1	-32.6	-13.3	-19.3	3.04	2.7
Pillar 2	-32.4	-13.1	-19.3	3.04	3.3
Pillar 3	-32.5	-13.2	-19.3	3.04	3.0

The above seam results for layout 3 are for a horizon 200m above the seam and are presented in Table 3-7.

Table 3-7 Layout 3 Above Seam Results for 200m Horizon

	$S_{max.}$ (mm)	$S_{rib.}$ (mm)	S_{50} (mm)	S_{10} (mm)	$\varepsilon_{max.}$
Parameter	7.53	5.44	3.76	0.75	0.000053
X Co-ord. (m)	141	0	-82	-324	-100

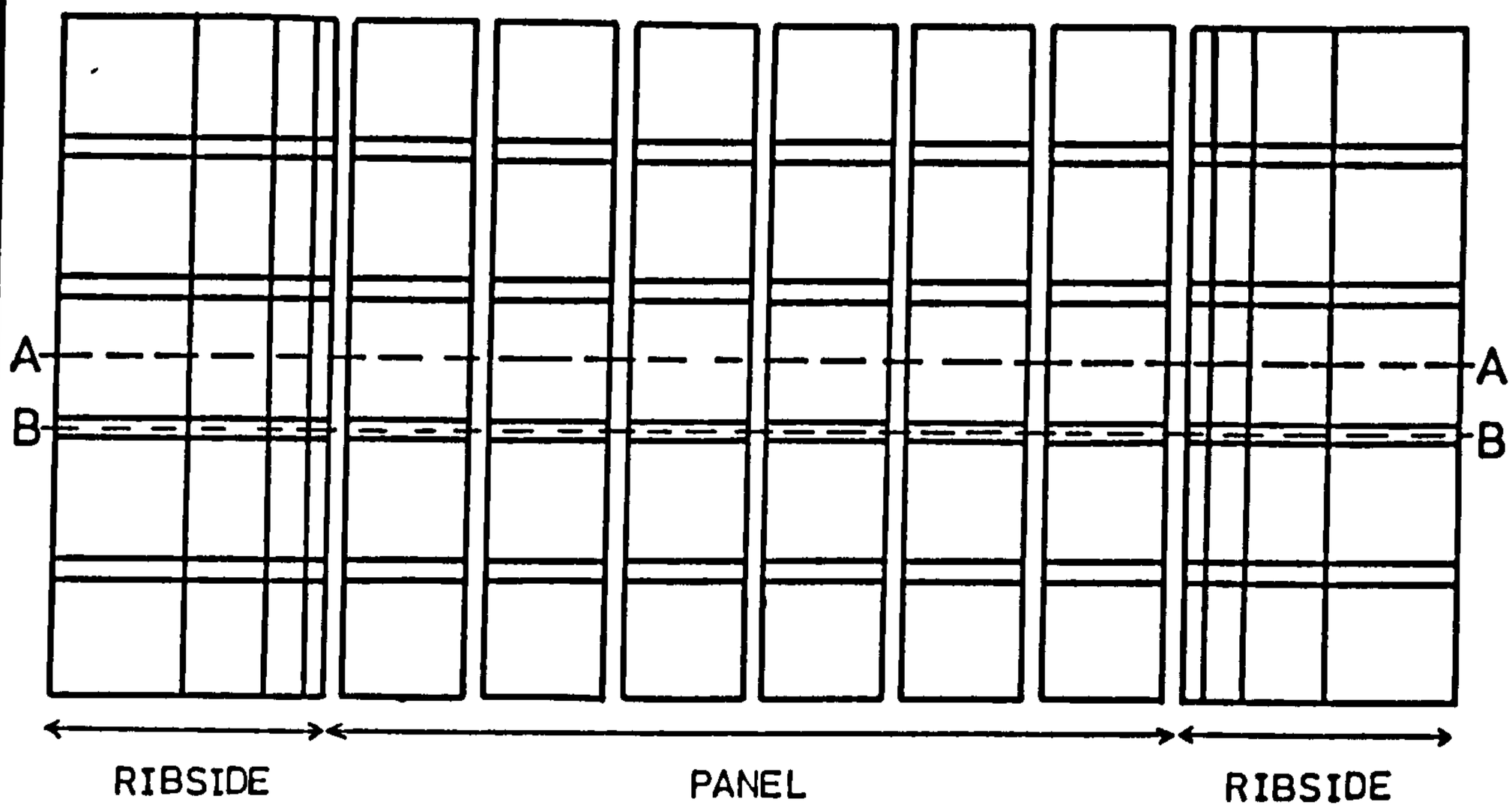

FIG. 3-8 LAYOUT 3 3D MESH (not to scale)

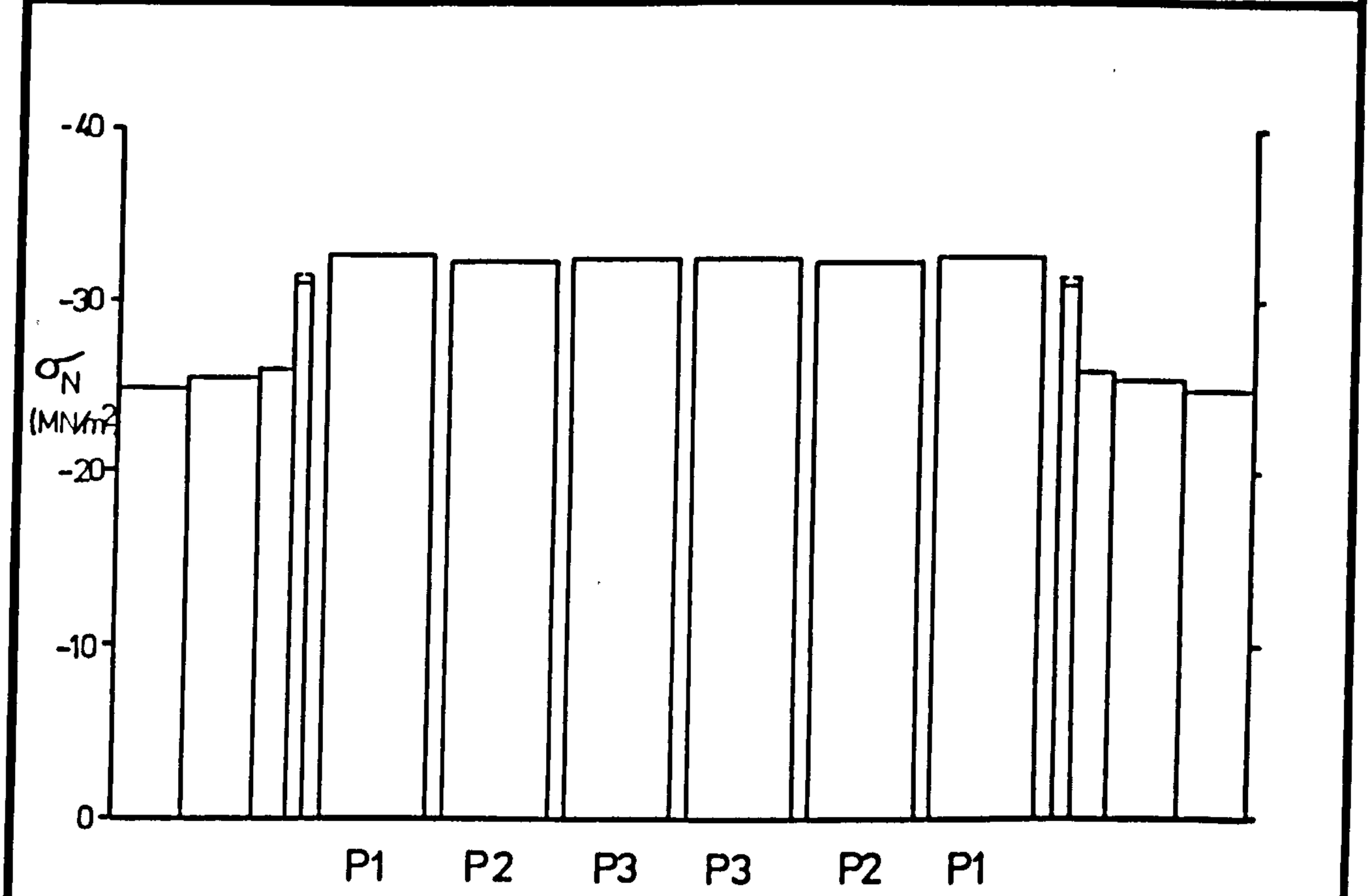

FIG. 3-9 LAYOUT 3 IN-SEAM NORMAL STRESSES

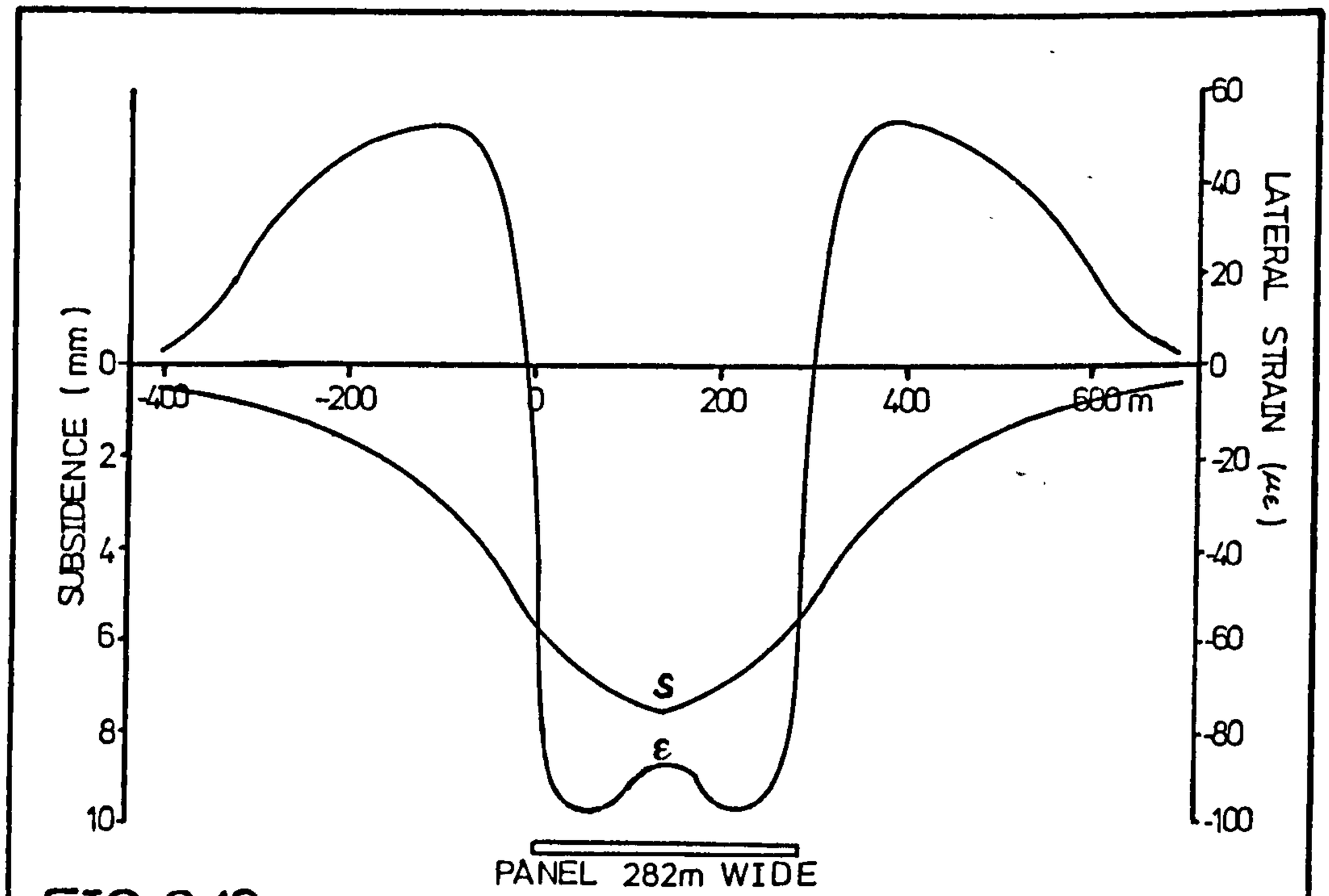

FIG. 3-10 SUBSIDENCE AND STRAIN 200m ABOVE LAYOUT 3

Fig. 3-10 shows the subsidence and lateral strain curves for layout 3.

3.3.4 Layout 4 - 7 Entries, 30m, 45m, 60m by 60m Pillars

Once again three compressible ribside zones have been used, in this case 5m, 10m, 45m wide. The panel layout has been varied in this layout to investigate the effect of a stiffer central region for central road protection. All the pillars are 60m long in the panel direction. Fig. 3-11 shows the mesh configuration while Fig. 3-12 shows the normal stress distribution.

The value of $\sigma_{T.A.}$ for this layout is -31.5 MN/m^2 which is based on uniform extraction across the panel width. This value

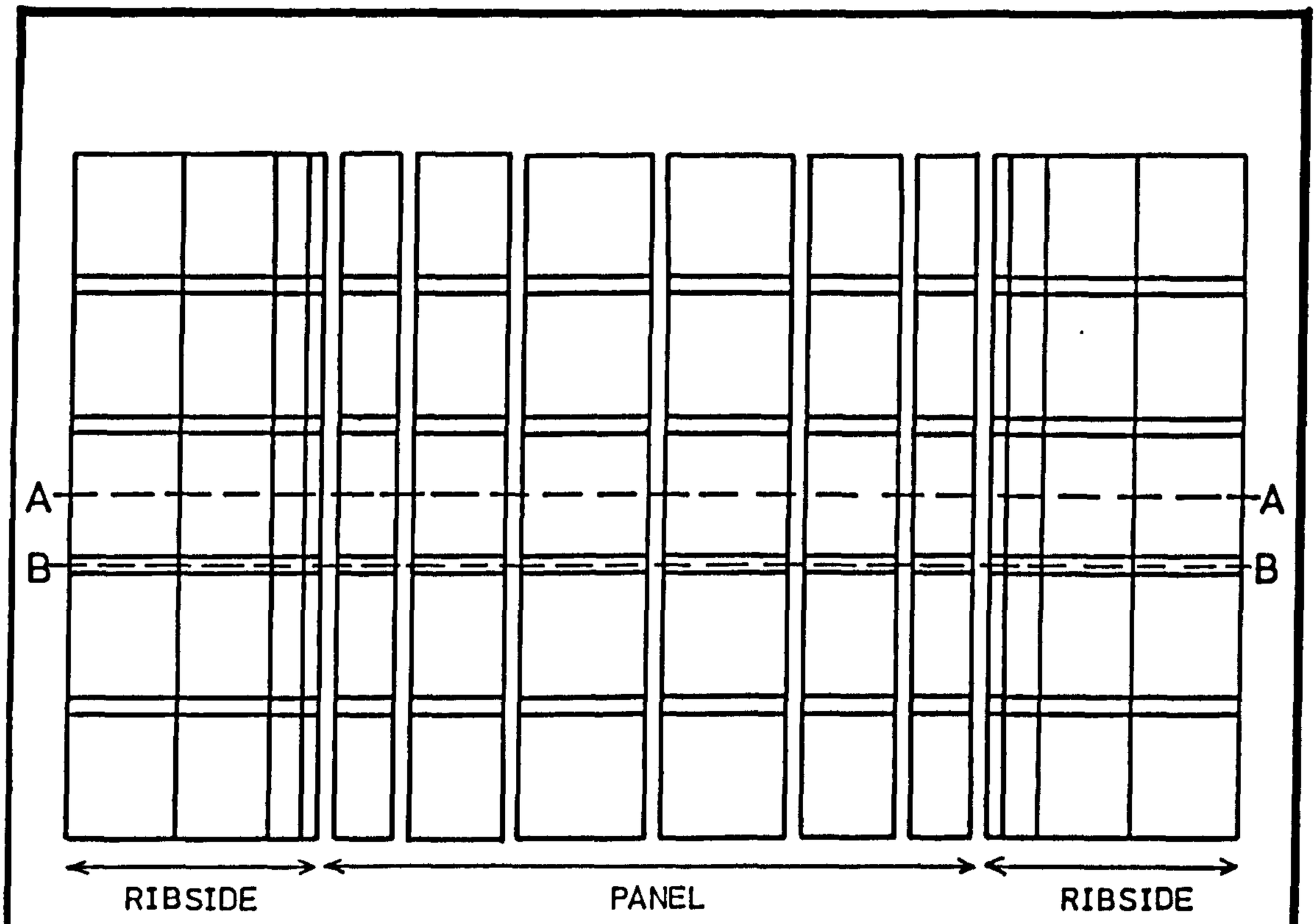

FIG. 3-11 LAYOUT 4 3D MESH (not to scale)

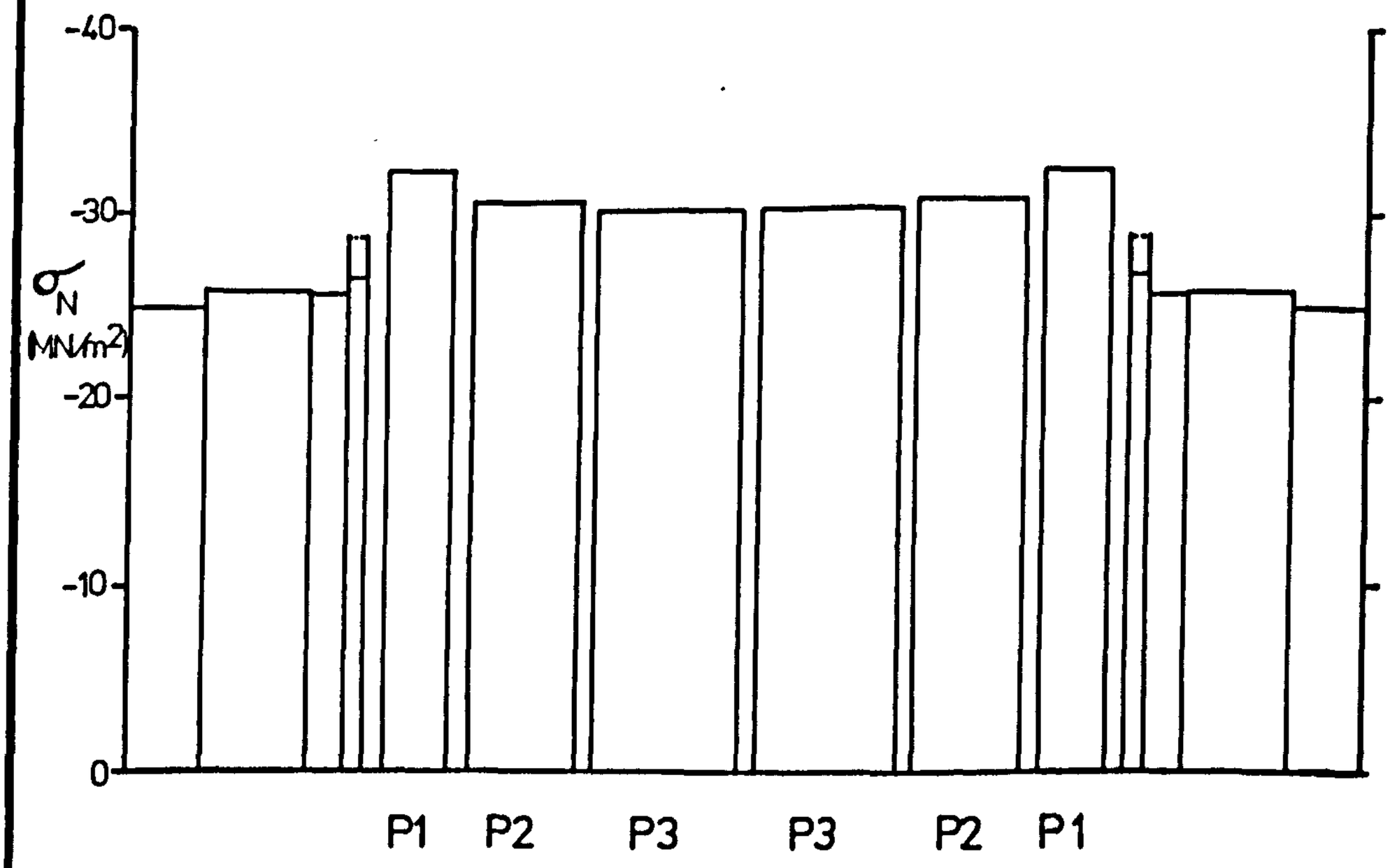

FIG. 3-12 LAYOUT 4 IN-SEAM NORMAL STRESSES

is lower than the actual stress on the outer pillars where extraction is higher than in the panel centre. This is the reason for the negative stress reduction factor in Table 3-8 which contains the stress results.

Table 3-8 Layout 4 In-Seam Stress Results

Panel Zone (AA and BB refer to Fig. 3-11)	σ_N (MN/m^2)	$\sigma_{Tang.}$ (MN/m^2)	$\sigma_{Dev.}$ (MN/m^2)	F_s	K (%)
1st Compr. Zone (AA)	-25.8	- 9.4	-16.4	3.29	
1st Compr. Zone (BB)	-25.8	- 9.4	-16.4	3.29	
2nd Compr. Zone (AA)	-25.6	- 9.2	-16.4	3.28	
2nd Ccmpr. Zone (BB)	-25.6	- 9.2	-16.4	3.28	
Ribside Zone (AA)	-26.5	-10.2	-16.3	3.34	
Ribside Zone (BB)	-28.8	-10.9	-17.9	3.14	
Pillar 1	-32.3	-13.8	-18.5	3.12	-2.5
Pillar 2	-30.7	-12.3	-18.4	3.12	2.5
Pillar 3	-30.2	-11.8	-18.4	3.14	4.1

The above seam results for layout 4 are for a horizon 200m above the seam and are presented in Table 3-9.

Table 3-9 Layout 4 Above Seam Results for 200m Horizon

	$S_{max.}$ (mm)	$S_{rib.}$ (mm)	S_{50} (mm)	S_{10} (mm)	$\varepsilon_{max.}$
Parameter	5.95	4.74	2.98	0.60	0.000051
X Co-ord. (m)	156	0	-94	-335	-140

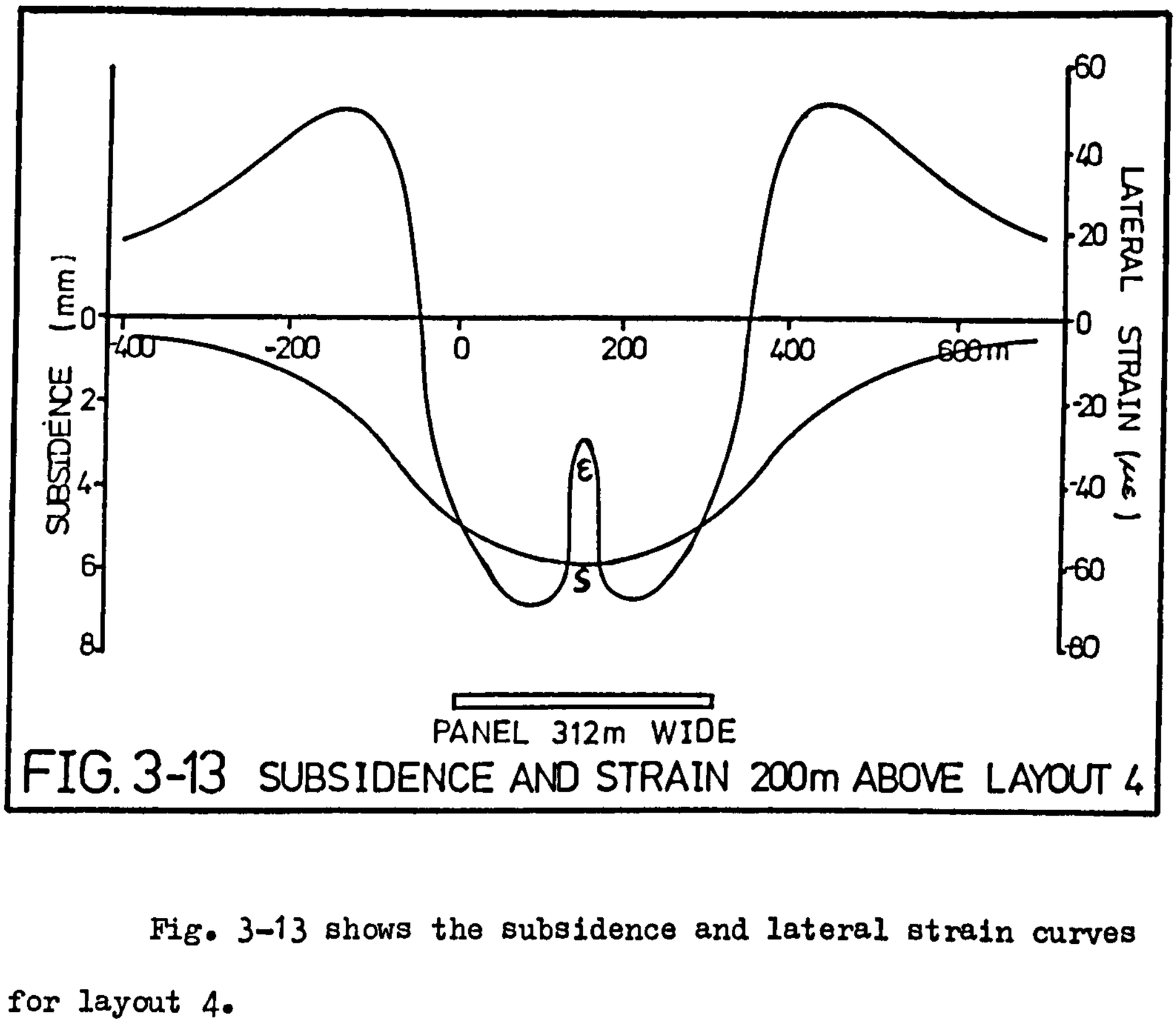

FIG. 3-13 SUBSIDENCE AND STRAIN 200m ABOVE LAYOUT 4

Fig. 3-13 shows the subsidence and lateral strain curves for layout 4.

3.3.5 Layout 5 - 11 Entries, 30m Square Pillars

This layout was the first to be analysed for a production panel, hence the larger number of entries and obviously higher extraction ratio. In this, and subsequent layouts, the ribside stress variation parallel with the panel direction has been neglected. However, in order to assess barrier pillar stability, more compressible ribside elements have been included. A total of five zones of compressible ribside have widths of 3m, 5m, 10m, 30m and 43m. Fig. 3-14 shows the mesh configuration while Fig. 3-15 shows the normal stress distribution.

The value of $\sigma_{T.A.}$ for this layout is -36.31 MN/m^2.

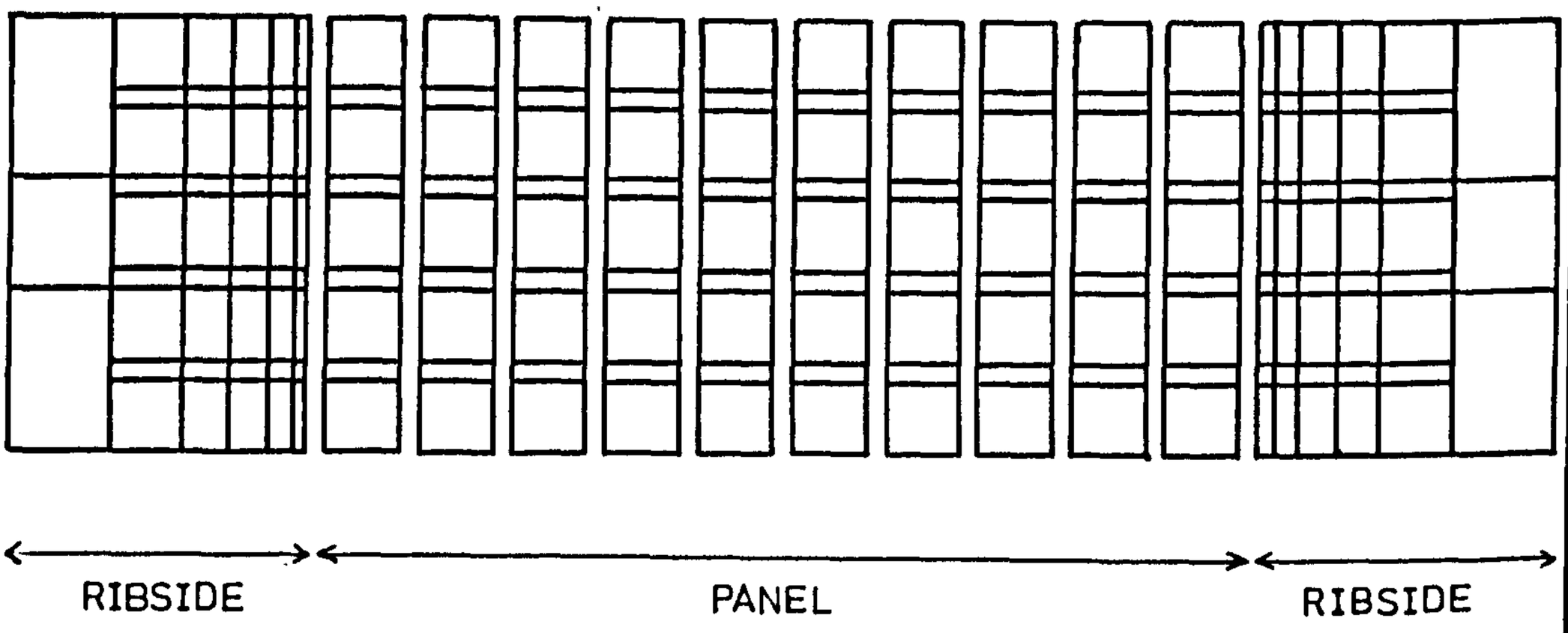

FIG. 3-14 LAYOUT 5 3D MESH (not to scale)

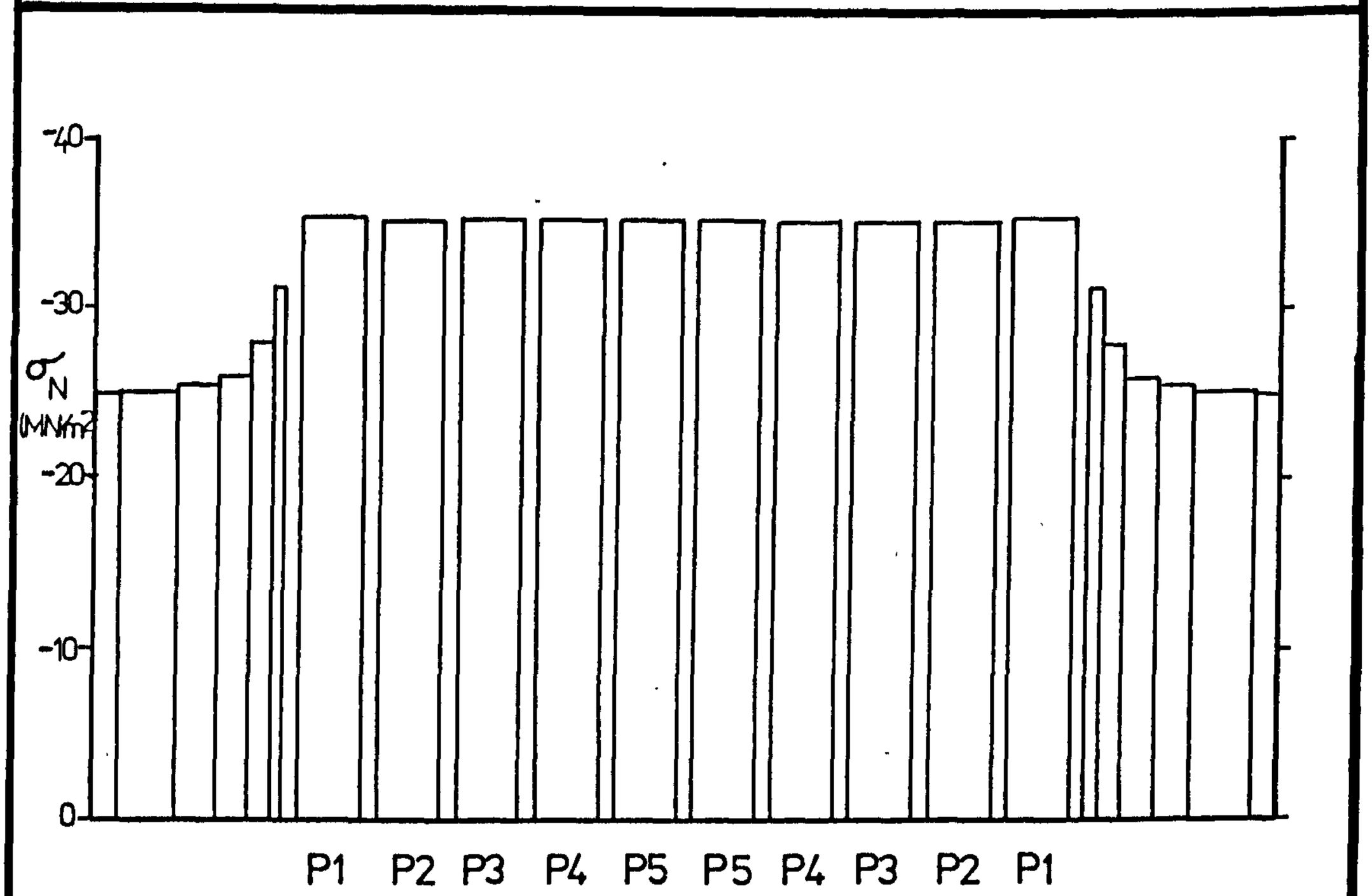

FIG. 3-15 LAYOUT 5 IN-SEAM NORMAL STRESSES

Table 3-10 contains the in-seam stress results which are quoted with an extra significant figure of accuracy from here on. This was due to increased field width of displacement output from the face element programs enabling better resolution of the influence matrix components. The previous layout analyses were less accurate, giving rise to slight fluctuations in stress which can be disregarded. The actual stresses derived were accurate to one more digit than is quoted in these tables and this accurate figure has been used to calculate the K factors.

Table 3-10 Layout 5 In-Seam Stress Results

Panel Zone	σ_N (MN/m^2)	$\sigma_{Tang.}$ (MN/m^2)	$\sigma_{Dev.}$ (MN/m^2)	F_s	K (%)
1st Compr. Zone	-25.00	- 8.50	-16.50	3.28	
2nd Compr. Zone	-25.46	- 8.96	-16.50	3.29	
3rd Compr. Zone	-25.95	- 9.45	-16.50	3.30	
4th Compr. Zone	-27.95	-11.45	-16.50	3.32	
Ribside Zone	-31.26	-14.76	-16.50	3.30	
Pillar 1	-35.25	-14.83	-20.42	2.95	2.92
Pillar 2	-35.11	-14.71	-20.40	2.94	3.30
Pillar 3	-35.17	-14.76	-20.41	2.94	3.13
Pillar 4	-35.20	-14.80	-20.40	2.95	3.04
Pillar 5	-35.22	-14.81	-20.41	2.95	3.01

The above seam results for layout 5 are for a horizon 200m above the seam. These results are contained in Table 3-11.

Table 3-11 Layout 5 Above Seam Results for 200m Horizon

	$S_{max.}$ (mm)	$S_{rib.}$ (mm)	S_{50} (mm)	S_{10} (mm)	$\varepsilon_{max.}$
Parameter	16.74	11.95	8.37	1.67	0.000072
X Co-ord. (m)	183	0	-65	-330	-120

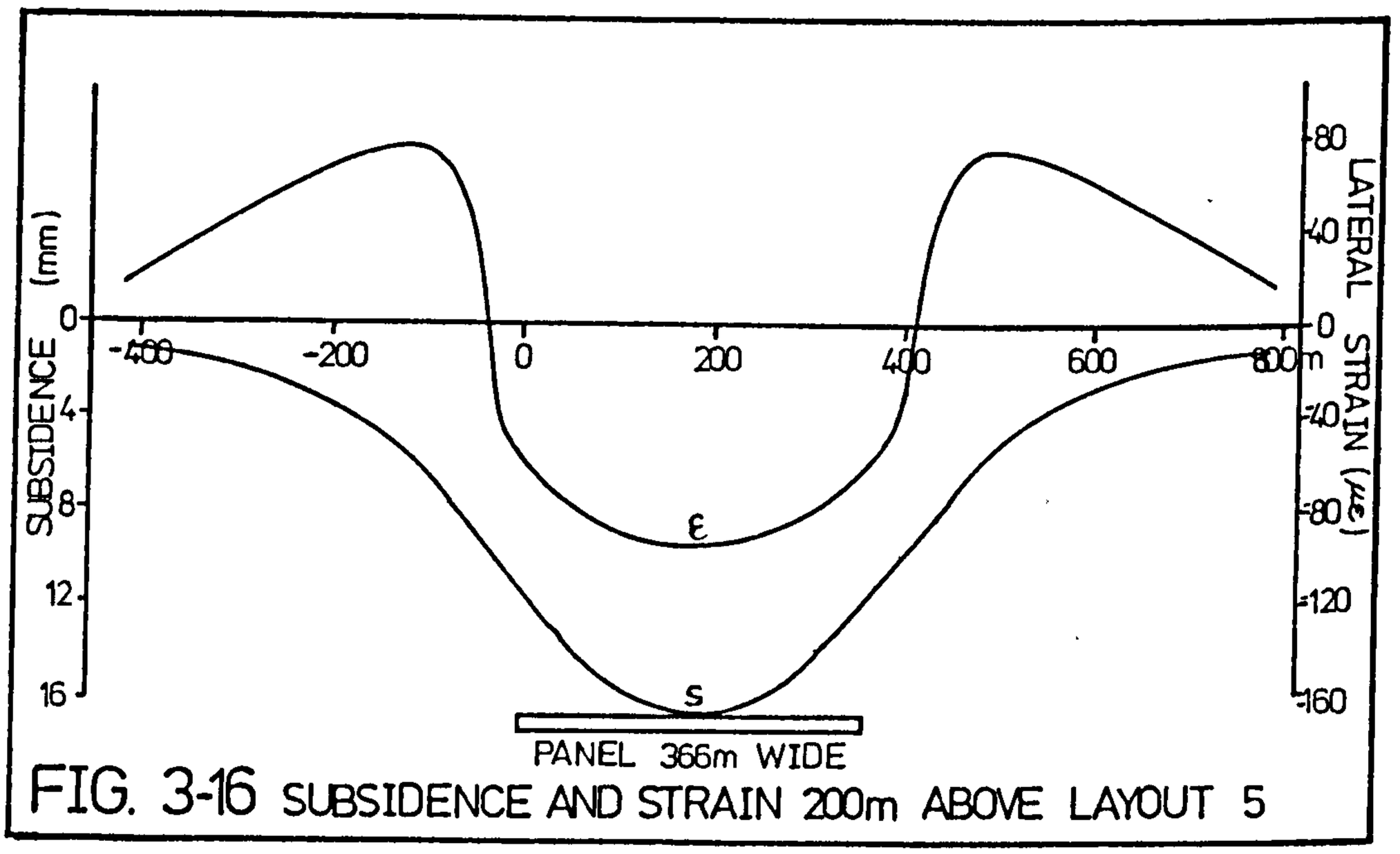

FIG. 3-16 SUBSIDENCE AND STRAIN 200m ABOVE LAYOUT 5

Fig. 3-16 shows the subsidence and lateral strain curves for layout 5.

3.3.6 Layout 6 - 11 Entries, 30m Herringbone Pillars

This layout represents a change to the herringbone concept of mining. This consists of inclining the cross-cuts at 60° to the panel direction rather than perpendicular to provide better ventilation and vehicle handling. Fig. 3-17

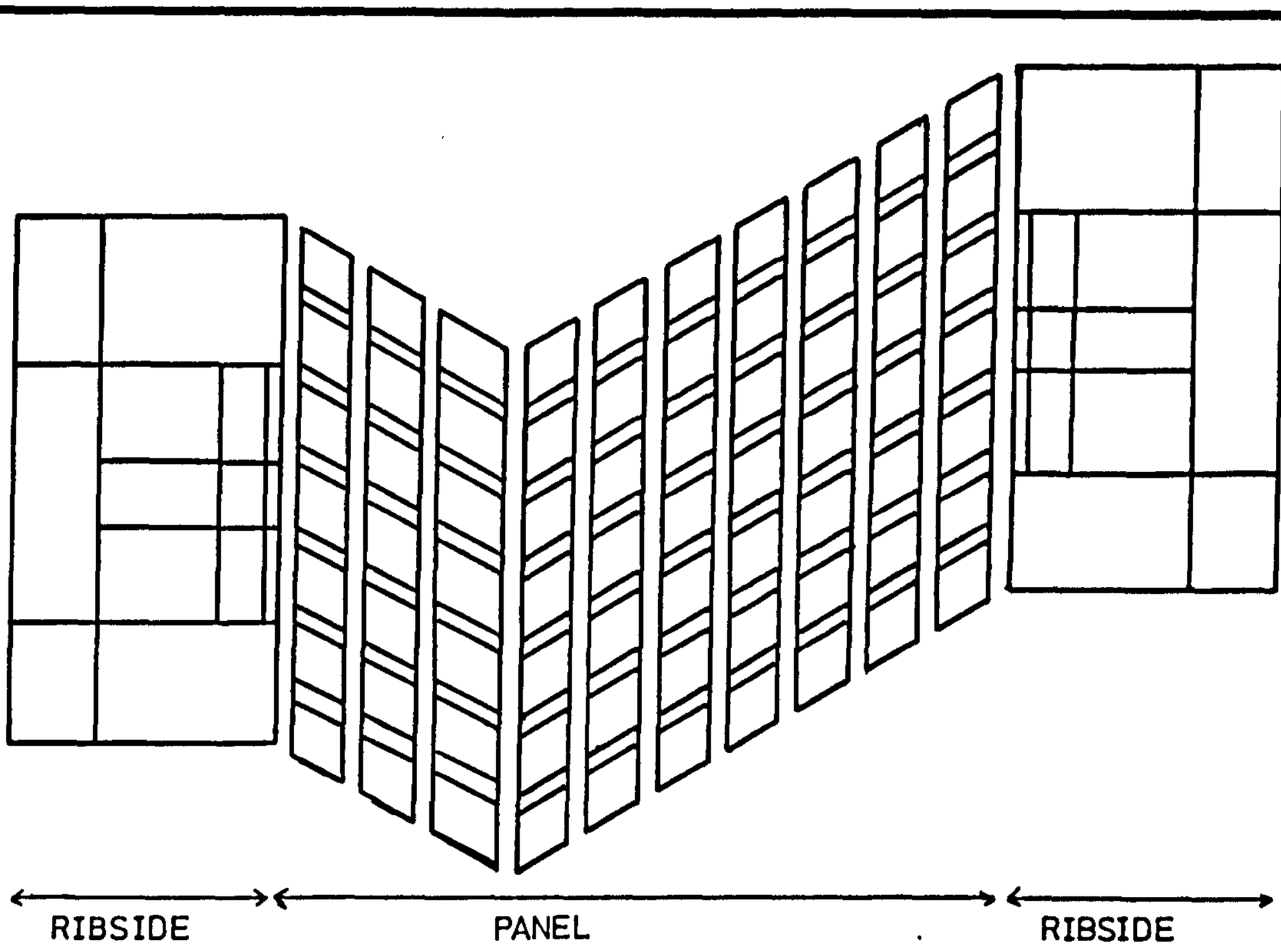

FIG. 3-17 LAYOUT 6 3D MESH (not to scale)

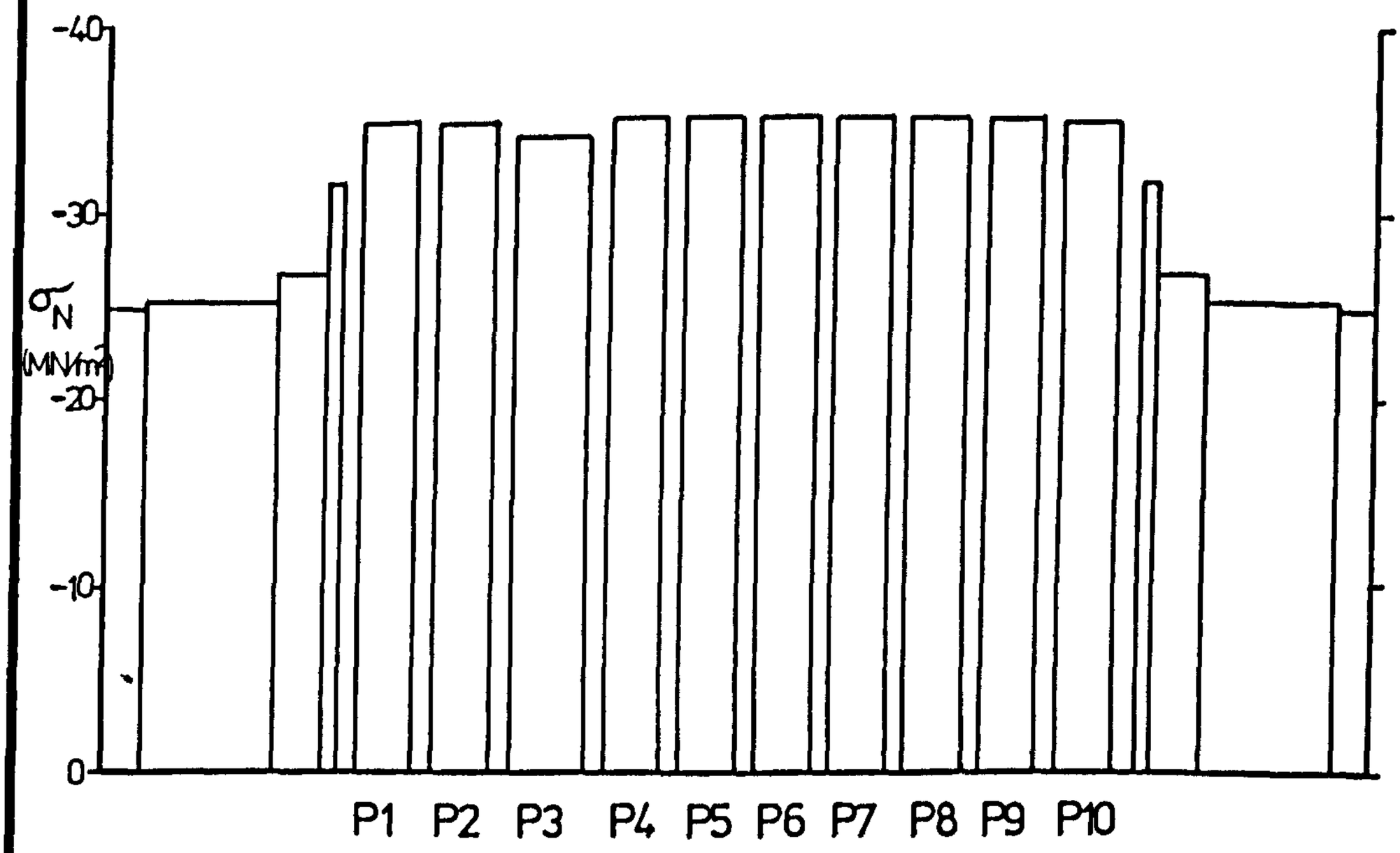

FIG. 3-18 LAYOUT 6 IN-SEAM NORMAL STRESSES

shows the mesh used for this layout. The layout was designed to provide basically the same strength of pillars as in layout 5. This was done by lengthening the dimension in the panel direction to 34m so that the shortest length between cross-cuts was still 30m and the total area was slightly greater.

The stable core concept can be represented geometrically by a circle within the pillar shape. This represents the area of pillar with minimal deviator stress where very little movement will occur compared with the sidewall movement. From early underground work a depth of 6m into pillar walls showed high deformation rates and obviously at corners the movement would occur even deeper due to greater stress concentrations. Therefore by removing 6m from each sidewall of the pillar and then drawing a circle inside that area an estimate of the probable confined core area can be obtained. For both the 30m square pillar and the 30m herringbone pillar an 18m diameter circle can be drawn representing 28% of the total square pillar area. Therefore it can be assumed that the main load bearing area of each of these pillar shapes is the same and so the resultant stresses provide a direct comparative measure of stability.

Another variation in this layout was that the main conveyor road, fourth from the left, was to be mined in the salt, 2m below the base of the potash and the next road to the right, a travel road, was to have its roof at the base of the potash. Each cross-cut had to drift up from the conveyor road into the potash on either side. This is the reason for the 40m pillar to the left of the conveyor road (pillar 3). The extra width was

necessary to provide sufficient cross-cut length at maximum gradient.

The face element technique used could incorporate the herringbone variation without any changes except that three pairs of balanced rows (rooms and pillars) were built into the mesh either side of the central pillar row instead of two. This was to ensure no boundary effects due to the closer proximity of the panel ends caused by angling of the rows. However, the variation of roadway elevations could not be incorporated in this type of model and so was neglected. The effect of this would be very small on the pillar loads.

The value of $\sigma_{T.A.}$ for this layout is -36.11 MN/m^2. Due to the lack of symmetry in this layout all the panel pillars and both ribsides had to be considered as separate variables. The normal stress distribution is shown in Fig. 3-18 and Table 3-12 contains the full in-seam stress results. Three compressible ribside elements were used on each side with widths of 4m, 16m, and 60m.

The above seam results for layout 6 are for a horizon 200m above the seam. These results are contained in Table 3-13. Two figures are quoted wherever the results refer to left and right hand ribsides, respectively.

Table 3-12 Layout 6 In-Seam Stress Results

Panel Zone	σ_N (MN/m^2)	$\sigma_{Tang.}$ (MN/m^2)	$\sigma_{Dev.}$ (MN/m^2)	F_s	K (%)
1st Compr. Zone	-25.22	- 8.72	-16.50	3.19	
2nd Compr. Zone	-26.78	-10.28	-16.50	3.26	
Ribside Zone	-31.66	-15.16	-16.50	3.26	
Pillar 1	-34.99	-14.60	-20.39	2.92	3.1
Pillar 2	-34.98	-14.59	-20.39	2.91	3.1
Pillar 3	-34.30	-13.99	-20.31	2.93	5.0
Pillar 4	-35.07	-14.67	-20.40	2.92	2.9
Pillar 5	-35.30	-14.88	-20.42	2.91	2.2
Pillar 6	-35.30	-14.87	-20.43	2.91	2.2
Pillar 7	-35.30	-14.87	-20.43	2.91	2.2
Pillar 8	-35.27	-14.85	-20.42	2.91	2.3
Pillar 9	-35.19	-14.78	-20.41	2.92	2.5
Pillar 10	-35.02	-14.63	-20.39	2.92	3.0
Ribside Zone	-31.66	-15.16	-16.50	3.26	
2nd Compr. Zone	-26.80	-10.30	-16.50	3.26	
1st Compr. Zone	-25.23	- 8.73	-16.50	3.19	

Table 3-13 Layout 6 Above Seam Results for 200m Horizon

	$S_{max.}$ (mm)	$S_{rib.}$ (mm)	S_{50} (mm)	S_{10} (mm)	$\varepsilon_{max.}$
Parameter	13.02	9.22 10.51	6.51	1.30	0.000067 0.000069
X Co-ord. (m)	220	0 0	-60 460	-350 765	-120 520

Fig. 3-19 shows the subsidence and lateral strain curves for layout 6.

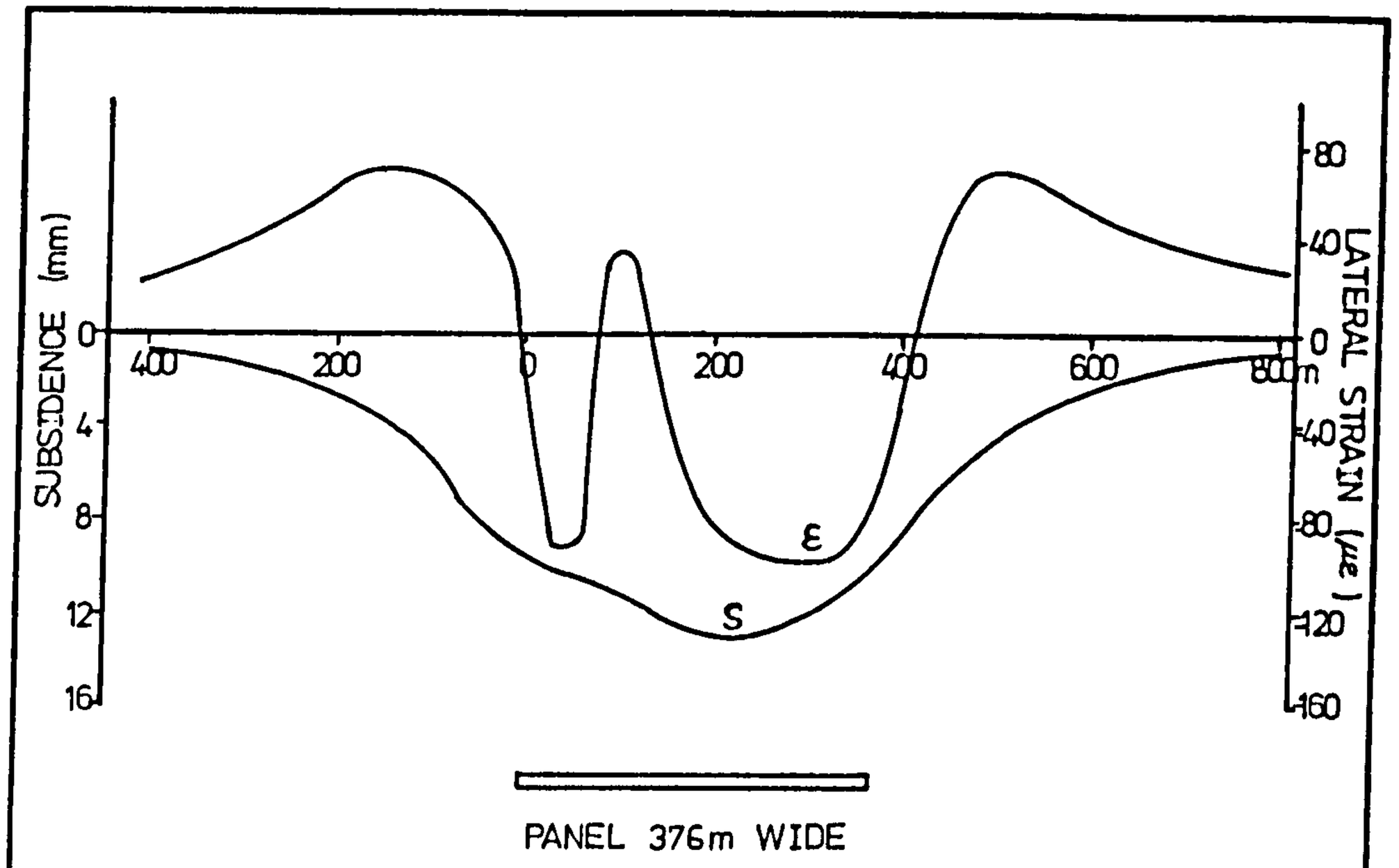

FIG. 3-19 SUBSIDENCE AND STRAIN 200m ABOVE LAYOUT 6

For the in-seam results of this layout a factor was introduced to modify the normal stresses to take into account overbreak in roadway dimensions. The 'overbreak' factor was calculated on the following basis.

i Reduce pillar sizes by 0.5m on all sides to allow for overwidth mining and excessive sidewall fracturing.

ii Reduce pillar sizes to allow for mining of equipment insets into two sides of each pillar, 5m by 1.5m each.

iii Reduce acute herringbone pillar corners by 2m along the pillar diagonal to allow for corner spalling.

The tangential stresses were not adjusted but the above reductions

resulted in an 8% area reduction for 30m herringbone pillars and 7% for the 40m herringbone pillars.

Obviously the overbreak factor in practice would lie somewhere between zero and the figure calculated on the above basis. Therefore, if a mid-range value of 4% was chosen the normal stresses increase by 4%, deviator stresses increase by approximately 7% and the safety factors reduce by approximately 3%. From these figures it becomes clear that the factors contributing to overbreak should be kept to a minimum wherever possible.

3.3.7 Layout 7 - 9 Entries, 24m Square Pillars

This layout returns to square pillars with only 9 entries. Once again five ribside zones have been used and they are 3m, 5m, 10m, 30m and 43m wide.

The value of $\sigma_{T.A.}$ for this panel layout is -39.72 MN/m^2. Fig. 3-20 shows the mesh used for this layout while Fig. 3-21 shows the distribution of normal stresses. The full in-seam stress results are contained in Table 3-14.

Unfortunately there was no subsidence analysis for this layout as it was only a hypothetical layout at the time.

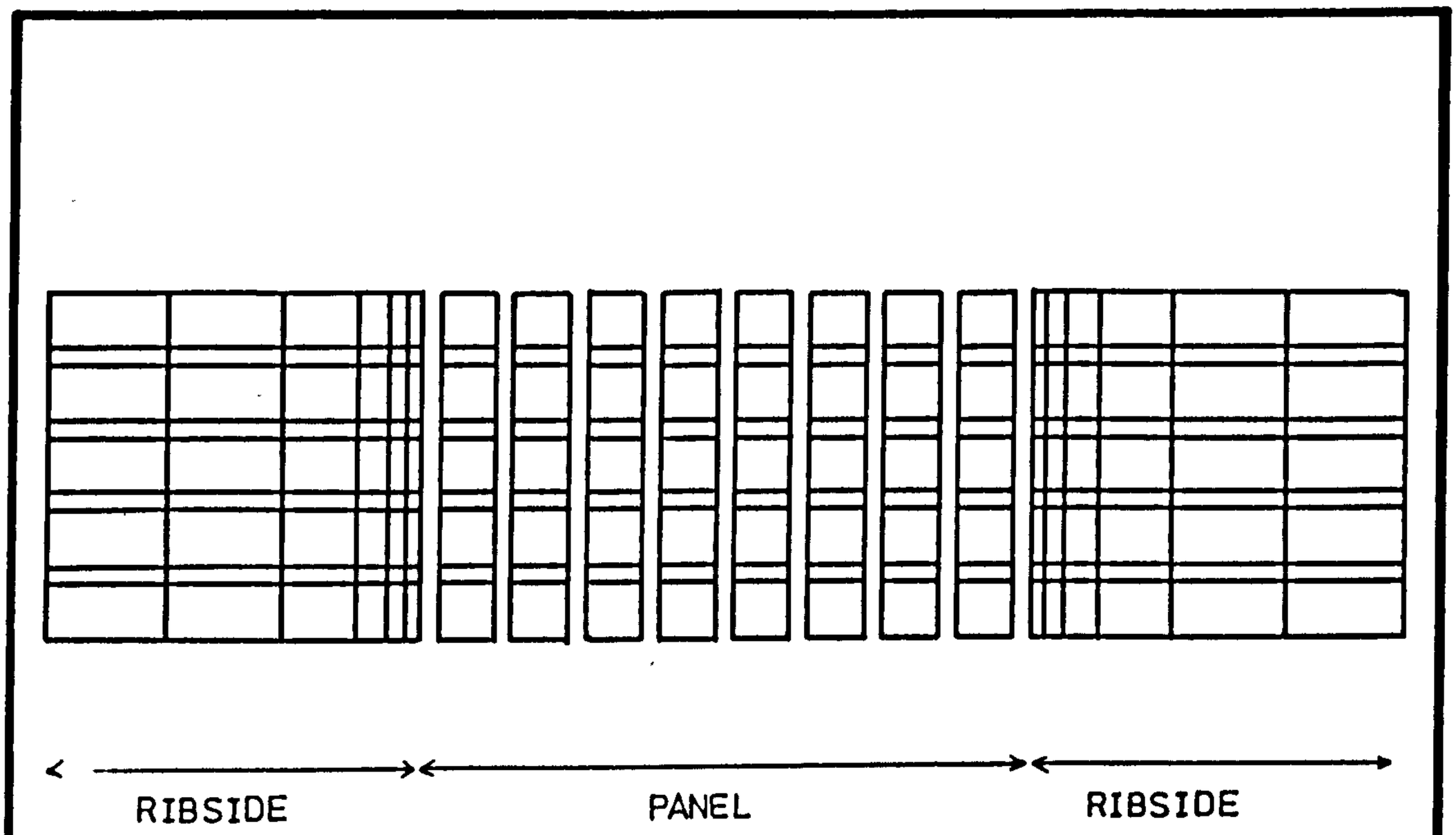

FIG. 3-20 LAYOUT 7 3D MESH (not to scale)

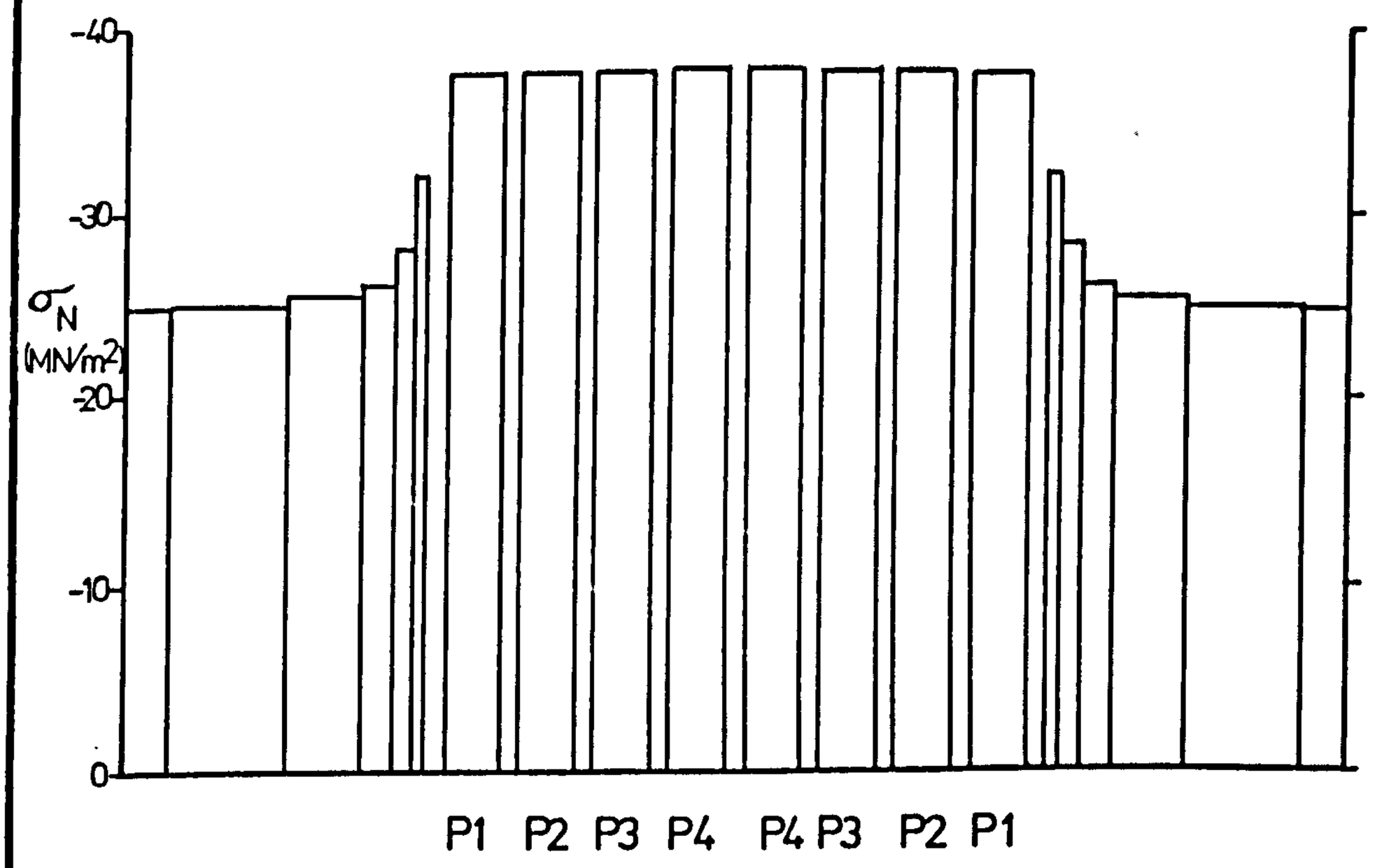

FIG. 3-21 LAYOUT 7 IN-SEAM NORMAL STRESSES

Table 3-14 Layout 7 In-Seam Stress Results

Panel Zone	σ_N (MN/m^2)	$\sigma_{Tang.}$ (MN/m^2)	$\sigma_{Dev.}$ (MN/m^2)	F_s	K (%)
1st Compr. Zone	-25.03	- 8.53	-16.50	3.22	
2nd Compr. Zone	-25.53	- 9.03	-16.50	3.21	
3rd Compr. Zone	-26.20	- 9.70	-16.50	3.21	
4th Compr. Zone	-28.46	-11.96	-16.50	3.30	
Ribside Zone	-32.35	- 9.38	-22.97	2.58	
Pillar 1	-37.73	-16.20	-21.53	2.85	5.0
Pillar 2	-37.82	-16.28	-21.54	2.85	4.8
Pillar 3	-37.92	-16.37	-21.55	2.85	4.5
Pillar 4	-37.95	-16.39	-21.56	2.85	4.4

3.3.8 Layout 8 - 7 Entries, 15m by 45m Herringbone Pillars

This layout once again adopted the herringbone concept with the same angle of 60° being used. For the analysis, five ribside zones were used, 3m, 7m, 10m, 30m and 50m wide.

The value of $\sigma_{T.A.}$ is -39.36 MN/m^2. Fig. 3-22 shows the mesh used for this layout while Fig. 3-23 shows the distribution of normal stresses. The full in-seam stress results are contained in Table 3-15.

The values of deviator stress and strength safety factor have been ommitted from the table due to the high values for $\sigma_{Tang.}$ which would lead to misleading results. For the same reason as ribside elements gave bad results for $\sigma_{Tang.}$, these

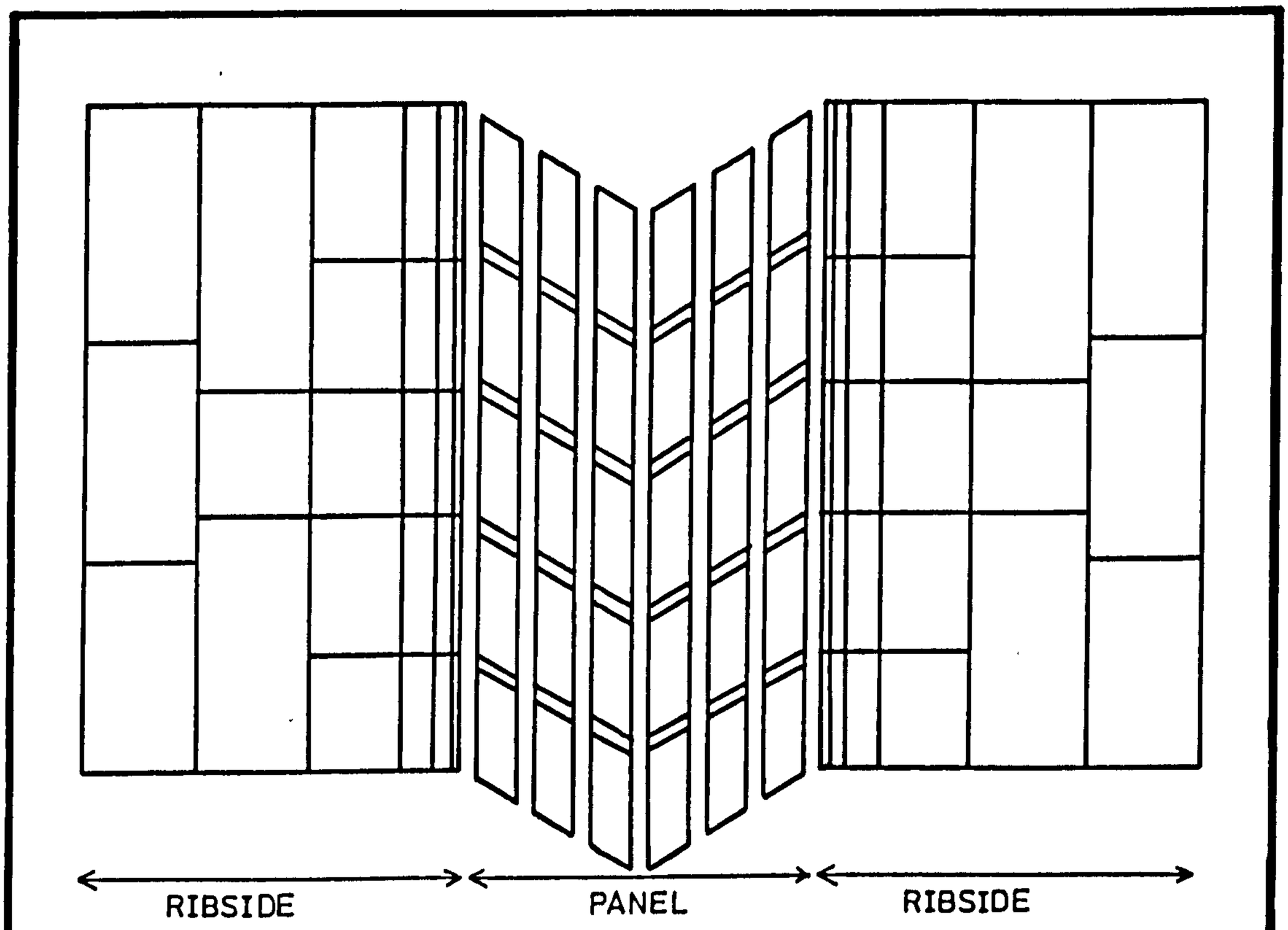

FIG. 3-22 LAYOUT 8 3D MESH (not to scale)

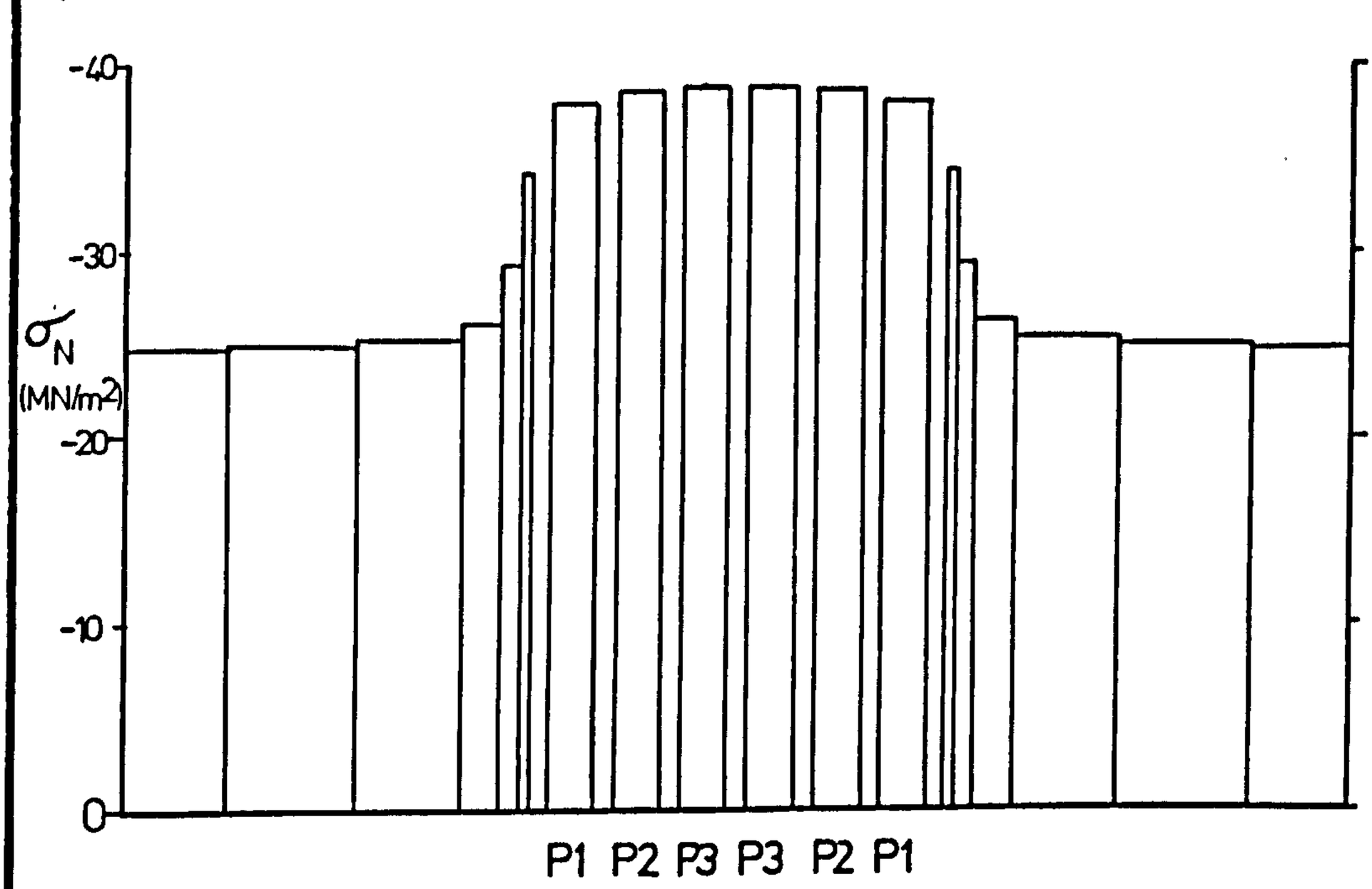

FIG. 3-23 LAYOUT 8 IN-SEAM NORMAL STRESSES.

long narrow pillar elements give excessive readings due to averaging over the whole element area. The high tangential stresses in the direction of the panel far outweigh the low stresses across the narrow width of the pillars resulting in the high average value.

Table 3-15 Layout 8 In-Seam Stress Results

Panel Zone	σ_N (MN/m^2)	$\sigma_{Tang.}$ (MN/m^2)	K (%)
1st Compr. Zone	-25.00	- 8.50	
2nd Compr. Zone	-25.44	- 8.94	
3rd Compr. Zone	-26.17	- 9.67	
4th Compr. Zone	-29.28	-12.78	
Ribside Zone	-34.30	-17.80	
Pillar 1	-38.00	-18.12	3.5
Pillar 2	-38.74	-18.81	1.6
Pillar 3	-38.77	-18.84	1.5

In order to obtain a more correct value of $\sigma_{Tang.}$ for the 15m pillar a series of two dimensional vertical plane strain analyses were carried out. A number of the layouts already analysed were re-assessed as if they were panels of long pillars with no cross-cuts. This was considered to give a better indication of pillar confinement for the long, narrow pillars since the minimum dimension of each pillar is the critical factor.

Fig. 3-24 shows the stress distribution obtained with bench marks through the mid-height of the central pillar of each panel considered. From these an average value for vertical and horizontal stresses has been calculated and these are listed in

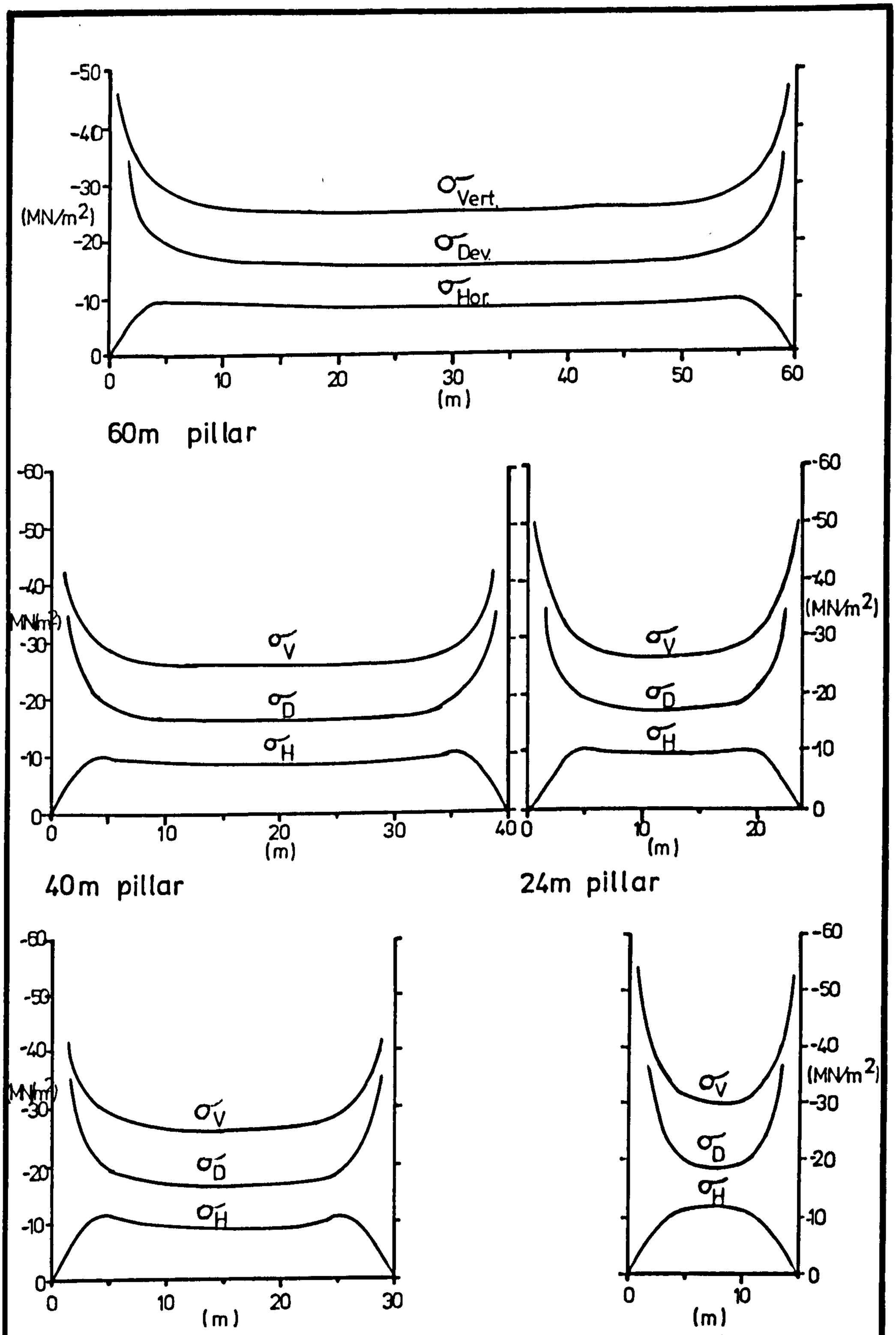

FIG. 3-24 STRESS DISTRIBUTION ACROSS PILLARS

Table 3-16.

Table 3-16 Average Pillar Stresses for Long Pillar Panels

Panel Type (No. of entries x minimum pillar width)	$\sigma_{Hor.}$ (MN/m^2)	$\sigma_{Vert.}$ (MN/m^2)	$\sigma_{Dev.}$ (MN/m^2)
5 x 60m	- 8.70	-27.11	-18.41
5 x 40m	- 8.89	-28.06	-19.17
11 x 30m	- 8.97	-29.30	-20.33
9 x 24m	- 9.10	-30.20	-21.10
7 x 15m	- 8.80	-34.50	-25.70

The deviator stresses obtained from the previous analyses for the central pillars of these panels were -18.4, -19.4, -20.41, -21.56 and -19.93 MN/m^2 respectively. The agreement is close for all but the last panel which is the one in question. The much lower value of $\sigma_{Hor.}$ for the 15m pillars verifies the previous reasoning that the stresses in the panel direction were causing the high average values in the three dimensional analysis. By applying the deviator stress from Table 3-16 to the normal stress in Table 3-15 (which takes into account cross-cuts) a more realistic value for $\sigma_{Tang.}$ across the minimum pillar width is obtained. This makes $\sigma_{Tang.}$ for the middle pillar -13.07 MN/m^2. The safety factor for the pillar becomes 2.42.

The above seam results for layout 8 are for a horizon 120m above the seam. From this layout onwards all subsidence analyses have been made for a 120m horizon. From the actual

subsidence curve, two strain determinations (described in Chapter 2) have been made representing the two extreme possibilities. A realistic estimate has been made by averaging the two values. Table 3-17 contains the subsidence results and they are plotted in Fig. 3-25. Strain curve A refers to the unrestrained strata interface (as for previous layouts) while curve B refers to the homcgeneous, fully welded type interface.

Table 3-17 Layout 8 Above Seam Results for 120m Horizon

	$S_{max.}$ (mm)	$S_{rib.}$ (mm)	S_{50} (mm)	S_{10} (mm)	$\varepsilon_{max.}$
Parameter	11.90	9.52	5.95	1.19	0.000101 (A) 0.000011 (B)
X Co-ord. (m)	66	0	-55	-210	-70 (A) -70 (B)

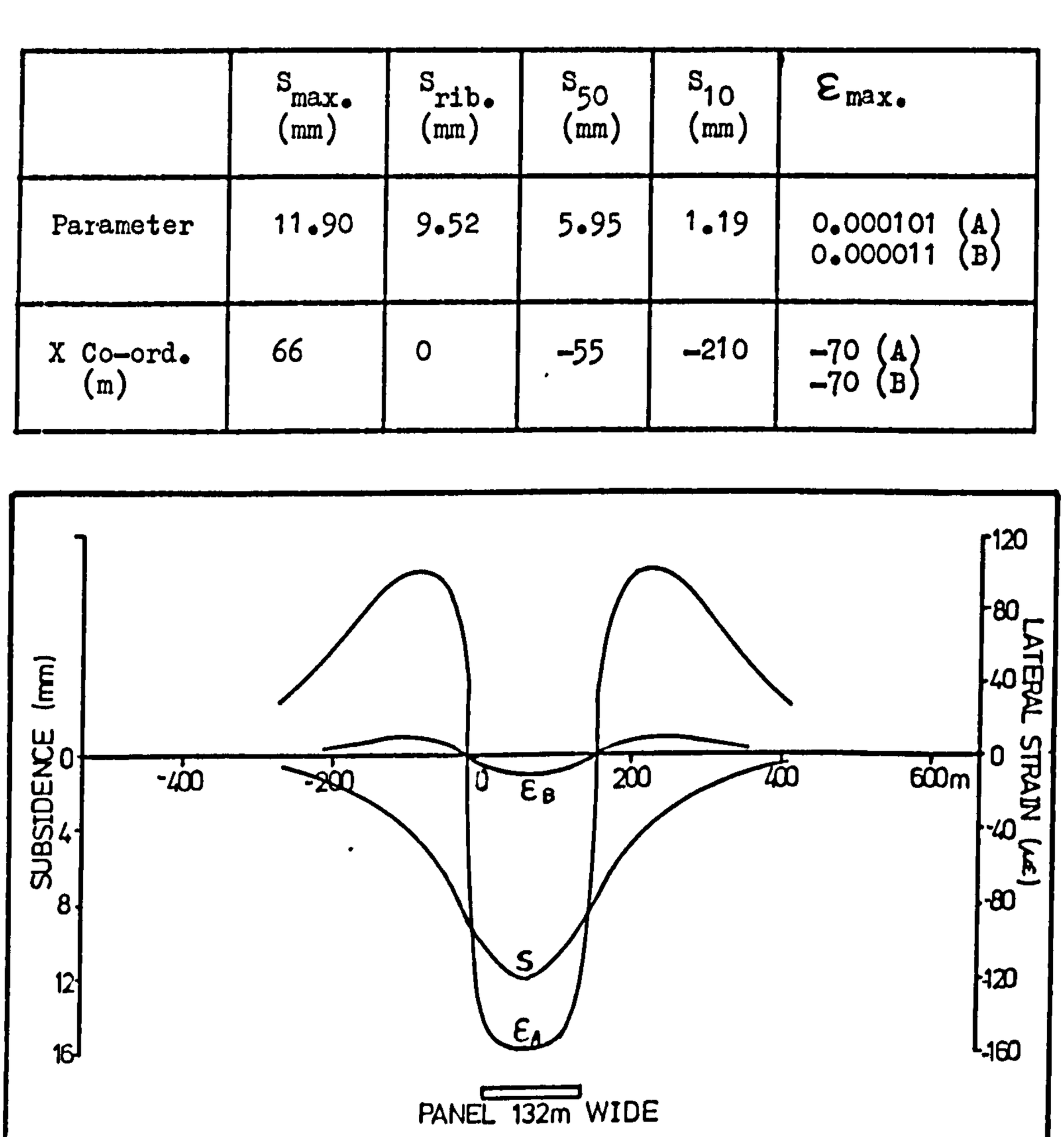

FIG. 3-25 SUBSIDENCE AND STRAIN 120m ABOVE LAYOUT 8

3.4 Comparison of Results

3.4.1 Panel Pillar Stability

The plotted results of normal stress distribution indicate a number of things concerning the panel geometries. Firstly, the slight variations in pillar stresses for the first four layouts should be disregarded as they are due to computer round-off error which was present in the early runs. Therefore, for the first three development panel layouts the stress distribution across the panel is uniform. This is due to the pillar sizes being sufficiently large so that the panel pillars are virtually as stiff as the ribside and no load build up occurs at the panel centres.

The pillar size variation in layout 4 shows a definite increase of stiffness in the panel centre due to 60m pillars protecting the central panel area. However, the smaller pillars near the ribsides are carrying very high stresses, possibly accentuated by excessive panel width.

Layouts 5 to 8 all show the characteristic of increasing stresses towards the panel centre due to the pillar stiffnesses being less than the ribside stiffness. The panel width in layout 5 appears to be excessive causing the outer pillars to carry very high loads. This would suggest that at least one pillar and road should be removed from each side reducing the panel width to 294m.

Layout 6 does not show the same problem as 5, although

the presence of the 40m pillar near the centre obviously stiffens the panel and shifts the peak stresses further to the right. Both layouts 7 and 8 appear to be within the critical panel width beyond which the load cannot be distributed away from the panel.

The K factors provide a measure of the effectiveness of the panel in redistributing load onto the ribsides. This is a function of extraction ratio within the critical width. The value of K for layout 8 is misleading due to the great length of the pillars relative to their width. This high ratio of length to width causes a lower extraction ratio although the stress distribution is not greatly affected until the length ratio is significantly reduced, the pillar width being the important dimension.

The effect of pillar shape on panel stability does not appear to be very significant in terms of the herringbone type layouts. Comparison of layouts 5 and 6 shows very little difference and so it can be concluded that provided the area of pillar core is not reduced then the angling of cross-cuts will not affect overall stability. However, excessive roof spans at herringbone roadway junctions could cause local instabilities.

A comparison of conditions for the central pillars of each panel provide the best indication of relative stability. Fig. 3-26 shows the relationship between the strength safety factor, F_s, and pillar width:height ratio. The latter is based on the minimum dimension of the panel pillars in each case. Fig. 3-26 also shows the influence of the overbreak factor on

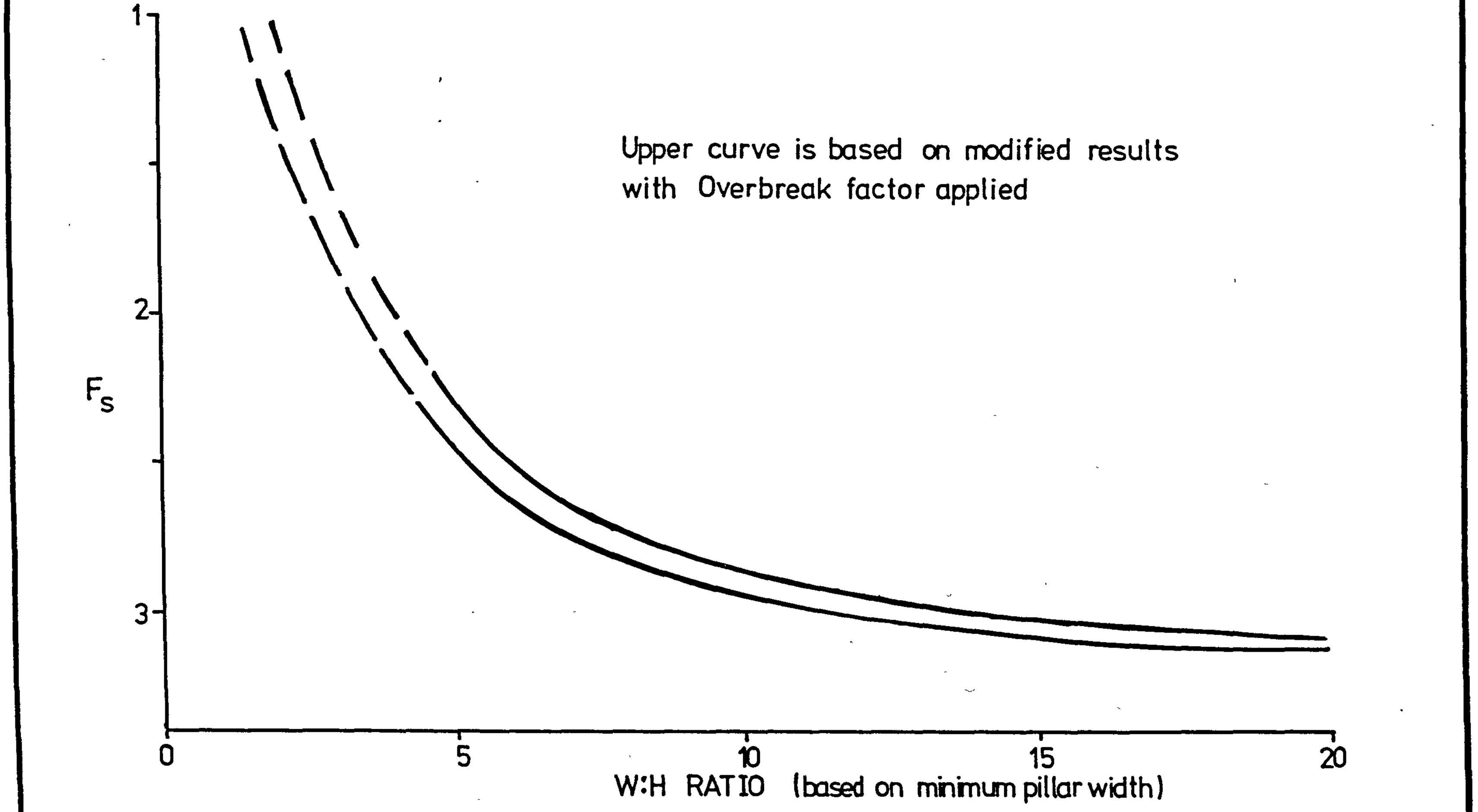

FIG. 3-26 STRENGTH SAFETY FACTOR (F_S) v. WIDTH:HEIGHT RATIO

this relationship. The mid-range factor has been applied in the way it was described for layout 6 and so the upper limit of the curve in this diagram should be used for interpretation.

In order to relate the pillar stress conditions to the time-dependent effects which will occur, Fig. 3-27 shows the relationship between average deviator stress and width:height ratio for the central pillars of each panel. Again the overbreak factor has been applied to this curve. Since the creep rate expected within these pillars is closely related to deviator stress, this curve gives a relative indication of the time-dependent yield which will occur with different sized pillars. This relationship is very important to the principle that these types of panels should consist of pillars with long term stability arising from triaxially confined cores. From the results plotted in Fig. 3-24 it can be seen that the deviator stress in the centre of the 15m pillars is as high as that within the outer 6m high creep zone of all the other pillar sizes. Obviously, 15m pillars (W:H ratio 5:1 in this analysis) will exhibit high creep rates throughout their width so that any core which may exist initially will diminish rapidly with time. The steep slope of Fig. 3-27 bears out this fact for the low width:height ratios.

From early work by Patchet (7) on model pillars and Cook (8) on triaxial creep of rocksalt with similar properties to potash, several parameters can be established. Patchet carried out tests (in excess of 500 days) showing that secondary creep strain rates of 5×10^{-6}/day and less for 10:1 width:height ratio pillars maintained long term stability and core confinement.

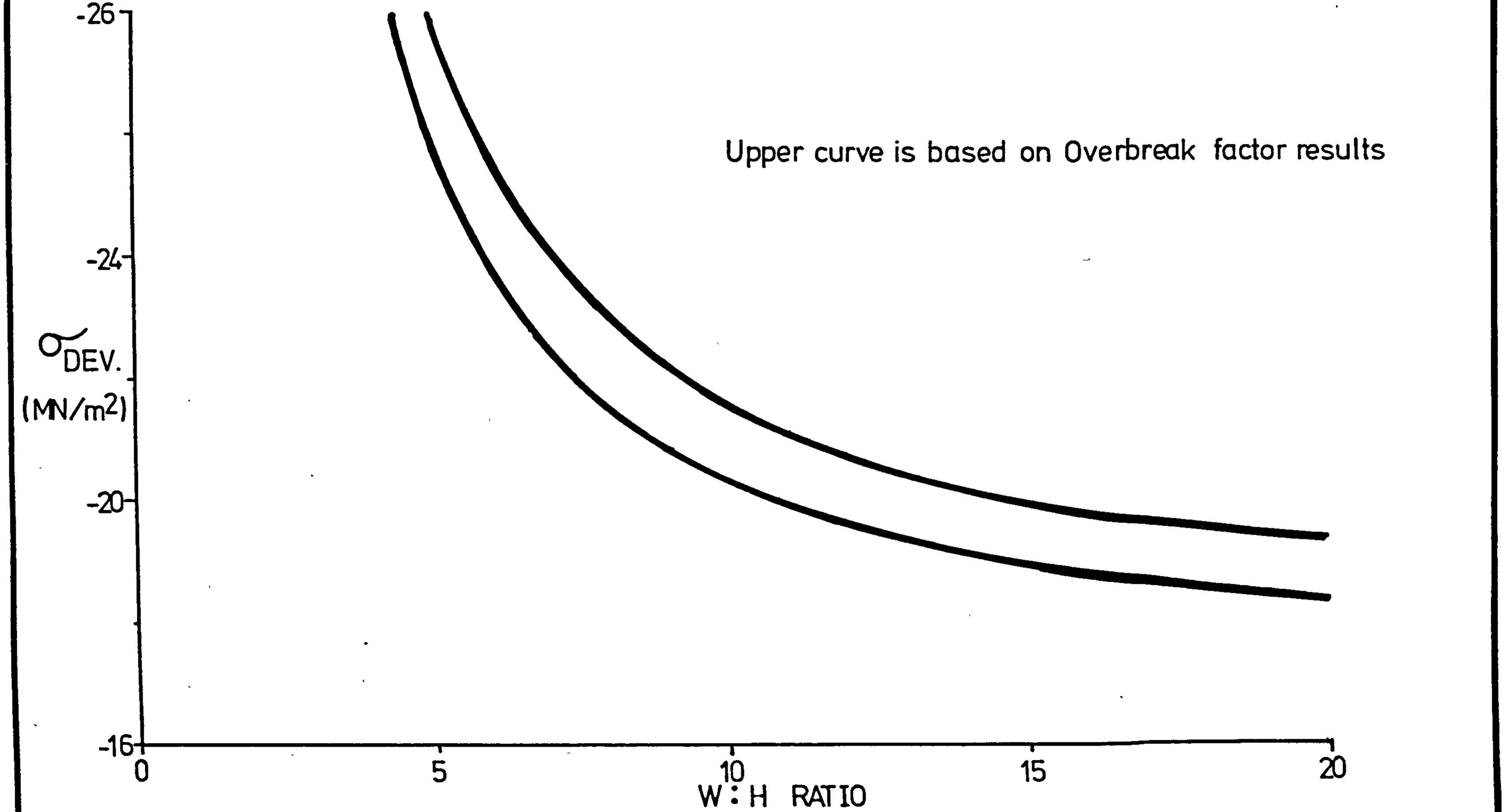

FIG. 3-27 AVERAGE PILLAR DEVIATOR STRESS ($\sigma_{DEV.}$) v. W:H RATIO

Cook's triaxial tests indicated that deviator stresses up to $-21\ MN/m^2$ could exist on specimens without the secondary creep strain rate exceeding 5×10^{-6}/day and once again these tests showed long term stability. A number of specimens with higher deviator stresses had equally low creep strain rates for times in excess of one year.

Numerous past and present tests of potash specimens from Boulby have indicated that deviator stresses up to $-10\ MN/m^2$ produce negligible creep effects. In these elastic analyses the in-situ virgin stress deviator has been assumed to be $-16.5\ MN/m^2$ at which it can be assumed that negligible creep would occur. Applying the $11\ MN/m^2$ range of deviator stress to this value gives a figure of $-27.5\ MN/m^2$ as being equivalent in this analysis to the figure found by Cook which represented the maximum deviator stress for long term stability. Therefore to relate the deviator stresses from this numerical modelling to a measure of time-dependent stability, an arbitrary safety factor, F_T, has been defined. When F_T equals 10 it represents an infinitely stable situation with a deviator of $-16\ MN/m^2$, and when F_T equals 1, for a deviator of $-27\ MN/m^2$, it represents the limiting value for long term stability. The relationship between F_T and $\sigma_{Dev.}$ is linear, as shown in Fig. 3-28.

Table 3-18 lists the values of F_T for the centre pillar of each of the layouts modelled.

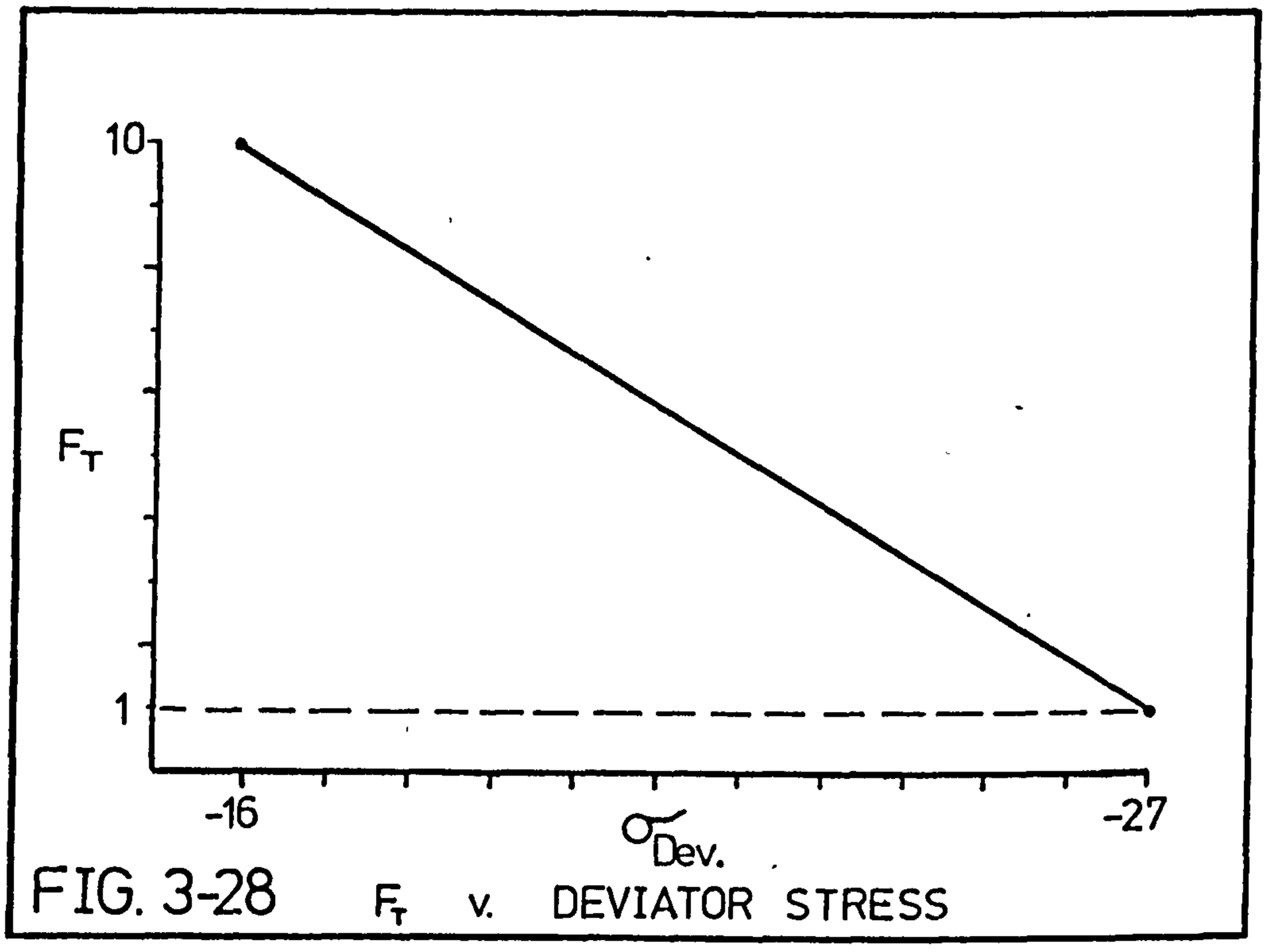

FIG. 3-28 F_T v. DEVIATOR STRESS

Table 3-18 Time-Dependent Safety Factors

Panel Layout No.	Width:Height Ratio	$\sigma_{Dev.}$	F_T
1	20:1	-18.4	8.0
2	13:1	-19.4	7.2
3	13:1	-19.3	7.3
4	-	-18.4	8.0
5	10:1	-20.41	6.4
6	10:1	-20.43	6.3
7	8:1	-21.56	5.4
8	5:1	-25.70	2.0

Fig. 3-29 shows the relationship between F_T and width:height ratio. The overbreak factor, as it affects deviator stress, has been applied to the curve and so the upper limit should be used. Obviously the end points of the F_T range have been chosen fairly

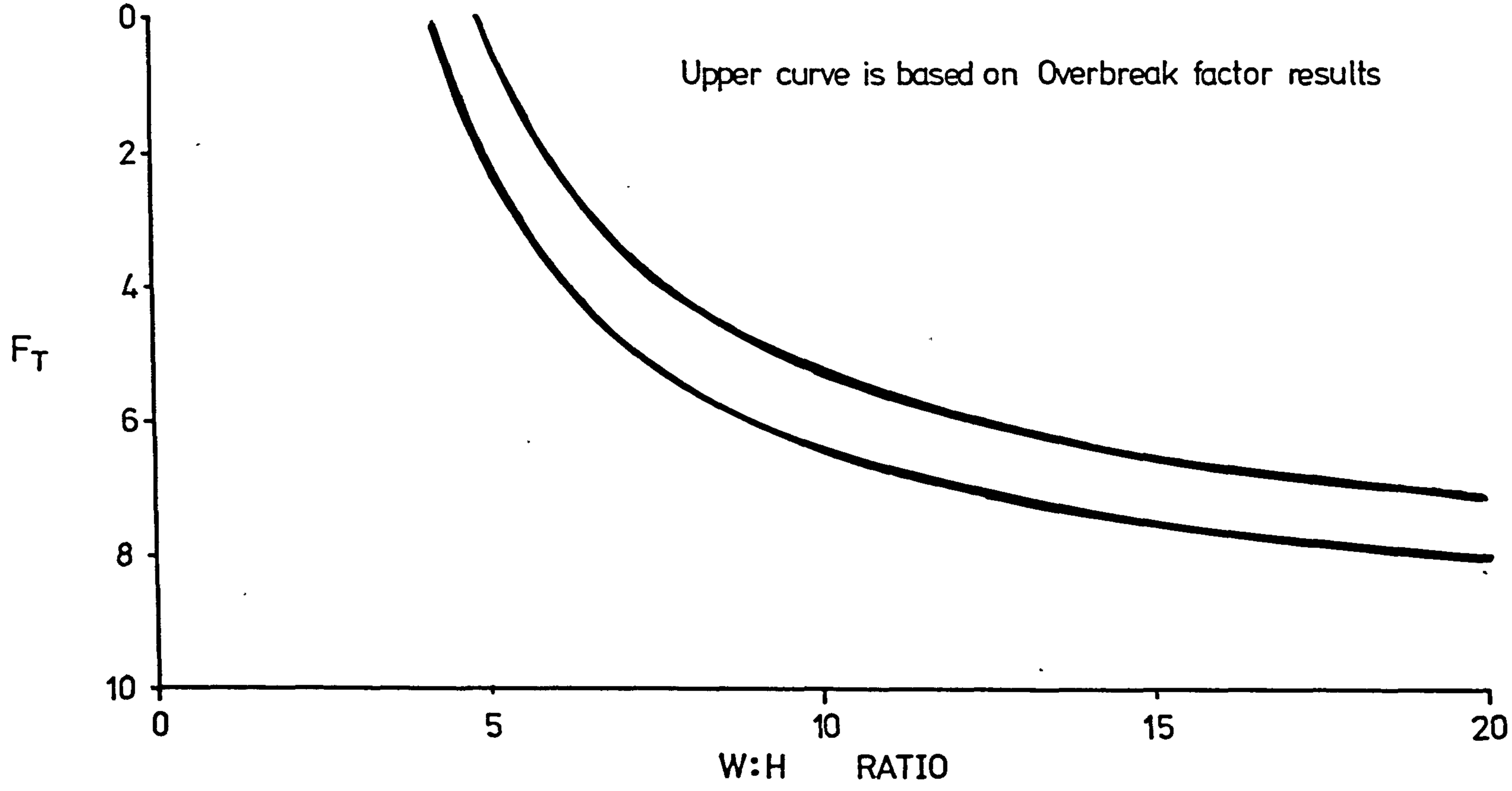

FIG. 3-29 TIME-DEPENDENT SAFETY FACTOR (F_T) v. WIDTH:HEIGHT RATIO

arbitrarily on the basis of laboratory test work and so a margin of safety should be allowed for in using this curve, especially since it approaches a vertical asymptote in the critical size region.

3.4.2 Barrier Pillar Stability

A number of rather empirical methods of barrier pillar width determination have been used in the past particularly for coal measures. These have included the pressure arch theory (28) which states that

$$B = \frac{W + P}{2} \qquad (3.4)$$

where B is the barrier width

P is the panel width ($\leq 0.75 \times W$)

W is the maximum pressure arch width,

where $W = 3(\frac{D}{20} + 20)$ (3.5)

where D is the depth to seam, in ft.

Another method, from the U.S.A., the Mines Inspectors' formula (29) states that

$$B = 20 + 4T + 0.1D \qquad (3.6)$$

where T is the seam thickness (ft.)

D is the depth to seam (ft.)

A third method, Holland's formula (30), uses measured

convergence data and predicts the barrier width as

$$B = 5\left(\frac{\log 2W_2}{0.09 \log e}\right) \qquad (3.7)$$

where W_2 is a convergence figure form Holland's table and

e is the base of the natural logarithm system.

These three methods predict barrier widths of 160m, 128m and 138m for the Boulby data although all are based on high extraction coal mining panels.

A fourth, more complicated method was devised by Wilson (31) based on a triaxial failure criterion. Wilson relates failure stress to confining pressure by a straight line with slope $\tan\beta$. His entire solution is extremely dependent on this value of $\tan\beta$. However, for potash, this linear relationship does not exist and so $\tan\beta$ cannot be defined accurately enough to use this method with any confidence.

In each of the layouts modelled in the present analysis, the stress distribution at depth into the barrier pillars has been very small. This is also evidenced by the low values of the K factor which represents the amount of excess load to be carried by the ribside barriers.

These values of K can be used to formulate a method of barrier pillar width determination. Assume that similar panel geometries are aligned in series with equal sized barriers between. Therefore the entire load redistributed from a panel can be carried by two half barriers. For the purposes of this model the load redistributed from one panel can be considered to be

carried by one barrier pillar of width, B.

For a panel with rows of n pillars, pillar areas A_i, factors K_i and a value of $\sigma_{T.A.}$ for the panel can be defined. The repetitive distance in the panel direction is ℓ (one pillar length plus one cross-cut). The load per unit length of panel, R, which is thrown onto the barrier, may be defined as,

$$R = \left(\sum_{i=1}^{n} K_i A_i\right) \sigma_{T.A.} / \ell \qquad (3.8)$$

Table 3-19 lists the values of R obtained from the results of each layout analysed.

Table 3-19 Barrier Loading Factor

Panel Layout No.	$\sigma_{T.A.}$ (MN/m^2)	R (MN/m)
1	-30.7	-131
2	-33.9	-186
3	-33.5	-210
4	-31.5	-162
5	-36.31	-280
6	-36.11	-277
7	-39.72	-287
8	-39.36	- 69

In order to generalise this relationship, assume that there is a constant value of K for each panel geometry. Then equation (3.8) may be redefined as

$$R = \left(\sum_{i=1}^{n} A_i\right) K \sigma_{T.A.} / \ell \qquad (3.9)$$

But in terms of panel width, W, and extraction ratio, e, the following relationship may be substituted.

$$\sum_{i=1}^{n} A_i = (1 - e) W \ell \qquad (3.10)$$

Also, by substituting the original definition of $\sigma_{T.A.}$ (equation (3.2)) then the definition of R reduces to

$$R = W \sigma_v K \qquad (3.11)$$

Fig. 3-30 shows the relationship between the average K values for the panels modelled and the panel extraction ratio. This appears to be quite linear provided the panel width is within certain limits. Layout 2 appears to be too narrow therefore giving an unusually high value of K whereas layout 5 is definitely too wide hence the lower value.

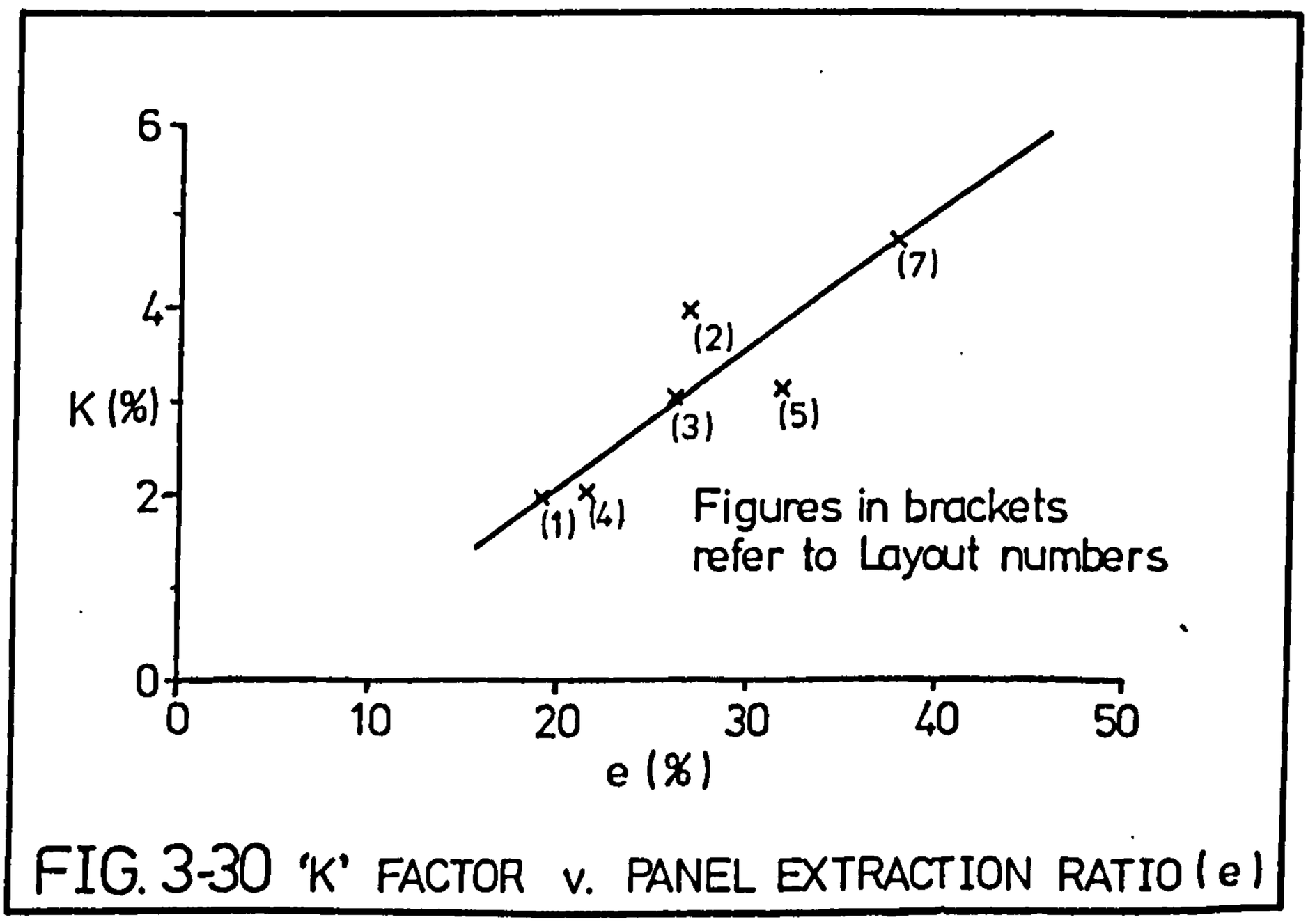

FIG. 3-30 'K' FACTOR v. PANEL EXTRACTION RATIO (e)

The relationship defined by Fig. 3-30 corresponds purely to the elastic load redistribution. For long term stability panels which satisfy the relationship in Fig. 3-29, K has a maximum of approximately 5%. In order to define a barrier pillar width with similar long term stability and central core confinement the value of K should be increased, say by a factor of 2. This should represent the total amount of load which the pillars will throw onto barriers on a long term basis, i.e. up to 10% of $\sigma_{T.A.}$. There is no reason to expect a higher figure here since the immediate roof strata at Boulby have an apparent stiffness less than that of the potash. Therefore most of the time-dependent load redistribution will be localised and minimal rather than in the form of a large scale roof beam effect across the panel width. The time-dependent value of R therefore becomes

$$R = 2W \sigma_v K \qquad (3.12)$$

This can be used to define a minimum barrier width by using the normal tributary area stress for a pillar with width: height ratio of 20:1 and applying an overbreak factor. The stability of such pillars (60m square) in the early shaft pillar investigations underground is obviously sufficient. By equating the average stress for such pillars to the virgin stress plus that defined by R over a barrier width B, the value of B may be determined.

$$1.30(\sigma_v) = \sigma_v + \frac{2WK}{B} (\sigma_v) \qquad (3.13)$$

By dividing by σ_v and rearranging, B is defined as

$$B = 6.67\ WK \qquad (3.14)$$

Reverting to Fig. 3-30, the relationship between K and e can be defined as

$$K = 0.15e - 0.01 \qquad (3.15)$$

Therefore the barrier pillar width can be defined in terms of panel extraction ratio and panel width as

$$B = W(1.00e - 0.07) \qquad (3.16)$$

Several important points must be made in conjunction with the interpretation of equation (3.16).

Firstly, it only applies to long term stability panels as defined by Fig. 3-29. Secondly, the value of W must include any additional short cross-cuts mined into the panel ribsides and the width of B must be taken from the extremities of such cross-cuts. Thirdly, any roadways mined through the barriers must be compensated for by an equivalent increase in barrier size, on an extraction ratio basis. Fourthly, a minimum barrier size of width:height ratio 16:1 should be used regardless of what equation (3.16) predicts. Finally, the barrier pillar must be wider than the pillar sizes within the panel to ensure greater stiffness and hence correct stress distribution.

The minimum barrier widths determined by this method represent basic load carrying ribs between stable panels. Where a major development entry is to be passed between two such panels, the barrier width determined above should be applied either side of the development entry. Similarly, where major

boundary pillars are required to isolate blocks of panels in the event of major panel collapse or water inrush, the double barrier width should be used as a minimum.

3.4.3 Above Seam Stability

The results of the above seam analyses for these layouts provide specific information on subsidence-induced strains for 200m above the seam. It has since been decided that the 120m horizon should be used as the level at which all lateral strains should be minimised. One important point concerning the six layouts analysed for 200m is that the peak strain occurred above a point 120m (±20m) into the ribside in each case. This represents an angle of draw of 31°. Similarly for layout 8 analysed at 120m, the peak was 70m into the ribside, an angle of 30°, which agrees well with the previous figure.

On the basis of this figure, barrier pillar dimensions in the vicinity of 140m will obviously produce the maximum lateral strain at 120m above the seam since the peaks induced by each panel will be superimposed on each other.

Obviously the local panel extraction ratio and geometry play an important part in the subsidence effects above the seam. However, to provide a comparative measure of subsidence strains caused by different barrier and panel widths, a two dimensional vertical plane strain analysis was implemented. Panels were considered as single excavations which would represent the maximum level of time-dependent pillar yield which might occur

within a panel. A block of four panels was modelled and for each panel width, seven different barrier widths were used. Panel widths modelled were 80m, 120m, 160m, 200m, 240m, 280m and 360m. For each run, the subsidence at 120m was analysed using the two methods described previously and an average value obtained for lateral strain. Fig. 3-31 shows a typical set of results obtained for the lateral strains above a 240m panel.

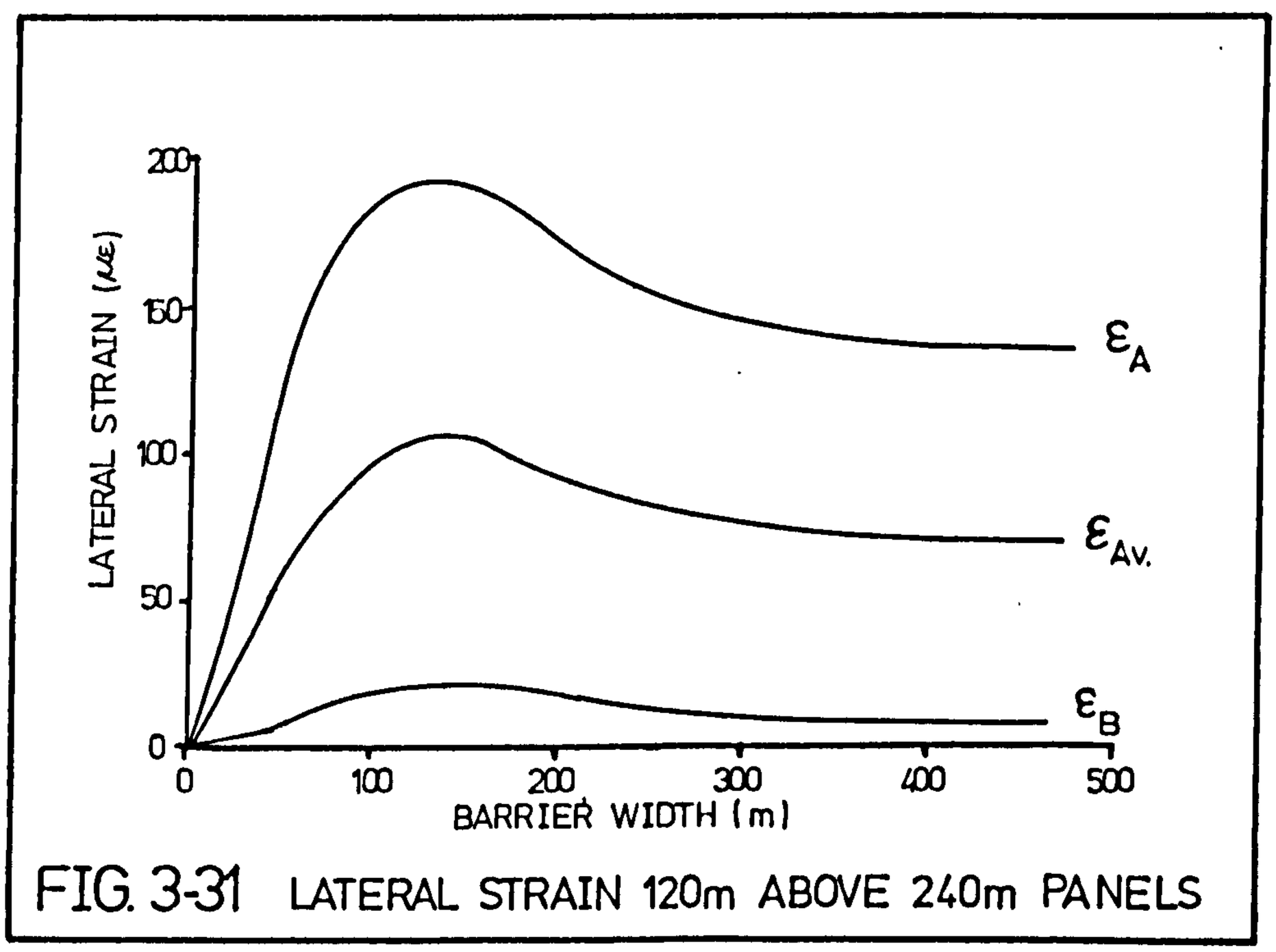

FIG. 3-31 LATERAL STRAIN 120m ABOVE 240m PANELS

From laboratory tests described in Chapter 5 on anhydrite specimens, a tensile failure strain of 106 microstrain was established. The properties of the Upper Permian Marl defined by Patchet (7) are very similar to those of the anhydrite with compressive Young's modulus being 6% higher and tensile strength 13% higher. Therefore using the anhydrite failure strain provides a 7% safety margin over the marl behaviour and so can be used for both the marl and the anhydrite band which exists below the

Bunter Sandstone. This is on the assumption that the marl and anhydrite tensile:compressive modular ratios are roughly the same. No specimens of the Permian Marl were available to verify this.

The full set of panel - barrier width results were converted to a safety factor on the basis of the above failure strain. Fig. 3-32 shows a series of curves corresponding to the magnitude, relative to failure strain, of the peak tensile lateral strain 120m above the centre of a barrier within a block of five identical panels. The panel and barrier widths are the two variables. Two points should be made about these results. Firstly, the magnitude of the strains is based on a theoretical analysis and therefore should only be used on a comparative basis. Secondly, the strata concerned is no doubt under a compressive horizontal stress field. The magnitude of this is unknown but due to the elastic nature of the ground and the low value of Poisson's ratio (0.07 obtained by Patchet) it could be extremely low especially in fissured or jointed ground. The stress represents an inherent compressive strain in the rock which must be overcome before any tensile strains develop and therefore it represents a small built-in margin of safety. However, it should not be relied upon to counteract the subsidence-induced strains and so has not been taken into account in this analysis.

3.5 Summary of Conclusions

From the results discussed in this chapter, the following

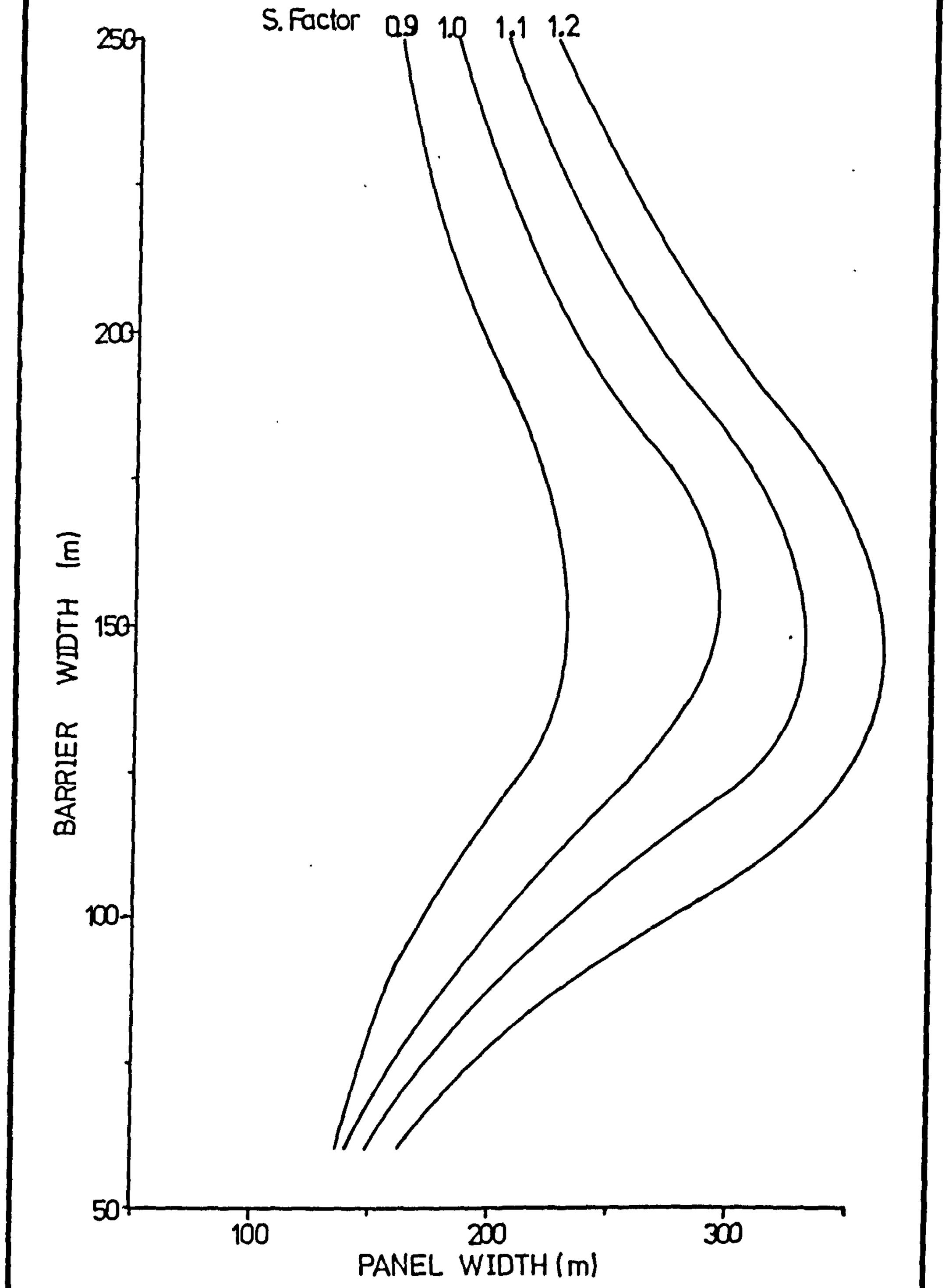

FIG. 3-32 LATERAL STRAIN SAFETY FACTOR CURVES

main conclusions may be drawn.

i Panel width should not exceed 290m if any load redistribution is to be achieved.

ii Herringbone pillar shapes do not signigicantly affect the overall panel stability provided the central core area is maintained.

iii Fig. 3-26 expresses a triaxial strength safety factor, F_s, in terms of width:height ratio. A factor of 1 represents immediate failure or excessive yield as soon as the full load has been applied.

iv Fig. 3-29 expresses a time-dependent safety factor, F_T, in terms of width:height ratio. A factor of 1 represents eventual failure due to long term creep.

v Applying the overbreak factor, a certain safety margin should still be maintained with the above factors due to the steepness of the curves in the critical region - safety factors should be at least in excess of 2. Also the overbreak factor has not allowed for roof overbreak and so the heights applied to W:H ratios should be adjusted accordingly.

vi Equation (3.16) should be used to define minimum barrier pillar widths between panels of stable pillars. This width should be increased according to the five associated points.

vii Major boundary pillars or pillars containing development headings should be at least double the

figure defined in (vi) to enable the central pillar region to be under virgin loading conditions.

viii The peak lateral strain above these panels occurs at an angle of 30° over the ribside.

ix Barrier widths between panels should be much less, or much greater than 140m so as to avoid maximum subsidence strains 120m above the seam.

x Fig. 3-32 defines relative safety factors in terms of lateral strain 120m above a set of panels and barriers.

CHAPTER 4

FACE ELEMENT AND FINITE ELEMENT ANALYSES OF HIGH EXTRACTION PANELS

4. FACE ELEMENT AND FINITE ELEMENT ANALYSES OF HIGH EXTRACTION PANELS

The analyses described in this chapter are concerned with layout designs utilizing narrow panels within which a high level of extraction takes place. The panel and barrier pillar widths are extremely critical to the stability of such layouts since it is assumed that the pillars within the panel carry very little of the overburden load, the barriers providing the main support. This type of mining has been described by many names - pressure arch method, yield pillar technique, stress relief technique - and has been applied, particularly in coal mining (32), in England and the U.S.A. for the past 20 years. The first reported use of this technique for mining evaporites has been from the Canadian potash mines where the method has been adopted over the past five years by the majority of mines. Further details of the Canadian methods are discussed in a later section but the basic principles of the technique are described here.

4.1 Yield Pillar Technique

This method, as used by the Canadian potash industry, has been most recently described by Serata (33). Serata discusses three methods which he calls the stress relief, parallel room and time control methods, each of which apply to slightly differing geological conditions. However, the basic principle behind the methods is the same as the original yield pillar technique.

This principle is one of stress redistribution away from the panel pillars and onto the adjacent barriers. The redistribution is brought about by mining the panel pillars sufficiently narrow so that there is very little horizontal confinement and the resultant uniaxial loading induces a large amount of yield throughout the pillar. The yield which occurs within the panel area relieves the stresses in the immediate roof and floor and creates a form of redistributed pressure arch above and below the panel. As a result the material within these arches, or envelopes, is protected from high stresses and so roof and floor stability is easily maintained and roadway closure rates and pillar yield rapidly diminish.

The resultant panel layouts obviously have a high extraction ratio due to the minimum pillar dimensions. However, the success of the technique is extremely dependent on a number of factors. The major ones are

i the relative dimensions of the barrier pillars and panel widths which determine the overall ground stability;

ii the dimensions used within the panel to initiate and control the yield;

iii the geology of the strata above and below the seam in its ability to maintain the stress redistribution created by the dimensions in (i) and (ii);

iv the sequence and rate at which the panel is mined to afford protection to the main roadways while the panel is being developed and to control the pillar yield correctly.

The theoretical work in this chapter primarily investigates these first two factors and comments on the influence of the third. The relevence of the fourth point is discussed in a later section in conjunction with the Canadian potash mining methods.

4.2 Face Element Analyses

In order to study the subsidence effects and barrier pillar load distribution associated with different panel and barrier widths, a two dimensional, vertical plane strain face element study was conducted. Each panel was considered as a single excavation without the intermediate yield pillars being included. This type of simulation was considered to be appropriate for representing the eventual time-dependent condition of the panel once the pillars had yielded and then stabilised to carry a minimal proportion of the overburden load. The simulation does not represent the situation where the combination of excessive panel width and incompetent geology causes breakdown of the pressure arch leading to excessive yield and panel collapse. Such a situation would result in greater subsidence and associated strains than predicted here and could possibly jeopardise the stability of the entire region where it occurred. Therefore these panel layouts must be designed in such a way that they maintain long term stability within the concepts of the yield pillar technique.

The face element model consists of four panel excavations with bench marks located in the central barrier and outer ribside to determine loading conditions and also at the 120m horizon to

monitor subsidence. A range of panel and barrier widths between 45m and 70m was modelled. The subsidence-induced lateral strains determined from this study were again average figures between the two extreme sets of values described earlier.

This work was conducted after in-situ stress measurements had been made underground. The virgin stresses based on these measurements and mechanical properties used were as follows:

σ_v = -31.0 MN/m^2

σ_H = -15.0 MN/m^2

E = 20.0 GN/m^2

ν = 0.32

4.2.1 Above Seam Results

From the results of each geometry considered, the peak lateral strains were determined and the anhydrite tensile failure strain referred to in Chapter 3 was used to determine a safety factor. In each case the peak strains above the barriers within the four panel block were of the same magnitude but the strain above the block ribside was slightly higher. The position of the peak ribside strain was above the point 70m (±5m) into the ribside in every case. This, once again, gives an angle of 30° from the ribside to the position of maximum lateral strain.

A horizontal line of bench marks was also positioned 1100m above the seam corresponding to the surface horizon. These were not extended far enough to obtain a peak strain value but were intended to give a relative indication of subsidence for different block

geometries and of subsidence relative to the 120m horizon.

Table 4-1 lists the maximum subsidence at 120m and at 1100m above each block geometry modelled. The maximum lateral strain above the block ribside at 120m is also included in the Table. The extraction ratio is calculated for a horizontal plane through the block within the block width assuming total extraction within each panel and infinite panel length.

Table 4-1 Maximum Subsidence Above a Four Panel Block

Panel Width (m)	Barrier Width (m)	Block Width (m)	Block Extr. Ratio (%)	$S_{max.}$ at 120m (mm)	$\varepsilon_{max.}$ at 120m ($\mu\varepsilon$)	$S_{max.}$ at 1100m (mm)
50	45	335	60	30.5	105	6.2
50	50	350	57	29.1	103	6.2
50	60	380	53	26.7	98	6.1
60	45	375	64	41.4	123	9.1
60	50	390	62	39.6	120	9.0
60	60	420	57	36.5	116	8.8
70	45	415	67	55.7	145	12.9
70	60	460	61	49.2	136	12.5

These figures indicate the relationship between block width, extraction ratio and subsidence. Fig. 4-1 shows the maximum ribside strain and maximum subsidence at 120m plotted against the product of extraction ratio and block width. Fig. 4-2 shows the maximum subsidence at 1100m plotted against the product of extraction ratio and block width.

Both of these diagrams suggest a linear proportionality

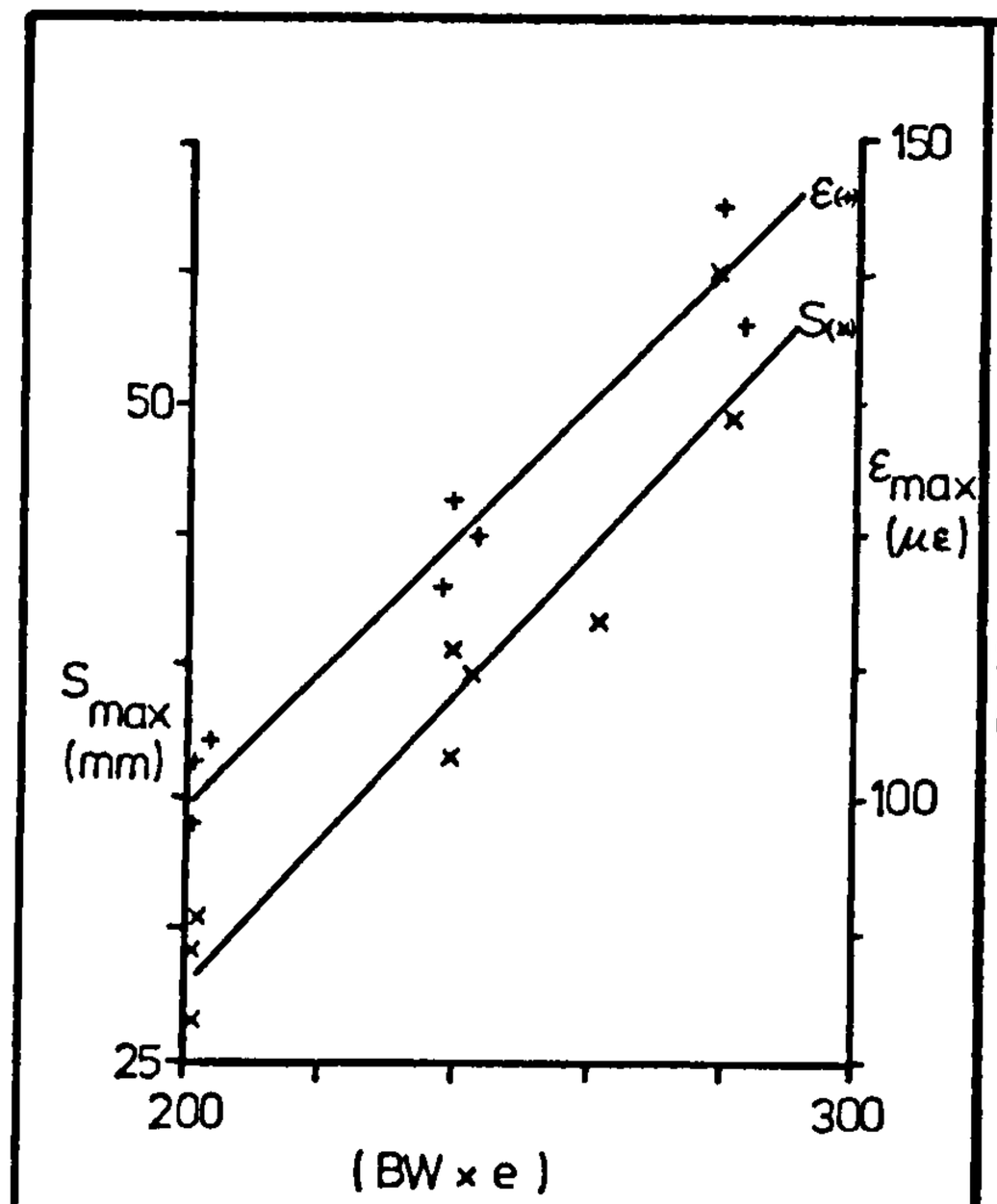

FIG. 4-1

120m ABOVE SEAM

$\varepsilon_{max.}$, $S_{max.}$ v. (BLOCK WIDTH × e)

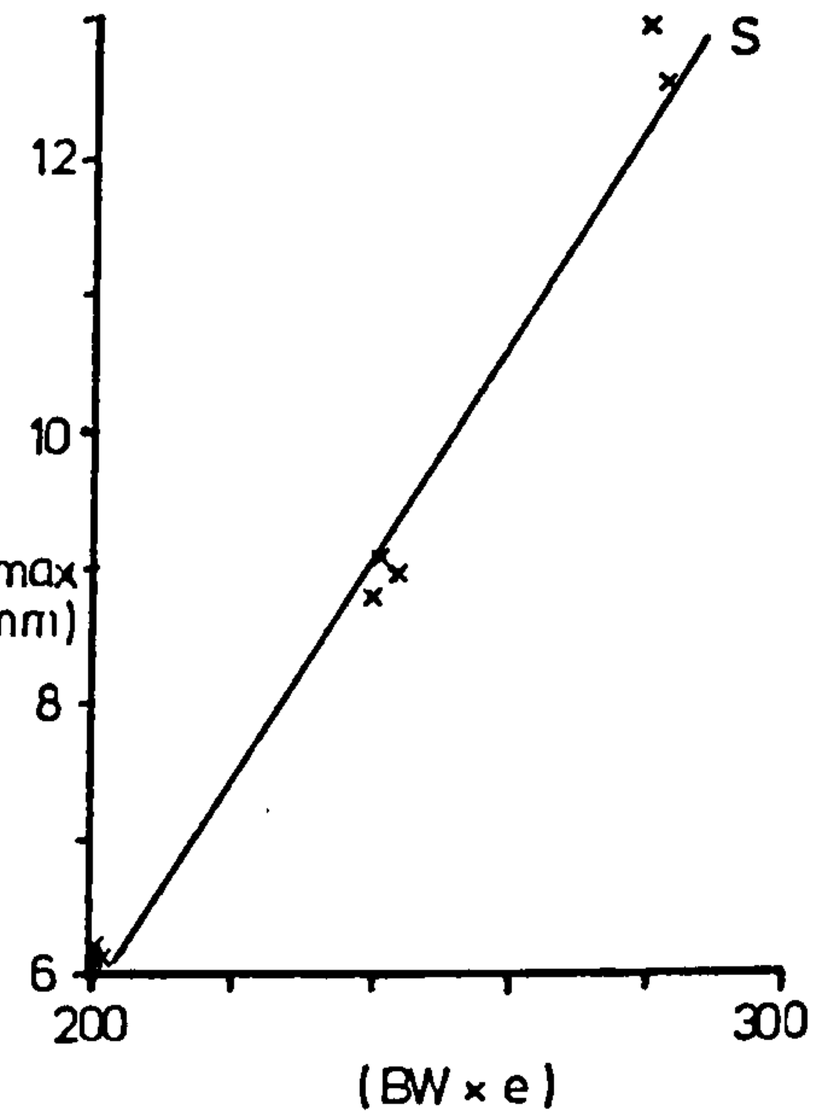

FIG 4-2

1100m ABOVE SEAM

$S_{max.}$ v. (BLOCK WIDTH × e)

between maximum subsidence, strain and the product of block width and block extraction ratio. Unfortunately this aspect of the problem was not being investigated particularly and there are insufficient points on the diagrams to quantify these relationships. However, it is clear that for a given block extraction ratio the block width critically affects maximum strains at 120m and at the surface. Therefore one dimension of the block should be kept within this critical width and the barrier between blocks should be of such a width that the lateral strain peaks are not superimposed, i.e. not close to 140m.

The lateral strains above the barrier pillars within a block are extremely sensitive to panel and barrier widths. Fig. 4-3 shows the relationship between the peak strain above the central barrier

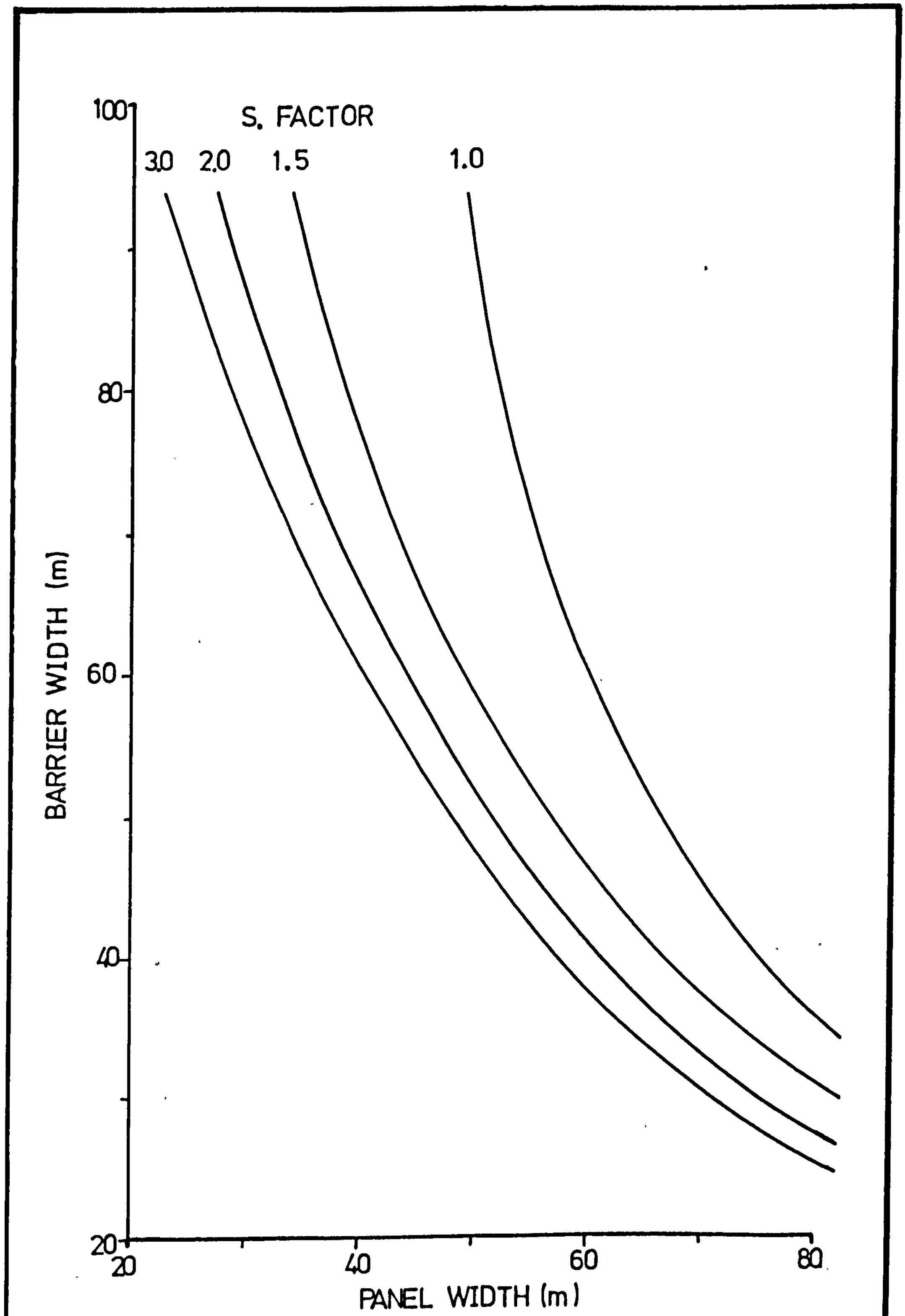

FIG. 4-3 LATERAL STRAIN SAFETY FACTOR CURVES

and the panel and barrier widths in terms of safety factors based on the anhydrite failure strain. These curves represent the same relationship as that established for the low extraction panels shown in Fig. 3-32.

The subsidence effects of the sequence of mining panels within a block were investigated for the same four panel block model using 60m panels and barriers. Fig. 4-4 shows the different strain profiles at 120m as the panels are mined in order 1, 2, 3 and 4. Fig. 4-5 shows the profiles produced by mining from each end of the block alternatively, in order 1, 4, 3 and 2. Clearly this second system produces almost double magnitude strains between panels 1 and 3 prior to mining panel 2 and so should be avoided. Each block should be mined, either in advance or retreat, but always in sequence either towards a ribside of virgin ground or a major boundary pillar, not towards a production panel area.

4.2.2 Barrier Pillar Results

The purpose of the barrier pillars within a block of yield pillar panels is to provide long term load-bearing capacity but also to provide controlled yield in order to prevent excessive tensile subsidence strains. In this sense the barrier pillars should fulfil the same role as the long term stable panel pillars of the low extraction panels while minimising subsidence strains according to Fig. 4-3.

The results from the bench marks located in the central barrier of the block were analysed for each geometry and Fig. 4-6

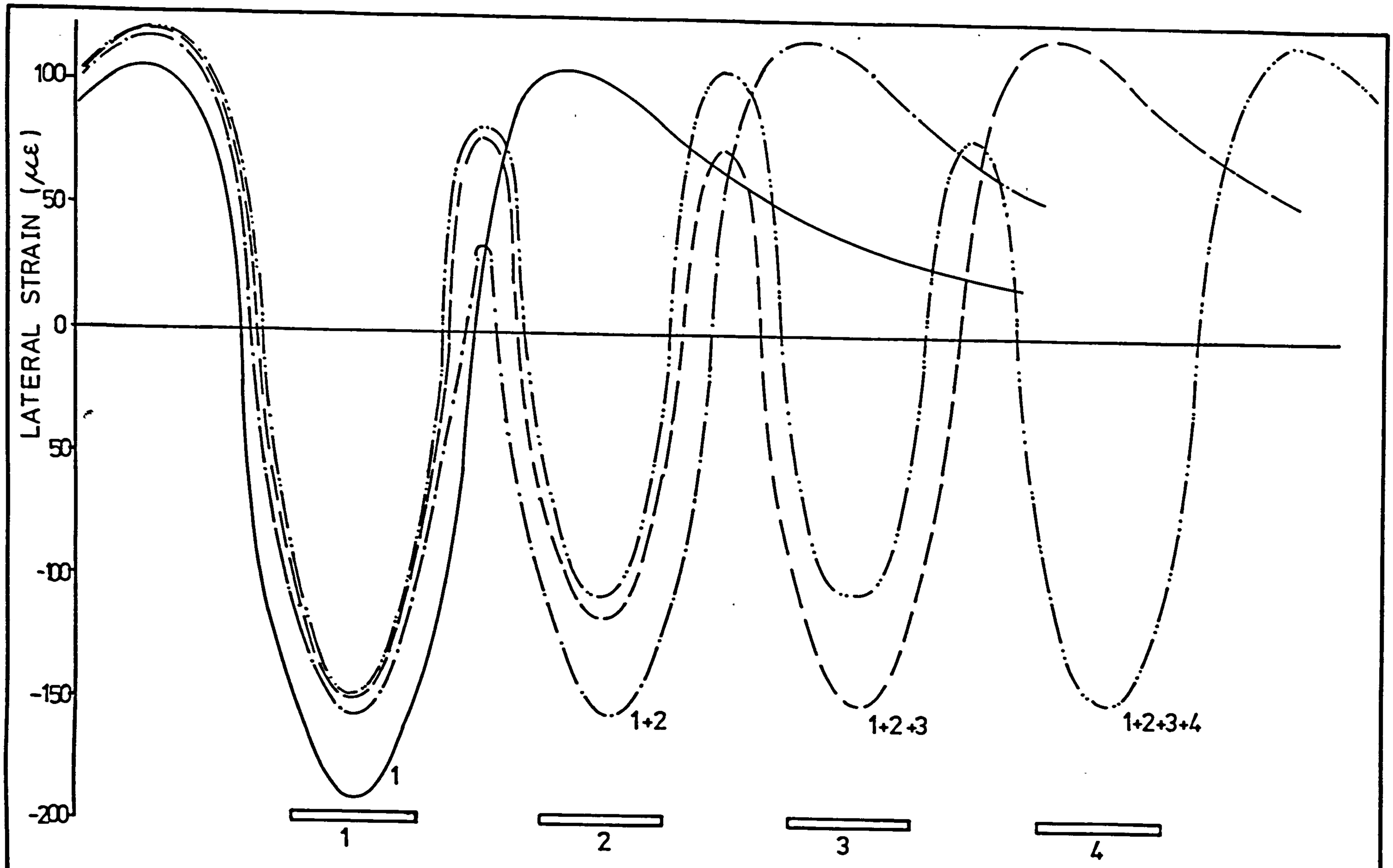

FIG. 4-4 LATERAL STRAIN PROFILE 120m ABOVE 4×60m PANEL BLOCK MINED 1,2,3,4

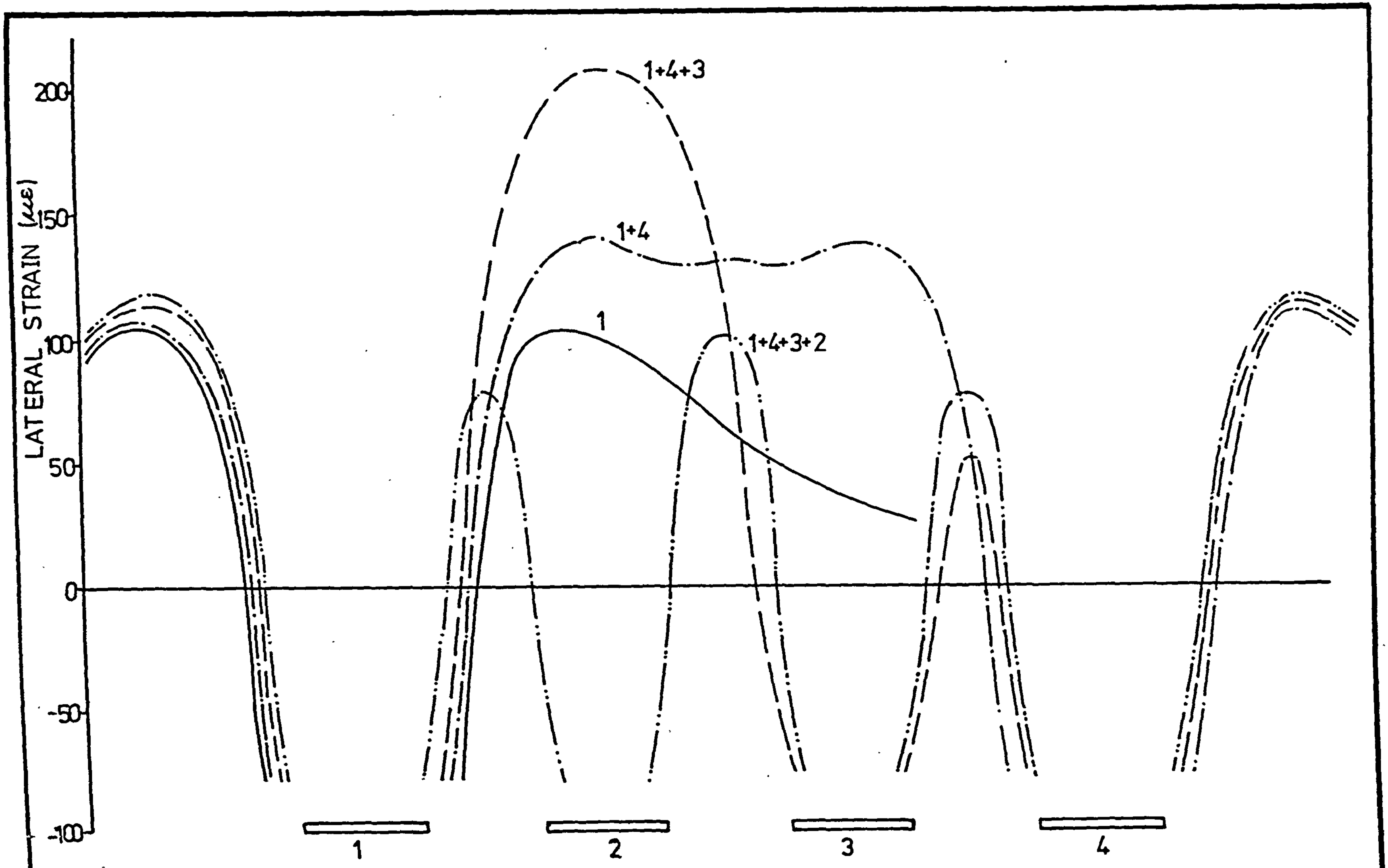

FIG. 4-5 LATERAL STRAIN PROFILE 120m ABOVE 4×60m PANEL BLOCK MINED 1,4,3,2

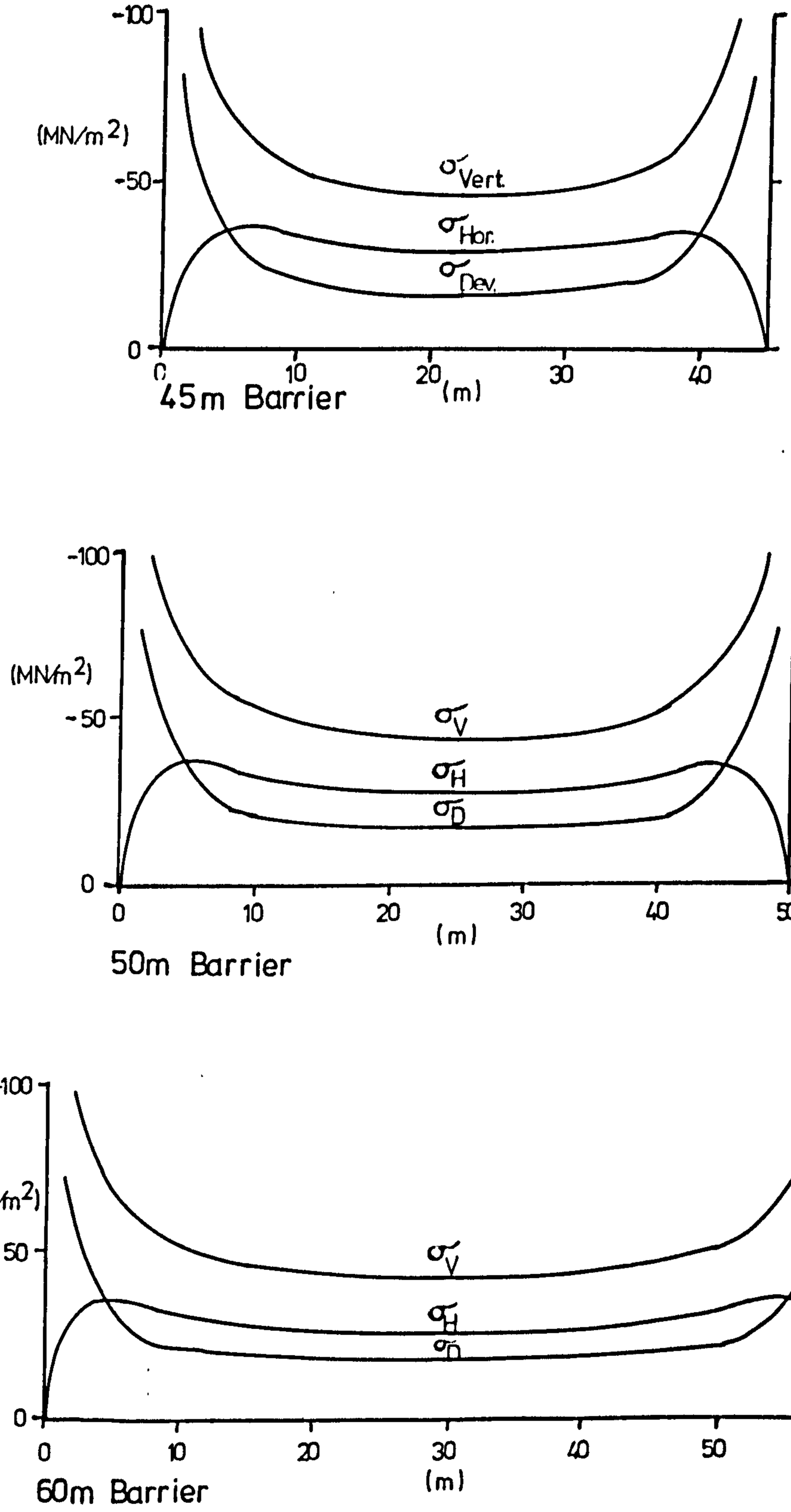

FIG. 4-6 STRESS DISTRIBUTION BETWEEN 50m PANELS

shows the stress distribution for the case of 50m panels with 45m, 50m and 60m barriers. The stresses in the ribside of the block were very similar to these in the barriers. For each block geometry, average values of σ_N, normal stress, and $\sigma_{Dev.}$, deviator stress, were obtained for the complete barrier width.

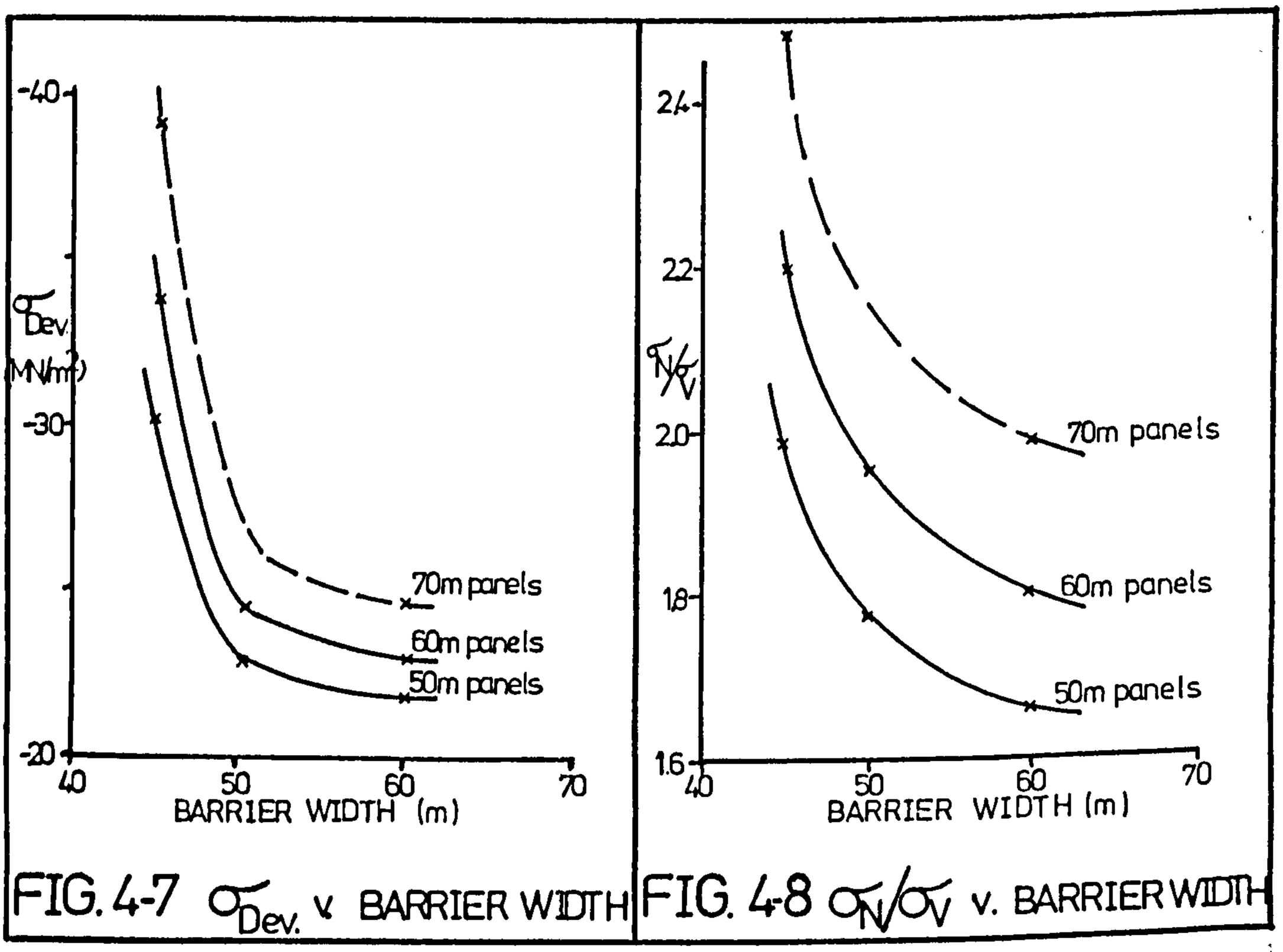

FIG. 4-7 $\sigma_{Dev.}$ v BARRIER WIDTH

FIG. 4-8 σ_N/σ_V v. BARRIER WIDTH

Fig. 4-7 shows the curves of $\sigma_{Dev.}$ against barrier width for the three panel widths considered while Fig. 4-8 shows similar curves for the ratio of σ_N to σ_V (virgin vertical stress) against barrier width. Although neither of these diagrams have sufficient points to use them for defining barrier widths accurately they do indicate several things. Firstly a barrier width of 50m appears to be an absolute minimum below which the loading increases rapidly and creep rates would be very high for this order of panel widths. Secondly, from the deviator stress to pillar size relationship shown in

Fig. 3-27, above a deviator of 22.5 MN/m^2 the curve rises steeply for only slight reductions in dimensions. Using this value in Fig. 4-7, a guide to barrier widths can be obtained. In each case the necessary barrier width is slightly in excess of the panel width used.

In order to obtain a method of barrier width determination in conjunction with the restrictions described above, an analytical approach has been used.

The yield pillars within each panel will carry a small amount of load for local roof support. Let the maximum permissible stress on the panel pillars be $\sigma_{Max.}$. For a given length of panel, ℓ, over which the yield pillar area is ΣA_i and beyond which the geometry is repetitive, the load supported by yield pillars per unit length of panel, R_y, is simply

$$R_y = \sigma_{Max.} \sum_{i=1}^{n} A_i / \ell \qquad (4.1)$$

But from equation (3.10) this may be reduced to

$$R_y = \sigma_{Max.} (1 - e)W \qquad (4.2)$$

where e is the panel extraction ratio

W is the panel width.

The total load to be thrown onto the barrier pillars by the panel, per unit length, is therefore

$$R_B = \sigma_v W - \sigma_{Max.}(1 - e)W \qquad (4.3)$$

where σ_v is the vertical virgin stress.

The barrier stress acting over width B and unit length, σ_B, is

$$\sigma_B = \sigma_v + W(\sigma_v - \sigma_{Max.}(1 - e))/B \qquad (4.4)$$

where B is the barrier width.

In the same way as for the low extraction panels, a maximum value of σ_B in terms of σ_v can now be chosen. In this case the barriers are required to remain stable in the long term but still permit as much yield as possible to create uniform subsidence. Therefore the minimum pillar size, i.e. 25m, used in the mine which has shown this capability has been chosen. The average normal stress for a fully loaded 25m square pillar, allowing for 7% overbreak, is $1.65(\sigma_v)$. Substituting this value for σ_B in equation (4.4) and re-arranging gives

$$B = \frac{W}{0.65}\left[1 - \frac{\sigma_{Max.}(1 - e)}{\sigma_v}\right] \qquad (4.5)$$

Equation (4.5) provides a minimum value for barrier pillar widths within a block of high extraction panels. The value for $\sigma_{max.}$ must be chosen initially in terms of uniaxial creep results. Patchet (7) shcwed that secondary creep strain rates for potash increased rapidly for uniaxial stresses in excess of -20 MN/m^2 for W:H ratio specimens of 2:1. A stress of -18 MN/m^2 gave a secondary creep strain rate of 10 microstrain per day and specimens showed stability over several years under such loading. In view of the fact that

the yield pillars will be roughly the same W:H ratio as Patchet's specimens, but will be fractured due to high initial loading, the pillar creep rates will no doubt be significantly higher and so a value less than -18 MN/m^2 should be chosen. Therefore the assumption is made that -16 MN/m^2 for $\sigma_{Max.}$ will allow for the fractured nature of the pillars. This maximum figure should prevent excessive yield and roadway closure once stress redistribution has taken place. However, the two restrictions described previously - a minimum barrier width of 50m, and barrier width always being larger than panel width - should be adhered to. Also the presence of roadways within the barrier should be compensated for, if they form pillars of smaller dimension than the barrier width.

The above method for determining barrier widths relates to barriers within a block of high extraction panels, provided the panels do form a stress relieved zone. Even with the correct widths, unless the geology is suitable and the mining sequence is correct the panels will not be stress relief panels and excessive subsidence strains and panel collapse will result.

Boundary pillars between blocks of high extraction panels should be determined according to the barrier widths within the blocks. Since these barriers have been designed to carry the full load for the block, the boundary pillars should only be sufficiently wide to be stiffer than the block barriers to ensure correct load distribution. On this basis, solid boundary pillars should be at least 10m wider than the block barrier pillars but less than the critical subsidence width. Where a boundary pillar contains the

main development entries, its width should be twice that of a block barrier pillar plus the width cf the development entries in the centre. Additional roadways within the boundary pillars should be compensated for by greater boundary widths. All barrier and boundary pillar widths must be determined with respect to the subsidence effects above the seam. Fig. 4-9 illustrates the configuration of development and production panels, and barrier and boundary pillars as they have been referred to in this section. The overall production area has been drawn as a square but could be rectangular with the long axis perpendicular to the panel lengths.

4.3 Finite Element Analyses

In order to analyse the effect of pillar yield on stress redistribution around a five entry panel, a finite element analysis was conducted using FEMITPLT, the two dimensional plane strain program. Fig. 4-10 shows the mesh used, with an axis of symmetry down the right hand side along which zero horizontal displacement was specified. Other boundary conditions used were all displacement restrictions, roller jointing on the left hand side and bottom with pin joints at the two bottom corners. The mesh geometry was not ideal for the problem with irregular element shapes along the left and lower boundaries causing inaccuracies. Insufficient element density in the upper left hand corner prevented a detailed subsidence strain analysis.

Table 4-2 lists the materials modelled and the mechanical properties used.

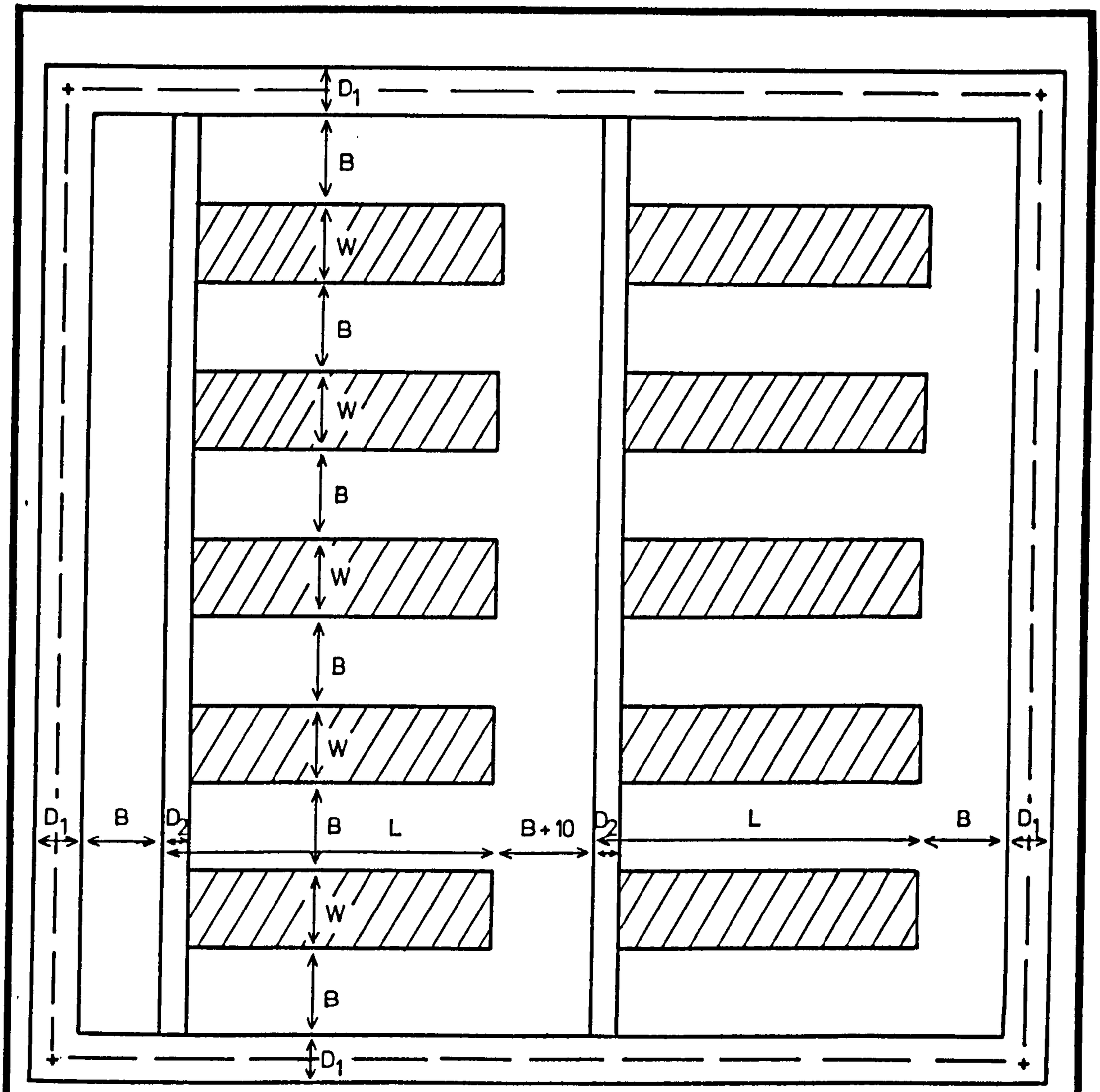

W = Production panel width

B = Barrier pillar width

$L - D_2$ = Production panel length

L = Block width

B + 10 = Width of solid boundary pillar between production blocks

D_1 = Width of primary development panels

D_2 = Width of secondary development panels

= Production panels

+——+ = Block perimeter within boundary pillars ($2B + D_1$ wide)

FIG. 4-9 BASIC LAYOUT FOR PRODUCTION BLOCKS

FIG.4-10 FINITE ELEMENT MESH

5 ENTRY PANEL SIMULATION - BOULBY MINE

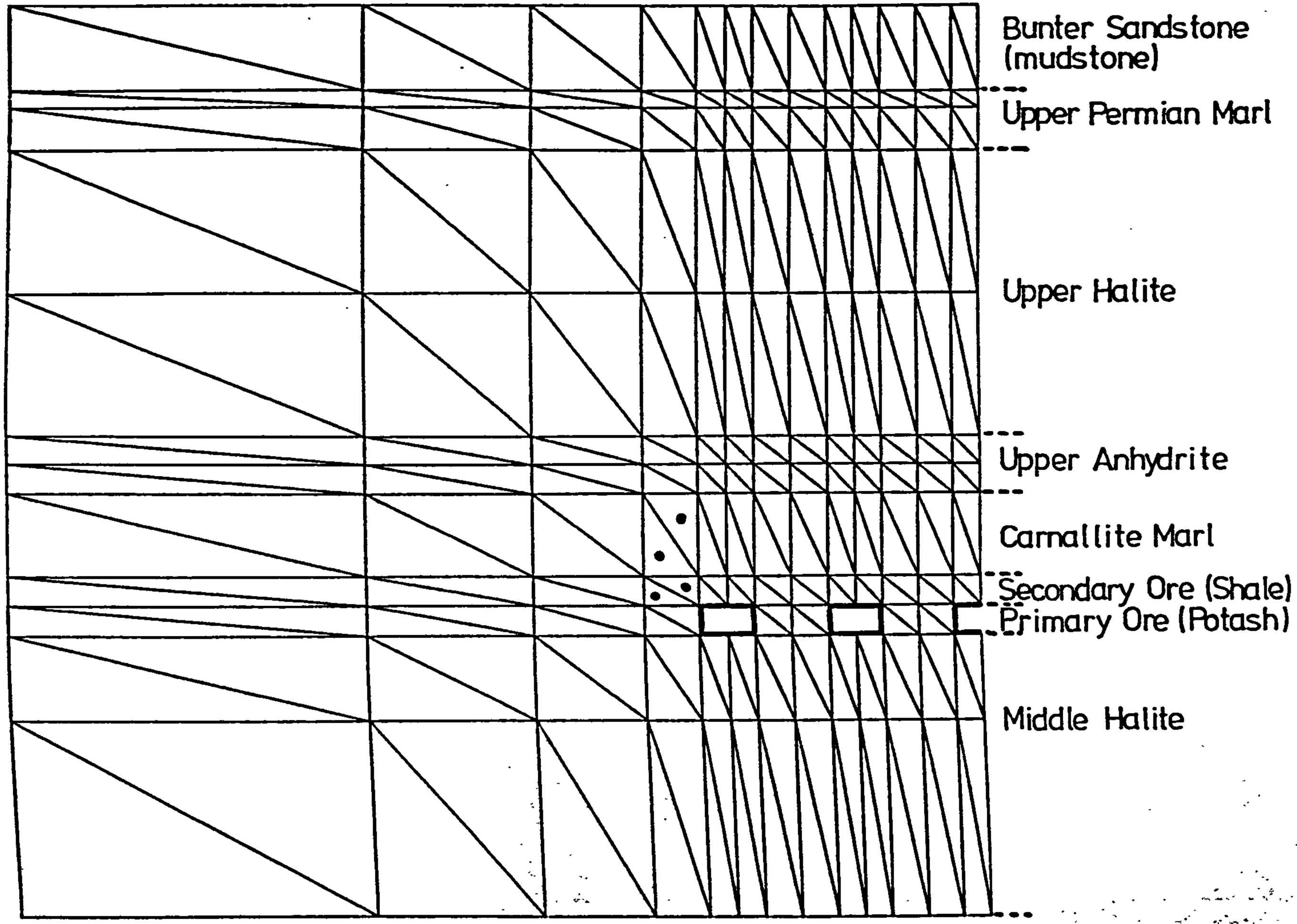

Table 4-2 Material Types and Properties for Finite Element Model

Material Type	Elastic Modulus (GN/m^2)	Poisson's Ratio
Bunter Sandstone	27.72	0.10
Upper Permian Marl	27.17	0.07
Upper Halite	22.06	0.24
Upper Anhydrite	25.99	0.20
Carnallite Marl	8.00	0.24
Secondary Ore (Shale)	11.03	0.24
Primary Ore (Potash)	20.00	0.32
Middle Halite	22.06	0.24

The 6m of potash adjacent to the outer roadway was assigned a lower modulus of 10.34 GN/m^2 and a Poisson's ratio of 0.36 to simulate ribside yielding. The potash elements in the twc yield pillars were assigned a value of 0.42 for Poisson's ratio while the moduli were varied between 5.52 GN/m^2 and 0.07 GN/m^2 in crder to simulate yield conditions.

The virgin stress conditions used were

$$\sigma_v = -30.13 \ MN/m^2$$
$$\sigma_H = -14.58 \ MN/m^2$$

at the seam level with the same ratio maintained along the linear stress gradient between seam and surface. The program uses imperial units for all data input and output but the approximate metric dimensions for the panel modelled were:

Roadway height - 3.05m

Roadway width - 6.10m

Pillar width - 7.92m

A number of alternative geometries were modelled but the main objective was to observe the effect of different amounts of pillar yield on stress redistribution for the five entry panel with the above dimensions.

4.3.1 Finite Element Results

A total of eight runs were conducted for this model. The first run used the original properties of potash as listed in Table 4-2 for all the seam elements including pillars. Subsequent runs used the reduced ribside and pillar properties with the pillar modulus being reduced further with each run.

Fig. 4-11 is a vector plot of the principal compressive stress field around the panel for the first run, using the initial properties. The length of the lines, plotted at element centroids, is proportional to the stress magnitude and the lines are angled according to the principal stress directions. This plot indicates the fairly uniform distribution of stresses around each roadway with very little distortion of stresses above the marl stratum.

The stress distribution for the other extreme, run 8, is shown with a similar plot in Fig. 4-12. The amount of yield for the inner pillar here is approximately 2% strain. This plot shows a significant reduction of stress on the pillars and around the inner

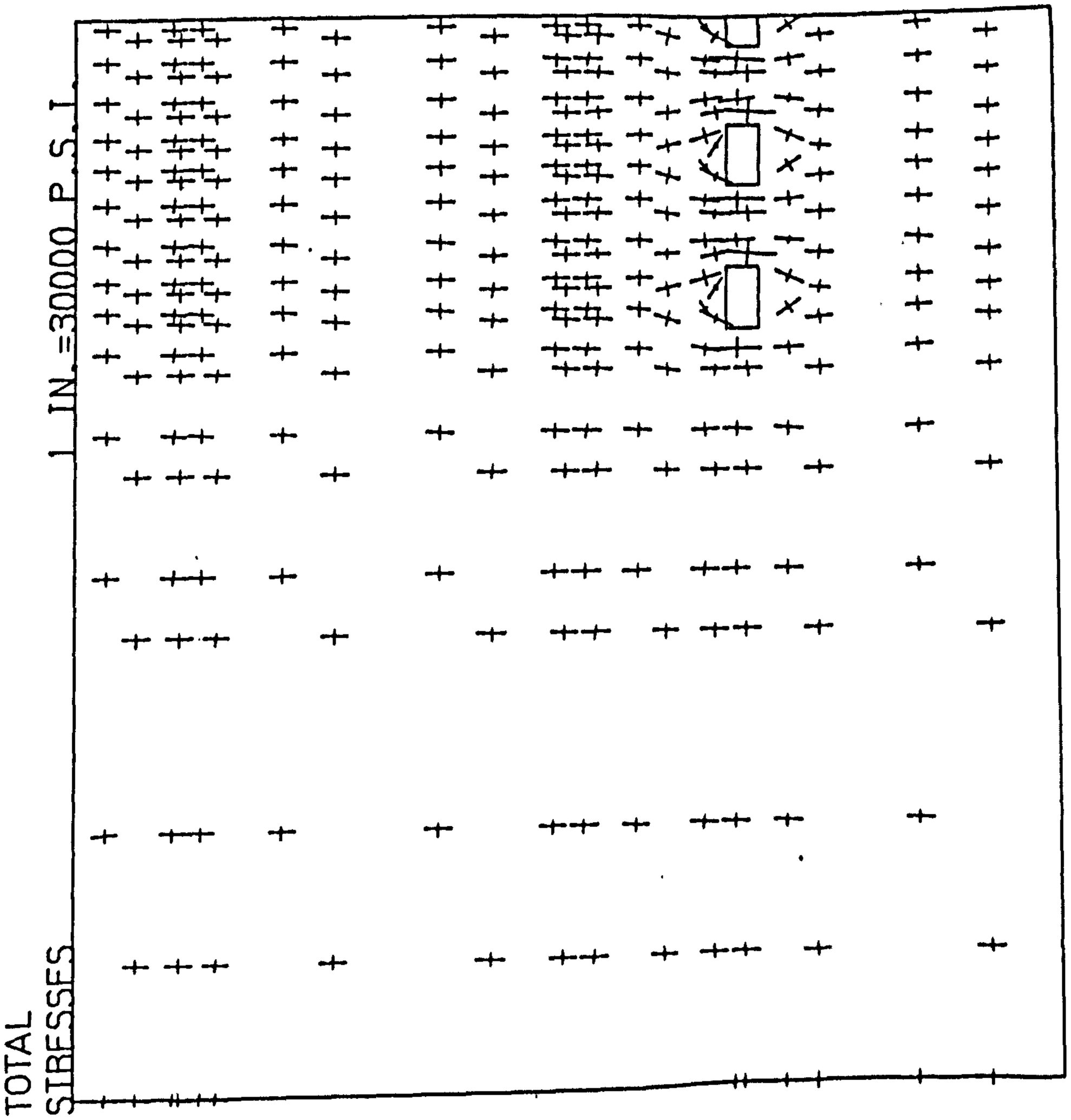

FIG. 4-11 PRINCIPAL COMPRESSIVE STRESS DISTRIBUTION AROUND 5-ENTRY PANEL WITH STIFF PILLARS

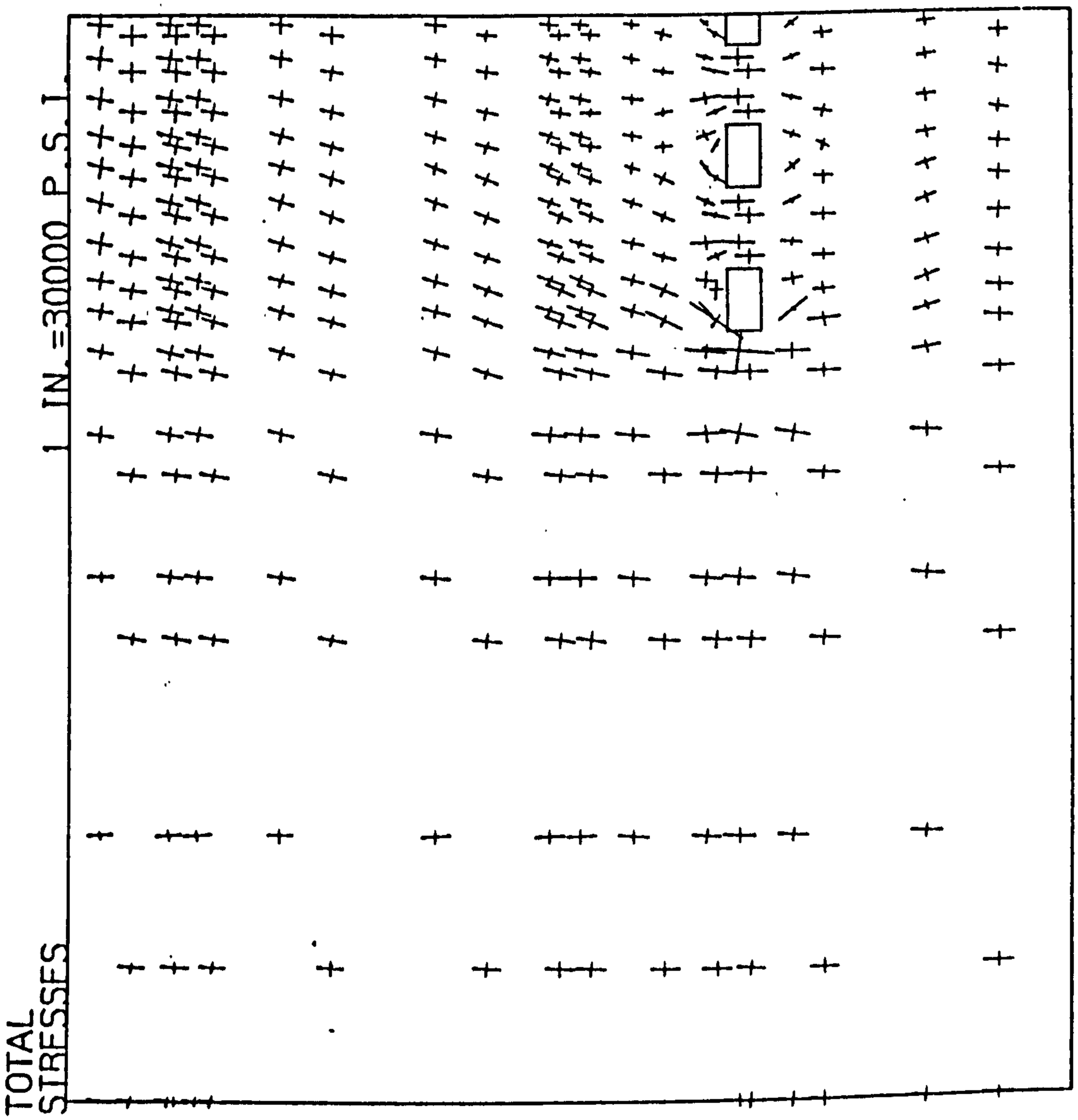

FIG. 4-12 PRINCIPAL COMPRESSIVE STRESS DISTRIBUTION AROUND 5-ENTRY PANEL WITH YIELDING PILLARS

and central roads but the stress field around the outer road and into the ribside is far greater than that of the first run. There is a definite bending effect in the Upper Anhydrite which is forming a bridge across the full panel width with the stresses in the halite above reflecting this overall redistribution away from the panel centre.

Fig. 4-13 and Fig. 4-14 highlight the pattern of stress redistribution for the results of run 8. They are vector stress plots of the principal induced compressive and tensile stresses respectively. The vertical and horizontal virgin stresses were subtracted from the final stress distribution to produce a better indication of the induced effects of the excavations. It should be noted that the original total principal stresses were all compressive so that the induced tensile stress vectors still represent a state of compression but with greatly reduced magnitude, i.e. a stress relief situation. Fig. 4-13 gives the clearest indication of the stress relief zone above and below the panel. It also shows the highly compressive stress redistribution above and beside the outer panel roadway. It is clear that the stress relief zone extends into the Upper Halite with significant influence on the Permian marls due to the highly yielding panel extraction. The proximity of the restrained boundary at the top left of Fig. 4-14 has caused distortion of the horizontal stresses. However throughout the Permian marl strata there have been far greater induced tensile strains than for the initial analysis with stiffer pillars.

In order to assess the degree of protection afforded to the immediate panel roof and pillars by the stress redistribution,

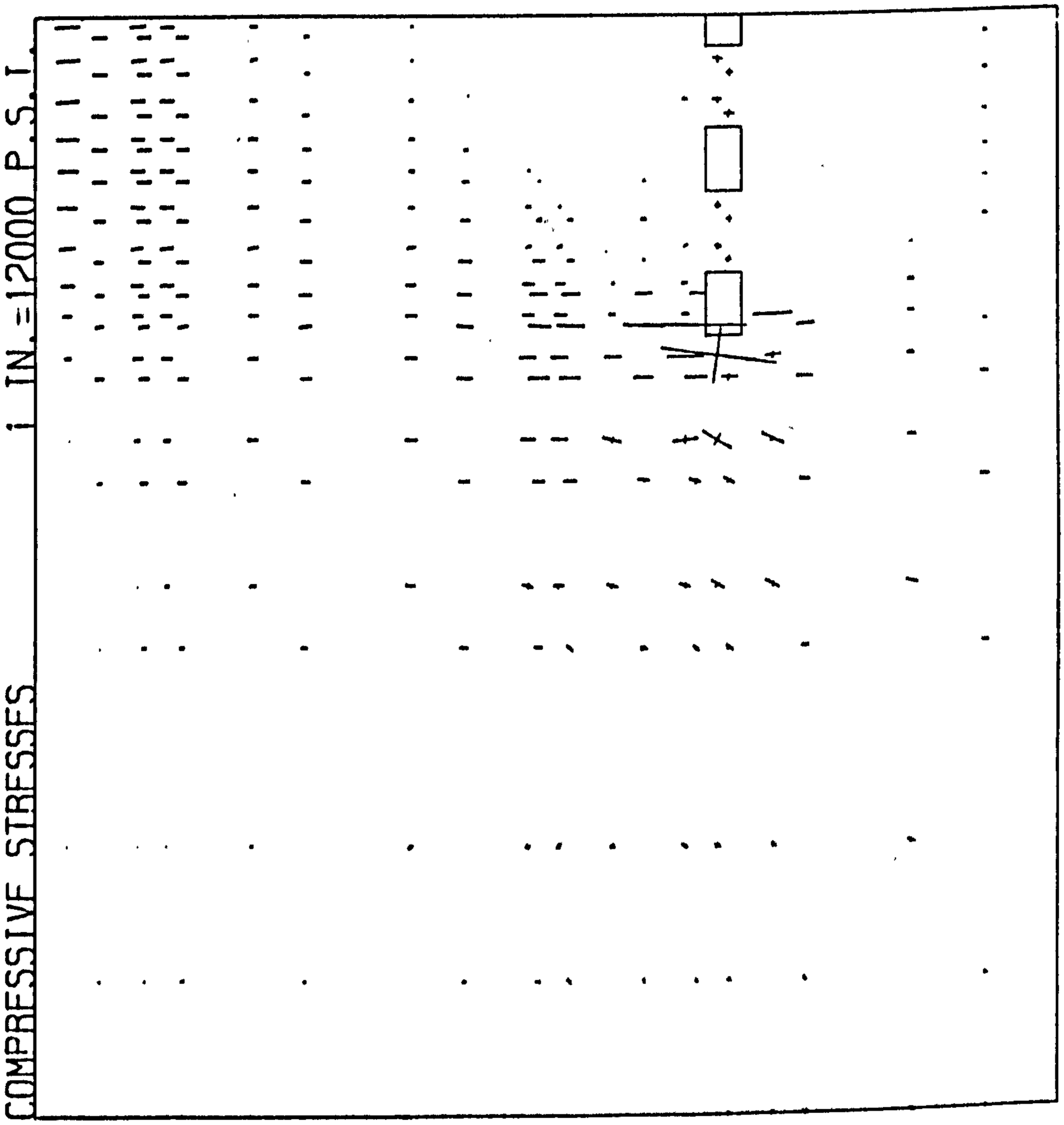

FIG. 4-13 INDUCED COMPRESSIVE STRESS DISTRIBUTION AROUND 5-ENTRY PANEL WITH YIELDING PILLARS

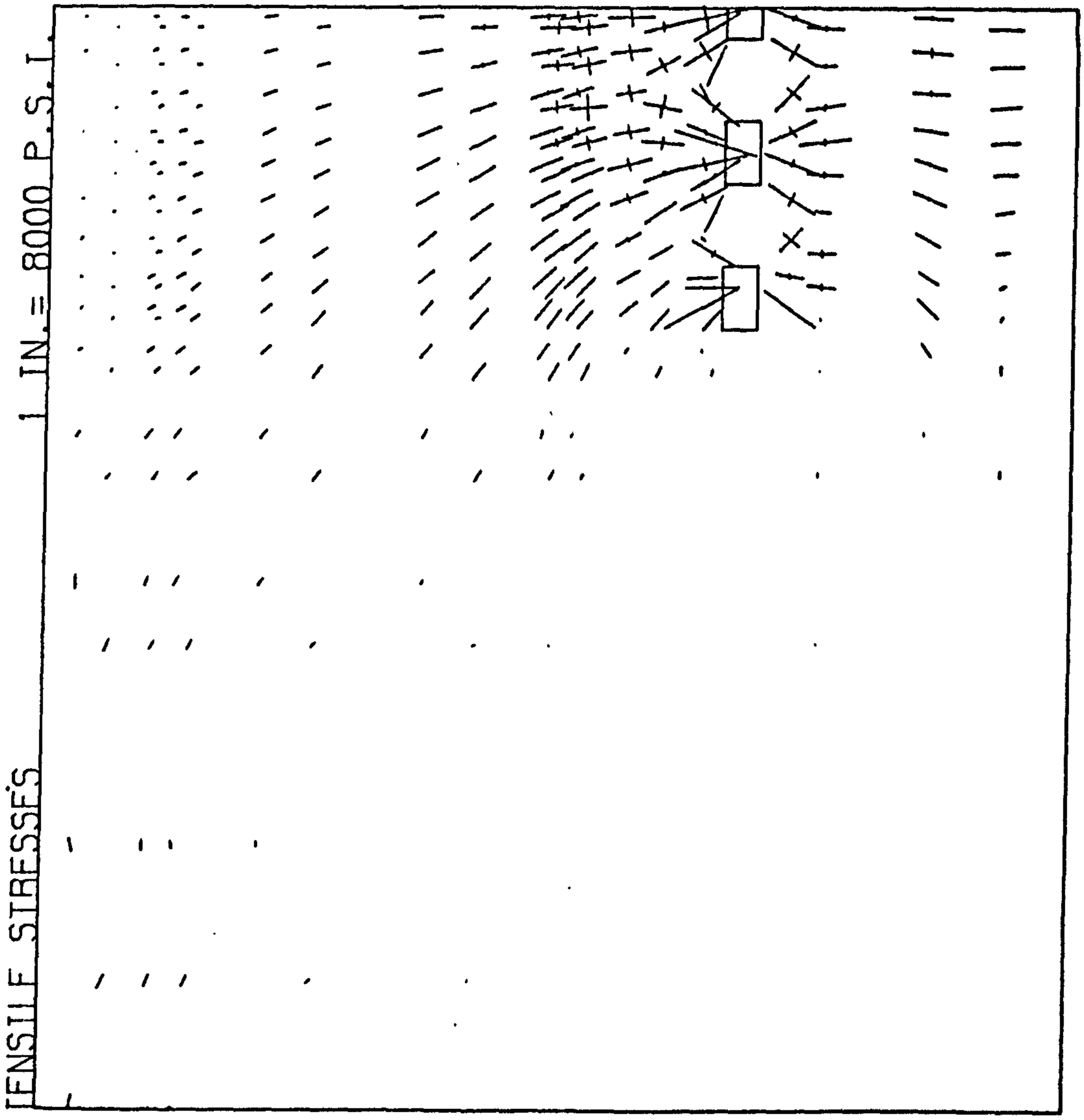

FIG. 4-14 INDUCED TENSILE STRESS DISTRIBUTION AROUND 5-ENTRY PANEL WITH YIELDING PILLARS

Fig. 4-15 has been included. It is a plot of the ratio of R_W to the average inner pillar yield for each run, where R_W has been defined as a roof warping ratio, as follows,

$$R_W = \frac{\text{Average Inner Pillar Yield}}{\text{Mid-Span Centre Road Closure}} \qquad (4.6)$$

This ratio provides a measure of the warping effect on the immediate roof and floor caused by excessively stiff pillars. As R_W approaches unity the roof and floor behave more as a flat plate undergoing uniform displacement and hence there is less chance of buckling failure due to the pillars punching into the roof and floor. From these results it appears that the curve flattens off after about 1.5% yield where the ratio is approximately 0.8. This yield percentage should therefore be used as an absolute minimum necessary to create sufficient stress relief such that warping failure cannot occur.

A second indication of stress relief is shown in Fig. 4-16 which is a plot of shear stress in the edge of the immediate shale roof stratum for each roadway of the panel against inner pillar yield. For the initial run there is very little difference between outer and central road shear stresses. However, with increased pillar yield the outer road roof shear stress builds up rapidly and would be likely to fail whereas the inner and central road roof shear stresses decrease similarly. This definitely indicates roof protection in the central panel roads and it appears to be fairly linear with pillar yield.

Shear tests carried out in the laboratory by Wiggett (9) indicated a shear strength for the shale in the range 9.00 MN/m^2

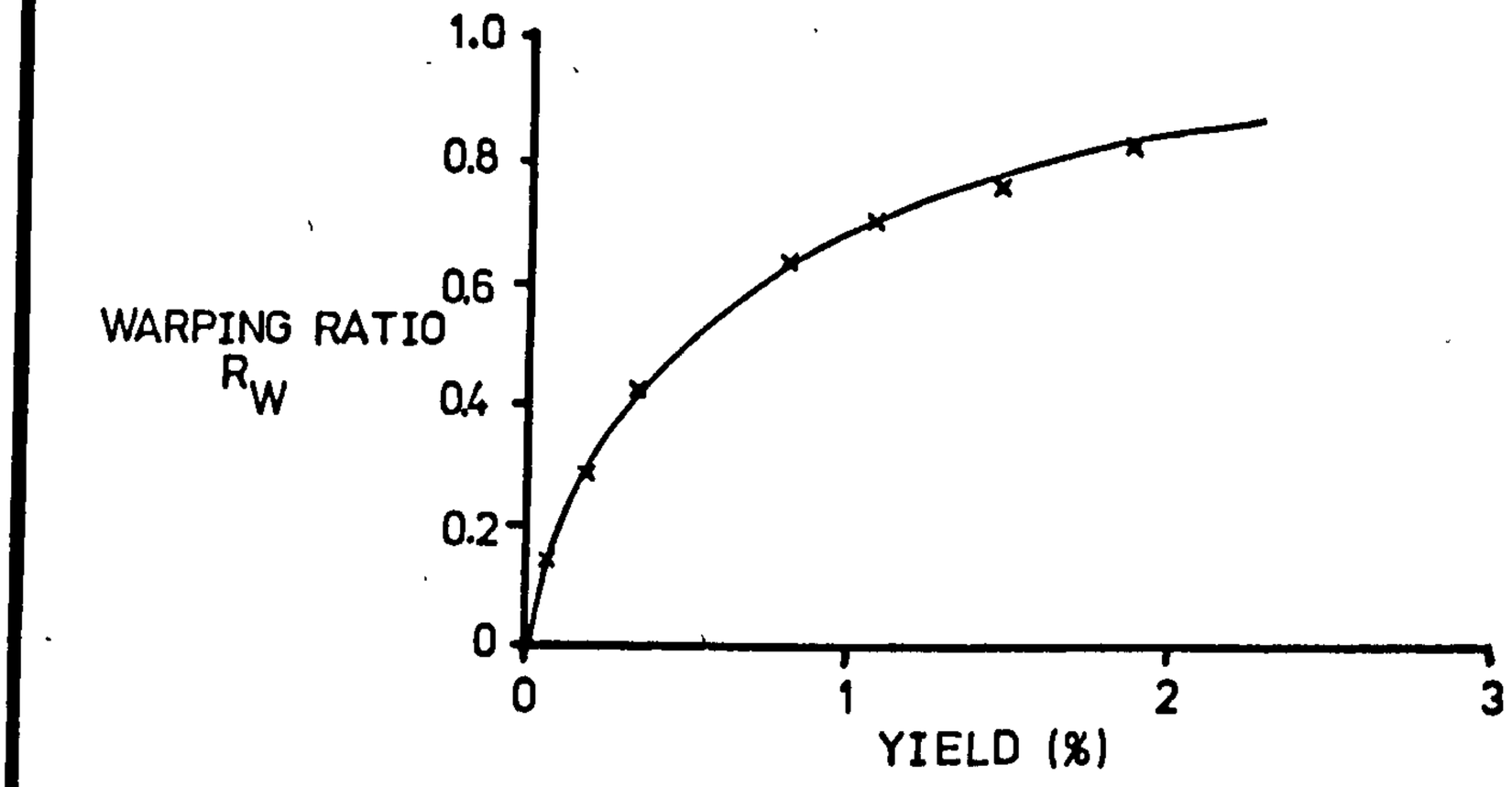

FIG 4-15 WARPING RATIO v. PILLAR YIELD

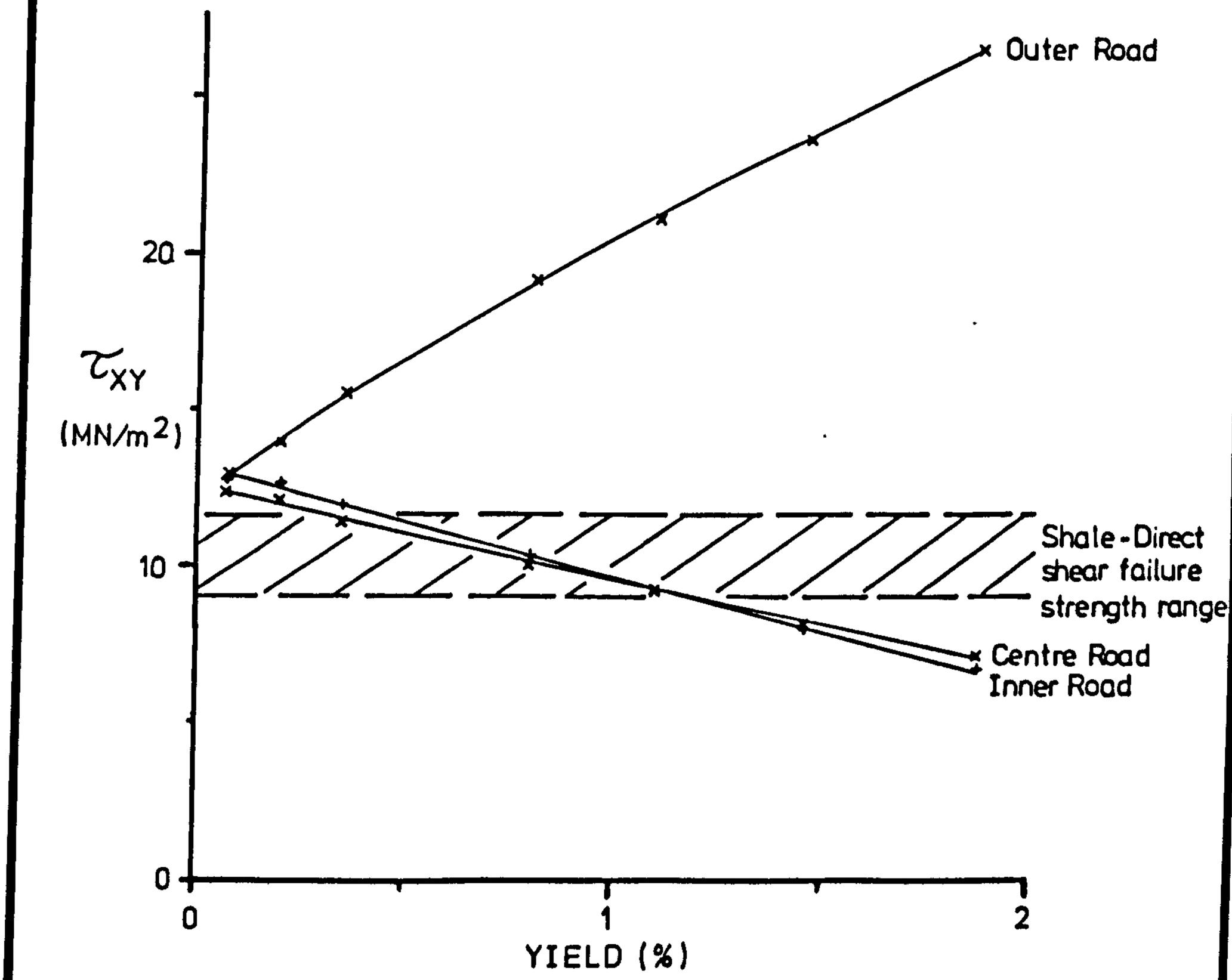

FIG. 4-16 ROOF SHEAR STRESS v. PILLAR YIELD

to 11.58 MN/m^2 using a confining stress of -6.58 MN/m^2. This range band has been marked on Fig. 4-16 and on this basis a yield of 1.3% will still cause shear failure in the central road roof. In order to allow for a margin of safety, particularly in view of the fact that the immediate roof will have higher shear stresses at the corners with negligible confinement, this minimum yield percentage should be increased to 2.4%. This corresponds to one full width of the failure band below the 1.3%-point.

Fig. 4-17 shows the vertical displacement profile along a line

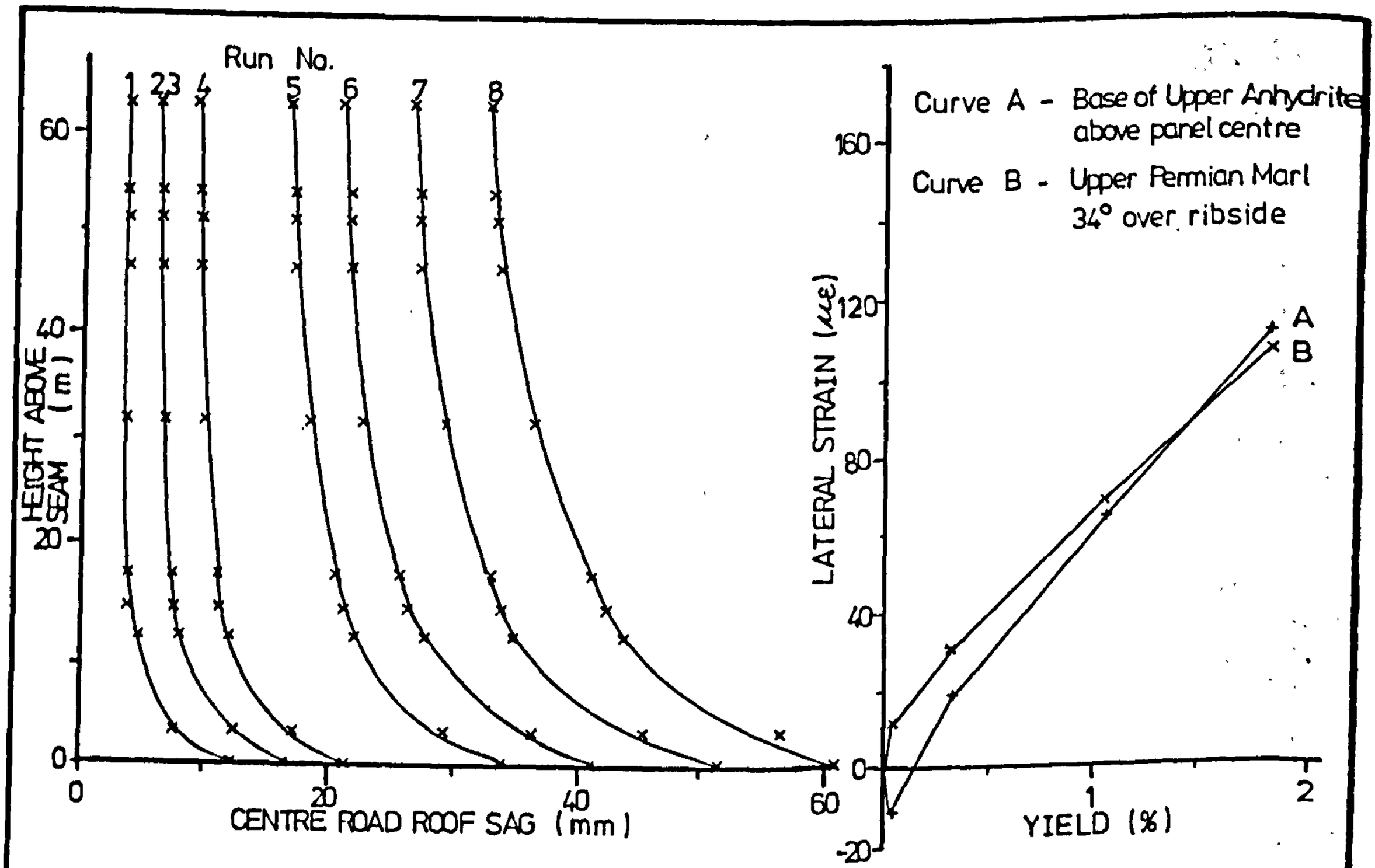

FIG. 4-17 ROOF SAG v. HEIGHT ABOVE SEAM

FIG. 4-18 LATERAL STRAIN v. YIELD

vertically up from the centre of the central roadway of the panel for each run. This indicates a number of points. The presence of the Upper Anhydrite 12m above the seam plays a major role in reducing subsidence and potential bed separation. There is much less vertical

strain apparent above this level suggesting that the anhydrite does form a significant bridge across the panel. However, there is significant strain within the marl and shale (indicated by the flatter slope of the displacement curves) which could quite possibly lead to bed separation and roof failure. This strain does not appear to reduce with increasing yield (corresponding to increasing run numbers). This implies that roof failure due to bed separation is equally, if not more likely in stress relief panels with a shale roof. Roadway widths must therefore be kept within acceptable limits to prevent excessive roof spans which could cause this type of failure.

As already mentioned, the Upper Anhydrite helps to reduce subsidence effects due to the panel, but as Fig. 4-17 shows, the total amount of subsidence increases significantly with increasing yield. Fig. 4-18 is a plot of subsidence-induced lateral strains against pillar yield. Curve A is for a point in the base of the Upper Anhydrite, 12m above the centre of the panel. It represents the tensile strain in the base of the beam formed by the anhydrite across the panel. Curve B is for a point in the Upper Permian Marl at an angle of 34° above the panel ribside. The point in the base of the Permian marl above the panel centre is in a state of increasing lateral compression. This is because it is in the region at the top of the stress redistribution arch which forms a band of increased compression extending around the entire stress relieved envelope of material. In the same way, the base of the Upper Anhydrite was initially in induced lateral compression (see Fig. 4-18, curve A) due to the localised stress redistribution around the central panel roadway. As the stress relieved zone extended outwards and upwards

the compressive arch moved up towards the Permian marl and the anhydrite underwent lateral tensile straining.

The relationship between lateral strain and yield appears to be almost linear with the marl and anhydrite both reaching the tensile failure strain used in previous analyses at 2% yield. The same safety margin exists here, that the material is still in overall compression due to the virgin stress field, but the 2% yield should be kept as a maximum yield to prevent excessive strains in both these strata. This is particularly important for the anhydrite, since if it fails, the entire stress relief envelope could break down which would significantly increase the overall subsidence and strain distribution in the strata above. Panel width is obviously critical to the Upper Anhydrite stability and so if the full 2% yield is necessary to create sufficient stress relief, then the panel width of this model, 62m, should be regarded as a maximum.

The total principal stress diagram for run 8 (Fig. 4-12) indicates the presence of very high stress deviators around the inner edge of the compressive stress arch referred to earlier. These deviators are most significant where the stress redistribution passes through the marl and shale strata above and to the left of the outer roadway. The lack of confinement due to the stress relieved ground on the inside of the arch together with the high compressive stresses of the redistribution are responsible for the increased deviator stresses. The maximum deviator stresses in these two strata occurred in the four elements marked on Fig. 4-10 with dots. Fig. 4-19 is a plot of this maximum deviator stress for the shale and marl against pillar yield from successive runs.

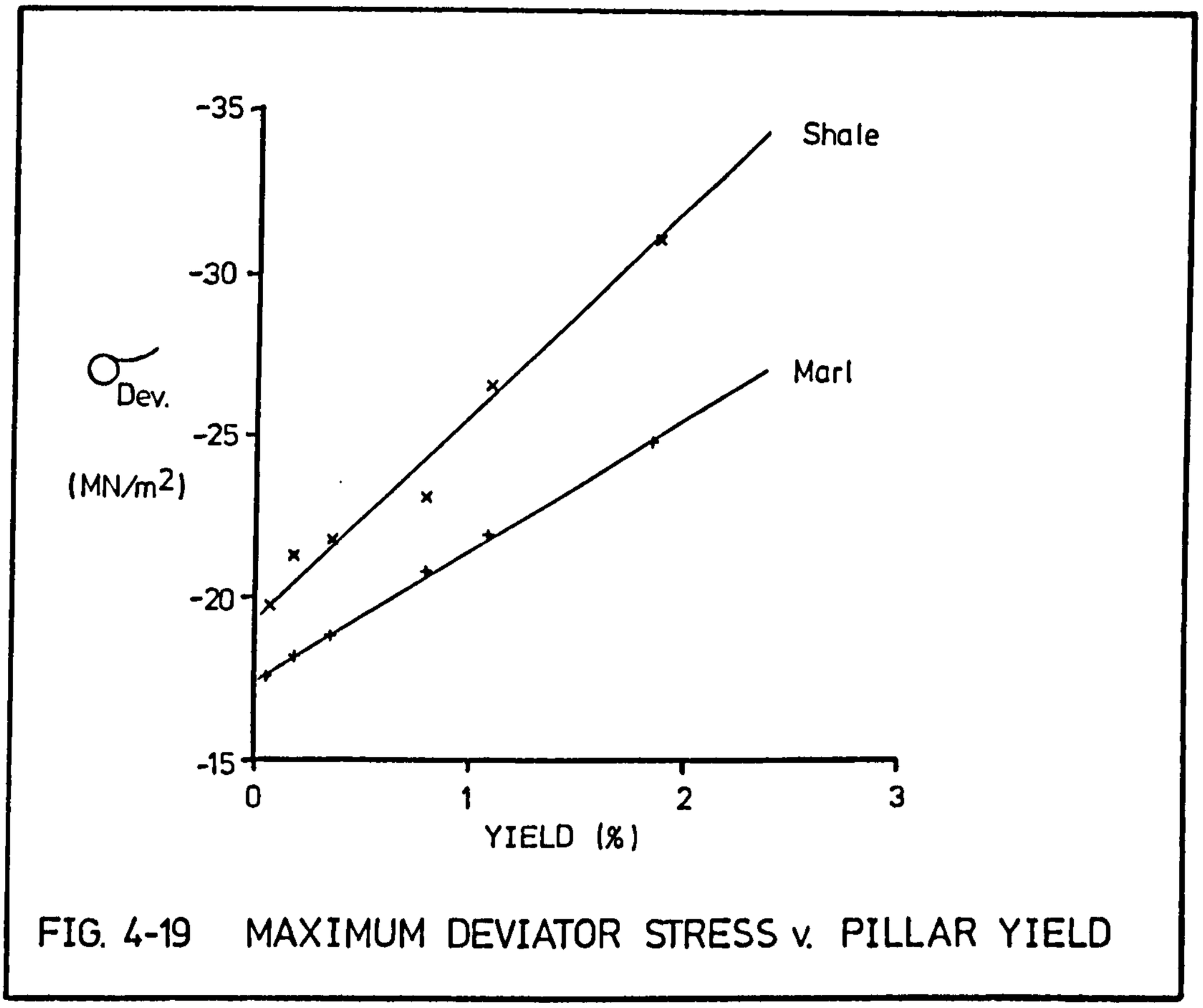

FIG. 4-19 MAXIMUM DEVIATOR STRESS v. PILLAR YIELD

The weak strength of both the marl and shale, and the low deviator stress at which both these materials appear to exhibit excessive creep properties suggest that any amount of panel pillar yield will cause major creep and possible failure of both strata in the vicinity of the pressure arch. Detailed creep data is not yet available on these materials but it is known that they are far less stable than potash for which a maximum deviator of -22.5 MN/m^2 has been defined with a margin of safety.

The consequences of excessive creep in this vicinity would be that as the stress relieved material stabilises on the yielded panel pillars, the marl and shale would become less confined, virtually under a uniaxial loading condition on the lower boundary of the

pressure arch. Large amounts of creep would take place, if not immediate failure, causing a reloading of the stress relieved material. This would be indicated in the panel by continued high closure rates and pillar deformation, even if roof conditions indicated a stress relieved roof stratum. (Normal closure rates should reduce rapidly once the redistribution has taken place.) The end result would be a breakdown of the pressure arch in the shale and marl causing excessive panel closures and possible collapse associated with increased subsidence and strains in the strata between the Bunter Sandstone and the seam. Fig. 4-20 shows hypothetical plots of central roadway closures to be expected for the case of a stable stress relief panel and several variations for an unstable panel.

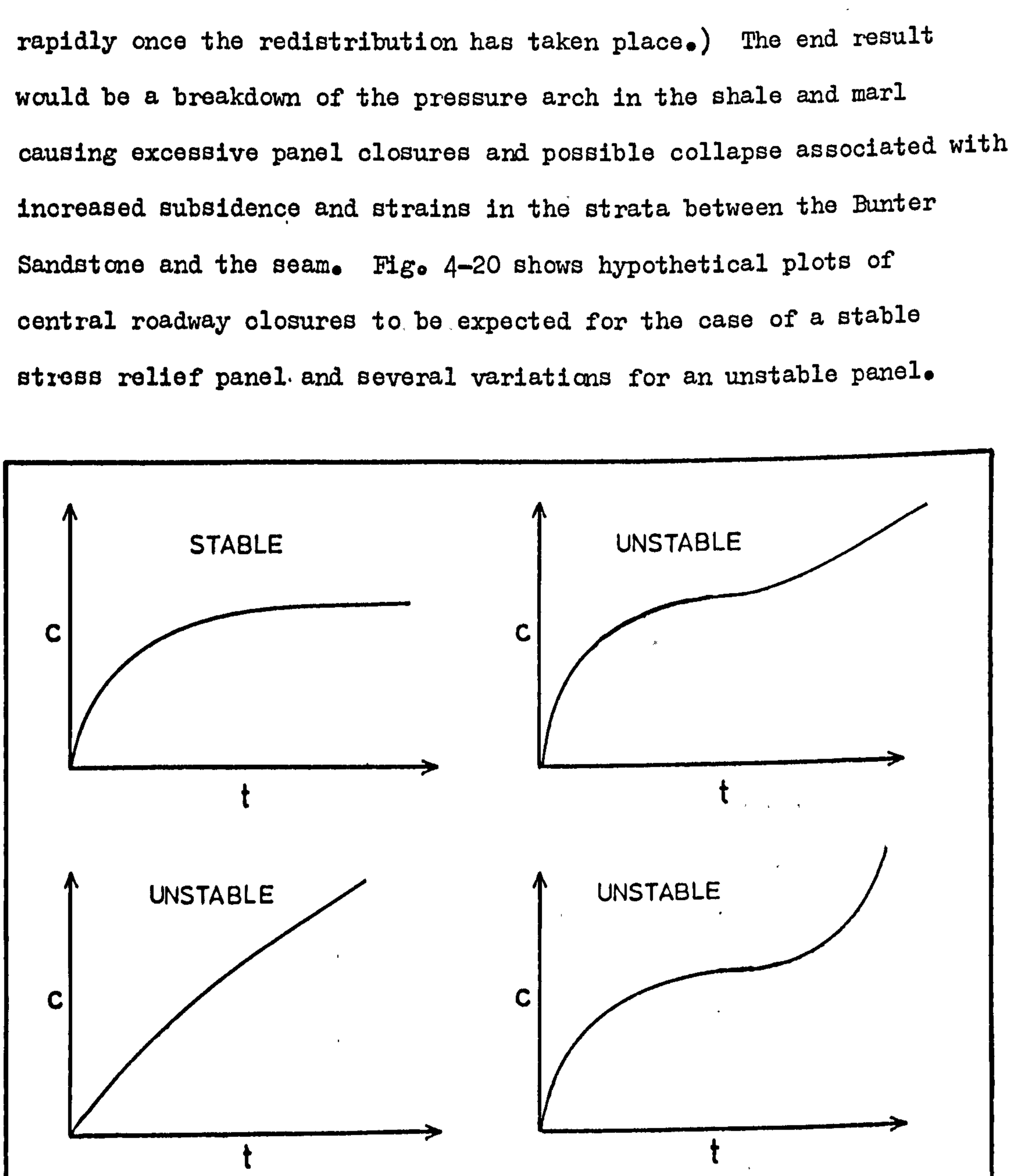

FIG. 4-20 CLOSURE v. TIME FOR STABLE AND UNSTABLE PANELS

4.4 Summary of Conclusions

From the results discussed in this chapter, the following main conclusions may be drawn.

i Fig. 4-3 presents the relationship between panel and barrier widths in terms of induced subsidence strains. The boundary pillar widths between blocks of panels should be much less or much greater than 140m to avoid maximum lateral strain above the seam.

ii Blocks of panels should be mined in sequence either towards a major boundary pillar or towards a virgin ribside, not towards an existing production panel.

iii Minimum barrier pillar widths within a production block should be defined according to equation (4.5) with an absolute minimum of 50m and the barrier width should be greater than the panel width and increased according to the amount of extraction within the barrier.

iv Boundary pillars between blocks must be stiffer than the block barrier pillars but only sufficiently so to maintain correct load distribution over the block. On this basis, solid boundary pillars should be approximately 10m wider than the block barrier pillars, provided this width satisfies the subsidence constraints.

v Boundary pillars containing development entries should be the width of the block barrier pillars either side of the development to prevent excessive loading on the development entries. Fig. 4-9 shows a general layout configuration on the basis of these constraints.

vi At least 1.5% pillar yield should occur to prevent roof warping failures within a stress relief panel due to excessively stiff pillars.

vii At least 1.4% pillar yield, and preferably 2.4%, should occur to prevent shear failures in a shale roof of the central panel roadways. The roof of the outer roads must be expected to fail.

viii Shale roof conditions will lead to failure due to bed separation in stress relief panels just as much as in conventional panels and so maximum roadway widths should be maintained at no more than 6m.

ix To prevent failure of the Upper Anhydrite above the panel centre and the Upper Permian Marl above the ribside a maximum of 2% pillar yield should be permitted to create the initial stress redistribution. On the basis that the full 2% yield is necessary (points (vi) and (vii)) to initiate redistribution, a maximum panel width of 62m should be used.

x Provided that the correct geometry is used for a stress relief panel, and that it is mined in sequence and with the necessary uniform rate of advance, the geology above the seam may still prevent such a panel from having any long term stability. Fig. 4-19 suggests that deviator stresses in the marl and shale will be excessive for any yield pillar panel and this will lead to continued high panel closures and possible excessive subsidence strains above the seam. Before this method is adopted for use

at Boulby an experimental panel should be mined and fully instrumented within the seam and above it to establish the stability, or otherwise, of the strata.

CHAPTER 5

MECHANICAL PROPERTIES OF NEAR-SEAM STRATA

5. MECHANICAL PROPERTIES OF NEAR-SEAM STRATA

The laboratory tests described in this chapter were conducted in order to complement the results obtained by Wiggett (9). Previous results by Patchet (7) had defined the mechanical properties for all the strata between surface and seam using exploration borehole core. As mentioned in Chapter 1, the existence of the secondary ore, predominantly shale, wasn't known at that stage and so Patchet's near-seam strata results did not include any tests on it. However, having encountered the shale material in the roof of most roadways outside the shaft pillar area it became necessary to establish some material properties for the shale.

In conjunction with Wiggett, a testing program was drawn up to re-assess the basic mechanical properties of all of the near-seam strata. This was particularly necessary due to doubt which had arisen over the values obtained by Patchet for Young's Modulus and Poisson's Ratio. Various occasional tests on different specimens invariably gave a much higher value for each of these properties than that obtained by Patchet. It was thought that Patchet's tests had only been conducted over a very low range of stresses incorporating initial crack closure effects. Therefore it was necessary to repeat these tests using rock collected from the mine itself in order to obtain more realistic values.

Rock samples were obtained from the mine and specimens prepared for testing. Rocks forming the potash seam were classified according to shale content with two grades of primary ore (potash)

and three of secondary ore (shale). These latter three types included the boracitic shale and anhydritic shale, both of which occur as bands within the shale raft above the primary ore. Wiggett carried out a large number of tests although he was unable to complete the testing program as it had been originally set out. Table 5-1 lists the mean values for mechanical properties obtained by Wiggett for the primary and secondary ore incorporating the geological variations within each type. The figures in brackets refer to the range of values obtained.

Table 5-1 Mean Values for Mechanical Properties of Potash and Shale (after Wiggett (9))

Rock Type	Young's Modulus GN/m^2	Poisson's Ratio	Uniaxial Compressive Strength MN/m^2	Tensile Strength MN/m^2	Shear Strength MN/m^2
Potash	22.42 (15.00–28.75)	0.372 (0.317–0.439)	-39.66 (-38.99--41.70)		
Shale	11.02 (8.25–14.09)	0.239 (0.125–0.280)	-12.20 (-8.42--14.83)	1.18 (0.61–2.24)	10.36 (9.00–11.58)

The following triaxial compression tests on potash, shale and Carnallite marl were conducted together with a Young's modulus and Poisson's ratio test on Middle Halite using the remaining specimens from Wiggett's testing program. Further tests using a servo-controlled testing machine were carried out and are described in Chapter 6.

5.1 Triaxial Compression Tests

These tests were carried out using an Avery Grade A 100 tonne testing machine and a triaxial compression cell designed by Buzdar (11). A cross-sectional diagram of the cell is shown in Fig. 5-1. The cell was designed specifically for testing evaporites under high confining pressures (up to 70 MN/m^2) and it allows for the large amount of lateral deformation which occurs with this type of material.

The specimens are cylindrical with a diameter of 75mm and length 150mm. Each specimen is sleeved in a rubber membrane (car tyre inner tubes have proved quite satisfactory for short term tests at room temperature) which is sealed against the top and bottom steel platens by a pair of 'O' rings. The top platen has a spherical seating between it and the loading ram. Confining pressure is applied by hydraulic oil once the cell containing the specimen is sealed and it is controlled by an external electric pump. For these tests the pore pressure control valves were sealed off as this control was not required.

The confining pressure was applied in stages as it was not possible to control the pump sufficiently to obtain a uniform rate of pressure increase. For each stage the axial load was applied by the testing machine and then held while confining pressure was increased. The axial pressure was always maintained slightly in excess of the confining pressure to prevent the specimen from becoming unseated within the cell. Once the required confining pressure had been reached the axial load was increased at a constant rate until failure occurred. The loading rate was approximately

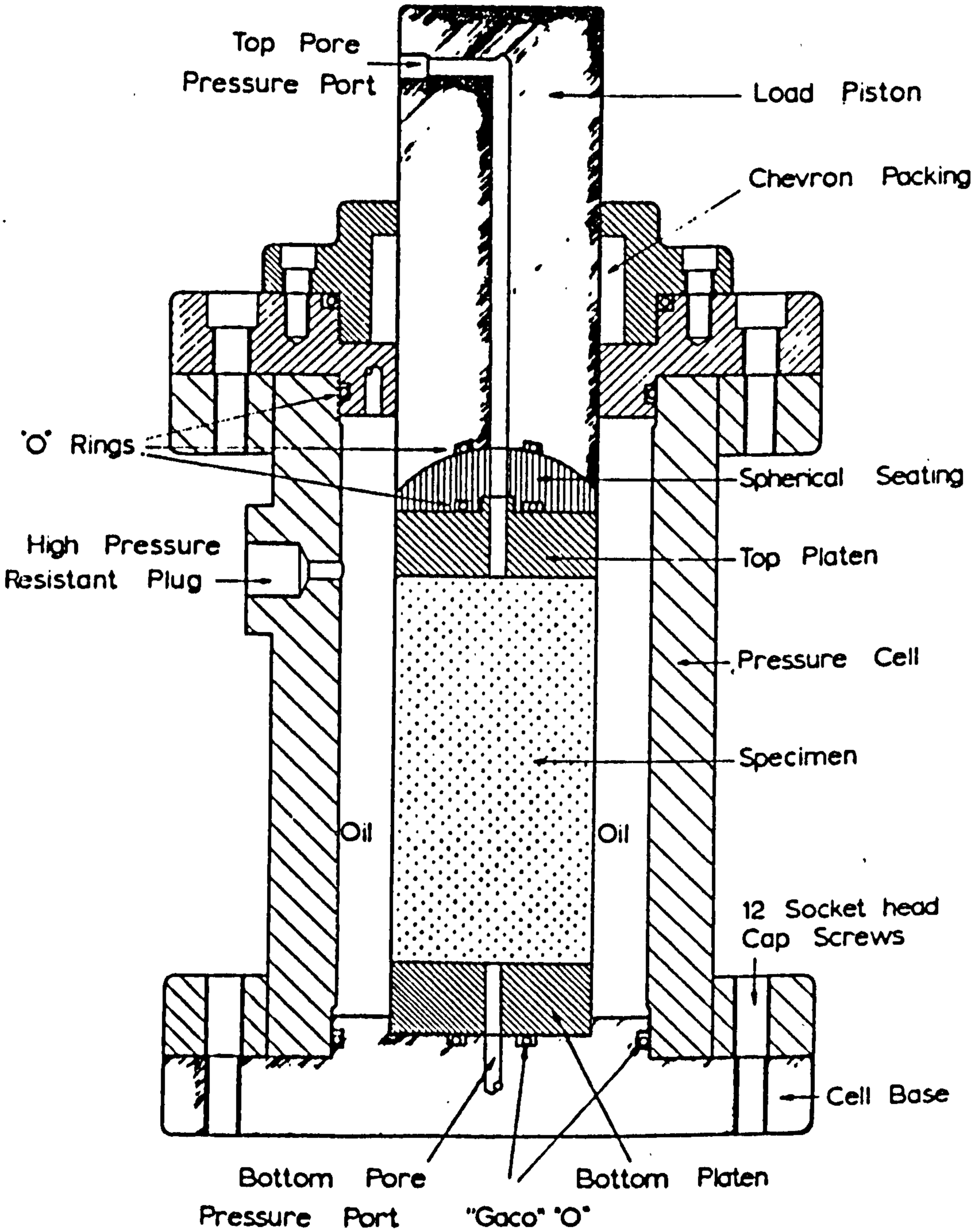

FIG. 5-1 CROSS-SECTION OF TRIAXIAL CELL
(after Buzdar)

700 kN/m^2 per second as recommended by the U.S. Bureau of Mines (34) although problems occurred in controlling the confining pressure and so not all the tests proceeded at a uniform rate. The main problem with controlling the confining pressure was due to the displacement of oil by the high level of lateral deformation of the specimens, particularly the potash. It was found that the most satisfactory technique was to keep the pump running fast at all times but with the bypass valve slightly open to maintain a constant pressure. This provided far more control over the cell pressure and was thus much more sensitive to changes in pressure due to volumetric changes within the cell.

Axial strain of the specimen was monitored continuously by means of a chart recorder connected to the platens of the testing machine. In all the results, failure stress and failure strain refer to the point of ultimate compressive strength for the specimen.

From the results of each test a Mohr's Envelope has been constructed tangent to the Mohr's circles as shown in Fig. 5-2.

5.1.1 Triaxial Compression - Potash Results

A total of five specimens, including one tested uniaxially, were tested to obtain the results for potash. Table 5-2 lists the results obtained and the stress-strain curves are plotted in Fig. 5-3. Fig. 5-4 shows the condition of the specimens when they were removed from the cell after testing.

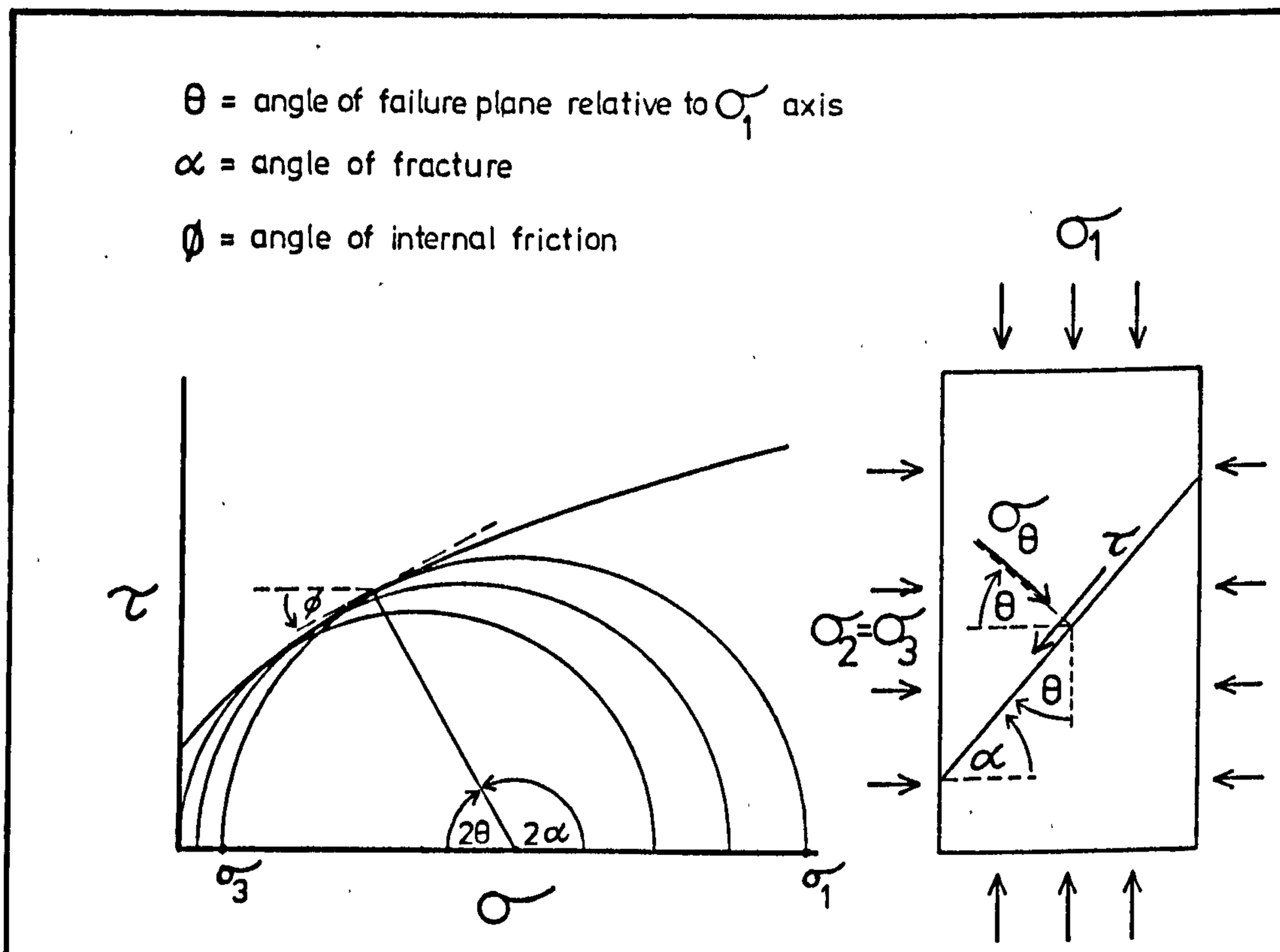

FIG. 5-2 RELATIONSHIP BETWEEN MOHR ENVELOPE AND SPECIMEN FAILURE MECHANISM

Table 5-2 Triaxial Compression Results - Potash

Specimen No.	Confining Pressure (MN/m^2)	Failure Stress (MN/m^2)	Failure Strain (%)
PP9	0.0	-32.23	3.5
PP5	- 5.17	-61.84	13.3
PP6	-10.34	-80.48	20.7
PP7	-16.55	-104.16	32.1
PP8	-24.82	-124.55	43.7

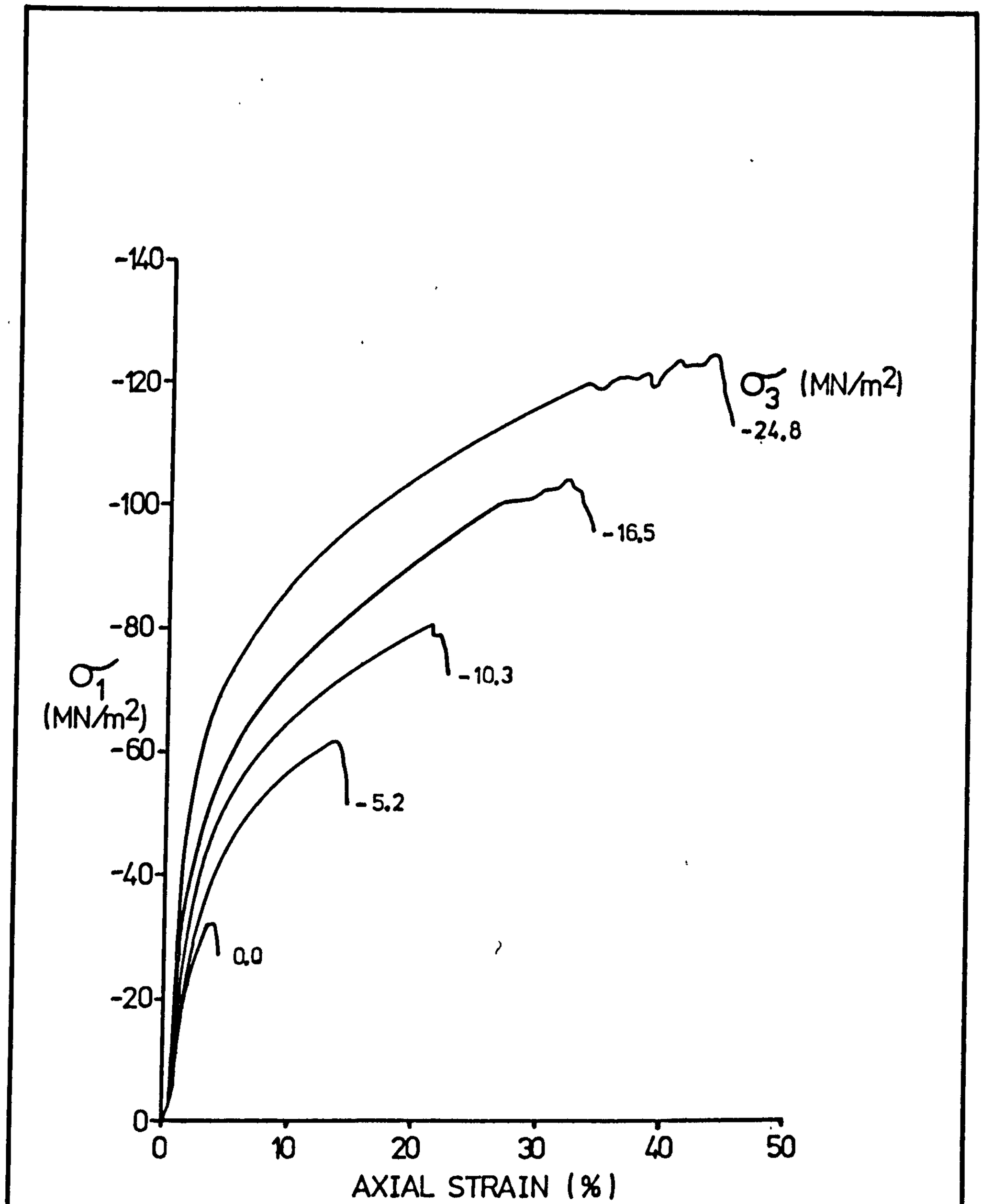

FIG. 5-3 EFFECT OF CONFINEMENT ON STRESS-STRAIN CURVE FOR POTASH

Specimen PP8
σ3 = 24.82MN/m2
σ1(fail) = 124.55 MN/m2
Specimen PP7
σ3 = 16.55MN/m2
σ1(fail) = 104.16 MN/m2
Specimen PP6
σ3 = 10.34 MN/m2
σ1(fail) = 80.48 MN/m2
Specimen PP5
σ3 = 5.17 MN/m2
σ1(fail) = 61.84 MN/m2
Specimen PP9
σ3 = 0.0 MN/m2
σ1(fail) = 32.23 MN/m2

Fig. 5-4

σ_3	$\sigma_{1(fail)}$	$\phi°$
0	-32	53
-5	-61	45
-10	-80	42
-15	-95	40
-20	-112	37
-25	-125	35

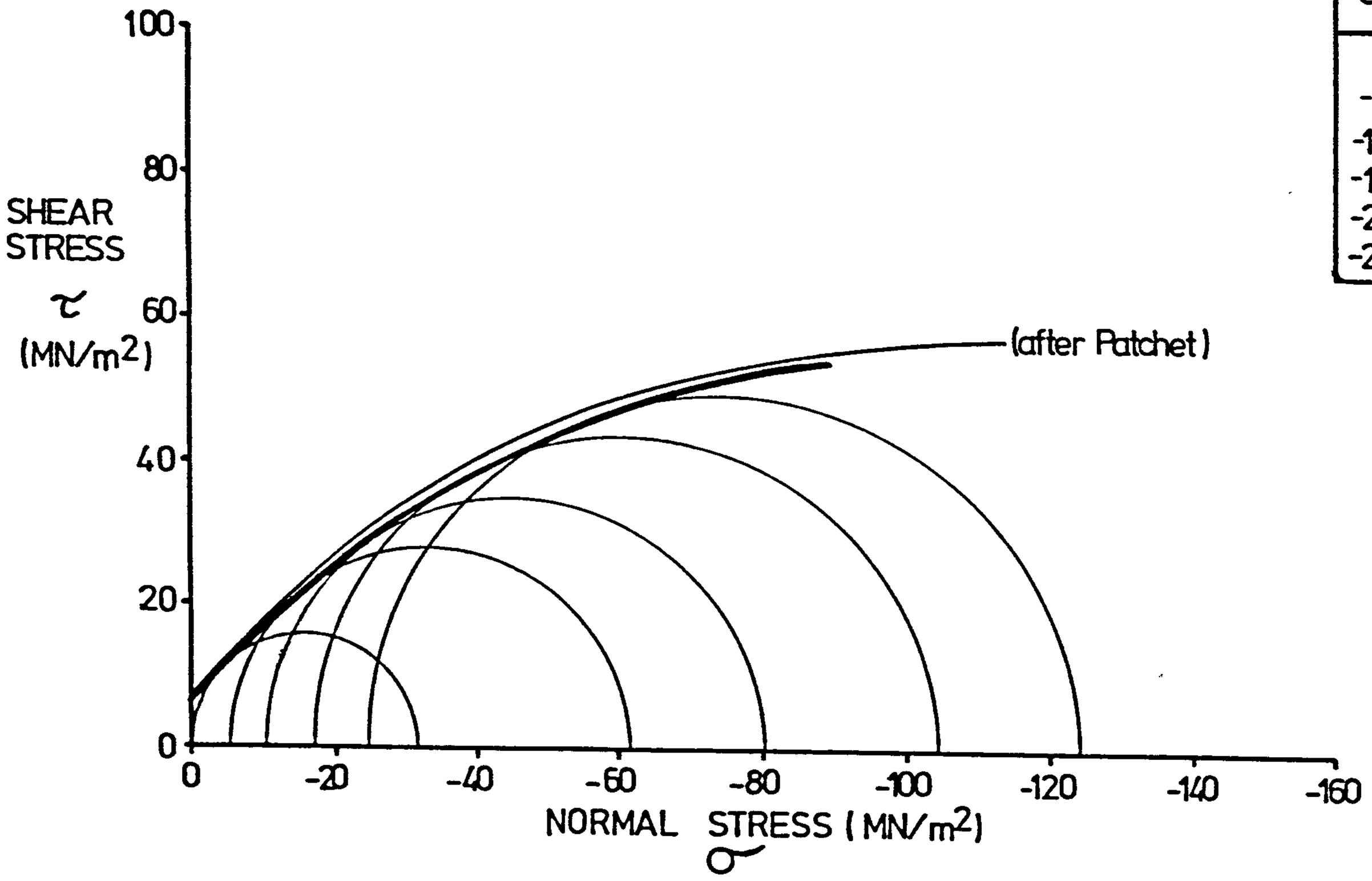

FIG. 5-5 MOHR ENVELOPE FOR POTASH

The last three specimens all show the presence of oil but it does not appear to have greatly influenced the results since it would only have penetrated the rubber membrane at the point of failure. As Fig. 5-3 and Fig. 5-4 show, considerable yield has taken place in the highly confined specimens which have deformed laterally to a great extent. There appears to be very little elastic behaviour even at high levels of confinement.

Fig. 5-5 is the Mohr envelope obtained from these results. The list of stresses and angles represent points along the failure envelope. Also included on Fig. 5-5 is the Mohr envelope obtained by Patchet which shows very close agreement with the present results.

5.1.2 Triaxial Compression - Shale Results

Six specimens were tested in this set, including the uniaxial one, and the results are listed in Table 5-3. Fig. 5-6 is a plot

Table 5-3 Triaxial Compression Results - Shale

Specimen No.	Confining Pressure (MN/m^2)	Failure Stress (MN/m^2)	Failure Strain (%)
SP13	0.0	- 11.84	2.3
SP 8	- 5.17	- 48.24	3.2
SP 9	-10.34	- 59.64	4.2
SP10	-16.55	- 66.66	5.4
SP11	-24.82	-100.21	7.3
SP12	-34.48	-115.12	12.5

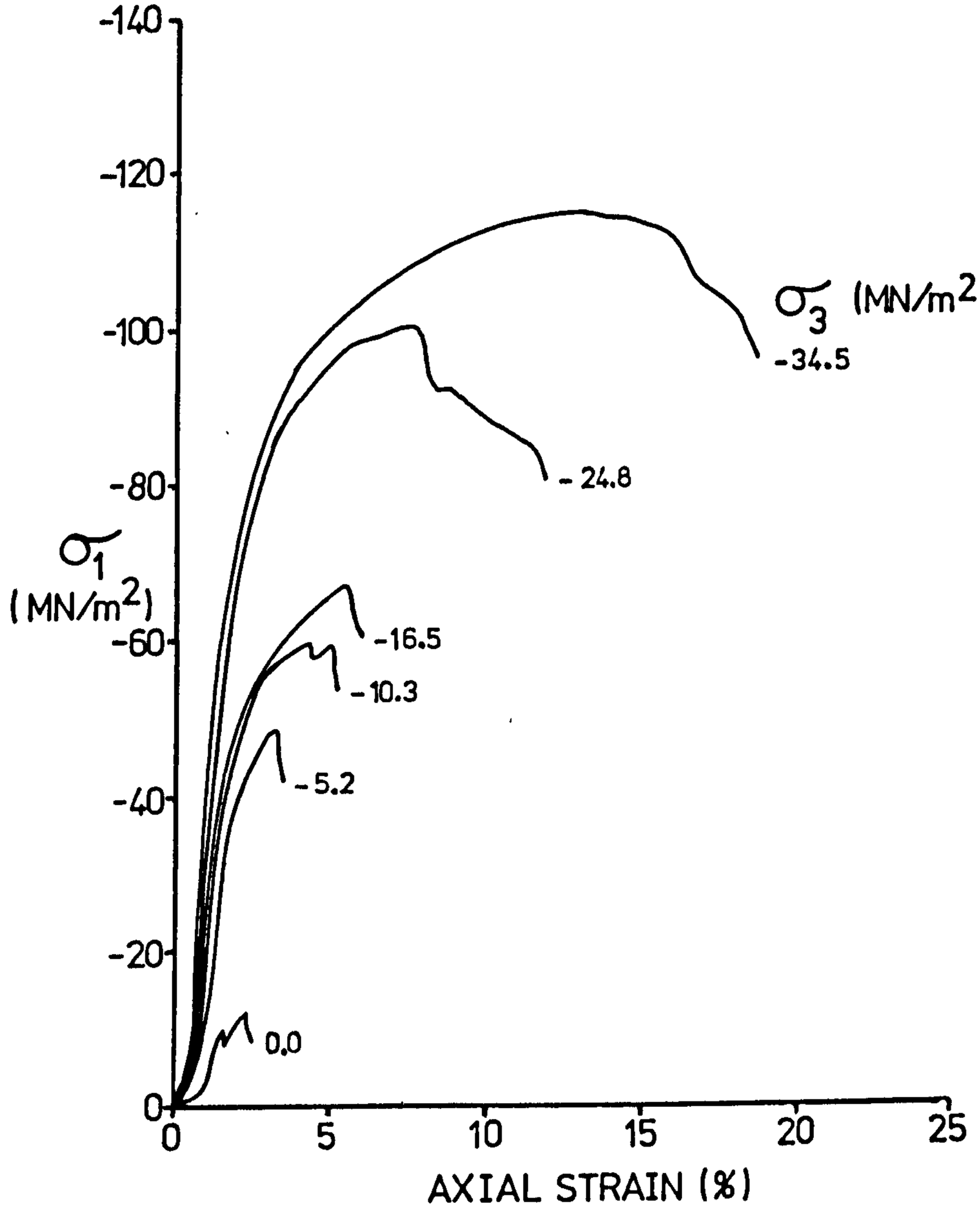

FIG. 5-6 EFFECT OF CONFINEMENT ON STRESS-STRAIN CURVE FOR SHALE

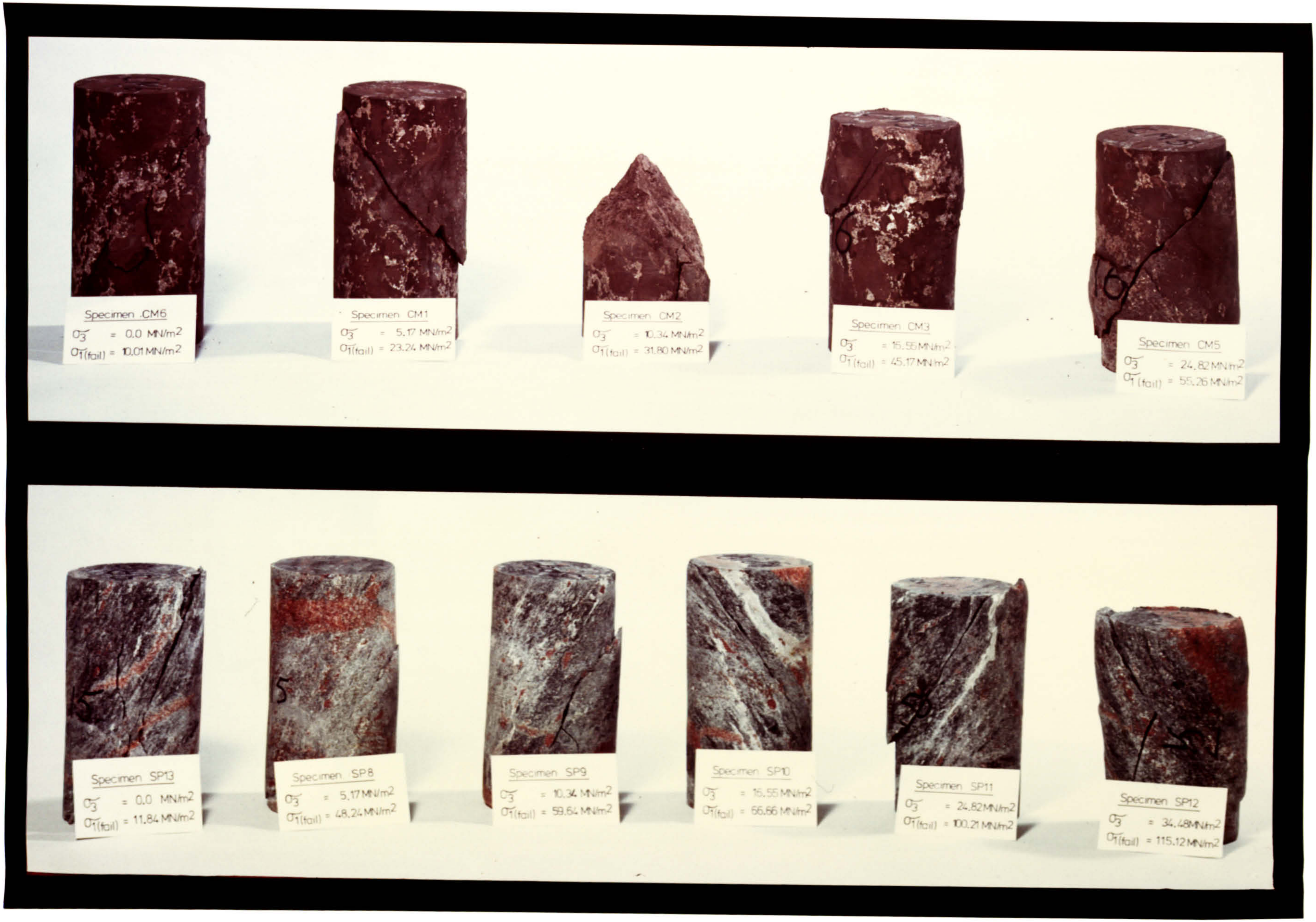
Specimen CM6
$\bar{\sigma_3}$ = 0.0 MN/m²
$\bar{\sigma_1}$(fail) = 10.01 MN/m²
Specimen CM1
$\bar{\sigma_3}$ = 5.17 MN/m²
$\bar{\sigma_1}$(fail) = 23.24 MN/m²
Specimen CM2
$\bar{\sigma_3}$ = 10.34 MN/m²
$\bar{\sigma_1}$(fail) = 31.80 MN/m²
Specimen CM3
$\bar{\sigma_3}$ = 16.55 MN/m²
$\bar{\sigma_1}$(fail) = 45.17 MN/m²
Specimen CM5
$\bar{\sigma_3}$ = 24.82 MN/m²
$\bar{\sigma_1}$(fail) = 55.26 MN/m²
Specimen SP13
$\bar{\sigma_3}$ = 0.0 MN/m²
$\bar{\sigma_1}$(fail) = 11.84 MN/m²
Specimen SP8
$\bar{\sigma_3}$ = 5.17 MN/m²
$\bar{\sigma_1}$(fail) = 48.24 MN/m²
Specimen SP9
$\bar{\sigma_3}$ = 10.34 MN/m²
$\bar{\sigma_1}$(fail) = 59.64 MN/m²
Specimen SP10
$\bar{\sigma_3}$ = 16.55 MN/m²
$\bar{\sigma_1}$(fail) = 66.66 MN/m²
Specimen SP11
$\bar{\sigma_3}$ = 24.82 MN/m²
$\bar{\sigma_1}$(fail) = 100.21 MN/m²
Specimen SP12
$\bar{\sigma_3}$ = 34.48 MN/m²
$\bar{\sigma_1}$(fail) = 115.12 MN/m²

σ_3	$\sigma_{1(fail)}$	$\phi°$
0	-17	40
-5	-37	38
-10	-58	37
-15	-75	36
-20	-89	34
-25	-100	32

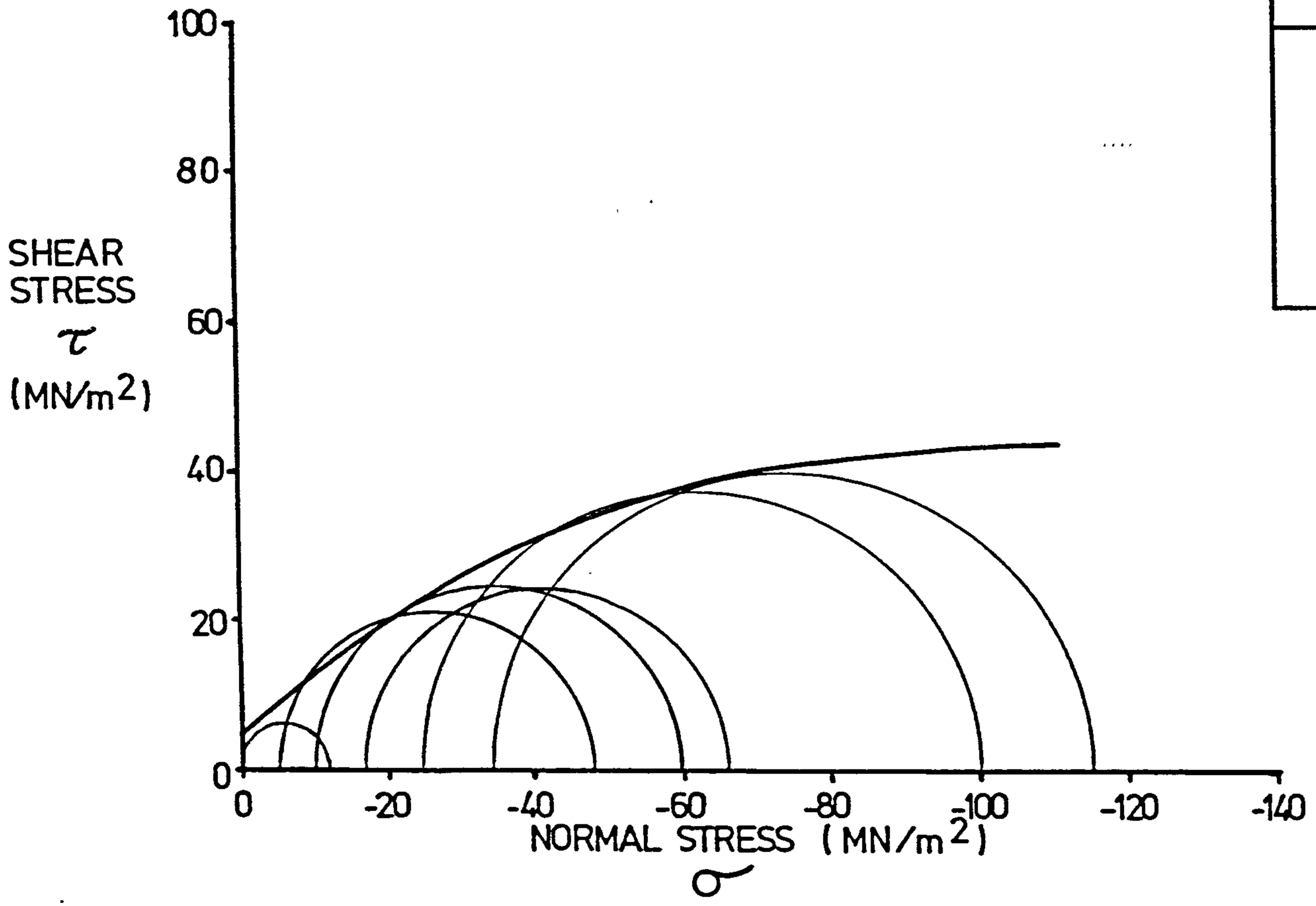

FIG. 5-8 MOHR ENVELOPE FOR SHALE

of the stress-strain results and the specimens are shown in Fig. 5-7 together with the marl specimens. Fig. 5-8 shows the Mohr envelope obtained from the shale results.

The plotted results and the photcgraphs both show the extremely elastic behaviour of the shale at all but the very high confining pressures. The specimens tested, particularly SP10 and SP11, both had pronounced bedding at approximately 45°, along which failure subsequently occurred. The last specimen, SP12, shows the effect of sylvinite (red colouring) in the shale. On both sides of the specimen, most of the lateral flow is from the sylvinite inclusions. Similarly, SP11 which contained sylvinite, showed the same characteristics.

It would appear that apart from the sylvinite content the shale behaves fairly elastically. The small increase in confinement between the uniaxial test and the first triaxial one has considerably increased the strength by providing a confining force across potential failure planes. However, with no confinement at all the shale shows very brittle, weak characteristics and at the depth at which it occurs it must be regarded as an incompetent material when unconfined.

5.1.3 Triaxial Compression - Carnallite Marl Results

Five specimens were tested but no strain results were obtained for the uniaxial test. Table 5-4 lists the results and the stress strain curves are plotted in Fig. 5-9. The specimens

are shown in Fig. 5-7. Fig. 5-10 is the Mohr envelope obtained for marl.

Table 5-4 Triaxial Compression Results - Carnallite Marl

Specimen No.	Confining Pressure (MN/m^2)	Failure Stress (MN/m^2)	Failure Strain (%)
CM6	0.0	-10.09	-
CM1	- 5.17	-23.24	2.3
CM2	-10.34	-31.80	3.7
CM3	-16.55	-45.17	6.3
CM5	-24.82	-55.26	7.8

As can be seen from the Mohr circles from each test there was some inconsistency due to the variability in the marl composition. Once again, oil had penetrated a number of specimens although presumably only at the failure point. This was the reason for the size of specimen CM2, the top half of which had completely disintegrated due to the oil penetration.

The results and the failure planes of the specimens suggest a fairly brittle, elastic material at low confinement. All the specimens show some degree of residual strength beyond peak strength presumably where sliding along fracture planes was taking place. However, the penetration of oil will have made the end points of these residual plateaux somewhat meaningless.

One point of significance in the results is the lack of lateral deformation or bulging in most of the specimens. Specimen CM3 shows the most bulging and possibly a more conical failure

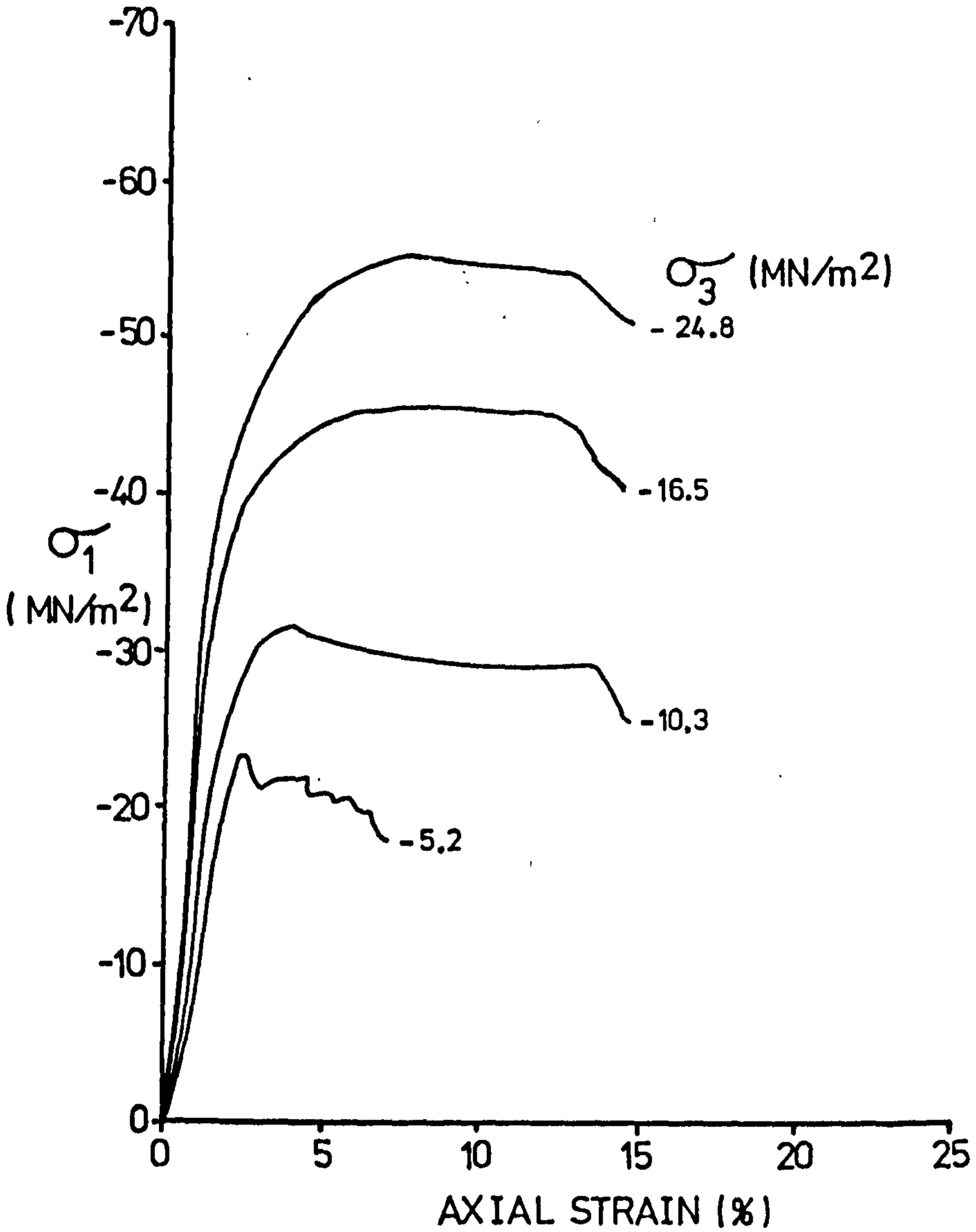

FIG. 5-9 EFFECT OF CONFINEMENT ON STRESS-STRAIN CURVE FOR CARNALLITE MARL

σ_3	$\sigma_{1(fail)}$	$\phi°$
0	-11	26
-5	-23	23
-10	-33	22
-15	-41	19
-20	-49	16
-25	-57	14

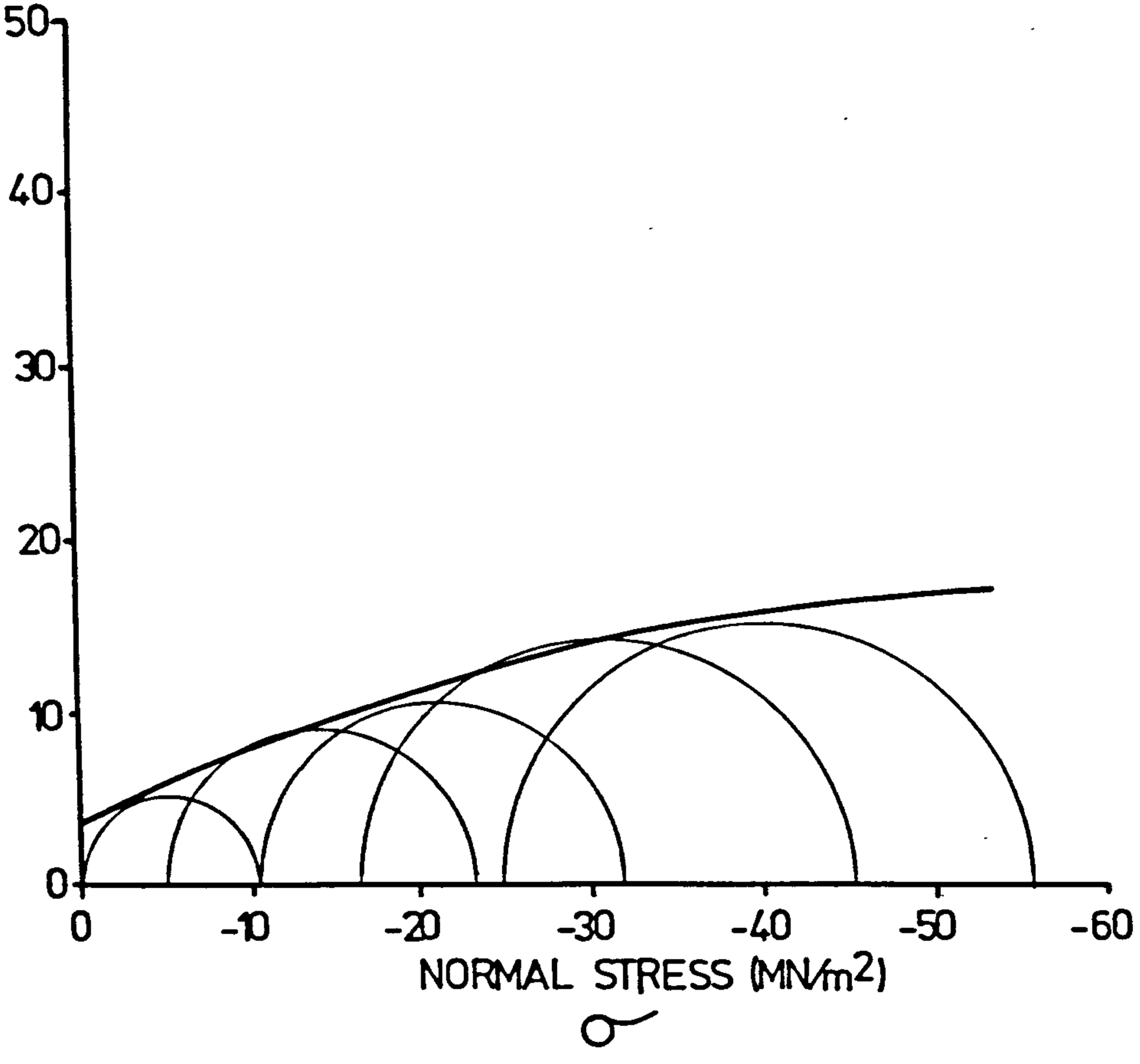

FIG. 5-10 MOHR ENVELOPE FOR CARNALLITE MARL

pattern. This appears to be associated with the increased halite content within the marl. This is similar to the phenomenon observed with the shale where apart from any evaporite content, the material has behaved virtually elastically.

5.1.4 Comparison of Results

The three sets of results provide a useful comparison of the competence of each rock type in-situ where they will almcst always have some degree of confinement.

Fig. 5-11 shows the relationship between failure strain and confining pressure for each rock type. In each case the relationship is virtually linear with marl and shale having similar results, but pctash markedly different. This gives an indication of the relative brittleness, or capacity for yield, possessed by each rock type. As either a pillar or a roof material the shale clearly has far less yield capacity than potash and so underground design should be modified accordingly.

Fig. 5-12 shows the effect of confinement on failure strength as compared with uniaxial strength. The shale shows the greatest increase in strength although this is due mostly to the initial 5 MN/m^2 of confinement. Within this amount the strength of the shale increases by a factor of four compared with approximately two for both potash and marl.

In order to compare absolute strengths relative to confinement, Fig. 5-13 is a plot of axial failure strength against confinement. This shows the weakness of the marl relative to the

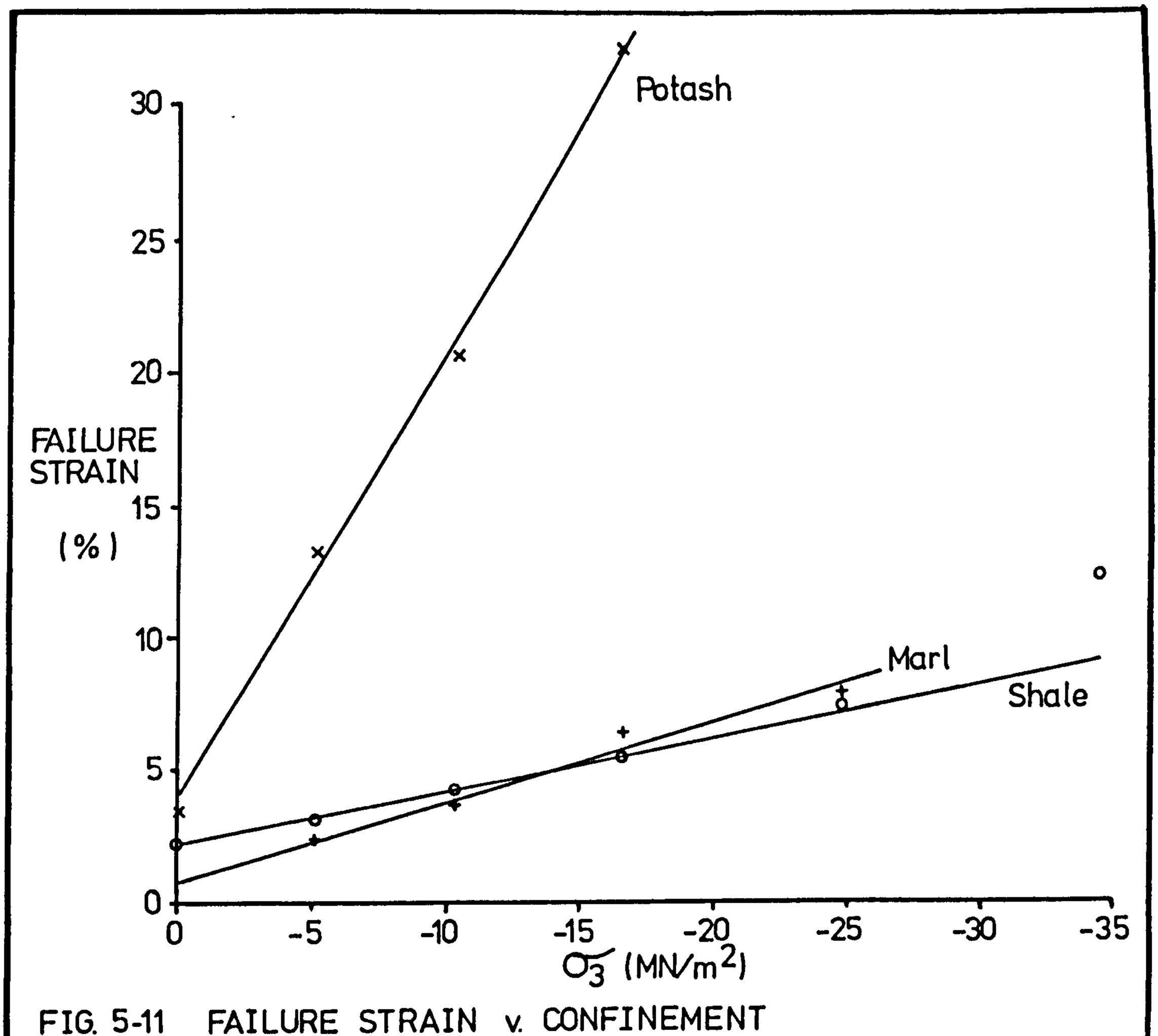

FIG. 5-11 FAILURE STRAIN v. CONFINEMENT

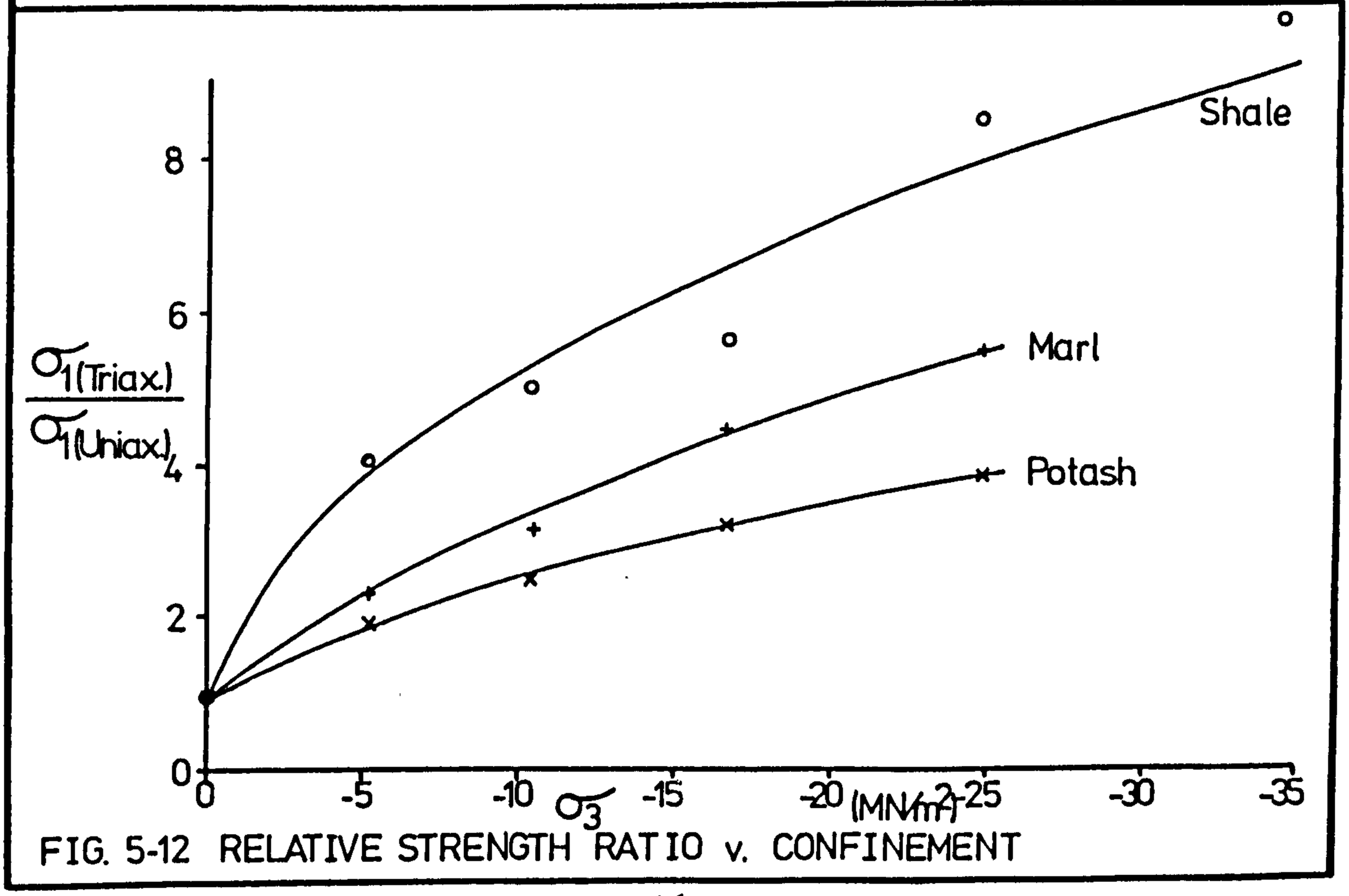

FIG. 5-12 RELATIVE STRENGTH RATIO v. CONFINEMENT

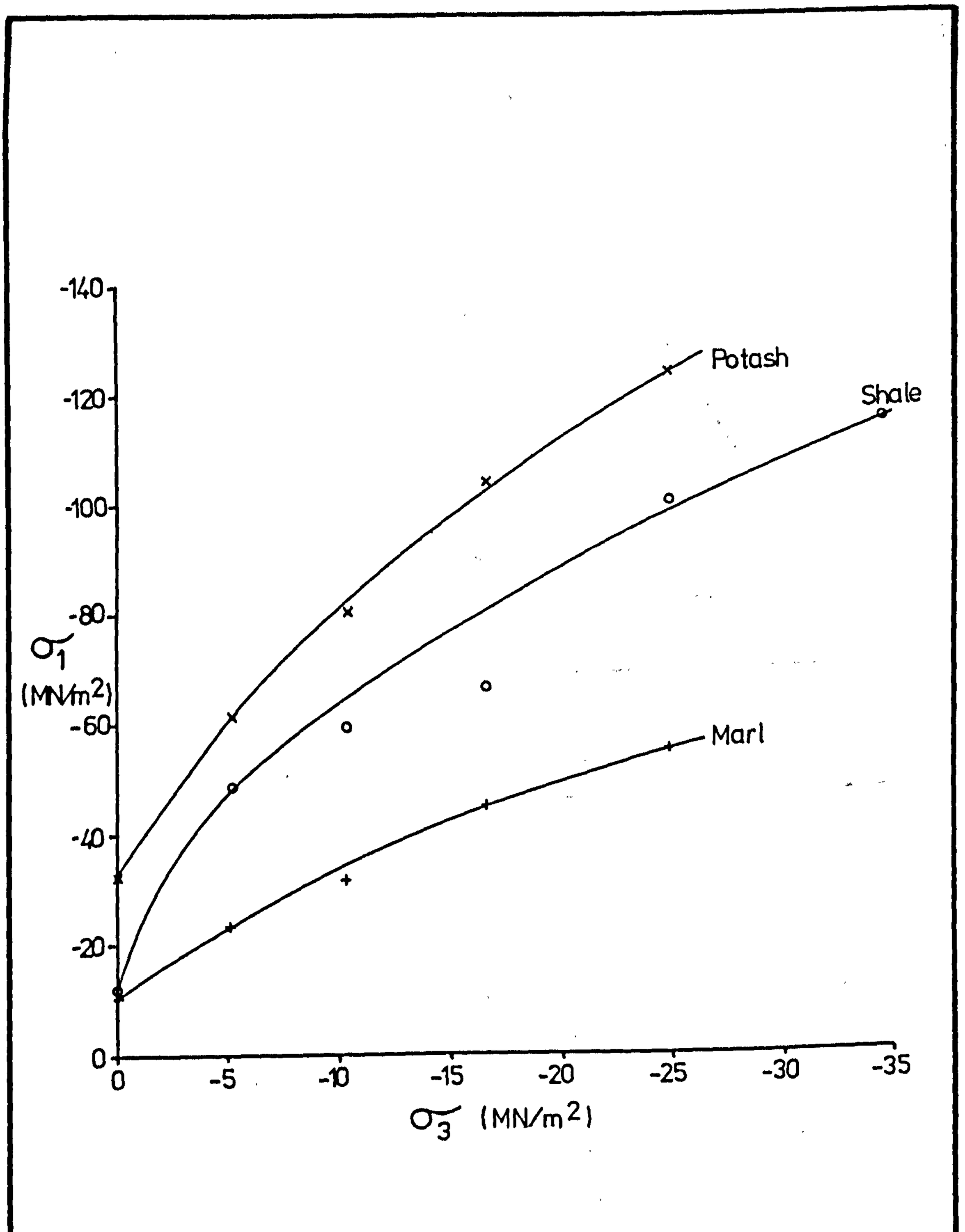

FIG. 5-13 STRENGTH v. CONFINEMENT

other two materials even under confinement. However, the shale strength is virtually 80% of the potash strength in all except the unconfined state where it is only 37%.

5.2 Middle Halite - Elastic Properties

This test was conducted purely as a check on Patchet's results (7) and only one specimen was available. Fig. 5-14 shows the value obtained for Young's Modulus and Poisson's Ratio for

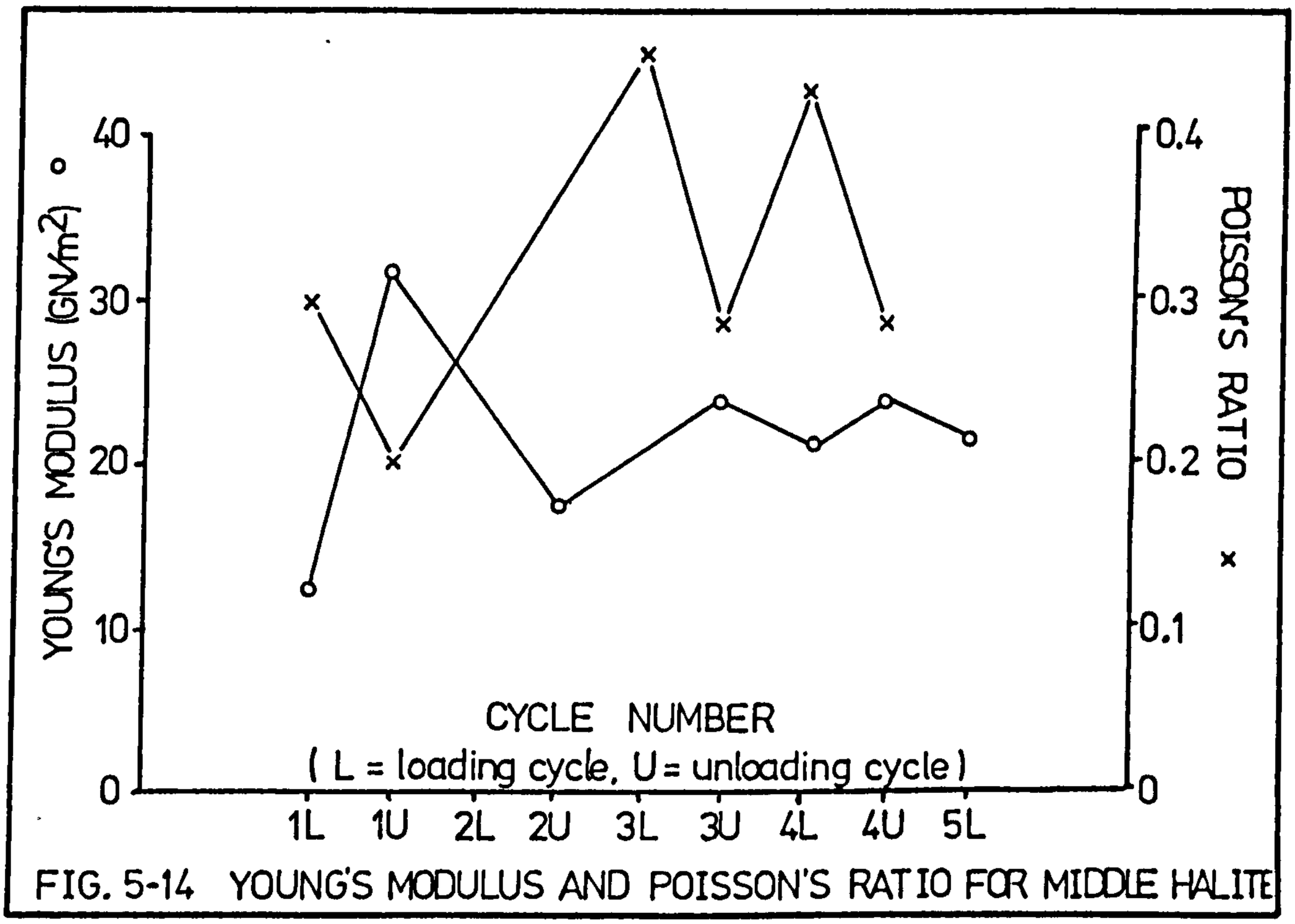

FIG. 5-14 YOUNG'S MODULUS AND POISSON'S RATIO FOR MIDDLE HALITE

five cycles prior to failure. The figures are based on results from 120 ohm strain gauges, two attached laterally and two axially to the 150mm by 75mm cylindrical specimen.

In view of the fact that the rock material underground is very rarely in an unloaded condition, the values obtained

on the unloading cycle from a state of confinement should be more appropriate than those from the loading cycle. It is also clear that several cycles are necessary before the values stabilise. These results were obtained from cycles between -2.29 MN/m^2 and -13.72 MN/m^2. The eventual uniaxial failure strength of the specimen was -23.60 MN/m^2.

The value of Young's Modulus obtained was 23.66 GN/m^2 and Poisson's Ratio was 0.284. Patchet obtained results of 4.20 GN/m^2 and 0.23.

5.3 Summary of Near-Seam Mechanical Properties

Apart from work by Patchet (7) and Wiggett (9), a program of testing on Carnallite Marl was carried out by Vutukuri (35). He obtained a mean value of Young's Modulus of 7.01 GN/m^2 and a Poisson's Ratio of 0.20.

In order to have a more realistic set of mechanical properties for the near-seam strata, Table 5-5 has been drawn up. This is based on Wiggett's results listed in an earlier section, the values for the elastic constants described above and Patchet's values for strengths. Triaxial properties are not included but are as shown earlier in this chapter.

Table 5-5 Summary of Near-Seam Mechanical Properties

Material Type	Young's Modulus (GN/m^2)	Poisson's Ratio	Uniaxial Compressive Strength (MN/m^2)	Tensile Strength (MN/m^2)
Carnallite Marl	7.01	0.20	-14.66	1.24
Shale	11.02	0.24	-12.20	1.18
Potash	22.42	0.37	-39.66	1.79
Middle Halite	23.66	0.28	-26.77	1.63

5.4 Anhydrite Tensile Strength and Modulus

In connection with subsidence analyses it was necessary to obtain a value for the horizontal tensile failure strain of anhydrite. Although no specimens of the thin band of anhydrite in the Upper Permian Marl were available some from the Upper Anhydrite were available from exploration borehole core. The purest of these cores were selected as being the most representative of the higher band of anhydrite.

A program of tests was initiated to define any anisotropy which might exist in the anhydrite tensile strength and also the tensile elastic modulus. From the vertical borehole core, cores were made horizontally and vertically and discs prepared for

Brazilian disc tests. The horizontal cores would allow tensile stresses in vertical and horizontal directions while the vertical cores would only allow horizontal stresses.

A total of 21 discs were prepared with a diameter, D, of 49mm and length, L, 26mm. The relationship between tensile strength, T, and failure load, F, given in equation (5.1) was used to obtain the results.

$$T = \frac{2}{\pi}\left(\frac{F}{DL}\right) \qquad (5.1)$$

Table 5-6 lists the mean values of the results obtained for each section of core tested in the 25 tonne Avery testing machine.

Table 5-6 Tensile Strength of Upper Anhydrite

Origin of Core (Borehole & Depth)	Direction of Failure Stress	Mean Tensile Strength (MN/m^2)	No. Specimens Tested
S8 (1177m)	Horizontal	4.868	3
S8 (1177m)	Vertical	3.740	3
S11-D4 (1165m)	Horizontal	4.530	3
S11-D4 (1165m)	Vertical	4.218	3
S11-D2 (1164m)	Horizontal	5.167	9

These results yield a mean vertical tensile strength of 3.979 MN/m^2 and a mean horizontal tensile strength of 4.980 MN/m^2.

The tensile elastic modulus was obtained using direct pull tests on two 150mm by 75mm specimens in the 25 tonne Avery testing

machine. Steel platens were glued to the specimen ends and coupled to wire ropes from the platens to ensure uniformity of loading. Specimens were strain gauged and the load cycled six times to obtain a modulus. The results of these tests are listed in Table 5-7.

Table 5-7 Tensile Elastic Modulus of Upper Anhydrite

Origin of Core (Borehole and Depth)	Tensile Modulus (GN/m^2)
S7 (1197m)	51.5
S11-D4 (1165m)	42.8
Mean Tensile Modulus	47.2

On the basis of the horizontal strength obtained above and this elastic modulus (2.47 times the compressive modulus obtained by Patchet (7)), a horizontal tensile failure strain of 106 microstrain is obtained.

5.5 Summary of Conclusions

From the results discussed in this chapter, the following main conclusions can be drawn.

i Potash exhibits very little elastic behaviour even under high confining pressures and shows large amounts of yield prior to the failure strength.

ii Both the shale and marl have basically elastic characteristics with low failure strains except under high confinement. However, the presence of any evaporites within either of these materials appears to cause non-elastic behaviour and increased yield.

iii The shale is very weak when unconfined and, together with marl, should be regarded as incompetent when in an unconfined state.

iv A small amount of confinement increases the shale strength to approximately 80% that of potash although the marl is considerably weaker, even under confinement.

v Table 5-5 summarizes the mechanical properties of the near-seam strata and their uniaxial strengths.

vi The Upper Anhydrite which is of a similar nature to the anhydrite band in the Upper Permian Marl, has a tensile failure strain of 106 microstrain.

CHAPTER 6

COMPLETE STRESS-STRAIN BEHAVIOUR OF MODEL POTASH PILLARS AND ADJACENT ROCK TYPES

6. COMPLETE STRESS-STRAIN BEHAVIOUR OF MODEL POTASH PILLARS AND ADJACENT ROCK TYPES

6.1 Importance of Post-Failure Characteristics

The ability to measure the relationship between stress and strain for a material, beyond the point of maximum strength, has only come about in recent years. Conventional testing machines (referred to as soft testing machines) have been used in the past to monitor stress-strain curves for materials, up to the point of peak strength. However, beyond this point, the behaviour of the failed material has generally been masked by the unloading characteristic of the testing machine itself. This is due to the energy stored up in the machine rig during loading being released as kinetic energy at failure point. The energy is released at a greater rate than that which the unloading, failed material can absorb.

However, with the advent of stiff testing machines and, more recently, servo-controlled testing machines, it has become apparent that many materials, including rocks, are still capable of supporting considerable loads even after the point of peak strength (referred to as failure point for definition purposes only). This capability of rocks is very important in the field of mining engineering since, in the majority of cases, the roof and floor strata of a mine are stiffer than the pillar material, even in a failed state. It is important that this be the case where pillars are to be loaded close to their failure strength, otherwise pillar failure could lead to violent rockbursts due to the release of energy similar to the explosive-type failures which

can occur in soft testing machines.

The purpose of this investigation is to define the post-failure characteristics of pillar material in relation to the yield pillar technique referred to in Chapter 4. In such a system the pillar is required to be strained beyond the failure point in order that load is redistributed away from the pillar vicinity. The failed pillar must still be capable of further straining to incorporate time-dependent pillar yield. Fig. 6-1 illustrates this principle. The line OABDE represents the stress-strain curve for a particular pillar. The

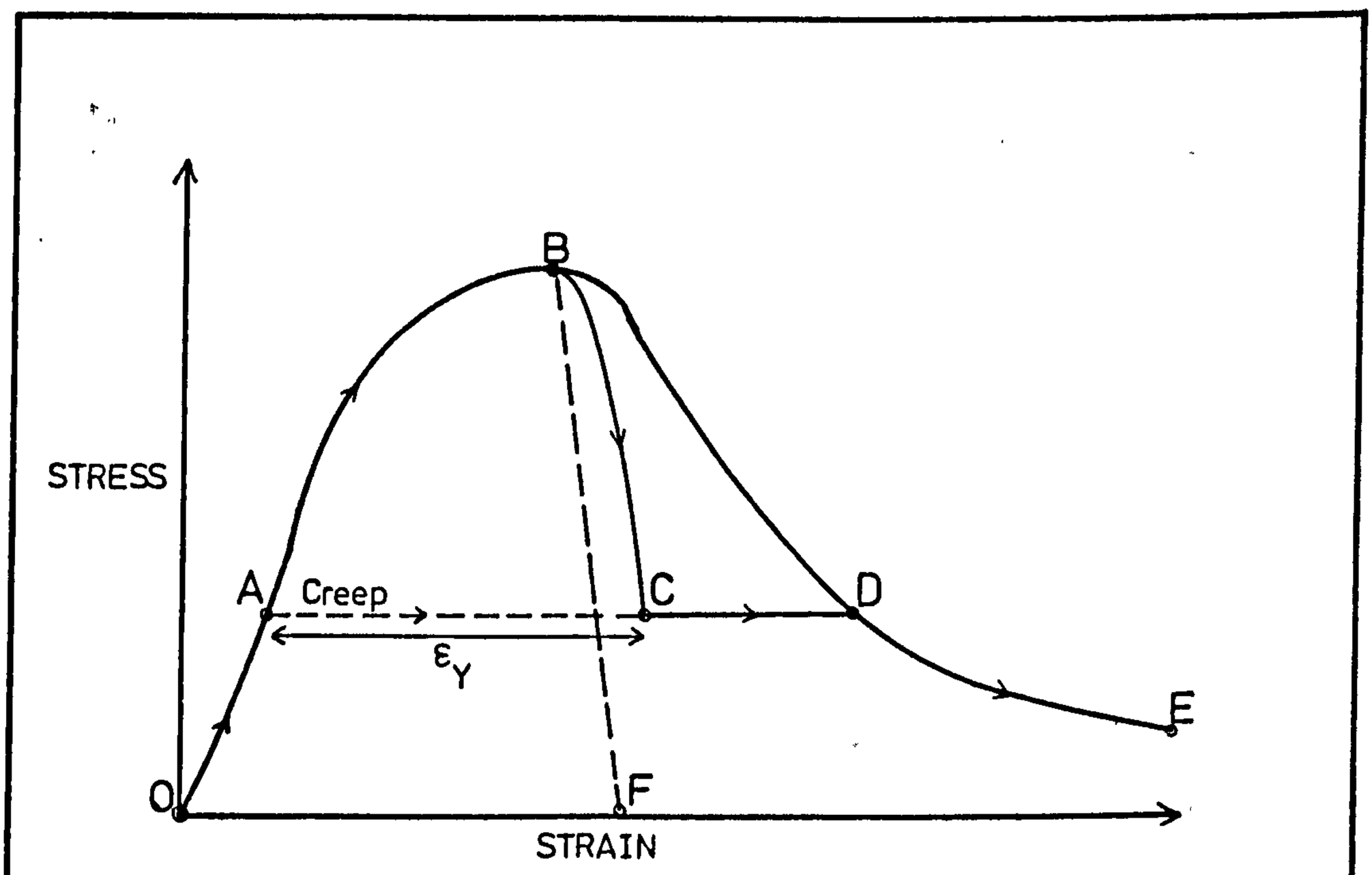

FIG. 6-1 STRESS-STRAIN PATH FOR YIELD PILLAR

geometry and geology require that the pillar yields by ε_y before there is significant stress relief and an equilibrium exists. The pillar must therefore be loaded to the point B if sufficient yield is to take place in a reasonably short time. (The alternative would be to load

the pillar to point A then allow it to creep until it reached C - this could take years). Beyond B the pillar sheds load, forcing stress redistribution to take place. The pillar reaches some point C at which an equilibrium exists in terms of stress, strain and time for both roof and pillar material. During the unloading between B and C the major stress relief has occurred as a result of sufficient yield taking place and competent strata above and below the pillar effecting the necessary redistribution. The pillar is now only slightly loaded and can creep under constant load along the line CD where it will again be forced to shed load. Provided CD represents sufficient strain, the pillar can be designed to remain stable for the life of the panel without shedding further load.

In the situation where the surrounding strata is incapable of redistributing or maintaining the redistributed stress field, if a load greater than that at B is applied to the pillar, it will continue to unload in the region between the strata stiffness curve, BF, and the pillar unloading curve BE. The pillar will eventually yield to such an extent that it can carry no further load.

The laboratory tests described in this chapter have been carried out in a servo-controlled testing machine. This type of machine has the advantage of being able to control any signal associated with the specimen. By comparing the feedback signal from the specimen with a pre-programmed signal in a servo-amplifier, a servo-valve on the machine hydraulic system is actuated to correct for the difference in the two signals compared. Such a closed loop system is shown in Fig. 6-2. By using a voltage transducer to monitor axial deformation of the specimen, a constant deformation (or strain) rate can be maintained and so the full stress-strain curve of the

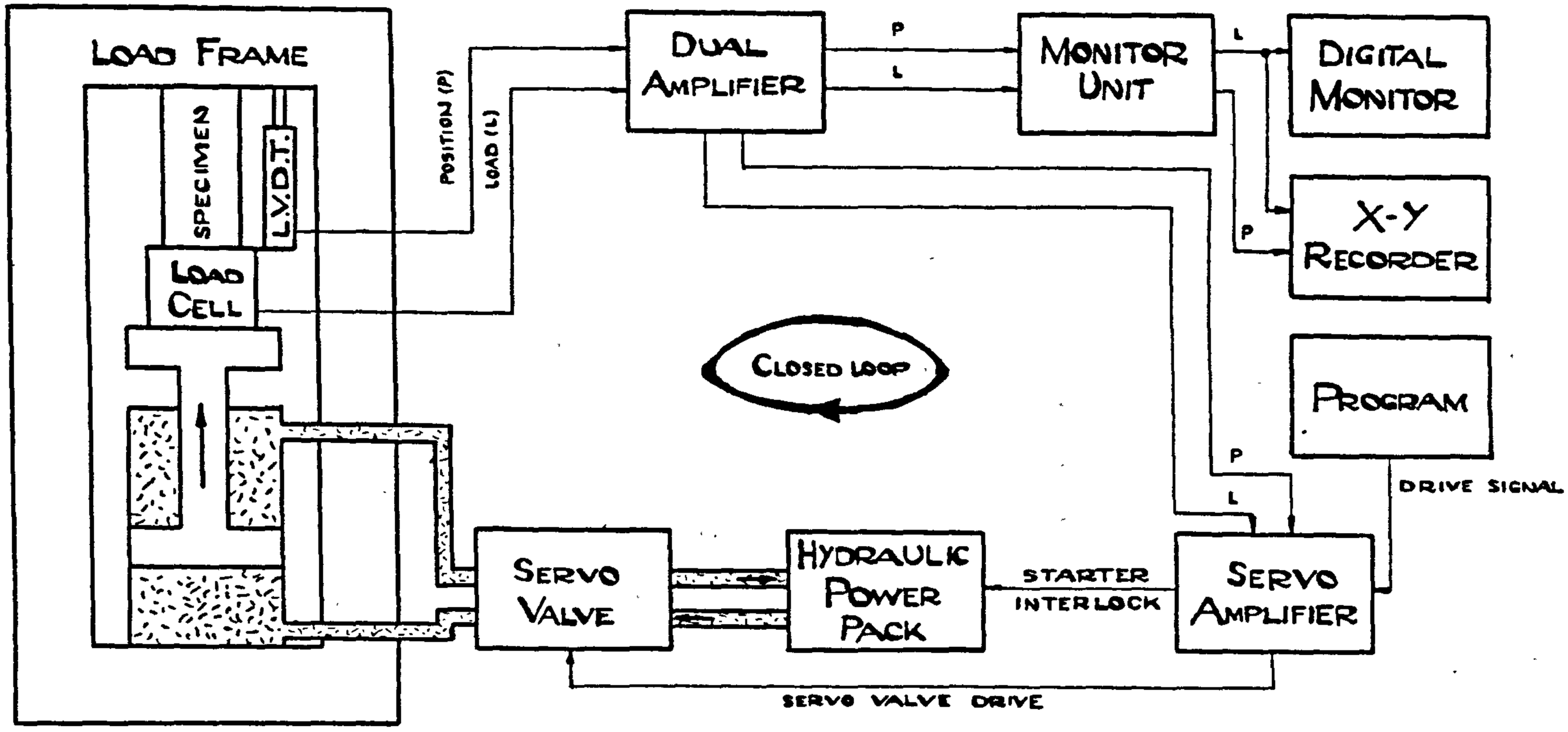

FIG. 6-2 A CLOSED LOOP SYSTEM FOR SERVO-CONTROLLED TESTING MACHINES

specimen can be monitored. A voltage ramp generator is used to provide the program signal for the servo-amplifier on this particular machine. The development of servo-controlled testing machines and discussion of soft and stiff machines is fully reviewed by Hudson et al. (36).

6.2 Equipment and Test Program

The servo-controlled testing machine in the Department of Mining Engineering, Newcastle University, has a capacity of 556 tonnes when operating at the maximum pump pressure of 24.8 MN/m^2. The hydraulic ram is double-acting with diameters of 0.533m and 0.476m. This enables rapid unloading when required by the control system.

Fig. 6-3 shows the testing machine and electronic control console in the laboratory. For these tests the specimen load was monitored by the strain-gauged 500 tonne load cell below the specimen. This was calibrated up to 450 tonnes at 1.0V per 50 tonnes. The maximum deviator from linearity occurred at the mid-point of the calibration curve and amounted to 1.2%. The LVDT used for axial deformation monitoring had a 0.10m travel and was linear to within 0.3% over the range of calibration. This varied for different specimens. Output from both the load cell and LVDT was monitored with an XY pen recorder, also shown in Fig. 6-3.

The testing program was designed primarily to investigate the effect of width:height ratio on the stress-strain characteristic of the potash. Rectangular prisms and cubes were used in order to simulate the actual pillar shapes underground. One of the major limitations was again the shortage of rock and so very few tests were

FIG. 6-3

able to be repeated under identical conditions. The results described in this chapter must therefore be viewed as an introduction to this area of work rather than a definitive set of results.

Other aspects investigated briefly were the effect of strain rate on rock behaviour, size and shape effects - these were from necessity since the specimens were of varied sizes in order to have any specimens at all - volumetric strain, the relationship between creep and the stress-strain curve, plus a number of tests on shale and halite samples.

One major problem throughout the testing program was with the machine itself. This was the first major set of tests to be carried out in the machine in the present laboratory and also the first to utilise the full range of the loading capability. Consequently there were numerous faults encountered during the course of the tests. Most of these were easily fixed but there was one fault which caused the machine to pick up transient signals from other equipment in the building from time to time. Such signals would cause the servo-amplifier to drive the ram its full 0.076m travel instantaneously and also to change the feedback signal mode. This resulted in the destruction of several specimens before and during the tests and has not as yet been eradicated. One smaller fault which was not corrected until after these tests was an interaction between the load and displacement signals, both of which used the same dual amplifier. This was found to cause a 1% reduction in apparent load voltage for an increase in displacement voltage. This has not been corrected for in these tests since the LVDT was also found to be non-linear beyond

its calibration range making overall compensation difficult. The results should therefore be regarded with at least a 3% error band in both directions for any given point on the curves.

6.2.1 Platen Effects

It was originally intended to use cut slabs of halite for platens above and below each specimen tested to represent more closely the underground end restraints on pillars. Once again lack of rock material ruled this out since it would probably be necessary to have new salt platens for each specimen. However, the variability of the material in the mine with shale, potash or salt as possible end materials above the pillars meant that any attempt to simulate end restraint would still not be correct for all situations. Also the confinement present in the roof and floor would tend to increase the pillar confinement and so any rock platens would require steel banding to provide sufficient confinement. Forster (37) found that the strength of rock salt was reduced by up to 17% for similar dimensions by using rock salt rather than steel platens. However, he had no confinement applied to his platens and so this 17% would be significantly reduced if the true pillar end confinement was able to be modelled correctly.

It was therefore decided that normal steel platens would be used since they would give consistent end conditions which should not be too different to those encountered in the mine.

6.2.2 Strain Rate

For realistic comparative results, a strain rate was chosen to represent the rate at which load is thrown onto a yield pillar when it is split into two by a central drive. On the basis of a continuous borer advance rate of 0.2m per minute maximum, a 22m pillar is split into two 8m pillars which, based on tributary area loading, represents a load increase from 73% to 100% of the 8m pillar failure strength assuming that the pillar should reach failure strength in order to promote stress redistribution. Taking into account creep effects at such a mining rate the strain increase between 73% and full load, from laboratory tests, is approximately 6% although this figure is fairly arbitrary. Underground tests have shown that with shale-potash roof conditions the support provided by the face is lost at a distance no greater than 4m from the face.

Therefore at the machine advance rate above, the heading will advance by 4m in 20 minutes. On the basis that the pillar becomes fully loaded in that time it will undergo a strain increase of 6%. This represents a strain rate of 1%/200 secs. for this final stage of pillar loading.

Obviously such a figure is fairly arbitrary. However, in order to realistically simulate the fastest strain rate to be expected as a result of normal mining procedures this figure has been used as the standard strain rate for the comparative width:height ratio tests.

6.3 Results

A summary of the specimens tested is given in Table 6-1 together with the strain rates and basic failure stress and strain figures. The bulk of the information obtained from these tests can be best presented graphically and so the various test results are compared in this way. Several points should be noted in regard to the results.

i) The first two letters of the specimen number refer to the rock type - primary potash, shale-potash, Middle halite, shale (anhydritic).

ii) L:W ratio relates to the specimens with a rectangular loading area and refers to length:width ratio.

iii) Failure stress and strain refer to the point of maximum strength although this is not necessarily a point of complete specimen failure.

iv) All the test results were obtained as load-displacement curves and have been converted to stress-strain curves for comparisons to be made. The stress is based on the original loading area of the specimen which is far greater than the true value in the later stages of most tests. The actual stresses present are therefore higher than shown due to this area reduction but pillars should be compared in terms of load-bearing capacity, not stress level to take into account this area reduction.

Table 6-1 Model Pillars - Specimen Details and Results

Specimen No.	Height (mm)	W:H Ratio	L:W Ratio	Specific Gravity	Initial Strain Rate (1%/_secs)	Failure Strain (%)	Failure Stress (MN/m^2)
PPMP 1	51	3.98	1.00		—(*)	—	—
PPMP 2	51	3.49	1.00		200	66.50	-135.71
PPMP 3	76	3.00	1.00		450	16.87	- 64.21
PPMP 4	76	3.00	1.00	2.18	180	15.10	- 65.42
PPMP 5	76	2.53	1.00	2.10	200	24.00	- 69.83
PPMP 6	102	2.00	1.00	2.09	192	13.36	- 52.20
PPMP 7	102	2.00	1.00		13	6.90	- 52.81
PPMP 8	51	1.50	1.00	2.10	200	5.50	- 41.83
PPMP 9	51	1.50	1.00	2.15	100	6.00	- 47.08
PPMP10	51	1.50	1.00	2.15	30	6.50	- 44.46
PPMP11	51	1.50	1.00	2.15	500	4.50	- 42.49
PPMP12	51	0.88	1.00		100	4.25	- 33.84
PPMP13	51	0.88	1.69		100	4.75	- 38.25
PPMP14	51	0.88	2.76		100	4.25	- 35.39
PPMP15	51	0.88	1.69		—(**)	—	—
PPMP16	102	1.49	1.00	1.77	—(***)	—	—
PPMP17	102	1.49	1.00	1.76	200	3.54	- 45.46
PPMP18	102	1.49	1.00		13	4.06	- 41.14
PPMP19	102	1.00	1.00		200	3.33	- 30.00
PPMP20	102	1.00	1.00		13	3.07	- 31.92
PPMP21	90	1.13	1.00		176	3.07	- 37.44

Table 6-1 Model Pillars - Specimen Details and Results - Cont.

Specimen No.	Height (mm)	W:H Ratio	L:W Ratio	Specific Gravity	Initial Strain Rate (1%/__secs)	Failure Strain (%)	Failure Stress (MN/m^2)
PPMP22	93	1.10	1.00		—(***)	—	—
SPMP 1	101	1.00	1.00	2.28	200	1.50	- 27.47
SPMP 2	101	1.51	1.00	2.08	100	1.50	- 35.10
SPMP 3	101	1.51	1.00	2.29	200	1.50	- 34.24
MH 3	150	0.50	—		236 (1)	2.38	- 19.16
PP10	150	0.50	—		3543 (2)	4.93	- 28.14
PP11	150	0.50	—		118	3.64	- 32.08
PP14	150	0.50	—		24	5.43	- 30.44
SA10	150	0.50	—	2.10	100 (3)	—	—
SA11	150	0.50	—	2.10	100 (3)	—	—
SA12	150	0.50	—	2.10	100 (3)	—	—
SA13	150	0.50	—	2.08	100	3.40	- 12.48
SA14	150	0.50	—		200	3.35	- 18.18
SP 3	150	0.50	—	2.18	200	3.06	- 19.27

* Specimen cut up to make PPMP8 - 11.

** Specimen used for creep test.

*** Specimen destroyed due to machine failure.

(1) Rate decreased to 1%/354 secs during test.

(2) Rate increased to 1%/354 secs during test.

(3) Output inaccurate due to faulty leads and plotter problems.

NB. Specimens MH3 - SP3 are all cylindrical specimens.

6.3.1 Width:Height Ratio Tests

The results of the tests carried out at 1% strain/200 secs are shown in Fig. 6-4. The results from PPMP2 (W:H 3.49) indicate that this ratio is sufficiently high that the pillar will continue to accept increasing load indefinitely. The test was stopped due to a lack of pump pressure to sustain any higher load. The specimen, when removed, had a width:height ratio of 10.6:1. PPMP4 (W:H 3.00) showed slightly lower strength than PPMP5 (W:H 2.53) but this was probably due to some irregular bedding planes present in the specimen. Both specimens showed considerable strength throughout and appeared to be maintaining a constant load at the end of the tests. This suggested that the material was creeping at the same rate as the machine strain rate (1%/200 secs).

The remaining three specimens all showed a decrease in load-bearing capacity with increasing strain. PPMP6 had to be tested in two stages hence the unloading curve at 41% strain. This shows the presence of elastic recovery even after such a large amount of strain. On a number of specimens unloaded from different loads this recovery was seen to be proportional to the load. From this particular specimen the area was recorded at the point of unloading and so a modulus of 17.8 GN/m^2 was calculated. This agrees quite well with the average value of 22.4 GN/m^2 quoted in Chapter 5.

Comparison of all six results shows the significant effect of width:height ratio and its associated confinement on peak strength and the post-failure curve. At this strain rate, only the specimens of W:H ratio 2.0 or less failed below the stress expected in a panel

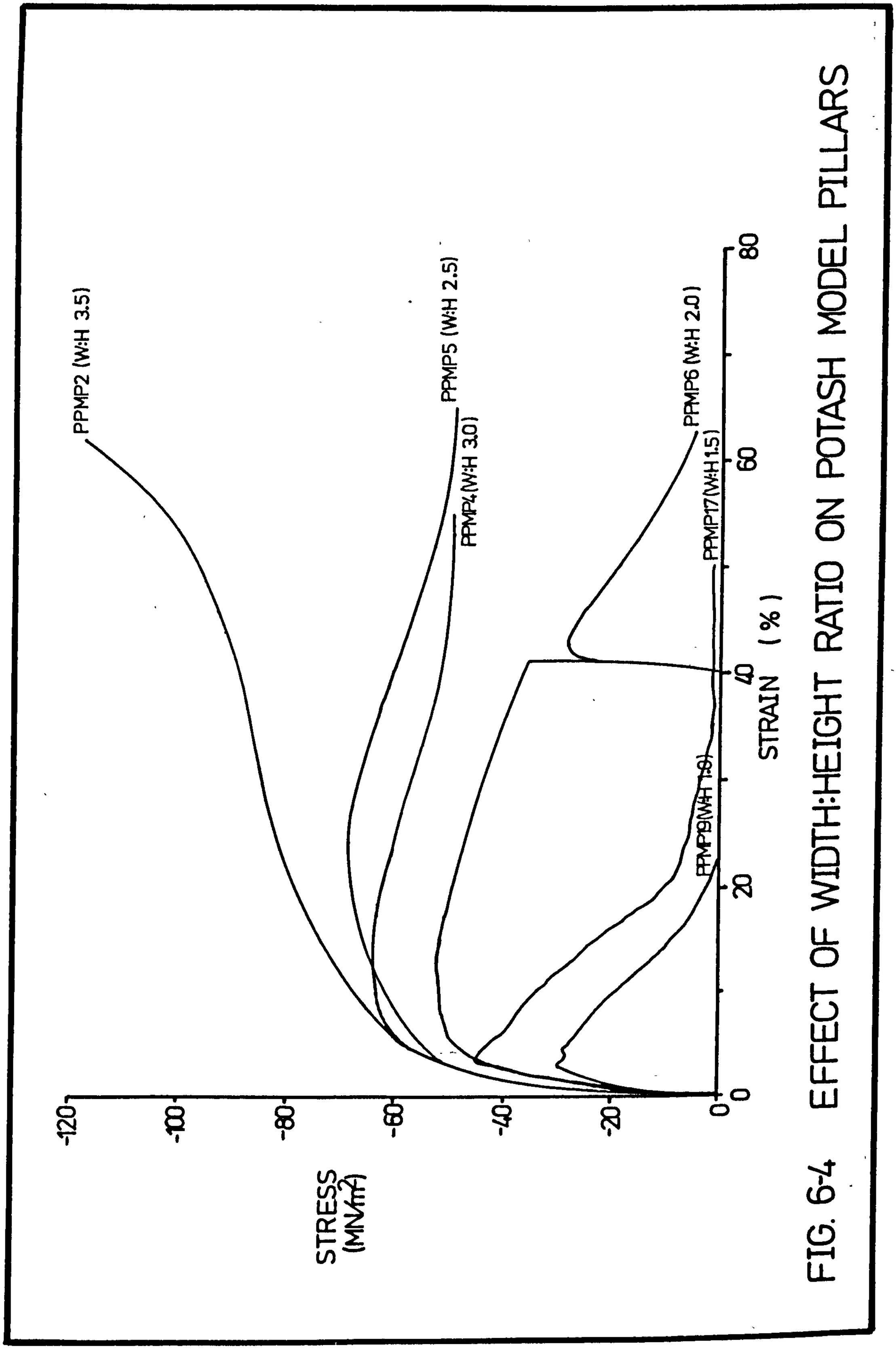
EFFECT OF WIDTH:HEIGHT RATIO ON POTASH MODEL PILLARS
PPMP2 (W:H 3.5)
PPMP5 (W:H 2.5)
PPMP4 (W:H 3.0)
PPMP6 (W:H 2.0)
PPMP17 (W:H 1.5)
PPMP9 (W:H 1.0)
80
60
40
20
0
STRAIN (%)
-120
-100
-80
-60
-40
-20
0
STRESS (MN/m²)

FIG. 6-4

due to tributary area theory. Therefore this ratio should be used as a maximum in order to promote stress redistribution. From the unloading curves, PPMP6 can still carry very high loads whereas a curve closer to that of PPMP17 would be more desirable to promote rapid yield and stress redistribution. PPMP17 (W:H 1.50) actually failed at 3.54% strain which is approximately 1.7% higher than the strain at -31 MN/m^2 representing approximately the virgin stress level. Therefore stress redistribution would start to take place after 1.7% yield for a pillar with this W:H ratio. However, the amount of remaining strain capability is less than 20% at any significant load for PPMP17 which may not prove sufficient for a long term yield pillar.

From these results, therefore, the width:height ratio range of 1.50 to 2.00 appears to be the maximum range for an effective yield pillar system. In order to have long term stability the ratio should be in the upper end of this range.

Fig. 6-5 shows the original shape of PPMP4 and the final shape of PPMP3 which began the test at the same size. The section shown is vertically through the centre of PPMP3. This shows the pattern of crystal deformation (the darker shale crystals are greatly distorted) and the overall flow pattern of the rock as a mass. The restraining influence of the platen can be seen by a confined core of relatively undisturbed material in the centre at top and bottom. In this and all specimens, however, this core exhibited a hemispherical shape, never extending more than about 6mm below the platen surface. The flow of material between and beside these zones appears to be relatively unaffected by the platen influence.

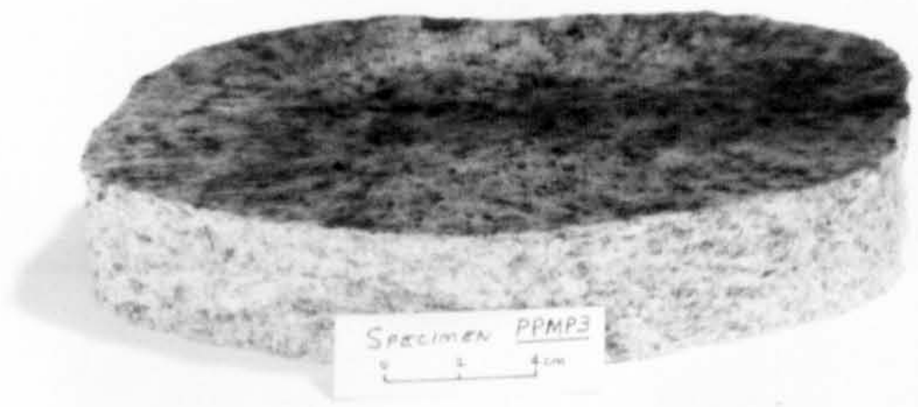

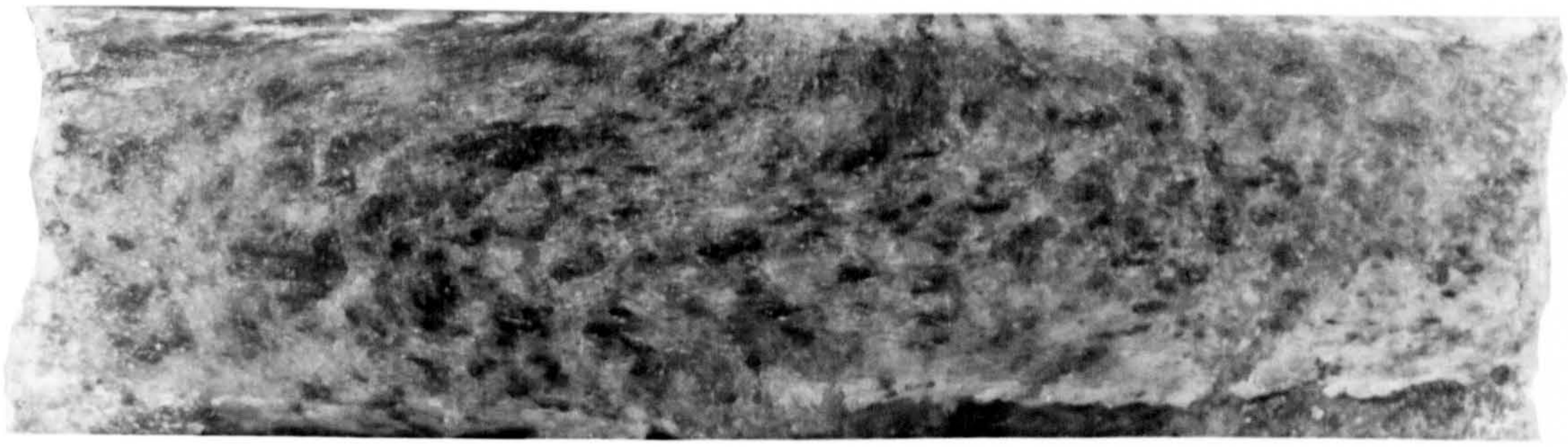

FIG. 6-5

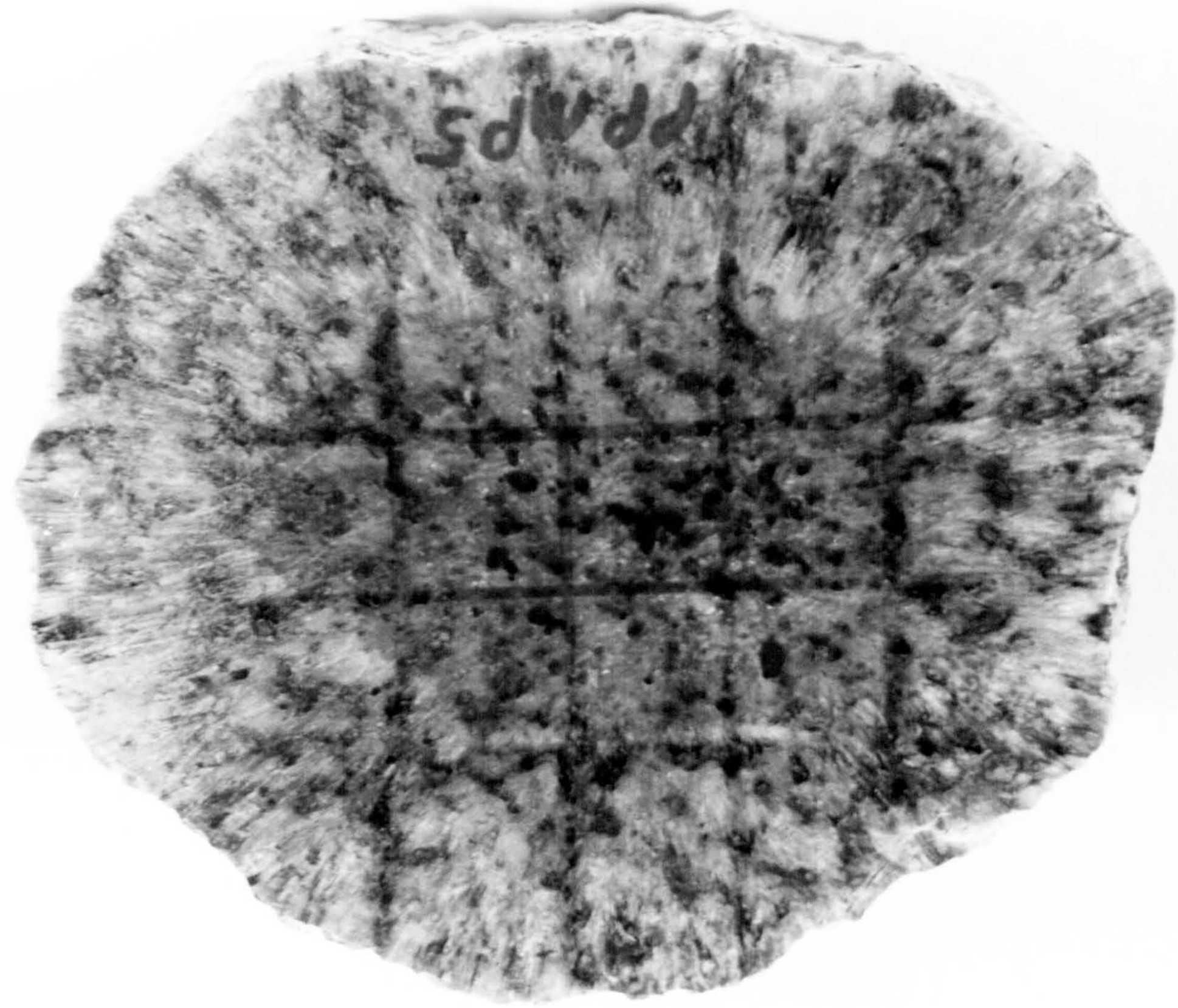

FIG. 6-6

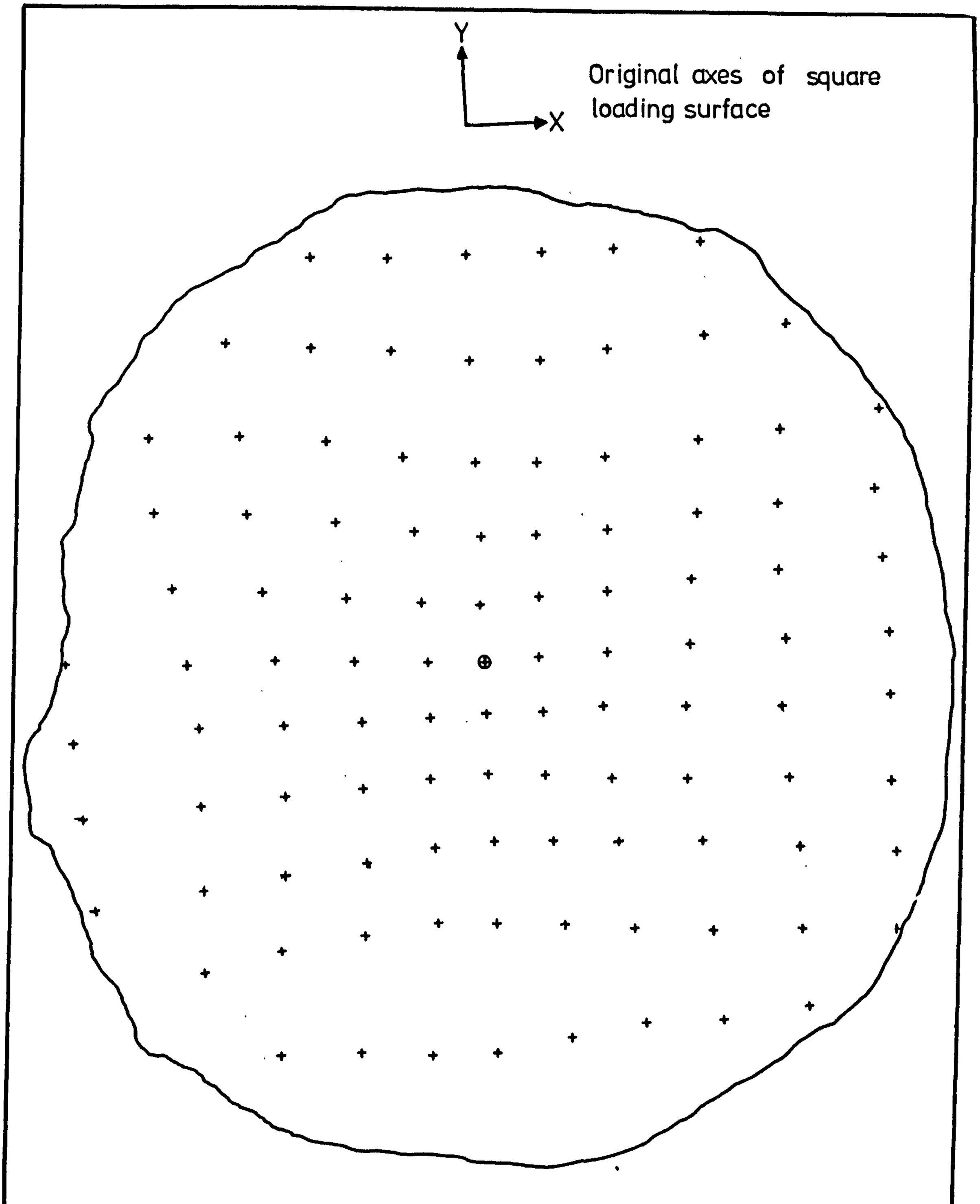

FIG. 6-7 DISTORTION OF 1cm SQUARE GRID ON BASE OF PPMP2

The same effect is shown in Fig. 6-6 for PPMP5. The upper picture shows distortion of a square grid which had been drawn on the base of the specimen while the lower section shows the flow patterns very clearly. In all specimens there was vertical microfracturing both around and within crystals and these are just visible in the sections in both Fig. 6-5 and 6-6. The maximum zone of fracturing, corresponding to the peak lateral strain zone, occurred between 15mm and 30mm into the side of each specimen examined. Fig. 6-7 shows the deformation of a grid of 1cm squares which was drawn on PPMP2. The lateral strains have been calculated along two opposite diameters of this grid and are plotted in Fig. 6-8. These clearly

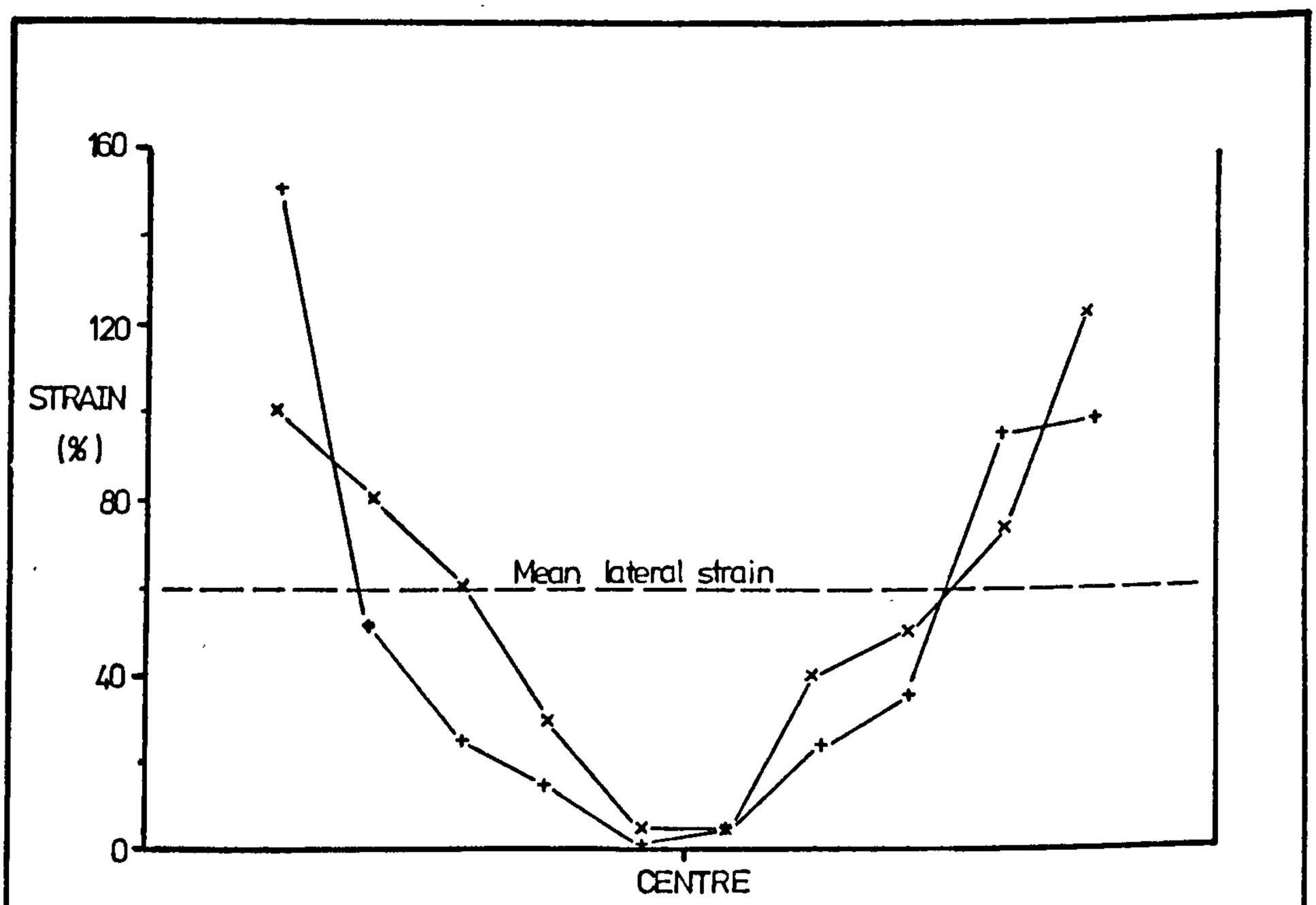

FIG. 6-8 LATERAL STRAIN ACROSS X AND Y DIAMETERS OF PPMP2

indicate the zone of confined material in the central core of the

specimen, even though this is based on a surface effect only. The average diametral strain is within 5% of the axial strain.

6.3.2 Volumetric Strain

The final perimeters of a number of specimens which remained as solid material were plotted and the area calculated. The specimens were also weighed in order to obtain a value for specific gravity. By comparing the ratios of specific gravity with those measured initially, an estimate of total volumetric strain was obtained. Three specimens provided this information and the results are listed in Table 6-2.

Table 6-2 Model Pillar Volumetric Strain

Specimen No.	Initial S.G.	Final S.G.	Volumetric Strain (%)
PPMP4	2.18	2.18	0.0 ± 2.8
PPMP5	2.10	2.06	1.9 ± 3.1
PPMP6	2.09	2.06	1.4 ± 3.4

The range of strain quoted was based on allowing 1mm variation in radius for the final area of each of the specimens which were virtually circular. Within the accuracy of this system of determination, it appears that the overall volumetric strain is approximately 0% or marginally greater, possibly due to the amount of fracturing within the solid material.

6.3.3 Strain Rate Effect

This is illustrated in Fig. 6-9 for five different strain rates ranging from 1%/13 secs to 1%/500 secs. All the specimens have a W:H ratio of 1.50 and are all the same height (51mm) except PPMP18 which is 102mm. From the results it appears that the variation in failure strength is not great (maximum range 14%) and in fact the highest strength was for the mid range of the strain rates used. Obviously specimen variation has affected these results also.

The major effect of the strain rate variation has been on the slope of the post-failure curves and hence the strain capacity of the pillars. The maximum slope change between the two extreme rates investigated is a slope reduction by a factor of 4:1 for the slower rate. Work by Bieniawski (38) showed similar effects of strain rate for tests on sandstone.

Fig. 6-10 shows similar strain rate effects for two samples with W:H ratio 1.0. The fast rate of 1%/13 secs for PPMP7 represented virtually a dynamic failure mechanism. Fig. 6-11 shows the condition of PPMP7 at the six stages of the failure curve indicated as 1 to 6 on Fig. 6-10. In this test as with all the others, the specimen corners fractured prior to peak strength and the remaining core gradually became more circular throughout each test.

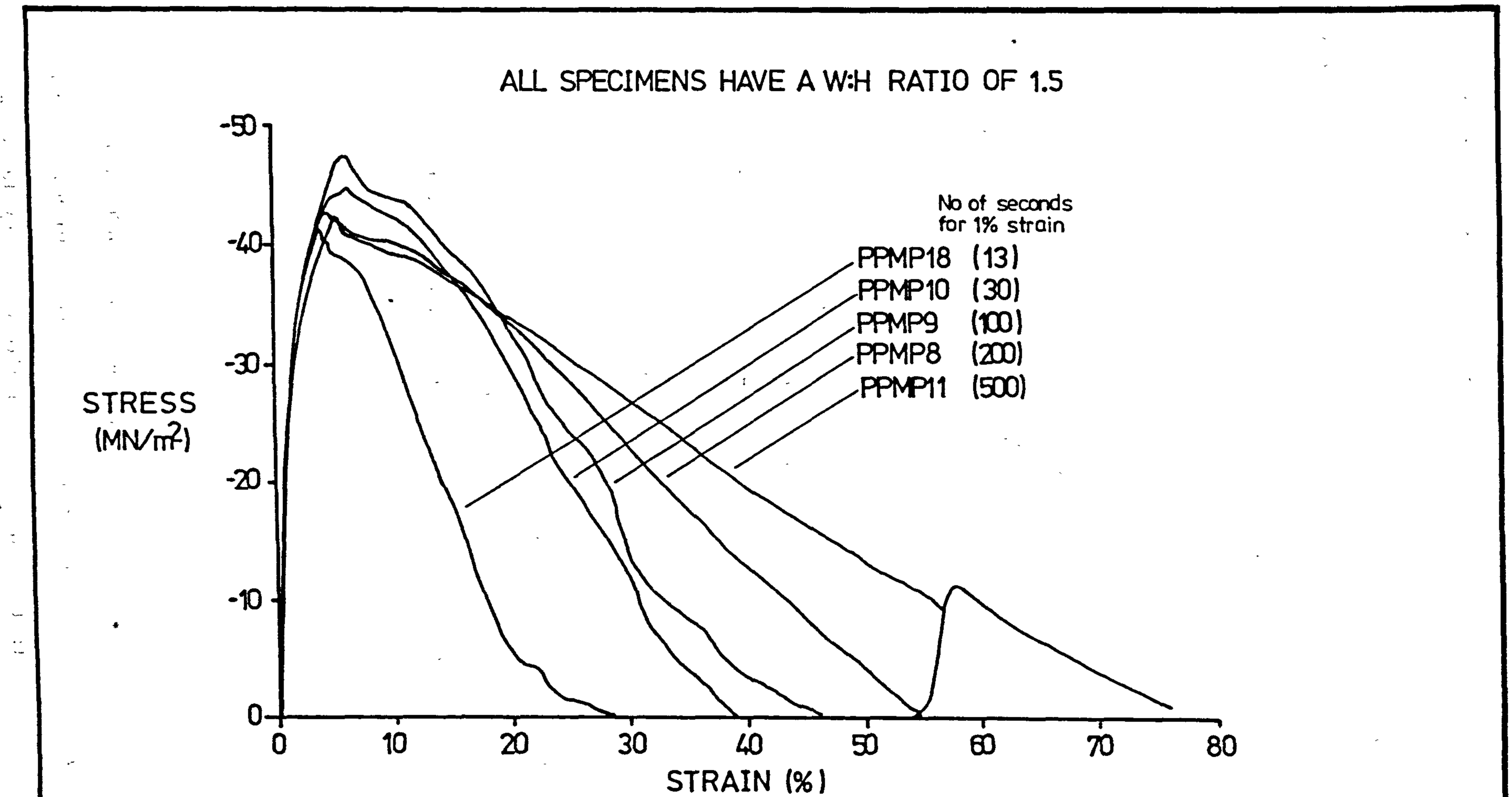

FIG. 6-9 EFFECT OF STRAIN RATE ON POTASH MODEL PILLARS

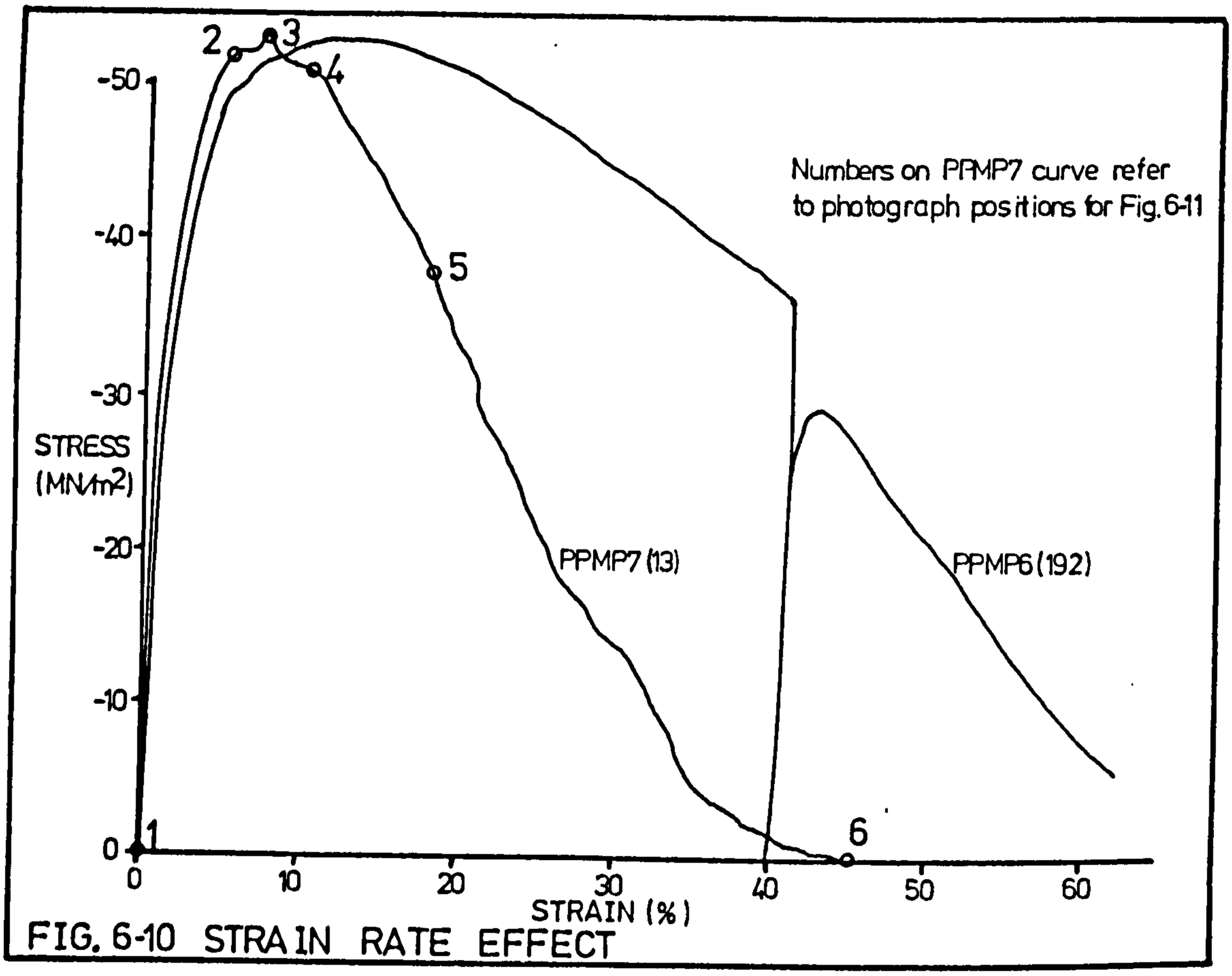

FIG. 6-10 STRAIN RATE EFFECT

6.3.4 Size Effect

Specimens PPMP17 and PPMP8 both had a W:H ratio of 1.5 and were tested at 1% strain/200 secs but PPMP17 was twice the height of PPMP8. Fig. 6-12 shows the curves for these specimens. As with the strain rate tests the strength variation does not appear to be significant but the post-failure curve is roughly double the slope for the taller specimen.

Size effects are often discussed as being very significant in relation to strength of materials. However, Brown (39) suggests that much of the so-called size effect is a function of the method of testing and related to soft testing machine strain energy assisting crack propagation. In material such as primary potash which is relatively fine-grained and homogenous compared with some evaporites, it is unlikely that strength will be altered to any large extent by

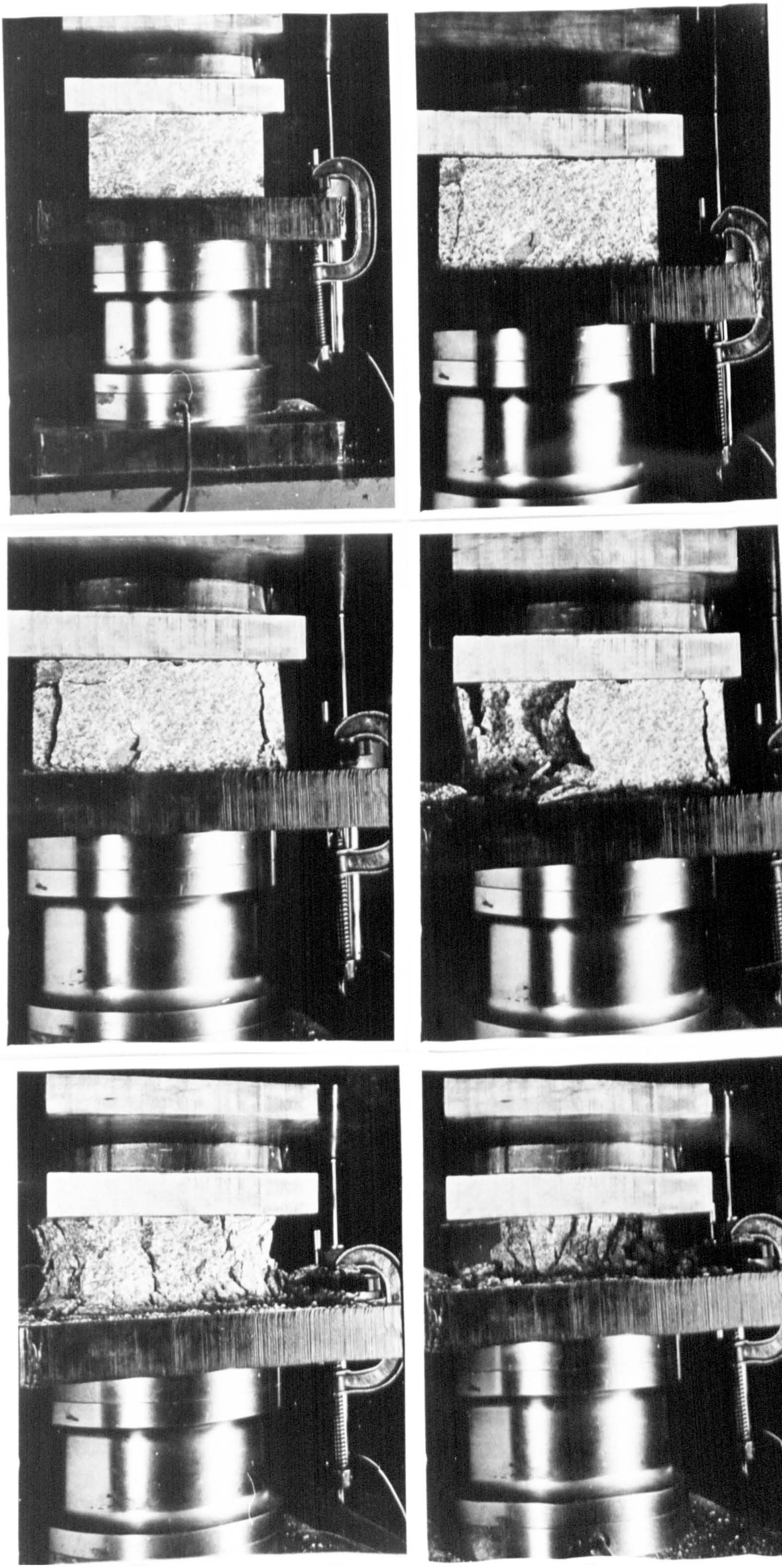

FIG. 6-11

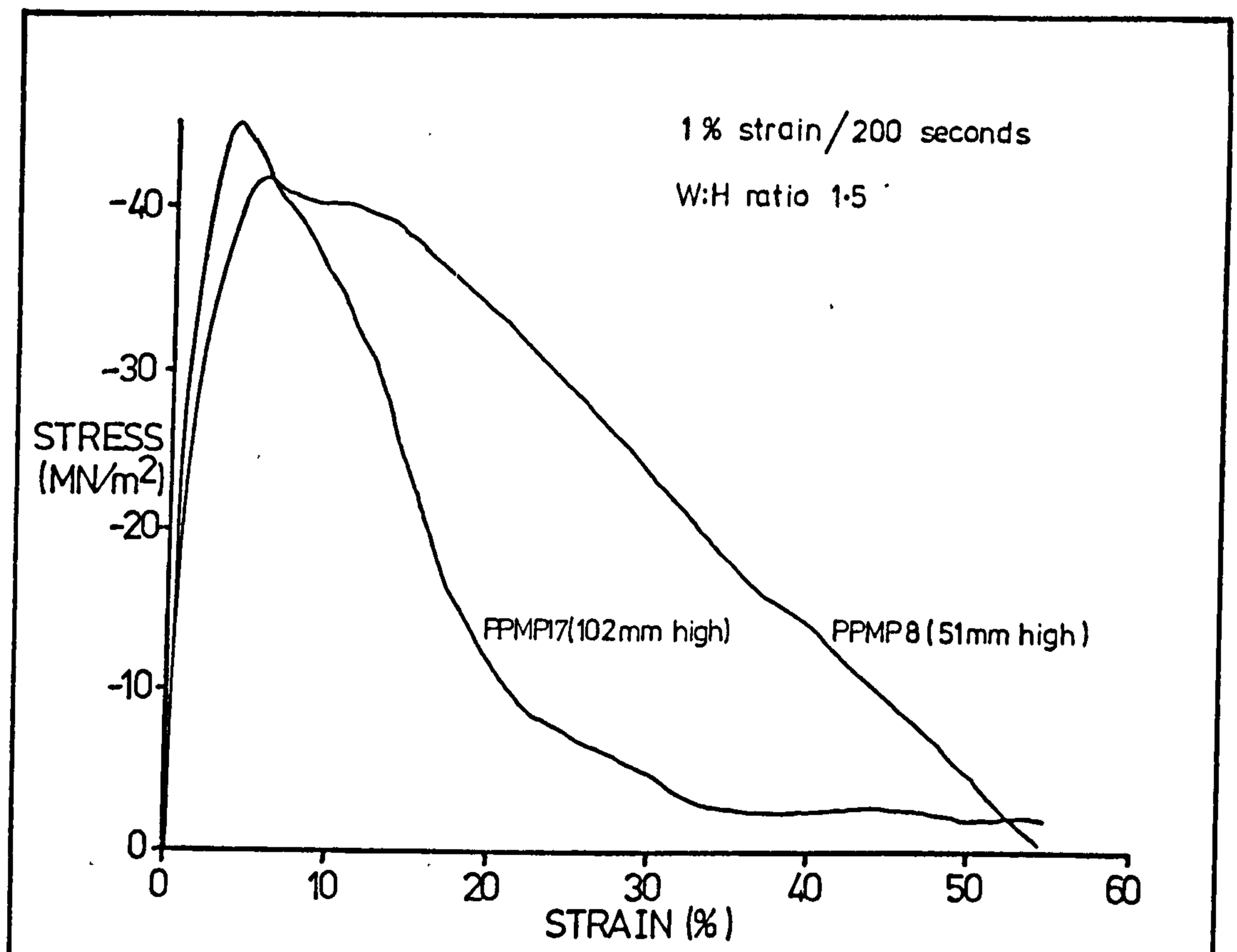

FIG. 6-12 EFFECT OF SIZE ON POTASH MODEL PILLARS

variations in size and this is suggested by the present results, although far from conclusively.

The flatter post-failure curve of the smaller specimen is most likely to be caused by platen effects having a more significant influence in restricting crack development and propagation.

6.3.5 Shape Effect

Three specimens of the same W:H ratio but L:W ratios of 1.00, 1.69 and 2.76 were tested to investigate the effect of the L:W ratio. The results are shown in Fig. 6-13. As expected, neither

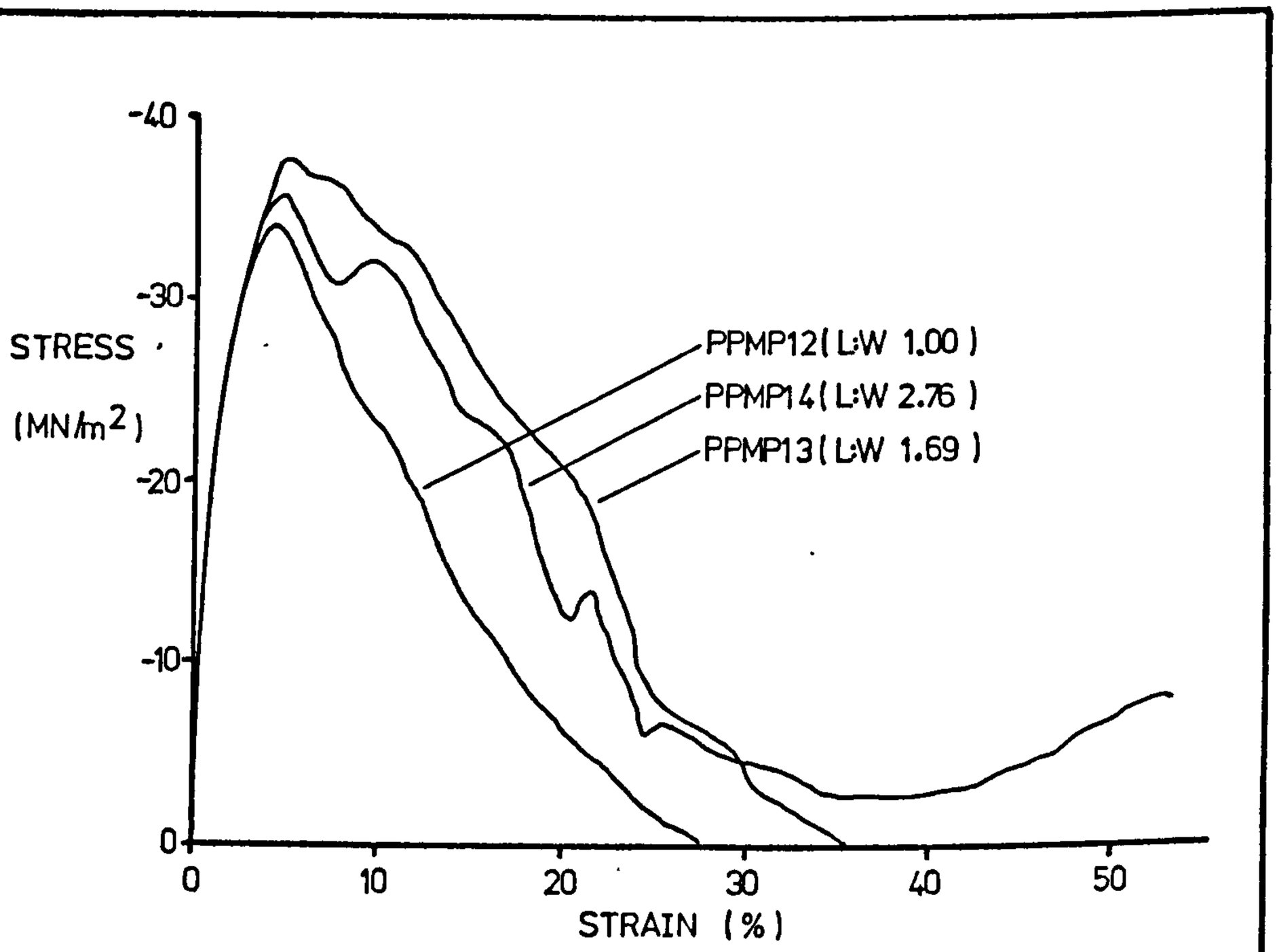

FIG. 6-13 EFFECT OF SHAPE ON POTASH MODEL PILLARS

the strength nor the pre or post-failure curves appears to be greatly affected. This supports the hypothesis that the minimum pillar dimension should be used for assessing the strength and stability of a pillar.

6.3.6 Creep in Relation to Stress-Strain Curves

Specimen PPMP15 was loaded in the Avery 100 tonne machine to -36.5 MN/m^2, just below the failure strength of PPMP13, which was of the same dimensions. The strain rate at which it was loaded was approximately the same as PPMP13 had been tested at throughout

(1%/100 secs). The specimen was allowed to creep under constant load until failure occurred. At this point the testing machine was operating with the bypass valve slightly open and so the specimen was able to unload slightly and continue straining before losing all load. The failed specimen was then reloaded for a second creep stage at a level of -27.8 MN/m^2 until a similar failure occurred. The strain rate to the creep level was inadvertently lower by a factor of 60% for this second stage. The two creep curves, indicating very typical creep characteristics, are shown in Fig. 6-14. The specimen was then reloaded for a third time at the correct rate until failure occurred.

Fig. 6-15 shows the three loading and two creep stages of PPMP15 superimposed on the stress-strain curve of PPMP13. Apart from specimen variation and the slower strain rate for the second loading, there is a remarkably good correlation between these sets of results. This concept of creep in relation to stress-strain curves is discussed by Hudson (40) although he doesn't present any actual creep results.

It does appear that the stress-strain curve defines the complete failure locus of a specimen, even for creep behaviour horizontally on the curve, for a given strain rate up to the creep stress level. This implies that the creep strain capability of a material is determined by the rate at which it is loaded to its stress level. This represents a form of strain energy mechanism for creep where the rate of energy input causes a proportional breakdown of the creep strain capability of the material.

Obviously this aspect of work requires further testing but

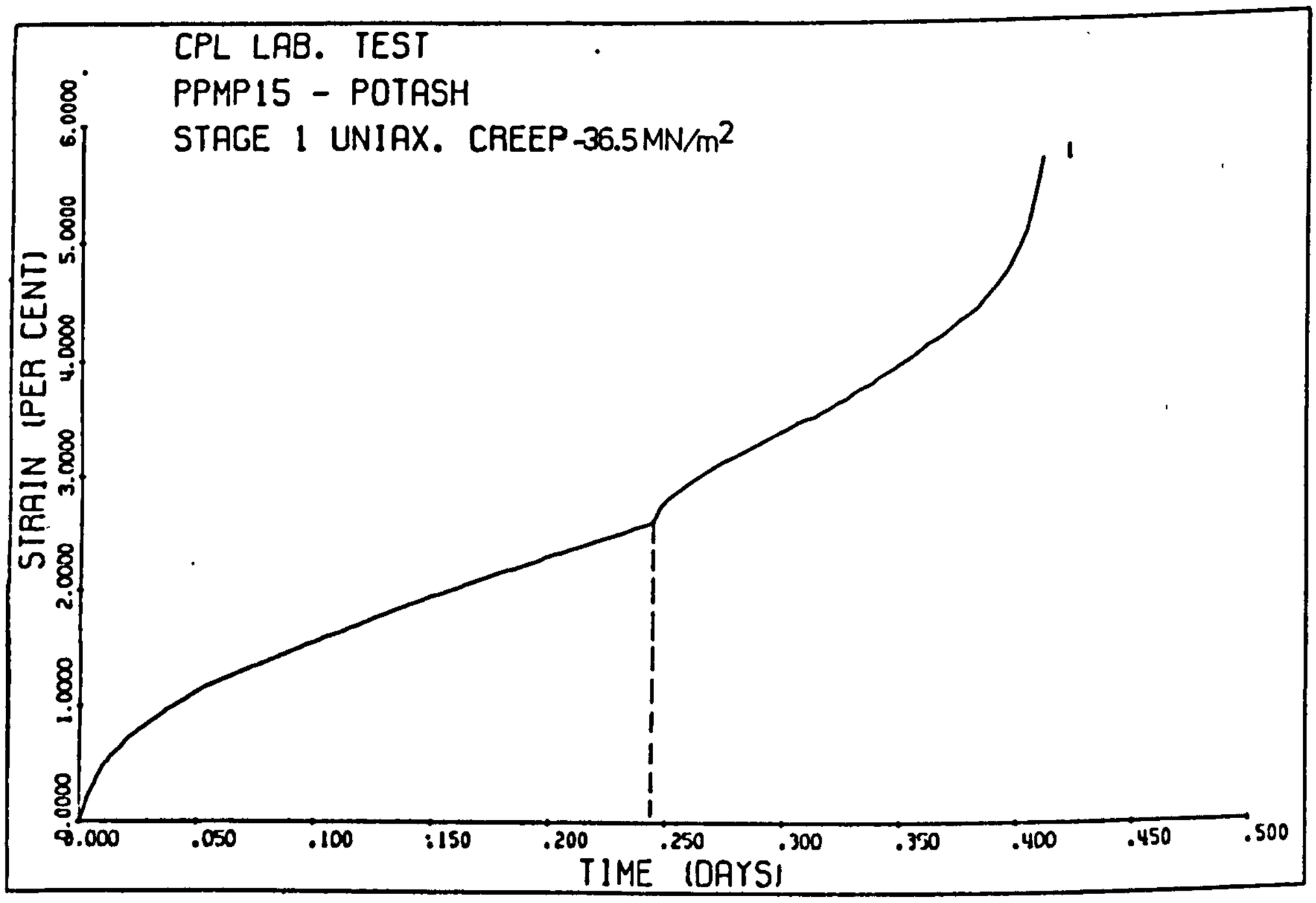

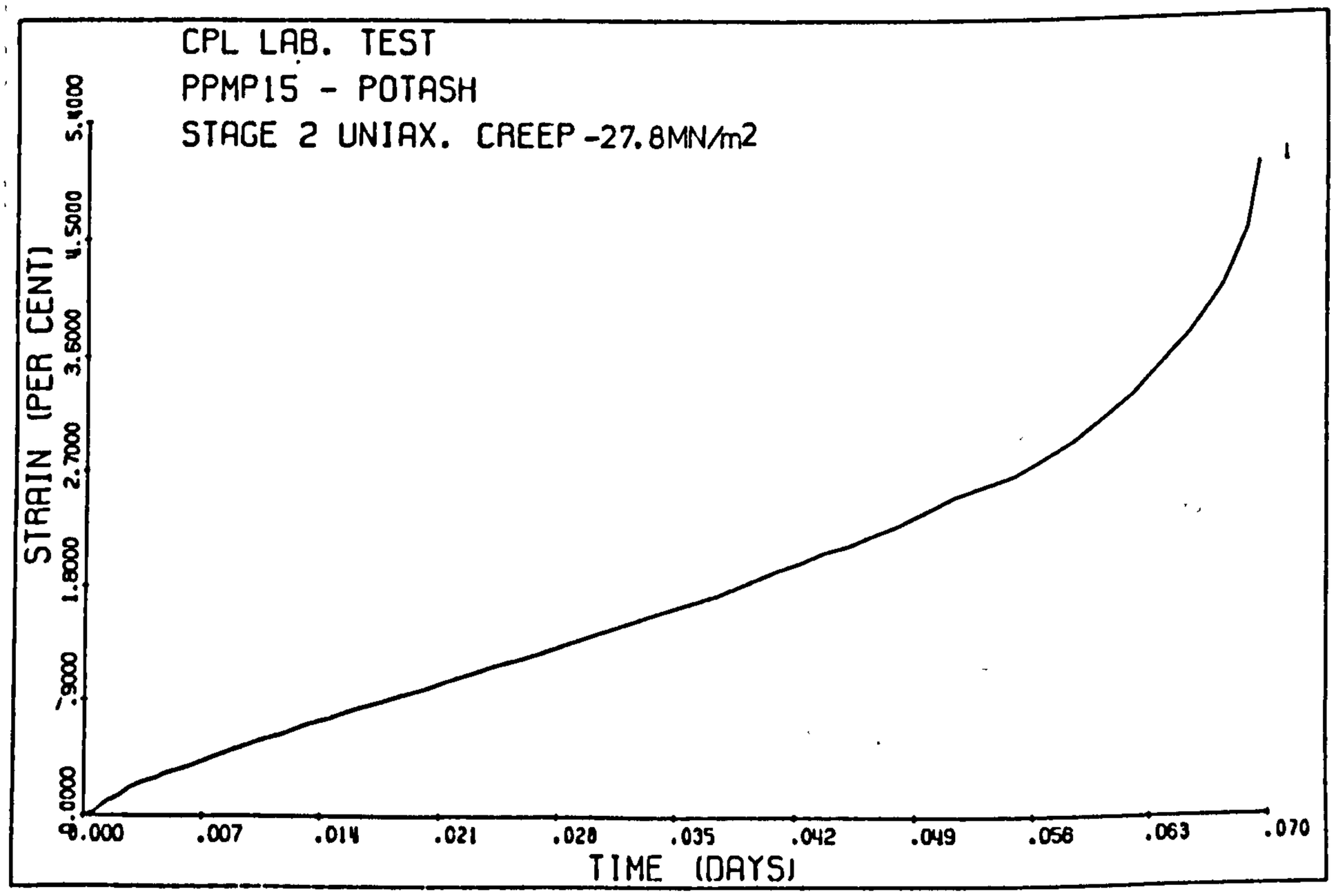

FIG. 6-14 CREEP OF MODEL PILLAR PPMP15

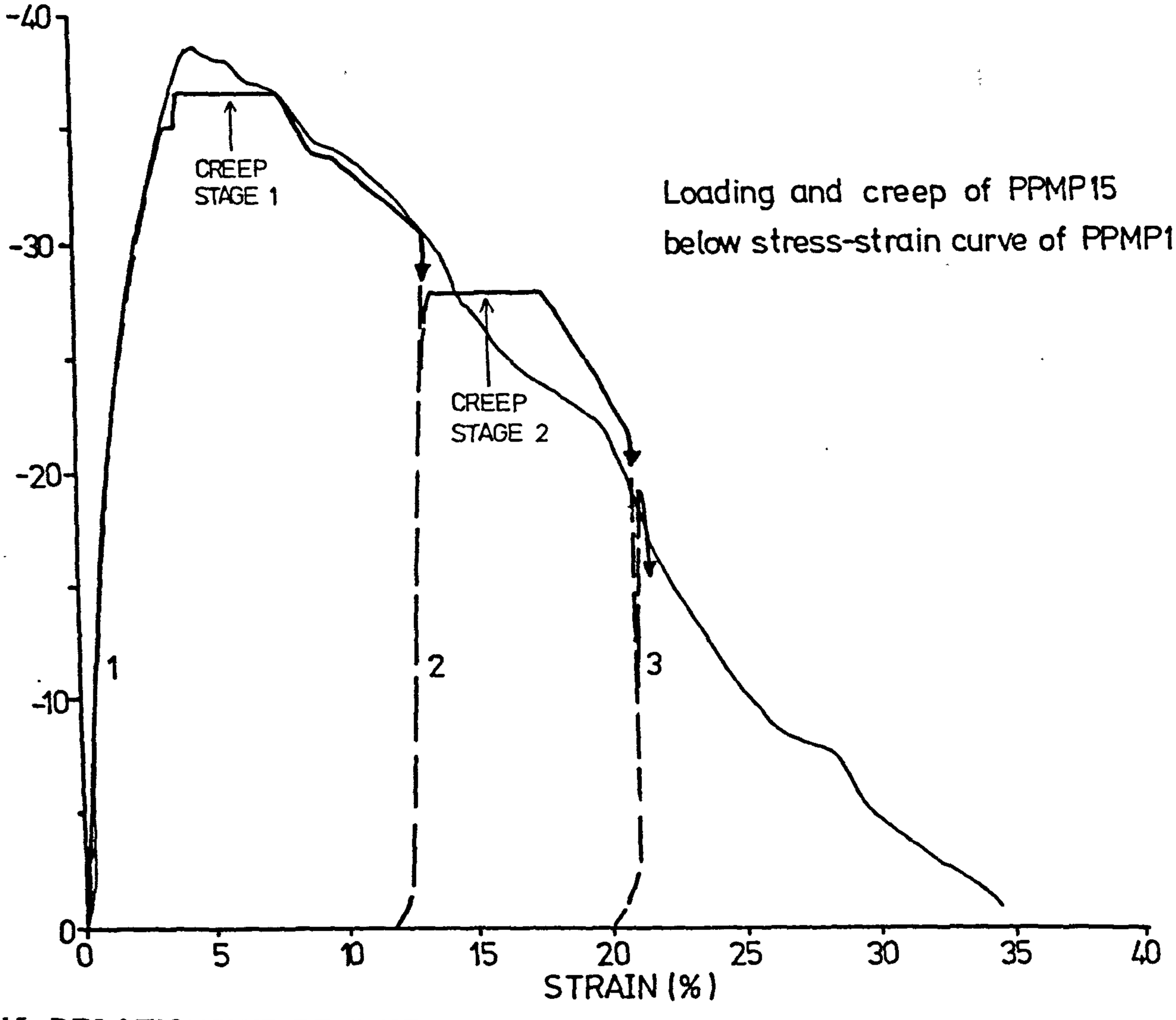

Loading and creep of PPMP15
below stress-strain curve of PPMP13

FIG. 6-15 RELATIONSHIP BETWEEN CREEP AND STRESS-STRAIN BEHAVIOUR

it provides an interesting method for predicting the creep life of a material based on its loading history and creep rate.

6.3.7 Shale v. Potash Results

Fig. 6-16 shows the results for SPMP1 and SPMP3 compared with PPMP19 and PPMP17 for W:H ratios of 1.0 and 1.5 respectively.

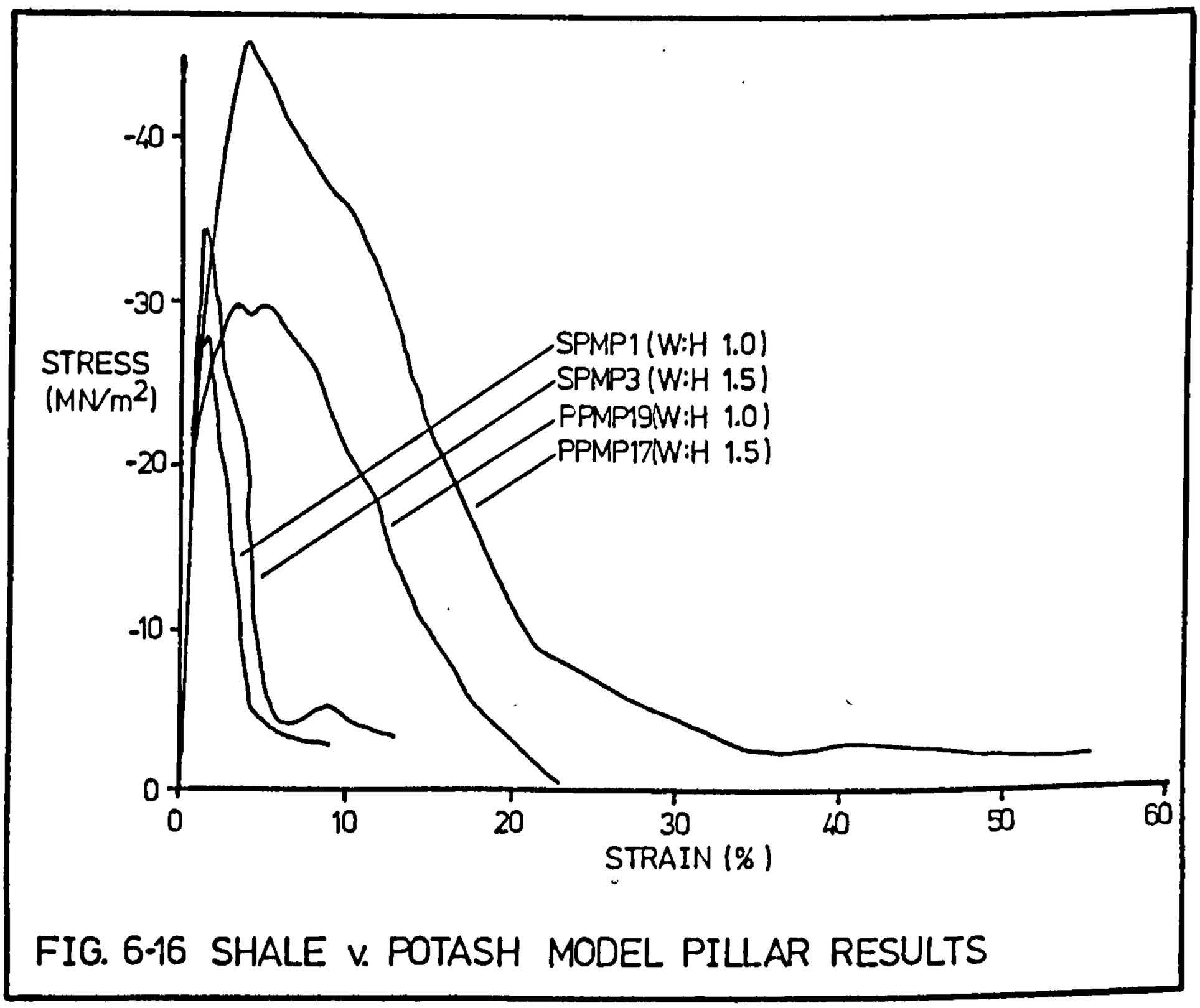

FIG. 6-16 SHALE v. POTASH MODEL PILLAR RESULTS

These indicate once again the very brittle nature of the shale material which possesses a far steeper unloading curve than the equivalent potash curves. This suggests that the shale has very little yield capacity so does not appear particularly suitable as a pillar material.

6.3.8 Shale v. Halite v. Potash Results

All the results for the cylindrical specimens are plotted in Fig. 6-17. Due to the variation in strain rates these are not directly comparable and so no major conclusions can be drawn. However, the results do suggest that the Middle Halite is closer to the shale in its stress-strain characteristics than to the potash. Its total strain capability is less than half that of the equivalent potash specimen, PP10, for any point on the unloading curve. This is mainly due to the large amount of yield exhibited by the potash prior to failure, rather than variation in post-failure stiffness.

6.4 Pillar Stability in Relation to Roof Stiffness

From the theoretical perturbation analyses in Chapter 3, the influence factors can be used to determine the roof strata stiffness. A modulus of 7.0 GN/m^2 was used for the initial analyses and that is approximately the same as for the combination of shale and marl in the mine roof. Using the method of 'local stiffness' of Starfield and Fairhurst (41), they defined the local stiffness as the change in deformation produced by a change in load on a hypothetical jack in place of a pillar. This stiffness factor, K, can be obtained from the self-induced influence factors obtained in Chapter 3, k_{ii}.

$$\text{Since } k_{ii} = \frac{\delta R_{ii}}{\delta Q_i}$$

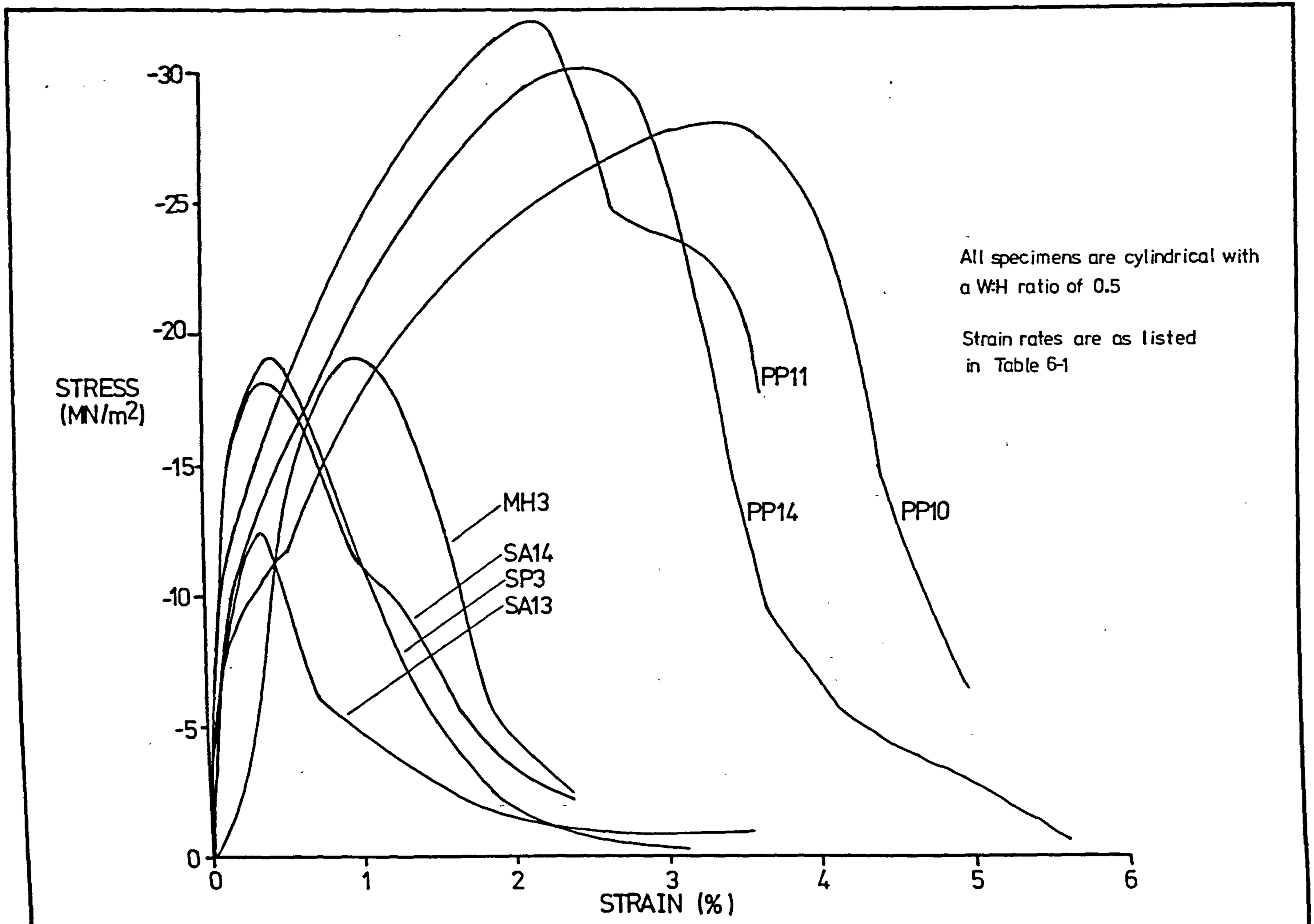

FIG. 6-17 SHALE, POTASH, MIDDLE HALITE RESULTS

and $\delta R_{ii} = \delta u_{ii} \times \left(\frac{2}{h}\right) \times E_{seam}$

where h = seam thickness,

then $$\frac{\delta P_i}{\delta u_{ii}} = \frac{2 E_{seam} A}{k_{ii} h} \qquad (6.1)$$

where $\frac{\delta P_i}{\delta u_{ii}}$ is the local roof stiffness

and A is the area of the pillar which has an influence factor of k_{ii}.

The roof stiffness is clearly a load-displacement function and from the runs described in Chapter 3, the average value of roof stiffness defined by equation (6.1) is 64 GN/m for all pillar sizes between 60m and 15m. In relating this to a stress-strain curve the correct dimensions rather than model dimensions should be used since it is a load-displacement rather than stress-strain function. However, in terms of the pillar dimensions modelled in this chapter, the roof stiffness curve is virtually a vertical line as shown in a sketch in Fig. 6-18. Using Salamon's (42) criterion for stability, the sum of the absolute roof stiffness, J, and the pillar unloading stiffness, $-\lambda$ should be greater than zero,

$$J + (-\lambda) > 0 \qquad (6.2)$$

On this basis, since J is a very large number for the Boulby situation, then the above condition should be satisfied to prevent dynamic energy releases with pillar failure. The area between the roof stiffness curve and the pillar unloading curve, shown shaded in Fig. 6-18, represents the extra energy required before an unstable collapse could occur.

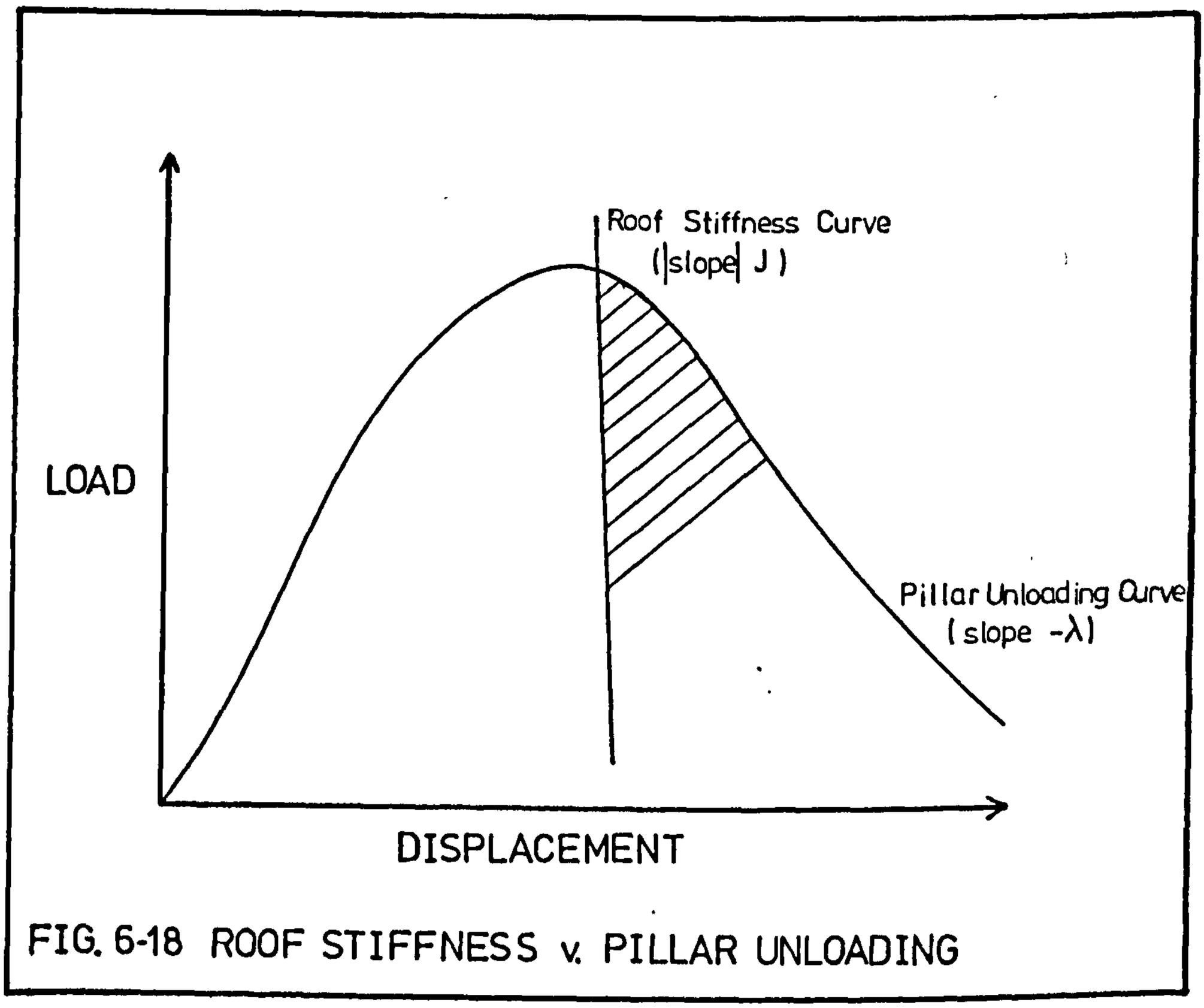

FIG. 6-18 ROOF STIFFNESS v. PILLAR UNLOADING

6.5 Summary of Conclusions

i) In order to create a stress redistribution, the pillar W:H ratio should be not significantly greater than 2.0 to induce failure and in excess of 1.50 to maintain stability after yielding.

ii) Potash is still capable of exhibiting elastic recovery proportional to load changes even after it has undergone large amounts of straining.

iii) Total volumetric strain in model pillars of primary potash is virtually zero.

iv) Strain rate greatly affects the post-failure curve of potash but only has a slight influence on the strength.

v) The size effect on strength does not appear to be very significant but it does affect the post-failure slope.

vi) Strength and post-failure behaviour are determined by the minimum width of a rectangular pillar.

vii) The stress-strain curve appears to define the absolute creep strain capability of a material in terms of the initial strain rate up to the creep stress level.

viii) The unloading curves for shale are much steeper than for potash and the shale shows very little capacity for yield.

ix) The roof stiffness is far greater than the unloading characteristics of any of the model pillars tested indicating no possibility of violent pillar collapse.

CHAPTER 7

MEASUREMENT OF THE STRESS

FIELD ABOVE THE MINING HORIZON

7. MEASUREMENT OF THE STRESS FIELD ABOVE THE MINING HORIZON

7.1 Estimated In-Situ Stress

In order to develop any type of numerical, physical or empirical model as an aid to mine design it is essential to have a knowledge of the virgin stress conditions which exist in the vicinity of the mining horizon. The virgin stress field is the fundamental boundary parameter for any model, prior to simulating the excavation process. Empirical modelling requires a knowledge of the stress field in order to interpret measured data correctly by relating rock movements to loading systems. In the simplest of such models the loading system is a function of the virgin stress field and the mining extraction ratio - the "tributary area" theory.

There are a number of methods for estimating the magnitude of the virgin stress field based on the assumption that there are no geological anomalies or tectonic forces present. On this basis, the stress directions are vertical and horizontal. A common 'rule of thumb' method states that the vertical virgin stress increases at the rate of $-22.6\ kN/m^2$ per metre of increase in depth (-1 p.s.i./ foot depth). Using this method the vertical virgin stress at Boulby would be $-24.8\ MN/m^2$.

A second method for estimating the vertical stress requires a knowledge of the overlying strata. This method calculates the gravitational force exerted due to the weight of the strata above. For a series of different strata the vertical virgin stress (σ_v) is given by

$$\sigma_v = -\rho \cdot g \cdot \left(\sum_{i=1}^{n} (d_i \cdot h_i)\right) \qquad (7.1)$$

where ρ is the density of water, g is the gravitational constant, d_i is the specific gravity of each stratum and h_i is the thickness of each of the n overlying strata. Table 7.1 lists the specific gravities for the general geological sequence at Boulby, as measured by Patchet (7), together with the stratum thicknesses. (The specific gravity for the Secondary Potash was calculated from laboratory testing described in Chapter 6.) Equation (7.1) predicts a value of

Table 7-1 Specific Gravity and Thickness of Geological Sequence

Stratum Type	Specific Gravity	Thickness (m)
Drift and Middle Lias	2.5	83
Lower Lias	2.6	295
Rhaetic	2.5	15
Keuper Marl	2.7	248
Bunter Sandstone	2.5	335
Upper Permian Marl	2.3	65
Upper Halite	2.2	34
Upper Anhydrite	2.8	8
Carnallite Marl	2.3	10
Secondary Potash (Shale)	2.2	4

$-27.4\ MN/m^2 \pm 0.5\ MN/m^2$ for vertical virgin stress using the above figures based on an accuracy of ±0.05 for specific gravity.

The elastic equilibrium condition which relates the horizontal stress to the vertical is given by equation (7.2),

$$\sigma_H = \sigma_V \left(\frac{\nu}{1-\nu}\right) \qquad (7.2)$$

where ν is Poisson's ratio. A value of 0.25 for ν predicts a horizontal virgin stress equal to one third of the vertical stress. This ratio of one third represents an elastic situation. The fact that the material concerned is a combination of weak shales and evaporites which exhibit time-dependent deformations suggests that the ratio would be higher than that predicted by equation (7.2). Typical values measured for this type of strata have a ratio between 0.8 and 1.0 (43).

These methods of estimating the stress field are an essential starting point for modelling a mining layout and analysing results. It is, however, an invaluable aid to be able to measure the stress field underground in the strata concerned. Such an opportunity arose in March, 1976 in connection with shaft lining problems in No. 2 shaft. The intention was to measure the virgin stress field in the potash and marl strata at a number of sites surrounding No. 2 shaft in order to predict closures of the shaft excavation. The method of stress measurement chosen was by overcoring using the Talbott strain cell developed by the Department of Mining Engineering, University of Newcastle upon Tyne (44, 45).

7.2 Stress Measurement by Overcoring Technique

The method of stress relief by overcoring is becoming quite widely practised, having taken over from the previously popular 'flatjack' methods of stress measurement. Merrill et al. (46) carried out extensive comparative testing of

flatjacks and borehole deformation gauges for the U.S. Bureau of Mines which yielded good correlation between the two methods of determination.

A number of different techniques were developed for measuring stress and strain distribution around boreholes. These included rigid, or high modulus inclusion stress meters (47, 48), photoelastic stress meters (49) and biaxial strain cells (50), all of which could be overcored to determine absolute stress conditions, uniaxially or biaxially. In South Africa, Leeman developed the C.S.I.R. triaxial strain gauge cell together with the mathematical solution for the three dimensional stress determination in an isotropic homogenous material (51, 52). There are now a number of both high modulus and soft inclusion triaxial strain cells in use, the Talbott cell being of the soft inclusion type.

7.2.1 The Talbott Mark II Strain Cell

The Mark II version of the Talbott strain cell is shown in Fig. 7-1. It consists of three rosettes each with three strain gauges, the rosettes being located at 0°, 90° and 225° around the circumference of the cell which is inserted into a 50mm (AWX) borehole. Attached to the central body of the cell are temperature compensating and bridge completion gauges. Insertion and setting of the cell in the hole is done by interlocking insertion rods with enclosed box keys one of which pressurises the cell while the other releases the cell from the leading insertion rod at the required orientation of rosettes.

FIG. 7-1

The cell consists of a moulded silicone rubber cylinder between steel end plates. Each rosette is located at the end of a nylon piston where it is fixed around the periphery. This piston is forced radially outwards by the pressure of silicone rubber due to axial compression of the cell end plates. The pistons are hexagonal in cross section and travel in a nylon bush within the rubber cylinder. This modification from the Mark I design prevents drag on the rosettes due to creep of the silicone rubber and the hexagonal shape prevents any rotation of the rosette before it makes contact with the rock.

One of the problems with the Mark I cell had been the effect of borehole surface irregularities on the strain gauges. The Mark II cell has reduced this problem considerably by allowing the rosettes to be bonded to the rock surface. In this way the bonding resin fills any voids in the rock surface and excess resin is allowed to flow into the trough surrounding the rosette. The curved, Teflon-coated end of the piston provides a smooth backing for the rosette and ensures that the gauges are not forced into irregular shapes associated with the borehole surface. As a result, under certain circumstances where the borehole surface is known to be clean and smooth, a frictional contact can be relied on rather than resin and this makes the cell re-usable after overcoring. However, it must be noted that with both frictional and resin contacts, the condition of the borehole surface is critical to the success of the overcoring. Apart from the problem of voids and troughs between crystals, the borehole must be cleaned thoroughly and dried before the cell is inserted to remove as much surface dust as possible as

this will affect the gauge response to rock movement regardless of the type of contact.

7.2.2 The Principle of Overcoring

As described previously there has been a great deal of development of instrumentation for stress measurement by overcoring. The basic principle of the method is that the annulus of rock within which the cell is installed is overcored to a sufficient depth so that the annulus deforms until it is in a condition of zero stress triaxially. The cell measures the elastic recovery on the inside surface of the annulus. The Talbott cell measures this recovery in terms of strain which is a function of the original triaxial stress field prior to overcoring. This relationship is obtained using a computer analysis developed by Maconochie (27) based on the solution of Hiramatsu and Oka (53). Values for Young's Modulus and Poisson's Ratio are required for this analysis and these parameters should be obtained for an unloading condition to simulate the overcoring process correctly.

This technique of stress relief is equally applicable to most rocks which exhibit inelastic or viscoelastic response to load changes as it is to elastic materials. Work by Gumperayarnnont (54) in the laboratory on rock salt showed that "The recovery strain of Cheshire rock salt on the instantaneous unloading cycle is independent of time but depends on the stress and is affected by the microscopic voids at the low stress levels. The void effect will be decreased as the stress increases." He tested specimens which had undergone

differing amounts of creep and established that there was still a direct relationship between applied load and elastic recovery. Work carried out by the author on potash specimens in a servo-controlled testing machine (see Chapter 6) confirmed that a proportional elastic recovery still took place after the specimens had undergone considerable straining.

Obviously an overcoring operation does not represent an instantaneous unloading and so there will be a component of time-dependent strain relaxation in viscoelastic type materials. However, provided the elastic properties of the material are obtained from a test simulating the time involved in overcoring then they also will contain a component of time-dependent relaxation. Obviously this does not provide a rigorous solution to the problem but for all practical purposes the elastic analysis will provide sufficient accuracy.

The Talbott cell is overcored using a 150mm diameter core barrel. This produces an annulus of 50mm thickness. This size is considered to be the minimum necessary to reduce heat effects on the cell and core during drilling and also to prevent premature discing of the annulus. This occurs when overcoring in areas of high stress fields or in weak rock where the pressure exerted by the cell itself can lead to tensile and shear failures. One major advantage with the drilling equipment used is the ability for continuous monitoring of all nine active gauges throughout the drilling operation. This is achieved by means of a specially built water swivel permitting the screened multi-core cable from the cell to be passed through the core barrel, drill rods and drill and connected to the logging

apparatus. As the results show, this facility is invaluable for identifying temperature effects on the rock, slip of gauges and any other possible causes of anomalies in the gauge readings. Such anomalies must be equally likely with any type of instrument and so continuous monitoring is considered as essential for confidence in the results of any overcoring operation.

7.3 Site of Overcoring Operation

Although it had been intended to carry out an overcoring at a total of five sites around the No. 2 shaft area, due to problems with drilling, costs and time, only one overcoring site was eventually used. The site chosen was a short cross-cut into the side of a 110m by 90m pillar adjacent to the shaft. Fig. 7-2 shows the location of the site on a section of the mine plan. Although

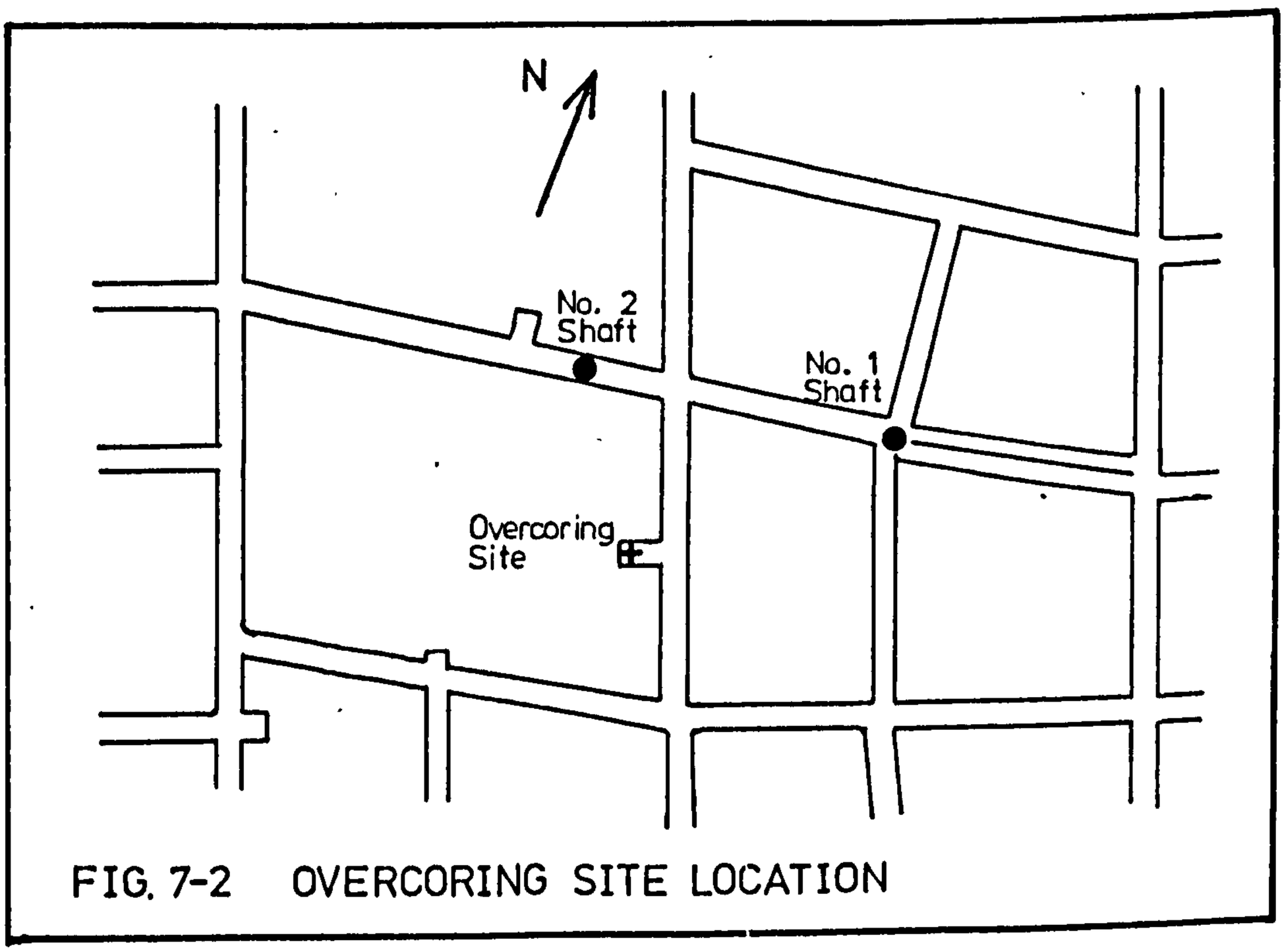

FIG. 7-2 OVERCORING SITE LOCATION

the stress distribution above the cross-cut would be influenced by the mine excavations the influence would be minimal at sufficient height above such a large pillar. The measured stresses could therefore be approximated to virgin conditions. It may have been possible to carry out the overcoring operation at the extremity of the mine workings in a long horizontal borehole and obtain more accurate results. However the purpose of the operation was primarily to define the stress field in the vicinity of the shaft and so this particular site was chosen.

The geology of the site is shown in Fig. 7-3 together with the location of the five cells which were installed. In this

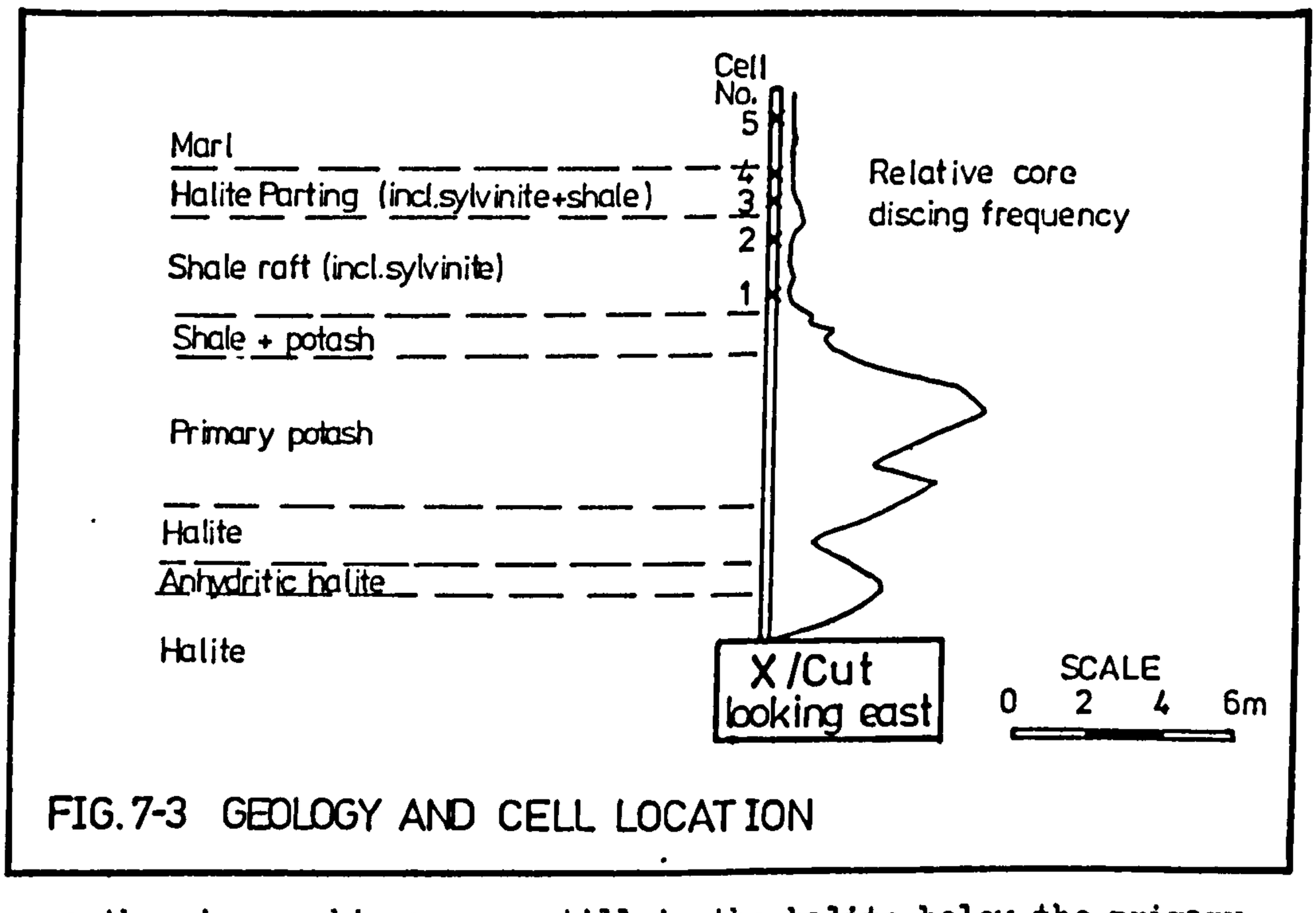

FIG. 7-3 GEOLOGY AND CELL LOCATION

area the mine workings were still in the halite below the primary potash seam in order to provide greater stability to the shaft pillar area. Above the halite was a thick bed of primary potash overlain by a secondary ore-bearing shale raft. The halite parting in

this area had pinched out to a very thin seam containing halite, sylvite and shale and then the Carnallite marl occurred above the halite parting with numerous sylvinite veins.

The drill site was located as close to the side of the cross-cut as possible and slightly back from the end of the cross-cut in order that the borehole would pass through the zones of induced stress due to the excavation in as short a distance as possible.

7.3.1 Equipment and Initial Drilling

The drill used was a compressed air drill mounted on a drill post wedged between roof and floor and surrounded by a scaffold working platform. Whenever possible compressed air was used as a flushing medium and the hole was cored the full length. However, due to lack of sufficient air pressure and irregularities in supply, it was necessary to use a diesel oil flushing system on a number of occasions to enable good core to be obtained. Although core recovery improved, the working conditions and morale of the drilling crew deteriorated rapidly!

The first 8m of drilling to the first cell position was very slow, especially due to discing of the core. The discing frequency is plotted on Fig. 7-3 and indicates the location of the relaxed zone of rock in the immediate roof followed by the zone of compressive stress which reaches a peak about 5m above the roof (this would be in excess of 6m above the centre of the cross-cut). Beyond this the discing frequency dropped rapidly suggesting the stress conditions were approaching the virgin stress level. Fig. 7-4 shows the drill

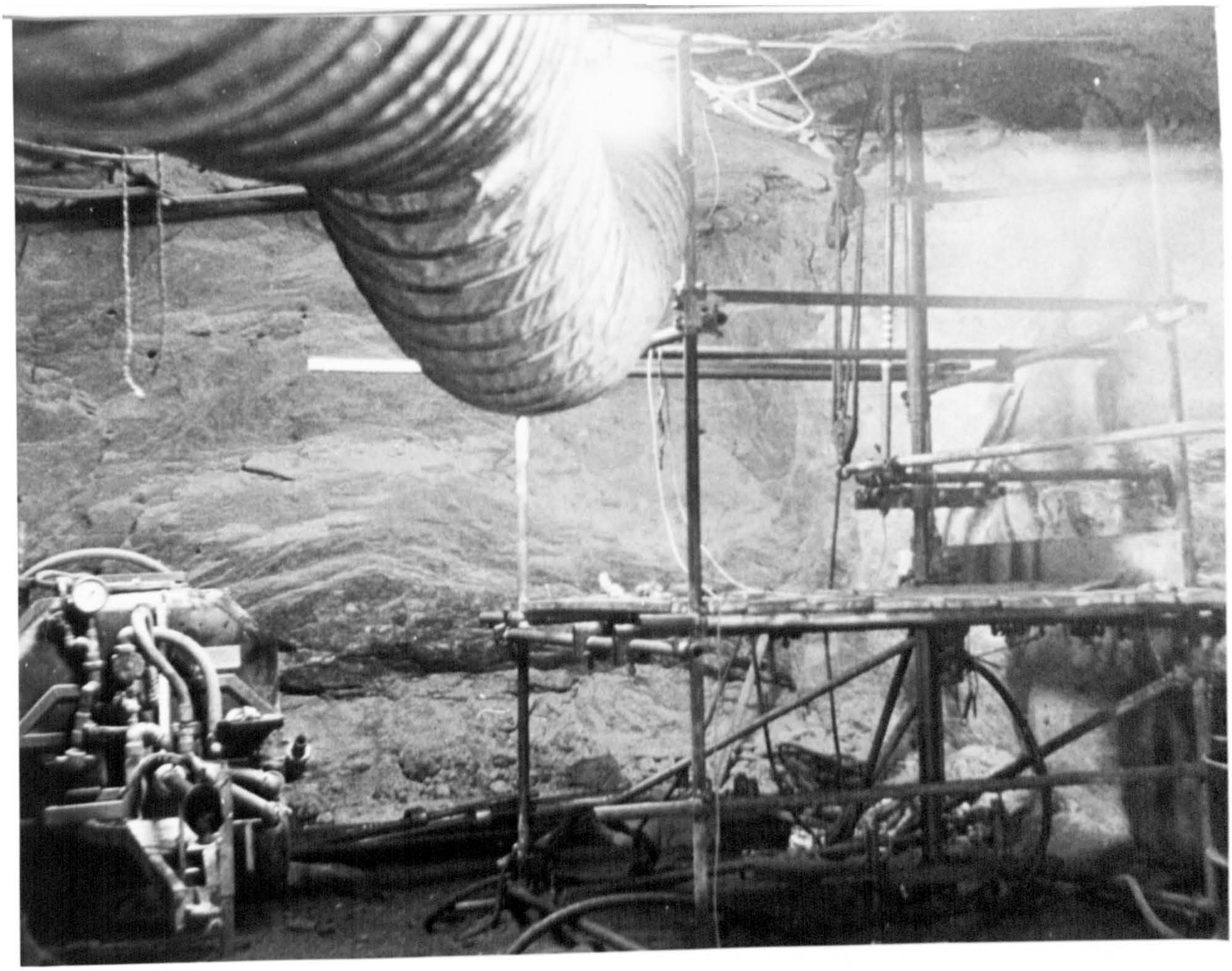

FIG. 7-4

FIG. 7-5

site, looking west into the cross-cut. Fig. 7-5 shows the core recovered up to the pilot hole for the first overcore (from left to right corresponds to going up the borehole). A detailed description of the entire operation is given in a report to Cleveland Potash Limited by Hebblewhite and Miller (55).

The data from the strain cells was logged using a system comprising a variable voltage stabilised power pack, Solartron scanner and data transfer unit, digital voltmeter, printout typewriter and paper tape punch. This provided a good back-up of data output since each one of the three output devices failed to work at some stage during the operation.

The convention used to describe the gauges and rosettes is that rosettes 1, 2 and 3 are located at 0°, 90° and 225° around the cell respectively. Within each rosette the gauge numbering is 1, 2 and 3 for circumferential, axial and 45° gauges respectively. For cells 1, 2 and 4 a positive strain represents tension while cell 3 was inadvertently reversed, so in the raw data only, a negative strain represents tension.

Fig. 7-6(a) illustrates the rosette orientation and the reference axes used for analysis. The z axis corresponds to the borehole while the circle in the x-z plane is the azimuthal reference circle with 0°(N) on the -z axis and the azimuth increases clockwise through the +x axis. Dip is measured between the x-z plane and the -y axis. Fig. 7-6(b) shows the rosette positions relative to the reference axes as viewed from above when the cell is installed in a vertical borehole.

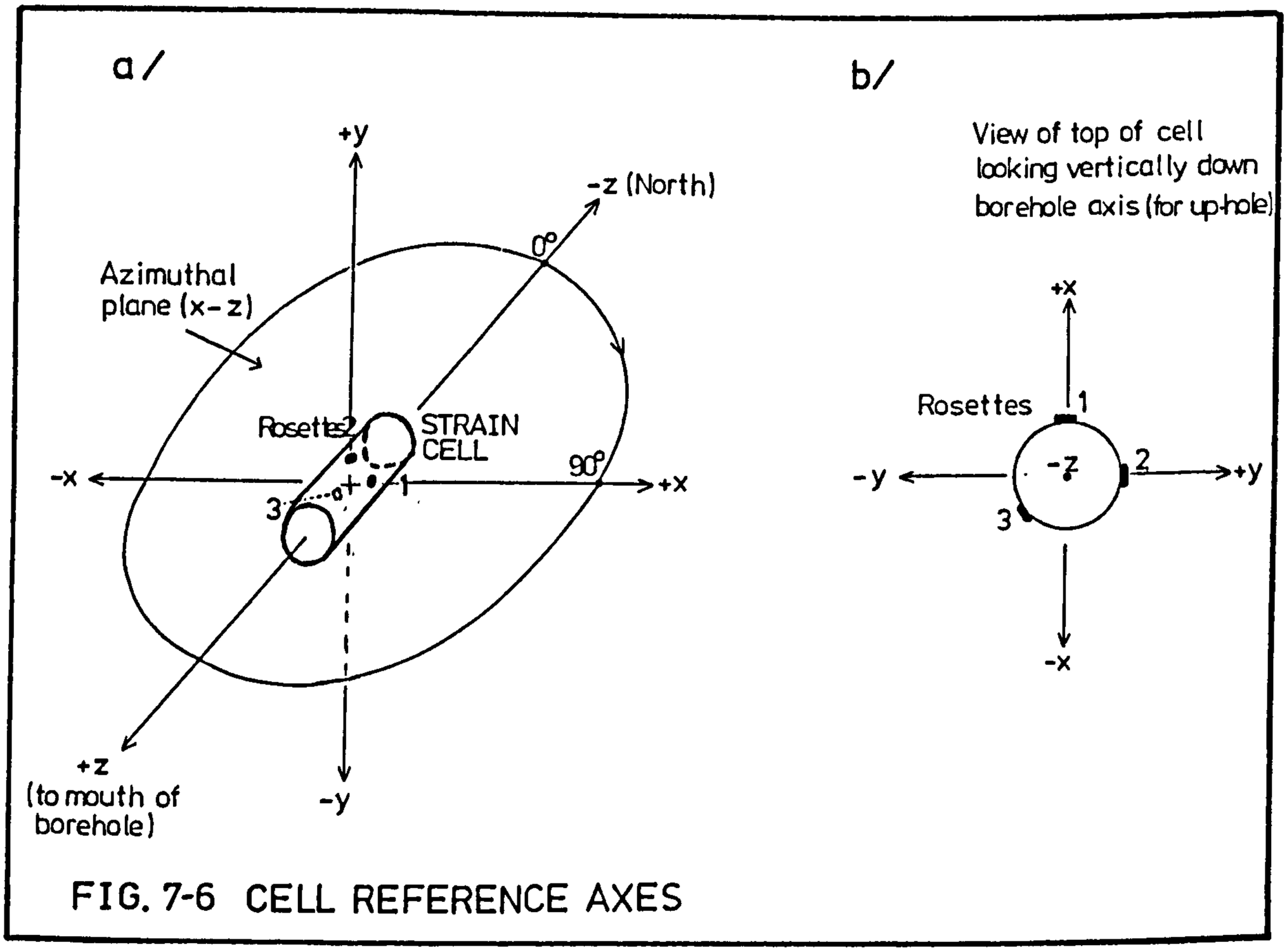

FIG. 7-6 CELL REFERENCE AXES

7.4 Discussion of Results

7.4.1 Cell 1

In this case and all others, the cell was connected to the logger during insertion so that the gauge outputs were used to indicate when sufficient pressure had been applied to the cell. The cell was tightened until all gauges had started to indicate large changes in reading. A resin bond was used for this cell. Laboratory tests had been carried out to find a bonding agent which had at least one hour pot life and yet hardened properly in a temperature of 35°C which was expected in the borehole. None of the resins were very satisfactory but a type of plastic steel performed best, using the slow hardener.

Cell 1 was left in the borehole overnight before being overcored using air flushing. Fig. 7-7(a,b,c) show the complete set of results while (d,e,f) show the strain results during the overcoring operation. Rosettes 1 and 3 both took two to three hours before they began reflecting the circumferential compressive creep of the rock mass. This delay in response could be caused by three factors.

i) Exothermic reaction while the resin is setting causing irregularities in the readings,

ii) Bad contact between resin and rock due to a build up of dust,

iii) The outward pressure due to radial expansion of the strain cell causing a tensile stress distribution in the rock surface initially before being overcome by the compressive creep strains.

Although the first factor no doubt exists, it would show fairly similar trends on all three rosettes which was not the case. Therefore a combination of (ii) and (iii) seems a likely explanation for the time delay.

As can be seen from the overcoring plots in Fig. 7-7 the overcoring was not a success. The gauge position of the cell was overcored after 42 minutes which was roughly when the gauges began slipping indicating a failure of the resin-rock bond. This stick-slip phenomenon continued for a further 10 minutes, the gauges still responding to a frictional contact with the rock before the core broke up completely inside the core barrel. The resin then exhibited a rapid strain recovery once free from any contact with the rock. This behaviour of the resin and the fact that the bond appeared to break prior to the break-up of the core highlighted another problem of using resin with low modulus rock. As soon as a strain exists on the resin-rock interface, an elastic mismatch develops due to the different elastic properties. This results in a shear stress

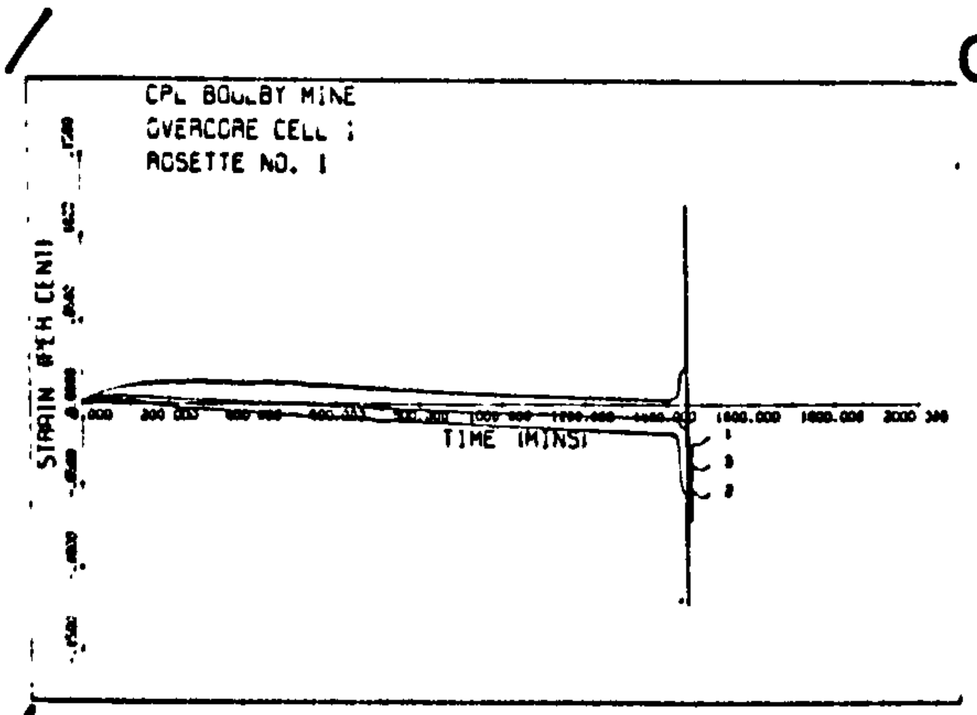

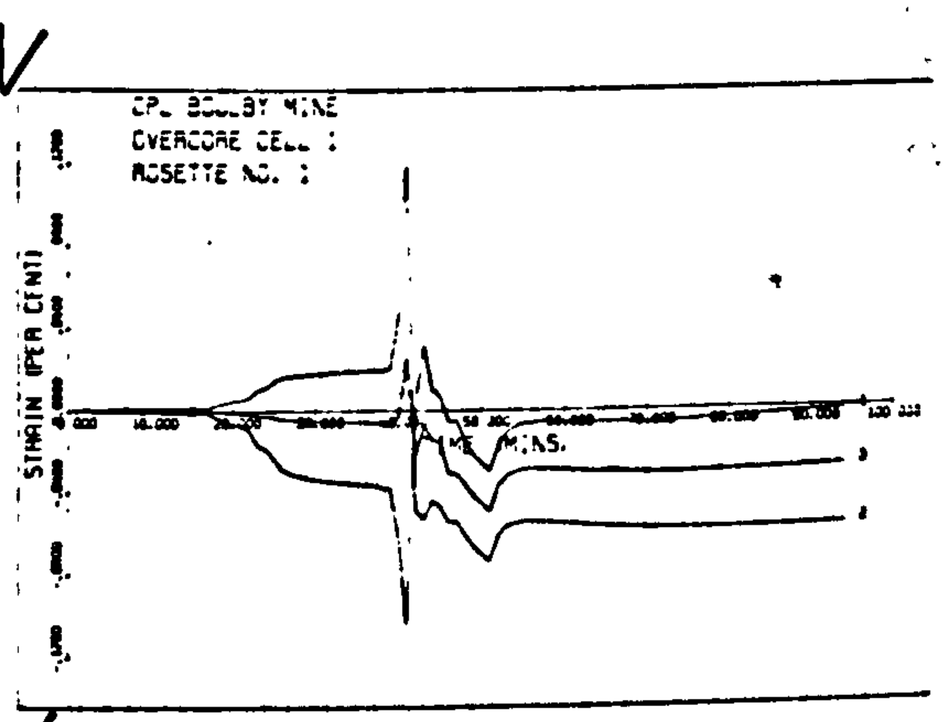

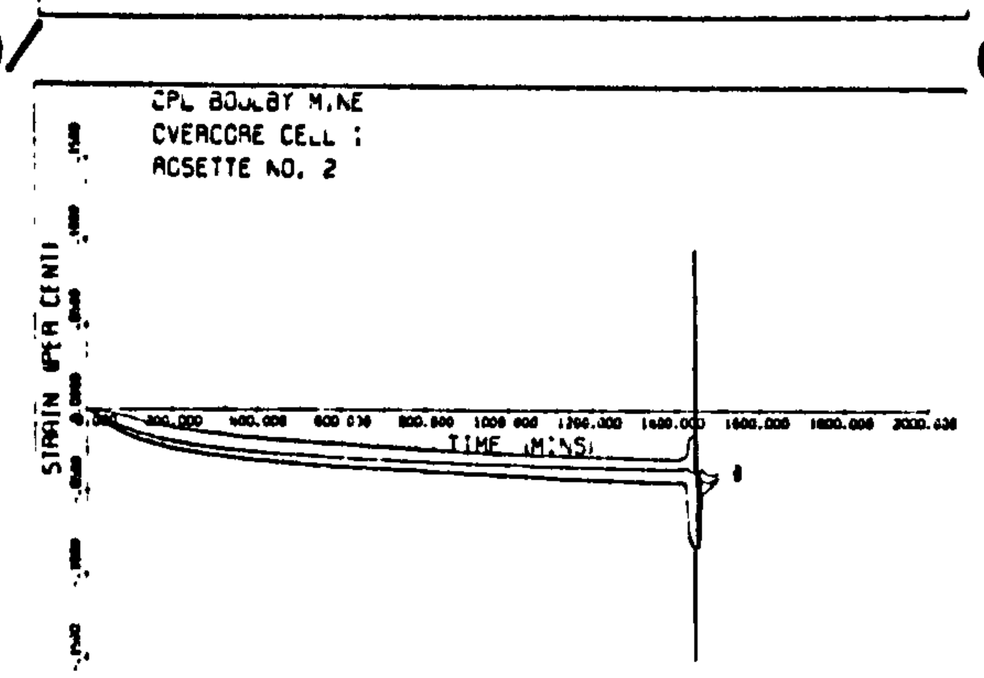

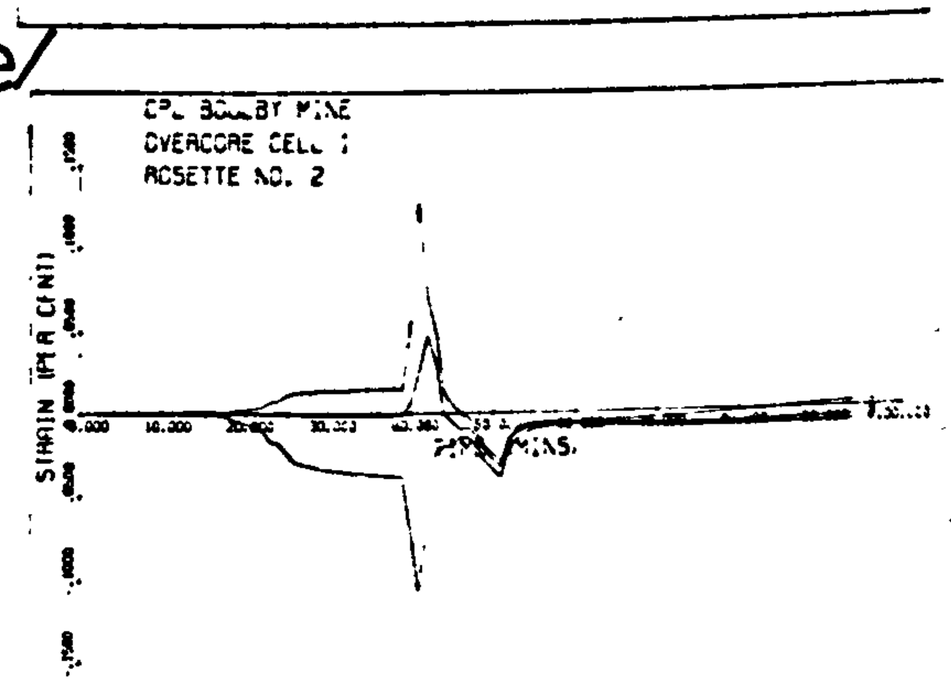

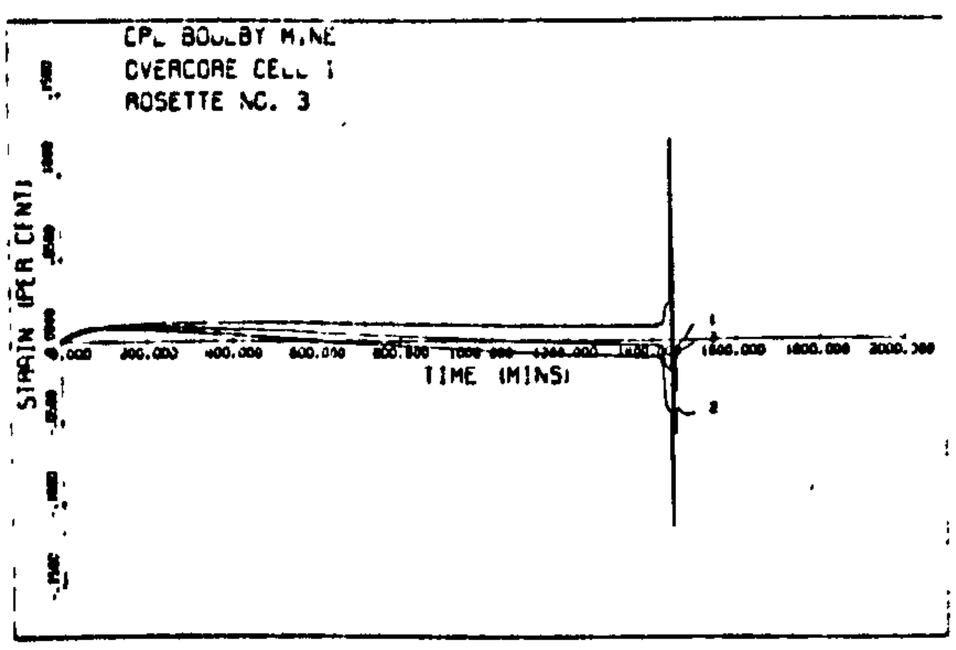

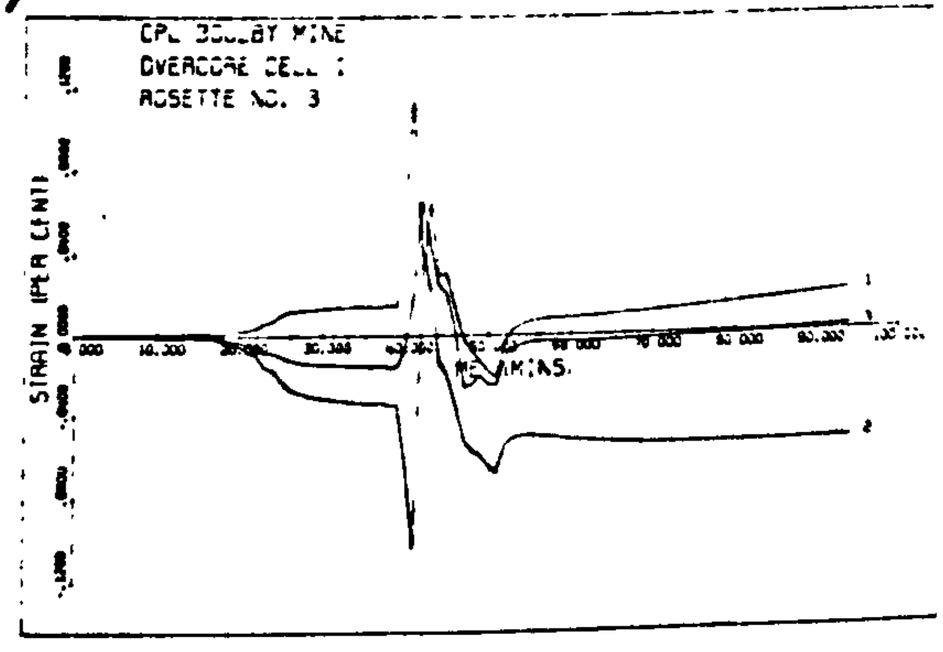

FIG. 7-7 CELL 1 RESULTS

developing along the interface. For recovery strains in excess of 2400 microstrain at a potash-resin contact the bond strength of the resin is likely to be exceeded and the bond will fail. A poor quality contact will fail at considerably less than that figure and once failed, the resin exerts a strong force attempting to overcome any frictional restraint and return the gauges and resin to an equilibrium condition. Therefore where high strains are expected in this type of rock a frictional contact has some advantages over a resin contact.

7.4.2 Cell 2

This cell was installed in the shale raft and once again resin bonding was used for the rosettes. A sample of the resin used was also kept for inspection once it had set. It was later found to have hardened to a certain extent but when placed in a high temperature room it became very ductile. This placed further doubt on the reliability of the resin bond in the borehole.

The results from this cell are shown in Fig. 7-8 where (a,b,c) show the complete data set for each rosette while (d,e,f) show the data obtained during the overcoring operation. Once again there is a time delay before the gauges respond to the rock closure and it is approximately 100 minutes though it varies with each rosette.

Drilling penetration was monitored having roughly established the cell position in the borehole. Diesel oil was used as the flushing medium during this overcore in an attempt to prevent the core breaking up. However, once again problems were encountered during the drilling and after 72 minutes all the gauges gave open-circuit readings and

a/

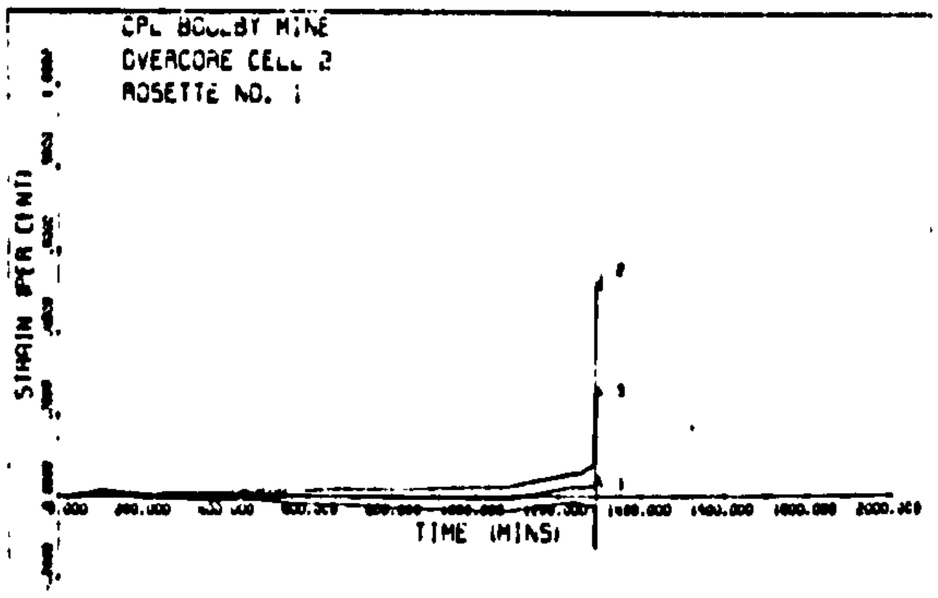

d/

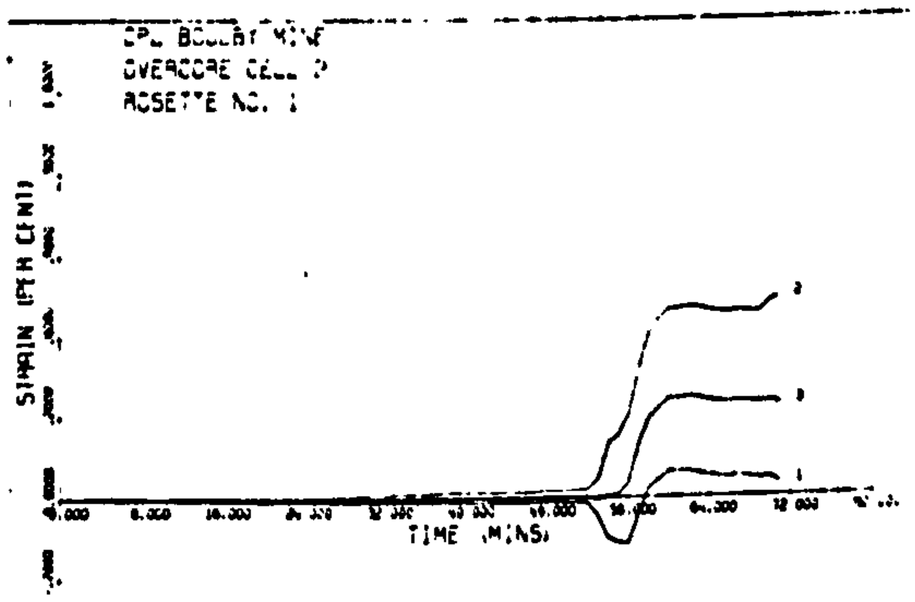

b/

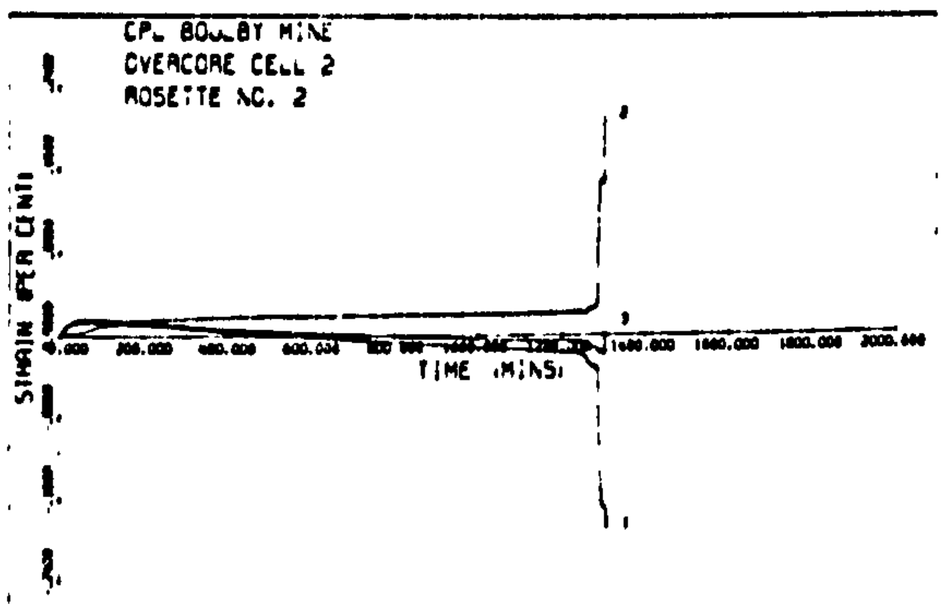

e/

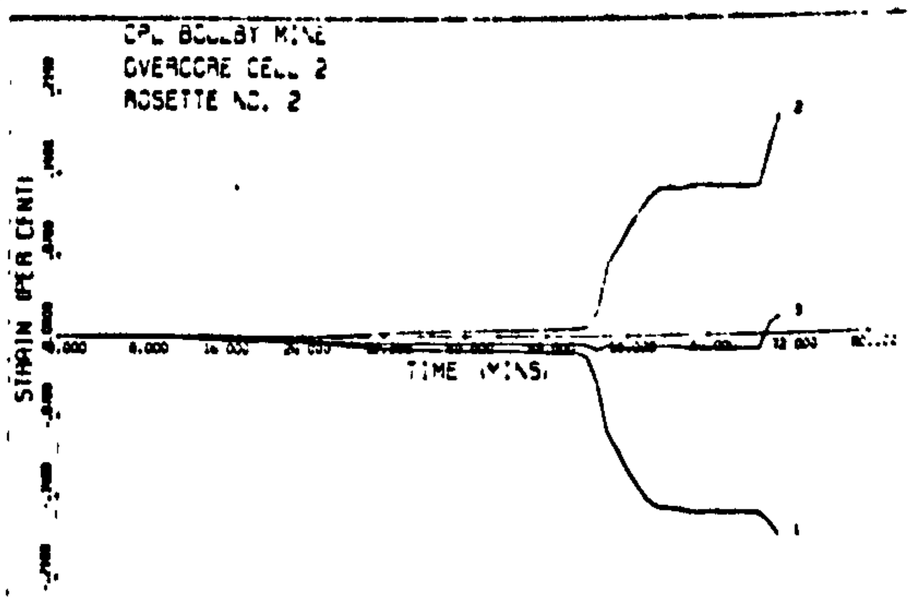

c/

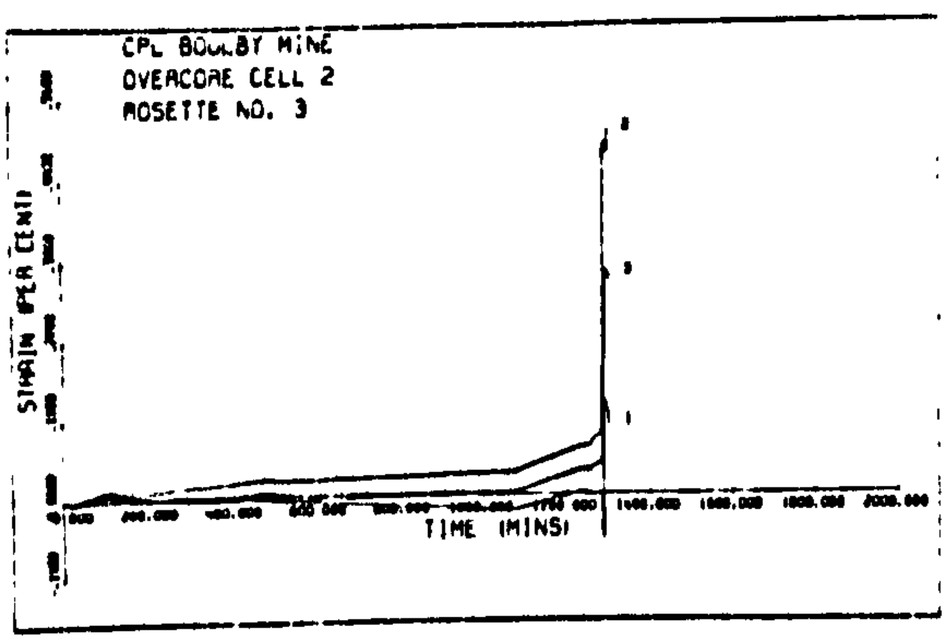

f/

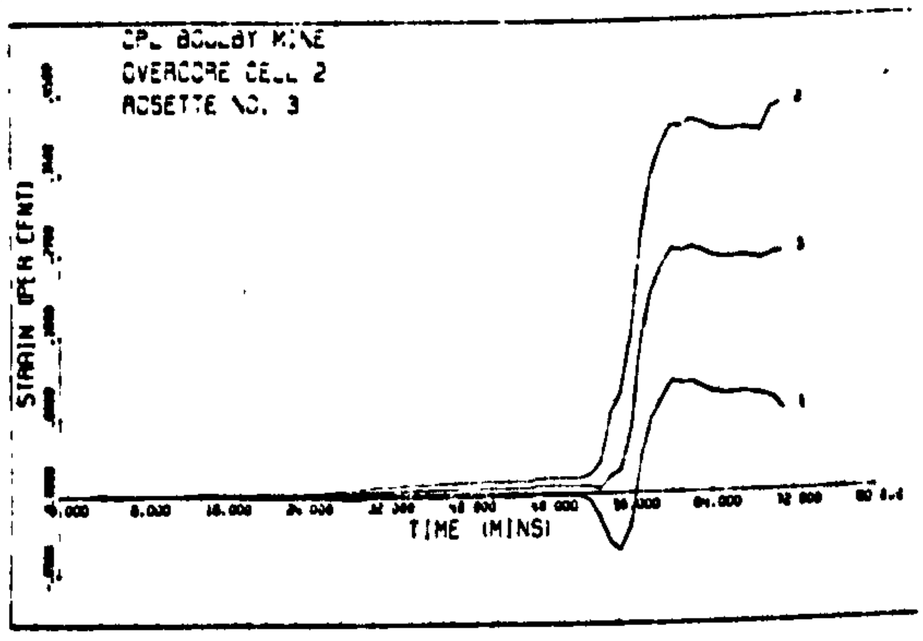

FIG. 7-8 CELL 2 RESULTS

again the core broke up. From the penetration measurements the drill had not even reached the cell position when the gauges ceased to function and so the results of this cell were disregarded in the initial analysis.

However, subsequent analysis of the data on paper tape produced the curves shown in Fig. 7-8. These curves indicate a successful overcoring operation prior to the gauge failure and so it must be assumed that the original position of the cell in the borehole was incorrectly logged. The flat plateau on all the curves between 62 and 69 minutes was caused by a halt in drilling but regardless of that it appears that virtually all the elastic recovery had taken place prior to the gauge failure at 72 minutes. From the results it could be estimated that the gauge position was overcored at approximately 57 minutes based on evidence from other overcoring results (45) and an axisymmetric finite element simulation of overcoring by Hooker et al (56).

The results from this cell were analysed using the endpoints of the curves as they are plotted on Fig. 7-8 (d,e,f). Table 7-2 lists the changes in microstrain for each of the nine gauges corresponding to the elastic recovery of the core.

Table 7-2 Cell 2 Overcoring - Elastic Strain Recovery

	Strain Recovery (Microstrain)		
	Circumferential Gauge	Axial Gauge	45° Gauge
Rosette No. 1	440	4557	2296
Rosette No. 2	-1553	1278	-127
Rosette No. 3	1106	4048	2616

Since the core was completely broken up when recovered there was no possibility of any laboratory testing to obtain elastic properties. For the purpose of the analysis, therefore, an estimate was used based on work by Wiggett (9). He obtained an average value of 11.02 GN/m^2 for the Young's Modulus of shale with a Poisson's Ratio of 0.24. This average included the shale-potash mixture already logged below the cell 2 position (see Fig. 7-3). All other shale types had moduli equal to or below the average value whereas the shale-potash mixture has a high modulus. The lowest modulus - for anhydritic shale - was 8.25 GN/m^2. Therefore a range of moduli from 8.25 GN/m^2 to 11.02 MN/m^2 was chosen to represent the shale in which cell 2 was located, i.e. 9.64 ± 1.38 GN/m^2. Since Poisson's Ratio does not have a large effect on the solution this was maintained at 0.24.

The principal stresses obtained from this overcore analysis are listed in Table 7-3 together with their azimuth and dip relative to the borehole axis. To relate the stress directions to the cross-cut geometry,

Table 7-3 Cell 2 Principal Stresses and Directions

	Principal Stresses (MN/m^2)	Azimuth ($^\circ$)	Dip ($^\circ$)
σ_1	-32.846	354	2
σ_2	- 6.158	88	61
σ_3	4.233	262	29

No. 1 rosette had a bearing of S21°E, i.e. it faced the southern wall of the cross-cut. Fig. 7-9(a) is a sketch of the triaxial stress distribution obtained from cell 2. Since the major principal stress

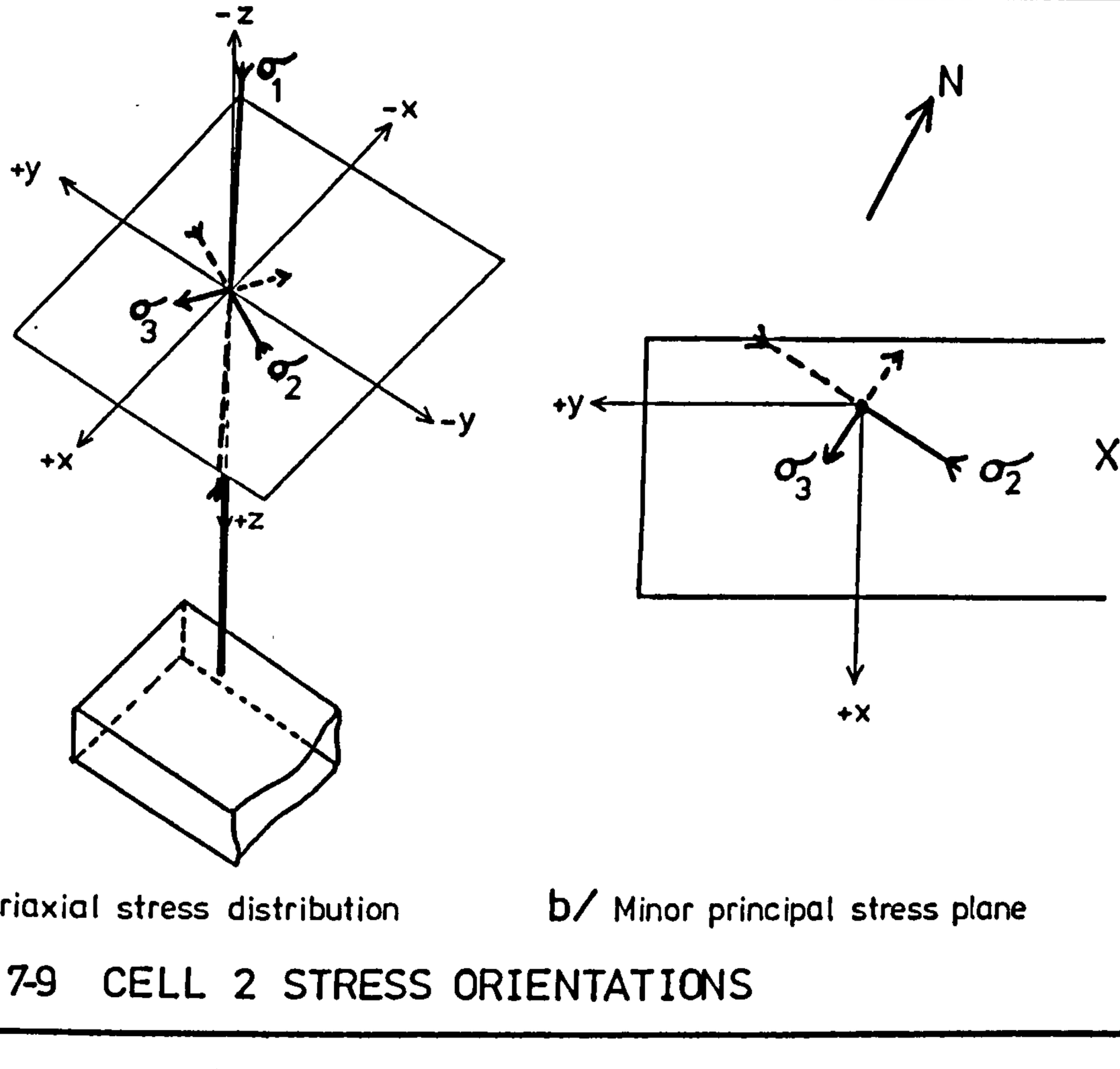

a/ Triaxial stress distribution b/ Minor principal stress plane

FIG. 7-9 CELL 2 STRESS ORIENTATIONS

is virtually vertical, the plane of the minor principal stresses is almost horizontal and so Fig. 7-9(b) shows the minor stress plane superimposed on a plan view of the cross-cut. The dashed lines represent the stress vector lying below the horizontal plane.

Since the modulus is the major assumption for these results then the modulus accuracy of ±14% should be applied to the stress magnitudes to give a meaningful range of magnitudes. The tensile value of σ_3 and the low compressive value of σ_2 could be associated with proximity to the cross-cut but they are still very hard to explain and could be due to anomalous results from rosette 2.

7.4.3 Cell 3

Following the problems with the bonding resin described

previously, this cell was installed with a friction contact only between gauges and rock. It was installed in the Halite Parting which contained both shale and sylvinite throughout the halite. The initial readings were not logged for this cell and since no resin setting time was required, the cell was overcored within a matter of hours. In this case diesel oil was used initially for flushing but then air was used for the actual overcoring. Once again it was thought that the results from this cell were of no use since the cell was not tightened sufficiently and it was thought the gauges had slipped. Although the core broke up to a certain extent and was permeated by oil, the annulus containing the gauges remained intact. It was only when the results were processed at a later date that it became apparent that the slip of the gauges was only a minor effect and could be corrected without significant loss of accuracy.

Fig. 7-10 (a,b,c) show the original overcoring data with the effects of flush and drilling indicated on (c). (Note the reversed sign convention here, tension is negative.) This highlights the influence of temperature on the rock and also the cell which is not fully independent of temperature effects. The period where the gauges slipped was between 42 and 44 minutes. A correction was made for this slip on the following basis. The curves were plotted against drilling penetration which was recorded correctly this time. Then, for each gauge, the gradients of the strain-distance curve immediately before and after the slip zone were averaged and this mean gradient was applied across the slip zone and subsequent readings adjusted accordingly. The corrected plots of strain against time are shown in Fig. 7-10 (d,e,f) while Fig. 7-11 shows the plots of strain against distance while drilling was in progress (from 21 to 49 minutes on the plots in Fig. 7-10).

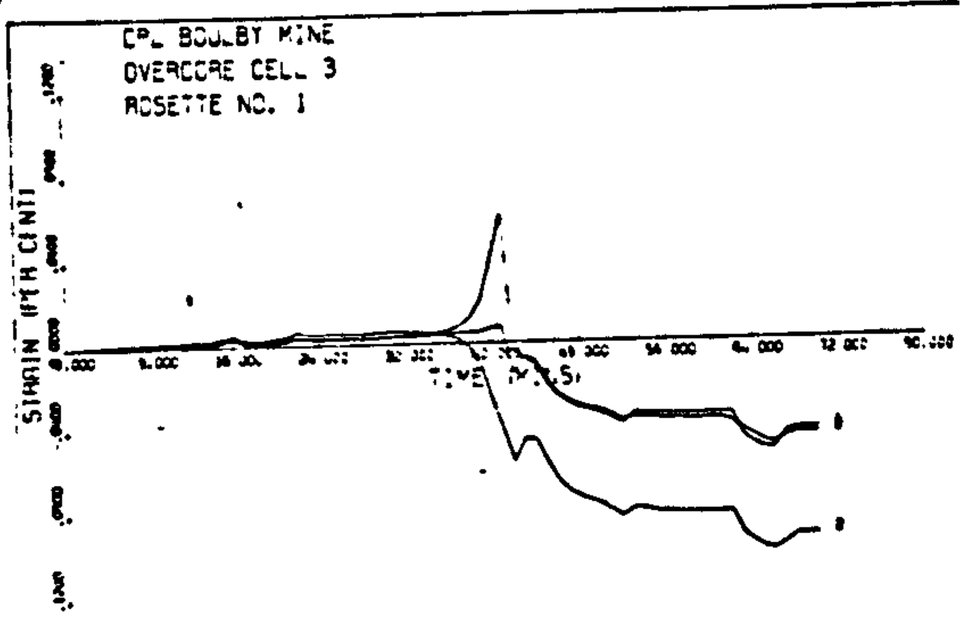

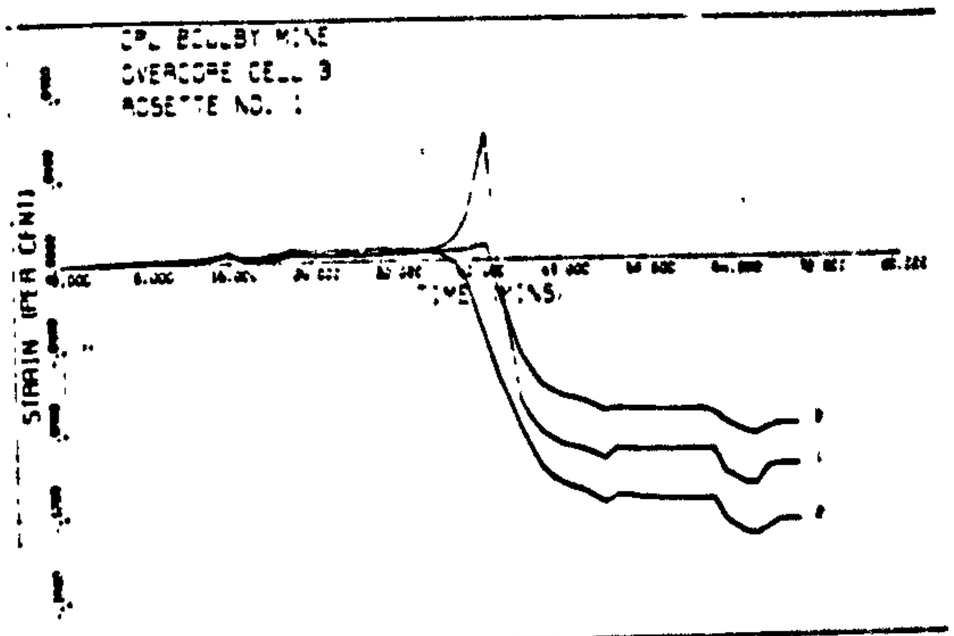

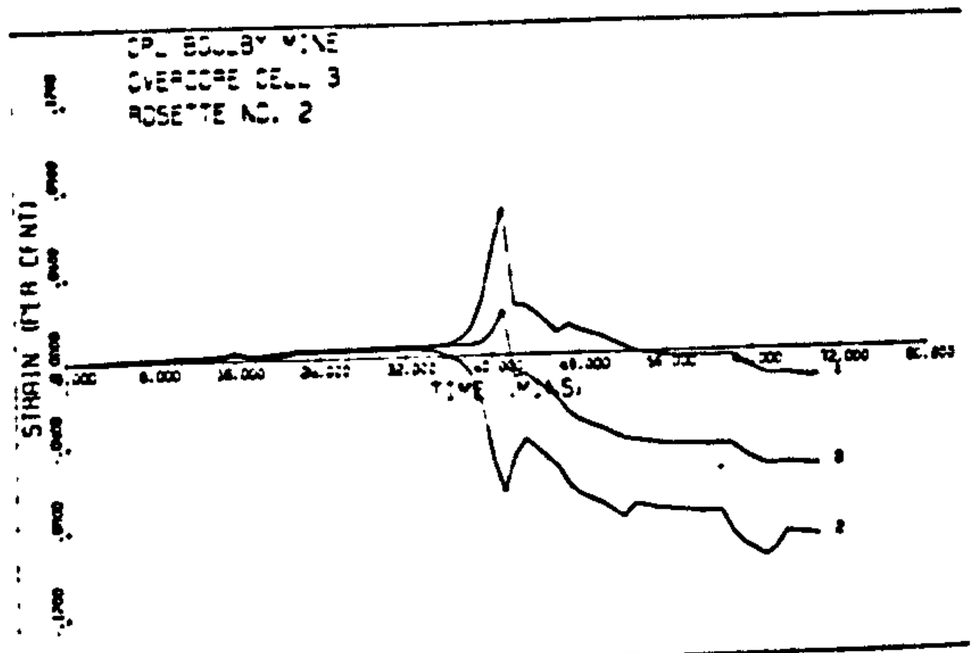

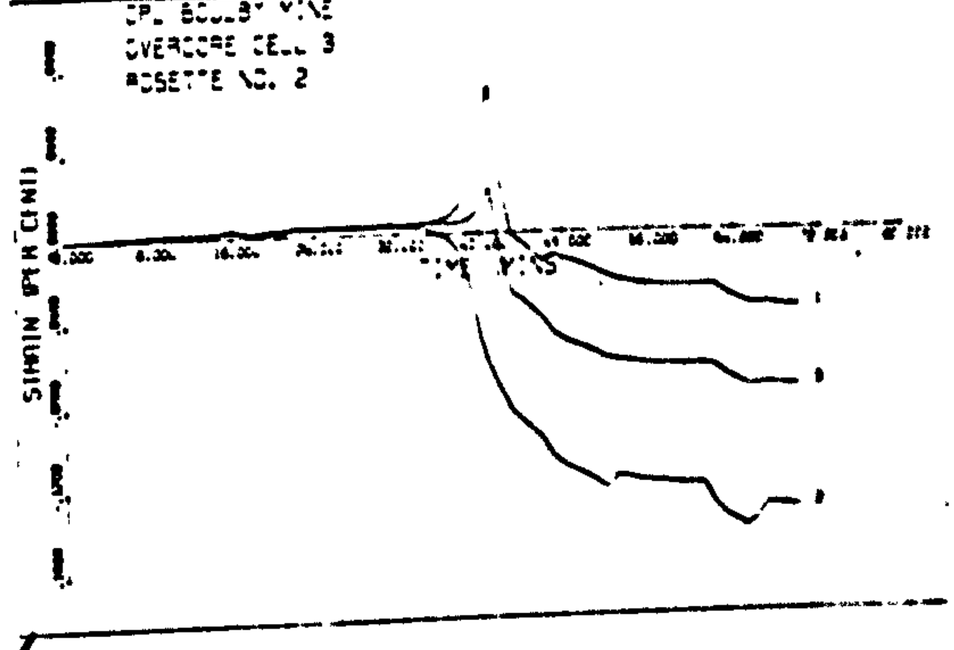

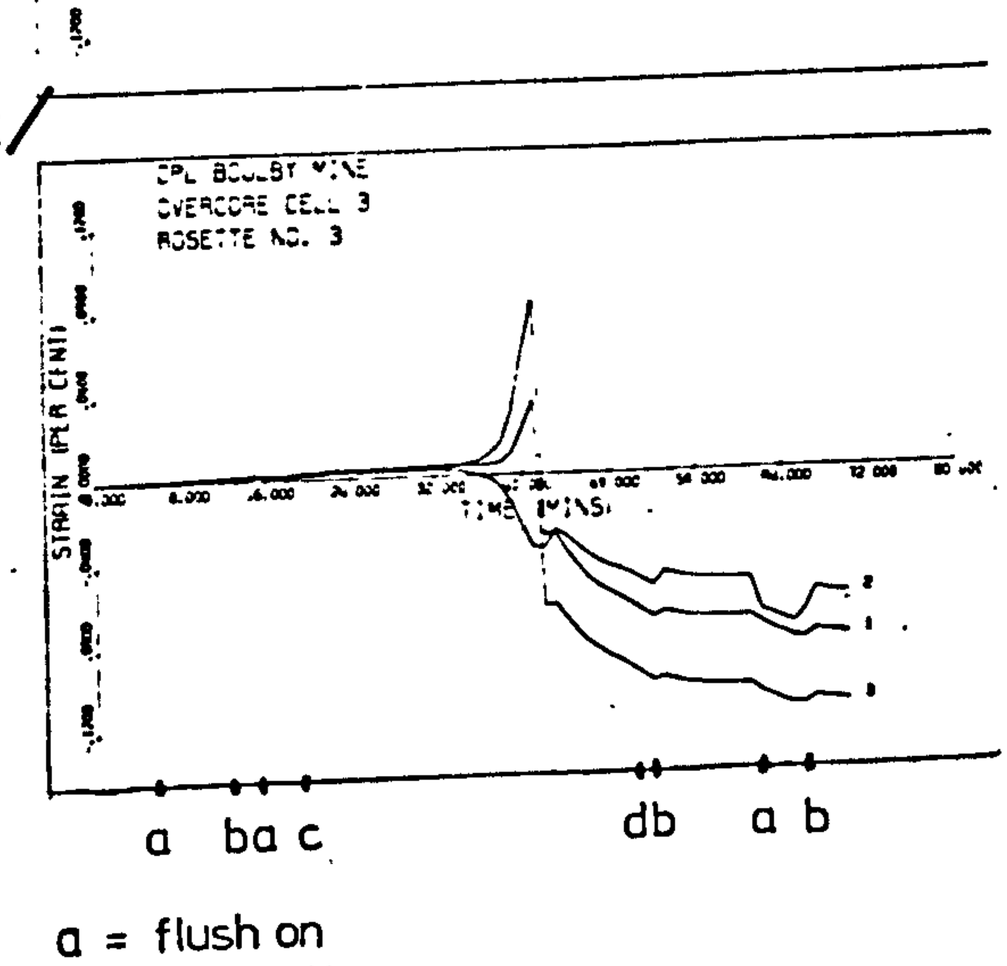

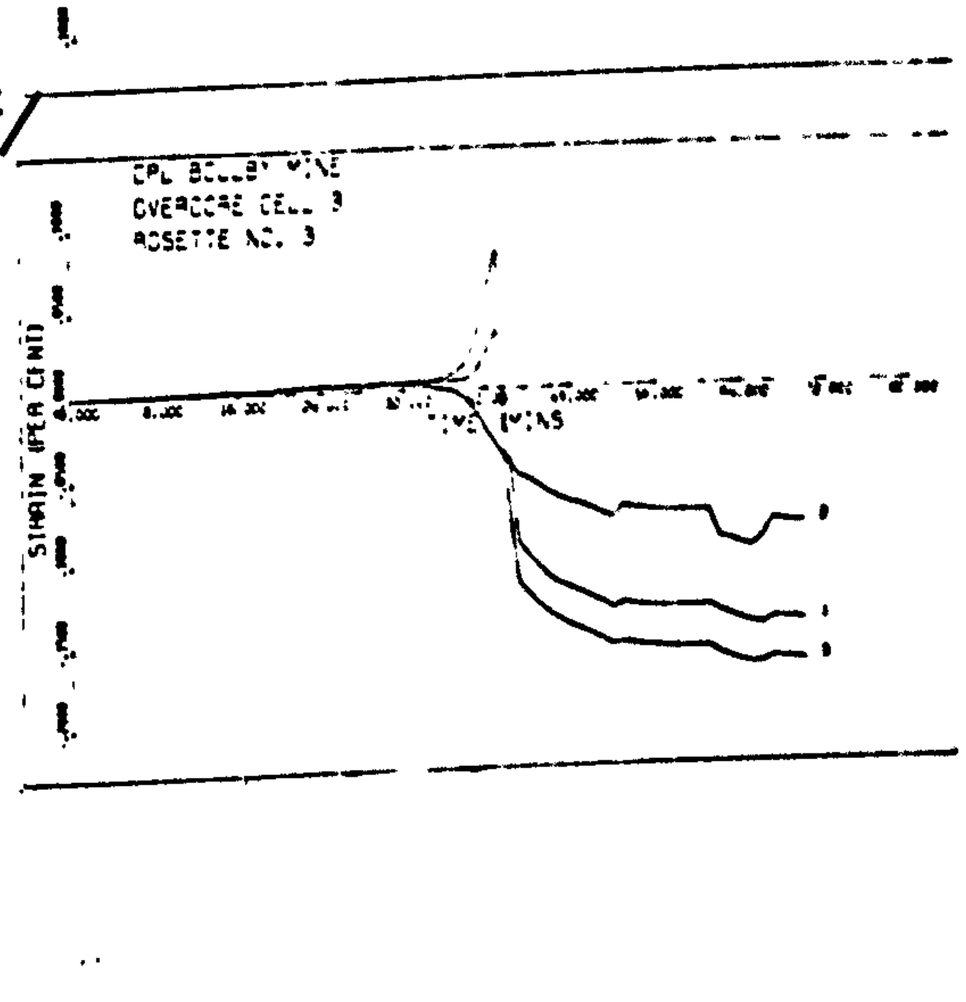

a = flush on
b = flush off
c = drill on
d = drill off

FIG. 7-10 CELL 3 RESULTS

a/

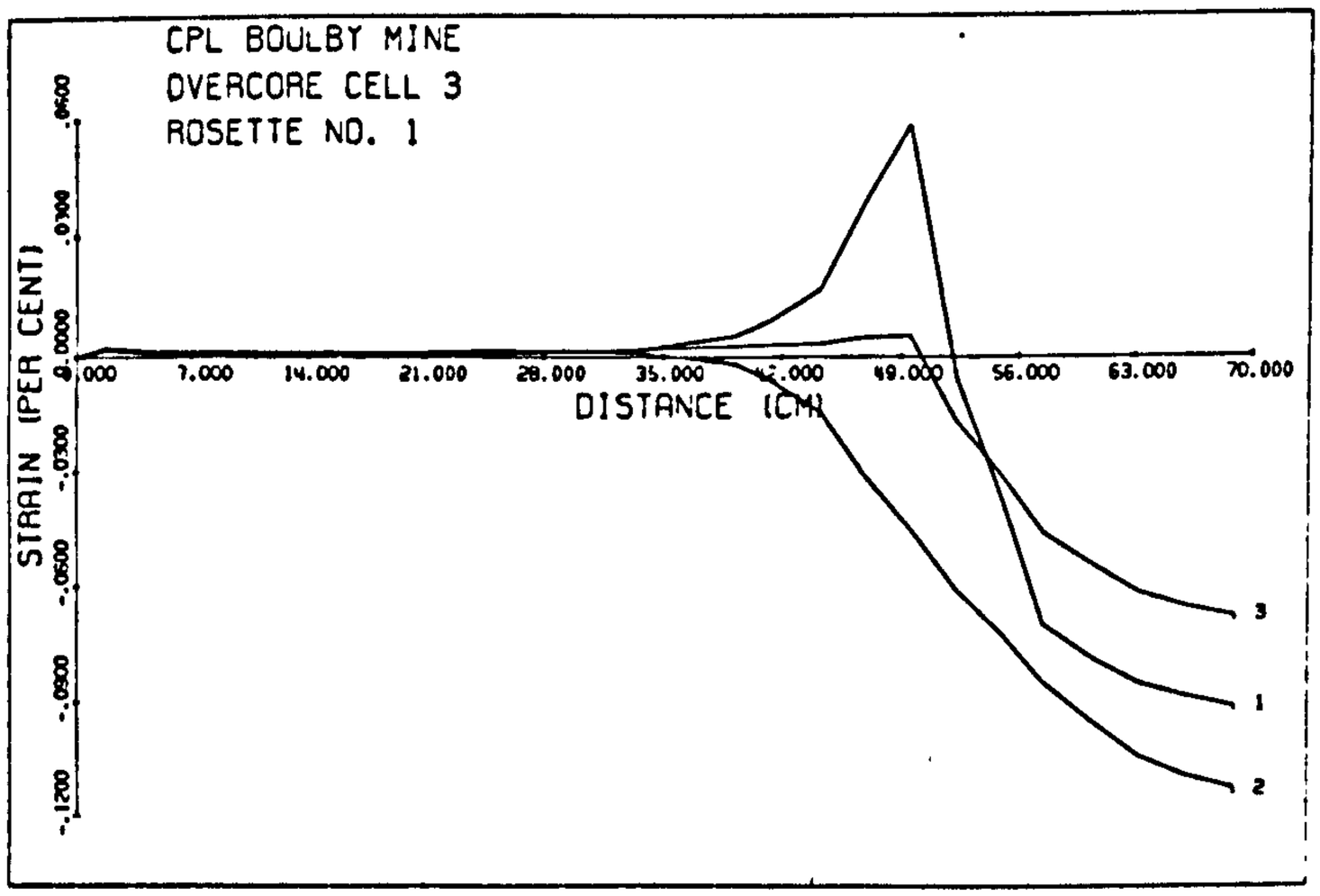

b/

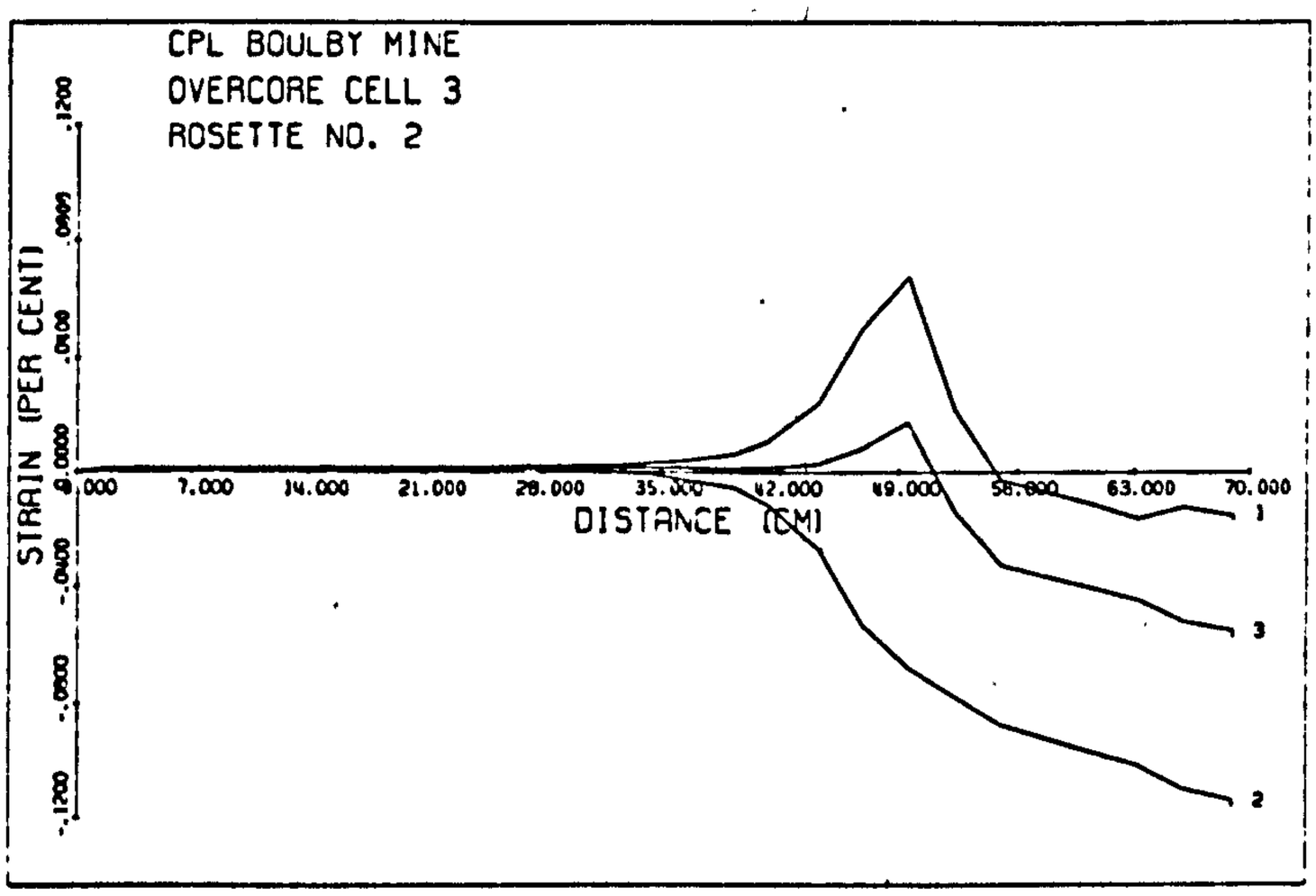

c/

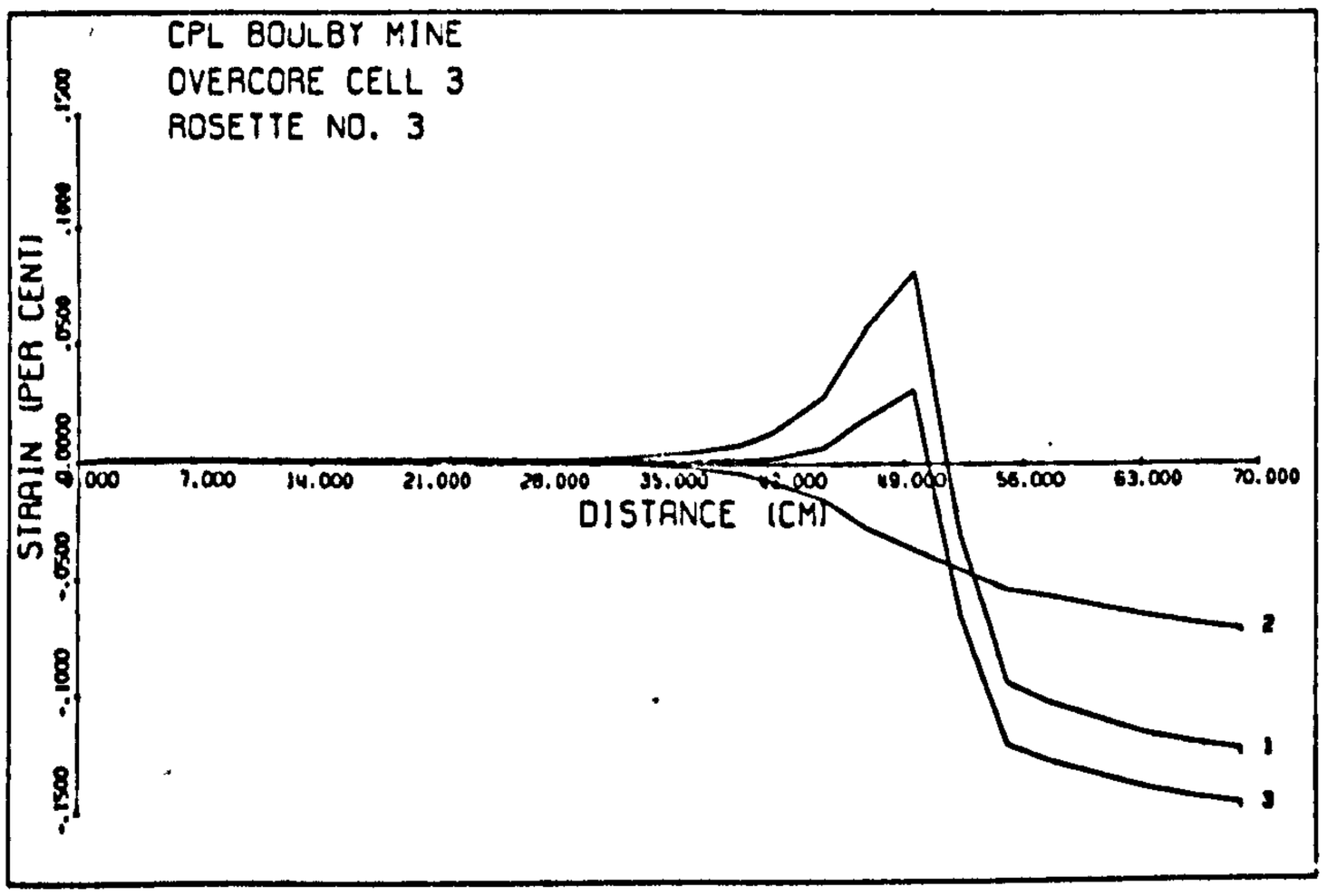

FIG. 7-11 CELL 3 - STRAIN v. DISTANCE

The position of the gauges was at 50cm in Fig. 7-11 and this confirms that the slip correction was of the right order on the basis of previous overcorings and theoretical work (45, 56). This has shown that the circumferential gauges commence to respond to overcoring in a compressive direction at a distance before the gauge position equidistant to the distance beyond the cell at which elastic recovery is complete. In the case of cell 3 the response began at about 31cm (19cm ahead of the gauges) and so it would be expected that the curves should be horizontal by about 69cm which they appear to be. Results of rosette 3 are the only ones which indicate a possible over-correction for slip but an estimated error band of ±10% on the strain values should allow for such differences.

The effects of flush on the rock temperature shown in Fig. 7-10(c) highlight the need for continuous monitoring in order to choose the correct endpoint for the strain recoveries. The starting point, relatively unaffected by the flush, was chosen at 21 minutes and the end point at 59 minutes where a long plateau had developed prior to the core being cooled by the air flush again. Table 7-4 lists the resultant strain recoveries recorded for each gauge.

Table 7-4 Cell 3 Overcoring - Elastic Strain Recovery

	Strain Recovery (Microstrain)		
	Circumferential Gauge	Axial Gauge	45° Gauge
Rosette No. 1	946	1209	751
Rosette No. 2	288	1241	679
Rosette No. 3	1356	792	1621

Once again no core was recovered so an estimate of the modulus had to be made. This cell was located in the same rock type as cell 4 and since it was analysed after the analysis of cell 4 results which included testing of an intact core, the elastic properties obtained for cell 4 have been used here with the same error band. A modulus of 20.43 GN/m^2 (±8%) and a Poisson's Ratio of 0.28 were used.

Table 7-5 lists the resultant principal stresses and directions.

Table 7-5 Cell 3 Principal Stresses and Directions

	Principal Stress (MN/m^2)	Azimuth ($^\circ$)	Dip ($^\circ$)
σ_1	-29.112	176	10
σ_2	-14.606	72	54
σ_3	- 5.986	273	34

To relate these stresses to the cross-cut, the No. 1 rosette had a bearing of N21°W (it faced the northern wall of the cross-cut). Fig. 7-12(a,b) are sketches of the triaxial stress distribution and the minor principal stress plane (again virtually horizontal) relative to the cross-cut.

The stresses listed in Table 7-5 are mean values within a range of ±18% based on error margins for the strain corrections and the modulus.

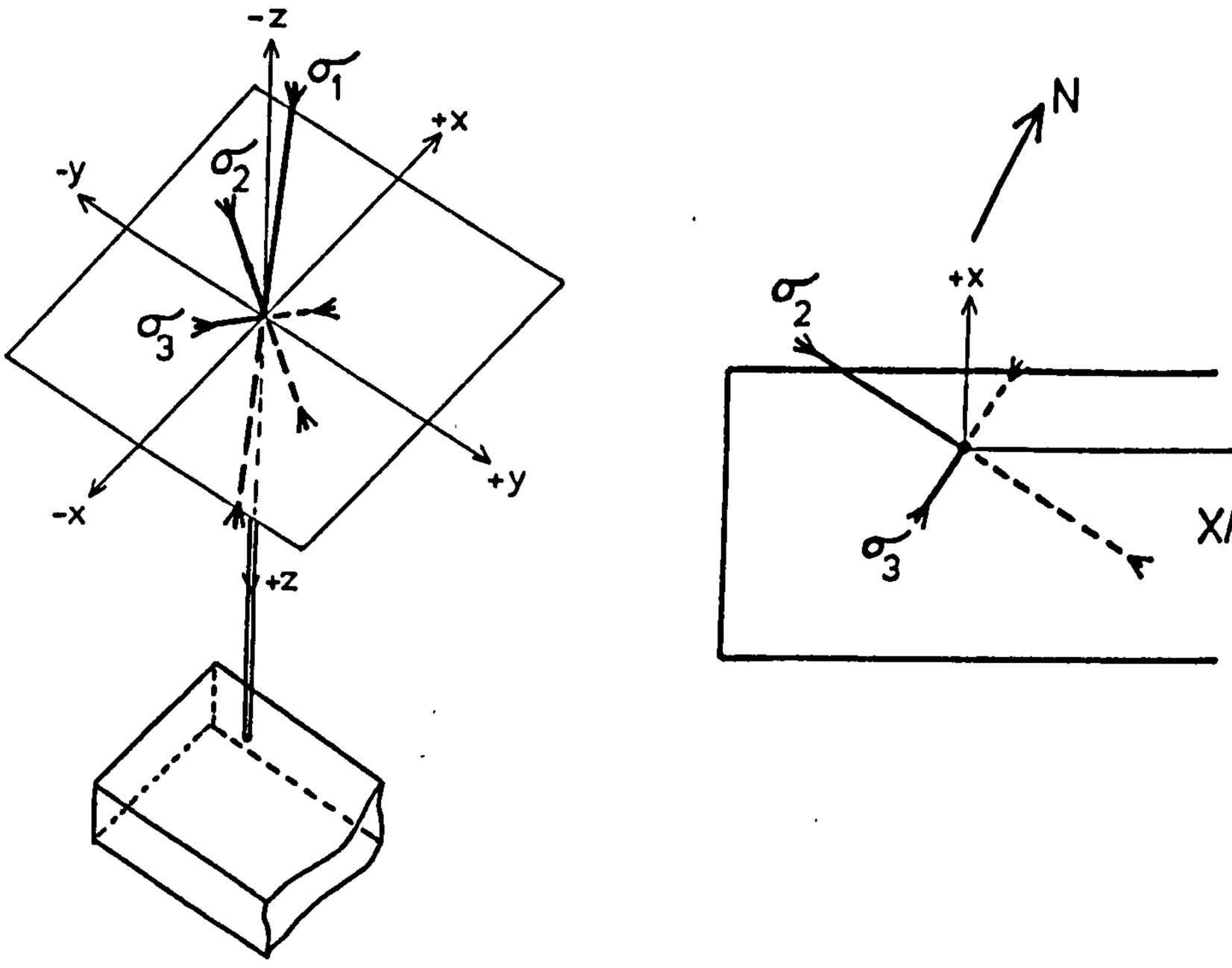

a/ Triaxial stress distribution b/ Minor principal stress plane

FIG. 7-12 CELL 3 STRESS ORIENTATIONS

7.4.4 Cell 4

This cell was installed with a friction contact but with more pressure applied to the cell to reduce the possibility of gauge slippage. Fig. 7-13 (a,b,c) shows the total strain-time curves for the complete operation which is described on (c). The cell was left in the hole over a weekend prior to overcoring. Fig. 7-13 (d,e,f) show the overcoring plots and once again there were problems with flush (air and diesel), drilling and gauge slippage. The drilling rate was very erratic and so the strain-distance plots are shown in Fig. 7-14 prior to any gauge slip correction.

Despite all the problems with this overcore, an intact core was obtained with the cell central in it. Every effort was made to interpret the results meaningfully since a realistic modulus would

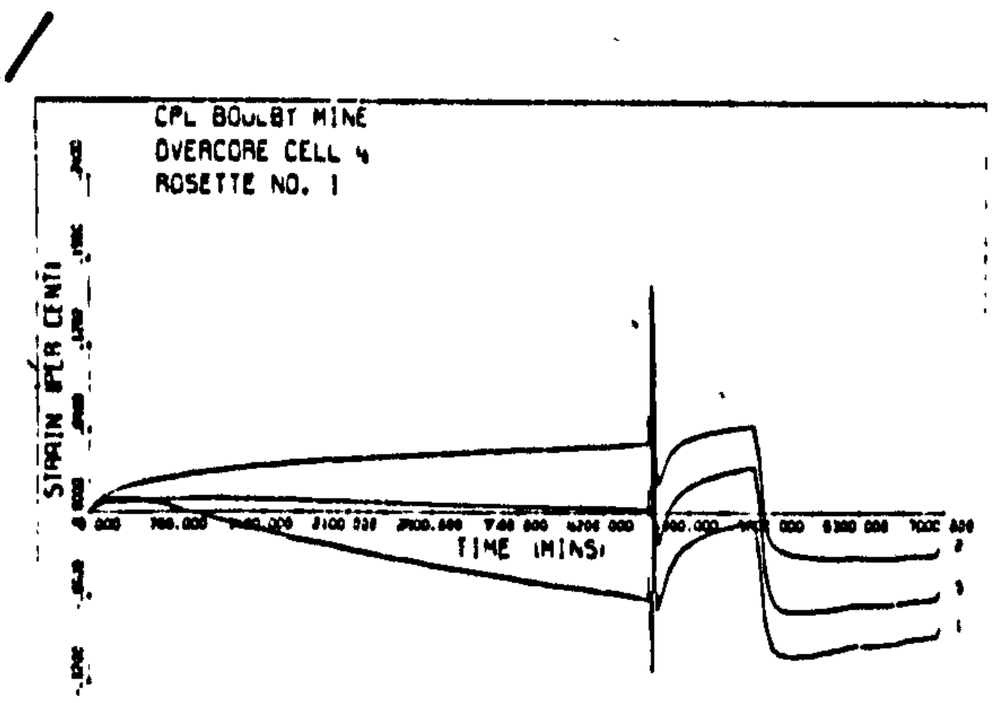

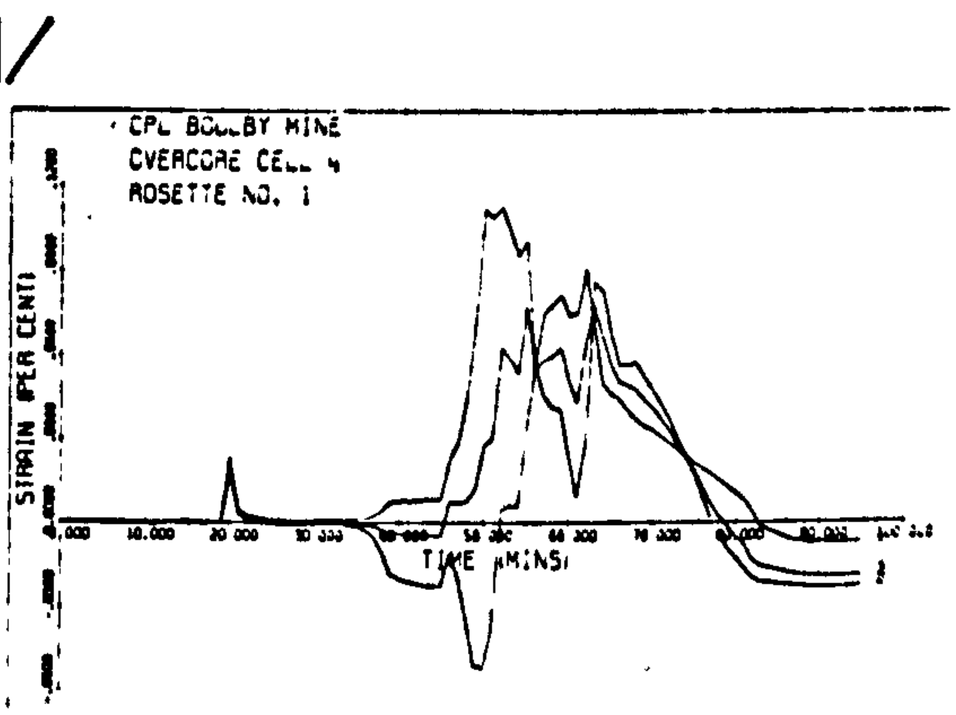

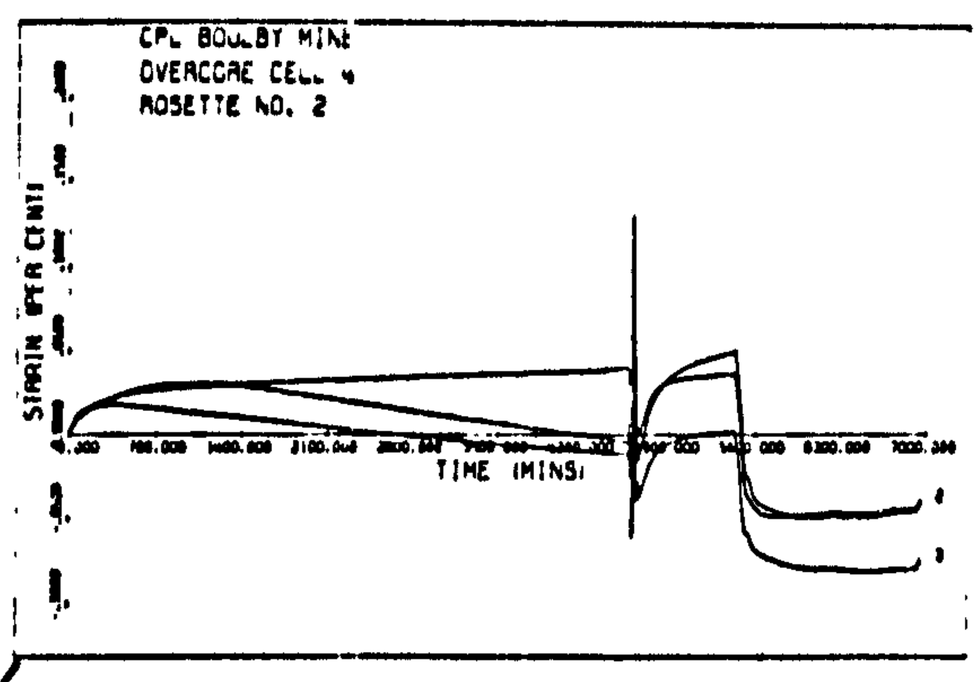

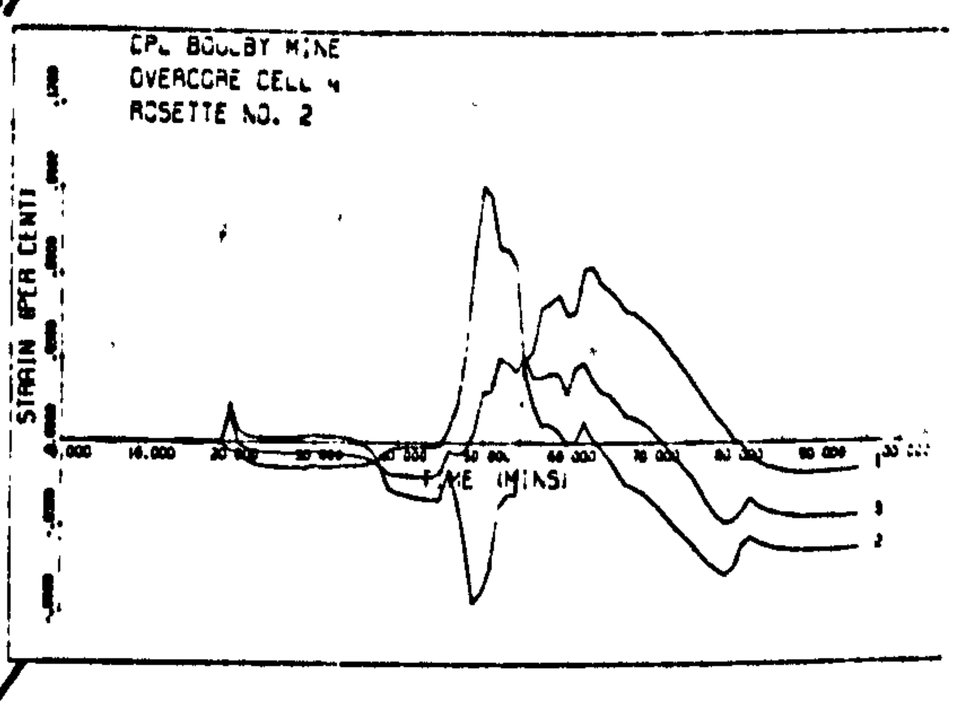

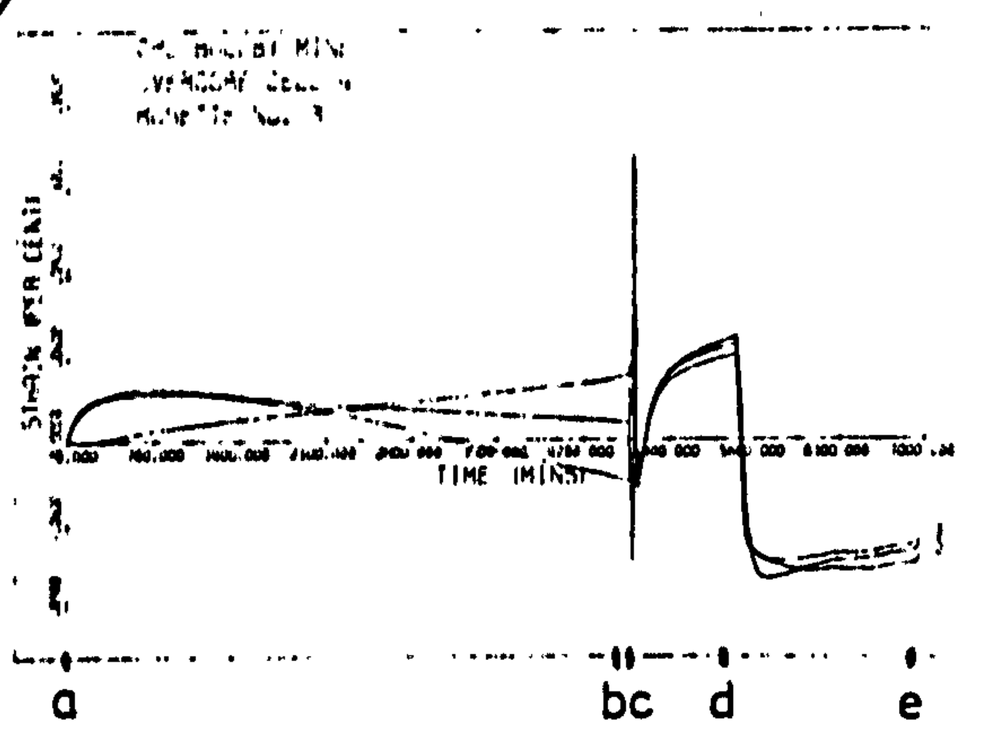

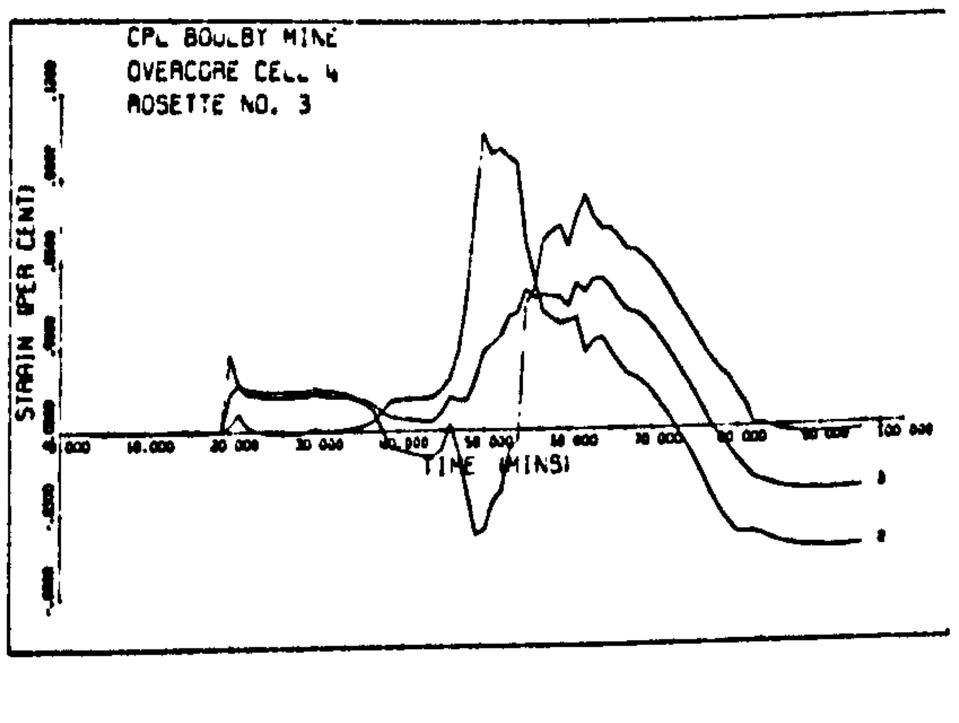

a bc d e

a = installation
b = start of overcoring operation
c = time-dependent relaxation
d = cooling of core when removed from borehole
e = core reheated slightly

FIG. 7-13 CELL 4 RESULTS

a/

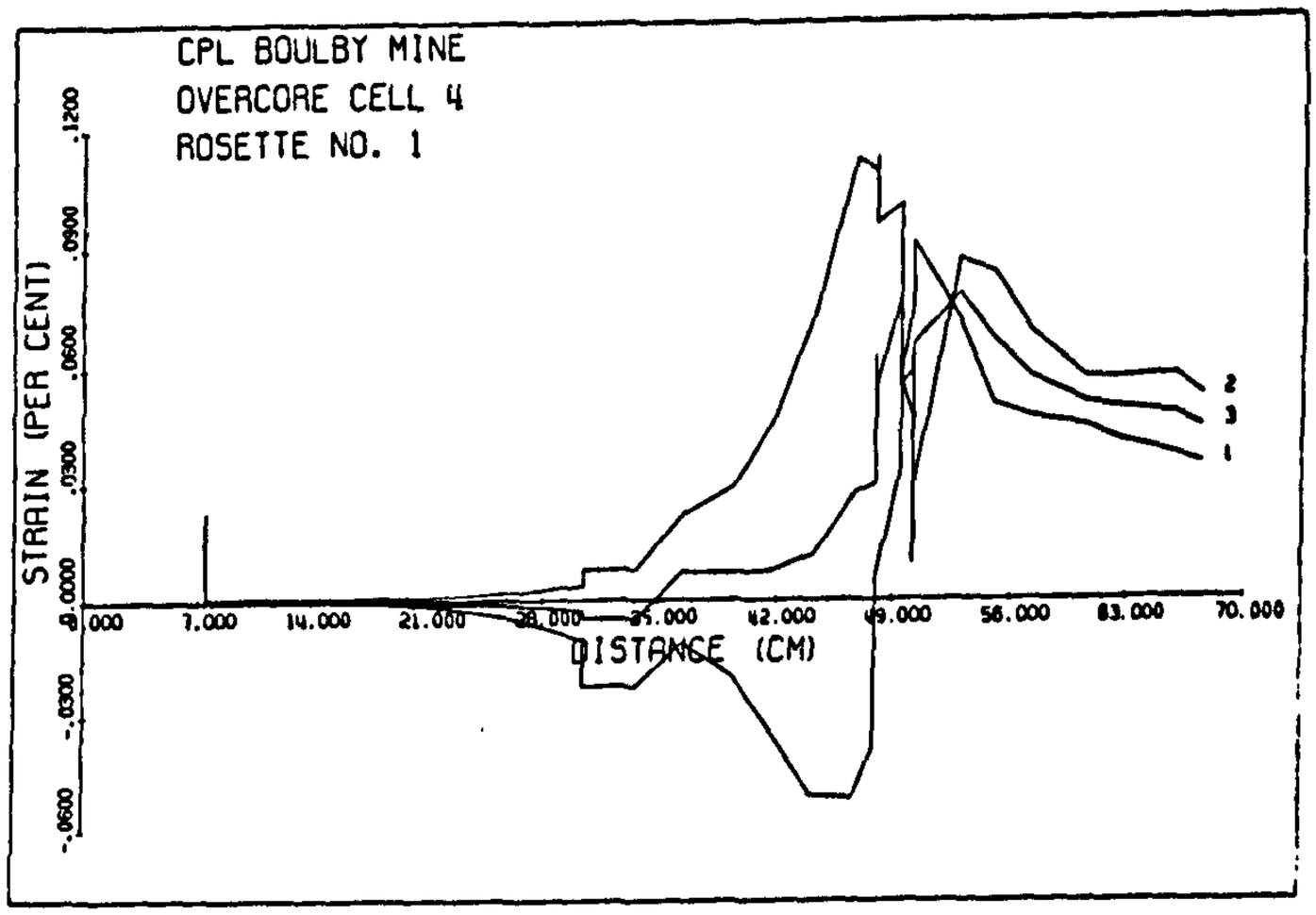

b/

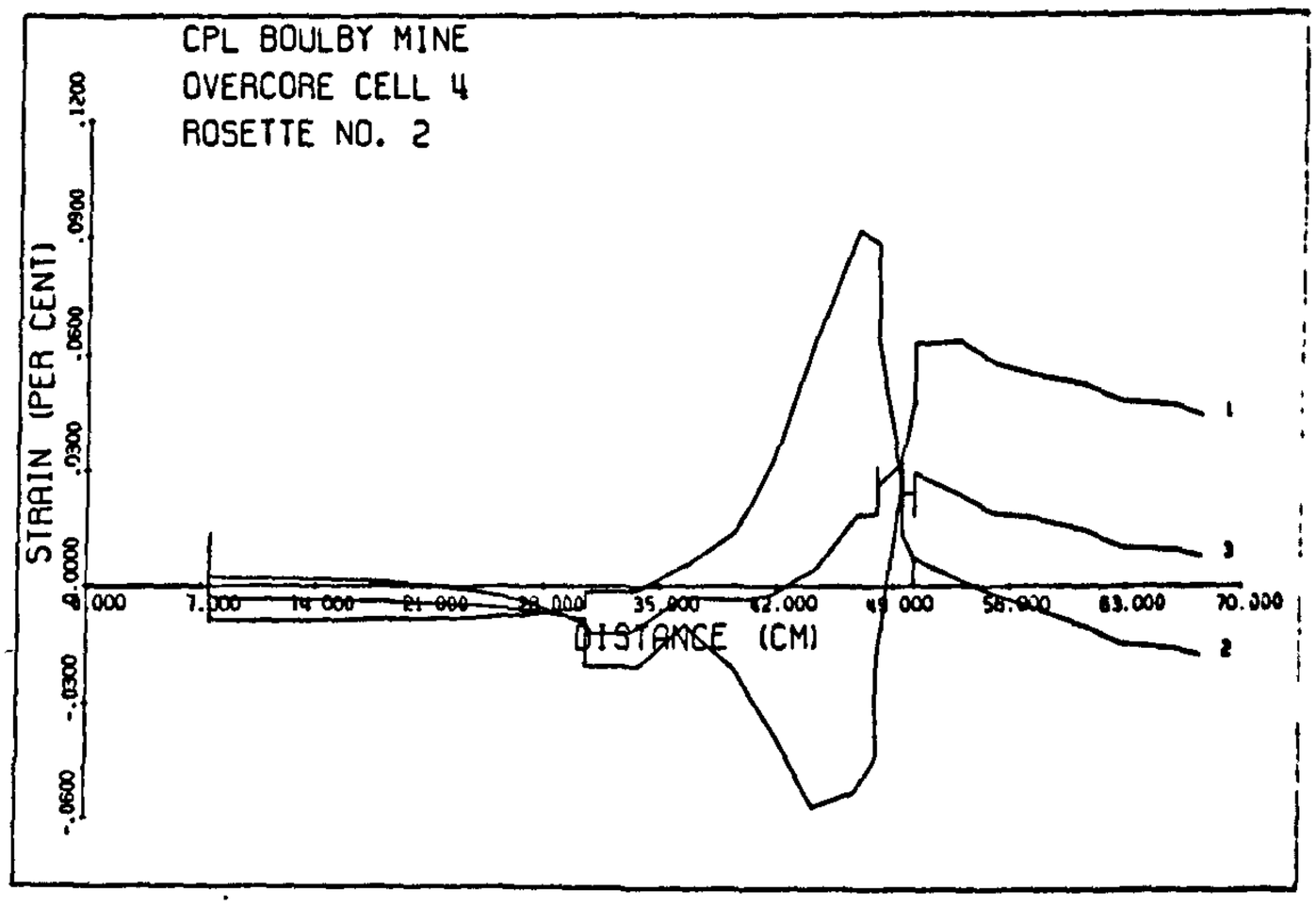

c/

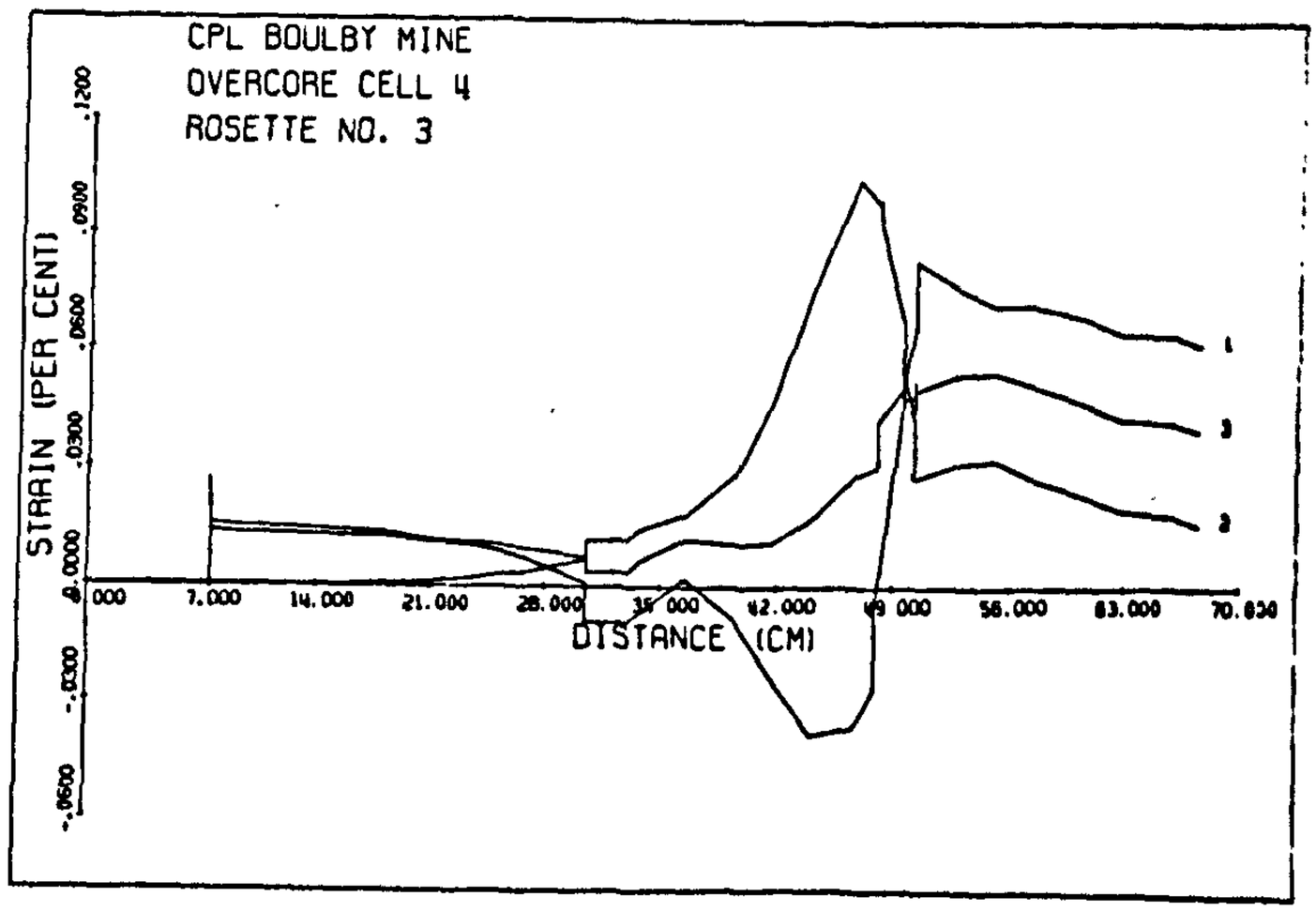

FIG. 7-14 CELL 4 STRAIN v. DISTANCE

be available from laboratory testing of the core.

Firstly, the time delay in initial gauge response is very apparent with this cell. This cannot be caused by heat effects since no resin was present. There is no reason why the hole should have been any dirtier than others and yet the delay is in excess of 10 hours for rosettes 2 and 3. This implies that the third factor suggested earlier is the most likely. The cell pressure is causing significant load to be applied to the rock surface causing tensile creep around the circumference until the loading can be counteracted by the compressive creep strains due to the rock. The fact that the cell was tightened more than previously would therefore account for the longer time delay.

The temperature effects are also very apparent both during the overcore due to flushing and afterwards when the core was cooled at 5500 minutes by lowering out of the borehole and then reheated slightly at 7000 minutes. Although no temperature readings were taken, it appears that this temperature effect is being magnified by poor temperature compensation within the cell.

The creep relaxation observed after overcoring is also significant. It is a maximum form 4650 minutes and continues for at least 15 hours. The initial maximum rate of relaxation strain monitored was approximately 5 microstrain/minute. This emphasises that in this type of material under these stresses the overcoring should be completed in as short a time as possible to avoid creep relaxation strains influencing the elastic recovery strains.

The actual slip corrections were carried out in a similar manner to cell 3 but with additional problems of penetration depth adjustments due to the drill seizing up short of the previous position. In the light of the creep relaxation strains it was also assumed that the axial elastic recovery should be complete at the time that the drill passes over the rosette location. Fig. 7-15 shows the corrections as carried out on No. 1 rosette.

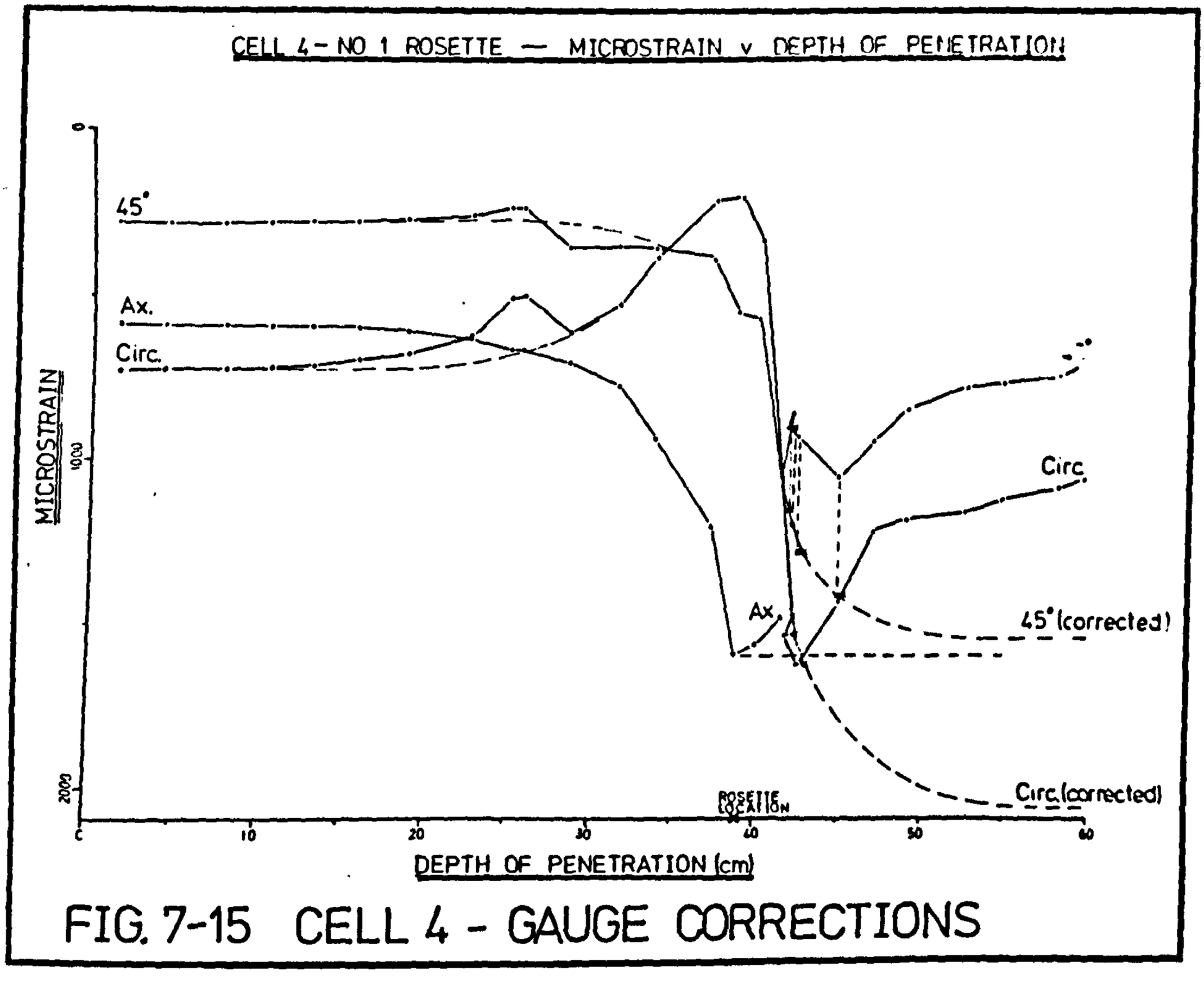

FIG. 7-15 CELL 4 - GAUGE CORRECTIONS

A further correction was made following inspection of the core recovered. It was found that there were very large halite and sylvinite crystals present together with large pockets of shale. The three

rosettes were consequently located on completely different materials. It was assumed that the major principal stress would be vertical and so the three axial gauges should indicate equal elastic recoveries. Therefore a 'modulus correction' was made to each rosette based on the deviation of the axial gauge from the mean axial recovery. The strain changes and final values for elastic recovery are summarised in Table 7-6. A margin of ±10% for the strain corrections should be applied to these values.

Table 7-6 Cell 4 Overcoring - Elastic Strain Recovery

	Rosette No. 1			Rosette No. 2			Rosette No. 3		
	Circ.	Ax.	45°	Circ.	Ax.	45°	Circ.	Ax.	45°
Raw recoveries prior to slip Correction	905	1118	775	628	915	291	843	1060	544
Corrected values for slip	1345	1118	1264	933	915	475	1253	1060	887
Modulus Correction Factor		0.922			1.127			0.973	
Final Corrected Values	1240	1031	1165	1051	1031	535	1219	1031	863

The overcored annulus was prepared in the laboratory and testing was carried out in the 25 tonne testing machine. The specimen was monitored with dial gauges and the stress was cycled between 0 and -10 MN/m^2 a total of six times. The unloading modulus from the final three cycles was used since it was the closest simulation of a triaxial elastic relaxation. The results of this laboratory test are shown in Fig. 7-16. The range of moduli obtained was between

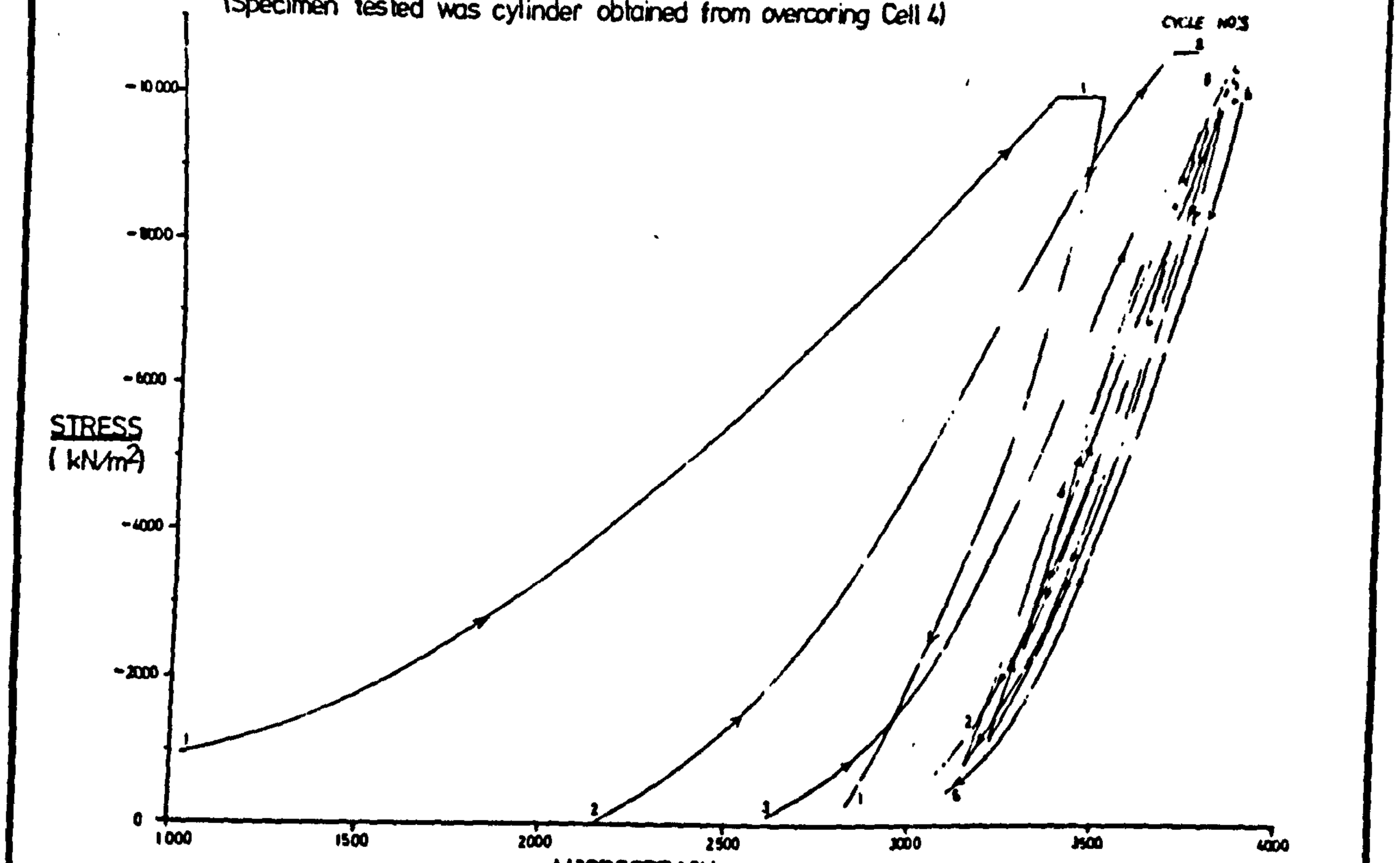

FIG. 7-16 CELL 4 - LABORATORY MODULUS TESTING

18.86 GN/m^2 and 22.00 GN/m^2 so a mean value of 20.43 GN/m^2 ±8% was used for the stress analysis. A value of 0.28 for Poisson's Ratio was obtained from previous laboratory testing.

Table 7-7 lists the resultant principal stresses and directions. To relate these stresses to the cross-cut the No. 1 rosette had a bearing of S21°E (it faced the southern wall of the cross-cut). Fig. 7-17 (a,b) are sketches of the triaxial stress distribution and the minor principal stress plane relative to the cross-cut.

Table 7-7 Cell 4 Principal Stresses and Directions

	Principal Stress (MN/m^2)	Azimuth (^{o})	Dip (^{o})
σ_1	-28.399	351	8
σ_2	-15.332	100	66
σ_3	-13.724	258	22

The stresses listed in Table 7-7 are mean values within a range of ±18% based on error margins for the strain corrections and the modulus.

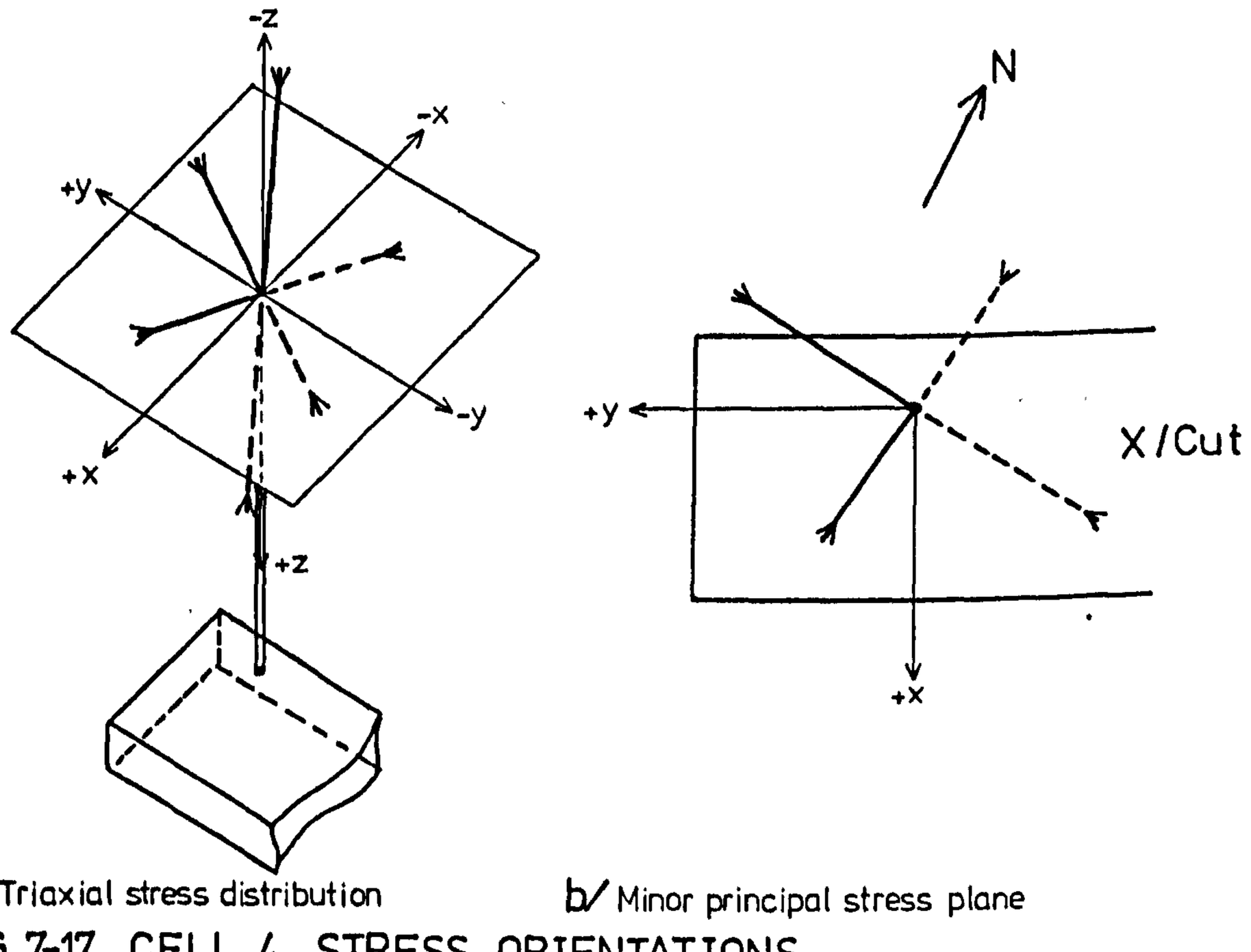

a/ Triaxial stress distribution b/ Minor principal stress plane

FIG. 7-17 CELL 4 STRESS ORIENTATIONS

7.4.5 Cell 5

This cell was installed in the marl strata but since it proved impossible to obtain a core, or maintain a hole in good

condition in the marl the cell was not overcored. It was left in the hole to monitor creep closure and this is being analysed as part of a separate project in connection with rheological properties of Carnallite marl.

7.5 Comparison of Results and Summary of Conclusions

Fig. 7-18 shows the condition of the cores which were obtained from cells 1, 3 and 4. From the three sets of stress measurements obtained, there appears to be quite good correlation in magnitude for the major principal stress. Within the accuracy of each set of results the values overlap. The mean value for the major principal stress is -30.1 MN/m^2.

The minor principal stresses improve with greater depth of borehole and are predominantly horizontal. There is very good correlation between the directions for all three cells, basically North-South and East-West (σ_3 and σ_2 respectively). From the magnitude of the minor stresses, those obtained by cell 4 seem to be most realistic in terms of virgin stress and within the accuracy of the solution the two minor stresses are equal with a mean value of -14.5 MN/m^2 for cell 4. This represents a ratio of 0.51 between horizontal and vertical principal stresses. On the basis of this ratio and the major principal stress obtained above, the mean value for the horizontal principal stresses is -15.4 MN/m^2.

These conclusions may be summarised as follows.

4

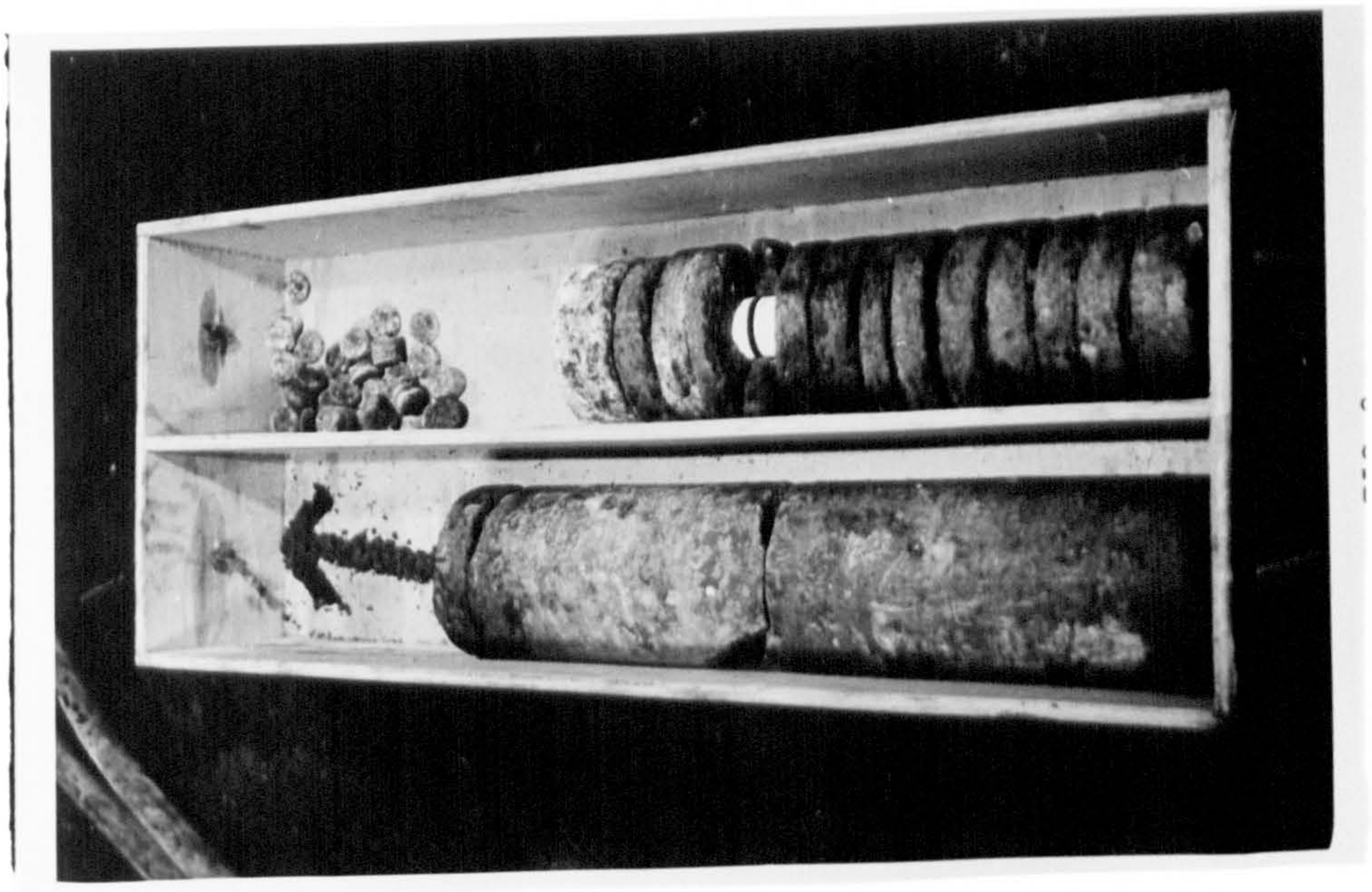

3

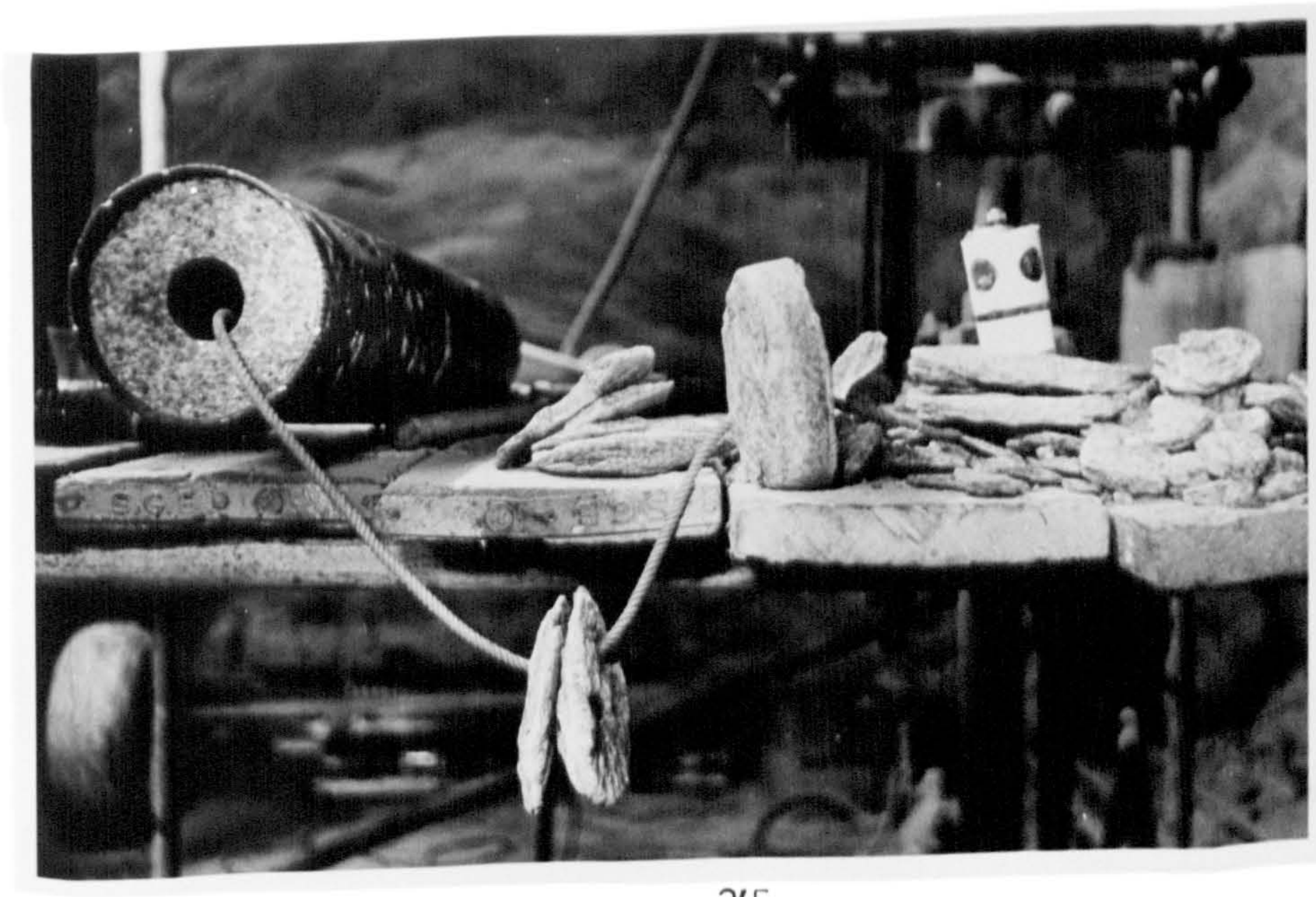

1

FIG. 7-18

In the vicinity of the potash seam the virgin stress distribution is:

i) orientated vertically and horizontally,

ii) the stress distribution within the horizontal plane is uniform in all directions,

iii) the major vertical principal stress is within the range -30.1 MN/m^2 ±18%,

iv) the ratio of horizontal to vertical stresses is 0.51 giving a horizontal stress field of-15.4 MN/m^2 ±18%.

The explanation for the low ratio of horizontal to vertical stress probably lies in the extremely irregular geology around the potash seam. The seam varies in thickness considerably and is very distorted along its upper boundary. This could easily prevent any time-dependent stress redistribution causing a higher ratio of horizontal to vertical stress.

These results are extremely dependent on the rock properties, since the Talbott cell is only measuring strain. For this reason the values are not definitive since the moduli used do not exactly represent the triaxial relaxation situation which takes place.

Other problems which arose during this overcoring operation which should be further investigated are:

i) the problem of rosette-rock contact, either friction or bonded,

ii) the problem of pressure exerted by the cell on the rock,

iii) quantifying this pressure and incorporating it in the stress analysis,

iv) the need for better temperature compensation within the cell,

v) the need for extremely good surface preparation within the borehole,

vi) drilling and associated problems in evaporite rock types under high stresses.

CHAPTER 8

ANALYSIS OF IN-SITU INSTRUMENTATION RESULTS

8. ANALYSIS OF IN-SITU INSTRUMENTATION RESULTS

Tha basic parameters of mine design have already been outlined and defined from a theoretical and laboratory point of view. However, the most important source of information must be the mine itself. In Chapter 7 the determination of the triaxial virgin stress field underground was discussed. This chapter deals with an cverall appraisal of the results from at least six hundred different extensometer and convergence anchors installed throughout the mine workings. These have provided essential information on roof, floor and wall components of roadway closures, together with deformation and strain distributions within varying roof materials and pillar geometries. Although confined to one chapter, the installation, monitoring and interpretation of results from these instrumentation sites has been the major concern throughout the course of the investigation. Obviously, it is not possible to present detailed analyses of every individual site and problems of local instability, however the important conclusions are discussed in the light of the overall stability of mining layouts.

The final section of this chapter concerns the analysis of the first complete set of surface subsidence data which was carried out on levelling results supplied by the mine Survey Department.

8.1 Instrumentation

Due to the large quantity of instrumentation installed underground, it has been essential to use simple and relatively cheap equipment rather than fewer, more sophisticated instruments. This

principle of numerous simple measurements over a large area has been ratified by the wide variability of conditions encountered in the mine.

All extensometer measurements have been made using a Newcastle Mark II 'Clip-on' extensometer which has a 150mm travel. This can be seen in Fig. 8-1 where it is being used to take initial readings for a roof borehole at Site 1P1. The photo also shows the drilling head of the Secoma roof bolter adjacent to the face. This drill has been used for all extensometer boreholes.

Monel wire has been used for all but the initial extensometer sites where stainless steel was found to become very brittle and corrode rapidly in the harsh environment. The monel has proved satisfactory but must be handled carefully as it is soft and liable to kink easily. The anchors used are normal expansion shell 'Rawlplugs' with hollow bolts through the centre to enable wires from deeper anchors to pass through. Two spring steel clips were fitted to later anchors to provide a grip on the side of the borehole for easier expansion of the anchors. This is done by coupled 2m lengths of insertion rods with the wires passed through the centre. Colour-coded brass nipples are used on the outer ends of the wires for attaching to the extensometer which provides a standard 111N tension. The stainless steel mouth of hole reference stations have machined ends to enable them to be used also for convergence stations. Initial boreholes were installed with a maximum of three anchors plus mouth station but later holes were installed with up to four anchors to depths of 27m into pillars. By positioning two parallel boreholes adjacent to each other it was

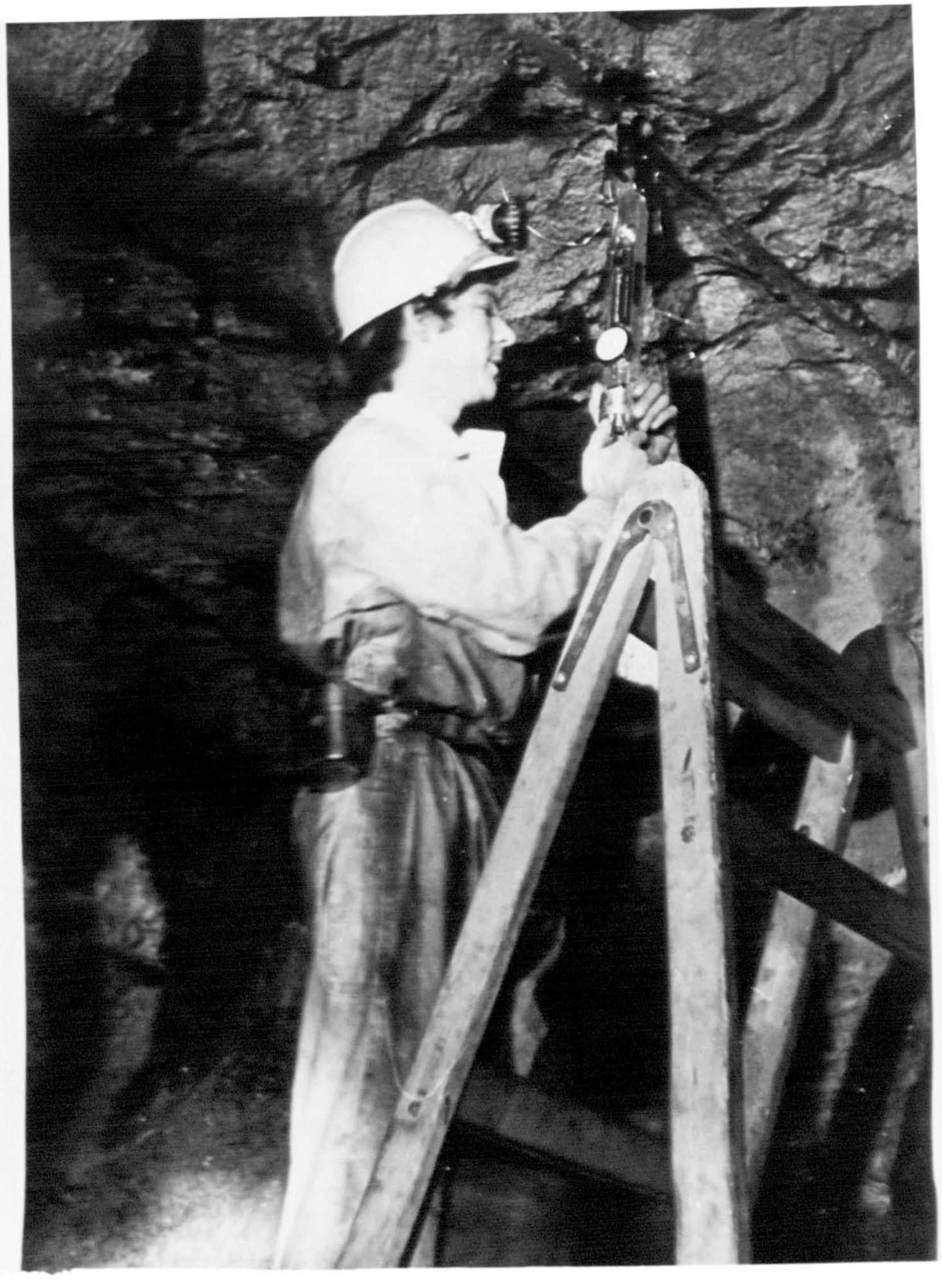

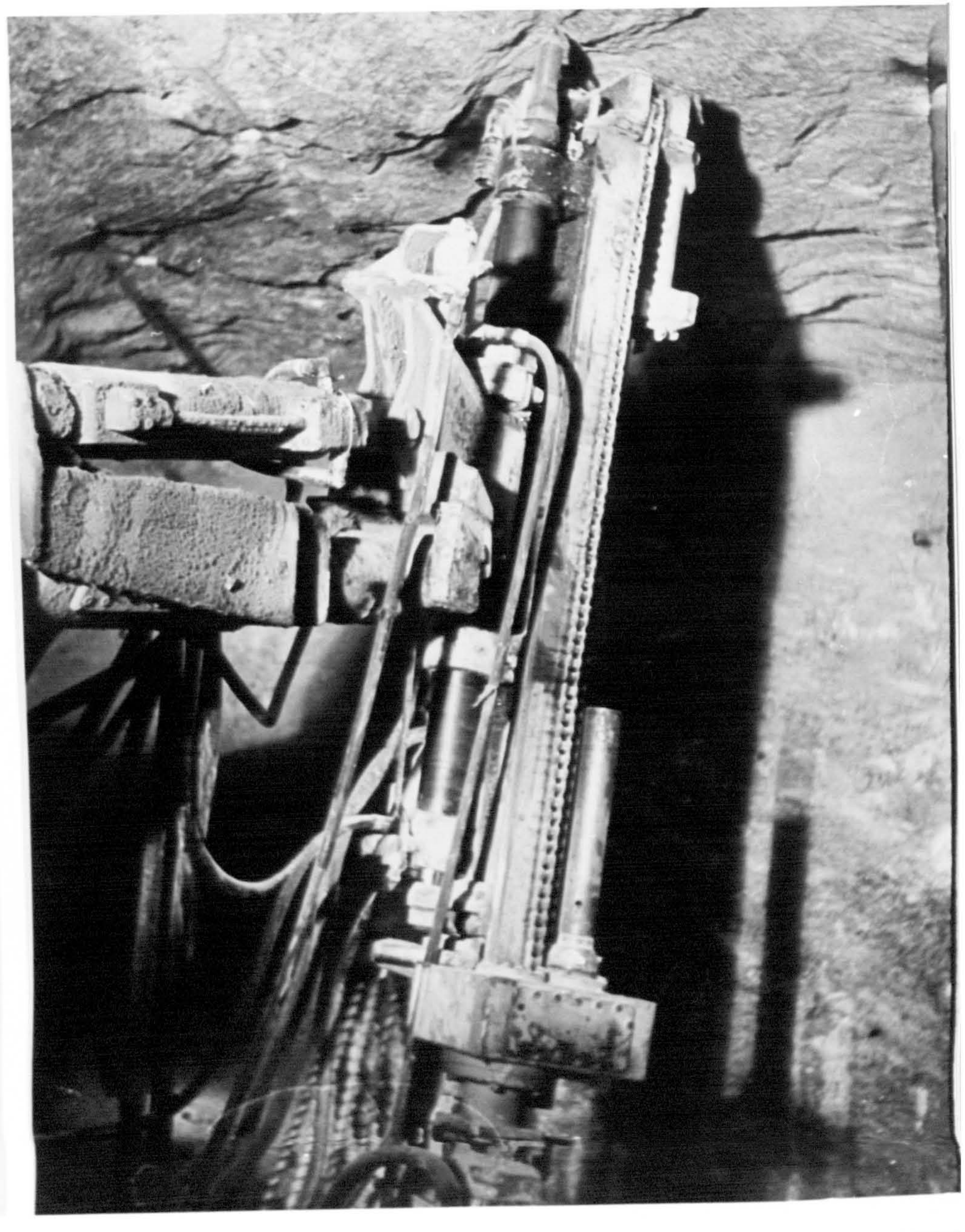

FIG. 8-1

therefore pcssible to measure from up to eight points within a pillar.

Initial convergence monitoring was carried out using stainless steel tapes and a Mark I Newcastle extensometer. However, due to the large amount of movement experienced, it was found to be much quicker and sufficiently accurate to use a conventional steel measuring tape. The convergence stations required were therefore simple bolts with expansion shell anchors and reference points on the bolt heads. These were set into 0.5m holes drilled in the roof, walls and floor. Roof sag and floor heave were monitored by levelling techniques using a pin at mid-height in a nearby pillar as the most stable bench mark available.

All the instrumentation sites in the shaft pillar plus the No.1 panel sites up to and including 1P4 were installed and initially monitored by Newcastle University. A rock mechanics section was then established at the mine to carry on this wcrk in conjunction with the University.

The location of all the instrumentation sites and their reference numbers is marked on the mine plan in Fig. 1-5. The results from Site 1P3, a roof bolting experiment, were reported by Wiggett (9) and are not included here. All other results have been analysed and are presented in graphical form as deformation-time curves in Appendix B. Each plot is marked with the relevant site number and is either an extensometer result, for which borehole numbers are given, or a convergence (i.e. total closure), roof sag or floor heave result. Table B1 in Appendix B lists the site and borehole numbers plus anchor depths for all the extensometer boreholes. They are indicated as being either roof, floor or wall boreholes. All roadways are approximately

6m wide and between 3.0m and 3.4m high unless described otherwise.

8.2 Shaft Pillar Results

Fig. 8-2 shows a plan of the sixteen sites installed in the shaft pillar area. Detailed site layouts and geological sections for these sites are included in Appendix B with the results.

The first of these sites were planned to investigate roadway geometry effects but initial results indicated the significant effect of geological variation on roadway stability. The remainder of the sites were installed in an attempt to correlate roadway stability with geological conditions.

Numerous problems were encountered during the shaft pillar program. These included the loss of valuable deformation data during the first few days after excavation. At a number of sites it was not possible to install the equipment immediately and in some sites it was three months before sites could be instrumented due to ventilation problems. (For correct interpretation, the time scale for all results starts at the date of excavation.) In other cases the stations were installed and then access was prevented by steel straps, conveyor belts etc. and so very few results were obtained.

Detailed discussion of the shaft pillar results is not included here but some general conclusions from the results may be drawn.

At Site N.U.02 the stability of the right-angled intersection has been established over an 800 day period although a fire in the area at 600 days damaged the extensometer wires and further results

FIG. 8-2 SHAFT PILLAR DEVELOPMENT
(Showing location of Rock Mechanics Sites)

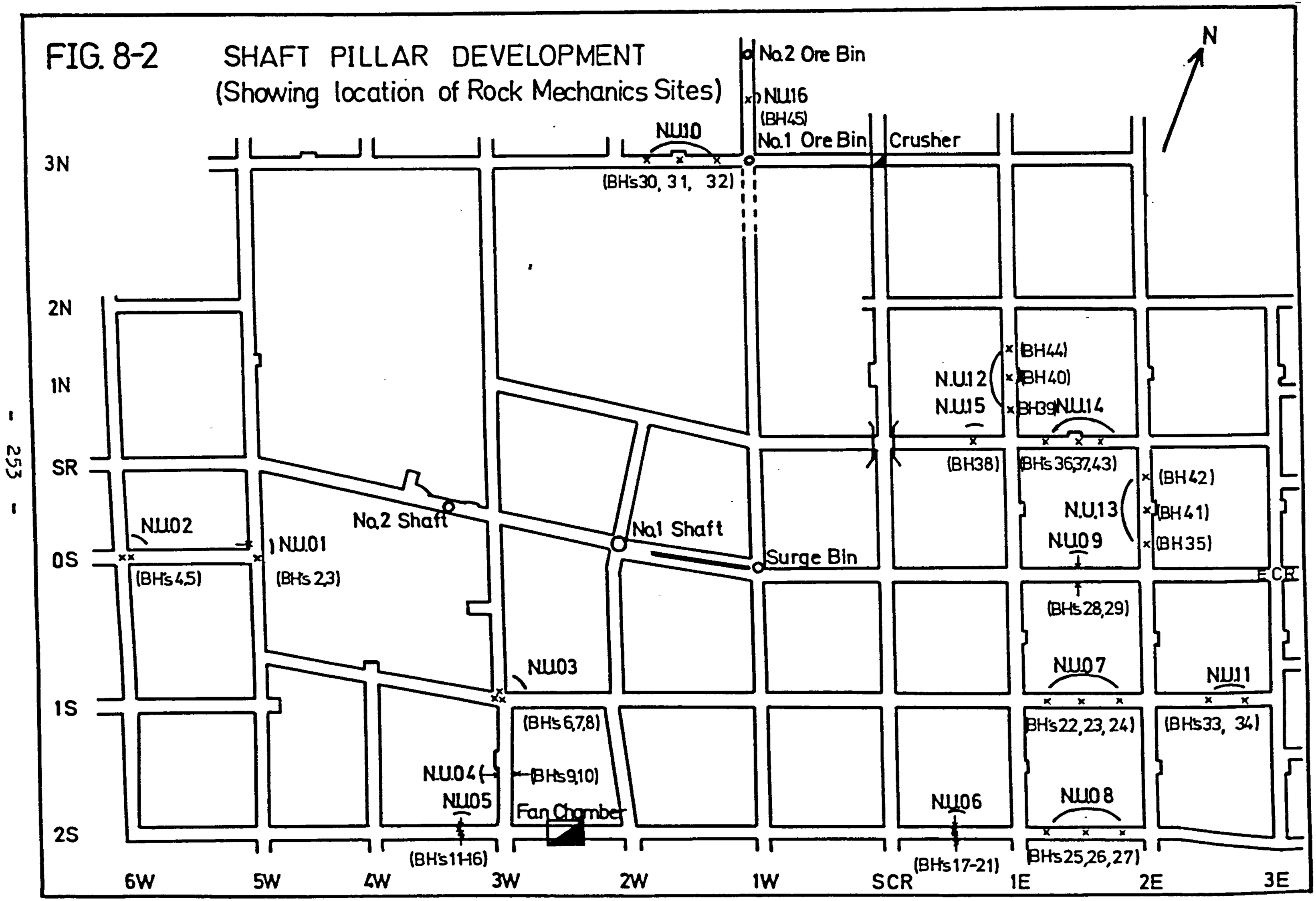

were inconsistent. Fig. 8-3 shows the distribution of strain along the length of borehole 4 in the roof of the junction centre at various time periods. This indicates a high level of strain at about 1.5m into the roof. This was also apparent for the borehole 5 results and in each case it corresponds to the geological interface between the halite parting and the potash. This suggests that bed separation is taking place at this level but the strain in the potash below is greatly reduced. As a result, the immediate roof material at the junction is in a stress relieved zone, similar to that described for the 1P1 results later. This accounts for the very low closure rates for this site (0.13mm/day by 800 days and still decreasing) and suggests that a roof beam of 1.5m of competent primary potash is sufficient for stability at this type of junction.

The results from Site N.U.01, a T junction, did not indicate any stress relieved roof strata even though the potash thickness was 2.4m in the roof. The maximum bay strain (average strain between anchors) occurred in the first bay, i.e. the immediate roof. Although no closure readings were taken, the roof did appear to have long term stability due to the thick potash roof beam. Therefore this suggests that T junctions do not provide any stress relief to the junction roof (and floor) strata, due to the presence of a solid pillar on one side, and so closure rates would be expected to be greater than for right-angled intersections. A thickness of 2.4m of primary potash in the roof does provide a competent roof structure for junction stability.

Sit N.U.05 was located in an experimental 8m wide road.

FIG.8-3 CPL BOULBY MINE

SITE NU02 OS/6W BH4

ROOF HOLE 2.89M DEEP

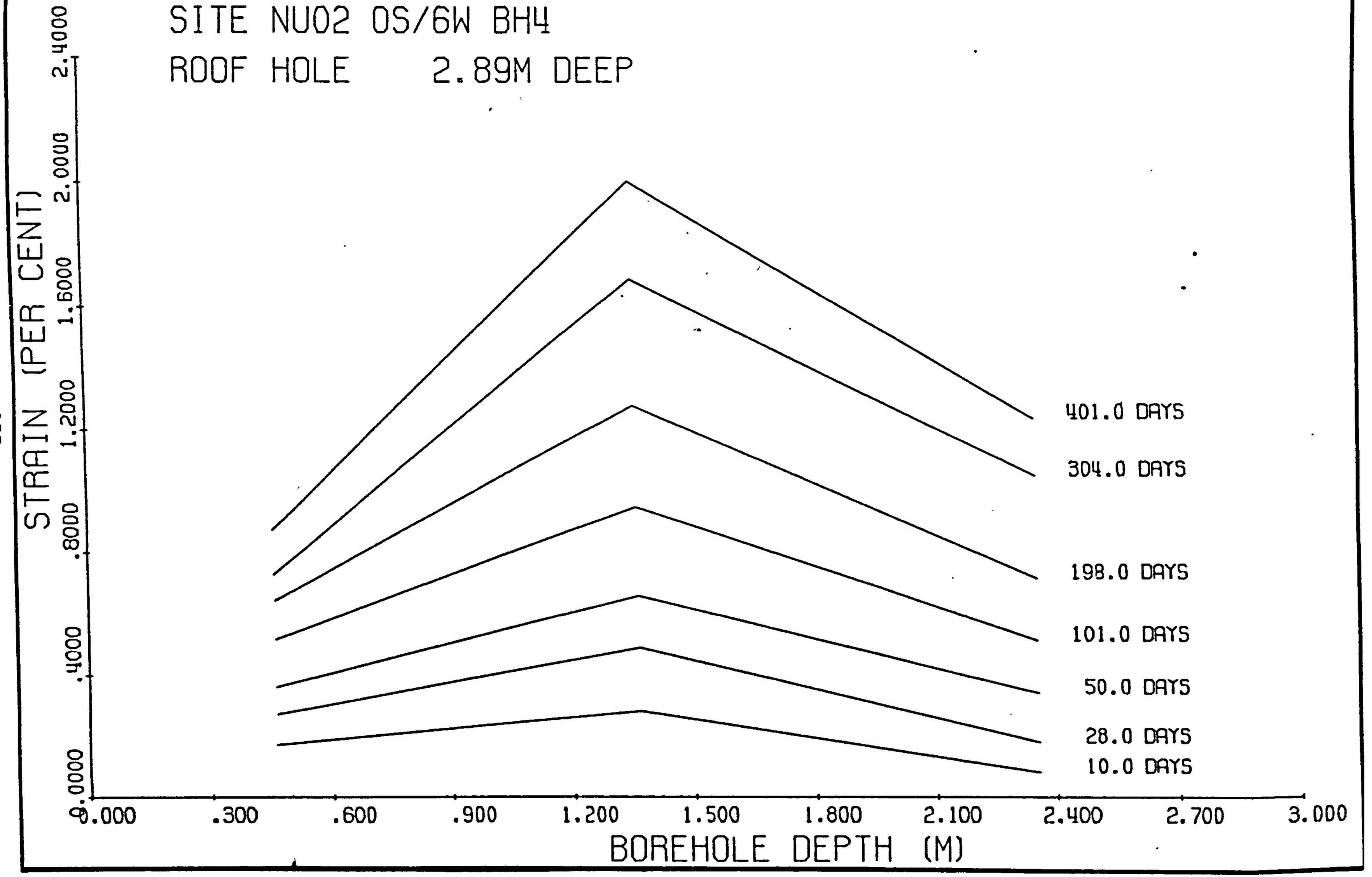

However, it was the first area where a shale raft existed in the roof strata. As a results, the roadway collapsed completely within a year. The instability leading to collapse developed in the shale raft as can be seen from the results of boreholes 14 and 15 in Appendix B. The rate of strain increase in the deepest bay of each of these boreholes began increasing from 280 days until collapse at about 370 days. The one conclusion which can be drawn from these results is that 8m wide roads with shale present within 3.5m of the roof will not ramain stable for any length of time.

Site N.U.06 was instrumented in conjunction with rock bolting experiments conducted by Dunham (12). Results of levelling at this and previous sites showed that with a halite floor and potash roof at least 2m thick, the floor closure contributed approximately 33% of the total roof-floor closure. On this basis, the absolute displacements of the extensometer anchors in the roof were calculated at 50 days and these are listed in Table 8-1.

Table 8-1 Site. N.U.06 - 50 day Anchor Displacements

Reference Point	Absolute Displacement (mm)		
	Borehole 17	Borehole 18	Borehole 19
Mouth Station (i.e. roof sag)	53	53	53
Anchor 1	31	44	38
Anchor 2	17	28	17
Anchor 3	13	13	11

These results are shown, with an exaggerated displacement scale, in Fig. 8-4.

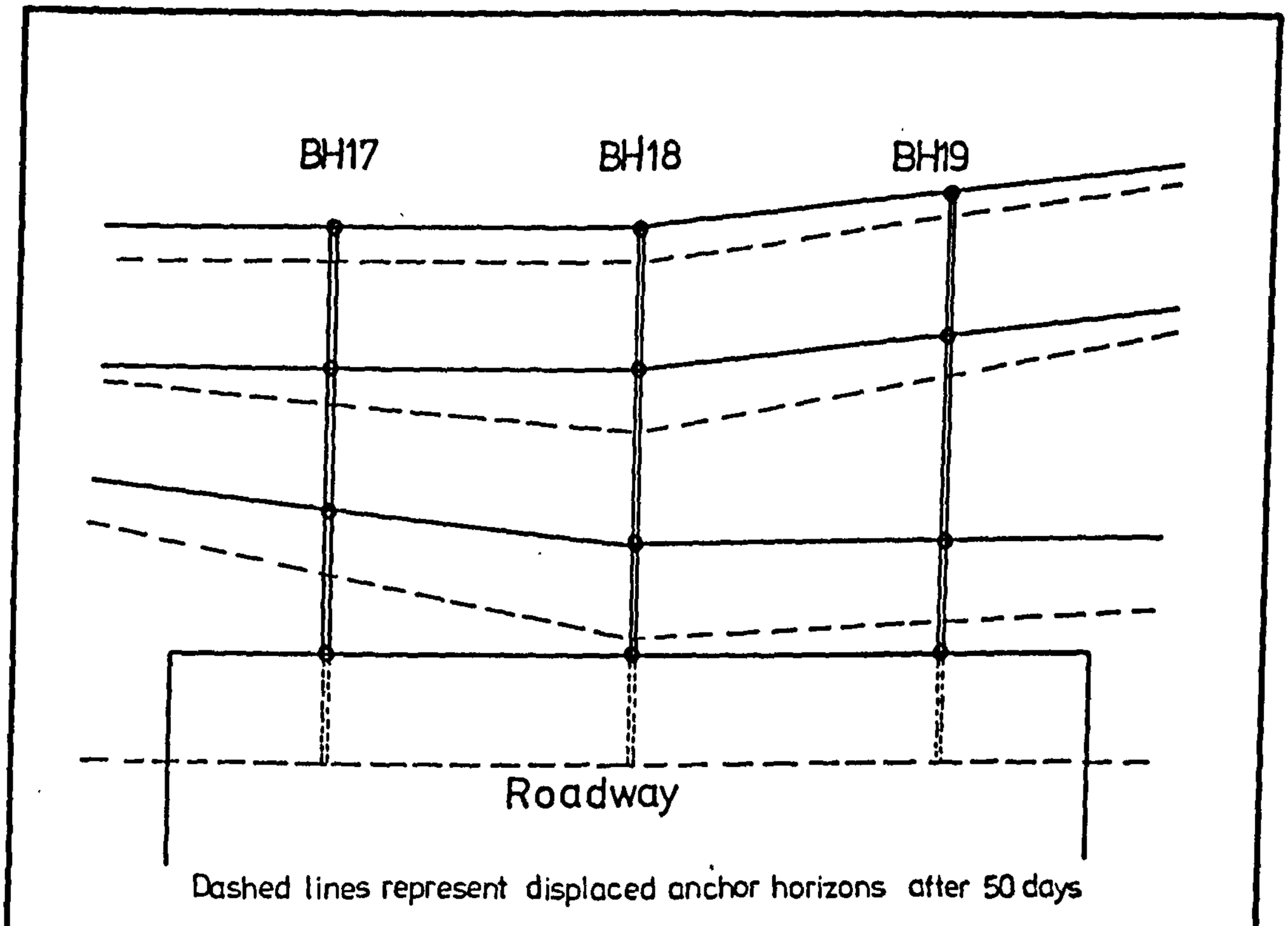

FIG. 8-4 SITE NU06 ROOF DISPLACEMENT

The results indicate two main points. Firstly, there is a uniform subsidence of at least 24% of the roof sag occurring beyond the 6m anchor horizon in the Carnallite Marl. Secondly, there is evidence of a tensile strain, arched zone of material above the roadway. This can be seen by the greater displacement of equivalent intermediate anchors in the centre borehole. The equal displacement of the deepest anchors suggests that the top of the arch is between 4m and 6m. This is similar to the lateral compressive peak stress anticipated at 6m above the cross-cut at the overcoring site, described in Chapter 7.

This site was supported using 1.5m long, full column, resin anchored bolts on a 1m staggered spacing. Previous support had been provided by mechanical bolts with steel straps between them.

The problems of roof bolting in highly stressed evaporites exhibiting time-dependent deformation are numerous. Lateral stresses acting on the immediate roof beam cause frequent shear failures over the sides of the roof strata. This can be seen in Fig. 8-5 where the time-dependent deformation has unloaded the steel straps which were originally installed flat across the roof. Also shown in Fig. 8-5 is the shear failure of potash around the end plate of a resin anchored roof bolt due to flow of the potash around the area supported by the plate.

The main conclusions reached by Wiggett (9) were that in this material, due to this type of behaviour, the influence of a bolt is virtually negligible within a radius of 0.5m along the full length of the bolt. Bolts considerably longer than 1.5m would be necessary to have any significant effect on confining a competent roof beam. Fig. 8-6 bears this out by showing two views of a shale-potash 1.5m thick roof beam failed along the length of the roadway as a solid mass parted from the above strata at a plane of weakness. Fig. 8-7 shows a junction shale roof failure in the start of No. 1 panel together with the consequences of attempting rigid steel support in this type of material.

Obviously, any roof support method is not going to prevent roof closure but should be designed to control the closure by providing confinement to a suitably thick roof beam. Such a system

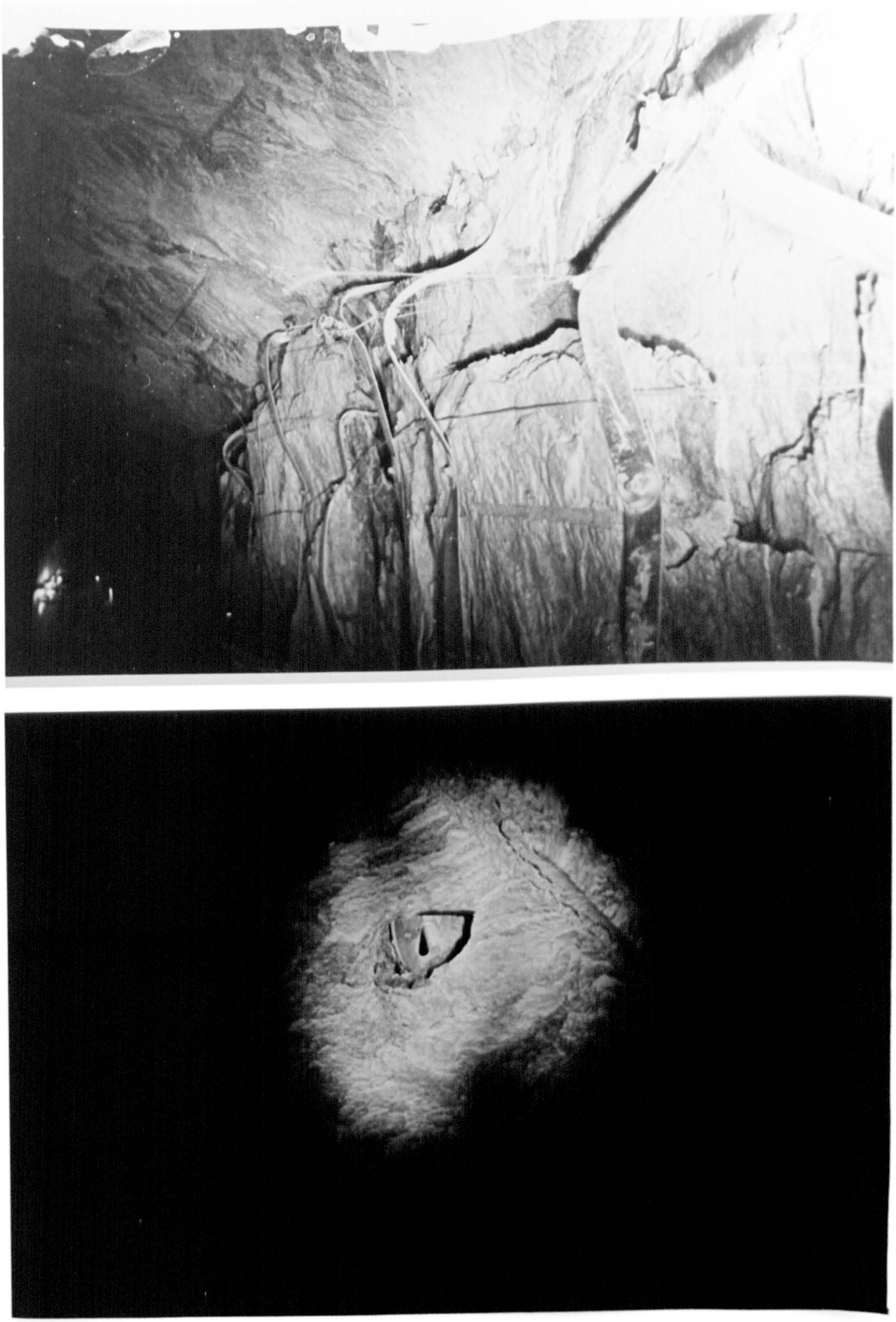

FIG. 8-5

FIG. 8-6

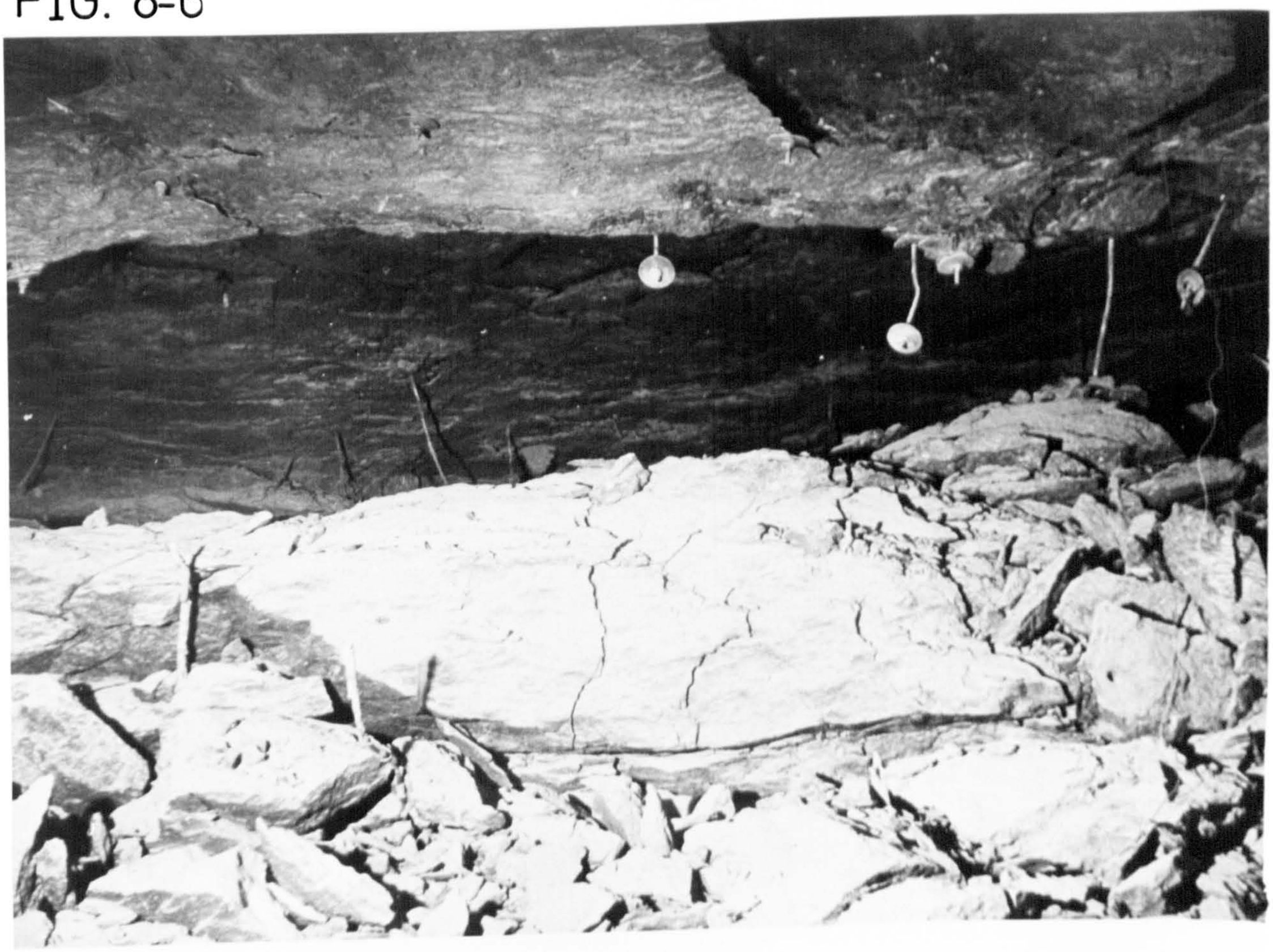

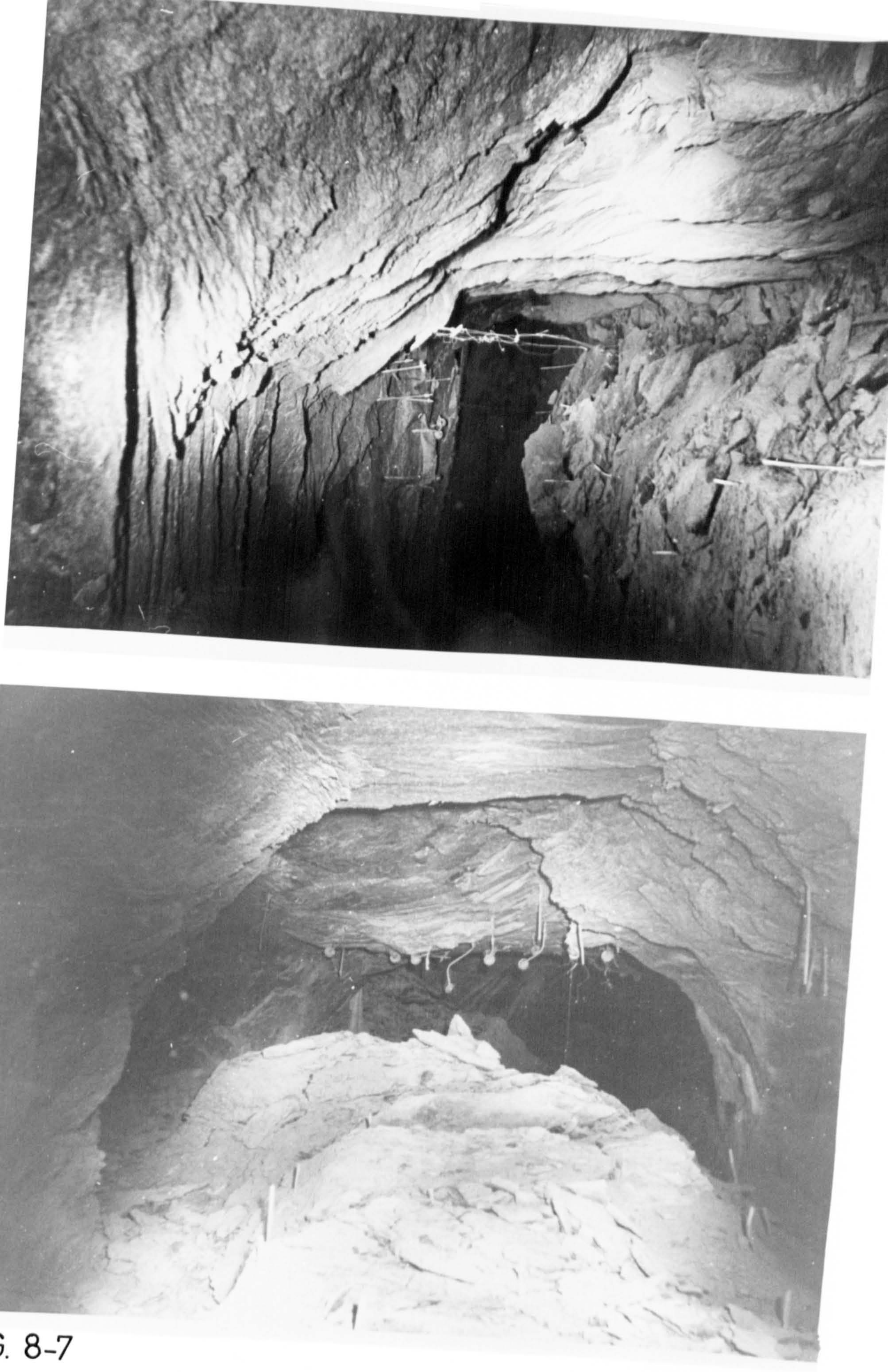

FIG. 8-7

would permit controlled yield rather than attempting rigid support. The N.U.06 results show that, in the centre of the roadway, bolts would have to be extremely long to even attempt to control roof yield by being anchored in compressively confined material. As Wiggett (9) recommends from the Site 1P3 results, side bolts should be angled over the solid pillar sides to achieve a confined anchorage and bolt lengths should be of the order of 2.5m.

The remaining sites in the shaft pillar were all normal roadways instrumented in connection with geology with the exception of N.U.09, a lateral pillar site. In each case the extensometer boreholes in the roof were difficult to instrument due to hole closure by shear planes or marl inflow. The roof to floor convergence rates provide the easiest way of comparing the various sites. Sites N.U.10 and N.U.16 both consisted of 5m wide roads with a salt roof while N.U.15 was 6m wide with a salt roof. All other sites were in potash with a mixture of potash, halite and shale in the roof.

In every case where roads have maintained overall stability, apart from minor slabbing, there has been at least 2m to 3m of competent material in the roof below the weak shales and marl. In some cases the competent roof beam has been made up of halite, potash and halite parting, or else the latter two. Where these strata are uniform and do not include shale weaknesses, they have formed a relatively stable composite beam, provided the lowest roof material is at least 1.5m thick, since the interfaces either side of the potash appear to be very weak.

None of the roadways between junctions have shown the stress

relieved roof layer that N.U.02 displayed. Even N.U.06 which was basically a stable roadway, had a very high strain profile in the immediate roof as shown in Fig. 8-8, in contrast to Fig. 8-3. This level of strain caused eventual slabbing of the surface layer of potash at borehole 19 although the overall roadway stability was maintained.

Fig. 8-9 shows the relationship between total closure rate and time for a representative sample of 6m wide potash roads in the shaft pillar. (The closure for salt roads, junctions etc. are compared later, with other results.) Apart from the N.U.08 curve (beneath borehole 26), most of the sites were still relatively stable up to 200 days. However, by 400 days, all but N.U.06 and N.U.04 were either collapsed, had been re-ripped due to bad conditions, or were rapidly becoming unstable.

In terms of both extensometer results and closure results, in every case where roadways have remained stable, the deformation and strain-time curves have shown a decreasing rate, even up to 800 days for the early sites. This cannot be directly related to a primary creep condition since it is associated with a changing loading condition in both roof and wall strata - greater stability with load relaxation around the excavation. However, it does appear that for any roadway where the extensometer or closure curves enter a steady state, constant rate of deformation against time, instability and eventual failure will result.

At a number of shaft pillar sites, wall extensometer boreholes were installed into adjacent 60m square pillars. The results from these have been analysed in terms of lateral strain rates against borehole

FIG.8-8 CPL BOULBY MINE

SITE NU06 2S BH19

ROOF HOLE 6.50M DEEP

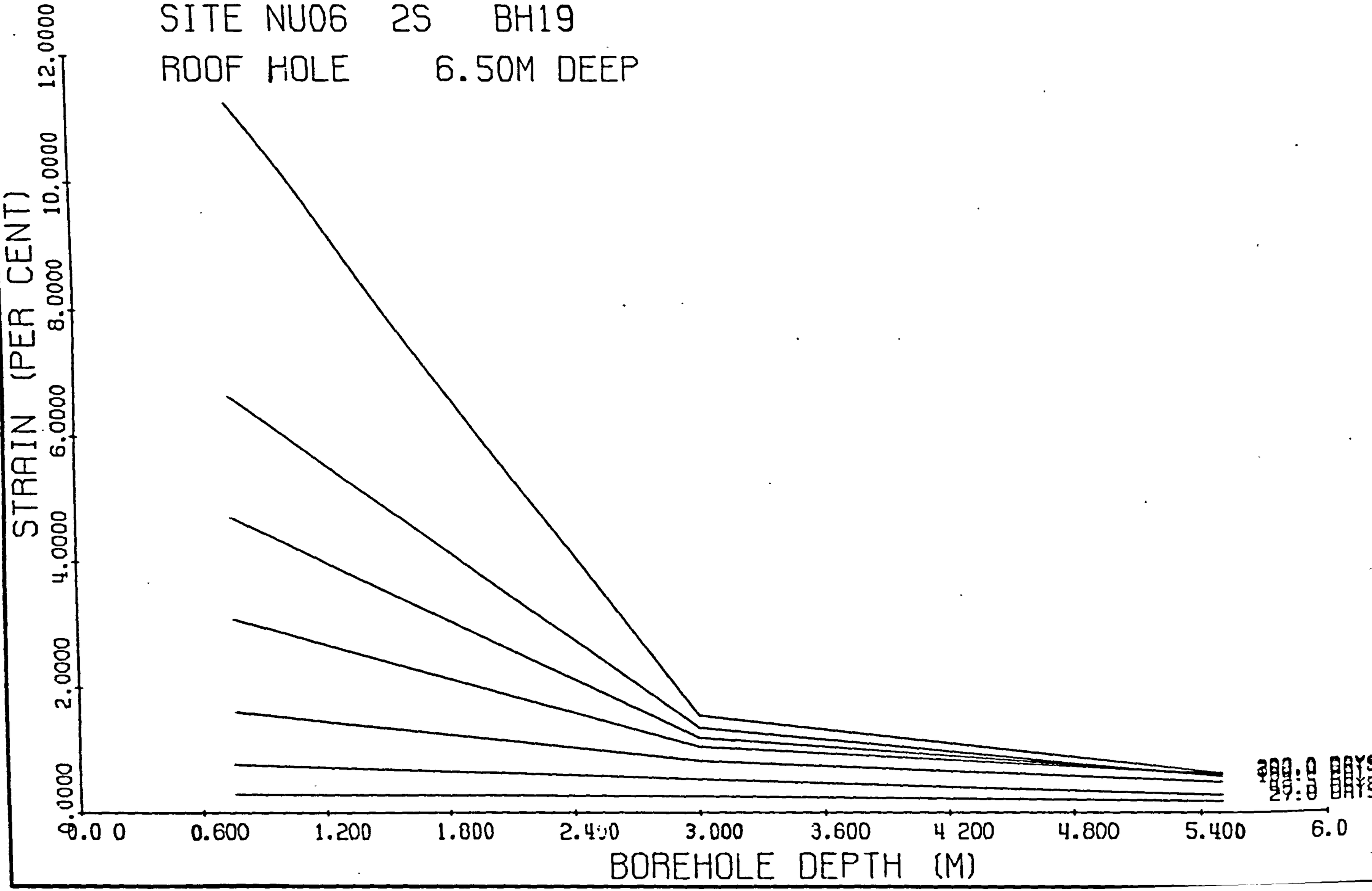

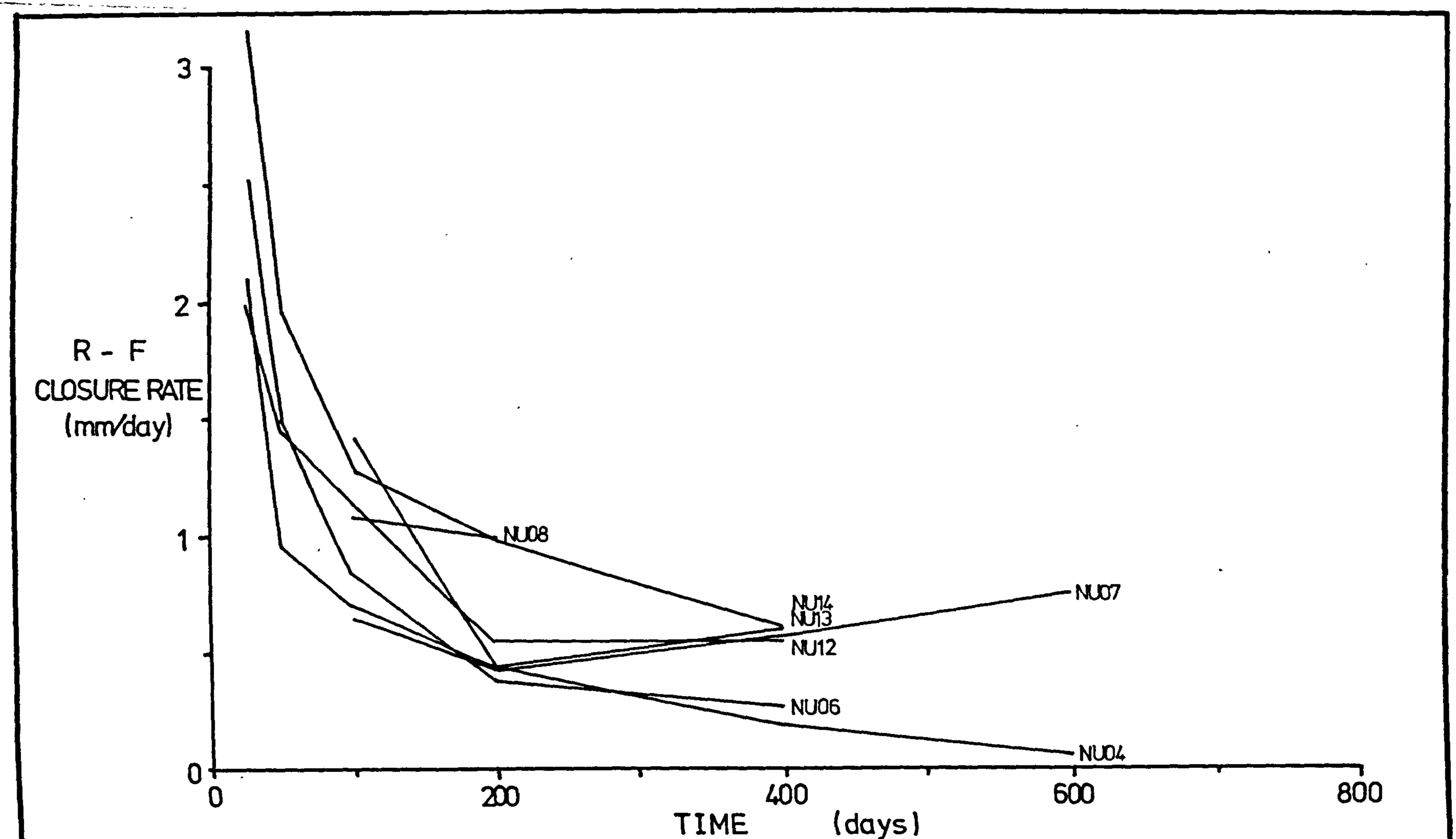

FIG. 8-9 SHAFT PILLAR POTASH ROAD CLOSURE RATES

depth, since this provides the best representation of the stress distribution on the pillar.

Fig. 8-10 shows the lateral strain rates after 50 days for each of the 60m pillar extensometers. All these curves are of the same magnitude and similar shape and indicate that the zone of high strain rate (and hence strain) is limited to the outer 5m to 10m of the pillar. This would suggest that the central core of confined material is approximately 45m wide. Fig. 8-11 shows the strain rates at various time periods between 50 days and 600 days for borehole 28 which, from Fig. 8-10, is a fairly typical case for 60m pillars. This indicates the stability of the outer 6m of the pillar with a decreasing rate indicating a relaxation zone developing at the pillar edge. However, the 200 day and 600 day curves show an increasing rate at depth, and at the pillar edge, respectively. This must be associated with some change in loading or a major fracture development.

In order to estimate the average strain which has taken place throughout the 60m pillar, the relationship between the natural logarithm of the smoothed strain rate, $\dot{\varepsilon}_s$, and time has been plotted for the 0 - 3 bay of borehole 28. This represents the average strain rate over the outer 6m of the 60m pillar. This is shown in Fig. 8-12 with two major regions of the curve. Up to 200 days there appears to be a very definite linear relationship between $ln\,\dot{\varepsilon}_s$ and time. Beyond 200 days another linear section has developed but there appears to have been a major reloading of the pillar and possible subsequent load variations. This major rate increase is apparent from the results of both boreholes 28 and 29 at this site. These boreholes are in opposite pillars which confirms that this phenomenon is not just a

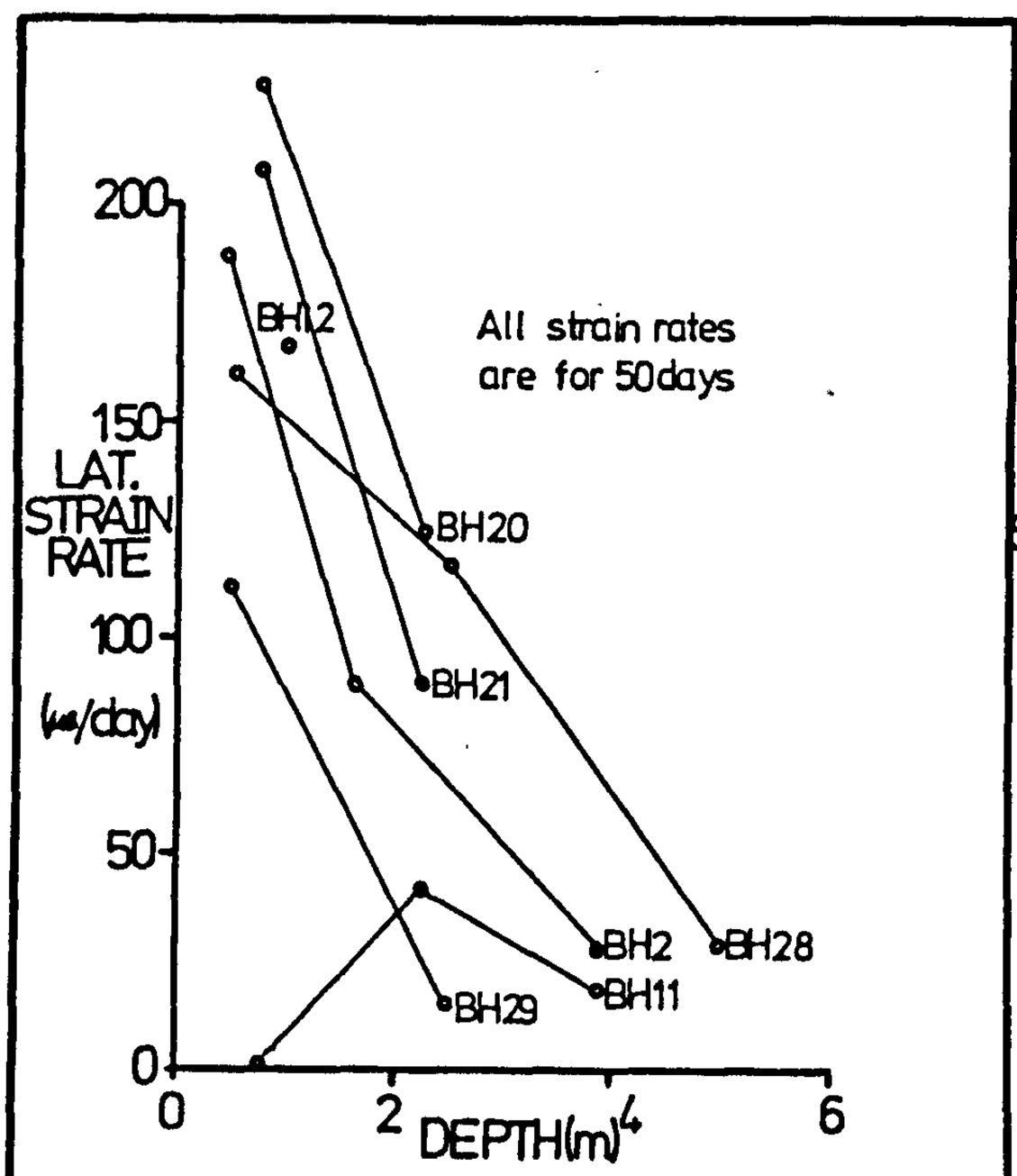

FIG. 8-10 60m PILLAR STRAIN RATES v. DEPTH

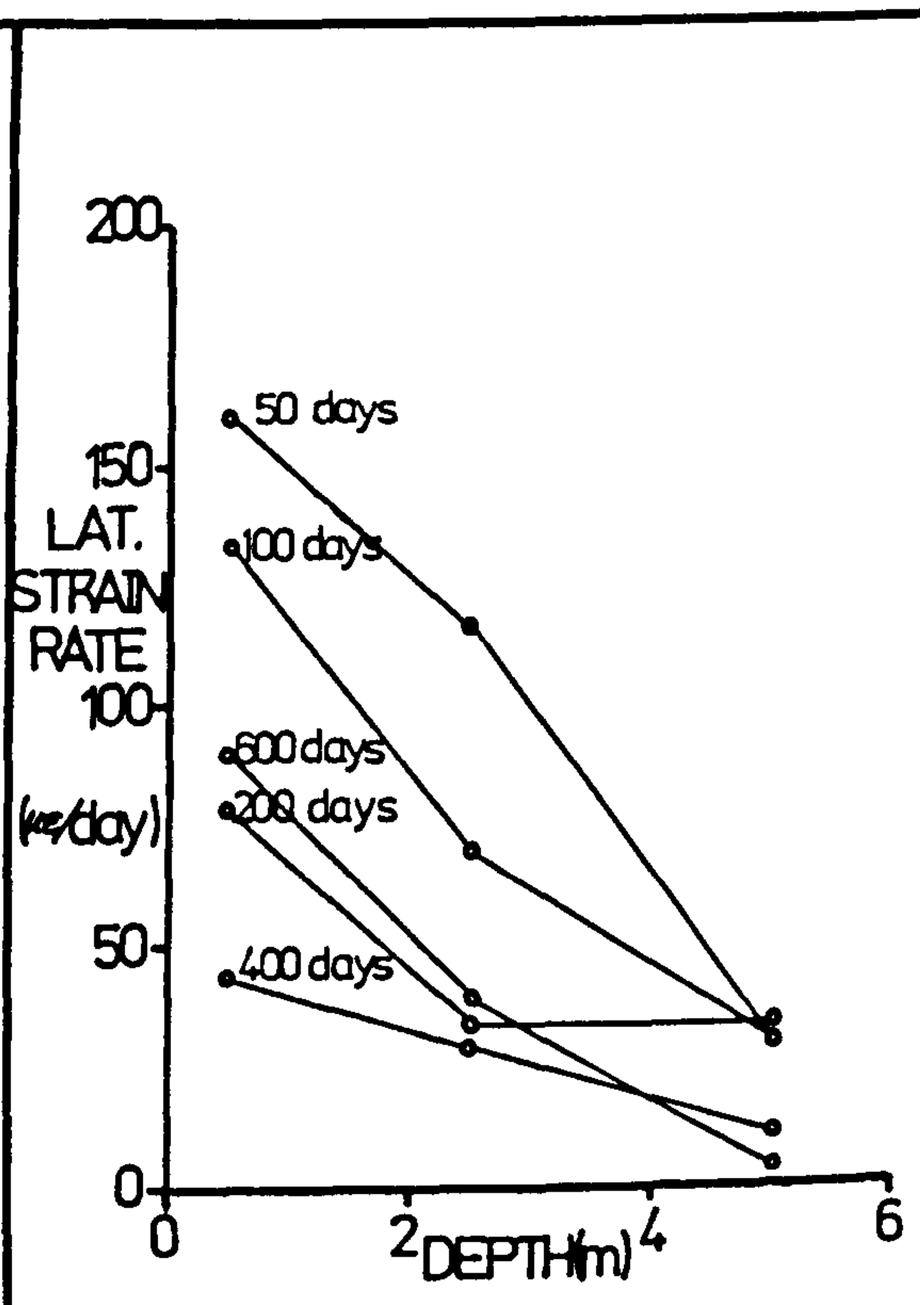

FIG. 8-11 BH28 STRAIN RATE v. DEPTH

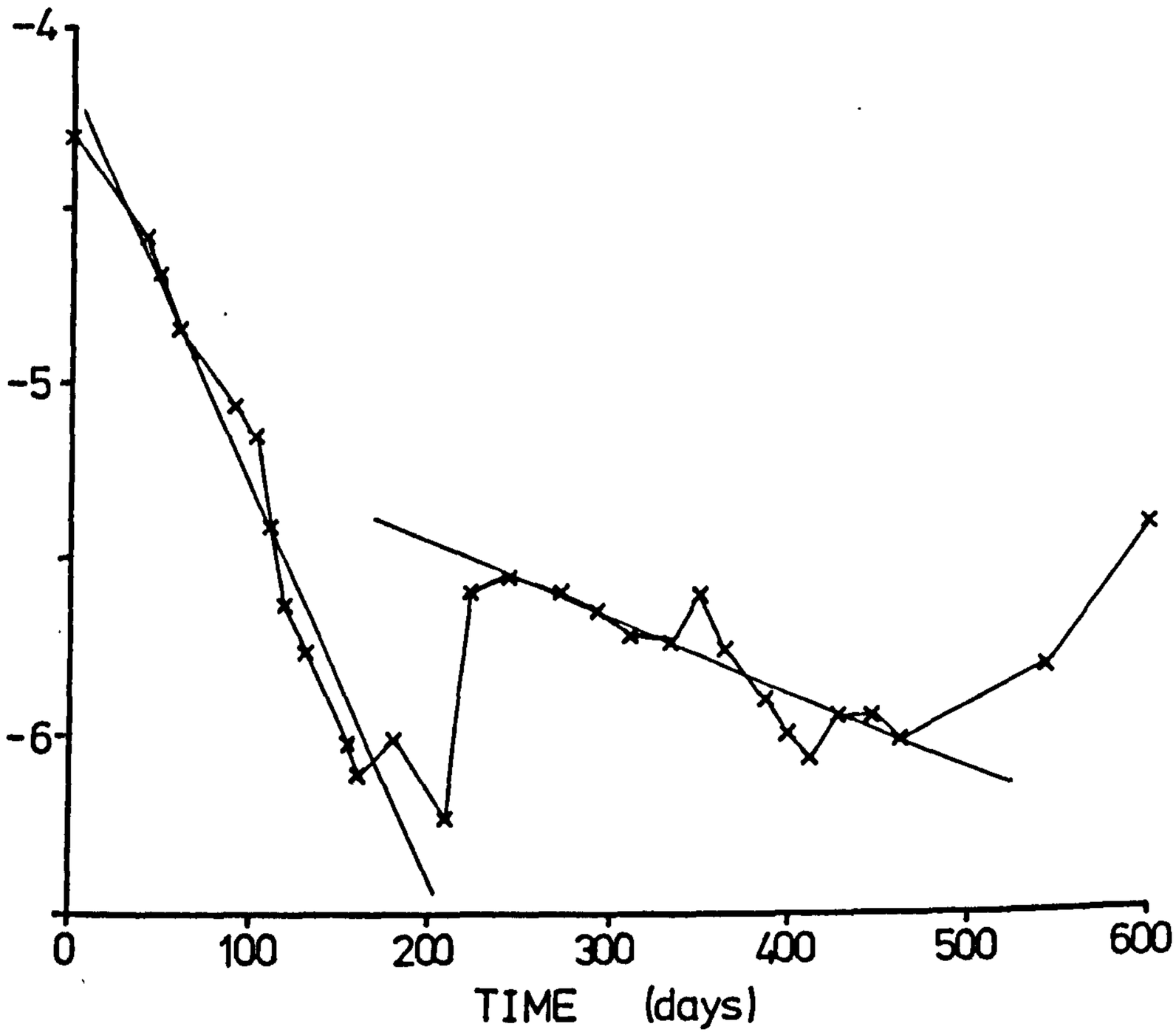

FIG. 8-12 BOREHOLE 28 ln STRAIN RATE v. TIME

local fracture effect.

The strain rate relationship up to 200 days can be approximated by the following equation,

$$\ln \dot{\varepsilon}_s = -0.01125t - 4.175 \qquad (8.1)$$

which reduces to

$$\dot{\varepsilon}_s = 0.015375\, e^{-0.01125t} \qquad (8.2)$$

where t is the time after excavation, in days
and $\dot{\varepsilon}_s$ is the average smoothed strain rate in %/day.

This can be integrated to obtain the following equation for average strain over the first 6m of the 60m pillar.

$$\varepsilon = 1.136667\,(1 - e^{-0.01125t}) \qquad (8.3)$$

The second stage in obtaining an estimate of average pillar strain consisted of relating the strain rate over the first 6m, defined by equation (8.2), to the wall to wall closure rate for site N.U.09. On the basis of extensometer strain rates for boreholes 28 and 29, the deformation from the borehole 28 side was contributing approximately two thirds of the wall to wall closure. The relationship between the equivalent displacement rate, $\dot{d}$, for the six metre pillar zone, and the contribution of the borehole 28 pillar to the closure rate, $\dot{c}$, was calculated for a number of time values, where

$$\dot{d} = \dot{\varepsilon}_s\left(\frac{6}{100}\right) \qquad (8.4)$$

The ratio $(\dot{d}/\dot{c})$ is plotted in Fig. 8-13 against the time values used.

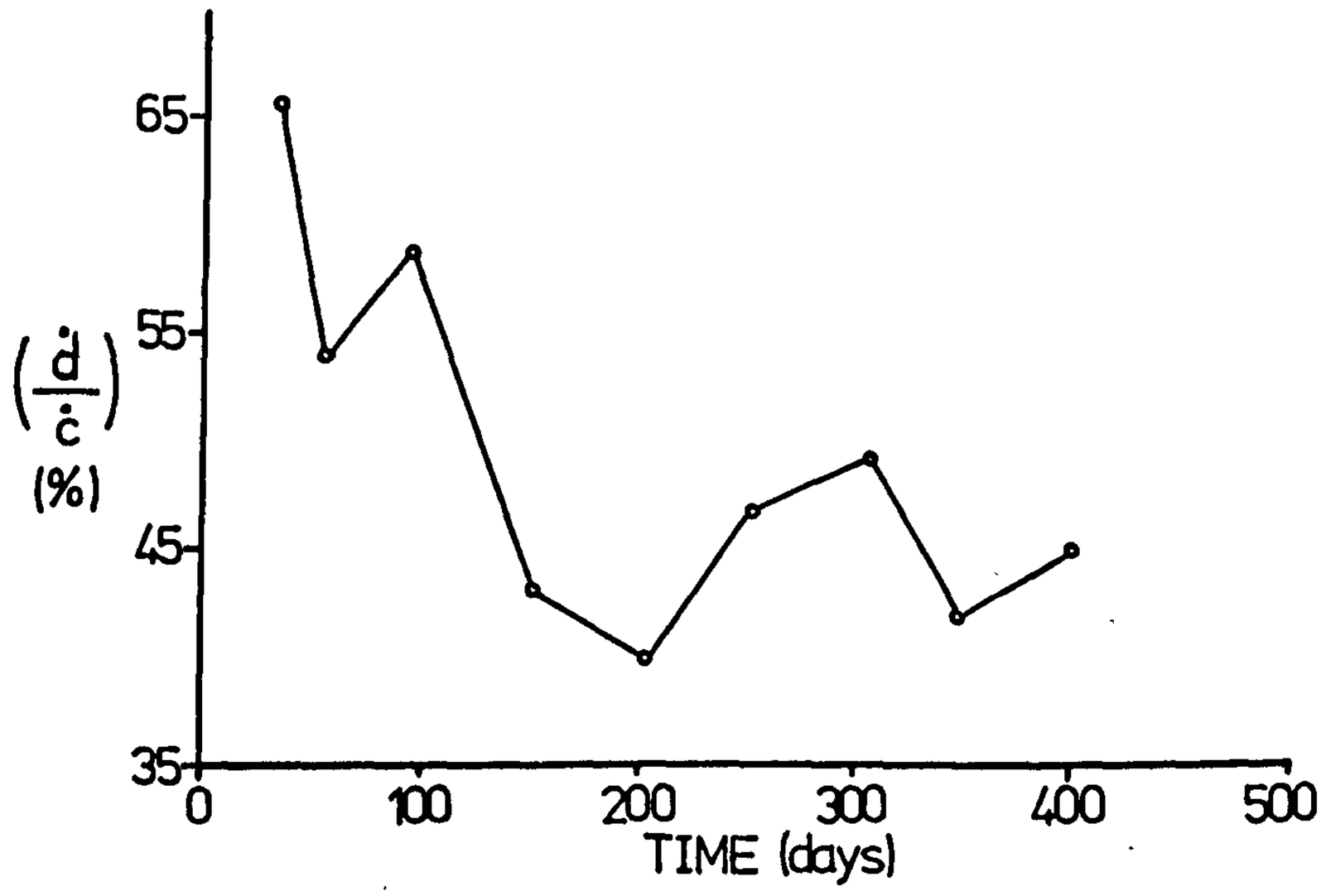

FIG. 8-13 $(\dot{d}/\dot{c})$ v. TIME

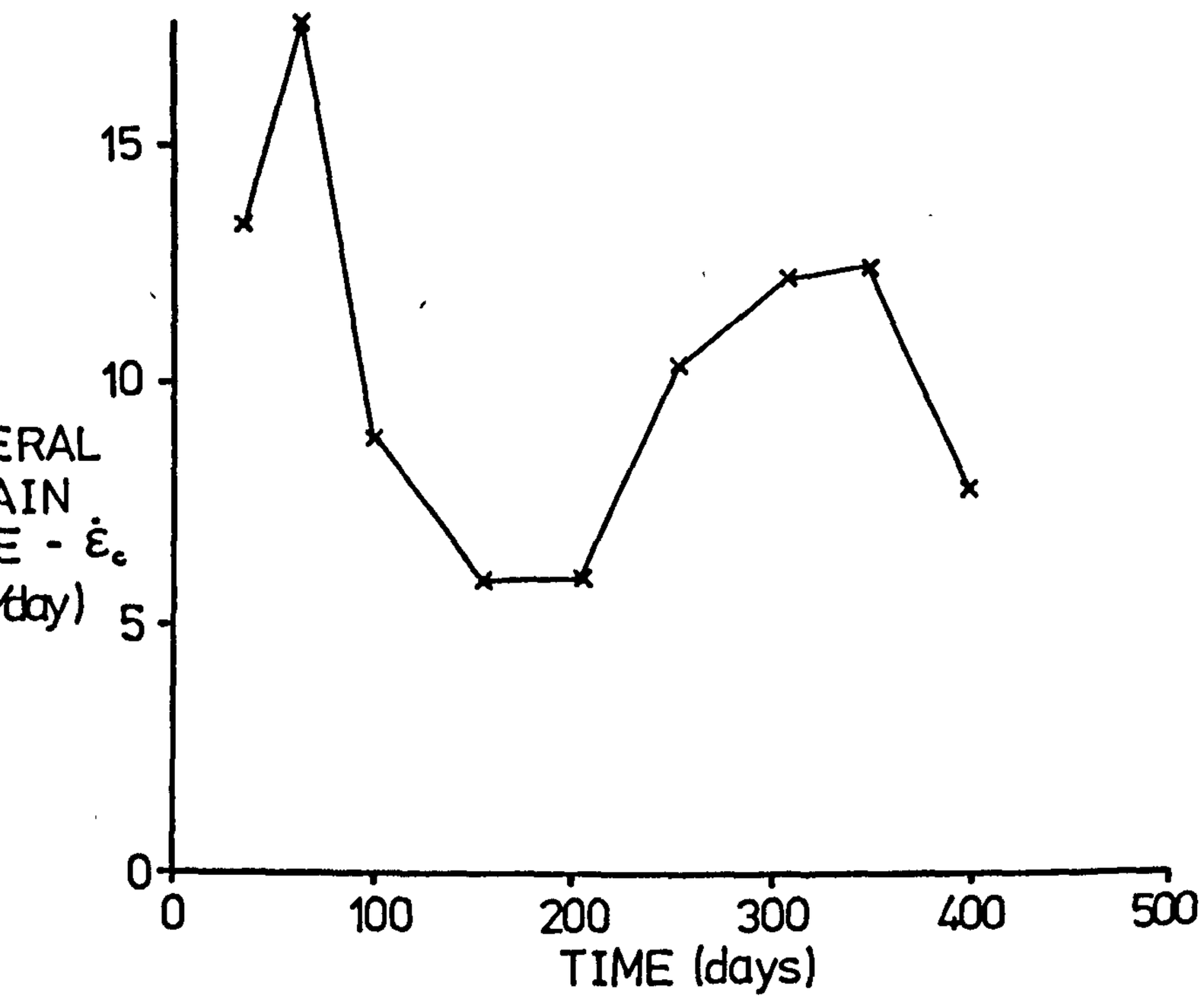

FIG. 8-14 $\dot{\varepsilon}_c$ v. TIME (for central 48m core of 60m pillars)

This indicates a decrease from about 65% to 45% of closure coming from strain in the first 6m of pillar, over 150 days. After 150 days the ratio levelled off at approximately 45%. This represents a movement of stress concentration beyond the 6m point in the pillar and subsequent shrinkage of the confined pillar core up to 150 days at which point it appears to have stabilised.

The difference between $\dot{d}$ and $\dot{c}$ represents displacement produced by strain developed between 6m and 30m into the pillar. Table 8-2 lists the values of $\dot{d}$, $\dot{c}$, $\dot{d}/\dot{c}$ and the resultant pillar core strain rate, $\dot{\varepsilon}_c$ for the various time values considered.

Table 8-2 60m Pillar Closure and Strain Rates

Time (days)	$\dot{d}$ (mm/day)	$\dot{c}$ (mm/day)	$\dot{d}/\dot{c}$ (%)	$\dot{\varepsilon}_c$ ($\mu\varepsilon$/day)
34	0.6293	0.9523	66	13.4
55	0.4969	0.9207	54	17.6
97	0.3098	0.5238	59	8.9
153	0.1650	0.3809	43	6.0
202	0.0951	0.2381	40	6.0
251	0.2243	0.4762	47	10.4
307	0.2788	0.5715	49	12.2
349	0.2228	0.5238	42	12.5
398	0.1503	0.3363	45	7.8

The pillar core strain rates listed above are plotted in Fig. 8-14. These also indicate the change in loading conditions which obviously

occurred at about 200 days. The only explanation for this change could be that 200 days was May, 1975 which was when mining commenced in No. 1 panel to the east of this site. This may have caused a load transfer back onto the shaft pillar area resulting in this quite significant increase in pillar strain rate.

The calculated strain rates, $\dot{\varepsilon}_c$, were plotted in the form $\ln \dot{\varepsilon}_c$ against time for the first 200 days and again a fairly linear relationship was obtained. This resulted in the following expression for $\dot{\varepsilon}_c$,

$$\dot{\varepsilon}_c = 0.001662e^{-0.006626t} \qquad (8.5)$$

which can be integrated to give

$$\varepsilon_c = 0.25075\ (1 - e^{-0.006626t}) \qquad (8.6)$$

for the average strain over the central 48m section of pillar. The above two terms are in units of (%/day) and (%) respectively.

A weighted average of the expressions in equations (8.3) and (8.6) therefore provides a measure of the average pillar lateral strain for a 60m pillar, at least for 200 days. This can be expressed as ε_{60},

$$\varepsilon_{60} = 0.22733\ (1 - e^{-0.01125t}) + 0.2006\ (1 - e^{-0.006626t}) \qquad (8.7)$$

The main interest in calculating an average pillar lateral strain is in relating it to a vertical strain and vertical pillar yield which is of importance for subsidence considerations.

Laboratory testing on potash model pillars (Chapter 6) indicated an average of zero volumetric strain even after large amounts of

deformation and fracturing of pillar edges. Analysis of in-situ shaft measurements in the Upper Halite (Appendix C) also suggested a zero volumetric strain mechanism away from the immediate vicinity of the excavation. In applying a zero volumetric strain criterion to the in-situ pillar results the tendency would be to over-estimate vertical strains if major fracturing has influenced the lateral strains. On the other hand it would under-estimate vertical strains if the average volumetric strain was compressive due to the large area of confined pillar material.

In view of these opposing effects, a zero volumetric strain criterion appears valid. On the assumption that the lateral strain occurs in the direction towards the closest pillar edge and is a function of that distance to the edge, the average vertical strain will be equal to the lateral strain. This was the case in the laboratory tests shown in Fig. 6-8 and has been assumed here. On the basis of an average pillar height of 3.4m, the average vertical deformation for a 60m pillar, d_{60}, can be obtained from equation (8.7) and written as

$$d_{60} = 0.007729(1 - e^{-0.01125t}) + 0.006820(1 - e^{-0.006626t}) \quad (8.8)$$

From the results plotted in Fig. 8-14 the strain rate appeared to level off after 150 days to a steady state condition. This may not be a specific point for all pillars, but to take into account effects such as the reloading of the borehole 28 pillar after 200 days, for subsidence prediction purposes, it has been assumed that all the pillars enter a steady state deformation rate after 150 days. In fact many pillars may continue to deform at a decreasing rate defined by the exponential function above.

Using the 150 day changeover point as the worst possible

subsidence criterion, the deformation of 60m pillars has reached 10.6mm at 150 days and then contimues to deform at a rate of 0.0361mm/day (based on the average pillar strain rate of 10.61$\mu\varepsilon$/day). In other words, a 60m pillar deforms by 18.3mm in the first year and 13.2mm in subsequent years.

8.3 No. 1 Panel Results

At the time when No. 1 panel was being developed, to the east of the shaft pillar area, a proposed layout of experimental roadways for rock mechanics investigations was put forward to the mine. This is shown in Fig. 8-15. This layout was accepted in principle and was to be incorporated in the planning of the north eastern section of the mine workings. Due to very bad geology in the area, however, the entire layout had to be incorporated within the normal panel layouts. Consequently, each rock-mechanics site in this panel represents a particular aspect of experimental investigation.

8.3.1 Site 1P1

This site was installed to investigate the stability of a herringbone roadway intersection located in halite below the potash seam. Fig. 8-16 shows the layout of the instrumentation in an isometric sketch and a plan view. Fig. 8-17 shows the site geology and the relative positions of the extensometer anchors.

Apart from the roof extensometers and roof and floor convergence pins in the junction itself, positions along each of the three roadways

FIG. 8-15

Layout of Experimental Roadways

(all distances in metres)

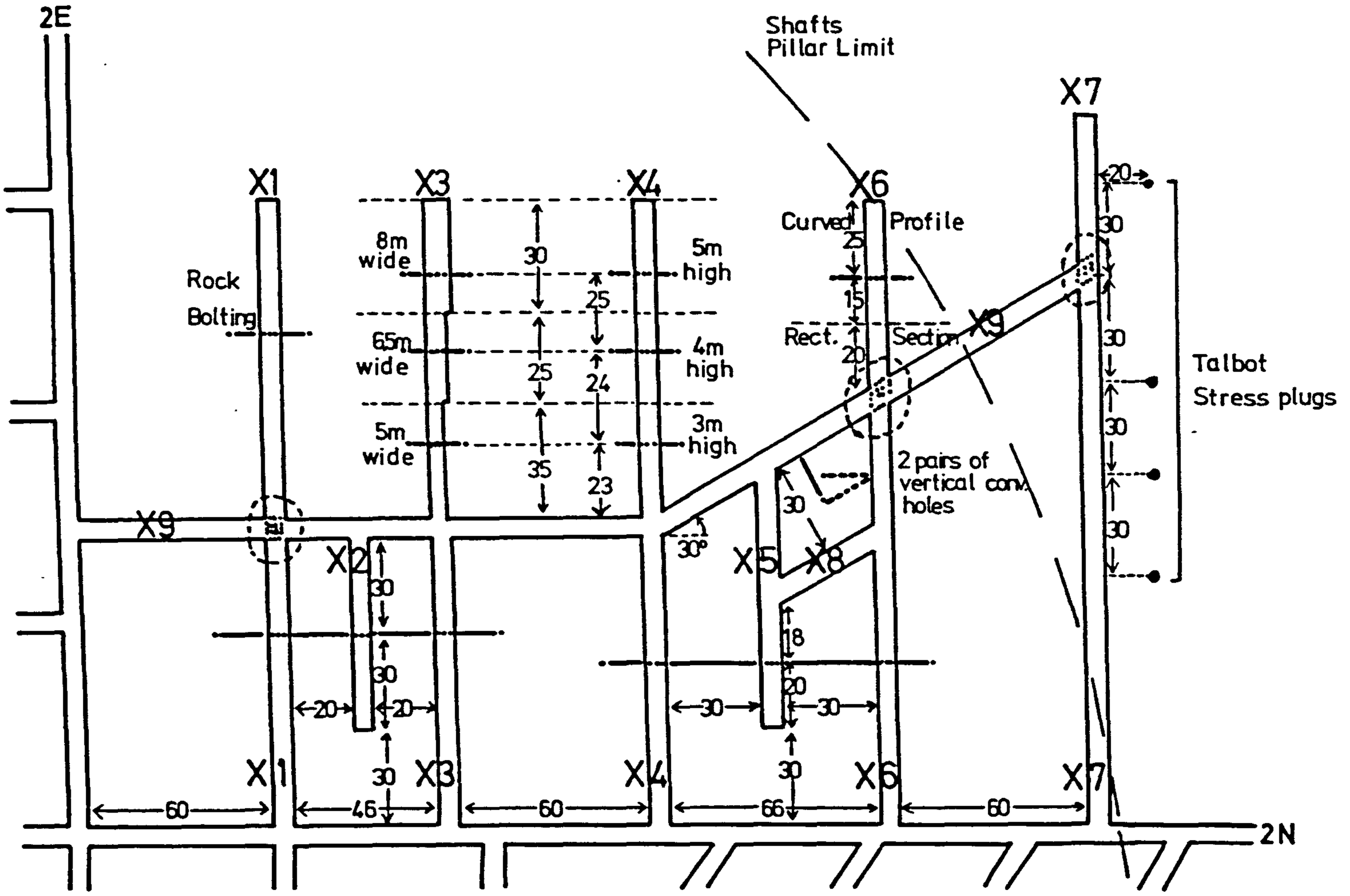

and ——— represent extensometer and convergence stations

G3 CONVEYOR ROAD INTERSECTION (No.1 Panel, Site 1P1)

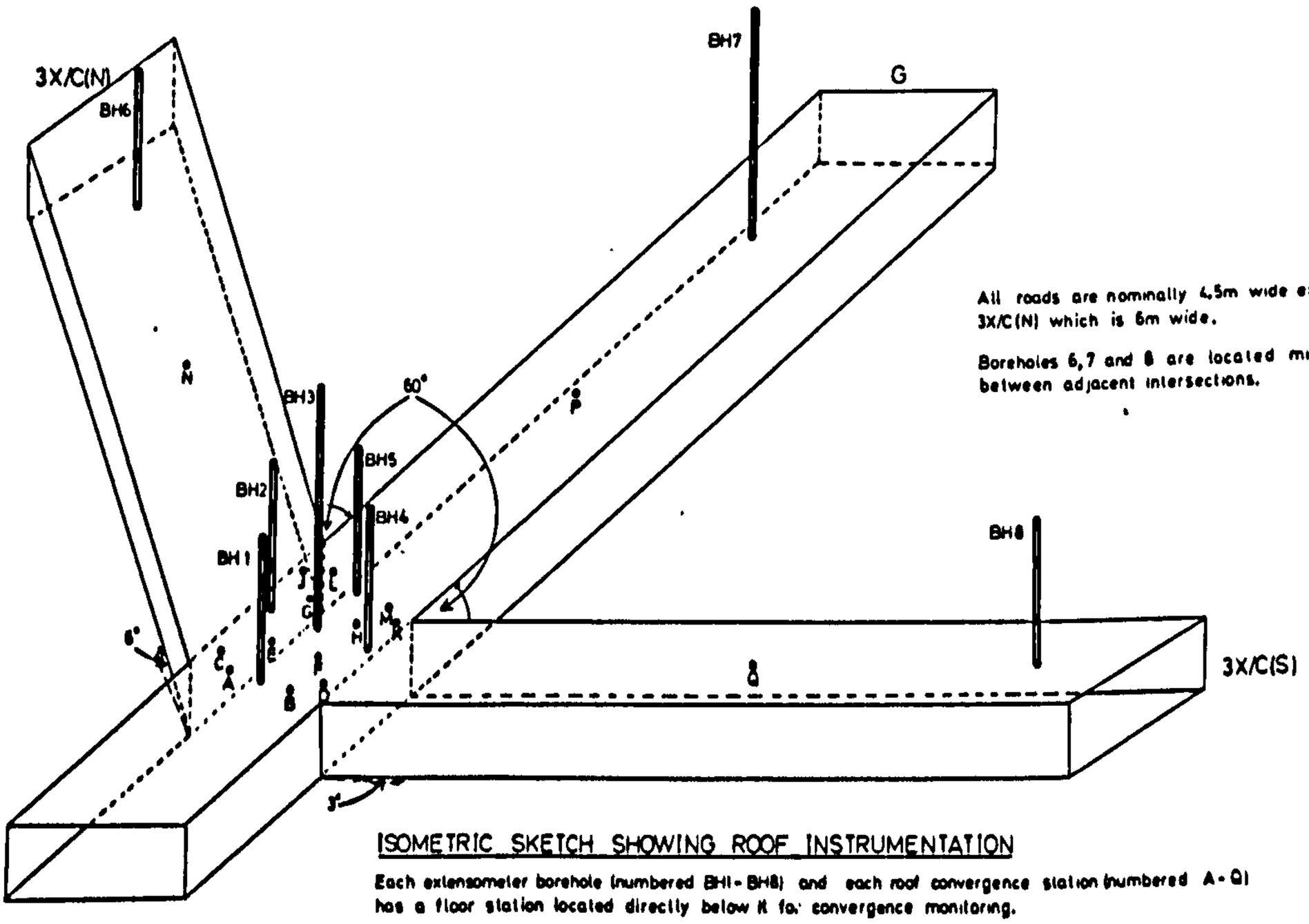

All roads are nominally 4.5m wide except 3X/C(N) which is 6m wide.

Boreholes 6, 7 and 8 are located midway between adjacent intersections.

ISOMETRIC SKETCH SHOWING ROOF INSTRUMENTATION

Each extensometer borehole (numbered BH1 - BH8) and each roof convergence station (numbered A - Q) has a floor station located directly below it for convergence monitoring.

FIG. 8-16 SITE 1P1 LAYOUT

G3 INTERSECTION - PLAN VIEW OF INSTRUMENTATION (No.1 Panel, Site 1P1)

BOREHOLE ANCHOR DEPTHS (metres)

Borehole	1	2	3	4	5	6	7	8
Anchor 1	1.8	1.8	1.8	2.0	1.8	2.0	2.0	1.8
Anchor 2	3.8	3.8	3.8	4.0	3.8	4.0	4.0	3.8
Anchor 3	5.5	5.6	5.8	5.5	5.5	5.7	6.0	5.6
Anchor 4			9.2				8.7	

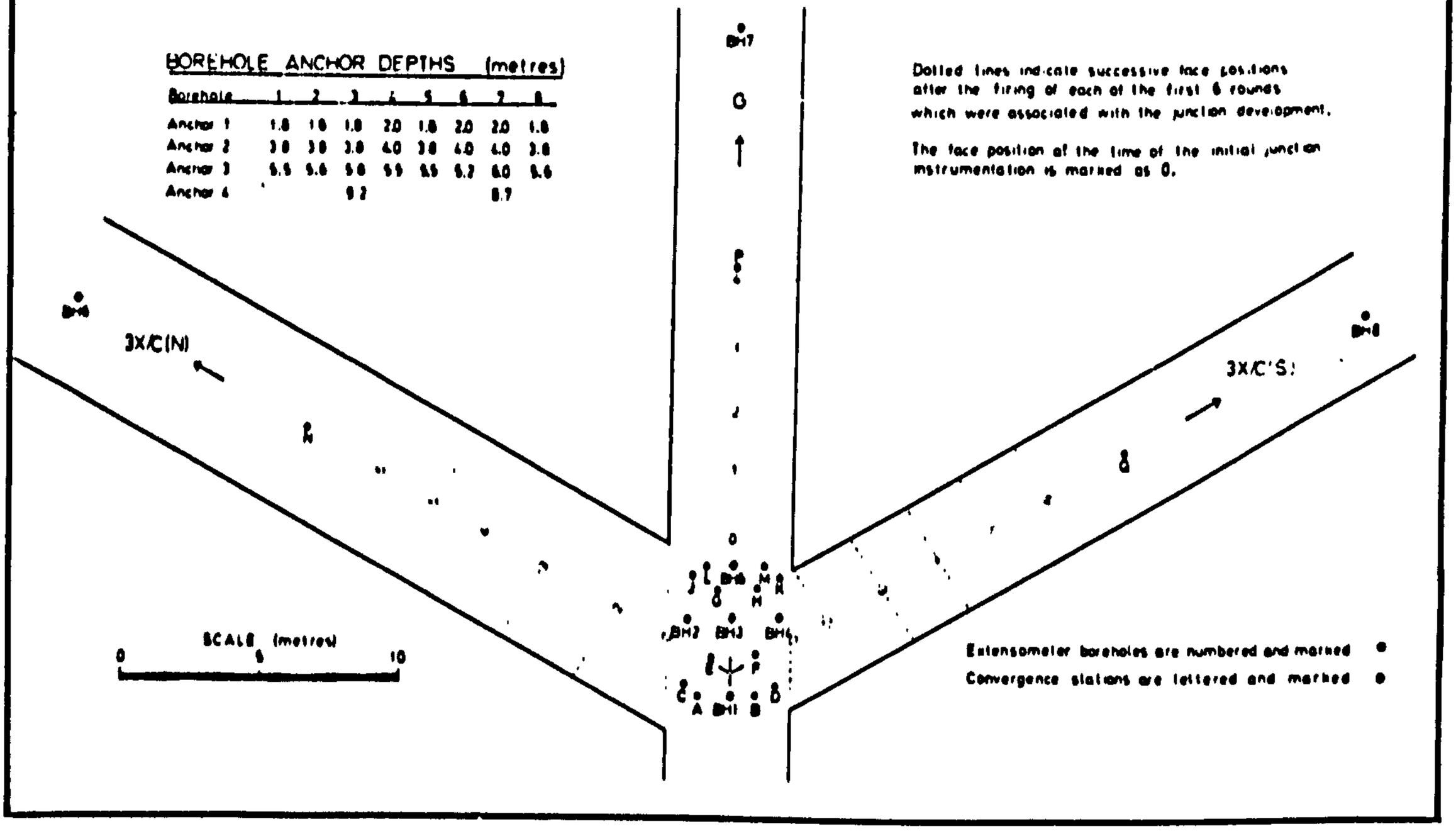

Dotted lines indicate successive face positions after the firing of each of the first 6 rounds which were associated with the junction development.

The face position at the time of the initial junction instrumentation is marked as 0.

Extensometer boreholes are numbered and marked ●

Convergence stations are lettered and marked ●

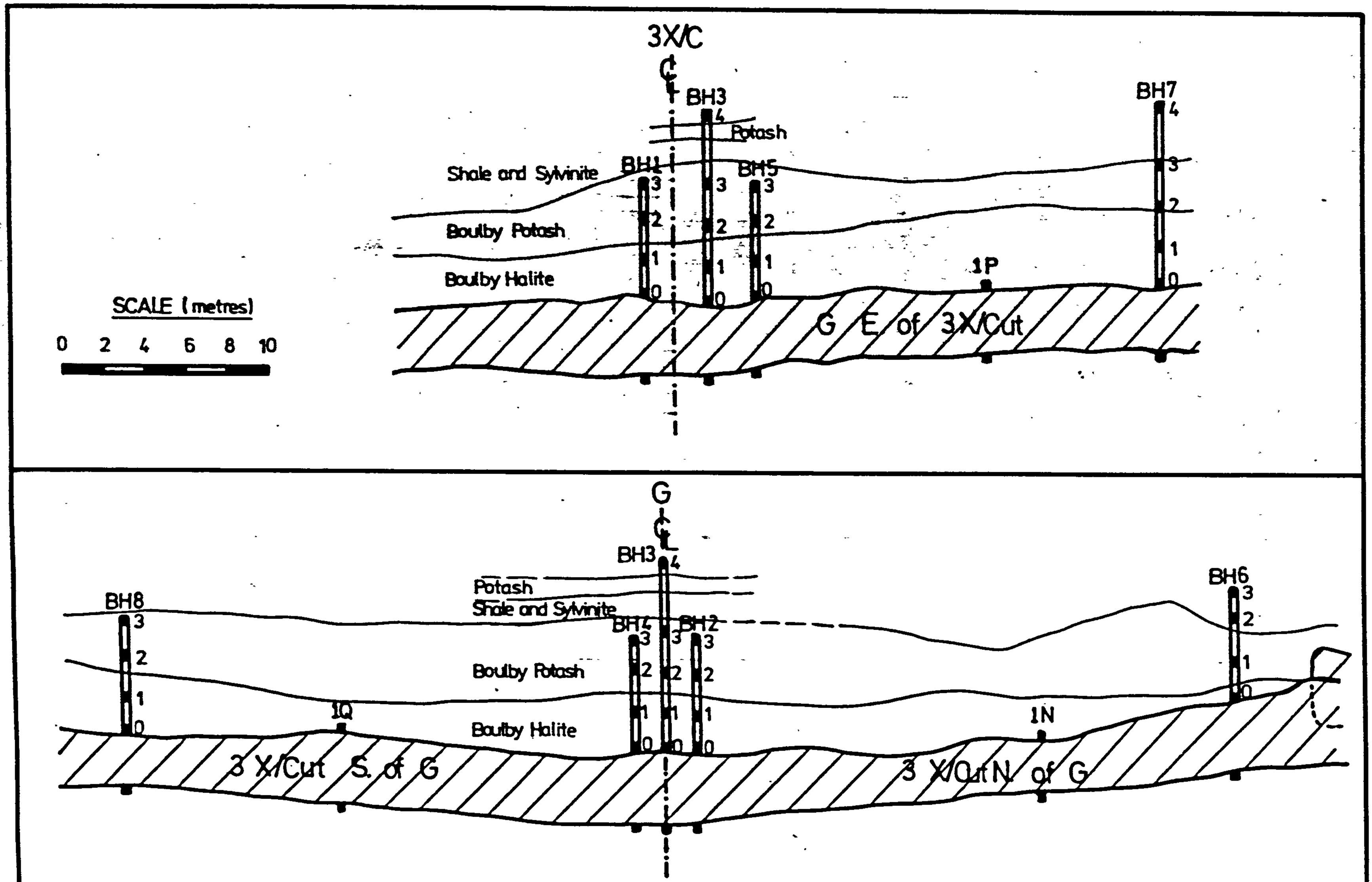

FIG. 8-17 GEOLOGICAL SECTIONS THROUGH G and 3X/C - SITE 1P1

out of the junction were instrumented. In order to obtain as much of the initial high deformation rate as possible, the equipment for the junction was installed within 0.5m of the face, before either of the cross-cuts had been turned off. The plan view in Fig. 8-16 indicates the face positions after successive blasts had been fired in each of the three headings to develop the junction. From the plotted raw results in Appendix B it can be seen that the very steep initial deformation rate was monitored by all the stations and some very consistent creep results were obtained.

Due to the thick layer of halite (3m) in the roof at this site, the roof and floor closures were virtually identical at every station. Therefore the 3m of halite must be providing sufficient confinement to the overlying potash which normally exhibits closures of double the amount of a halite floor.

Fig. 8-18 shows the effect on total closure of the junction development after successive firings. The firing numbers refer to the resultant face positions marked on Fig. 8-16. Firing 1 appeared to influence borehole 5, which was closest to the face, far more than borehole 1 which showed very little increase in closure. This indicates that the distance beyond which the face has minimal support influence lies between 3m and 6m in this material. Firing 2 caused a widening of the span from 4.5m to 8m, since both cross-cuts were fired for the first time. Subsequent firings had far less effect on the junction stations which indicates that 4.5m is well within the critical stable span width for this material whereas only beyond 8m does the loading require redistribution in order to maintain stability.

FIG. 8-18 TOTAL CLOSURE AT SITE 1P1 DURING JUNCTION DEVELOPMENT

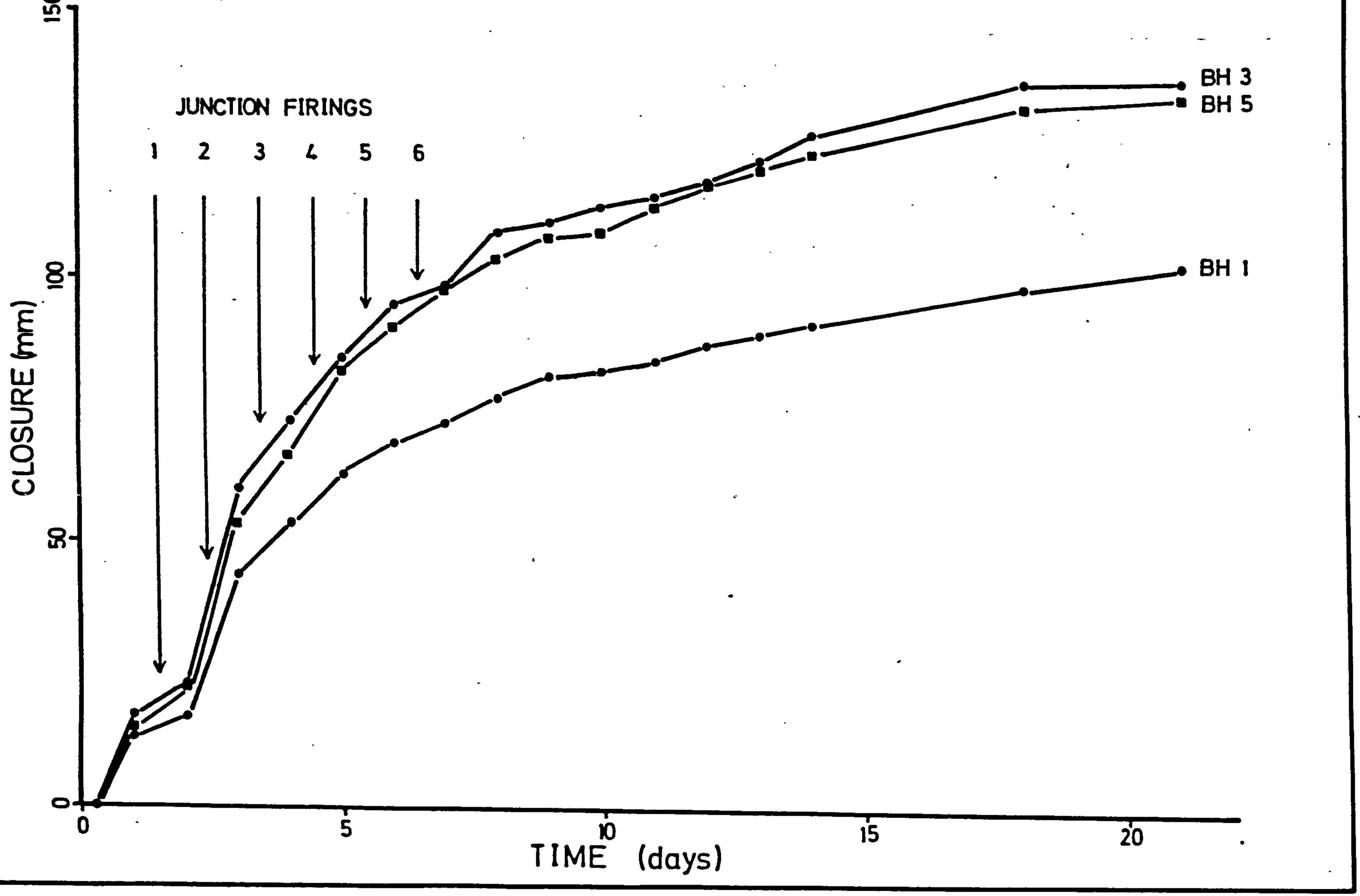

The effect of roadway width on deformations is shown in Fig. 8-19 for No. 3 cross-cut where the width changes from 6m to 4.5m across the junction. Although the halite roof thickness is less at borehole 6 due to the incline of the cross-cut, stations N and Q have similar geology and yet the closures in the 6m wide road are more than double those of the 4.5m road.

The difference between the 10 day and 100 day deformations, for both closure and extensometer anchors, highlights the most important aspect of these results. This concerns the stress redistribution away from the immediate junction, which has taken place after about 30 days. The 10 day results indicate very high deformation in the main junction area with only small movements away from the junction. However, after 100 days, the junction has not even doubled its 10 day deformation whereas the cross-cut stations and extensometers have increased their deformation by many orders of magnitude.

The redistribution away from the junction can be more precisely defined in terms of the floor closure rates along the central road G between the junction and borehole 7. These are not complicated by geological variation. Fig. 8-20 shows the actual floor closure rates for the junction, the quarter pillar station and the half pillar station (midway between two junctions). The curves drawn through the points are based on a least squares regression analysis of the closure rates and are defined by,

for borehole 3,

$$\dot{u}_f = 13.031\ t^{-0.999} \qquad (8.9)$$

for station 1P,

$$\dot{u}_f = 2.248\ t^{-0.543} \qquad (8.10)$$

FIG. 8-19 VERTICAL SECTION ALONG 3 X/C LOOKING EAST THROUGH SITE 1P1 SHOWING DISPLACEMENTS AT 0 DAYS AND AFTER 10 AND 100 DAYS.

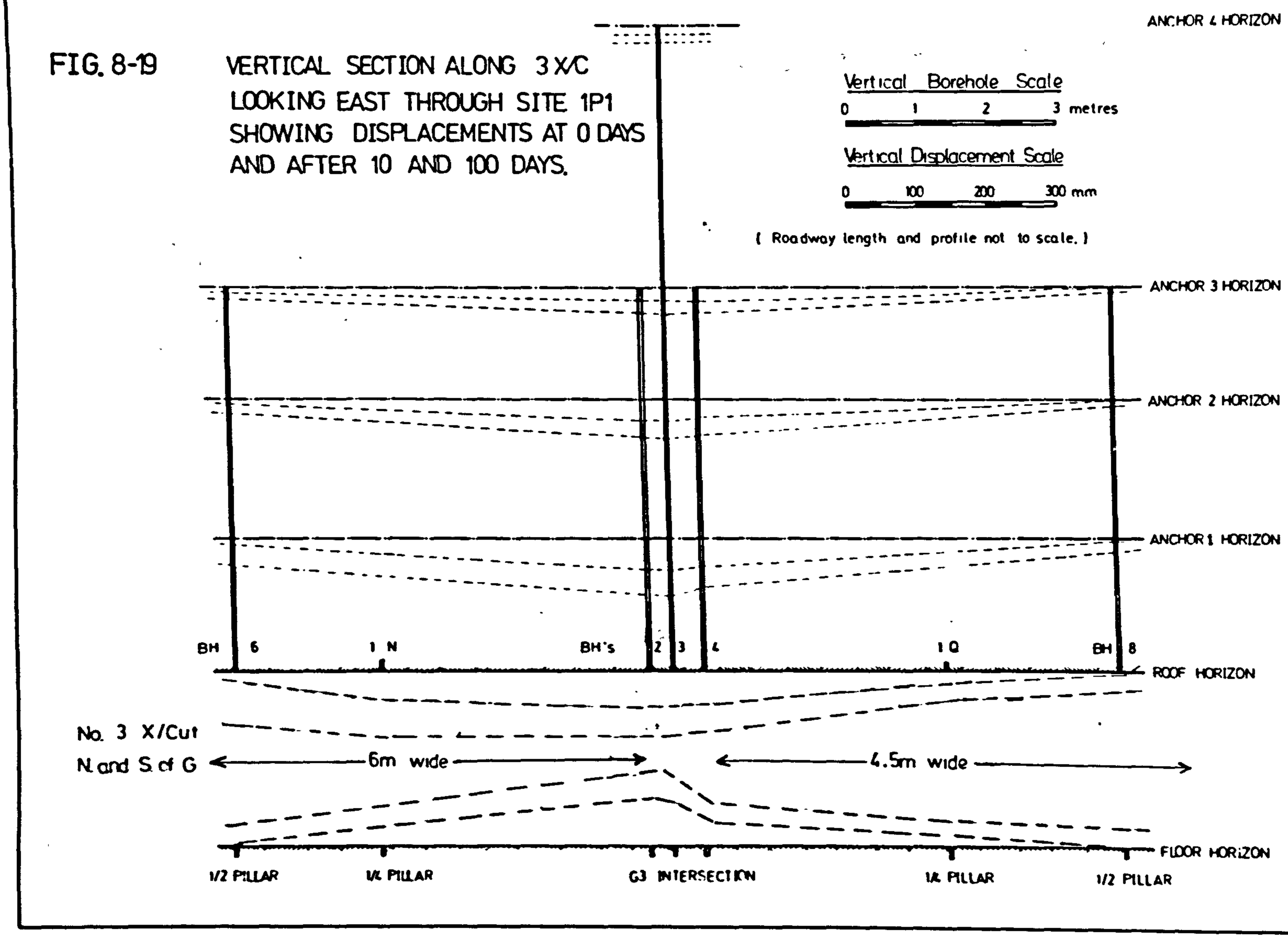

FIG. 8-20 FLOOR CLOSURE RATE v. TIME - SITE 1P1

• = BH3 (Junction floor)

+ = 1P (1/4 pillar floor)

x = BH7 (1/2 pillar floor)

| indicates starting point of time scale (0 days) for fitted curves to avoid dynamic loading effects on closure rate due to face advance.

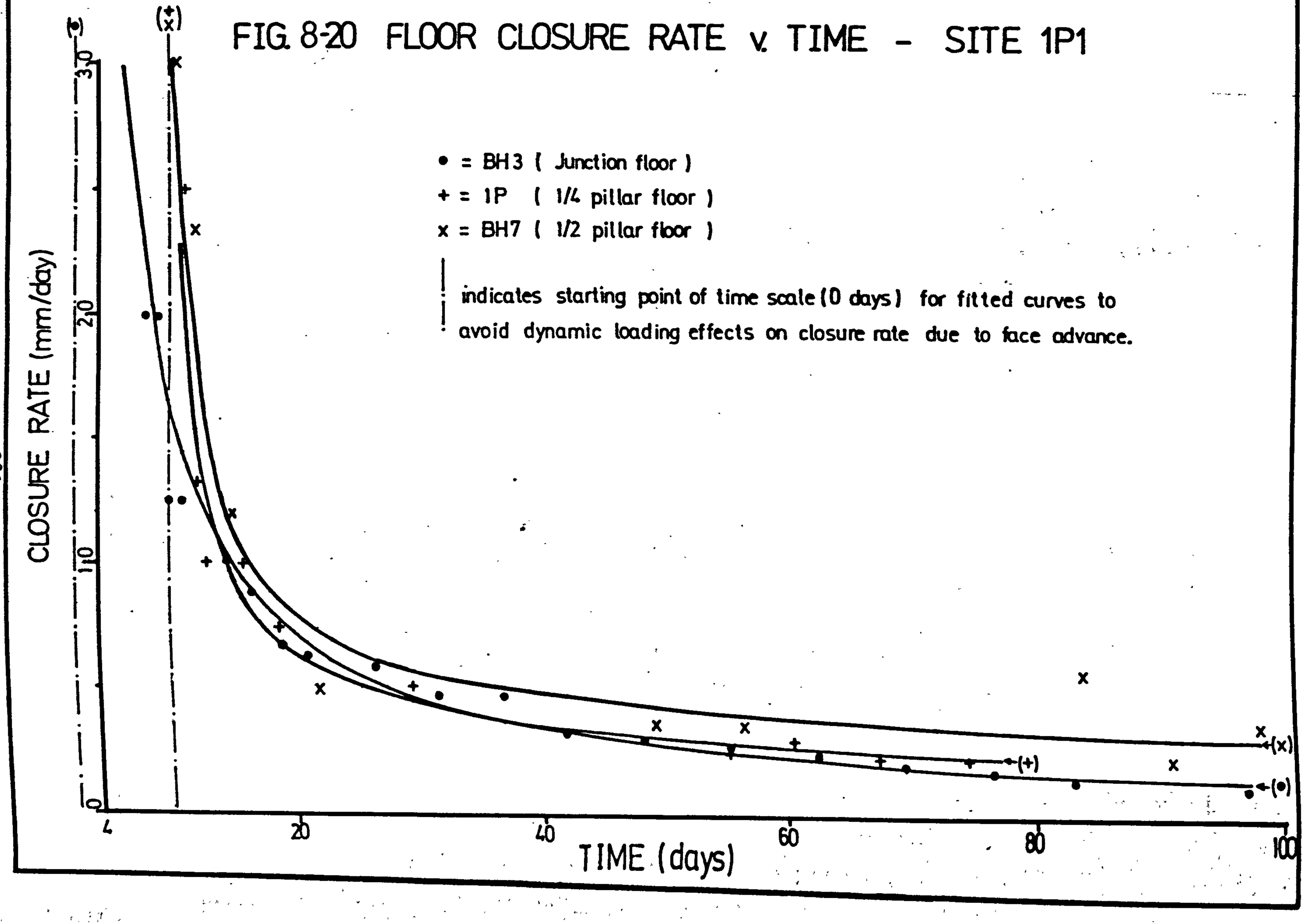

for borehole 7,

$$\dot{u}_f = 2.382\ t^{-0.465} \qquad (8.11)$$

where t is the time in days after the initial dynamic loading effects of roadway advance,

and $\dot{u}_f$ is the floor closure rate in mm/day.

These results show clearly the very high initial closure rate at the junction, but by 75 days the quarter and half pillar rates are 1.4 and 2.0 times the junction rate, respectively. This corresponds to the existence of a stress relief mechanism developing after the high initial yield created at the junction area. Due to the thick, competent roof (halite and primary potash) and floor, the load has been redistributed away from the immediate junction area onto the surrounding pillars.

Fig. 8-21 shows the effect of this stress relief in terms of borehole strain in the roof strata above boreholes 3 and 7 - junction and half pillar stations. Borehole 3 shows the peak strain existing deep into the roof with very little strain development in the immediate roof, which is the reverse of the borehole 7 results.

Consequently, the herringbone junction appears to have great stability as a result of this stress redistribution and the fact that the roadway is in halite. However, the mechanism is fairly finely balanced as can be seen from Fig. 8-22 and Fig. 8-23. These results, and all the 1P1 results, indicate the sharp increase in closure rates which occurred at approximately 200 days. The difference between junction and mid-pillar rates vanished due to an obvious reloading of the strata in this vicinity. The time corresponds to March, 1976

FIG. 8-21 STRAIN v. DEPTH - BOREHOLES 3,7 - SITE 1P1

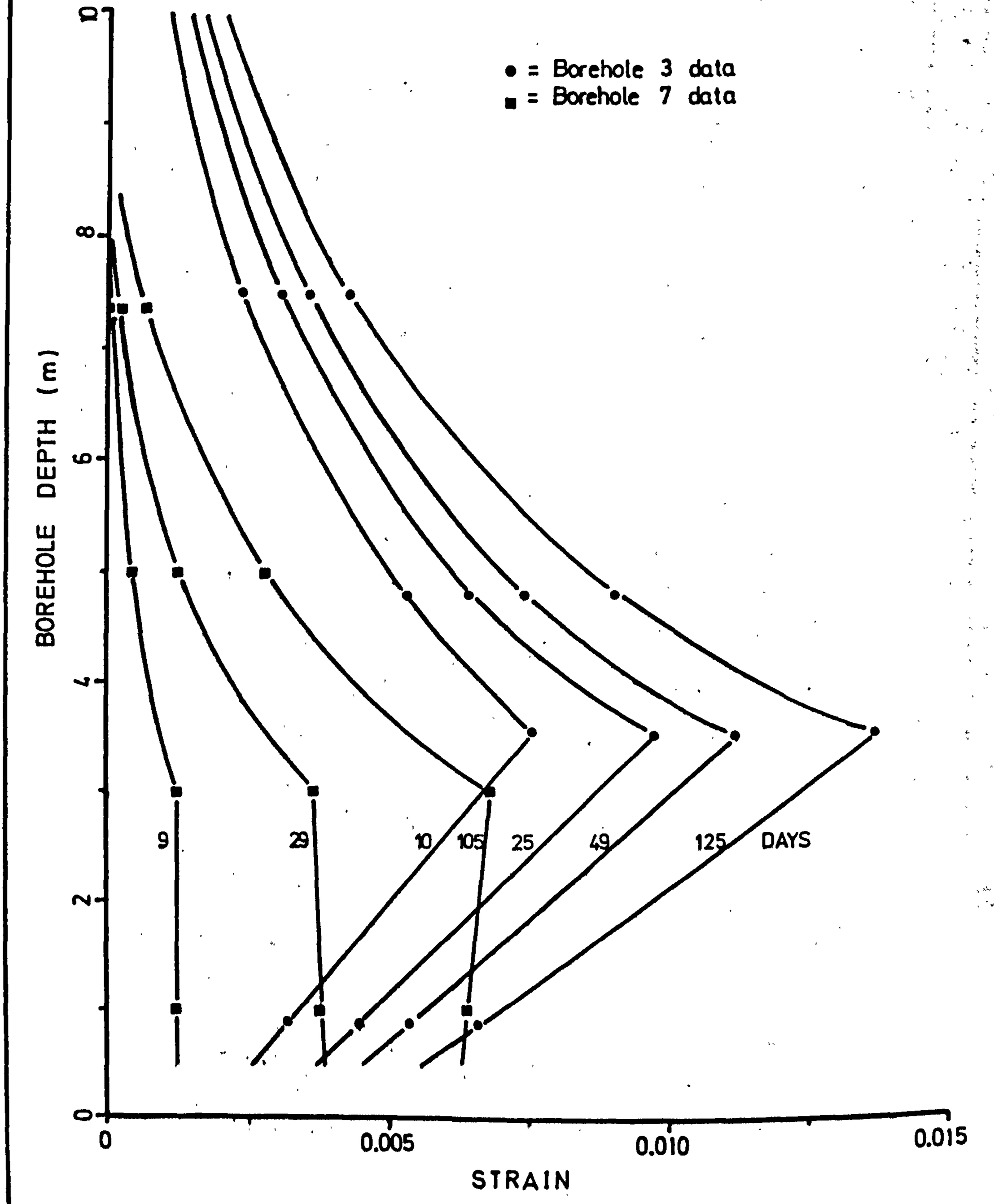

PAGE
NUMBERS
CUT OFF
IN
ORIGINAL

FIG.8-22 CPL BOULBY MINE SITE 1P1

ROOF SAG

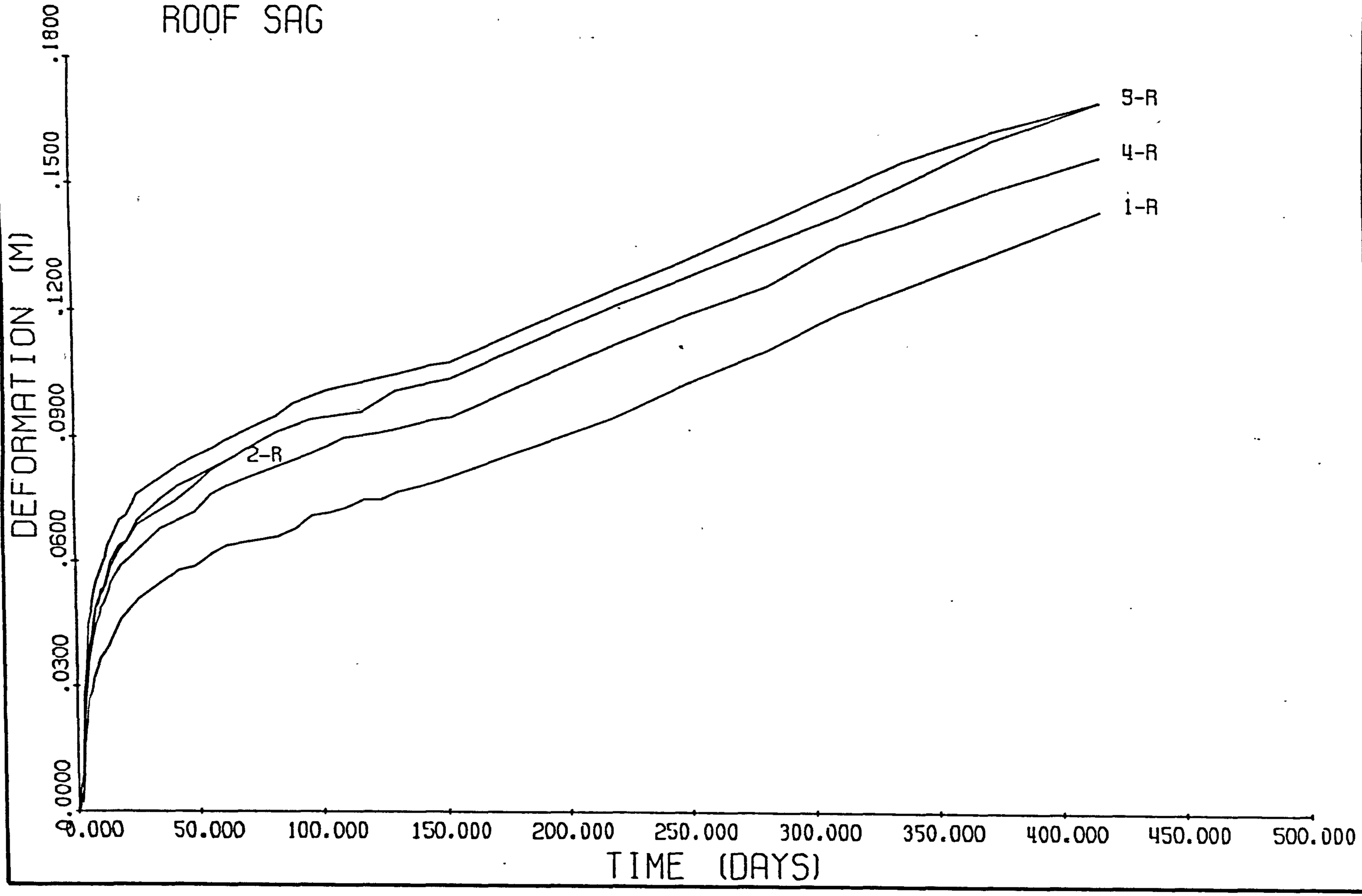

FIG 8-23 CPL BOULBY MINE SITE 1P1

ROOF SAG

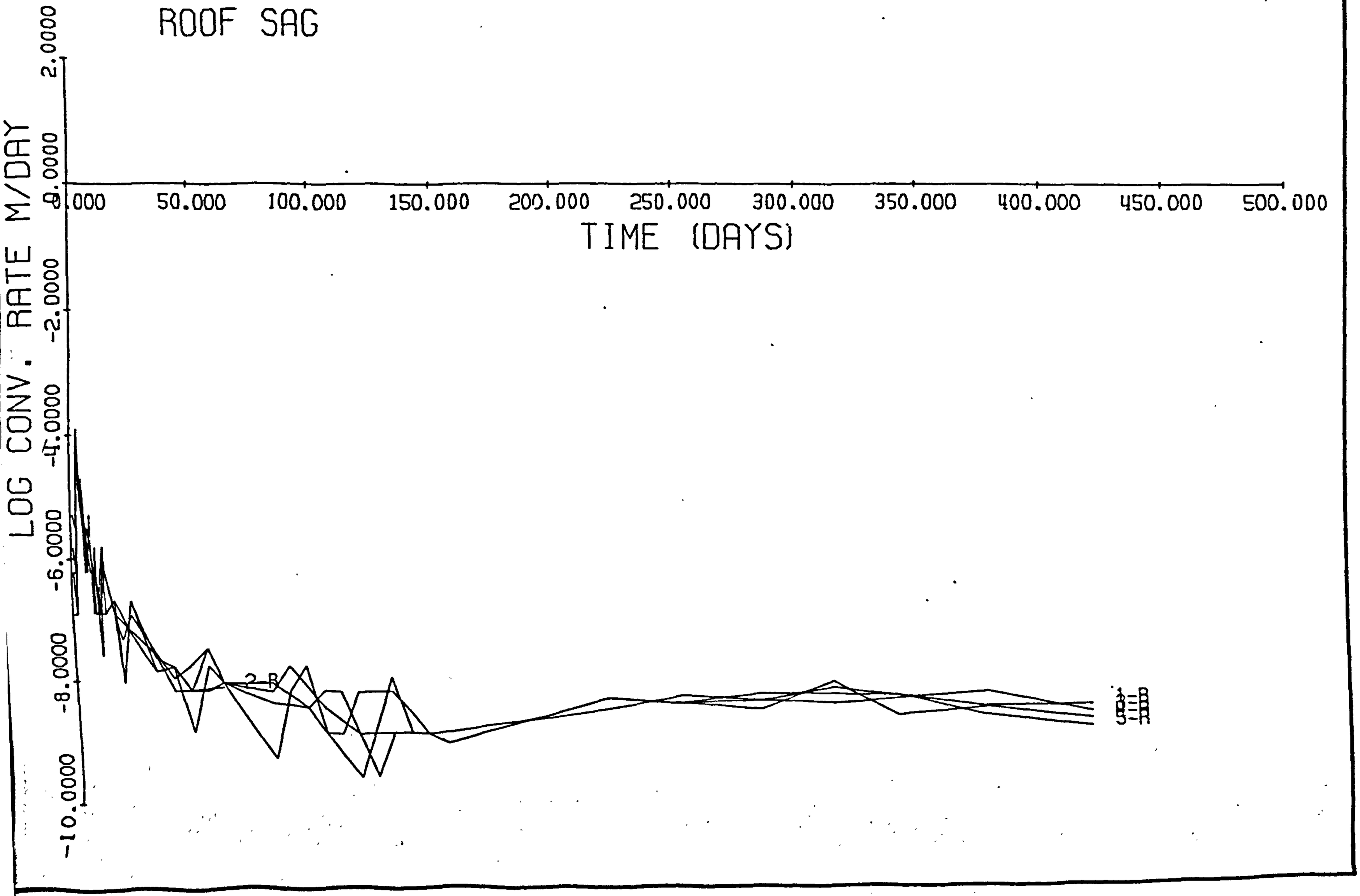

which was when the high extraction mining on the north and south flanks of No. 1 panel increased the effective panel width from approximately 244m to in excess of 400m. This suggests that although 244m was below the critical span width for a low extraction panel, 400m was clearly in excess of it and caused a load transfer onto the stiffer, central panel region where 1P1 was located.

8.3.2 Site 1P2

This site was another herringbone junction investigation but of a slightly different geometry and completely different geology. Fig. 8-24 shows the site layout, on a similar pattern to 1P1, and Fig. 8-25 shows the geology. In this area the primary potash seam was very thin and so the secondary ore, or shale, was being mined in the roadways as well as forming the roof strata.

The junction development was monitored but no conclusive results could be obtained due to lack of access to all stations between blasts. However, it was ascertained that the influence of the face proximity on roof support was lost within 3.5m for this material.

The junction showed some degree of stability for the first 50 days although closure rates continued at a high level. As can be seen from the borehole 11 results in Appendix B, however, there was major bed separation and instability in the junction itself within 80 days of excavation.

Fig. 8-26 shows the floor closure rates for the junction and

K3 INTERSECTION - PLAN VIEW OF INSTRUMENTATION (No 1 Panel, Site 1P2)

BOREHOLE ANCHOR DEPTHS

Anchor	1	2	3
Borehole 9	-	-	-
" 10	2.0	4.0	5.6
" 11	2.0	4.0	5.6
12	2.0	4.0	5.6
13	-	-	5.6
14	2.0	4.0	5.5
16	0.9	1.3	

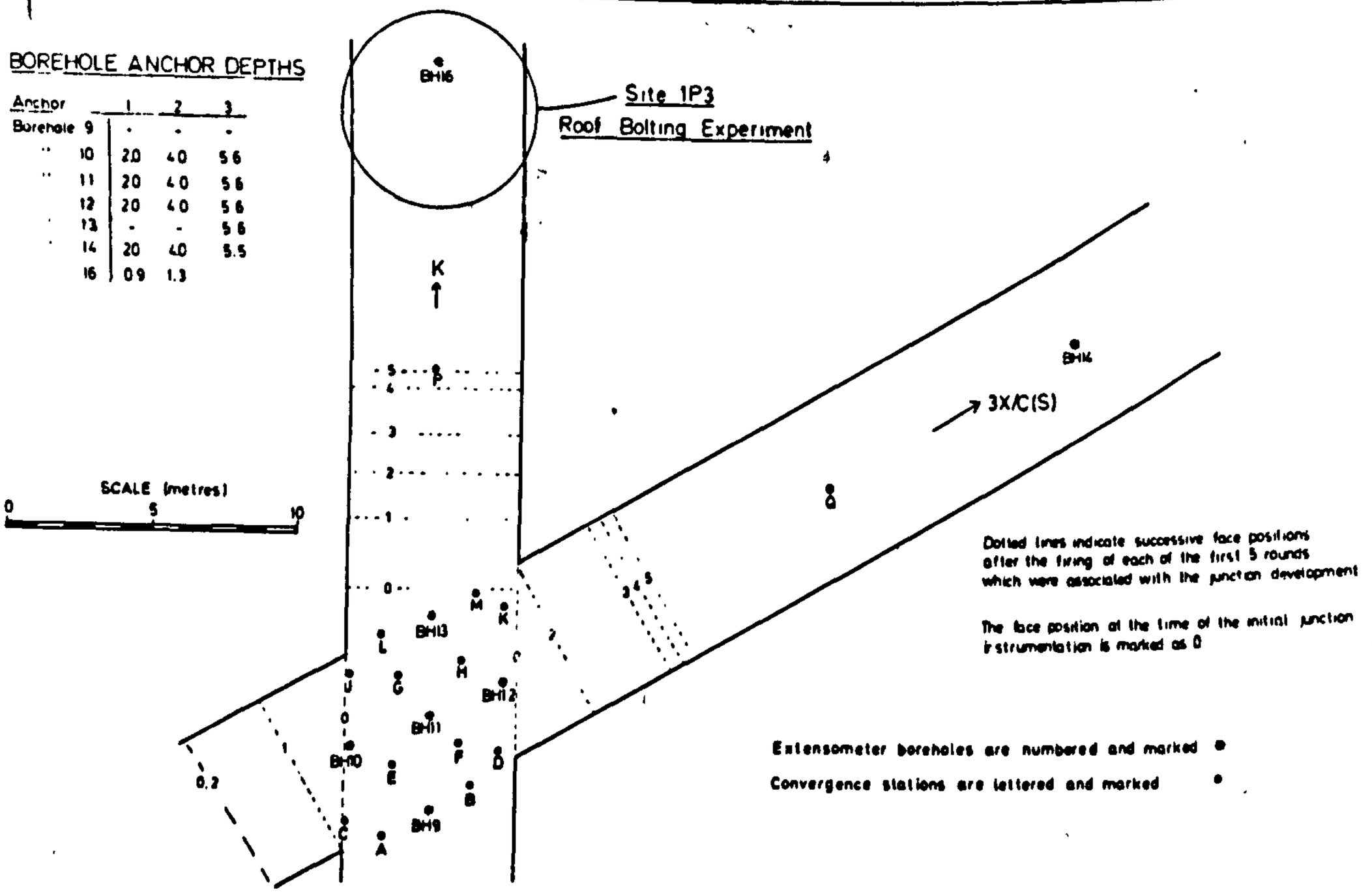

FIG. 8-24 SITE 1P2 LAYOUT

K3 HERRINGBONE TYPE INTERSECTION (No 1 Panel, Site 1P2)

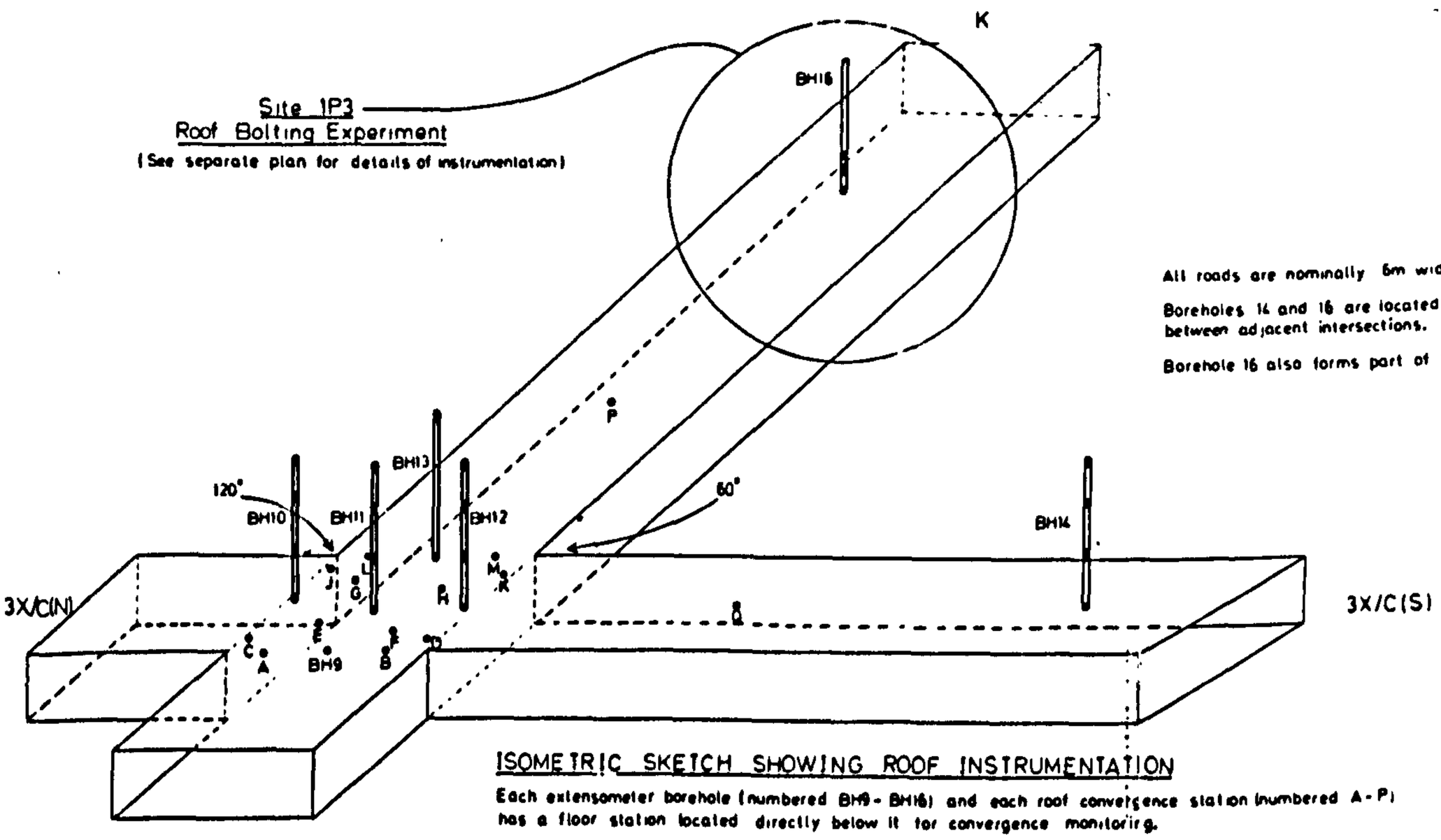

All roads are nominally 6m wide.

Boreholes 14 and 16 are located midway between adjacent intersections.

Borehole 16 also forms part of Site 1P3.

ISOMETRIC SKETCH SHOWING ROOF INSTRUMENTATION

Each extensometer borehole (numbered BH9 - BH16) and each roof convergence station (numbered A - P) has a floor station located directly below it for convergence monitoring.

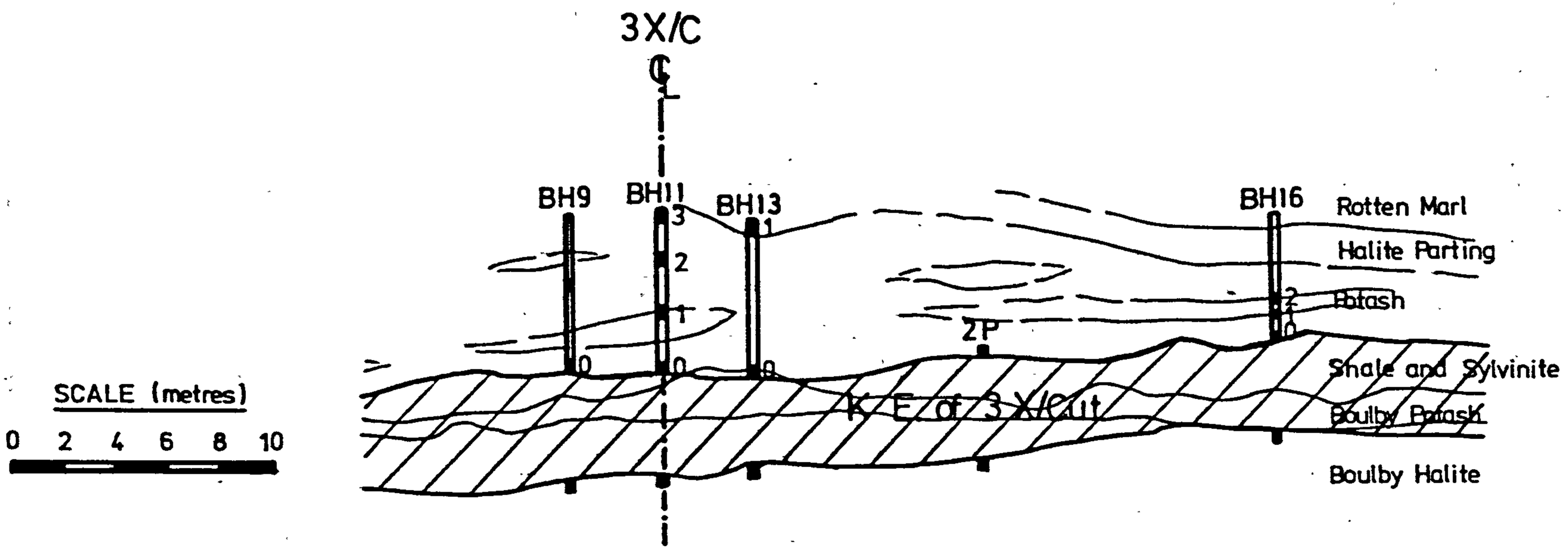

FIG.8-25 GEOLOGICAL SECTIONS THROUGH K and 3 X/C - SITE 1P2

FIG. 8-26 FLOOR CLOSURE RATE v. TIME - SITE 1P2

• = BH11 (Junction floor)
+ = 2P (1/4 pillar floor)
x = BH16 (1/2 pillar floor)

| indicates starting point of time scale (0 days) for curves to avoid dynamic loading effects on closure rate due to face advance.

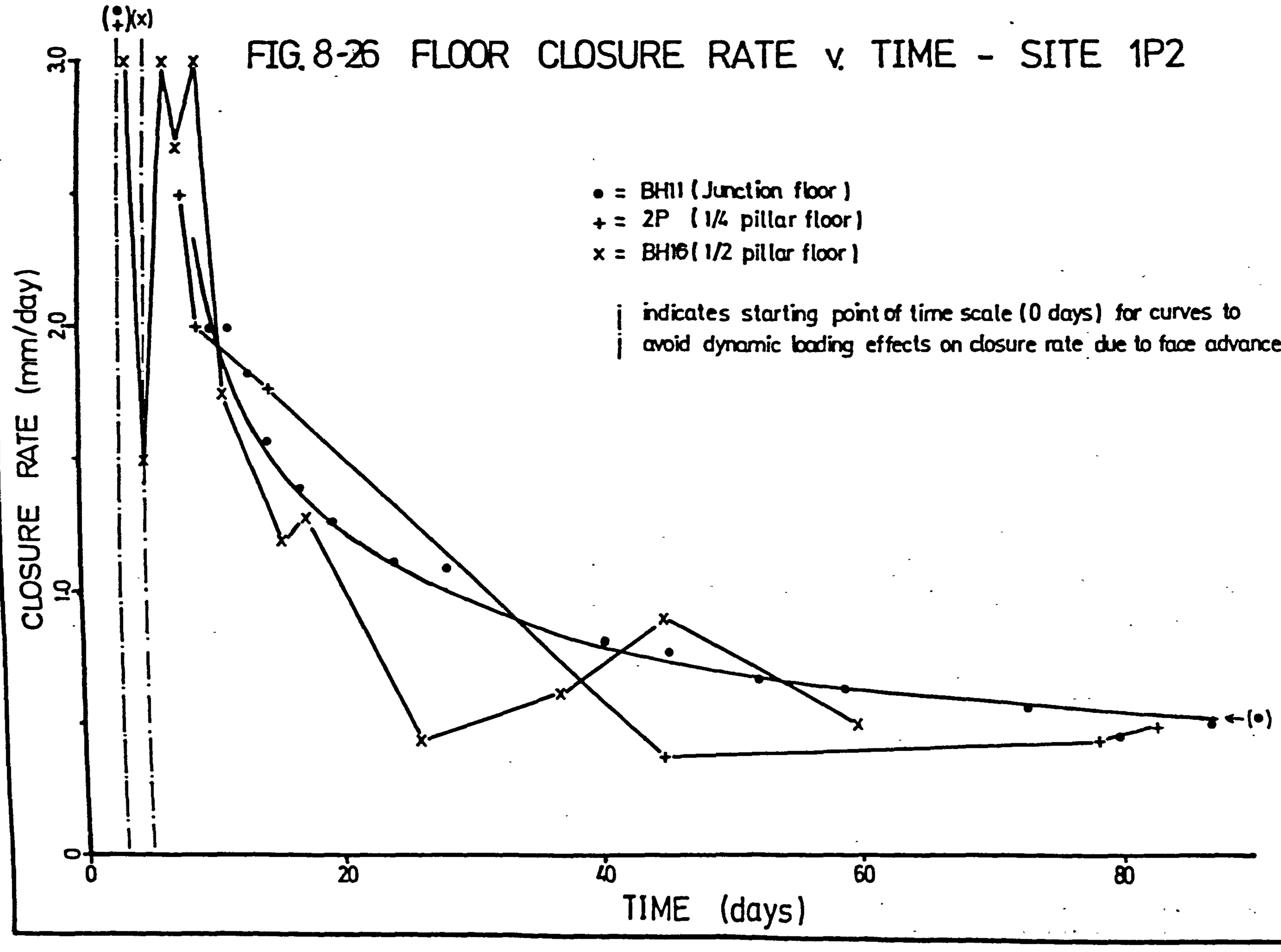

mid pillar stations for this site, but due to wide scatter of readings, only borehole 11 could be approximated by an equation, as follows,

$$\dot{u}_f = 5.670\, t^{-0.536} \qquad (8.12)$$

The results showed no decrease in junction closure rate compared with the mid pillar sites.

Fig. 8-27 shows the strain profile against depth into the roof for borehole 11. Although this shows some degree of stress relief in the immediate roof initially, the rate of strain increase along the entire borehole length suggests an unstable condition developing with time. The 94 day curve shows the resultant instability in the immediate roof of the junction.

On the basis of these results, it appears that although the shale material may have been capable of sustaining an initial stress redistribution around the junction, this did not last for any length of time.

8.3.3 Comparison of 1P1 and 1P2 Results

The difference in closure between the two sites is apparent from Fig. 8-28. This shows the total closure curves for the junction stations (boreholes 3 and 11) and the half pillar stations (boreholes 7 and 16).

Another comparison of the two sites is given in Fig. 8-29 where the displacement of extensometer anchors above the roof has been expressed as a percentage of the roof sag. It has been found that

FIG. 8-27 STRAIN v. DEPTH - BOREHOLE 11 - SITE 1P2

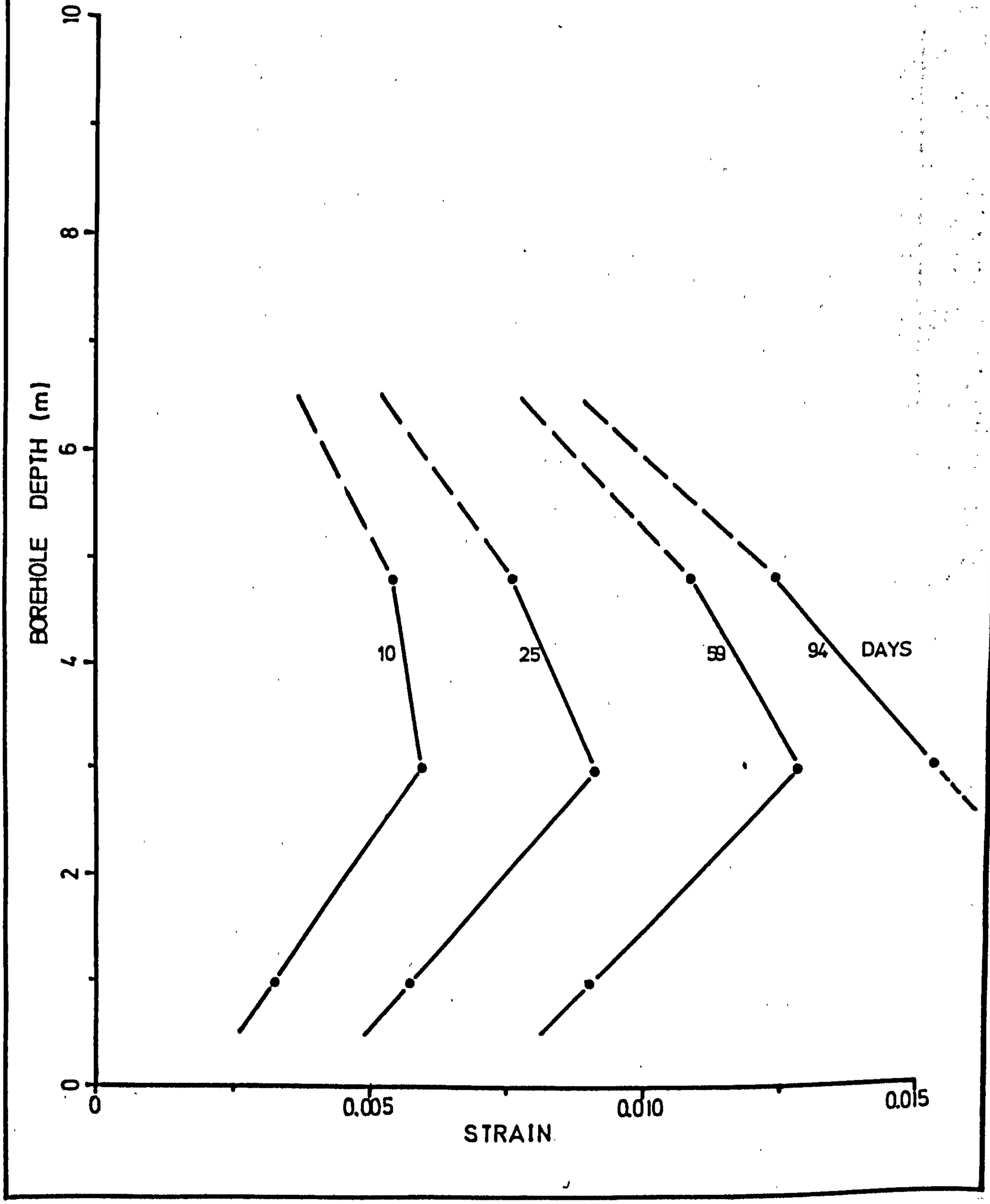

FIG. 8-28
CPL BOULBY MINE
SITES 1P1, 1P2
CONVERGENCE

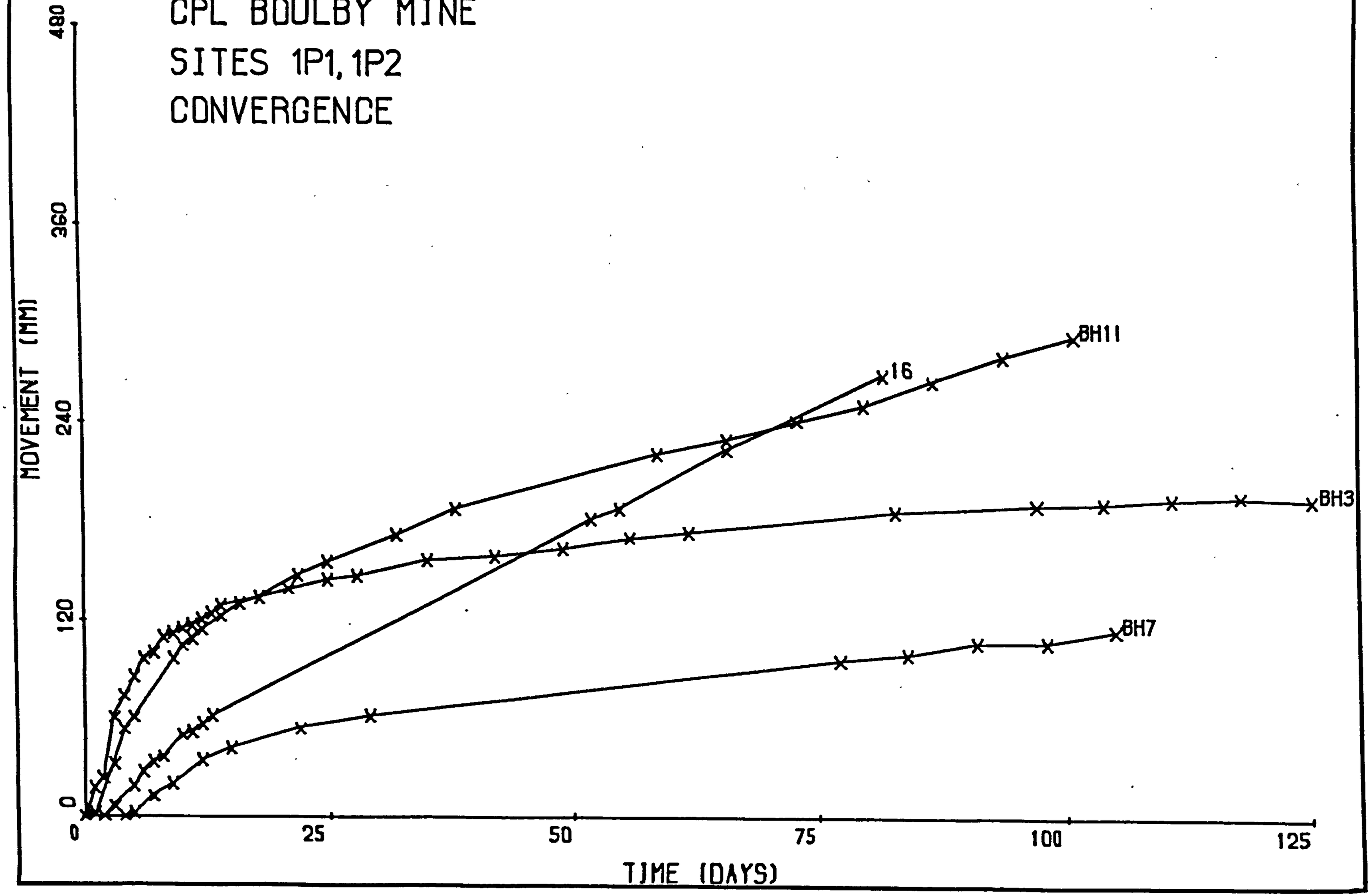

FIG. 8-29 Subsidence v. Depth above Mine Openings (as a function of roof sag)

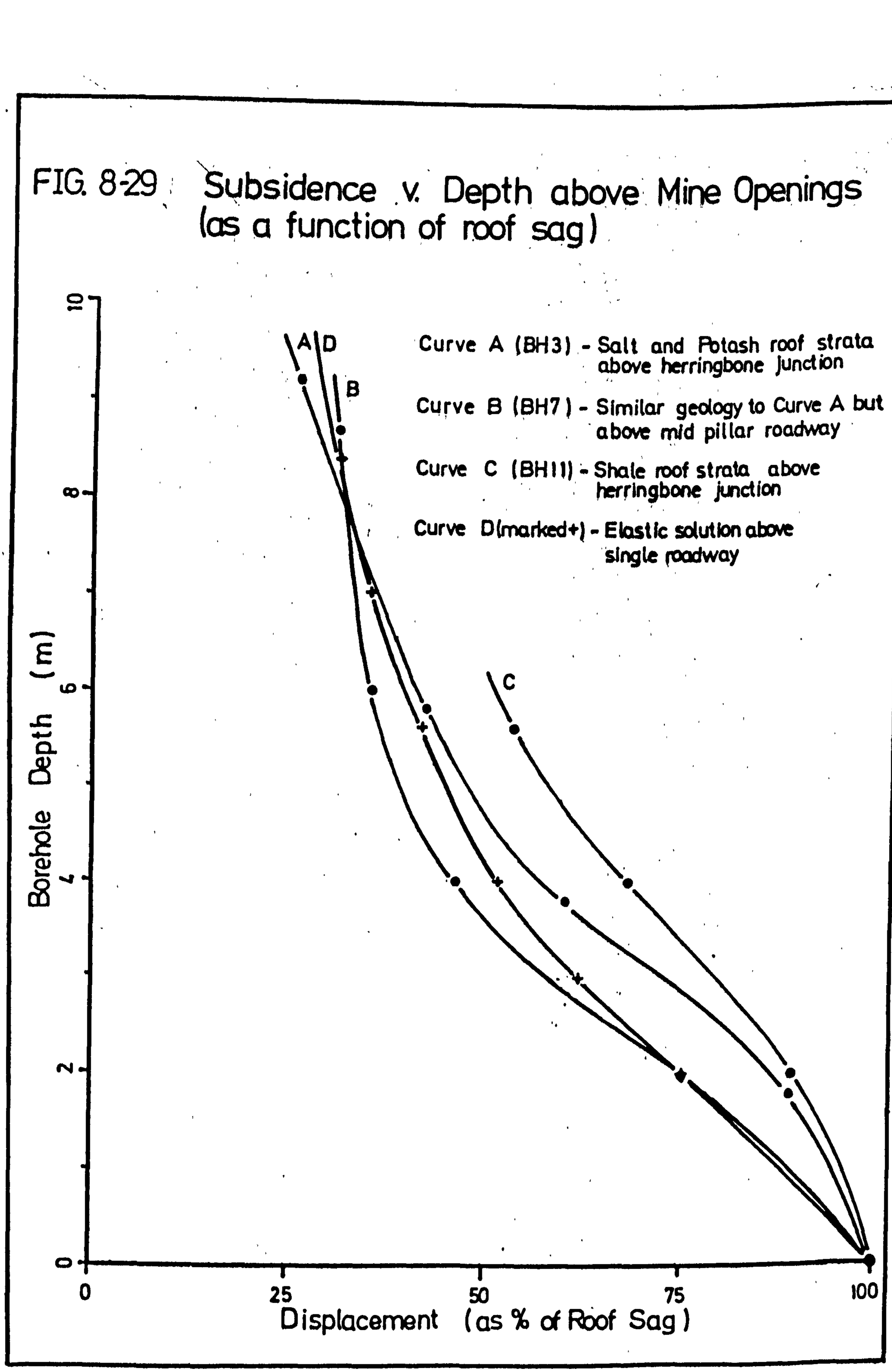

whenever stable conditions have prevailed without major bed separation, this percentage has remained constant with time. The borehole 11 figures have been included on this diagram since they did display this stability initially. However, as soon as bed separation develops at a particular horizon the percentage for an anchor above that horizon decreases, whereas the anchor below the bed separation maintains its ratio with the roof sag. Therefore, on the basis of these percentages, where extensometers have been installed, any major bed separation can be located and quantified to monitor roadway stability.

8.3.4 Site 1P4

This site was the first to investigate the effects of varying pillar dimensions. This was achieved by creating a 46m pillar and then progressively splitting it into two 11m pillars and a central 12m pillar. Fig. 8-30 shows the site layout and Fig. 8-31 shows the relative sequence of mining each of the roads. As shown on Fig. 8-30, it was intended to monitor roadway profiles using a photographic time-exposure technique. This was carried out on a number of occasions with considerable success, using a point light source to illuminate the roadway profile. The system proved to have an accuracy of approximately 0.2% of the roadway width. However, it was not continued, since the regular fracturing of rock and spalling from sidewalls and roof were causing apparent increases in roadway size although the overall profile was reducing in size with respect to the original datum.

The geology of this site was quite variable and although most

FIG. 8-30

C - D PILLAR SPLITTING EXPERIMENT (No. 1 Panel, Site 1P4)

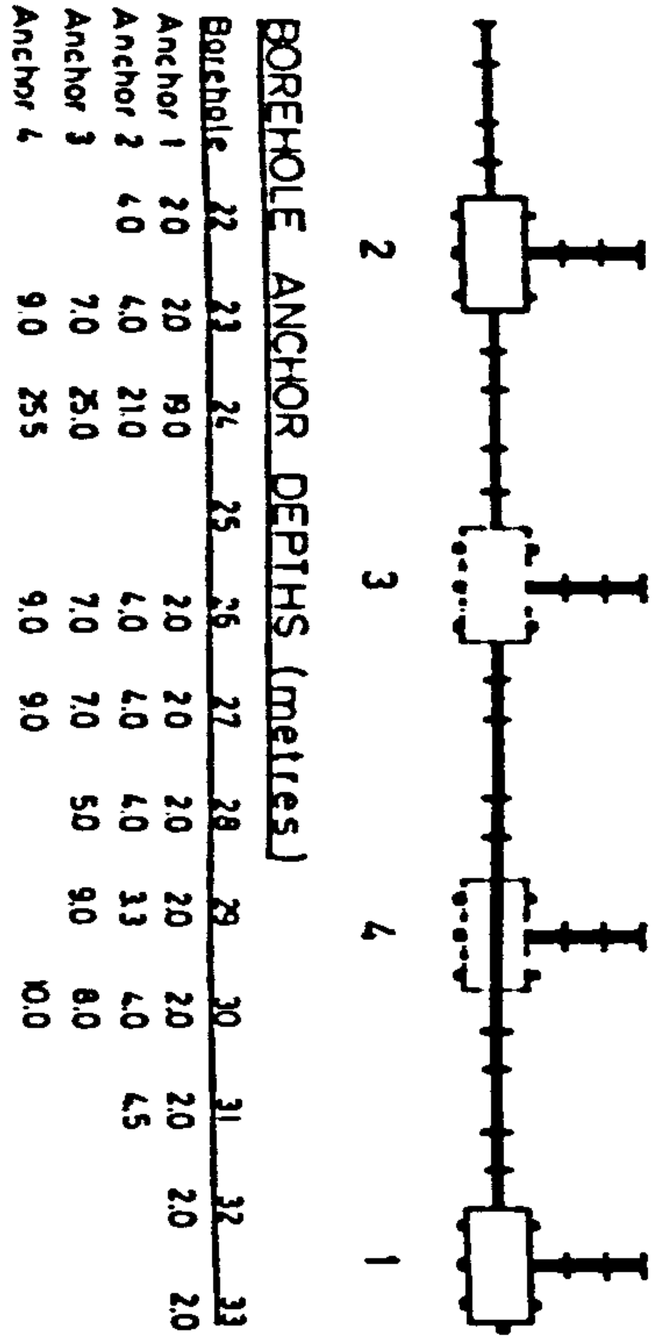

VERTICAL SECTION VIEW (A-A)

PLAN VIEW

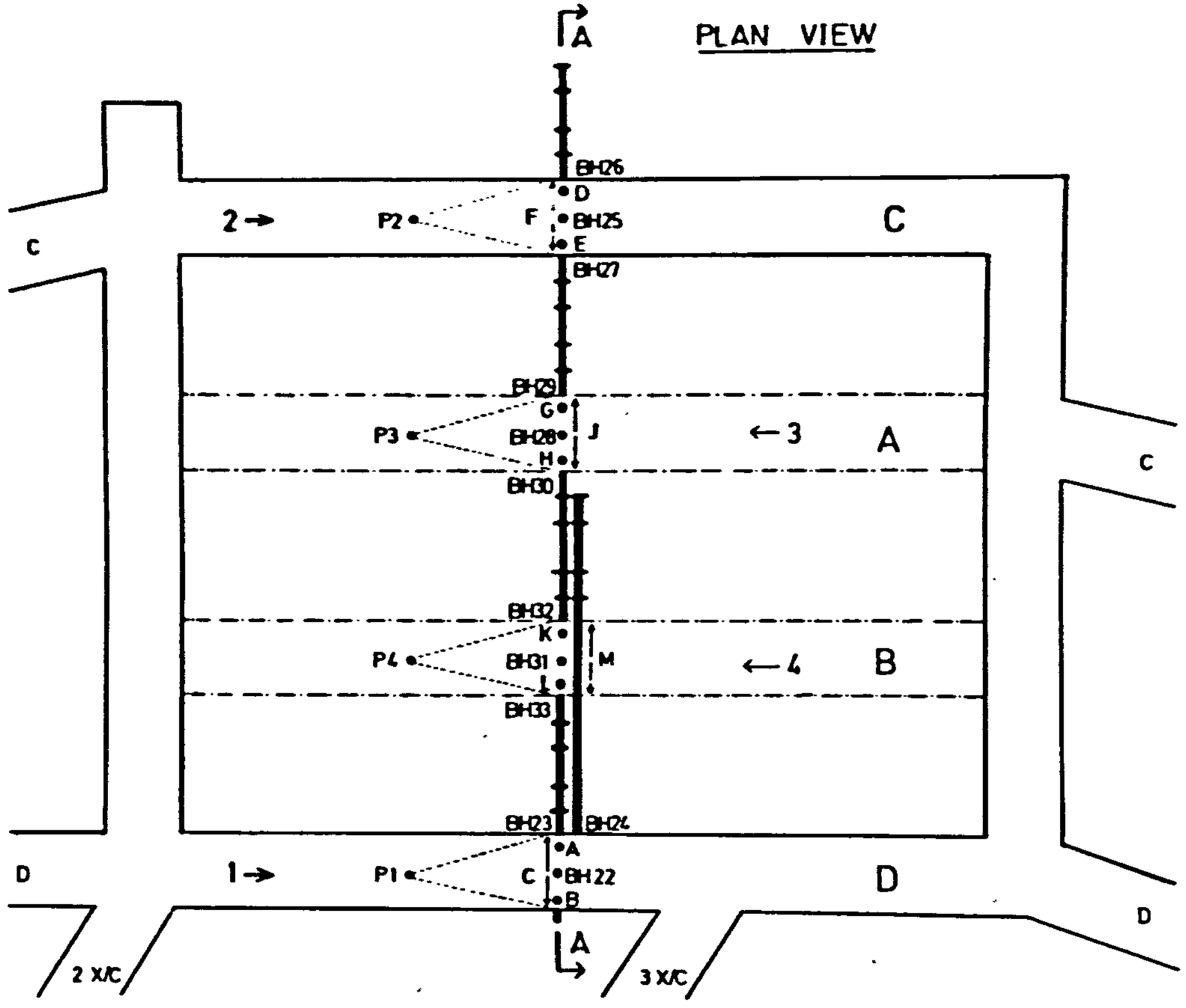

MINING and INSTRUMENTATION SEQUENCE

1. Mine Road 1 and instrument boreholes 22, 23 and 24 and associated convergence stations.
2. Mine Road 2 and instrument boreholes 25, 26 and 27 and associated convergence stations, then complete mining of perimeter roads.
3. Mine Road 3 and then Road 4 and instrument boreholes 28, 29, 30, 31, 32, 33 and associated convergence stations.

SCALE (m)
0 10 20

(P1, P2, P3 and P4 are camera positions for photographic monitoring of road profiles)

FIG. 8-31 RELATIVE SEQUENCE OF MINING PAST PLANE OF INSTRUMENTATION SITE 1P4

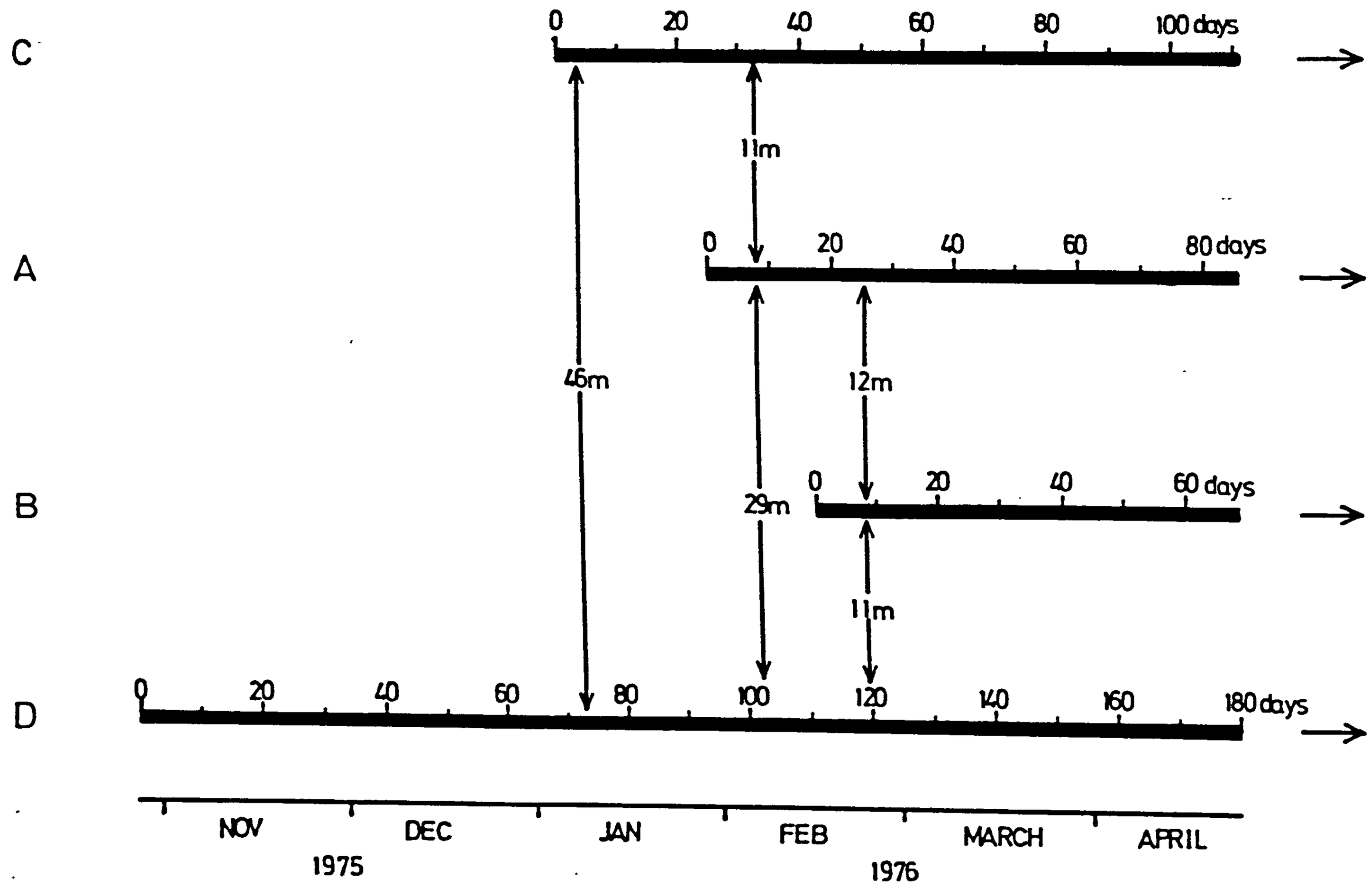

roads had a thin layer of potash in the roof, the conditions were influenced by large quantities of shale above this. Consequently, many of the roof stations were either not installed, or lost very quickly due to local roof falls.

Fig. 8-32 shows the floor and roof closure rates in roads A, B and D. The peaks in the floor rates have been identified in terms of the adjacent roadway advance. These indicate that the increase in closure rate in road D was greater due to the furthest road, C, being mined, than it was when A was mined. This suggests that A was mined through at least a partially stress relieved zone and hence there was not a major transfer of load onto the flank road, D. However, the same cannot be said for when B was mined. In fact the closure rates in A and B continued at a fairly high level and resulted in unstable conditions throughout the area.

Fig. 8-33 shows the sharp increase on the bay strains for borehole 23, installed through to road A from D, when B was mined. The deeper anchors were cut off but the shallower four all show a very significant increase representing a high degree of pillar yield, particularly adjacent to road B (bay 3 - 4).

Fig. 8-34 shows the lateral strains developed in each different pillar width, after it was created. These provide the best indication of pillar yield and load distribution. The initial ribside adjacent to D and the 46m pillar between C and D both show only a shallow depth of movement, hence a large core of confined material. The 30m pillar between A and D indicates strain occurring across the full pillar width although clearly confined in the central

FIG 8-32 FLOOR AND ROOF CLOSURE RATES v. TIME SITE 1P4

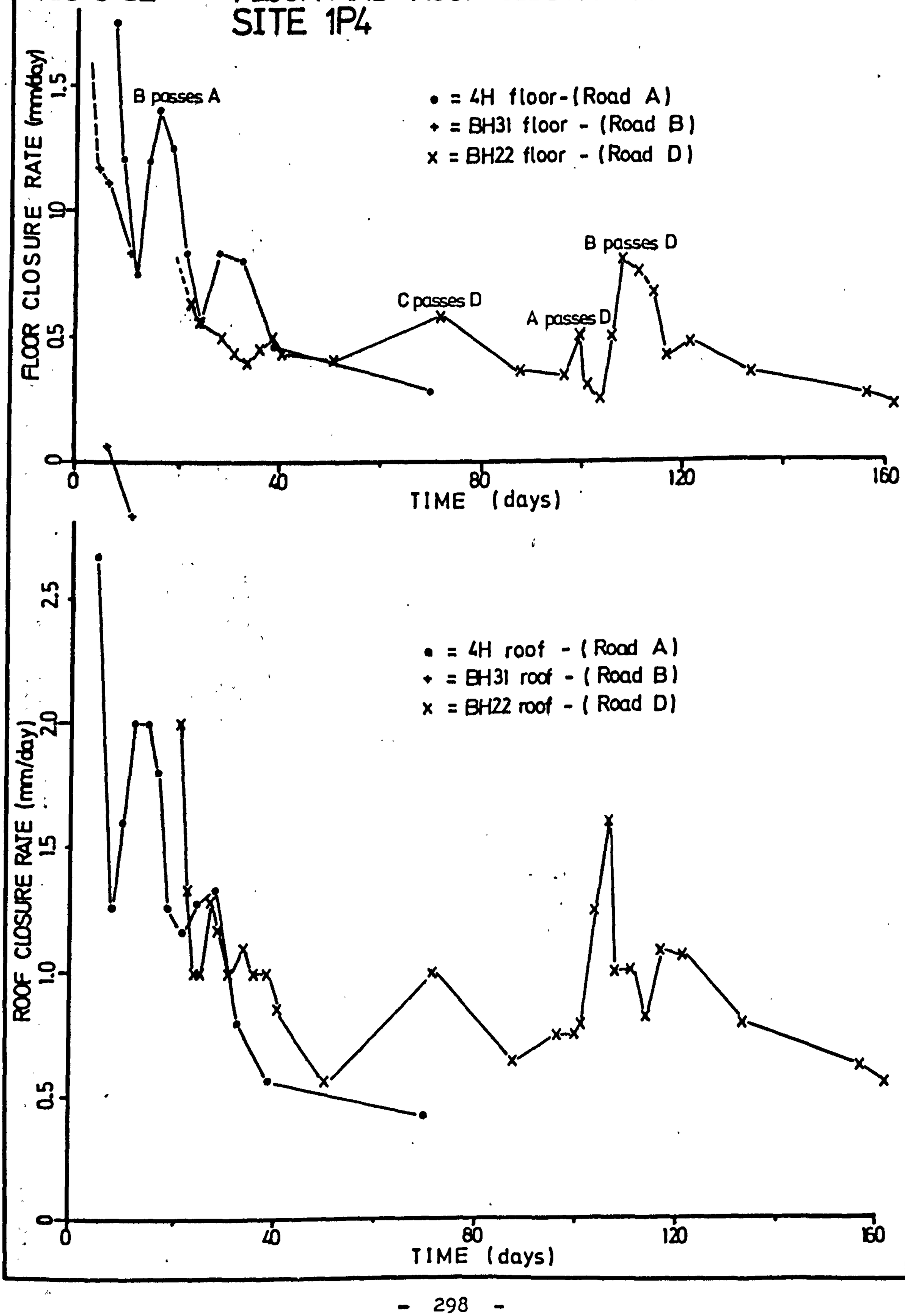

FIG. 8-33 CPL BOULBY MINE

SITE 1P4 D BH23

WALL HOLE 25.00M DEEP

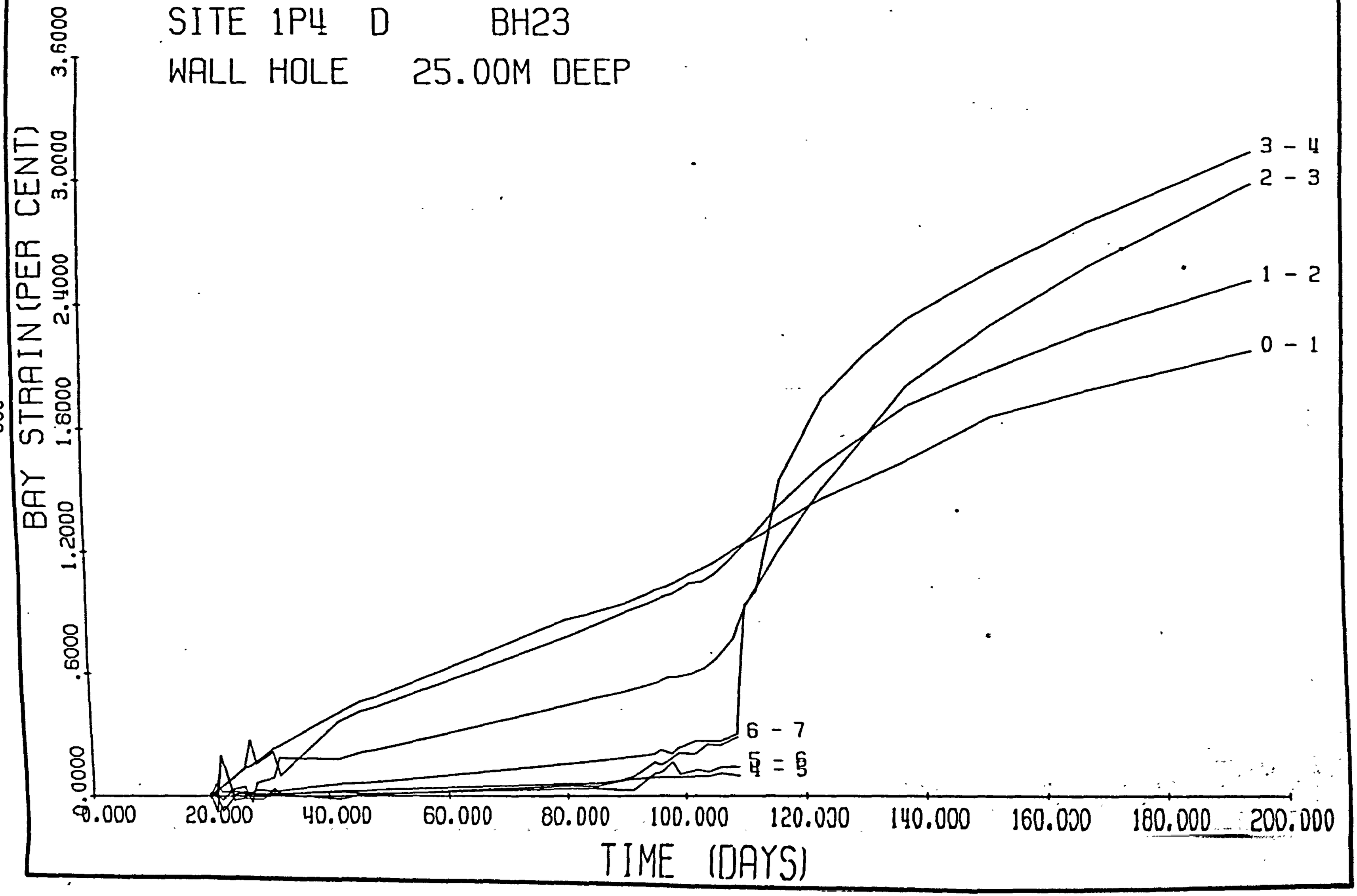

FIG. 8-34 LATERAL STRAIN RATES INDUCED IN PILLARS AT TIME PERIODS AFTER CREATION OF EACH NEW PILLAR WIDTH (sections facing East)

(The columns of number of days indicate the sequence of curves below each arrow.)

SITE 1P4

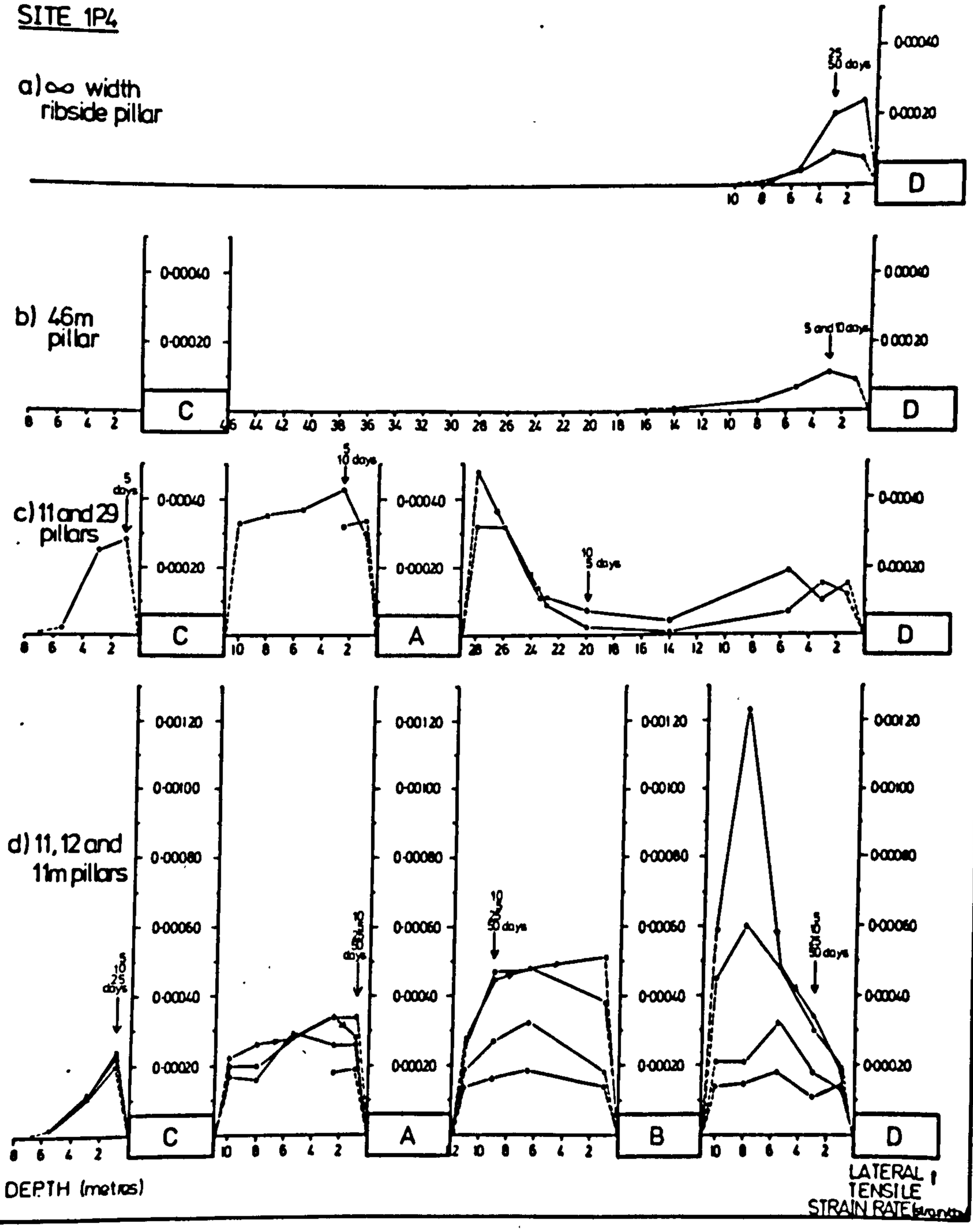

zone. The three narrow pillars all indicate high strain rates across the full pillar width. These do show some reduction with time although they are still very high even after 50 days.

The overall condition of the site initially showed some stress redistribution effects, however the pillars did not appear to be narrow enough to yield rapidly, and they continued to carry load. Conditions eventually deteriorated in all roadways. The combination of bad geology and excessive pillar widths appears to have caused excessive closure effects and roadway deterioration.

Fig. 8-35 (a,b,c) shows the progressive deterioration in roof conditions in the flank road, C. These photos were taken approximately 15 days, 71 days and 226 days after the date of excavation. Fig. 8-36 shows the presence of shale in the immediate roof in the form of large slickenside planes, and as a buckled failure due to horizontal stresses. Fig. 8-37 shows the effects of closure on a ventilation stopping in road D, and also the condition of No. 2 cross-cut along the western end of the site. The considerable yield and influence of a softer roof material is evidenced by the outward sloping narrow pillar side on the left (between A and B) compared with that on the right which is a 40m pillar.

8.3.5 Sites 1P7, 1P8, 1P9

The layout for these sites is shown in Fig. 8-38, the site being located in the south east of No. 1 panel. The sites are all pillar dimension and stress relief experiments carried out by the mine. Once again, although most of the roadways had some potash in

c.

b.

a.

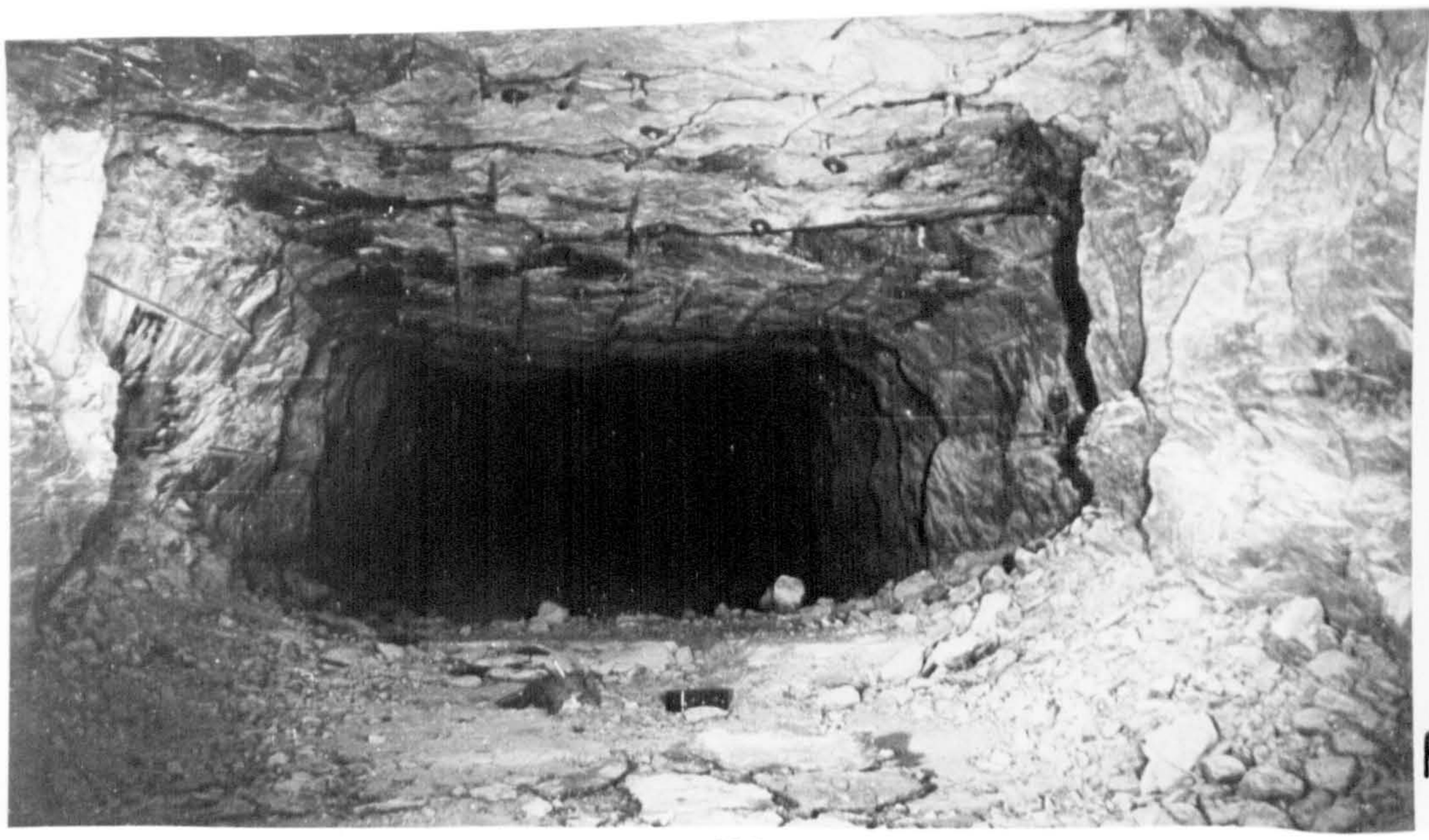

FIG. 8-35

FIG. 8-36

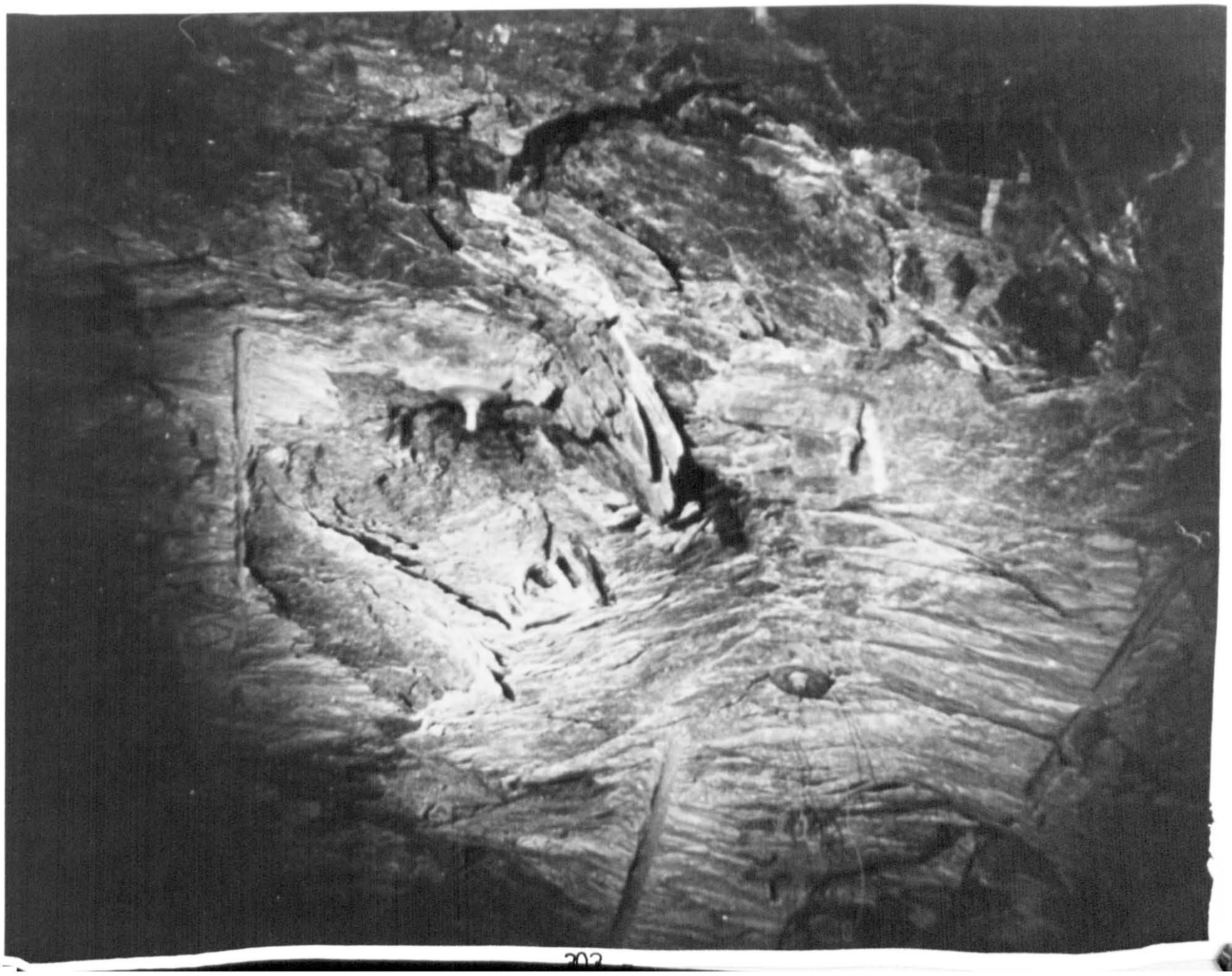

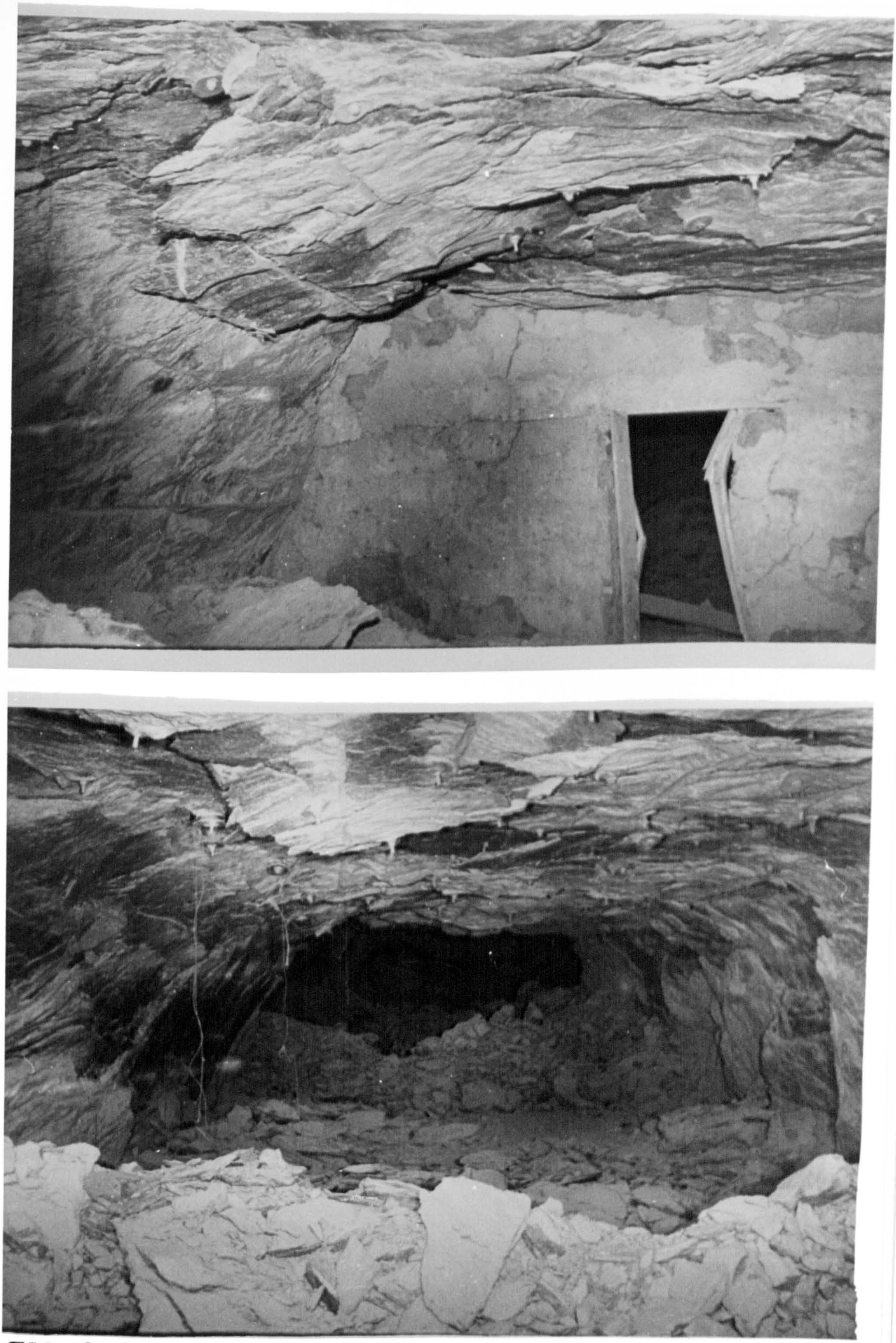

FIG. 8-37

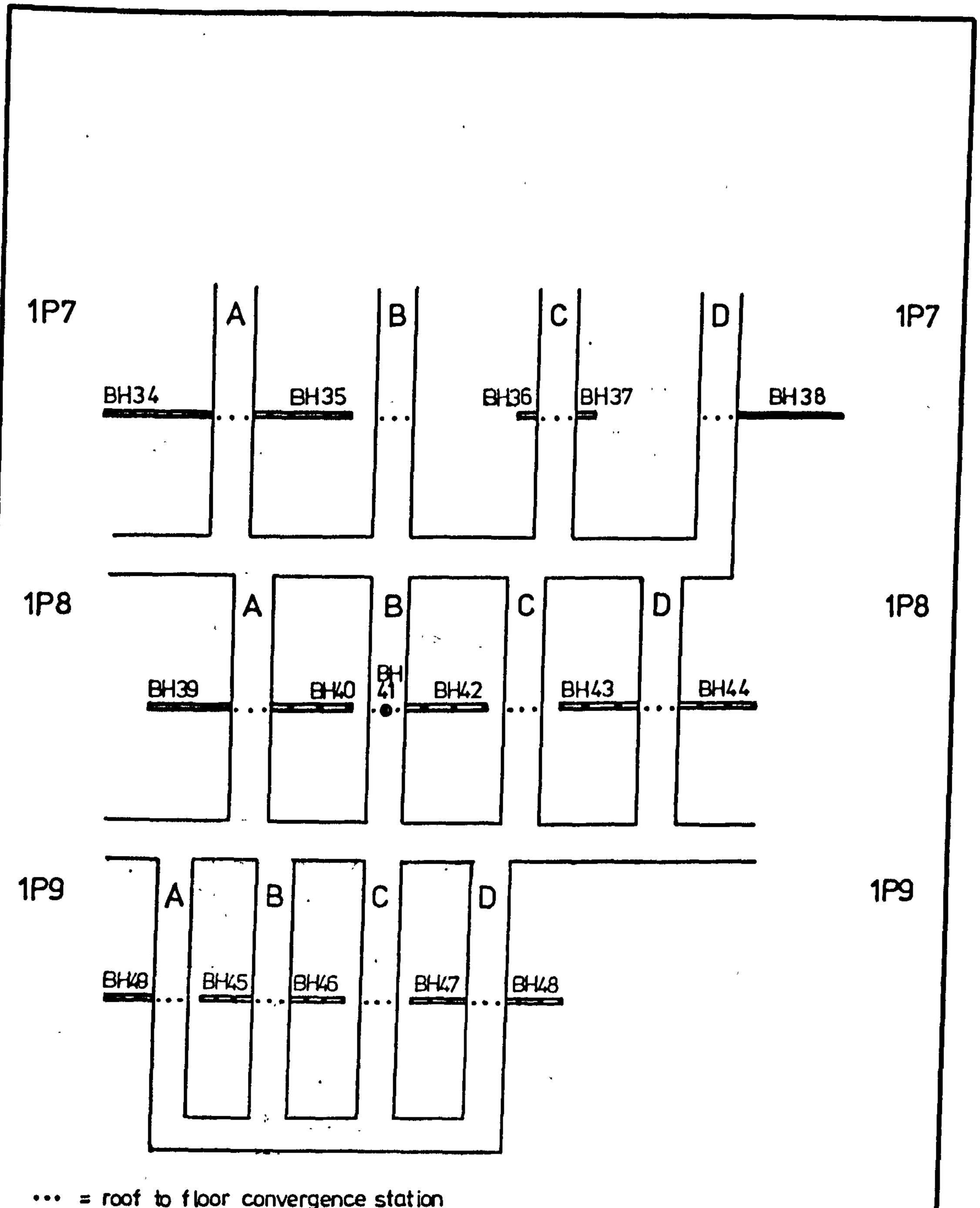

FIG. 8-38 LAYOUT OF 1P7, 1P8, 1P9

the roof, it was only thin, and roof material was basically shale. A number of roads in this area were also influenced by gas blowholes in the shale which caused large variations in road and pillar dimensions. It was not possible to install the equipment immediately in some roads and so some initial information was lost. In all but 1P7, the sequence of mining was not correct from a stress relief point of view and the results should be interpreted in the light of this. The sequence and the relative timing between mining each road is indicated on the result diagrams.

Site 1P7 consisted of 20m wide pillars, 1P8 of 12m wide pillars, and 1P9 of 8m wide pillars. The results of lateral strains in the pillars and total closure rates for the roads, where available, are shown in Figs. 8-39, 8-40 and 8-41.

The 1P7 results, although incomplete, indicate that the 20m pillars are definitely yielding throughout the pillar width. However, the centre of the A-B pillar shows some confinement rendering it too stiff to permit stress redistribution to take place. The fact that the pillar centre is yielding to such an extent (50μs/day after 50 days) indicates that the pillar is too narrow to have any long term strength or stability due to a confined core. This dimension is therefore wrong for each of the two alternative pillar mechanisms. The pillars merely attract excessive loading and this creates bad roof and floor conditions. The site was abandoned due to the deteriorating conditions.

The 1P8 results, however, show definite signs of stress relief at least in the initial stages represented by these results.

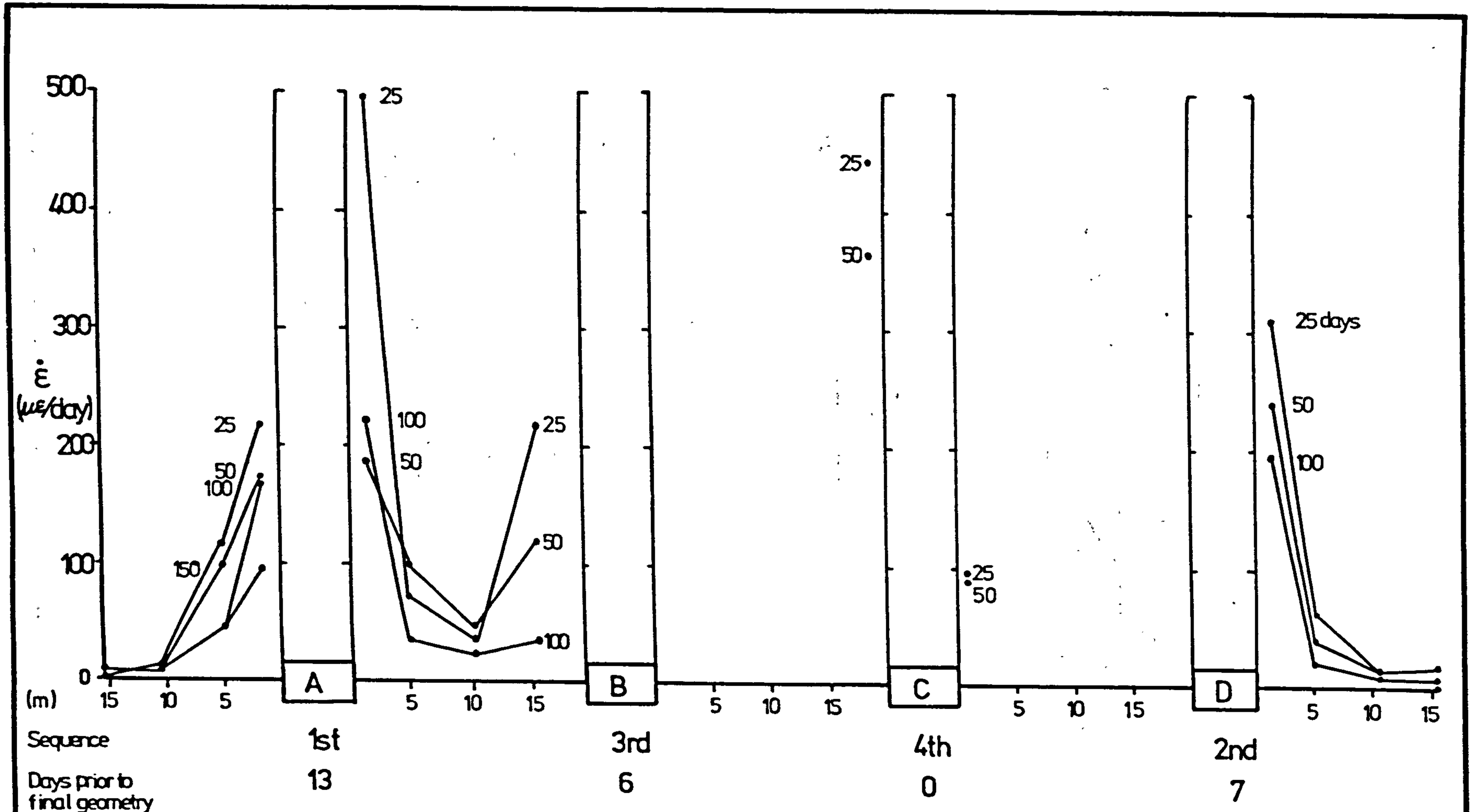

FIG. 8-39 1P7 RESULTS

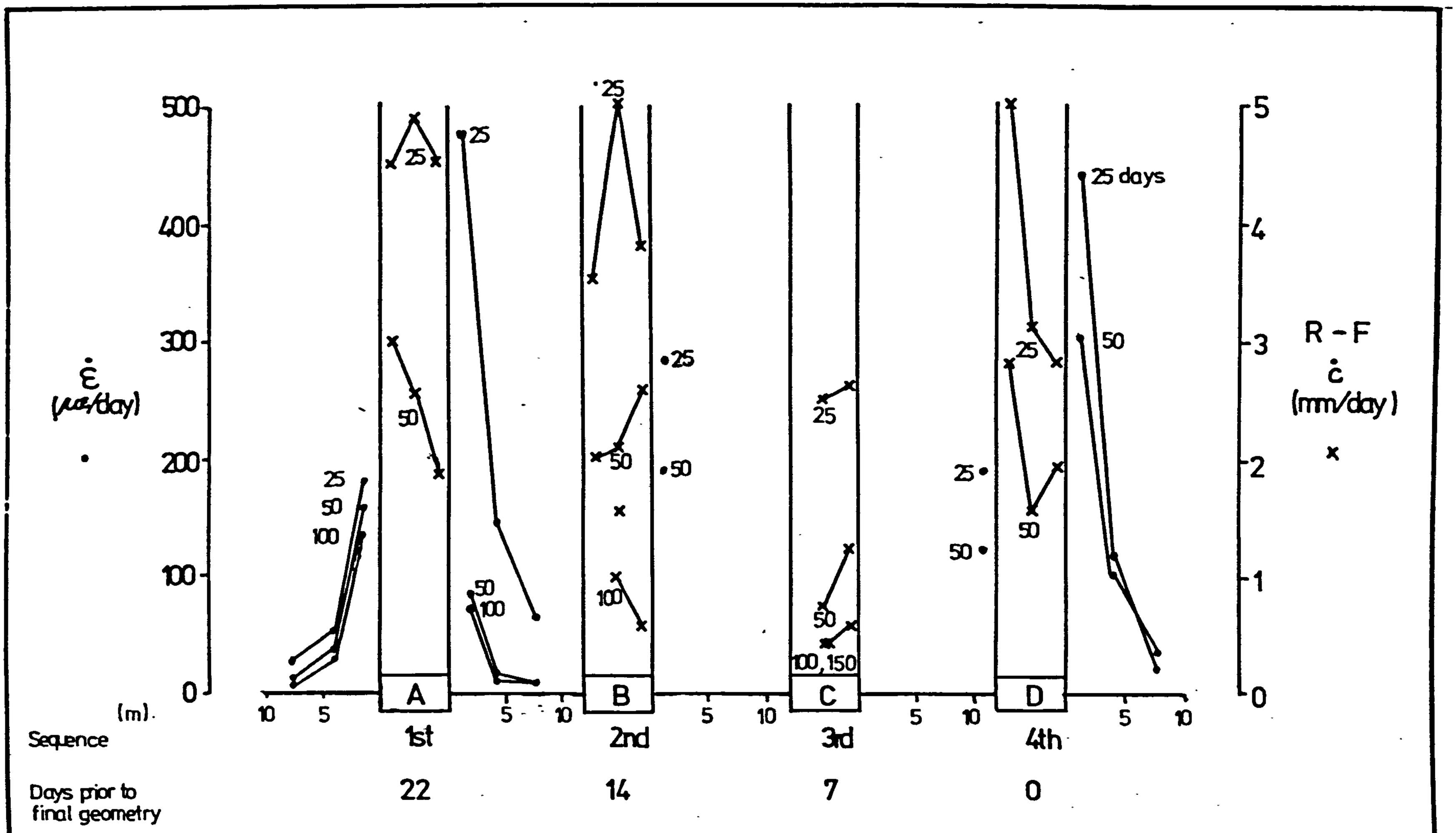

FIG. 8-40 1P8 RESULTS

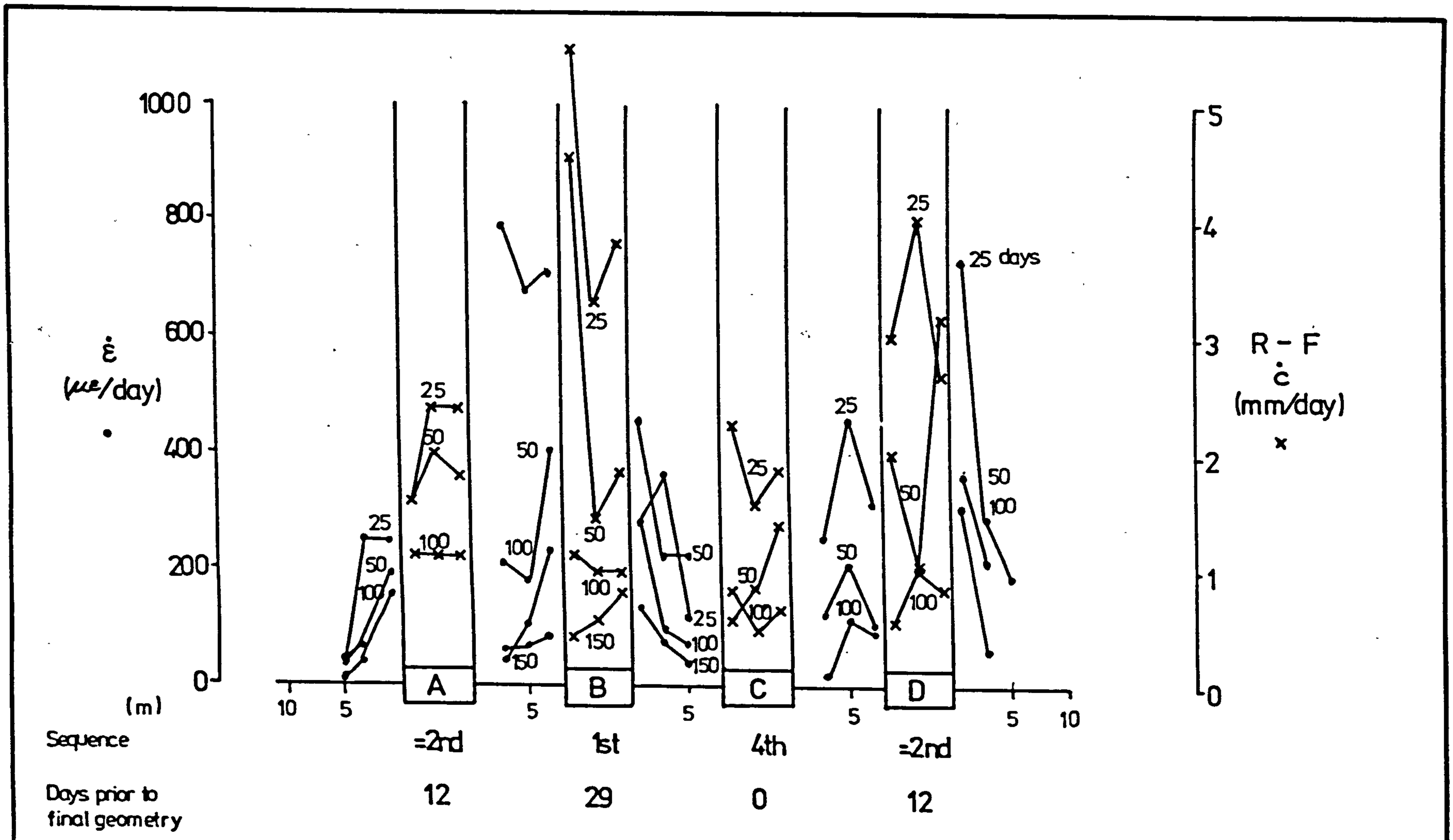

FIG. 8-41 1P9 RESULTS

Although mined third, road C is the one afforded the greatest protection due to stress redistribution, as can be seen by the road closure rates. Further evidence of load redistribution can be seen by the greatly increased ribside strain rates where the load is being carried, and the resultant high level of road closure rates in A and D, the flank roads. Although the data is incomplete, the pillar strain rates all appear to have reduced considerably, again indicating some degree of stress redistribution.

It is important to note that these pillars, and those of 1P7, contained a high shale content and many gas blowholes which have caused pillar dimensions, on average, to be reduced by several metres, in terms of load bearing width. This is why the apparent stress relief is more noticeable here than at 1P4 with similar theoretical dimensions. The 1P8 pillars should therefore be considered as roughly 8m - 9m pillars due to this geological condition.

Since the strain rates on all three pillars are less than on the ribsides after 50 days, it appears that the stress redistribution is capable of taking place over the full width of the panel, 60m in this case.

The results for 1P9, where 8m pillars of primary potash were mined, again indicate a significant amount of stress relief, at least in roadway C. The fact that B was mined first caused very high closure rates, and the 25 day strain rate to the left of B indicates a large amount of load being carried since the material formed the ribside, at least until A was mined.

Apart from the incorrect sequencing, road C shows definite

stress relief with low closure rates and relatively low strain rates in the adjacent pillars. The rates for B and the adjacent pillars have eventually decreased after 50 days, although the initial high strain and closure rates no doubt caused a lot of bad ground conditions.

It therefore appears that, apart from instability and high levels of yield in the vicinity of B, due to wrong sequencing, this site is showing stress relief effects. It is interesting to note that the total amount of lateral pillar strain for the C - D pillar was 1.29% after 25 days, 1.69% after 50 days and 2.26% after 100 days. Although the first few days were missed and so these strains are not total, as the borehole 47 results in Appendix B show, the level of deformation, and hence strain, has flattened off considerably after the first 25 days. This is another indication of a stable stress relief condition where the pillar has yielded, shed load, and then stabilised. Applying a zero volumetric strain criterion, the amount of vertical pillar yield has not been much more than 2% to create the stress relief condition. Referring back to the 1P8 results, neither borehole 42 or borehole 43 have shown a similar significant flattening off in terms of deformation against time. Therefore even if a stress relief situation has developed at 1P8, the pillars are still continuing to yield under high loading, resulting in excessive subsidence effects. The slightly greater pillar widths could account for the extra loads being carried by these pillars.

8.4 No. 2 Panel Results

These sites, 2P1 and 2P2, were another investigation of yielding

pillar and stress relief systems. The layout is shown in Fig. 8-24. Only three parallel roads were driven here, with angled cross-cuts into the solid ribside. The pillar widths were nominally 8m. However

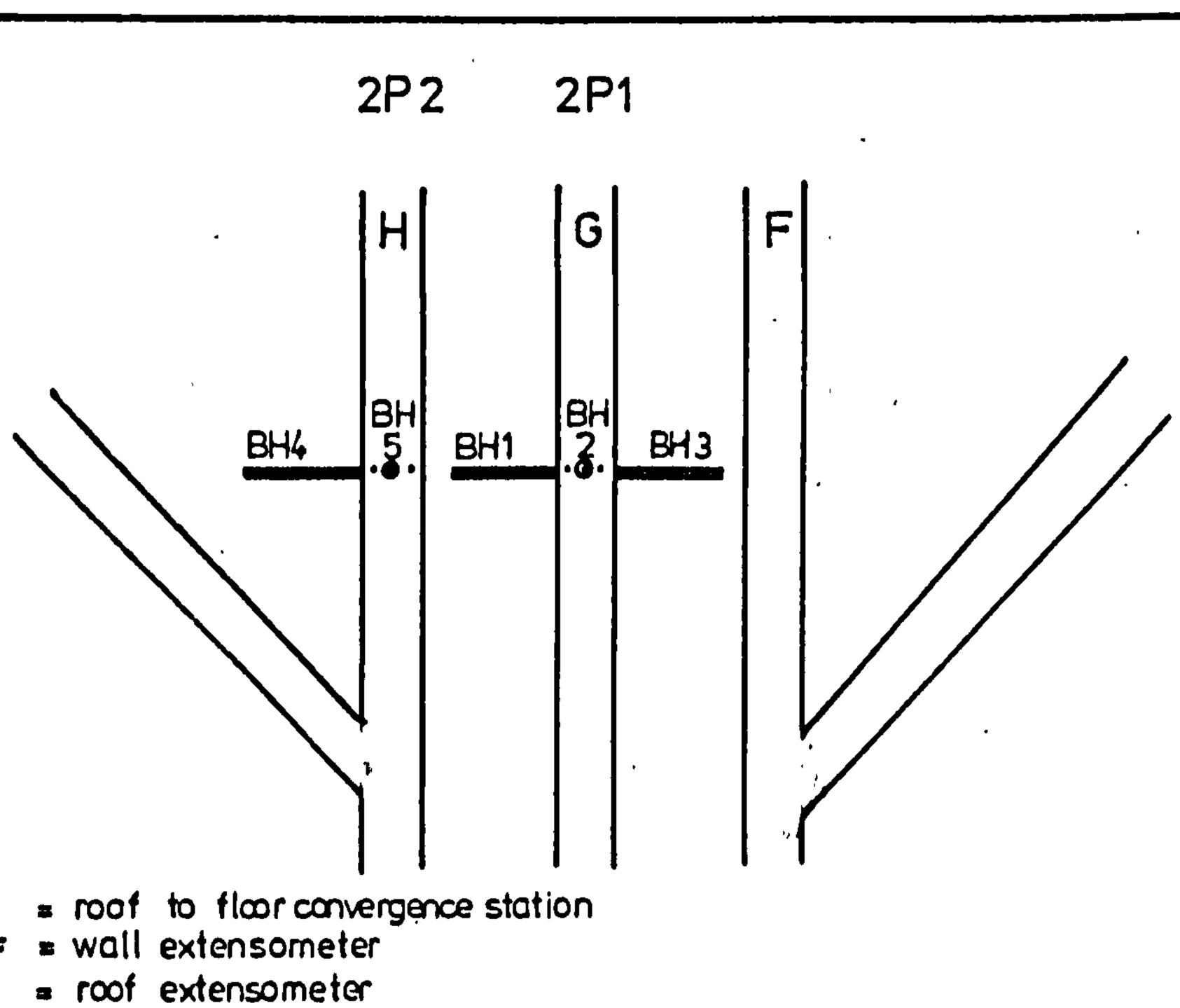

FIG. 8-42 LAYOUT OF 2P1, 2P2

again the geological influence of gas blowholes in the shale content of the pillars effectively reduced the widths to about 6m. The immediate roof at these sites was a combination of primary potash and shale.

The results from sites 2P1 and 2P2 are presented in the same format as previously, in Fig. 8-43. These do not show any similarity with those of 1P9, particularly in terms of magnitude. Although there has been a reduction in strain and closure rates suggesting some stress redistribution, the level of strain in the pillars is extremely high even

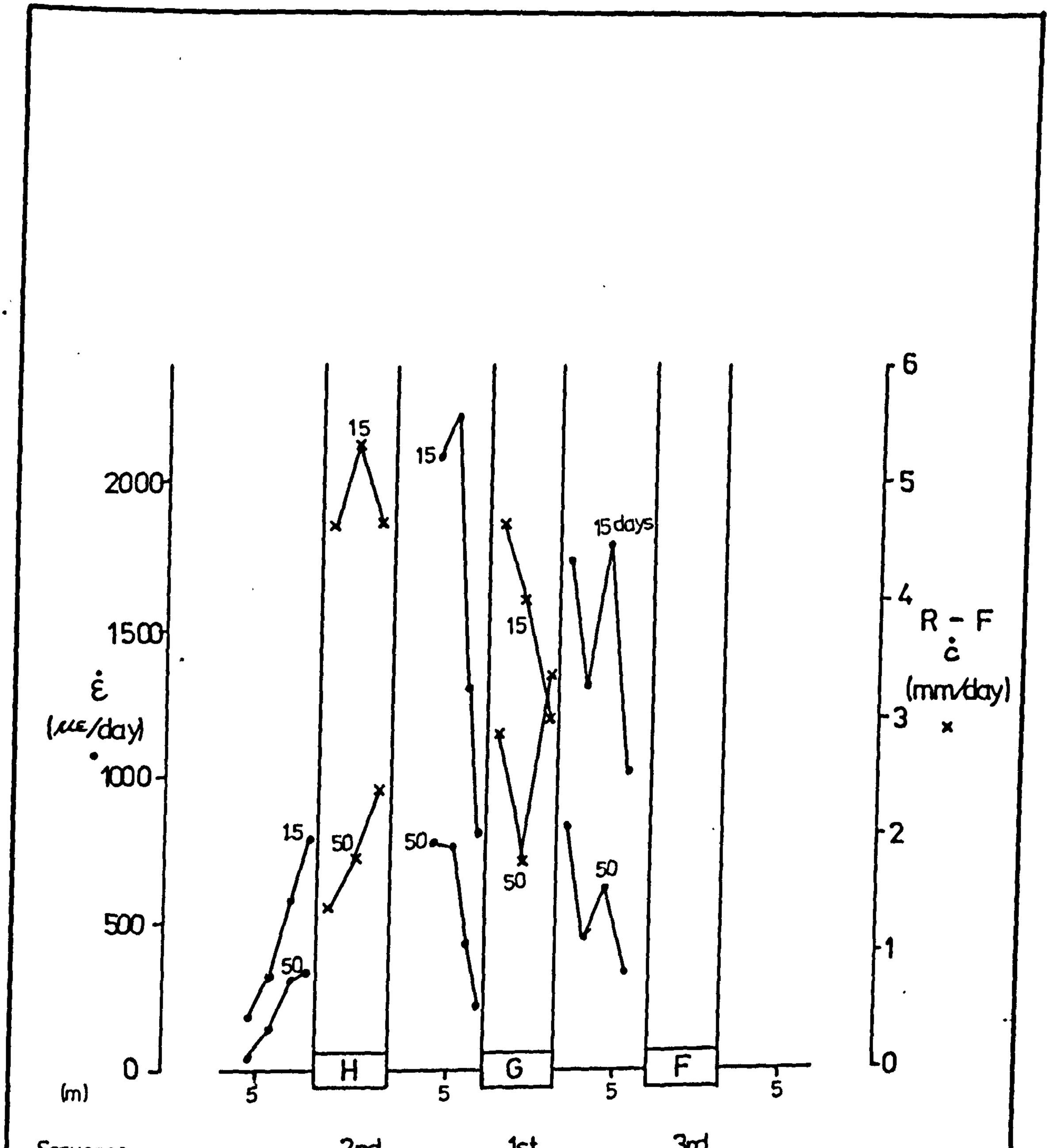

Sequence	2nd	1st	3rd
Days prior to final geometry	2	4	0

FIG. 8-43 2P1, 2P2 RESULTS

at 50 days and the closure rates are more than double those of 1P9C. The pillar strains from boreholes 1 and 3 at 15 days were 1.45% and 1.57%, but by 50 days they had reached 3.70% and 3.99%.

Visual inspection of the site indicates very good roof conditions as a result of some stress relief, but the amount of closure which has taken place is extremely high and not showing any sign of further decrease in rate. This must be creating far higher levels of subsidence above the panel than if the system had stabilised correctly.

There are a number of possible mechanisms which may have caused this continuing high closure. Firstly, the reduced pillar sizes would initially create excessive yield, but if a complete stress redistribution had taken place, even 6m pillars should have shown greatly reduced strain and closure rates with time. The wrong sequence of mining the panel would also have had a major detrimental effect on closure rates, but again, as in 1P9, once the final geometry existed, the system should have stabilised. The cross-cuts mined into the ribsides were extended at least 30m either side of the panel so that the effective panel width was approaching 100m. This excessive width definitely would have caused some reloading of the central area of the panel. The only other possible mechanism would be that suggested from the theoretical work in Chapter 4. The high deviator stresses in the shale and marl above the panel could have caused failure of the redistributed pressure arch and continual reloading of the panel area. A combination of these last two mechanisms seems to be the most likely cause of the extremely high closures in No. 2 panel.

8.5 South Development Results

A series of sites was planned to extend across the full width of the southern development panel. These were to monitor closure and lateral deformation in order to correlate with the theoretical work on panel layouts and relative pillar loading. Unfortunately, not all the stations could be installed and due to drilling problems, most of the sites, SD1 to SD7, were installed late and so the main objective of the exercise was defeated. However, some results were obtained and these have provided information on individual pillar stability. The site layout is shown in Fig. 8-44. The central section of the development is in halite, below the potash, and so the pillars, H - G and G - F, can be regarded as halite pillars. Although parts of the other pillars are in halite, they are predominantly potash pillars with a halite floor. The pillars all form a row across a 7 entry, 40m herringbone panel.

Fig. 8-45 shows the results from the six extensometers which were functioning correctly. The total closure rates for the road centre stations are shown at 100 days. The ribside pillars appear to be carrying higher loading than those in the panel centre. However, the fact that the central pillars are in salt means that strain rates for equivalent loading will be lower due to the lower creep rates of halite compared to potash.

Fig. 8-46 shows the detailed strain rate distribution obtained from boreholes 4 and 5, through pillar J - H, at 50 and 100 days. This clearly shows some degree of straining through the entire width of the 40m pillar although at least the central 25m is considerably confined.

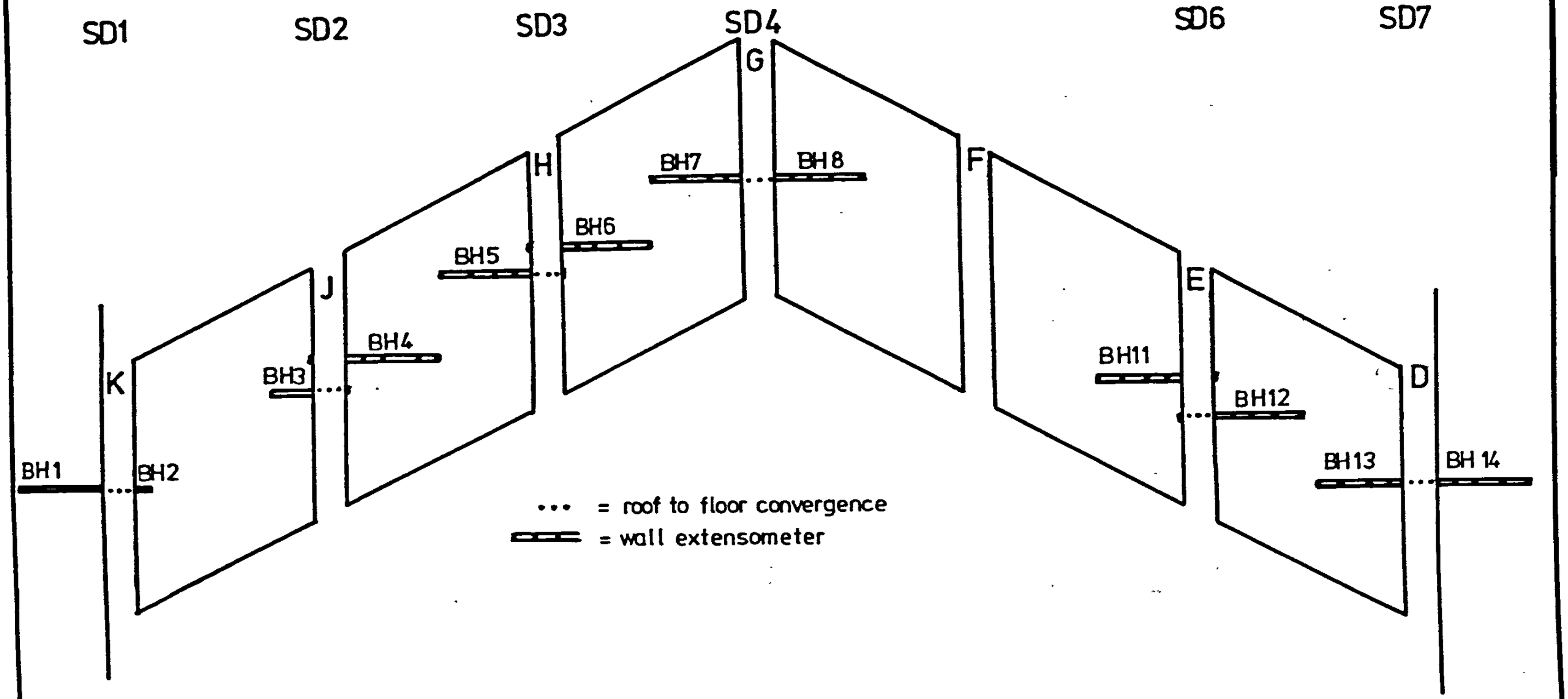

FIG. 8-44 SOUTH DEVELOPMENT LAYOUT

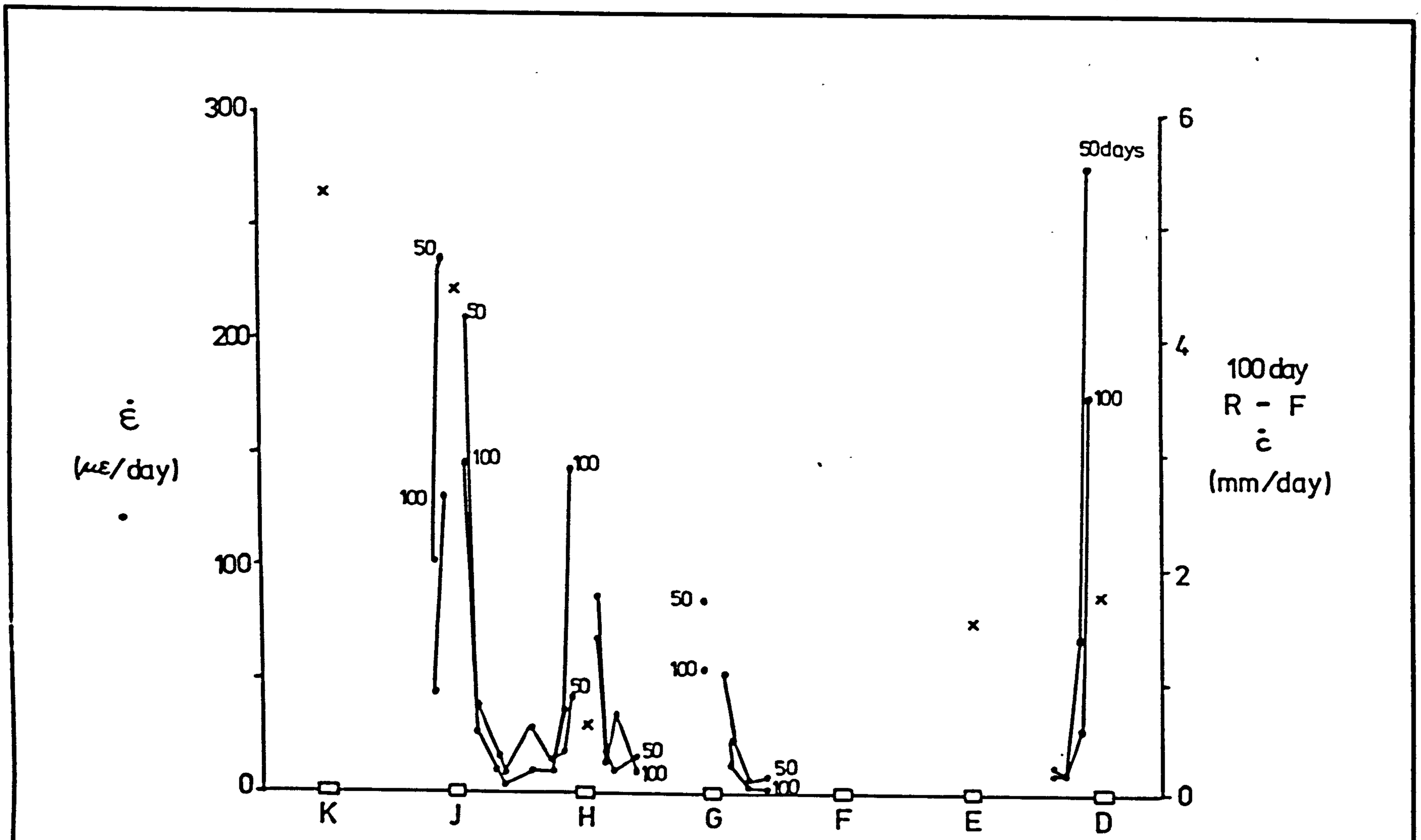

FIG. 8-45 SOUTH DEVELOPMENT RESULTS

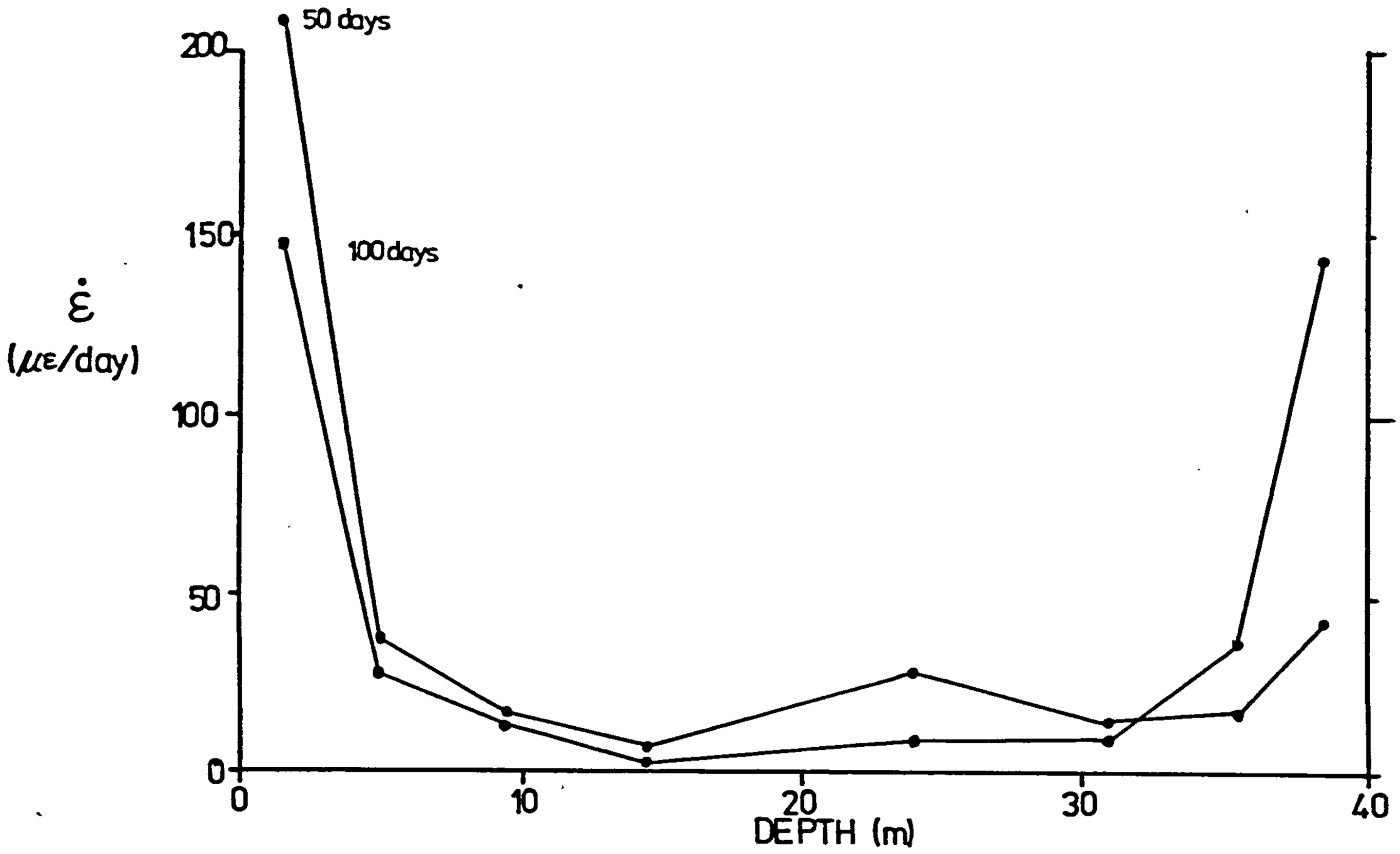

FIG. 8-46 J-H PILLAR STRAIN RATES

In order to estimate the average vertical strain and deformation for a 40m pillar, using the same approach as for the 60m pillars, Fig. 8-47 shows a plot of the natural logarithm of the 0 - 4 bay, smooth strain rate against time, for boreholes 4 and 8. These represent

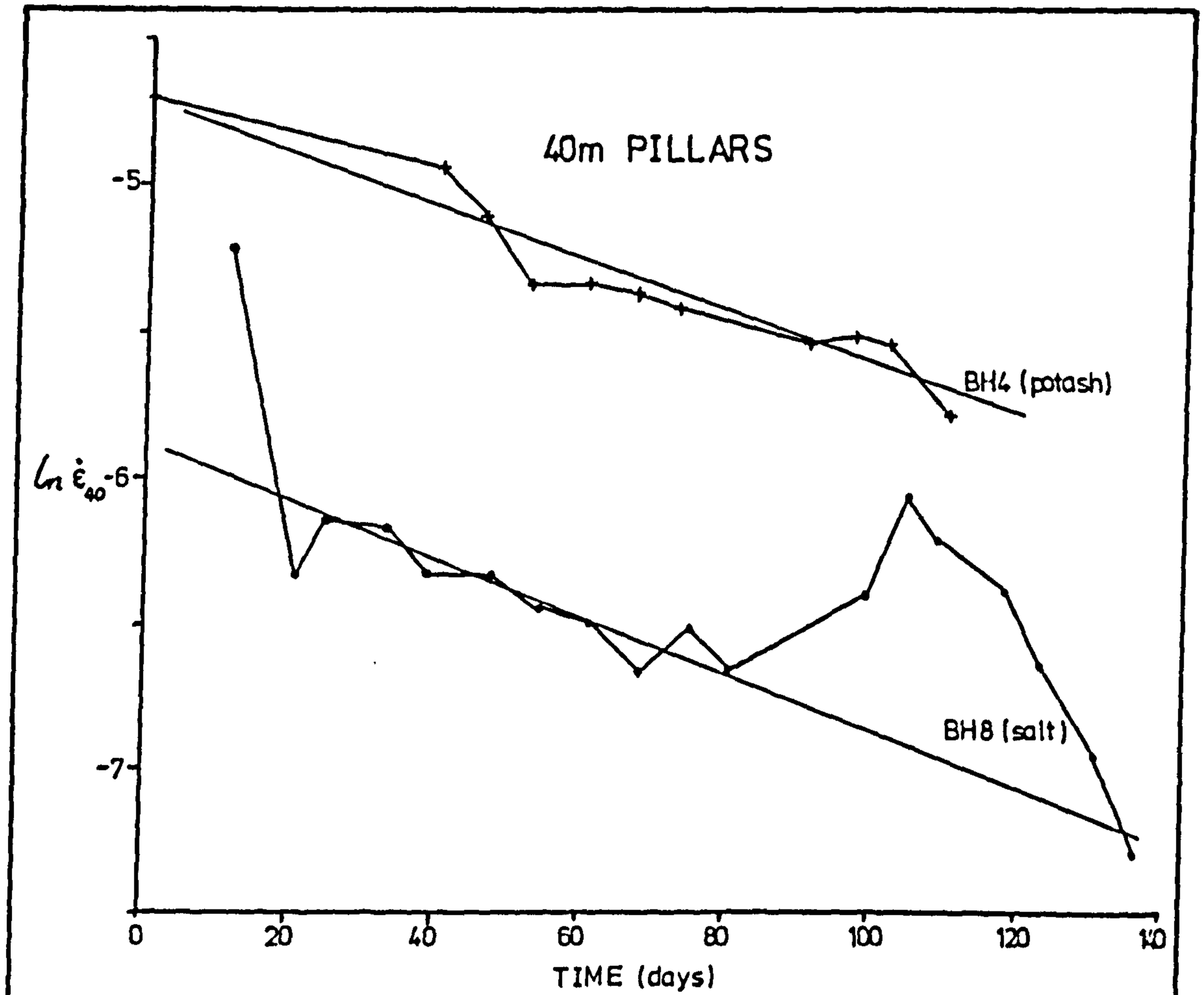

FIG. 8-47 $\ln \dot{\varepsilon}_{40}$ v. TIME

40m potash and halite pillars, respectively. Once again these results can be defined as linear relationships, although there are a number of fluctuations, particularly with borehole 8 which appears to have been reloaded, then unloaded, between 100 and 120 days (July, 1976).

The linear relationships indicated by Fig. 8-47 are defined as,

$$\ln \dot{\varepsilon}_s = -0.00873t - 4.725 \qquad (8.13)$$

for the potash pillar, and

$$\ln \dot{\varepsilon}_s = -0.00984t - 5.900 \qquad (8.14)$$

for the salt pillar.

These reduce to

$$\dot{\varepsilon}_{potash} = 0.008871\, e^{-0.00873t} \qquad (8.15)$$

and

$$\dot{\varepsilon}_{salt} = 0.002739\, e^{-0.00984t} \qquad (8.16)$$

which, when integrated, give

$$\varepsilon_{40(potash)} = 1.0162(1 - e^{-0.00873t}) \qquad (8.17)$$

and $$\varepsilon_{40(salt)} = 0.27835(-e^{-0.00984t}) \qquad (8.18)$$

These final two equations represent the average strain across the full width of 40m pillars of potash and salt. By the same zero volumetric strain criterion as used previously, for 3.4m high pillars, the vertical pillar deformations may be defined by

$$d_{40(potash)} = 0.03455(1 - e^{-0.00873t}) \qquad (8.19)$$

and $$d_{40(salt)} = 0.009464(1 - e^{-0.00984t}) \qquad (8.20)$$

Using the above equations and the 150 day changeover tc steady state yield, the potash pillars will deform by 25.2mm in 150 days then

at a rate of 0.0814mm/day (23.95$\mu\varepsilon$/day), i.e. 42.6mm in the first year and 29.7mm in subsequent years.

The 40m salt pillars, however, are far more rigid and deform by only 7.3mm in 150 days, then 0.0213mm/day (6.26$\mu\varepsilon$/day), or 11.8mm in the first year and 7.8mm in subsequent years. In order to relate these to surface subsidence effects, a weighted average for two salt and 4 potash pillars across a panel gives a deformation of 32.3mm in the first year and 22.4mm in subsequent years.

8.6 East Panel Results

The east panel sites are located in the 9 entry, 25m square pillar section of No. 1 panel. Once again it was intended that the full width of the panel be instrumented, as planned for the south development, but again this did not eventuate. Only three sites were established and within these, only a limited number of stations were installed. Fig. 8-48 shows the layout of the sites installed.

The geology at these sites varied across the panel but in general a shale roof predominated with shale also occurring in the primary potash at floor level in some locations.

Fig. 8-49 shows the lateral strain rate profile across the panel for the pillars instrumented. These results indicate, at least initially, that the loading across the panel is distributed with a maximum in the centre. The low load on the ribside pillar indicates that the panel width is not excessive. The ribside pillar between the East conveyor road and road C does not appear to be carrying a

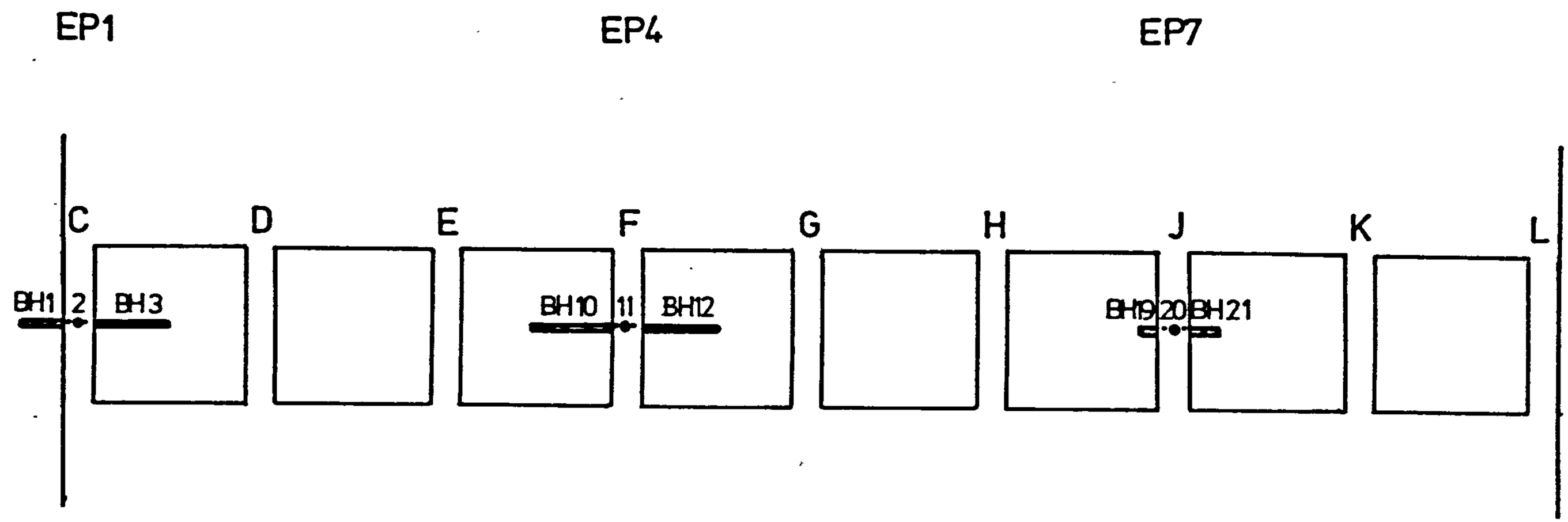

FIG. 8-48 EAST PANEL LAYOUT

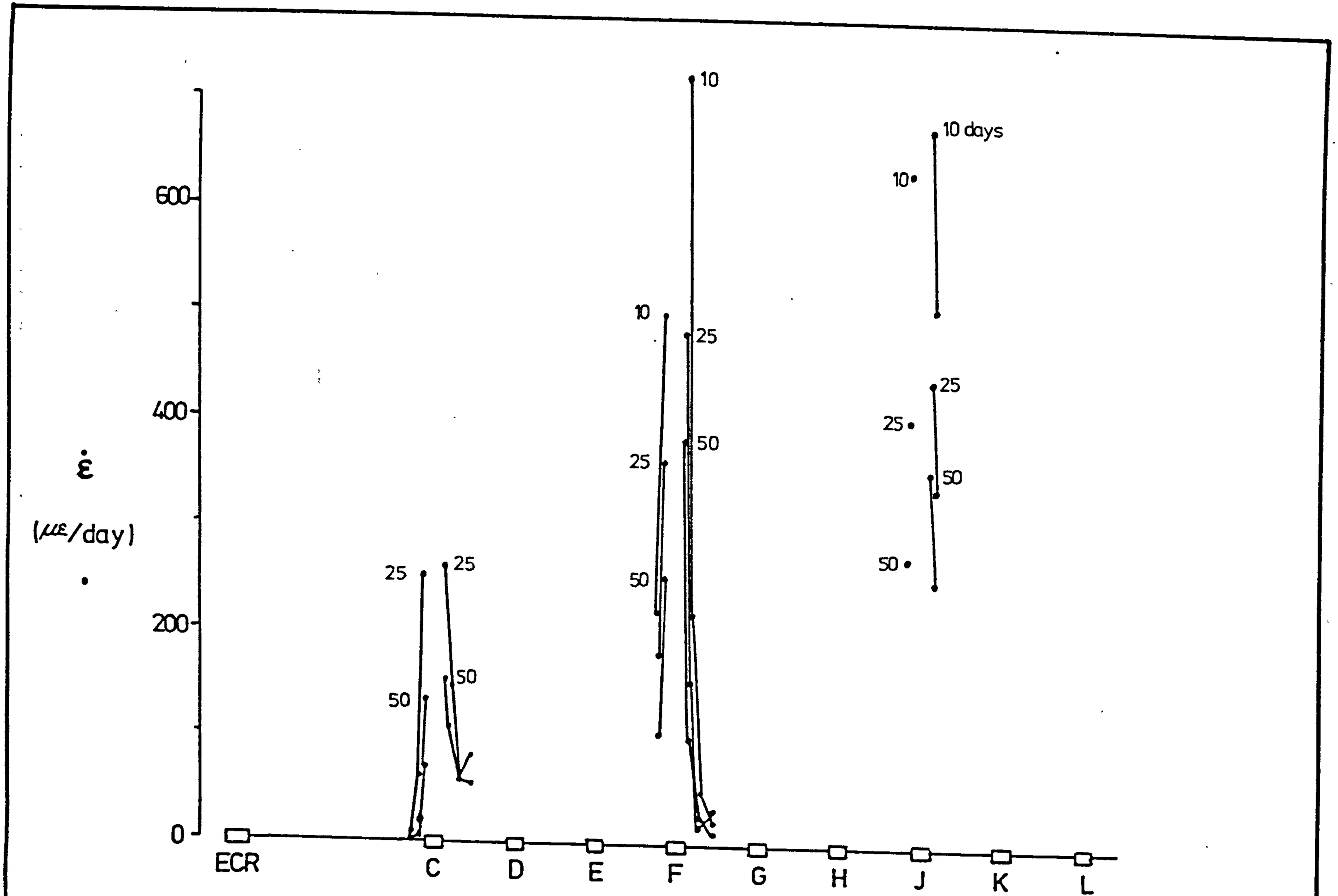

FIG. 8-49 EAST PANEL RESULTS

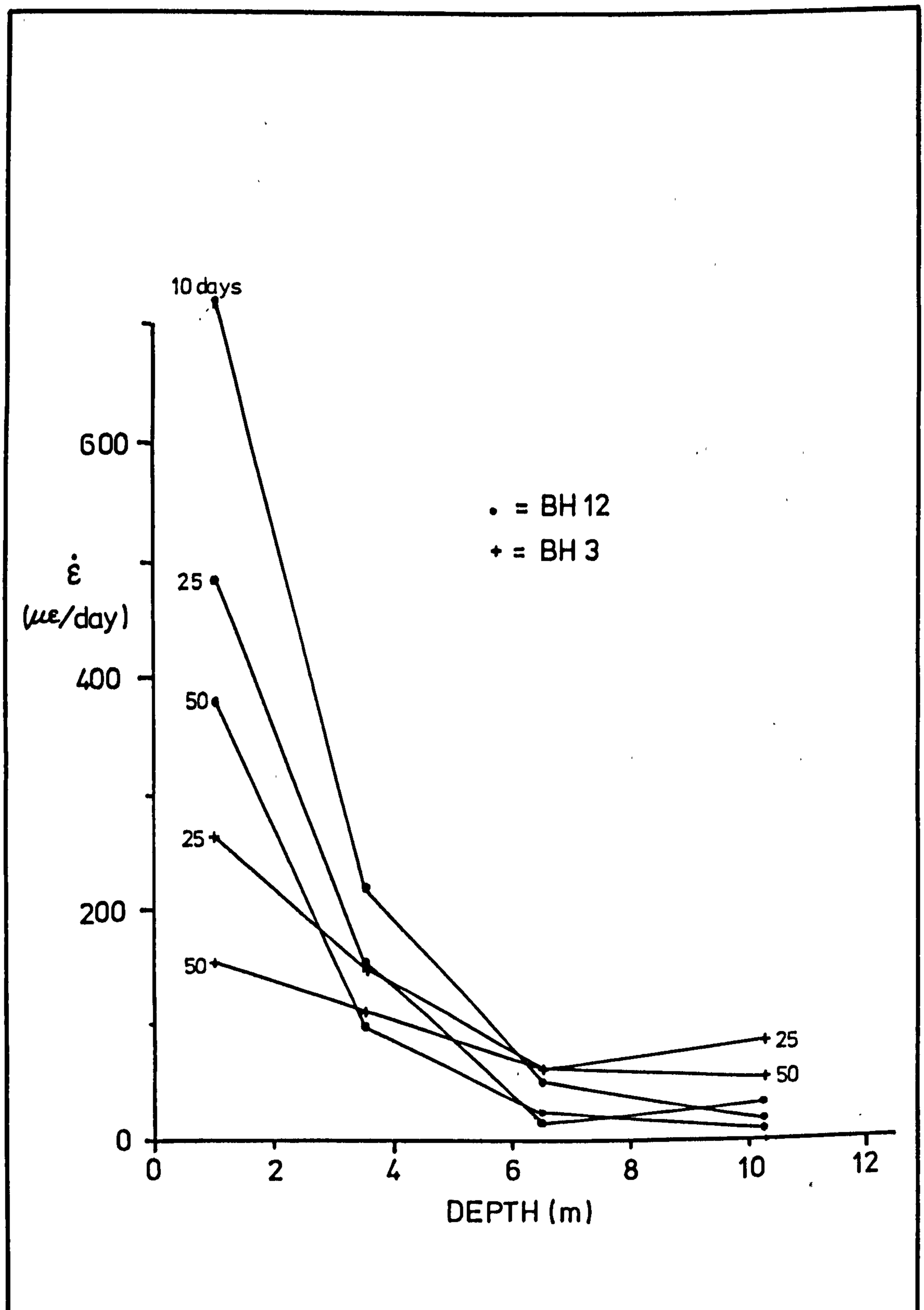

FIG. 8-50 STRAIN RATE v. DEPTH
25m PILLARS

large amount of load. This confirms the theoretical conclusion that the panel pillars carry virtually the entire cover load and so large barrier pillars are not necessary.

Fig. 8-50 shows a detailed profile of strain rates against borehole depth for borehole 3 and 12, in pillars C - D and F - C. It is apparent from these plots that the high strain rates in the panel centre (borehole 12) are only a surface effect and the overall strain distribution is fairly similar to that of the ribside pillar. The confined pillar core does not appear to be more than about 10m in width even after 50 days. Therefore this pillar size (W:H ratio 7.4) should be considered as the smallest size capable of maintaining a reasonable core. These pillars should be closely monitored to establish the long term condition of the pillar core.

Fig. 8-51 is a plot of the $\log_e$ smooth strain rates against time for the 0 - 4 bays of boreholes 3 and 12. These coincide almost

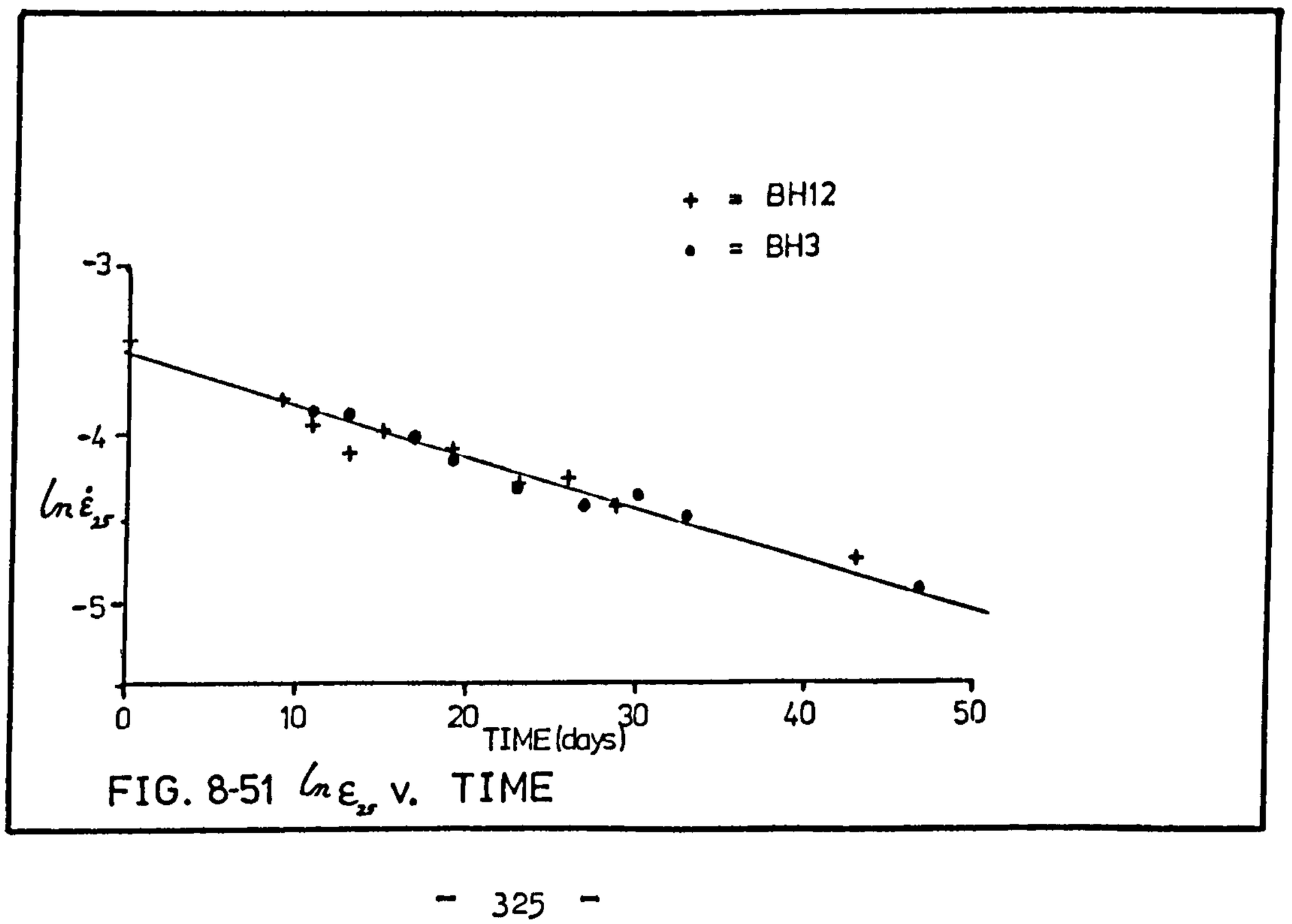

FIG. 8-51 $\ln \varepsilon_{25}$ v. TIME

exactly along a straight line defined as,

$$\dot{\varepsilon}_n = -0.030t - 3.575 \qquad (8.21)$$

which can be rearranged to,

$$\dot{\varepsilon} = 0.02802e^{-0.030t} \qquad (8.22)$$

By integrating this equation, the average lateral strain for the pillar may be defined as,

$$\varepsilon_{25} = 0.9567(1 - e^{-0.030t}) \qquad (8.23)$$

For a 3.4m high pillar, on the same principle as before, the average pillar deformation can be defined as

$$d_{25} = 0.03250(1 - e^{-0.030t}) \qquad (8.24)$$

Since these pillars are much smaller than the other types considered, a changeover point of 100 days, to a steady strain rate, has been applied. On this basis the pillar deforms by 30.9mm after 100 days then at 0.0474mm/day (13.95$\mu\varepsilon$/day), i.e. 43.5mm in the first year and 17.3mm in subsequent years.

8.7 Comparison of 25m, 40m and 60m Pillars

Fig. 8-52 shows the 50 day lateral strain rates for the typical 60m, 40m and 25m pillars analysed in this chapter. This clearly indicates that although the strain rate in the first 6m of each pillar size is a function of size and load, beyond that depth the strain rates are virtually identical and greatly reduced in magnitude due to confinement. Therefore the size of the pillar core is directly related

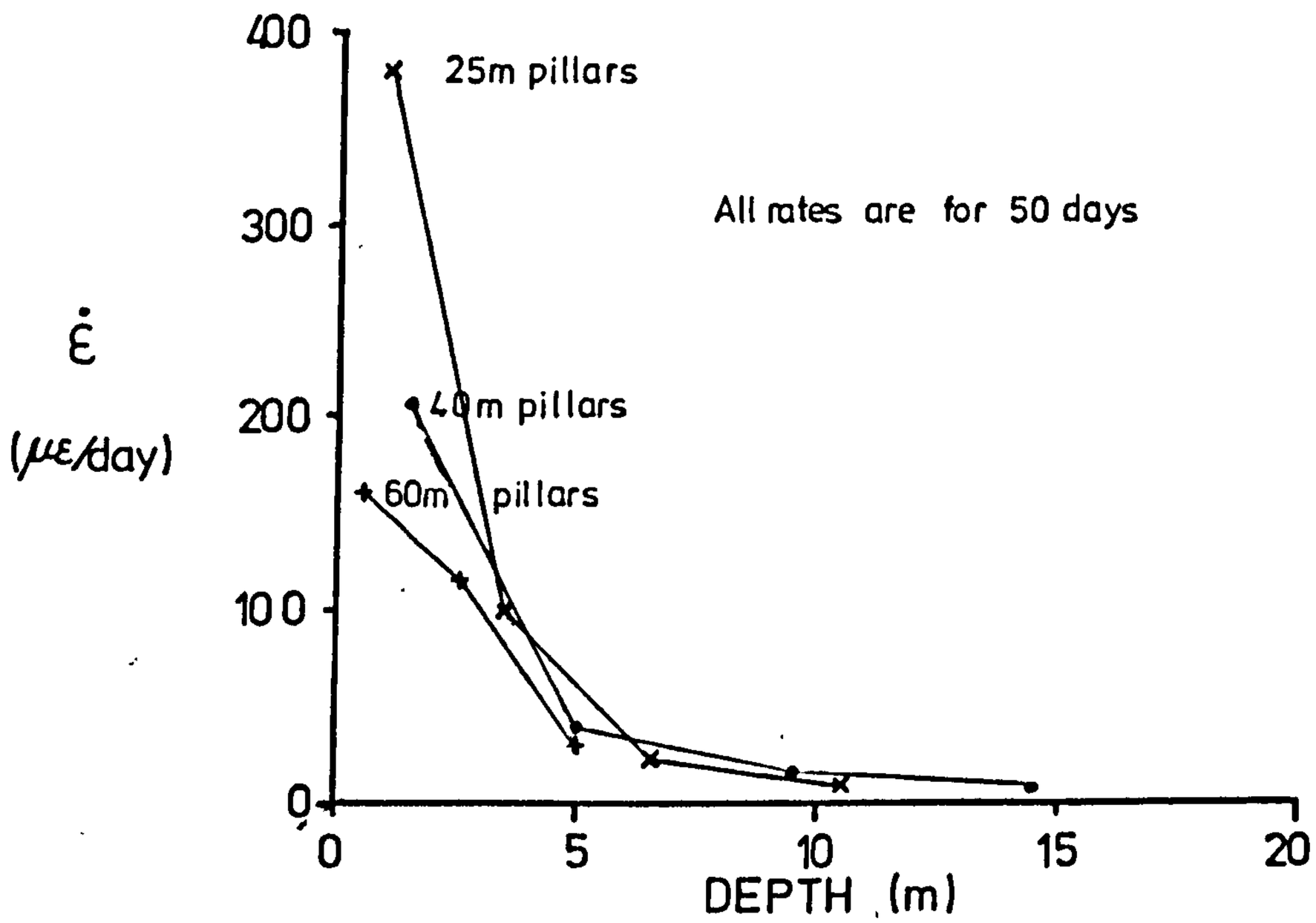

FIG. 8-52 PILLAR STRAIN RATES v. DEPTH

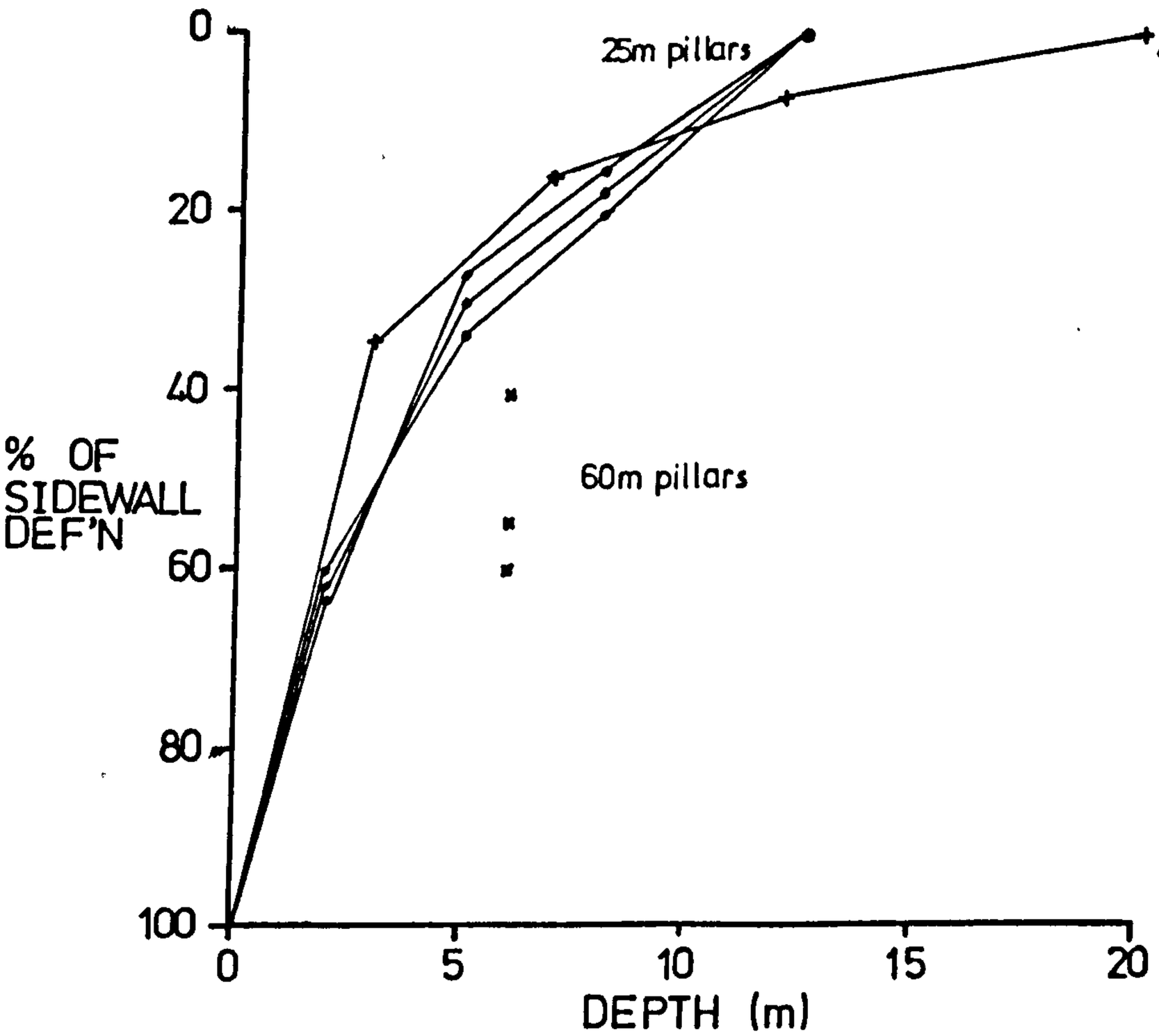

FIG. 8-53 PILLAR DEFORMATION RELATIVE TO SIDEWALL

to overall pillar size, being approximately 15m less than the minimum pillar dimension.

Fig. 8-53 also shows the presence of a confined core in each pillar size. It expresses the absolute displacement of any point at depth in terms of the sidewall displacement. This indicates that movement is occurring right to the pillar centre, at least for the 25m and 40m pillars. The steepness of the curves is a measure of the strain at any depth. Since the 25m pillar curves do not flatten any further between 5m and the pillar centre at 12.5m, then the core must be close to its minimum stable size since the strain does not decrease any further towards the centre. Pillar sizes below 25m should not be used unless within a stress relief panel.

Fig. 8-54 shows the relationship established for average pillar strain and deformation against time, for each of the pillar sizes. One point of apparent contradiction is the lower steady deformation rate of the 25m pillars compared with the 40m potash pillars. The most likely explanation for this is that the 25m pillars are in an area with shale roof and floor and so they are punching into the shale rather than yielding themselves. This is evidenced in the panel by considerable floor heave and deteriorating roof conditions. This damage to roof and floor could only be reduced by larger pillar sizes. In terms of subsidence, however, the subsidence above the 25m pillars is obviously the sum of pillar yield plus the deformation of the pillar into roof and floor. This could be considerably greater than that predicted from these curves.

The 40m salt pillars are very stable structures, even more rigid

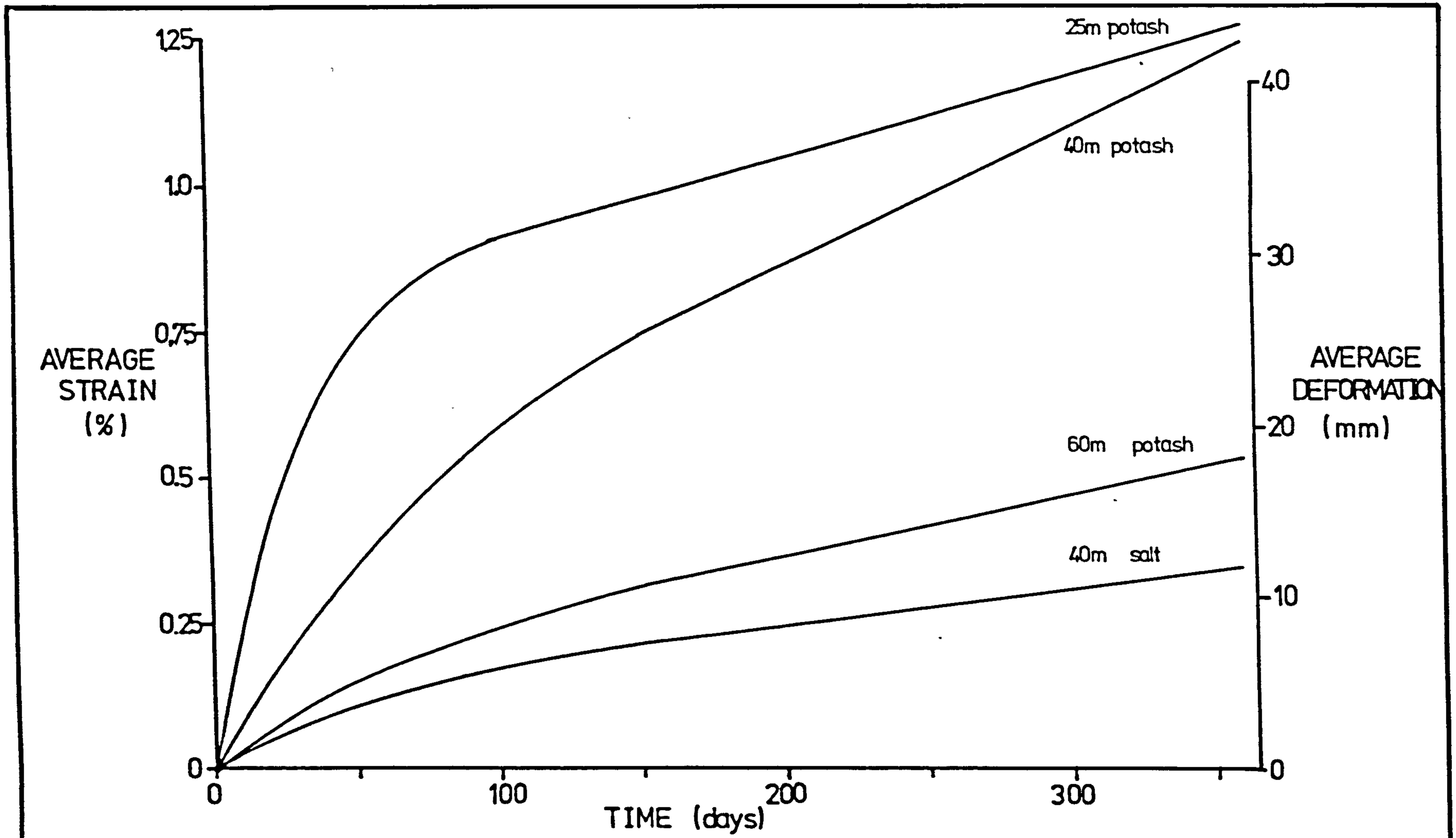

FIG. 8-54 AVERAGE VERTICAL PILLAR STRAIN AND DEFORMATION v. TIME

than the 60m potash pillars which have exhibited surprisingly high levels of yield. Some of this yield could account for cracking of the concrete shaft linings which has occurred since the shaft pillar was developed, particularly in No. 2 shaft. A series of parallel cracks which have been mapped in a section of lining between 945m and 1020m all lie in a set of parallel planes, the normal of which dips at 50° towards the south east. This part of the lining is poured in direct contact with the Upper Permian Marl and so it is likely that these cracks reflect rock movement. The normal to the planes intersects the potash seam close to site N.U.03 which also happens to correspond to the closest point of 60m potash pillars to the shaft. (It is surrounded by larger halite pillars on all other sides.) The yield of the potash pillars therefore provides a feasible explanation for these cracks, due to subsidence of the section of strata at this point in the shaft, towards the south east. The apparent limit of such subsidence is at least an angle of 40° from vertical.

8.8 Comparison of Roadway Closure Rates

From the analysis of potash road closure rates in the shaft pillar it was established that closure rates similar to those of site N.U.06 represented a maximum for long term stability. On the basis of this and other potash results shown in Fig. 8-9, an envelope of closure rates for stable conditions has been established and this is shown in Fig. 8-55. Superimposed on this envelope are closure rates from various other sites which have been discussed in this chapter. Table 8-3 lists the roof to floor closure rates for all these stations.

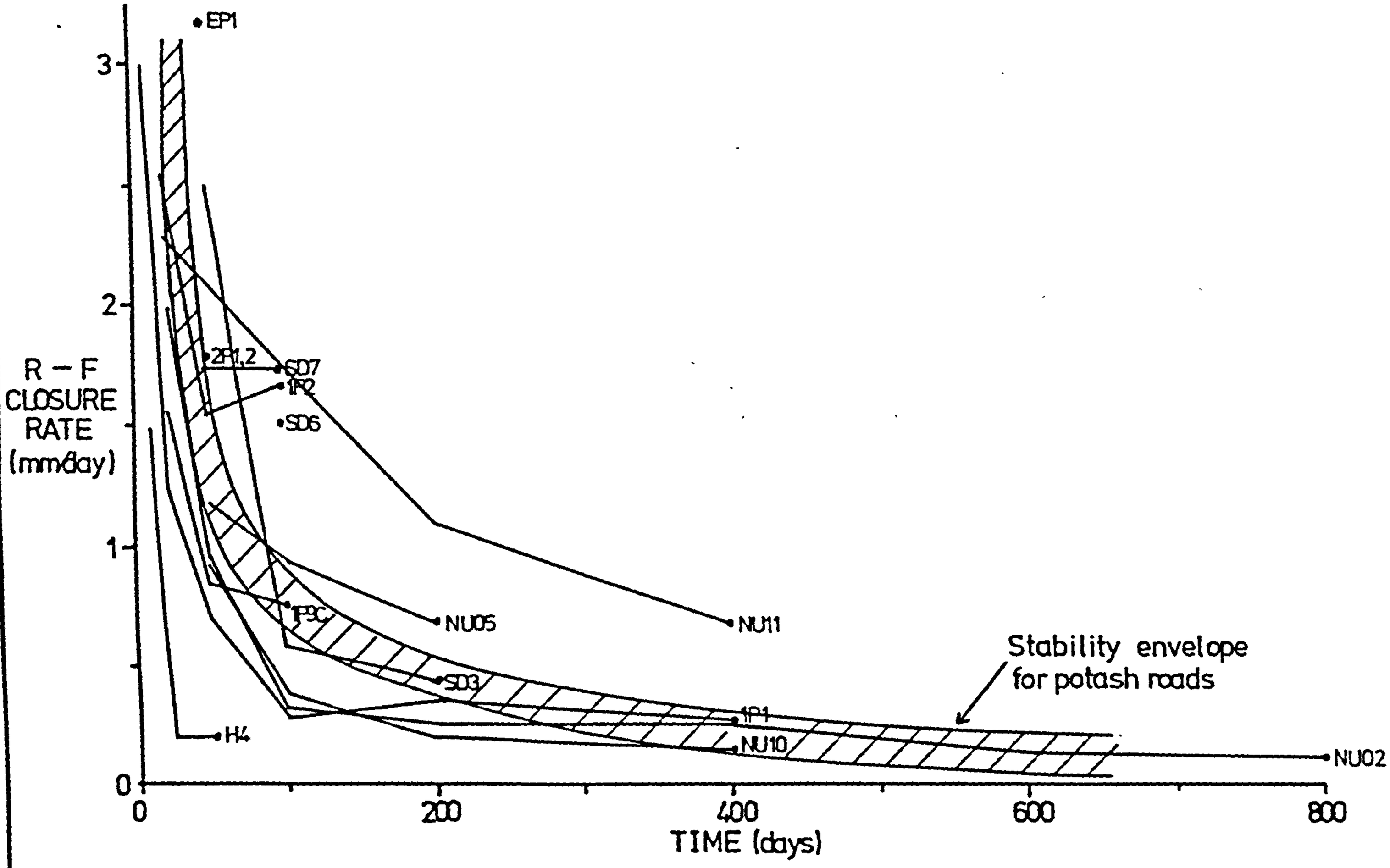

FIG. 8-55 ROADWAY CLOSURE RATES

TABLE 8-3 ROOF - FLOOR CLOSURE RATES (mm/day)

Site	Station	10 days	25 days	50 days	100 days	200 days	400 days	600 days	800 days
NU02	C-1		2.00	0.94	0.37	0.26	0.28	0.14	0.13
NU04	C3		2.11	0.96	0.71	0.44	0.20	0.14	
NU05	C7	6.01	-	1.19	0.94	0.69			
NU06	C11		2.57	1.49	0.84	0.38	0.28		
NU07	C14		2.00	1.47	1.14	0.57	0.57	0.77	
NU08	C17		3.17	1.95	1.29	1.00			
NU10	C21		0.88	0.92	0.39	0.21	0.14		
NU11	C23		2.25	-	-	1.10	0.68		
NU12	C25				1.44	0.43	0.57		
NU13	C30				0.67	0.57	0.60		
NU14	C26				1.10	1.00	0.62		
NU15	C29					0.57	0.34		
NU16	C32				0.43	0.57	0.14	0.36	
1P1	BH3	3.00	1.25	0.71	0.28	0.36	0.30		
1P1	BH6	3.00	1.71	0.86					
1P1	BH7	4.00	1.57	-	0.50	0.38	0.44		
1P1	BH8	0.30	0.57	-	0.31	0.31	0.19		
1P2	BH11	8.00	2.56	1.57	1.71				
1P2	2P	5.80	-	-	1.43				
1P2	2Q			1.81	1.18				

TABLE 8-3 Cont. ROOF - FLOOR CLOSURE RATES (mm/day)

Site	Station	10 days	25 days	50 days	100 days	200 days	400 days	600 days	800 days
1P7	A C2			2.75	1.86				
1P8	A C2		4.88	2.56					
1P8	C C2		2.50	0.75	0.43				
1P9	B C2	5.80	3.30	1.43	0.86				
1P9	C C2	3.67	1.57	0.86	0.50				
SD1	C2			9.33	5.33				
SD2	C2			7.28	4.43				
SD3	C2		1.25	2.50	0.61	0.43			
SD4	C2		1.25	0.62					
SD6	C2				1.52				
SD7	C2			1.75	1.75				
H4	C5	1.50	0.20	0.21					
H5	C5	0.75	1.00	0.29					
EP1	C2		4.25	3.14					
EP7	C2	6.00	5.33	7.20					
2P1	C2	8.00	3.67	1.80					
2P2	C2		5.33	1.80					

In every case, the sites which have remained stable have fallen below or within the envelope and those which are above have all had major roof falls.

The upper limit of the potash closure rate envelope is therefore the most accurate criterion for assessing potential roadway instability. This limiting curve may be approximated by the following equation, since it is linear when plotted on log-log axes.

$$\dot{c} = 34.81\ t^{-0.785} \qquad (8.25)$$

where $\dot{c}$ = roof to floor closure rate in mm/day

and t = time in days.

It is interesting to note that the 1P9 stress relief road closure rates are well within the envelope and virtually all the salt roadways are below the envelope.

Although not discussed previously due to very few readings available to date, the salt roadways excavated with a Heliminer, rather than blasted, are represented by the H4 results. These show a much lower closure rate than any other site, at least initially, and so it appears that without the effects of blasting, the strata surrounding roadways is far more stable.

8.9 Surface Subsidence

This section is only an initial attempt to correlate surface subsidence measured by the mine Survey Department with underground mining layouts. Initially, two traverse lines were established on the

surface and these are shown on Fig. 8-56 in relation to the development of the underground workings. Fig. 8-57 shows contours of face positions at different times between October, 1975 and September, 1976, based on the development shown in Fig. 8-56.

The initial levelling results along these lines were carried out in July, 1976, and so the subsidence deduced from following surveys is only that which has occurred since July, 1976, not necessarily the total subsidence.

Fig. 8-58 and Fig. 8-59 show the results of three surveys carried out along each of the two traverse lines. The mid-date of each survey has been used for this analysis and these are as follows.

Line 1	Mid-date of survey
Survey 1	28.8.76
Survey 2	9.11.76
Survey 3	11.2.77
Line 2	
Survey 1	20.9.76
Survey 2	1.12.76
Survey 3	20.3.77

The zero position of the x axis in each case was arbitrarily fixed from the traverse results, and for each traverse, the positions of various stations along the survey lines are marked on the profiles.

The main purpose of this analysis was to establish some basic data on angle of draw and time effects in relation to underground mining. This has been done by interpreting the various changes in

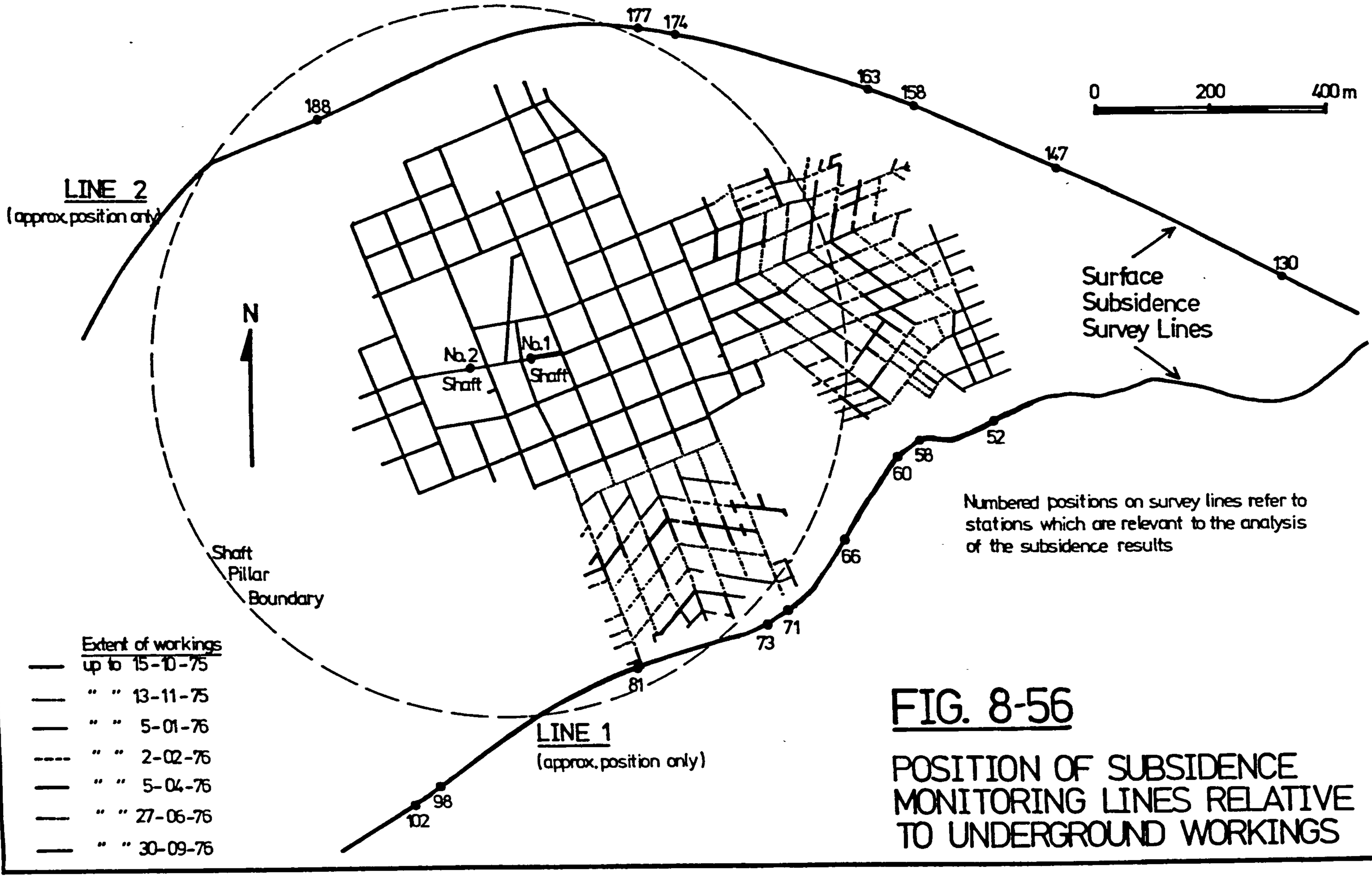

FIG. 8-56

POSITION OF SUBSIDENCE MONITORING LINES RELATIVE TO UNDERGROUND WORKINGS

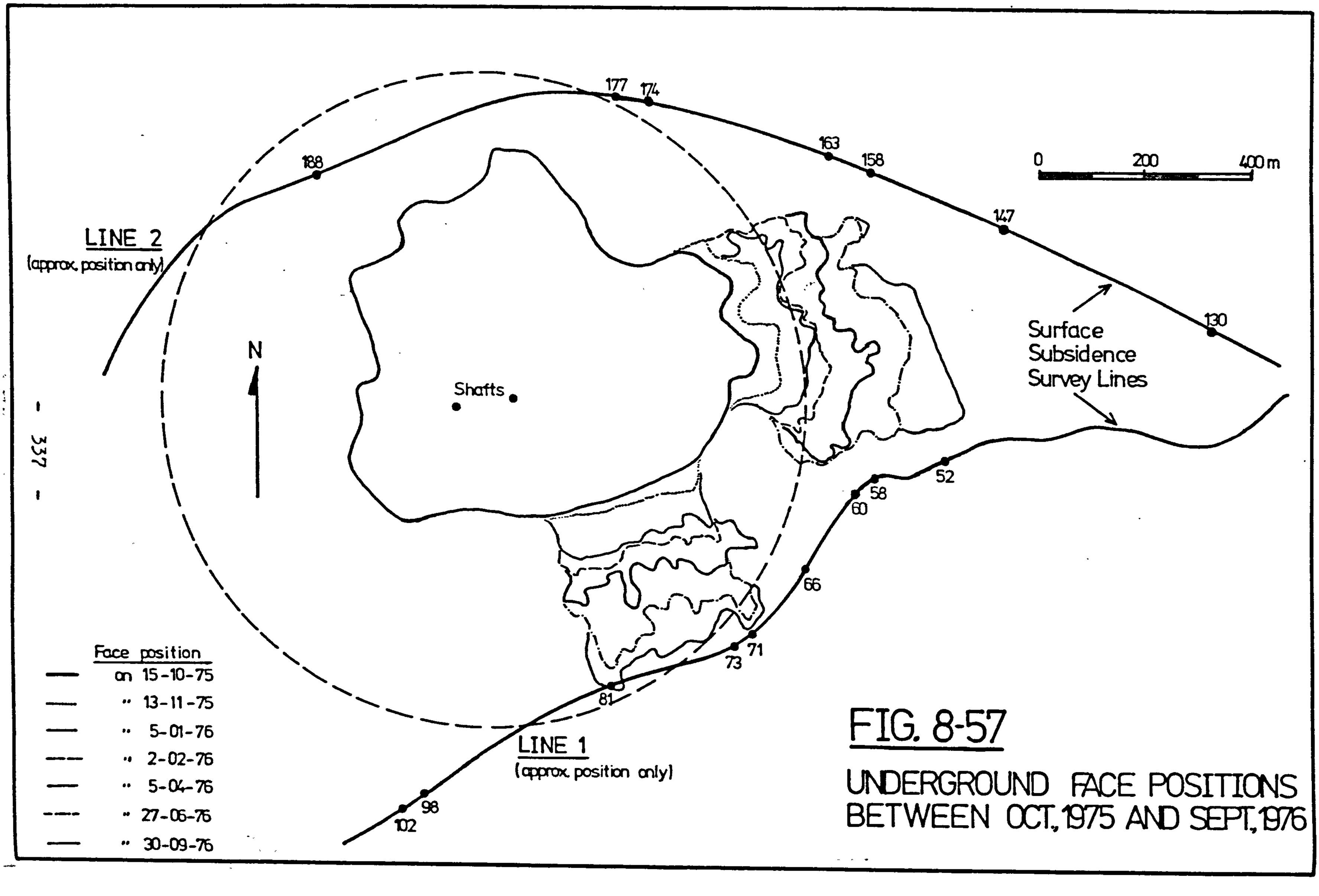

FIG. 8-57

UNDERGROUND FACE POSITIONS BETWEEN OCT., 1975 AND SEPT., 1976

FIG. 8-58

CPL BOULBY MINE - SURFACE SUBSIDENCE - LINE 1

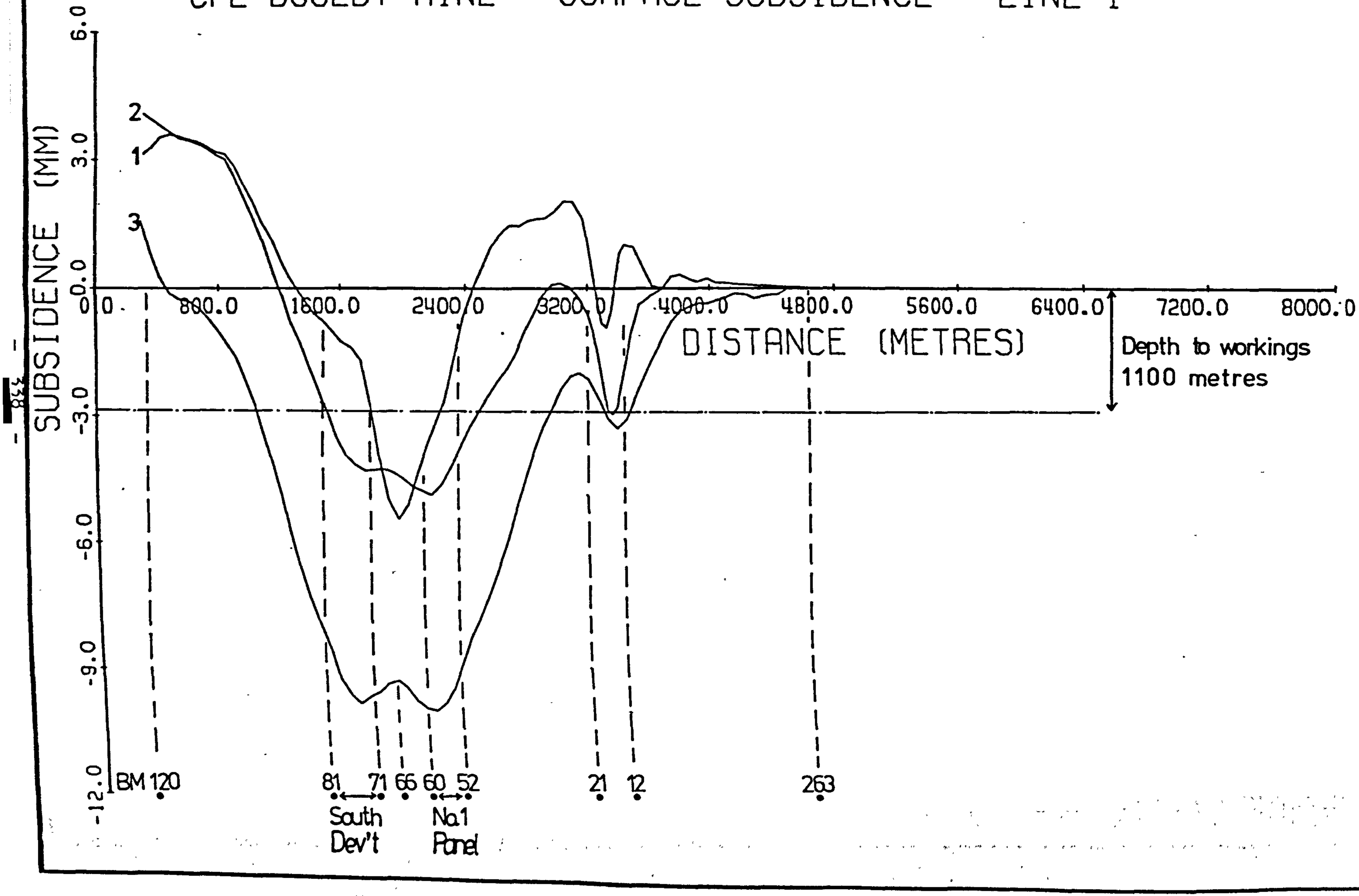

FIG. 8-59

CPL BOULBY MINE - SURFACE SUBSIDENCE - LINE 2

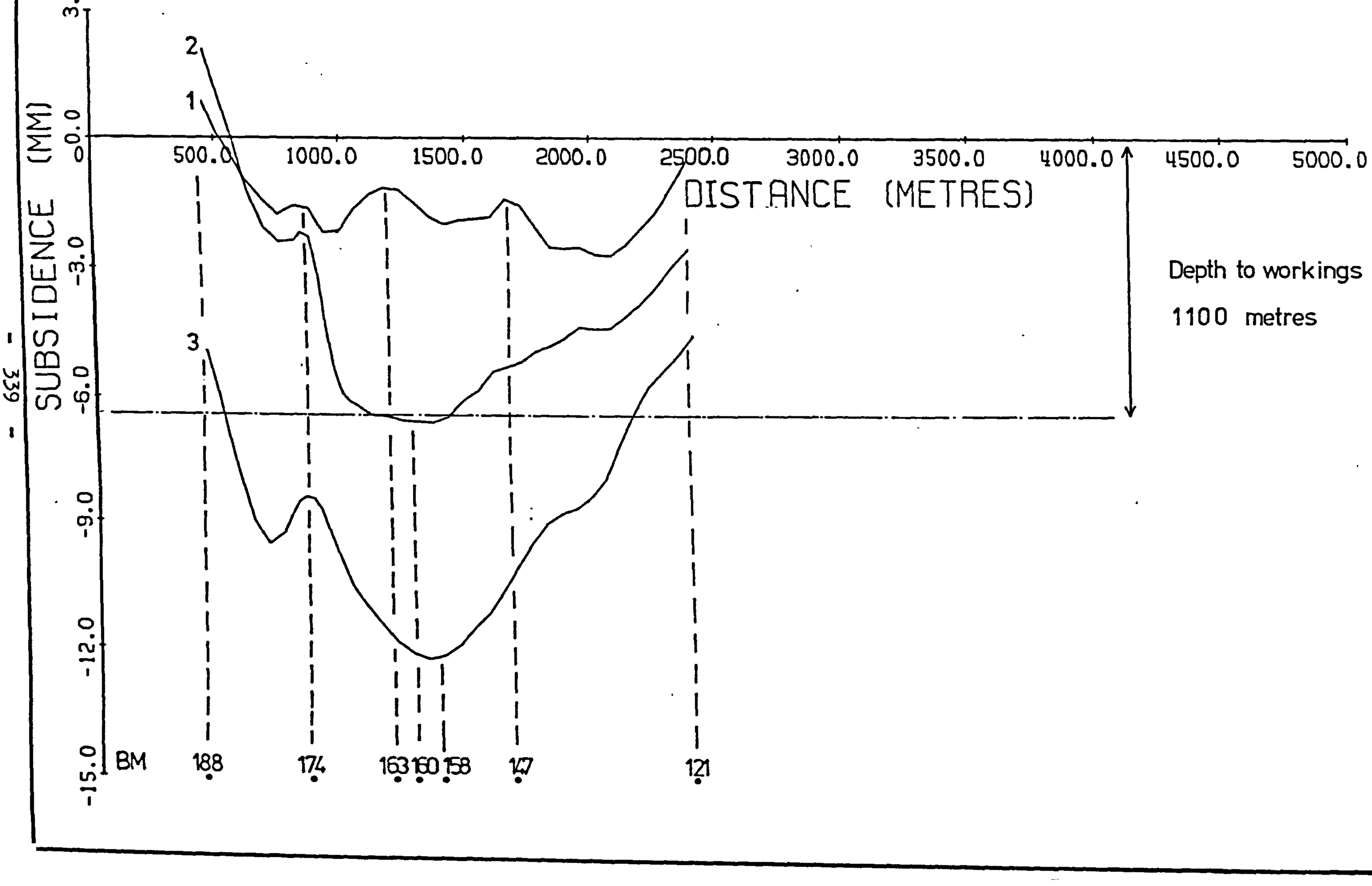

- 339 -

shape of the subsidence profiles with respect to changes in the underground face positions.

8.9.1 Angle of Draw

i) Line 1

a) Survey 1: The zero point for the limit of subsidence effects appears to be at least as far to the left as the arbitrary zero used as the x axis origin on the plot. This corresponds to an angle of at least 54° for pre-November 1975 facelines or 53° for pre-April 1976 facelines. For the eastern faceline at the time of the survey, the angle would be 47°.

b) Survey 2: The plot axis is too close to fit the left of curve 2 and so the angle is at least 52° for even the most recent faceline. At the right hand end the angle is at least 43°, even for the faceline at the date of the survey.

c) Survey 3: As in b) the angle is at least 52° at the left and 47° at the right for the closest faceline.

ii) Line 2

Since both end points are still indicating uplift on this traverse line, it is impossible to reach any conclusions concerning angle of draw without any fixed reference for the profiles.

8.9.2 Time Lag

This refers to the time delay between a change in face position underground and the initial subsidence, due to that change, occurring at the surface.

i) Line 1

a) Survey 1: The base of the trough is at station 66 which is closer to the South District (SD) than No. 1 Panel (1P). This curve therefore reflects a faceline prior to the development of these areas and the pillar between them, i.e. pre-November 1975.

b) Survey 2: The effect of the pillar between SD and 1P is appearing and the trough over 1P is deeper, indicating the start of the high extraction mining in 1P, i.e. after November 1975 and up to February 1976.

c) Survey 3: The 1P trough is still only slightly deeper than the SD one indicating development of both areas, but not the very high June 1976 extraction in 1P, i.e. approximately April 1976, but pre-June 1976. The pillar between SD and 1P is clearly reflected in the peak at station 66.

On all three surveys the trough between stations 21 and 12 appears to be an anomaly, unrelated to mining. It could be due to road slippage where the traverse line follows a road on the side of a steep hill.

ii) Line 2

a) Survey 1: Peaks exist at stations 174, 163 and 147. The

first of these has a slightly deeper trough to the right due to 1P development and corresponds to the solid corner in the north east of the shaft pillar, i.e. between November 1975 and January 1976. The other two peaks appear to be anomalies and virtually disappear in subsequent surveys.

b) Survey 2: The trough to the right of 174 is much deeper due to the north east extraction in 1P with the lowest point at 160 indicating a faceline between February 1976 and April 1976.

c) Survey 3: The trough has moved to the right and deepened, reflecting the development up to June 1976.

8.9.3 Summary of Angle of Draw and Time Lag Conclusions

Using the notation A for angle of draw in degrees, and t for time lag in months, these conclusions may be summarised as follows.

Line 1 - Survey 1: $A \geq 53$ or $A = 47$ if $t = 0$,
$t \geq 9.3$

Line 1 - Survey 2: $A > 52$ or $A = 43$ if $t = 0$,
$t < 11.8$, $10.2 > t > 9.2$

Line 1 - Survey 3: $A > 52$ or $A = 47$ if $t = 0$,
$t \leq 10.3$, $t > 7.6$

Line 2 - Survey 1: $t > 8.6$

Line 2 - Survey 2: $8.4 \leq t \leq 10.0$

Line 2 - Survey 3: $t \geq 8.8$

From these ranges, the time lag is approximately 9.5 months ±

1 month. Using 9.5 months time lag, the angle cf draw is 53°. Even if the time lag were 0, the angle would still be 46°.

On the basis of 9.5 months time lag the surveys reflect face positions at the following dates.

Line 1	Date of face pcsition
Survey 1	mid-Ncvember, 1975
Survey 2	late January, 1976
Survey 3	late April, 1976
Line 2	
Survey 1	early December, 1975
Survey 2	mid-February, 1976
Survey 3	early June, 1976

8.9.4 Lateral Strains

Using the program, SURFSUB, the subsidence profiles were used to predict lateral strains on the surface. Fig. 8-60 and Fig. 8-61 show the predicted lateral strains for the third survey profile on each traverse line. Each plot shcws considerable fluctuation due to the very small magnitude of the subsidence and strains but the peak tensile strains range between 30 and 80 microstrain. The position of peak lateral strains is not conclusive, but from the general trend of the curves, using a 9.5 month time lag, several estimates can be made.
On line 1 a peak to the left of the South District occurs at approximately 32° over the ribside. On line 2, there is an indication of a peak to the right of the No. 1 panel front at an angle of about 36°.

FIG. 8-60

CPL BOULBY MINE - SURFACE SUBSIDENCE - LINE 1 - SURVEY 3

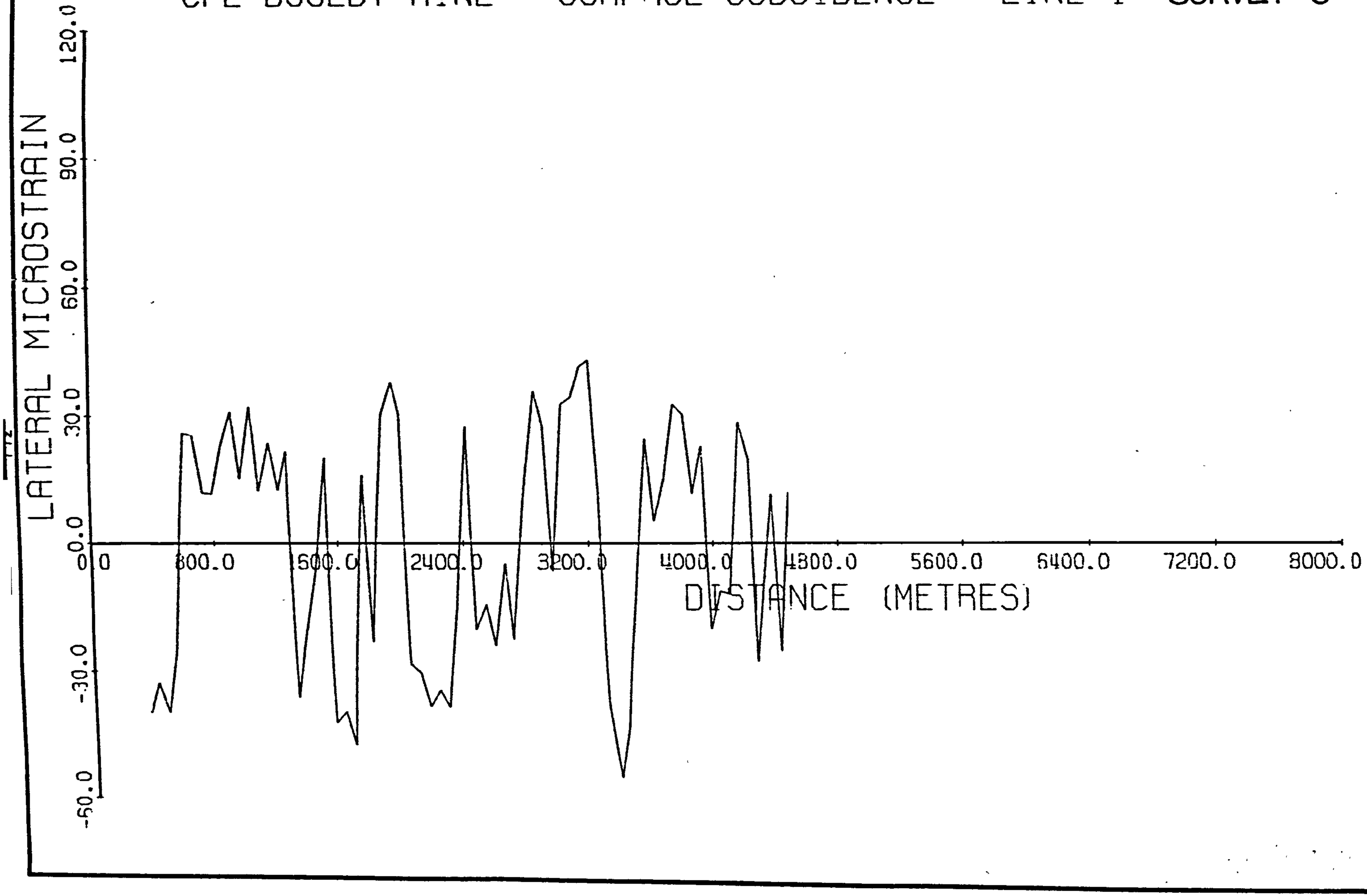

FIG. 8-61

CPL BOULBY MINE - SURFACE SUBSIDENCE - LINE 2 - SURVEY 3

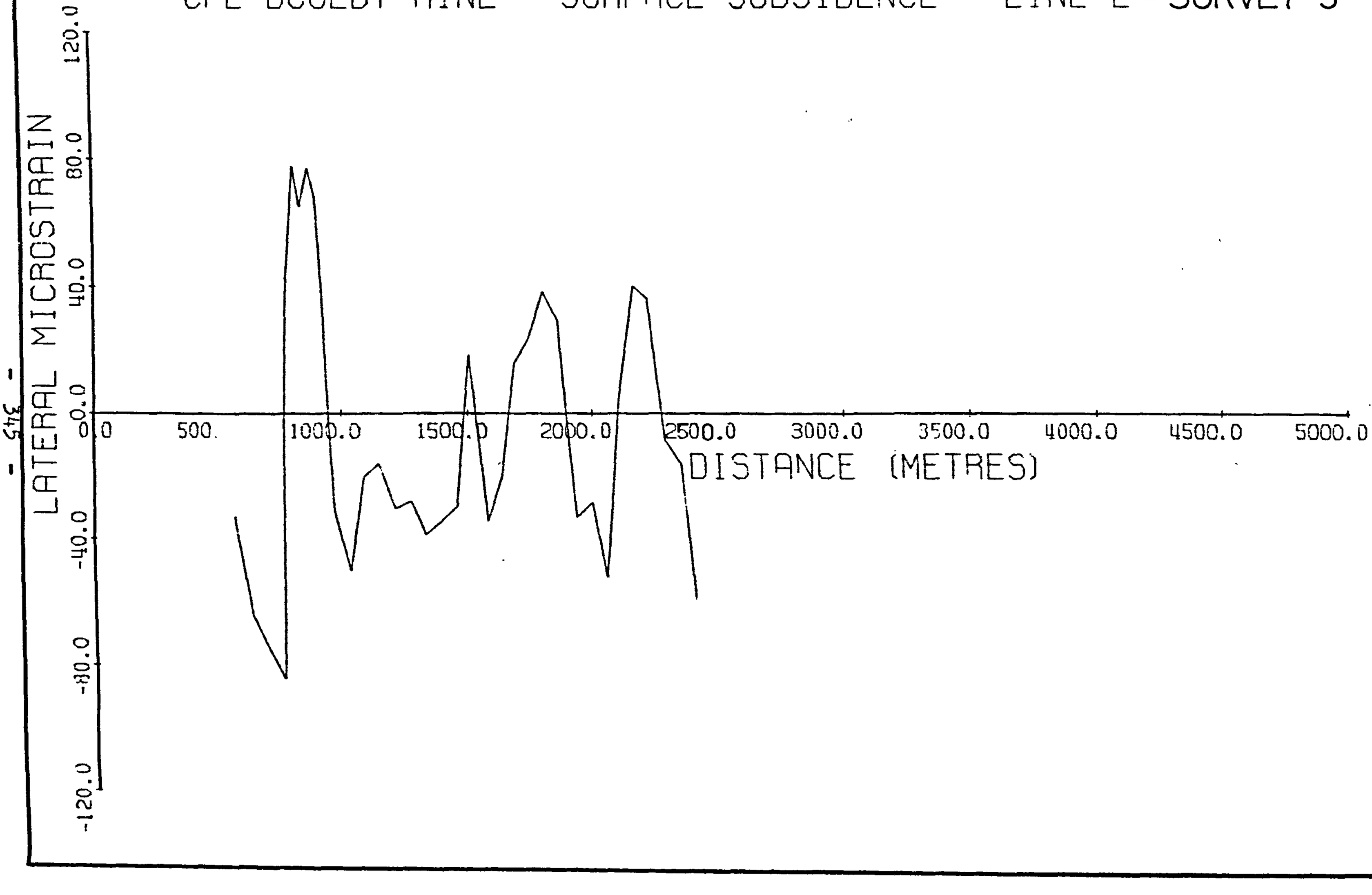

8.10 Summary of Conclusions

(All pillar widths referred to are in connection with pillar heights of between 3m and 3.4m.)

i) Road intersections with at least 1.5m of competent potash or halite exhibit stress relief and resultant lower closure rates than surrounding roads.

ii) T junction intersections do not create stress relieved ground and behave as normal roadways which are stable with 2m to 3m of competent potash in the roof.

iii) 8m wide potash roads which have shale within 3.5m of the roof are likely to become unstable.

iv) Any roof strata made up of composite, competent material should be at least 2m to 3m thick with the bottom layer at least 1.5m thick.

v) Roads which exhibit steady state closure, or roof strata deformation rates, are likely to become unstable. Continually decreasing rates indicate stability and should be below the level defined by equation (8.25).

vi) 60m pillars show a migration of load away from the outer 6m, up to 150 days and then they appear to stabilise.

vii) All long term stable pillars exhibit high strains in the immediate 5m to 10m proportional to their size, but a confined core beyond this zone. The core is generally about 15m narrower than the minimum pillar width.

viii) Pillars below 25m width should not be used for stable low extraction panels.

ix) All the pillars investigated (up to 60m pillars) have shown significant yield which would produce subsidence, even from the shaft pillar area alone.

x) The halite pillars are up to four times as rigid as the equivalent potash pillars.

xi) The irregular development around the immediate shaft area appears to have been respcnsible for some of the shaft lining cracking due to subsidence.

xii) Junctions in halite exhibit very stable conditions due to stress relief but are vulnerable to reloading effects of panel development.

xiii) 8m wide salt roads should be quite stable.

xiv) Low extraction panel widths of 244m are within the critical width defined by geological conditions, but 400m is in excess of this width. (Observations in No. 1 panel have also shown that, with stubs mined either side of the panel, the total width of 290m has caused excess loading on the ribside pillars, i.e. the critical width is less than 290m.)

xv) Shale roof conditions do not permit stress redistribution around intersections for any length of time.

xvi) 20m pillars are too small to remain stable and too large to yield sufficiently to be used in stress relief panels.

xvii) 11m pillars indicate some stress relief effects but not sufficient for roadway protection.

xviii) Pillars between 8m and 9m are small enough to create a stress relief panel, though the mining sequence is

critical to roadway protection and subsidence effects, due to excess pillar yield. (No long term data is available, as yet, on continued stability of such panels.)

xix) A stress relief panel width of 60m is capable of redistributing the load onto both ribsides.

xx) Pillars of 6m are too narrow and create excessive yield. The presence of shale in the pillars makes their behaviour and strength unpredictable.

xxi) The presence of weak shale and marl above a stress relief panel, together with excessive panel width (up to 90m), causes reloading of the panel and excessive closure and subsidence effects.

xxii) Surface subsidence has occurred due to mining of 60m pillars in the shaft pillar. The subsidence profiles have reflected the development of the twc main production areas.

xxiii) There is an apparent time lag of about 9.5 months between a face advance and the associated subsidence appearing on the surface. This is no doubt associated with the time-dependent closure effects on the pillars and the strata deformation above.

xxiv) The maximum angle of draw for surface subsidence is approximately 53° with the maximum tensile strains occurring between 32° and 36° over the ribside.

CHAPTER 9

SUMMARY OF OTHER RELEVANT EVAPORITE MINING OPERATIONS

9. SUMMARY OF OTHER RELEVANT EVAPORITE MINING OPERATIONS

This chapter is intended to provide a brief review of various mining operations which are similar to the Boulby situation. In particular, the Canadian potash mines in Saskatchewan are discussed, following a visit to them by Potts (57) and the author, in 1976. This review has been left until this stage, in order that the other mining operations may be considered in the light of conditions and results from Boulby, which have already been discussed.

9.1 Rock Salt Mines

Numerous rock salt mining operations have been instrumented to obtain rock mechanics information related to their stability. Only a few of these are discussed here, in terms of particular points of interest arising from the results reported.

The I.C.I. Meadowbank Mine at Winsford, Cheshire, has been the site of a continuing research project by the Department of Mining Engineering, University of Newcastle upon Tyne. Papers by Potts (58) and Potts et al. (59) have reported the use of extensometer and closure data for assessing room and pillar stability. In particular, the latter paper discusses the results of optical techniques for measuring vertical deformations within the pillar material. Results taken over 18 months, up to a distance of 9.1m into a 19.8m pillar, showed that the average vertical pillar strain up to that depth was no more than 1.25 times the average lateral strain in the direction of the borehole. This confirms the previous hypothesis that the lateral strains normal to the pillar

edge provide a reasonable and direct estimate of vertical pillar strain for each sector defined by the horizontal pillar diagonals. Clearly, the lateral strain parallel to the nearest pillar edge is only small, relative to the strain normal to the edge, apart from near the pillar diagonals.

McClain (60) describes experiments carried out in the Lyons, Kansas mine, U.S.A., in connection with Project Salt Vault for the Oak Ridge National Laboratory. He monitored lateral strain at a depth of 3.0m, in salt, below a 16m wide potash pillar as it was created. Within one year the induced strain had reached a tensile value of 700 microstrain and was still increasing with time. This indicated the significant punching effect of the pillar on the mine floor, even in a material such as rock salt. This effect, in floor and roof strata, would undoubtedly cause subsidence greater than that due simply to pillar yield, as well as high stress concentrations in the roof and floor strata of the adjacent rooms.

Hedley (61) investigated problems of roof falls in a Canadian salt mine. Conventional room and pillar mining at a depth of 535m had been used. He found that in 18m wide rooms, 4.3m roof bolts were having very little effect, except for preventing surface (up to 0.6m) slabbing. Attempts to prevent shear failures along the roof edges by undercutting the pillars to a depth of 3m, to unload the pillar edge, did not have any significant effect on roof deformations or stability.

9.2 European Potash Mines

McClain (62) carried out extensometer studies on the deformation of potash barrier pillars located between production panels. These had been

mined between 40m and 80m wide with a series of yield pillars which were later mined on retreat. The barrier pillars, between 50m and 70m wide, showed lateral strains in excess of 2.0% after 100 days, at the pillar edge, but within 5m the strain had reduced to 0.1% and in the central core region of the pillar the strains were below 0.04%. This confirms that pillars of this size, even when highly loaded due to complete extraction on either side, maintain a sufficiently large confined core to support the overlying strata.

A number of papers have been published on the German potash mining industry. One of the principal authors has been Höfer (63, 64) who has established a rheological model for carnallite which he has correlated with underground measurements. However, laboratory triaxial compression tests published by Menzel et al.(65) indicate the marked difference in behaviour between the carnallite potash ore, predominant in Germany, and sylvinite, which occurs at Boulby. The failure strain plotted against confinement shows that while sylvinite strain increases from 2.5% to 35%, the carnallite only increases from 0.5% to 2.5%. On a plot of σ_1 against σ_3 the carnallite strength increases significantly with a small amount of confinement from 43% of the sylvinite strength in the uniaxial case, to an average of 80% for a confined condition. This shows a remarkable similarity to the behaviour of the secondary ore at Boulby, as compared with the primary ore (see Chapter 5).

The German potash mines have had considerable problems with rockbursts and gas outbursts. These are discussed by Gimm and Pforr (66) who state that, "it was found that genuine rockbursts only occur in the German potash industy when the pillars in the potash seam consist wholly

or partially of carnallite". Photographs of the German rockbursts and gas outbursts show a remarkable resemblance to the so-called gas blowholes in the secondary ore at Boulby. The similarities in properties between carnallite and the secondary ore should therefore serve as a warning against the use of secondary ore as either a pillar or immediate roof material where it will be under very high stress concentrations.

9.3 Canadian Potash Mines

There has been a considerable amount of material published concerning the potash industry in Saskatchewan and only a selection of it is referred to here.

Serata (67) has investigated the rheological aspects of potash behaviour in the laboratory and theoretically, although his theories are not universally accepted. There has been a continuing controversy between Serata and Baar (68, 69) concerning the application of Serata's theories to the mining situation. Baar claims that Serata's mining method, referred to previously (33), does not create a stable stress arch above a mining panel but develops into a steady state creep condition. This ultimately leads to large amounts of subsidence, possible panel collapse and water inrush. (The Canadian mines are situated below a number of water-bearing strata, the closest of which, though often dry, is the Dawson Bay limestone, which can occur within 12m of the potash horizon.)

King (70) carried out a program of laboratory creep testing on model pillars of Saskatchewan potash. He simulated the clay bands which occur at the top and base of most pillars underground and act as friction

reducers. These play a vital part in the yield pillar system, removing much of the confinement applied by the roof and floor strata. King found that pillars with a W:H ratio of 8, and clay bands, fail due to tertiary creep in the same way as W:H ratio of 4 pillars with no clay bands.

Most of the mines have published data recorded underground in various panel and experimental layouts. Zahary (71) has reported work at I.M.C., Serata and Schultz (72) at Syvite of Canada, McKinlay (73) at Allan Potash Mine and Mackintosh (74) at Cominco Potash Mine. All the mines are at a depth between 975m and 1070m.

The Sylvite and I.M.C. workings in the Esterhazy region of Saskatchewan are in a flat sylvite depcsit with at least 30m of homogenous halite as the immediate roof strata. This enables them to mine extremely wide rooms, on the stress relief principle, without the need for regular yield pillars for local roof support. Sylvite is presently mining 20m wide rooms and they are experimenting with 24m rooms, all 2.5m high. The 20m rooms are mined in pairs with an 8m yield pillar in the centre and 65m barrier pillars (increased from 53m initially). Fig. 9-1 shows the four rotor, Marietta borer which is used at Sylvite and the face profile cut by it after the second pass. The bottom photograph shows a cantilever roof failure at Sylvite in a 20m room, caused by the adjacent 15m yield pillar being excessively stiff and punching into the roof.

Each of the other mines, in the Saskatchewan region, mines a potash seam which is overlain by salt between 12m and 20m thick, then 5m of red beds (weak shales and marls) and at least 35m of Dawson Bay limestone. The salt is cut by a series of thin, parallel clay bands up to 10cm thick, one of which occurs at the top of the mining horizon, in

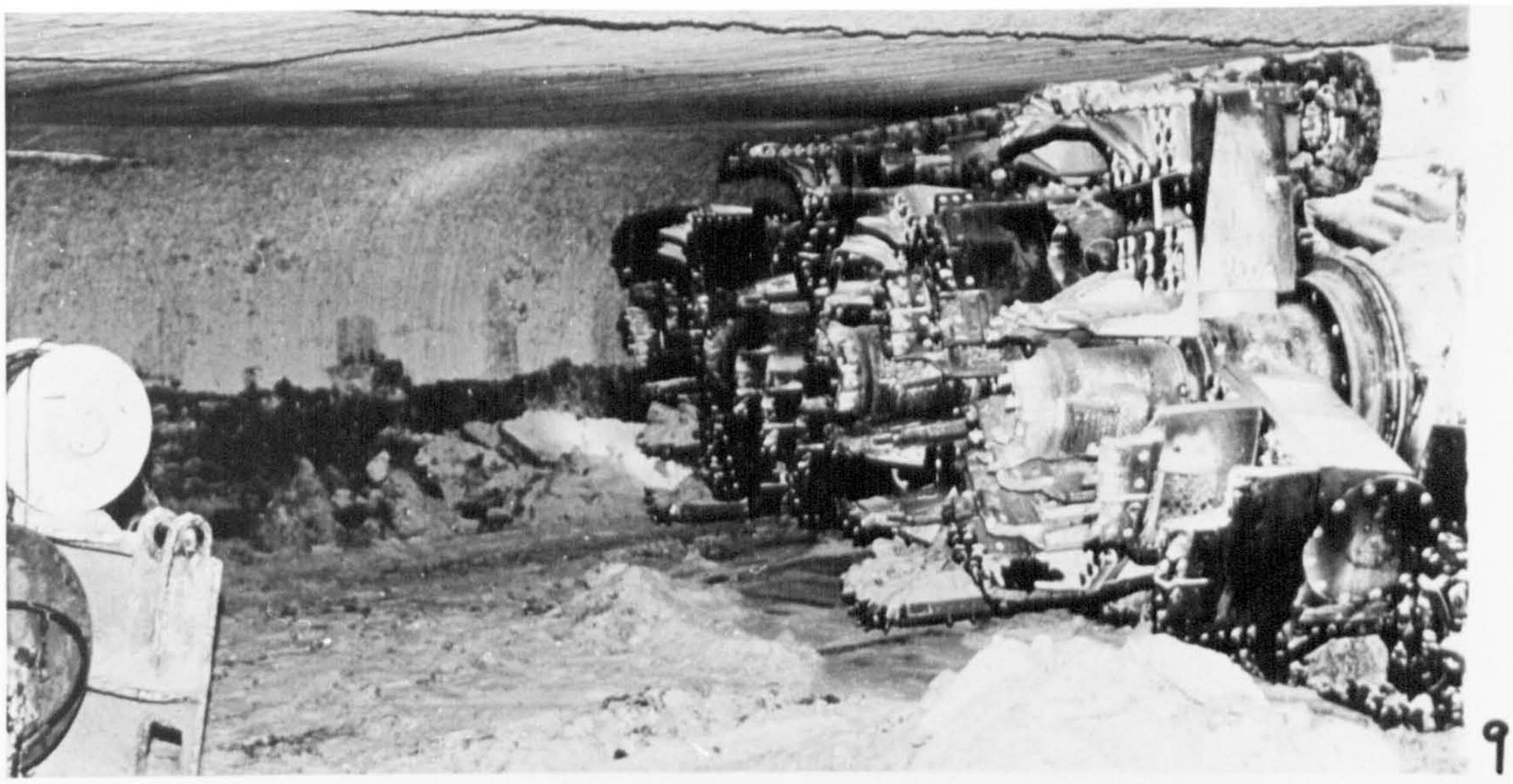

9

FIG. 9-1

each pillar. The mining height is approximately 3m at each of the mines.

Although the mining method varies at each mine - from five parallel rooms with no cross-cuts at Cominco, to double chevron (herringbone) panels at Allan - the method employed is fundamentally the same. Only Alwinsal mine still uses a conventional room and pillar system.

Fig. 9-2 illustrates the basic technique using a 5 entry panel. The sequence of mining is critical to provide the necessary protection to the central roadways. The outer roads are mined first and allowed to fail (minimal roof support is installed). The arched roof failure in these roads forces the horizontal stress field upwards, thereby protecting the central salt plate roof structure from any horizontal loading. Clay bands below the floor cause floor heave to persist, at least in roads 3 and 4, since the outer roads do not provide the same protection as in the roof. This is one reason why the Canadian mines use at least 4 or 5 entry systems to eliminate effects of horizontal stresses on the central region.

The maximum width of panels is obviously a function of the geology. The Dawson Bay limestone forms a bridging strata for these panels, and for all the mines, the ratio between height to the Dawson Bay limestone and panel width is within the range 0.20 to 0.35. Once the final panel geometry has been mined, the function of the yield pillars is purely to hold the plates of salt in the roof together, and carry a minimal load to support the immediate strata. Pillar dimensions vary but are in the range of 5m to 9m. At Cominco they found that slightly wider pillars adjacent to the central roads (8m) gave added stability to the panel and reduced closure rates, while 6.5m pillars

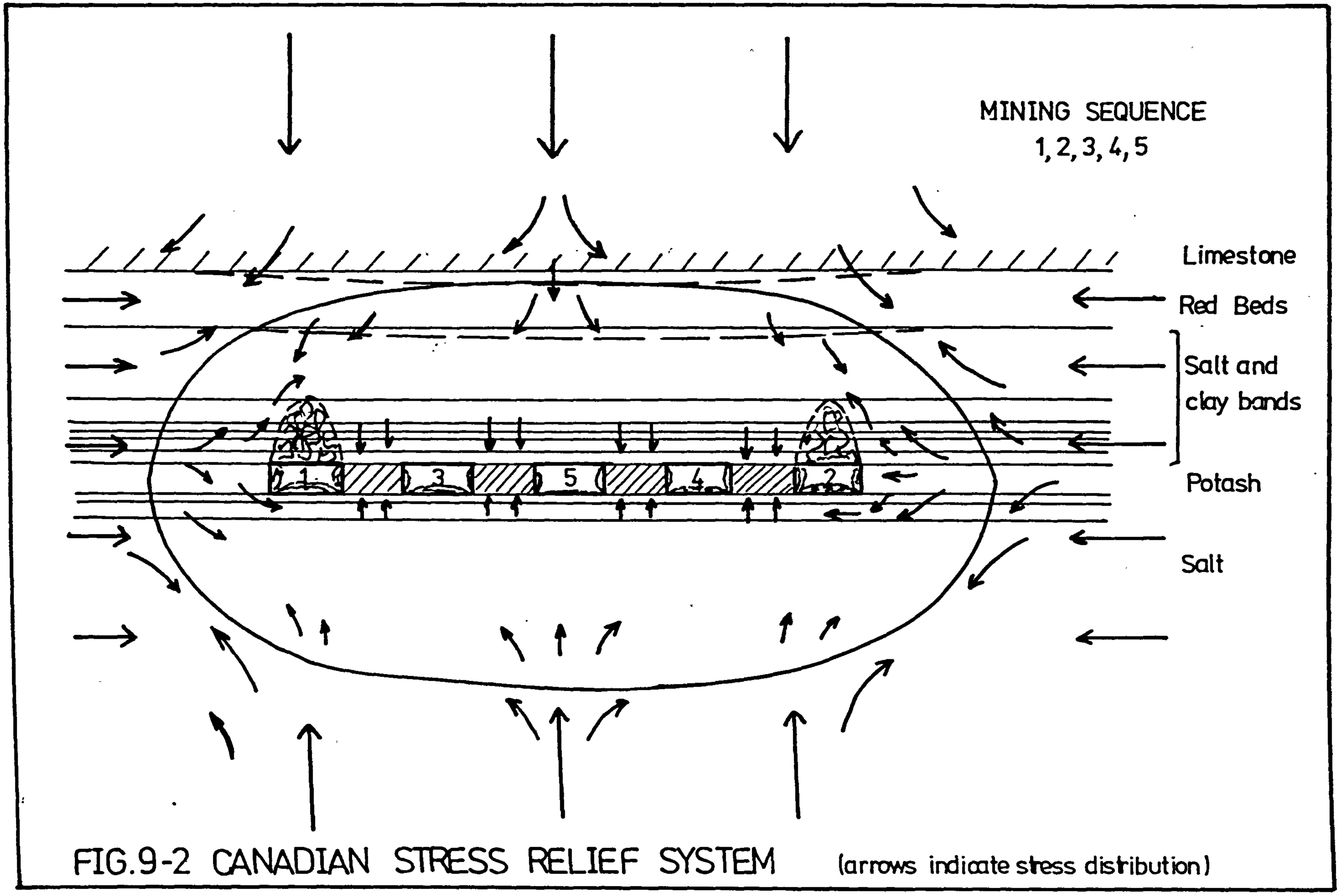

FIG.9-2 CANADIAN STRESS RELIEF SYSTEM (arrows indicate stress distribution)

at the sides promoted the initial necessary redistribution. A typical closure rate for the central two roads of a 4 entry panel at Cominco after 10 days is 2.7mm/day.

Fig. 9-3 shows conditions at Noranda mine (C.C.P.). The top photo is looking across the central region of a chevron panel, showing the angled, yield pillars at a very early stage, and the very good roof condition across such a wide unsupported span (at least 30m). The middle photo is an end view of a yield pillar with vertical tensile fracturing indicating the effect of the clay bands in eliminating all confinement from the pillar. The bottom photo shows the use of wooden blocks with mechanical anchored roof bolts, to absorb the initial high level of time-dependent deformation in the roof. At Noranda they monitor, on average, about 50mm closure in the first 2 days for the central road of a panel, and then another 50mm over the next 200 days by which time a steady state condition has developed. Boreholes in the roof of a panel have indicated that at a height of 10m above the panel centre the deformation is 90% of the roof sag. This indicates a virtually completely stress relieved zone in the immediate roof.

Fig. 9-4 shows conditions at the Cominco mine. The top photo shows the remains of an early shaft pillar drive (8m by 3m) which had been re-intersected. Without any major roof collapse, it had closed to about 4m by 1.5m in the space of 3 to 4 years. The middle photo shows the cutting head of a Heliminer being used to re-cut a floor where extensive floor heave had occurred. The bottom photo shows the caved roof of an outer road in a stress relief panel.

Barrier pillars vary considerably in width throughout the mines,

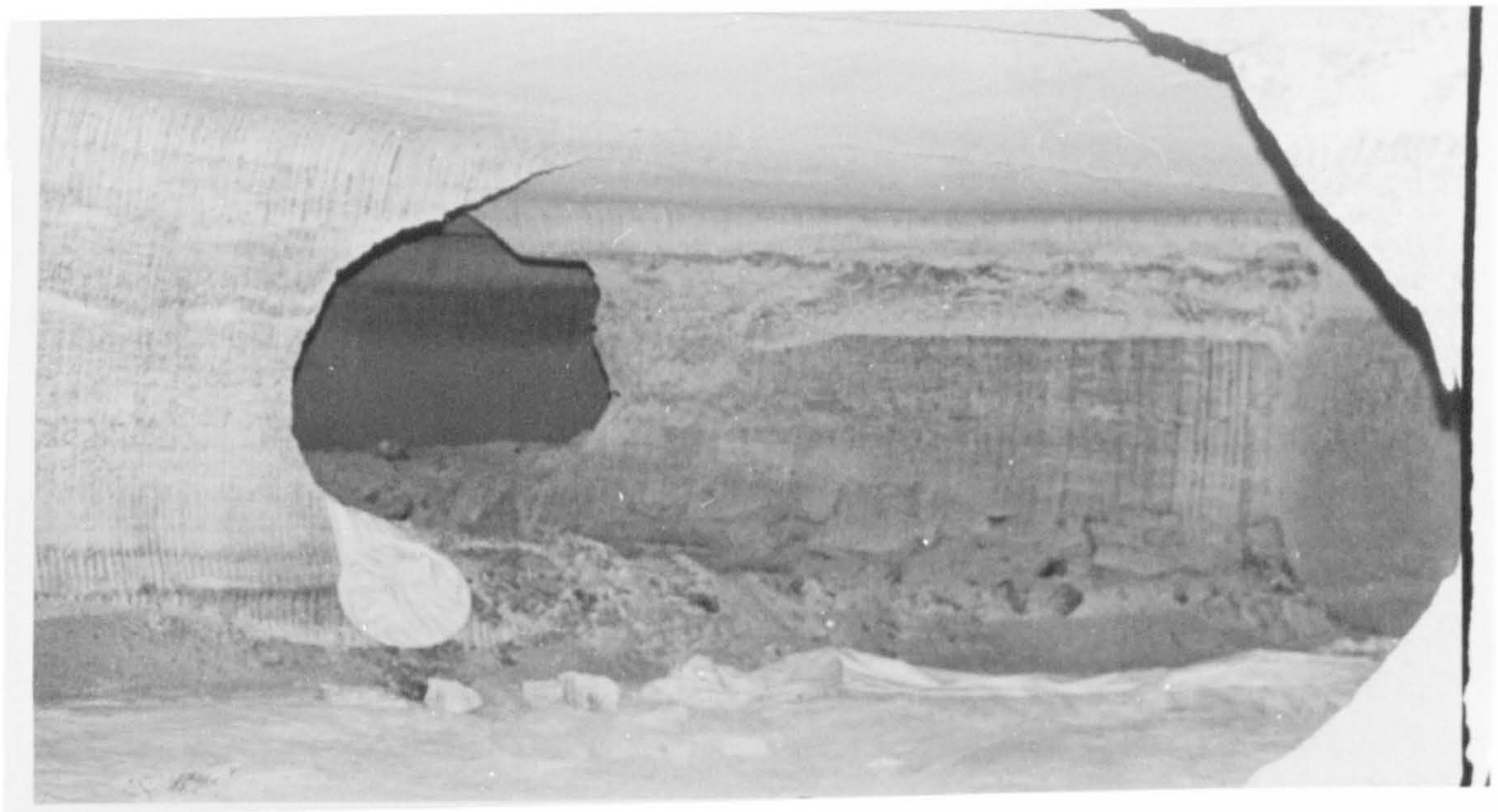

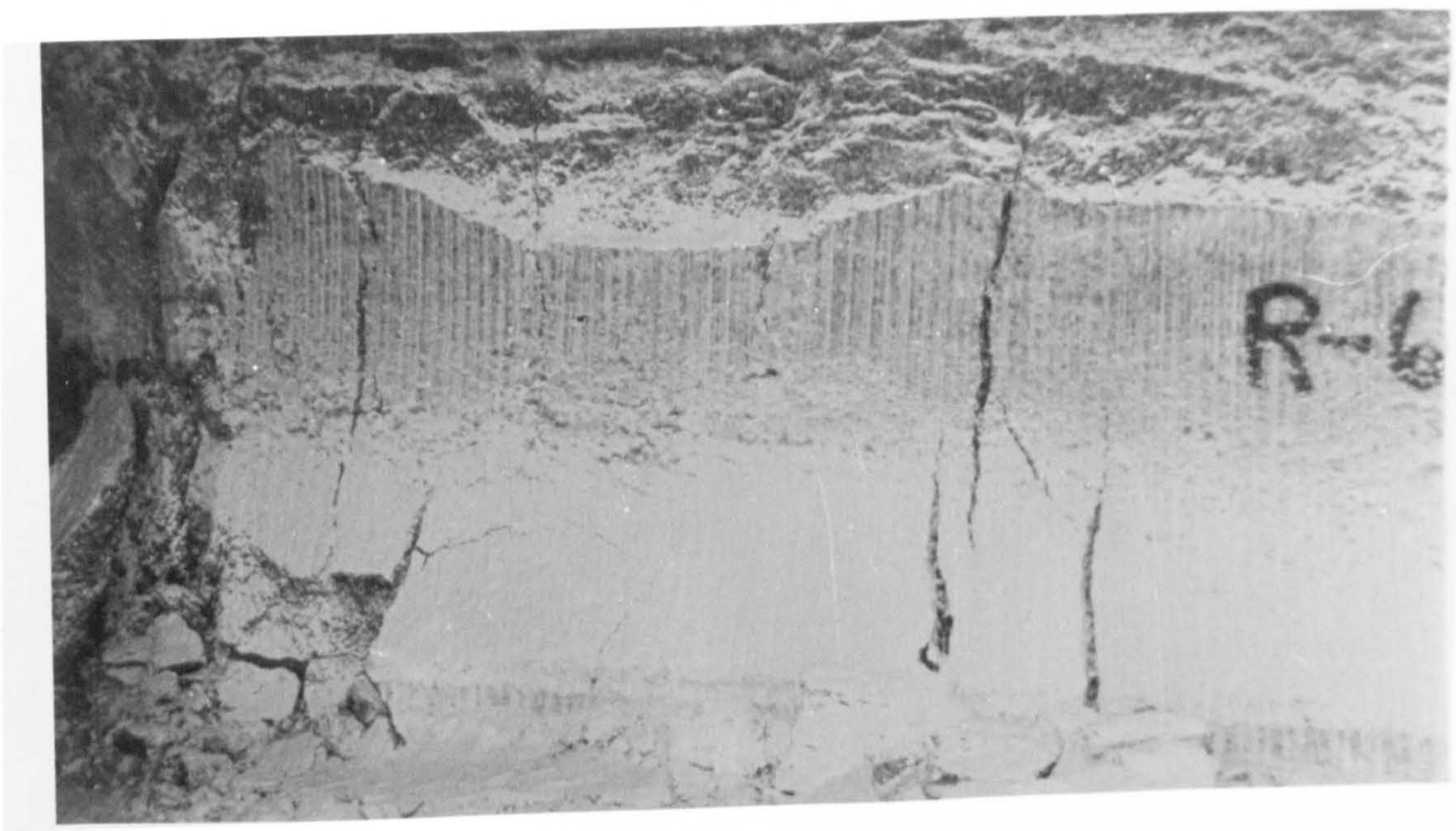

FIG. 9-3

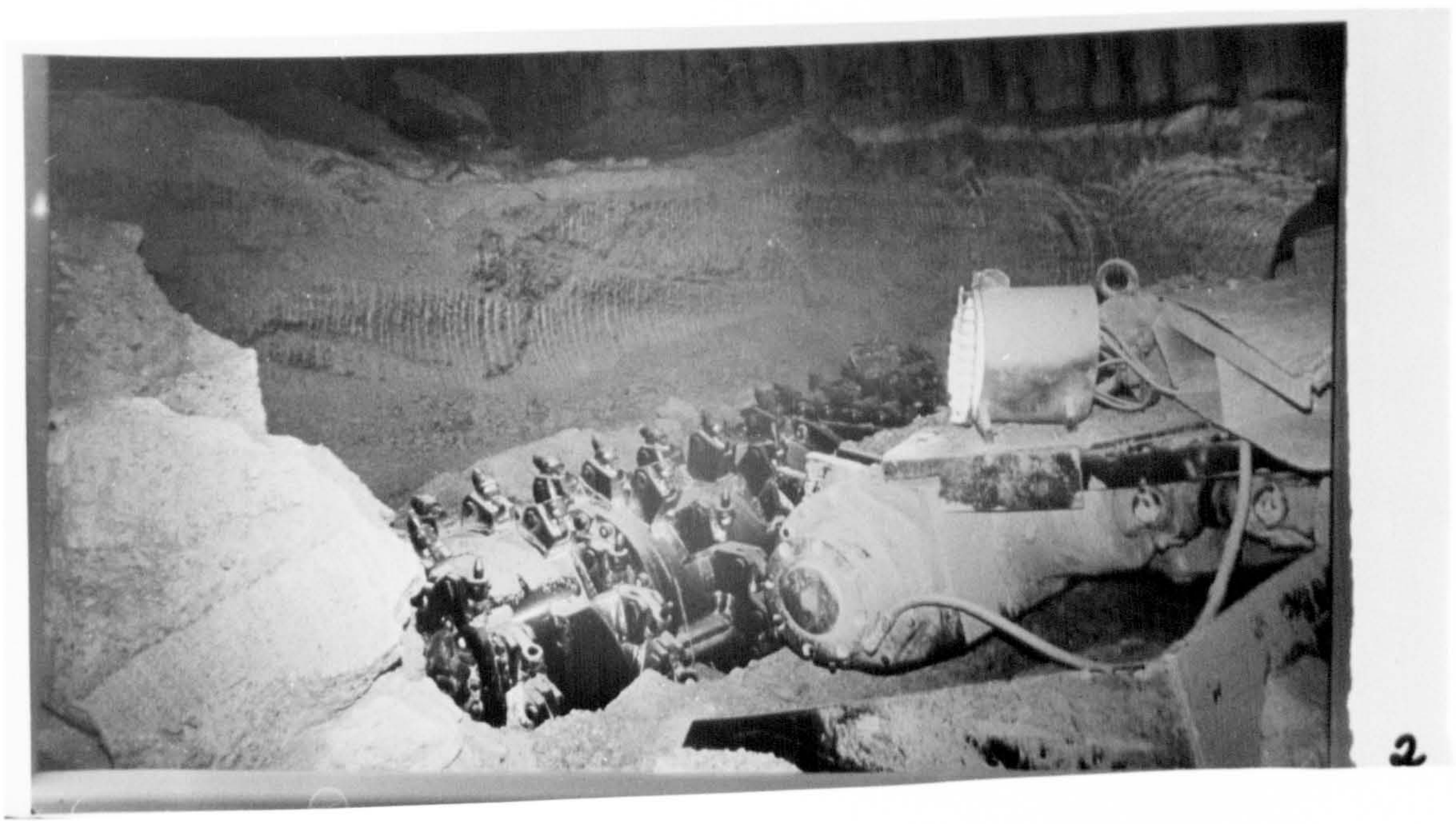

2

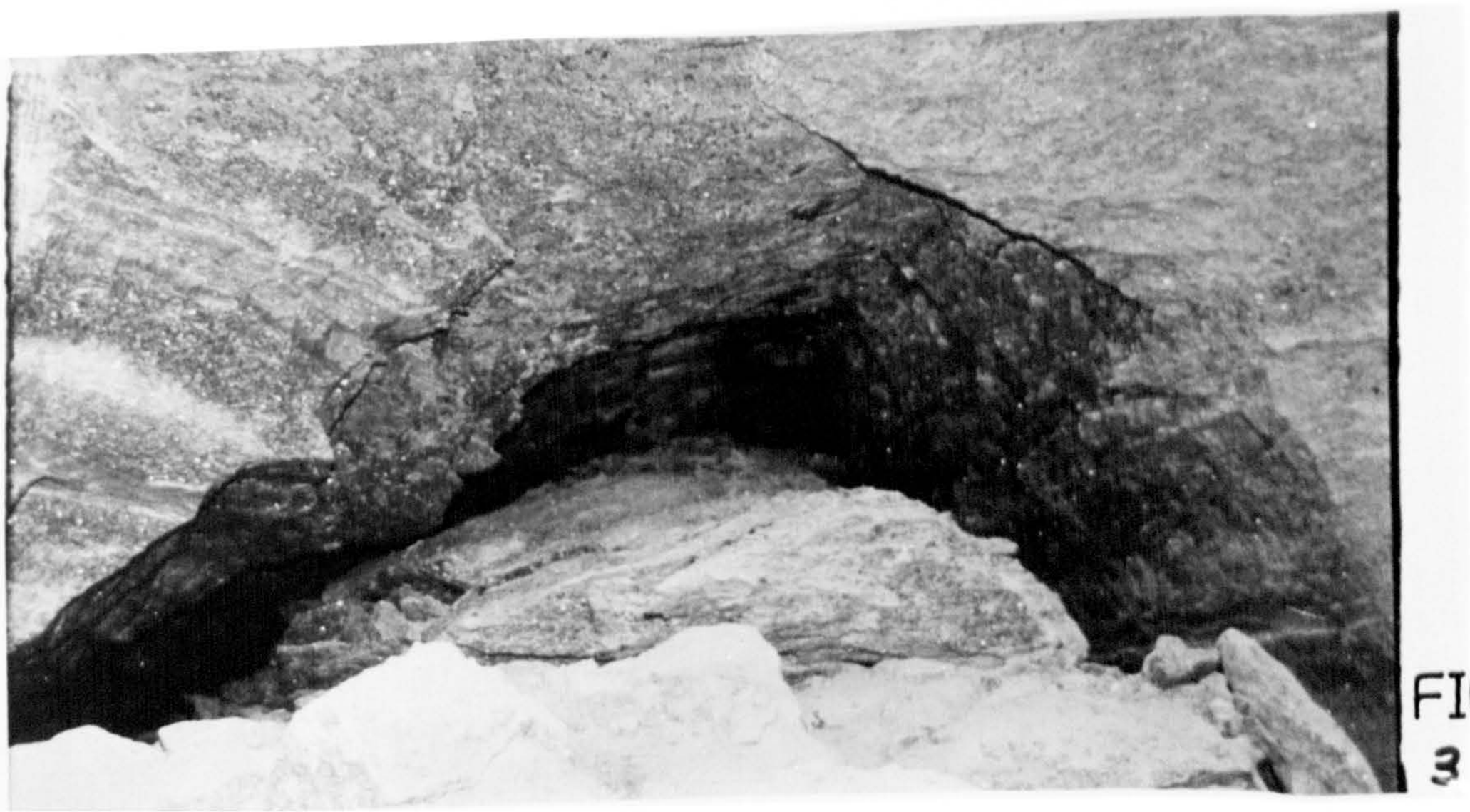

FIG. 9-4

3

from about half the panel widths to double the width. The barriers at Sylvite, where they are carrying the full load in each panel, are approximately 1.3 times the panel width. All the mines have recorded surface subsidence, though not necessarily since the start of mining. Sylvite have a maximum of 75mm subsidence, whereas Allan have recorded almost 200mm subsidence due to very haphazard block development and minimal regional support by barrier pillars. Allan have also recorded 50mm uplift under the shaft head frames as a result of one-sided development away from the shaft pillar.

9.4 Application of Canadian Method to Boulby

Specific details of panel layouts at the Canadian mines were reported by Potts (57). The comparison of Canadian conditions with those at Boulby shows that the Boulby geology is not as favourable. The massive weak shale and marl at Boulby are not represented in Canada, except for the red beds, which are not as close to the seam. The Canadians report stress conditions to be virtually hydrostatic at about $-24.1\ MN/m^2$, considerably lower than at Boulby. There are no equivalent clay bands at Boulby to permit frictionless pillar yielding.

On the basis of these factors, there is still the question of whether the Boulby geology is capable of maintaining a stable stress relief panel. On the assumption that it is, the following points should be made. Due to the higher vertical stress field at Boulby, the upper range of the ratio quoted (for height to bridging strata against panel width) should be applied. The Upper Anhydrite is 15m above the seam and so a range of panel widths between 40m and 60m should be adhered to.

In view of the subsidence measured in Canada, regional support should be provided at regular intervals between production blocks, and barrier pillars should be wider than the panel widths.

Yield pillars would need to be wider than those in Canada to allow for the higher vertical virgin stresses. However, the lack of clay seams would require narrower pillars to create the necessary uniaxial loading and yield. Therefore the range of pillars in Canada (6m to 9m) should provide for these two opposite effects. The exact, optimum dimensions will only be determined by experimentation underground. The Cominco practice of wider pillars in the central region of each panel should be attempted, to reduce central closure rates. In all panels, as was found in Canada, the maximum yield pillar width should be used, compatible with sufficient stress relief and good roof and floor conditions.

CHAPTER 10

CONCLUSIONS

10. CONCLUSIONS

The work described in this thesis has been concerned with the stability of various panel layouts for an underground potash mining system. The individual pillar and room components of such a system have been considered, as well as the induced effects of the mining system on the overlying geological strata.

Stability has been assessed in terms of theoretical analyses, laboratory testing and in-situ experimentation. The theoretical work has defined the relative effects of changes in each of the mining layout parameters. The laboratory work has been a continuation of previous work using standard testing techniques to assess the properties of various rock types encountered in the mine. Some model studies were conducted to investigate the post-failure characteristics of the material which will form the mine pillars. The in-situ investigations have been used to define the absolute conditions of stability for various layouts and thus provide a comparison with the theoretical results. A study of other potash mining operations has been included as a comparison and guide for the design of the mining layouts. The conclusions reached from these investigations are summarized in the following sections.

10.1 Panel and Barrier Dimensions

i) From both the theoretical and underground results, a panel width of 290m is excessive, for low extraction panels, whereas 240m is within the critical width. Therefore a figure of 260m should be used as a maximum for panel widths. This should also be used as the maximum

critical block width for a stress relief mining block.

ii) The width of a barrier pillar between low extraction panels should be defined by

$$B = W(1.00e - 0.07) \qquad (10.1)$$

where B is the minimum barrier width

W is the maximum panel width (including stub-ends off the panel)

e is the panel extraction ratio

B should always be of such a dimension that its W:H ratio exceeds 16:1.

iii) A barrier pillar which contains a development panel or forms a major block boundary should be at least double the width predicted by (10.1) plus the width of the development panel.

iv) For a stress relief panel, the maximum panel width should be 60m, based on theoretical results and Canadian experience. (This figure is a function of the geology, not the mining height, and so is an absolute maximum.)

v) The barrier pillars between stress relief panels, within a mining block, should be wider than the panel width on the basis of Canadian and theoretical results. The minimum width should also be defined by

$$B = \frac{W}{0.65}\left[1 - \frac{\sigma_{Max.}(1 - e)}{\sigma_V}\right] \qquad (10.2)$$

where B is the minimum barrier width,

W is the panel width,

$\sigma_{Max.}$ should be taken as -16 MN/m^2, subject to further investigations,

σ_v should be taken as $-30\ MN/m^2$

e is the panel extraction ratio.

B should have a minimum W:H ratio of 16:1.

vi) Solid boundary pillars within a production block of stress relief panels should be marginally wider than the barrier width used between panels, i.e. barrier width + 10m.

vii) Barrier pillars containing development panels or forming a major block boundary, adjacent to stress relief panels, should be at least double the width predicted by (10.2) plus the width of the development panel.

viii) All barrier, boundary pillar and panel widths defined in i) to vii) must satisfy the subsidence restrictions represented by Fig. 3-31 and Fig. 4-3. These imply that barrier and boundary pillar widths should be either much greater, or much less than 140m - a range between 90m and 190m should be avoided completely and the further from 140m, the better. Panel widths, similarly, should be either no greater than 60m or no less than 150m.

10.2 Pillar Dimensions

i) Pillars in a low extraction panel should have a minimum W:H ratio of 7 (i.e. 25m for 3.4m high pillars).

ii) Pillar shape does not have a significant influence on pillar stability provided the central core area is not reduced.

iii) The confined core in a stable pillar has a width approximately 15m narrower than the minimum pillar width, for a mining height of 3.4m. Beyond the core zone the lateral strain rates increase rapidly to the pillar edge.

iv) Pillars in a stress relief panel should have a W:H ratio in excess of 1.75 and less than 2.6, and should be as wide as possible, subject to roof conditions. Central pillars in a stress relief panel should be wider than outer pillars for greater stability. An average vertical yield of approximately 2% for a 3.4m high pillar should be sufficient to create stress relief. The pillar should then stabilise at a much lower yield rate.

v) Pillar sizes between the limits defined in i) and iv) should not be used as they will attract load and cause excessive yield, but be too stiff for a stress relief system. Roadway conditions will suffer due to these factors.

vi) Due to the brittle nature of the secondary ore (shale) in both pre and post-failure modes, it should not be used as a pillar material.

10.3 Roadway Stability

i) Roadway junctions should have at least 1.5m of a competent, homogenous material in the roof and floor.

ii) Normal roadways between pillars, and at T junctions, should have at least 2m to 3m of competent material in the roof and floor.

iii) Where the material in ii) is a composite structure, the exposed outer layer should be at least 1.5m thick.

iv) Potash roads should not be greater than 6m wide where shale is present within 3.5m of the immediate roof.

v) Salt roads with the correct roof conditions (see ii)) are stable at least up to 8m wide.

vi) Shale and marl should be regarded as incompetent when unconfined, and so should not form the immediate roof, wall or floor strata.

vii) Wherever closure rates around a roadway enter a steady state condition, the roadway is likely to become unstable.

viii) For maximum stability, long term development roads should be mined in the salt, at least 3m below the base of the potash seam.

10.4 Subsidence

i) The 60m potash pillars have shown considerable vertical yield and their proximity to the shafts appears to be responsible for some of the lining cracking, at least in No. 2 shaft.

ii) Salt pillars are far more rigid than potash pillars and their time-dependent yield is far less. (40m potash pillars exhibited four times as much yield as 40m salt pillars.)

iii) Surface subsidence results indicate a 9.5 month time lag between a face advance underground and the first indication of subsidence induced by it appearing on the surface.

iv) The maximum angle of draw for surface subsidence appears to be approximately 53° and the maximum tensile strain occurs between 32° and 36°.

10.5 Other Conclusions

i) The secondary ore (shale) and Carnallite marl, in a pure state, exhibit virtually elastic properties. However, the non-elastic and time-dependent properties are caused by evaporite inclusions and planes of weakness due to impurities.

ii) The strength of the shale increases considerably with confinement to almost 80% of potash strength.

iii) Potash exhibits elastic recovery when unloaded, even after large amounts of strain. A modulus, based on this recovery, is very similar to one obtained prior to significant straining.

iv) Stress measurements in the potash horizon using an overcoring technique, indicate that the major principal virgin stress is approximately -30 MN/m^2 and is vertical. The horizontal stress distribution is uniform in all directions and is 0.51 times the vertical stress.

v) Theoretical and some underground results suggest that the shale and marl above the seam will be incapable of maintaining a stress redistribution arch over a stress relief panel. If this is the case, excessive closure and subsidence effects will result, and so this type of mining should not be adopted unless it can be proven to have long term stability.

10.6 Recommendations for Future Work

There are obviously a number of aspects of this investigation which need to be carried further in order to modify or complete the conclusions outlined above. These can be summarized as follows.

i) Laboratory work: Comprehensive laboratory creep testing program on all near seam rock types, particularly shale, for which there is no creep data available at all, as yet.

Model testing on creep of pillars, particularly creep of pillars which have been loaded beyond their failure point in the servo-controlled testing machine and unloaded to various stress levels. This will define the long term stability of yield pillars in stress relief panels, and provide an accurate assessment of the value of $\sigma_{Max.}$ in equation (10.2).

ii) Theoretical work: Subsidence analyses can now be carried out using face element techniques with the pillar yield relationships as the boundary conditions. Using the three dimensional program, any variations of the mine layout can be incorporated and the results correlated with surface subsidence data as it is obtained. Once the rheological data from i) is obtained, finite element simulations of stress relief panels can be conducted using a suitable program to assess the long term stability of such mining systems.

iii) In-situ work: Monitoring of experimental stress relief panels is an essential area where data is required. This should include not only the conditions within the panel itself but strain

distributions within adjacent barriers.

Sub-surface subsidence effects induced by mining should be measured above mining blocks and above boundary pillars, if possible, to provide data in this area where only theoretical data have been available in the present investigation.

Regular monitoring of existing stations should be continually assessed to provide further information on the long term behaviour of roads and pillars.

CHAPTER 11

APPENDICES

APPENDIX A

COMPUTER PROGRAM CONTROL DATA AND LISTINGS

The following control cards are for use on the N.U.M.A.C. M.T.S. system at Newcastle University.

1. To run the face element programs, compiled in MNI1:2DOBJ and MNI1:3DOBJ on disk MTS945,

```
$H MTS945
Signon
Password
$R *GETDISK PAR=MTS945
$CRE -A TYPE=SEQ
$CRE -B TYPE=SEQ
$CRE -C TYPE=SEQ
$CRE -D TYPE=SEQ
$CRE -F TYPE=SEQ
$R MNI1:2DOBJ 1=-A 2=-B 3=-C 4=-D 5=-Q 7=-E 8=-F 10=-G
$SIG
File -Q is the data file
```

To run the 3D program, change 2DOBJ to 3DOBJ

2. To run the subsidence program, UGSUB, which is compiled in MNI1: SUBSOBJ on MTS945, with the 2D face element program, insert the following in the above controls before the $SIG card.

```
$CRE -S
$GET -S
$NUMBER
```

.... i

.... j .... k .... l ....

$UNNUMBER

$R MNI1:SUBSOBJ 3=-G 5=-S

Where i is the number of horizons of bench marks in the -Q data set and j, k, l ... are i values for the number of bench marks within each horizon.

3. To run the perturbation analysis program, FACSOLVE, which is on MTS945,

$H MTS945

Signon

Password

$R *GETDISK PAR=MTS945

$R *FORTRAN SCARDS=MNI1:FACSOLVE SPUNCH=-A

$R -A+*NAG 5=-Q

$SIG

File -Q is the stresses and displacements data file from the 2D and 3D face element runs.

4. To run DATAPLOT which is compiled in MNI1:DPOBJ2 on MTS945

$H MTS945 PLOT 20M 10F

Signon

Password

$R *GETDISK PAR=MTS945

$R MNI1:DPOBJ2+*PLOTLIB+*NAG 5=-Q 7=-W 8=-E 9=-R 10=-T 11=-Y 12=-U

$R *UNEPLOT SCARDS=-R

$SIG

File -Q is the data file.

5. To run FEMITPLT which is compiled in MNI1:FEMOBJ2 on MTS945

$H MTS945 PLOT 10M 10F

Signon

Password

$R *GETDISK PAR=MTS945

$R MNI1:FEMOBJ2+*PLOTLIB 1=-Q 3=*SINK* 5=-S 9=-R

$R *UNEPLOT SCARDS=-R

$SIG

File -Q is the data file.

6. To run STRAINPLOT which is on MTS945,

$H MTS945

Signon

Password

$R *GETDISK PAR=MTS945

$R *FORTRAN SCARDS=MNI1:STRAINPLOT SPUNCH=-A

$R -A 1=-B 5=-C 6=-Q

$SIG

Where -B contains the basic DATAPLOT controls and title cards and

-C contains the Talbott cell output as times plus 9 readings for each scan on each line,

-Q is the input file for DATAPLOT.

7. To run SURFSUB and plot the subsidence and strain data with XYPLOT (both on MTS945)

$H MTS945 PLOT 10M 10F

Signon

Password

```
$R *GETDISK PAR=MTS945
$R *FORTRAN SCARDS=MNI1:SURFSUB SPUNCH=-A
$R -A 5=-Q 7=-J 8=-K
$R *FORTRAN SCARDS=MNI1:XYPLOT SPUNCH=-B
        $R -B+*PLOTLIB 5=-J 6=-R 9=-P1
        $R -B+*PLOTLIB 5=-K 6=-T 9=-P2
        $C -P1+-P2 To -P3
        $R *UNEPLOT SCARDS=-P3
        $SIG
```

Where -Q is the subsidence data file

-J is the subsidence output file

-K is the lateral strain output file.

The following pages are listings of the two programs, FACSOLVE and DATAPLCT.

DAMAGED

TEXT

IN

ORIGINAL

BEST COPY

AVAILABLE

Variable print quality

```
$SIG MNI1 T=2 P=10
CHARGING RATE = UNIVERSITY, EATCH
**LAST SIGNON WAS: 12:15:04    TUE   2-AUG-77
 USER "MNI1" SIGNED ON AT  10:20:19 ON THU 18-AUG-77
$L FACSOLVE
      1       C         PROGRAM TO CALCULATE 2D AND 3D INFLUENCE FACTORS FROM
      2       C         FACE ELEMENT PERTUREATIONS
      3             DIMENSION STRESS(20),STNEW(20),STIN(20),DISPL(20,20),
      4            1DELU(20,20),STOUT(20,20),FAC(20,20),RHS(20,1)
      5             DIMENSION                          SOLN(20,20),AL(20),CROUT(20,20)
      6             DIMENSION RESID(20,20)
      7             DIMENSION FINAL(20)
      8       C
      9       C         INPUT DATA IS YOUNG'S MODULUS,SEAM THICKNESS,NO. OF STRESS
     10       C         VARIABLES,NO. OF NON-PERTURBED VARIABLES,(E.G. IN RIBSIDE),
     11       C         VERTICAL VIRGIN STRESS VALUE USED,
     12       C         BASE AND PERTURBED STRESS VALUE, (NRUN-NZERO) SETS OF
     13       C         (NVAR) DISPLACEMENTS. OUTPUT IS IN NVAR SETS OF NVAR FACTORS
     14       C         IN (I,J) MATRIX FORM WHERE I REFERS TO THE INPUT PERTURBATION
     15       C         AND J TO THE OUTPUT INFLUENCE.
     16       C
     17             REAL*8 FAC,RHS,SOLN,AL,CROUT,RESID
     18             DO 14 NR=1,2
     19             DO 2 I=1,20
     20             STRESS(I)=0.0
     21             STNEW(I)=0.0
     22             STIN(I)=0.0
     23             DO 2 J=1,20
     24             DISPL(J,I)=0.0
     25             DELU(J,I)=0.0
     26             STOUT(J,I)=0.0
     27             IF(NR.EQ.2) GO TO 2
     28             FAC(J,I)=0.0
     29             RHS(J,1)=0.0
     30           2 CONTINUE
     31             READ(5,1) YMOD,THICK,NVAR,NZERO,VIRGY
     32             WRITE(6,101) YMOD,THICK,NVAR,NZERO,VIRGY
     33             NZ=NZERO+1
     34             NRUN=NVAR+1
     35             DO 4 I=NZ,NVAR
     36             READ(5,3) STRESS(I),STNEW(I)
     37             WRITE(6,103) STRESS(I),STNEW(I)
     38             WRITE(6,9)
     39             IF(NR.EQ.2) GO TO 4
     40             FINAL(I)=STRESS(I)
     41             RHS(I,1)=STRESS(I)-VIRGY
     42           4 STIN(I)=STNEW(I)-STRESS(I)
     43             DO 6 I=NZ,NRUN
     44             K=I-1
     45             KL=NVAR/5
     46             IF((5*KL).LT.NVAR) KL=KL+1
     47             DO 12 II=1,KL
     48             J1=5*II-4
     49             J2=5*II
     50          12 READ(5,11) (DISPL(J,I),J=J1,J2)
     51             WRITE(6,5) (DISPL(J,I),J=1,NVAR)
     52             IF(K.EQ.NZERO) GO TO 6
     53             DO 6 J=1,NVAR
     54             DELU(J,K)=DISPL(J,I)-DISPL(J,K)
     55             STOUT(J,K)=2.0*(DELU(J,K)*YMOD/THICK)
```

```
      FAC(J,K)=FAC(J,K)+STOUT(J,K)/STIN(K)
    6 CONTINUE
      DO 14 J=1,20
      RHS(J,1)=RHS(J,1)-(DISPL(J,NZ)*2.0*YMOD/THICK)
   14 CONTINUE
      WRITE(6,9)
      DO 8 K=1,NVAR
      DO 10 M=1,NVAR
      IF(K.EQ.M) FAC(M,K)=FAC(M,K)-1.0
   10 WRITE(6,7) K,M,FAC(M,K)
    8 WRITE(6,9)
C       PROGRAM TO SOLVE SIMULTANEOUS LINEAR EQUATIONS
      ISIM=20
      DO 88 I=1,NVAR
      AL(I)=0.0
      DO 88 I=1,NVAR
      SOLN(J,I)=0.0
      CROUT(J,I)=0.0
   88 RESID(J,I)=0.0
      DO 32 I=1,NVAR
   32 WRITE(6,33) RHS(I,1)
   33 FORMAT(2X,F12.2)
      WRITE(6,9)
      I=1
      CALL F04AEF(FAC,ISIM,RHS,20,NVAR,1,SOLN,NVAR,AL,CROUT,NVAR,RESID,
     1NVAR,I)
      IF(I.EQ.0) GO TO 40
      WRITE(6,200) I
  200 FORMAT(1HO, 25HFAILURE IN F04AEF, IFAIL=,I5)
      STOP
   40 WRITE(6,201) (SOLN(I,1),I=1,NVAR)
      WRITE(6,105)
      DO 77 I=1,NVAR
      FINAL(I)=FINAL(I)+SOLN(I,1)
   77 WRITE(6,101) FINAL(I)
    1 FORMAT(2(1PE9.2),2I2,1PE9.2)
  101 FORMAT(2X,2(1PE9.2),2I2,1PE9.2)
    3 FORMAT(2(1PE12.5))
  103 FORMAT(2X,2(1PE12.5))
    5 FORMAT(2X,15(1PE11.4,1X))
    7 FORMAT(2X,'(',I2,',',I2,')',4X,F10.5)
    9 FORMAT(///)
   11 FORMAT(  5(1PE11.4,5X))
  201 FORMAT(1H ,1P216.9)
  105 FORMAT(///,2X,' FINAL SOLUTION STRESSES',/)
      STOP
      END
END OF FILE


$SIG
```

```
$SIG MNI1 T=5 P=40
CHARGING RATE = UNIVERSITY, BATCH
**LAST SIGNON WAS: 12:14:38
 USER "MNI1" SIGNED ON AT  12:15:04 ON TUE  2-AUG-77
$R *GETDISK PAR=MTS945
EXECUTION BEGINS
DONE MTS945
EXECUTION TERMINATED


$L DATAPLOT
C*****************************************************************************
C
C                    ****** "DATAPLOT" PROGRAM ******
C
C                    MARCH, 1977  VERSION
C
C                    THIS PROGRAM IS IN COMPILED FORM IN FILE MNI1:DPOBJ
C
C*****************************************************************************
C
C          THIS PROGRAM IS A GENERAL PROGRAM FOR ANALYSIS AND OPTIONAL PLOTTING OF
C          TIME-DEPENDENT SEQUENTIAL DATA. THE TYPE OF DATA SUITABLE FOR ANALYSIS
C          INCLUDES MULTI-ANCHOR BOREHOLE EXTENSOMETER DEFORMATIONS(UP TO 10
C          ANCHORS), ANY OTHER FORM OF DEFORMATION READINGS SUCH AS MINE ROOF SAG
C          AND CONVERGENCE DATA, ANY LABORATORY TIME-DEPENDENT DEFORMATION OR
C          STRAIN DATA, PLUS MULTI-GAUGE OVERCORING OR MONITORING STRAIN AND
C          STRESS DATA. THE FACILITIES AND OPTIONS AVAILABLE ARE DESCRIBED FULLY
C          IN THE USERS MANUAL. THE PROGRAM HAS BEEN DEVELOPED FOR USE WITH DATA
C          FROM THE CLEVELAND POTASH LTD RESEARCH PROJECT ON BOULBY POTASH MINE.
C
C*****************************************************************************
C
C          FOR FURTHER REFERENCE, CONTACT:  B. K. HEBBLEWHITE
C                                           DEPT. OF MINING ENGINEERING,
C                                           UNIVERSITY OF NEWCASTLE UPON TYNE
C
C*****************************************************************************
      DIMENSION D(22),C(22,200)
      DIMENSION CC(22,200)
      DIMENSION HE(22,22)
      DIMENSION A(200),B(200),HM(17),KOUNT2(10)
      DIMENSION KPLOT(17),DEP(10),RDAY(10,150),RDEF(10,150),RST(10,150)
      DIMENSION RSTR(10,150),PLNO(10),RSSTR(10,150),RSST(10,150)
      DIMENSION NBAY1(10),NBAY2(10),RT(10)
      REAL*8 A,B,C,D,CC,RDAY,RDEF,RST,RSTR,RSSTR,RT,RSST
  997 CONTINUE
C
C          UNLESS NOREAD=0, THE PROGRAM WILL NOT START TO READ THE DATA REQUIRED.
C          THIS ENABLES OTHER CONTROL CARDS TO PRECEDE THOSE REQUIRED.
C          IN1 IS THE NO. OF COMPLETE DATA SETS(EG NO. OF BOREHOLES, ETC. )
C          THIS SHOULD BE THE ONLY INPUT NO. ON THE FIRST DATA CARD.
C                                                                  (2X,I2)
      READ(5,998) NOREAD, IN1,(HM(IH),IH=1,17)
      IF(NOREAD.NE.0) GO TO 997
  998 FORMAT(2I2,17A4)
C
C          JPLOT=0 IF NO PLOTS ARE REQ'D, 1 FOR A4 SIZED PLOTS,
C          MSC=0 FOR AUTOMATIC SCALING OR 1 IF MANUAL SCALING IS TO BE SUPPLIED
```

```
C        FOR ALL PLOTS
C                                                                    (2I4)
      READ(5,999) JPLOT,MSC
      DO 115 IN2=1,IN1
C
C        ALL INPUT FROM HERE IS SUPPLIED 'IN1' TIMES
C
      DO 7000 IM=1,22
      D(IM)=0.0
      DO 7000 I=1,200
      CC(IM,I)=0.0
 7000 C(IM,I)=0.0
C
C        NO IS THE NO. OF BLOCKS OF DATA SUPPLIED WITHIN EACH SET(UP TO 10)
C        WHEN PLOTTED, THERE ARE 'NO' PLOTS PER PICTURE (I.E. NO OF ANCHORS, ETC
C        JTYPE DEFINES THE DATA TYPE 0,1,2 FOR EXTENSOMETER DATA,
C        3 FOR CONVERGENCE DATA, 4 FOR LAB. DATA, 5 FOR OVERCORING DATA.
C        JTIME=0 FOR TIME DATA AS HRS,MINS,DATE OR =1 FOR DIRECT ELAPSED TIME
C                                                                    (3I4)
      READ(5,999) NO,JTYPE,JTIME
      JTYPE=JTYPE+1
      IF(JPLOT.EQ.0) GO TO 7001
C
C        IF PLOTTING HAS BEEN REQUESTED, KPLOT DEFINES THE TYPES OF PLOT REQ'D
C        A 0 VALUE MEANS NO PLOT, A 1 MEANS PLOT, IN EACH SUCCESSIVE I4 RECORD.
C        THE ORDER OF PLOT TYPES IS, DEFORMATION V TIME, STRAIN V TIME, STRAIN
C        RATE V TIME, SMOOTHED STRAIN RATE V TIME, BAY STRAIN V TIME, BAY STRAIN
C        RATE V TIME, SMOOTHED BAY STRAIN RATE V TIME, CONVERGENCE V TIME, CONV.
C        RATE V TIME, SMOOTHED CONV. RATE V TIME, BAY STRAIN V DEPTH, BAY STRAIN
C        RATE V DEPTH, SMOOTHED BAY STRAIN RATE V DEPTH, STRESS V TIME, STRAIN V
C        DISTANCE, SMOOTH STRAIN V TIME, SMOOTH BAY STRAIN V TIME
C                                                                    (17I4)
      READ(5,999) (KPLOT(J),J=1,17)
 7001 CONTINUE
      IF(JTYPE.EQ.5) IEXC=0
      IF((JTYPE.EQ.5).OR.(JTYPE.EQ.4)) GO TO 6060
C
C        IEXC IS THE NO. OF ELAPSED DAYS PRIOR TO THE START OF READINGS. FOR LAB
C        DATA IT IS SET TO 0, FOR CONV. IT IS SUPPLIED LATER.
C                                                                    (I4)
      READ(5,999) IEXC
 6060 CONTINUE
  999 FORMAT(17I4)
      DO 6010 J=1,10
      NBAY1(J)=0
      NBAY2(J)=0
      RT(J)=0.0
      DEP(J)=0.0
      DO 6010 K=1,150
      RDAY(J,K)=0.0
      RDEF(J,K)=0.0
      RST(J,K)=0.0
      RSTR(J,K)=0.0
      RSST(J,K)=0.0
 6010 RSSTR(J,K)=0.0
      DAYMAX=0.0
      DEFMIN=0.0
      DEFMAX=0.0
      STMIN=0.0
      STMAX=0.0
```

```
      STRMIN=10.0
      STRMAX=0.0
      SSTRMN=10.0
      SSTRMX=0.0
      SSTMIN=0.0
      SSTMAX=0.0
      NNN=0
      N4=0
      DO 2 JW=1,NO
C
C        THE FOLLOWING DATA IS INPUT 'NO' TIMES FOR EACH DATA SET
      DO 3 I=1,200
      A(I)=0.0
      B(I)=0.0
    3 CONTINUE
      NN=0
C
      CALL READIN(A,B,HM,RAY,NN,JW,NO,IFAC,IFACY,IEXC,JTYPE,JTIME,DAYMAX,
     1DEFMIN,DEFMAX,STMIN,STMAX,STRMIN,STRMAX,SSTRMN,SSTRMX,
     2RDAY,RDEF,RST,RSTR,RSSTR,DEP,KOUNT2,NUNIT,PLNO,
     3SSTMIN,SSTMAX,RSST,NBAY1,NBAY2)
C
      INN=NN
      DO 200 I=1,NN
  600 CONTINUE
      IK=I
  203 CONTINUE
      IF (A(I).NE.0.0) GO TO 200
      INN=INN-1
      IK=IK+1
      DO 202 II=I,NN
      IJ=II+1
      A(II)=A(IJ)
      B(II)=B(IJ)
  202 CONTINUE
      IF (A(I).NE.0.0) GO TO 200
      IF (IK.GE.INN) GO TO 200
      GO TO 203
  200 CONTINUE
    7 FORMAT(2F11.4)
      IF(NNN.GT.NN) GO TO 4
      NNN=NN
    4 CONTINUE
      DO 5 I=1,200
      J=JW
      JJ=2*J-1
      C(JJ,I)=A(I)
      JJ=JJ+1
      C(JJ,I)=B(I)
    5 CONTINUE
      HC(J,I)=HM(9)
      HI(J,2)=HM(10)
      D(J)=RAY
    2 CONTINUE
      IF(JPLOT.EQ.0) GO TO 8000
C
      CALL PLOT(HM,KELCT,DEP,RDAY,RDEF,RST,RSTR,RSSTR,
     1DAYMAX,NUNIT,JPLOT,NN,DEFMIN,DEFMAX,STMIN,STMAX,STRMIN,
     2STRMAX,SSTRMN,SSTRMX,IEXC,JTYPE,KOUNT2,PLNO,MSC,NBAY1,NBAY2,RT,
     3SSTMIN,SSTMAX,RSST)
```

```
 8000 CONTINUE
      IF((JTYPE.EQ.4).OR.(JTYPE.EQ.5).OR.(JTYPE.EQ.6)) GO TO 115
      DO 10 I=1,NNN
      DO 530 K=1,NO
      JJ=2*K-1
      JK=JJ+1
      DO 520 K2=1,NO
      IF(K2.EQ.K) GO TO 520
      J2=2*K2-1
      J3=J2+1
      IF(C(JJ,I).EQ.0.0) GO TO 15
      IF(C(JJ,I).LE.C(J2,I)) GO TO 15
      IF(C(J2,I).EQ.0.0) GO TO 16
      DO 1000 J=1,NNN
      CC(JJ,J)=C(JJ,J)
      CC(JK,J)=C(JK,J)
 1000 CONTINUE
      DO 11 II=I,NNN
      III=II+1
      C(JJ,III)=CC(JK,II)
      C(JK,III)=CC(JK,II)
   11 CONTINUE
      C(JK,I)=0.0
      C(JJ,I)=C(J2,I)
      GO TO 15
   16 C(J2,I)=C(JJ,I)
      C(J3,I)=0.0
   15 CONTINUE
  520 CONTINUE
  530 CONTINUE
      IF (C(1,I).EQ.0.0) GO TO 66
      N4=N4+1
   66 CONTINUE
   10 CONTINUE
C
      CALL BAYSTN(C,D,N4,NO,IFAC,HM,IFACY,IEXC,MSC,JTYPE,DEP,KPLOT)
C
  115 CONTINUE
      STOP
      END
C
C*****************************************************************************
      SUBROUTINE RLADIN(A,B,FM,BAY,NN,JW,NO,IFAC,IFACY,IEXC,JTYPE,JTIME,
     1DAYMAX,DEFMIN,DEFMAX,STMIN,STMAX,STRMIN,STRMAX,SSTRMN,SSTRMX,
     2RDAY,RDEF,RST,RSTR,RSSTR,DEP,KOUNT2,NUNIT,PLNO,
     3SSTMIN,SSTMAX,RSST,NBAY1,NBAY2)
      DIMENSION MONTH(12),IM(6,150),DATA(3),RM(18,50),FM(8,150)
      DIMENSION KS(8),PLNO(10),TIM(150)
      DIMENSION A(200),B(200),HM(17),RSST(10,150)
      DIMENSION KPLOT(17),DEP(10),RDAY(10,150),RDEF(10,150),RST(10,150)
      DIMENSION RSTR(10,150),RSSTR(10,150),KOUNT2(10)
      DIMENSION XP(200),FP(200),WP(200),SL(5),P(5)
      DIMENSION NBAY1(10),NBAY2(10),BTIME(10,150),BST(10,150)
      DIMENSION II(10),XN(5),FN(5),W(5),PCEF(4),SI(4)
      REAL*8 XN,FN,W,PCEF,SI,BTIME,BST
      REAL*8 XP,FP,WP,SL,P,T,S,XX,RLSID,RMEAN,RMS
      REAL*8 A,B,FM,RDAY,RDEF,RST,RSTR,RSSTR,RSST
      LOGICAL LPOLY
C     HM CONTAINS [illegible]RINGS, IM DATE AND ELAPSED DAYS, FM DATA AND
```

```
C     CALCULATED VALUES, RM REMARKS.
      NBRATE=0
      MONTH(1)=31
      MONTH(2)=28
      MONTH(3)=31
      MONTH(4)=30
      MONTH(5)=31
      MONTH(6)=30
      MONTH(7)=31
      MONTH(8)=31
      MONTH(9)=30
      MONTH(10)=31
      MONTH(11)=30
      MONTH(12)=31
C     ZERO AND SET INITIAL VALUES
      GO TO 95
C
      ENTRY READ2(HM,NO,NBAY1,NBAY2,BTIME,BST,DEP,II,MSC,JTYPE,KPLOT,IEXC
     1,RDAY,RSTR,RSSTR,DAYMAX,STRMIN,STRMAX,SSTRMN,SSTRMX,KOUNT2,RST,
     2SSTMIN,SSTMAX,RSST)
C
      NBRATE=1
      KB=1
      JW=1
      DAYMAX=0.0
      STRMAX=0.0
      STRMIN=10.0
      SSTRMX=0.0
      SSTRMN=10.0
      SSTMIN=0.0
      SSTMAX=0.0
   95 CONTINUE
  415 DO 309 I=1,150
      DO 310 J=1,6
  310 IM(J,I)=0
      DO 311 J=1,7
  311 FM(J,I)=0.0
      TIM(I)=0.0
  309 CONTINUE
      DO 312 I=1,18
      DO 312 J=1,50
  312 RM(I,J)=0.0
      KOUNT=1
      IYEAR=0
      HK=1
      DEFSTO=0.0
      ADJUST=0.0
      IF(NBRATE.NE.0) GO TO 80
C     READ HEADER CARD
      GO TO (5000,5000,5000,5010,5020,5020),JTYPE
 5000 NTYPE=0
C
C         EXTENSOMETER TITLE CARDS-TITLE,BAY=ANCHOR DEPTH(FROM MOUTH STATION),
C         NRD=NO. OF READINGS TO BE AVERAGED FOR EACH TIME SCAN, NUNIT=1 IF ALL
C         INPUT AND OUTPUT IS TO BE IN INCHES, =0 FOR OUTPUT IN METRES.
C         THE DEEPEST ANCHOR DATA SHOULD BE READ IN FIRST AND IS NUMBERED 'NO'
C                                                                (14A4,F8.0,I2,6X,I2)
      READ(5,101) (HM(I),I=1,14)     ,NRD,NUNIT
      GO TO 5030
 5010 CONTINUE
```

```
C        CONVERGENCE TITLE CARDS - TITLE AND IEXC AS EARLIER
C                                                              (17A4,5X,I4)
         READ(5,5011) (HM(I),I=1,17),IEXC
         PLNG(JW)=HM(14)
         NRD=1
         NUNIT=0
         BAY=1.0
         GO TO 5030
C
C           LAB DATA TITLE CARDS-TITLE, BAY=SPECIMEN HEIGHT(=1.0 FOR STRAIN DATA
C           INPUT), NRD AS BEFORE, NTYPE=0 FOR DEFN INPUT,  1 FOR STRAIN INPUT AND
C           2 FOR MICROSTRAIN INPUT,NUNIT AS BEFORE.
C                                                              (15A4,F6.0,3I4)
 5020    READ(5,5015) (HM(I),I=1,15),BAY,NRD,NTYPE,NUNIT
 5015    FORMAT(15A4,F6.0,3I4)
 5030    CONTINUE
  101    FORMAT (14A4,F8.0,I2,6X,I2)
         RD=NRD
         NALTER=0
C    READ DATA CARDS
C
C           FOR ALL TYPES OF DATA, THE TIME VALUE CAN BE USED AS AN OPTION CONTROL.
C           TIME=40.00 TO CHANGE BAY LENGTH - NEW VALUE IN DATA COLUMNS
C           TIME=50.00 NEW BASE READING(IE PREVIOUS READING IN TERMS OF NEW SCALE)
C           TIME=60.00 INSTRUMENT ADJUSTMENT, + OR - CHANGE
C           TIME=70.00    LOWS REMARKS TO BE INSERTED IN FOLLOWING CARD
C           TIME=80.00 IF INPUT IS IN INCHES BUT OUTPUT IS REQ'D IN METRES
C           TIME=85.00 IF CHANGING FROM MULTIPLE READINGS TO SINGLE READINGS/SCAN
C           THE 2 PREVIOUS OPTIONS ARE ONLY REQ'D FOR THE FIRST DATA CARD AFFECTED
C           AND THE TRUE TIME FOR THAT DATA IS DEFAULTED TO 12.00
C           TIME=88.88 USED AFTER LAST DATA CARD IN EACH BLOCK, AS END MARKER.
C
         DEP(JW)=BAY
         IREAC1=0
         IPUNCH=0
         BASE=0.0
 5001    CONTINUE
         IF(JTYPE.EQ.4) GO TO 5007
         IF(JTIME.NE.1) GO TO 505
C
C           THIS IS FOR ALL DATA TYPES EXCEPT CONVERGENCE, WHERE DIRECT TIME
C           READINGS ARE SUPPLIED
C           TIME IS USED PURELY AS AN OPTION CONTROL, EDAY=ELAPSED DAYS THEN NRD
C           SETS OF DATA VALUES ARE SUPPLIED
C                                                              (F5.2,1X,F9.4,6F10.0)
         READ(5,5005) TIME,EDAY,(DATA(K),K=1,NRD)
 5005    FORMAT(F5.2,1X,F9.4,6F10.0)
         GO TO 5006
C
C           THIS IS FOR ALL EXCEPT CONVERGENCE DATA, WHERE TIME, DATE ARE SUPPLIED.
C           TIME IS GIVEN IN HRS, WITH THE DECIMAL PART BEING THE MINS. IM(I,KOUNT)
C           IS THE DATE (DAY,MONTH,YR) AND THEN DATA AS BEFORE.
C                                                              (F5.2,I2,1X,I2,1X,I2,2X,6F10.0)
  505    READ(5,102) TIME,(IM(I,KOUNT),I=1,3),(DATA(K),K=1,NRD)
         GO TO 5006
 5007    IF(IPUNCH.NE.0)  GO TO 5013
C
C           THIS IS FOR CONVERGENCE DATA AND IS USED TO HANDLE OLD DATA HENCE THE
C           ..ODULAR FORMAT. IEND IS 0 EXCEPT AFTER LAST DATA CARD WHEN IT IS -1.
```

```
      C        DATE AS BEFORE. ONLY ONE DATA VALUE. HOLE IS EQUIVALENT TO NEW BASE
      C        VALUE WHEN TAPES USED-REPRESENTS DISTANCE BETWEEN OLD AND NEW HOLE.
      C        IREAD IS NON ZERO WHEN DATA CHANGES FROM TAPE EXTENSN TO DIRECT READ
      C        FROM FOLLOWING TIME SCAN. TIME CAN BE USED AS BEFORE.
      C                                                    (2I2,2I4,2F10.5,I5,3X,F5.2)
            READ(5,5012) IEND,(IM(I,KOUNT),I=1,3),DATA(1),HOLE,IREAD,TIME
            DBA=DBASE
            DBASE=DATA(1)
            IF(IREAD1.EQ.10) TIME=50.00
            IREAD1=0
            IF(IEND.LT.0) TIME=88.88
            IF(HOLE.EQ.0.0) GO TO 5014
            TIME=50.00
            DNEW=DATA(1)
            KI=IM(1,KOUNT)
            LI=IM(2,KOUNT)
            MI=IM(3,KOUNT)
            DATA(1)=DBA+HOLE
            IPUNCH=1
            GO TO 5006
         5013 DATA(1)=DNEW
            IM(1,KOUNT)=KI
            IM(2,KOUNT)=LI
            IM(3,KOUNT)=MI
            HOLE=0.0
            TIME=0.0
            IPUNCH=0
         5014 IF(IREAD.EQ.0) GO TO 5006
            IREAD1=10
            IREAD=0
         5011 FORMAT(17A4,5X,I4)
         5012 FORMAT(2I2,2I4,2F10.5,I5,3X,F5.2)
         5006 CONTINUE
            IF(NTYPE.NE.2) GO TO 6080
            DO 6075 K=1,NRD
         6075 DATA(K)=DATA(K)/10000000.0
         6080 CONTINUE
            TIM(KOUNT)=TIME
            IF(TIME.EQ.00.00) TIME=12.00
            IF(TIME.EQ.80.00) MALTER=1
            IF(TIME.EQ.81.00) GO TO 5001
            IF((TIME.EQ.80.00).AND.(IM(1,KOUNT).EQ.0)) GO TO 5001
            IF(TIME.EQ.80.00) TIME=12.00
            IF(MALTER.NE.1) GO TO 599
            DO 598 K=1,NRD
          598 DATA(K)=0.025400*DATA(K)
          599 CONTINUE
            IF(JTYPE.NE.5) GO TO 5036
         5036 CONTINUE
            IF(TIME.EQ.85.00) GO TO 600
            GO TO 610
          600 RD=1.0
            NRD=1
            TIME=12.00
          610 CONTINUE
          102 FORMAT (F5.2,I2,1X,I2,1X,I2,2X,6F10.0)
            IF (TIME-88.88) 401,402,402
          401 IF (TIME-30.0) 403,404,404
          404 NCK=(TIME/10.0)-2.0
            GOTO (501,502,503,504),NCK
```

```
      LA=1
      KA=1
C     "IF" TESTS FOR NON-DATA VALUES
  429 IF (IM(6,KA)) 999,427,428
  428 KA=KA+1
      GOTO 429
  427 KS(LA)=KA
      IF (LA-4) 430,431,999
  430 LA=LA+1
      KA=KA+1
      GOTO 429
  431 CONTINUE
      LA=5
      KA=KOUNT
  434 IF (IM(6,KA)) 999,432,433
  433 KA=KA-1
      GOTO 434
  432 KS(LA)=KA
      IF (LA-8) 435,436,999
  435 LA=LA+1
      KA=KA-1
      GOTO 434
  436 CONTINUE
      K1=KS(1)
      JST=1
      K2=KS(2)
      K3=KS(3)
      K4=KS(4)
      K7=KS(8)
      K8=KS(7)
      K9=KS(6)
      K10=KS(5)
      SUM23=FM(2,K1)+FM(2,K2)+FM(2,K3)
      FM(3,K1)=SUM23/3.0
      SUM24=SUM23+FM(2,K4)
      FM(3,K2)=SUM24/4.0
      SUM23=FM(2,K10)+FM(2,K9)+FM(2,K8)
      FM(3,K10)=SUM23/3.0
      SUM24=SUM23+FM(2,K7)
      FM(3,K9)=SUM24/4.0
      K5=KS(4)+1
      M=1
  439 IF (IM(6,K5)) 999,437,438
  438 K5=K5+1
      GOTO 439
  437 CONTINUE
      FM(3,K3)=(FM(2,K1)+FM(2,K2)+FM(2,K3)+FM(2,K4)+FM(2,K5))/5.0
      XN(1)=FM(9,K1)
      XN(2)=FM(8,K2)
      XN(3)=FM(8,K3)
      XN(4)=FM(9,K4)
      XN(5)=FM(8,K5)
      FN(1)=FM(4,K1)
      FN(2)=FM(4,K2)
      FN(3)=FM(4,K3)
      FN(4)=FM(4,K4)
      FN(5)=FM(4,K5)
      DO 450 L=1,5
  450 W(L)=1.0
      IF(JST.EQ.1) W(1)=100.0
```

```
      XP(M)=XN(1)
      FP(M)=FN(1)
      WP(M)=W(1)
      LPOLY=.TRUE.
      CALL E02AEF(5,XN,FN,W,4,ND,SI,PCEF,LPOLY)
      FM(5,K3)=PCEF(1)+PCEF(2)*XN(3)+PCEF(3)*XN(3)**2+
     1PCEF(4)*XN(3)**3
      FM(7,K3)=PCEF(2)+2.*PCEF(3)*XN(3)+3.*PCEF(4)*XN(3)**2
      IF(JST.NE.1) GO TO 452
      FM(5,K1)=PCEF(1)+PCEF(2)*XN(1)+PCEF(3)*XN(1)**2+
     1PCEF(4)*XN(1)**3
      FM(7,K1)=PCEF(2)+2.*PCEF(3)*XN(1)+3.*PCEF(4)*XN(1)**2
      FM(5,K2)=PCEF(1)+PCEF(2)*XN(2)+PCEF(3)*XN(2)**2+
     1PCEF(4)*XN(2)**3
      FM(7,K2)=PCEF(2)+2.*PCEF(3)*XN(2)+3.*PCEF(4)*XN(2)**2
  452 CONTINUE
      IF(K5.NE.K10) GO TO 454
      FM(5,K4)=PCEF(1)+PCEF(2)*XN(4)+PCEF(3)*XN(4)**2+
     1PCEF(4)*XN(4)**3
      FM(7,K4)=PCEF(2)+2.*PCEF(3)*XN(4)+3.*PCEF(4)*XN(4)**2
      FM(5,K5)=PCEF(1)+PCEF(2)*XN(5)+PCEF(3)*XN(5)**2+
     1PCEF(4)*XN(5)**3
      FM(7,K5)=PCEF(2)+2.*PCEF(3)*XN(5)+3.*PCEF(4)*XN(5)**2
  454 CONTINUE
      IF (K5-K1C) 440,441,999
  440 K1=K2
      K2=K3
      K3=K4
      K4=K5
      K5=K5+1
      M=M+1
      JST=0
      GO TO 439
  441 CONTINUE
      DO 456 IL=1,4
      M=M+1
      ILN=IL+1
      XP(M)=XN(ILN)
      FP(M)=FN(ILN)
  456 WP(M)=W(ILN)
      LPOLY=.FALSE.
      CALL E02AEF(M,XP,FP,WP,5,ND,SL,P,LPOLY)
C     PRINT-OUT HEADINGS
      WRITE (6,201)
  201 FORMAT (1H1)
      IF(JTYPE.NE.5) GO TO 6050
      WRITE(6,6055) (HN(I),I=1,15),BAY
 6055 FORMAT(5X,15A4,3X,19H SPECIMEN HEIGHT - ,F8.5,//)
      GO TO 6052
 6050 CONTINUE
      IF(NBRATE.NE.1) GO TO 6046
      WRITE(6,6045) (HN(I),I=1,9),NBAY1(JW),NBAY2(JW)
 6045 FORMAT(5X,9A4,25X,25H BAY BETWEEN ANCHOR NO.,I3,15H AND ANCHOR NO.
     1,I10,//)
      GO TO 6052
 6046 CONTINUE
      WRITE (6,202) (HN(I),I=1,17),BAY
      FORMAT(5X,17A4,16H DATUM HEIGHT - ,F8.5,//)
 6052 CONTINUE
      IF(OUTPUT.NE.2) GO TO 6047
```

```
      IF(JTYPE.EQ.6) GO TO 6043
      WRITE (6,203)
  203 FORMAT(1X,4HTIME,2X,
     1       2X,4HDATE,5X,7HELAPSED,2X,4HMEAN,4X,11HDEFORMATION,1X,
     2 26HSTRAIN,5X,8HSMOOTHED,3X,8HRESIDUAL,3X,7HLOG SM.,4X,6HSTRAIN,5X,
     3 38HSMOOTHED,3X,7HLOG SM.,/18X,4HDAYS,5X,7HREADING,1X,8H(METRES),
     4 44X,10H(PER CENT),1X,6HSTRAIN,5X,9HS.S.-POLY,2X,6HSTRAIN,5X,
     5 54HRATE,7X,9HSTR. RATE,2X,9HSTR. RATE,//)
      GO TO 6049
 6043 WRITE(6,6044)
 6044 FORMAT(1X,4HTIME,2X,
     1       2X,4HDATE,5X,7HELAPSED,2X,4HMEAN,4X,11HDEFORMATION,1X,
     2 26HSTRAIN,5X,8HSMOOTHED,5X,8HRESIDUAL,3X,7HLOG SM.,4X,6HSTRAIN,5X,
     3 38HSMOOTHED,3X,7HLOG SM.,/18X,4HMINS,5X,7HREADING,1X,8H(METRES),
     4 44X,10H(PER CENT),1X,6HSTRAIN,5X,9HS.S.-POLY,2X,6HSTRAIN,5X,
     5 54HRATE,7X,9HSTR. RATE,2X,9HSTR. RATE,//)
      GO TO 6049
 6047 WRITE(6,6048)
 6048 FORMAT(1X,4HTIME,2X,
     1       2X,4HDATE,5X,7HELAPSED,2X,4HMEAN,4X,11HDEFORMATION,1X,
     2 26HSTRAIN,5X,8HSMOOTHED,5X,8HRESIDUAL,3X,7HLOG SM.,4X,6HSTRAIN,5X,
     3 38HSMOOTHED,3X,7HLOG SM.,/18X,4HDAYS,5X,7HREADING,1X,8H(INCHES),
     4 44X,10H(PER CENT),1X,6HSTRAIN,5X,9HS.S.-POLY,2X,6HSTRAIN,5X,
     5 54HRATE,7X,9HSTR. RATE,2X,9HSTR. RATE,//)
 6049 CONTINUE
      IF(JTYPE.EQ.5) GO TO 6070
      WRITE(6,212) IEXC
  212 FORMAT(12X,' BOREHOLE LOCATION EXPOSED',I4,' DAYS PRIOR TO INSTRUM
     1ENTATION',/)
 6070 CONTINUE
C     PRINT-OUT RESULTS
      HK=1
      IM(6,1)=5
      KOUNT1=KCLNT-1
      RIEXC=IEXC
      WRITE(7,6056) KCLNT
      WRITE(7,6057) RIEXC
      WRITE(8,6056) KCLNT
      WRITE(8,6057) RIEXC
      WRITE(11,6056) KOUNT1
      WRITE(10,6056)  KOUNT1
 6056 FORMAT(I5)
 6057 FORMAT(F5.4)
      KOUNT2(JW)=KCLNT
      RESID=0.0
      NPLS=0
      DO 3213 I=1,KCLNT
      IF (IM(6,I)) 999,413,414
  413 CONTINUE
      IF(FM(5,I).LE.0.0) GO TO 472
      SLC=DLOG(FM(5,I))
  477 CONTINUE
      IF(FM(7,I).LE.0.0) GO TO 473
      SRL=DLOG(FM(7,I))
      GO TO 474
  472 SLC=-9.999
      GO TO 477
  473 SRL=-9.999
  474 CONTINU
      XX=FM(8,I)
```

```
      N1=ND+1
      S=P(N1)
      DO 475 IC=1,ND
      I1=N1-IC
  475 S=S*XX+P(I1)
      T=(FM(5,I)-S)
      RESID=RESID+DABS(T)
      NRES=NRES+1
      WRITE(6,204) (TIM(I),(IM(J,I),J=1,3),FM(8,I),(FM(K,I),K=1,2),
     1(FM(K,I),K=4,5),T,SLO,(FM(K,I),K=6,7),SRL)
      A(I)=FM(8,I)
      B(I)=FM(2,I)
      RDAY(JW,I)=FM(8,I)
      RDEF(JW,I)=FM(2,I)
      RST(JW,I)=FM(4,I)
      RSST(JW,I)=FM(5,I)
      RSTR(JW,I)=FM(6,I)
      RSSTR(JW,I)=FM(7,I)
      IF(RDAY(JW,I).GT.DAYMAX) DAYMAX=RDAY(JW,I)
      IF(RDEF(JW,I).LT.DEFMIN) DEFMIN=RDEF(JW,I)
      IF(RDEF(JW,I).GT.DEFMAX) DEFMAX=RDEF(JW,I)
      IF(RST(JW,I).LT.STMIN) STMIN=RST(JW,I)
      IF(RST(JW,I).GT.STMAX) STMAX=RST(JW,I)
      IF(RSST(JW,I).LT.SSTMIN) SSTMIN=RSST(JW,I)
      IF(RSST(JW,I).GT.SSTMAX) SSTMAX=RSST(JW,I)
      IF((RSTR(JW,I).LT.STRMIN).AND.(RSTR(JW,I).GT.0.000000001))
     1STRMIN=RSTR(JW,I)
      IF(RSTR(JW,I).GT.STRMAX) STRMAX=RSTR(JW,I)
      IF((RSSTR(JW,I).LT.SSTRMN).AND.(RSSTR(JW,I).GT.0.000000001))
     1SSTRMN=RSSTR(JW,I)
      IF(RSSTR(JW,I).GT.SSTRMX) SSTRMX=RSSTR(JW,I)
      WRITE(7,6020) RDAY(JW,I),RDEF(JW,I)
      WRITE(8,6020) RDAY(JW,I),RST(JW,I)
      WRITE(11,6020) RDAY(JW,I),RSTR(JW,I)
      WRITE(12,6020) RDAY(JW,I),RSSTR(JW,I)
 6020 FORMAT(F5.4,1PE11.4)
  204 FORMAT(1X,F5.2,1X,
     1          I2,1H-,I2,1H-,I2,1X,F9.4,1X,F9.6,8(1PE11.4))
      GOTO 313
  414 RDAY(JW,I)=RDAY(JW,(I-1))
      RDEF(JW,I)=RDEF(JW,(I-1))
      RST(JW,1)=RST(JW,(I-1))
      RSST(JW,I)=RSST(JW,(I-1))
      RSTR(JW,I)=RSTR(JW,(I-1))
      RSSTR(JW,I)=RSSTR(JW,(I-1))
      NCK=IM(6,I)-3
      GOTO (513,510,511,512),NCK
  513 WRITE(6,205) (IM(J,I),J=1,3),FM(1,I)
  205 FORMAT (2X,I2,1H-,I2,1H-,I2,24H  NEW BAY LENGTH=    ,F9.5)
      GOTO 313
  510 CONTINUE
      IF(FM(7,I).GT.0.0) SRL=DLOG(FM(7,I))
      IF(FM(7,I).LE.0.0) SRL=-9.999
      WRITE(6,206) (IM(J,I),J=1,3),FM(1,I),FM(5,I),FM(7,I),SRL
  206 FORMAT (2X,I2,1H-,I2,1H-,I2,21H  NEW BASE VALUES=,F9.5,
     1 1PE11.4,35X,2(1PE11.4))
      IF(I.EQ.1) SSTRMX=FM(7,I)
      IF(I.EQ.1) RSSTR(JW,I)=FM(7,I)
      IF(I.EQ.1) RDAY(JW,I)=RICXC
      IF(I.EQ.1) GO TO 313
```

```
      WRITE(10,6020) RDAY(JW,I),RSSTR(JW,I)
      GOTO 313
  511 WRITE(6,207) (IM(J,I),J=1,3),FM(1,I)
  207 FORMAT (2X,I2,1H-,I2,1H-,I2,31H  INSTRUMENT ADJUSTMENT=    ,F9.
     25)
      GOTO 313
  512 WRITE(6,208) (IM(J,I),J=1,3),(RM(K,HK),K=1,18)
  208 FORMAT (2X,I2,1H-,I2,1H-,I2,10X,18A4)
      HK=HK+1
      GOTO 313
  313 CONTINUE
      NN=NN+1
 3313 CONTINUE
      TMARK=-1.0
      WRITE(7,6025) TMARK
      WRITE(8,6025) TMARK
      WRITE(11,6025) TMARK
      WRITE(10,6025) TMARK
 6025 FORMAT(F9.4)
      WRITE(6,209)
  209 FORMAT (2X,14HEND OF SUMMARY)
      IF (TIME-88.88) 999,416,416
  999 WRITE(6,210)
  211 FORMAT (2X,33H***WARNING*** ERROR BRANCH TO END)
  416 WRITE(6,210)
  210 FORMAT (2X,14HEND OF PROGRAM)
      WRITE(6,460)
  460 FORMAT(////,90H  LEAST SQUARES FIT OF SMOOTHED STRAIN V. TIME BY O
     1RTHOGONAL POLYNOMIALS USING NAG E02ADF)
      WRITE(6,465)
  465 FORMAT(//5X,15HCOEFFICIENTS OF,10X,8HGOODNESS/5X,
     115HBEST POLYNOMIAL,11X,6HOF FIT)
      DO 466 I=1,5
  466 WRITE(6,470) P(I),SL(I)
  470 FORMAT(4X,E14.6,8X,E14.6)
      RMEAN=RESID/NRES
      WRITE(6,476) RMEAN
  476 FORMAT(/5X,58HRESIDUAL = SMOOTHED-(POLY. FITTED STRAIN)   MEAN RES
     1IDUAL=,1PE11.4)
      IF(NBRATE.EQ.0) GO TO 96
      JW=JW+1
   95 KB=KB+1
      IF(KB.LE.NC) GO TO 80
      NJ=JW-1
   96 CONTINUE
      RETURN
      END
C
C
      SUBROUTINE EAYSTR(C,D,NN,NO,IFAC,HM,IFACY,IEXC,MSC,JTYPE,DEP,KPLOT)
      DIMENSION C(22,200),D(22),CO(200,55),IX(55),IY(55),HM(17)
      DIMENSION DEP(10),KPLOT(17)
      DIMENSION RTIME(10,150),RST(10,150),IJ(10),IBAY(10),IBAY1(10),
     1IBAY2(10),RDAY(10,150),RSTR(10,150),RSSTR(10,150),KOUNT2(10)
      DIMENSION RT(10),RST(10,150),RDEP(10,150),RSTD(10,150),
     1RSTRD(10,150),RSSTRD(10,150),RSST(10,150)
      REAL*8 C,D,CO,RTIME,RST,RDAY,RSTR,RSTR,RT,RSTD,RSTRD,RSSTRD,RDEP
      REAL*8 RSST
C
      RMIN=0.0
```

```
      BMAX=0.0
      DAYMAX=0.0
      XFAC=IFAC/10.0
      XFACY=IFACY/10.0
      WRITE(6,1000)
 1000 FORMAT(1H1,20X,16HBAY DEFORMATIONS)
      DO 666 J=1,55
      IX(J)=0
  666 IY(J)=0
      ISB=0
      KBNEW=1
      KBMAX=1
      DO 667 I=1,10
      II(I)=0
      NBAY(I)=0
      NBAY1(I)=0
      NBAY2(I)=0
      BT(I)=0.0
      DO 667 I1=1,150
      BTIME(I,I1)=0.0
  667 BST(I,I1)=0.0
      DO 500 I=1,NNN
      DO 2000 J=1,55
 2000 CD(I,J)=0.0
      IBS=I+1
      IF((C(1,I).EQ.0.0).AND.(C(1,IBS).NE.0.0)) ISB=ISB+1
      ISB1=I+ISB
      C(1,I)=C(1,ISB1)
      DO 300 JI=1,NC
      JK=2*JI
  300 C(JK,I)=C(JK,ISB1)
      IF(ISB1.EQ.NNN) NNN=I
      WRITE(6,1) C(1,I)
      IF(C(1,I).GT.DAYMAX) DAYMAX=C(1,I)
    1 FORMAT(1H0,4X,7HTIME = ,F9.4,5H DAYS)
      WRITE(6,1002)
      WRITE(6,1002)
 1003 FORMAT(1H )
 1002 FORMAT(1H ,4X,3HBAY,10X,10HBAY LENGTH,10X,7HBAY DEF,10X,20HBAY STR
     1AIN(PER CENT))
      IST=1
      DO 320 IP=1,NO
      IF(IP.LT.IST) GO TO 320
      NOP=NO-IP+1
      JC=2**NOP-1
      KC=JC+1
      NIT=1
  330 IF(C(KC,I).NE.0.0) GO TO 100
      KC=KC-2
      IF(KC.EQ.0) GO TO 499
      NIT=NIT+1
      GO TO 330
  100 IC=KC+2**NIT
      IA=KC/2
      IB=IA+NIT
      BAYD=C(KC,I)-C(IC,I)
      IF(JTYPE.EQ.2) BAYC=-BAYC
      DD=D(IA)-D(IB)
      IXX=NO+2-IP
      IYY=NO+2-IP
```

```
      IZZ=IXX+1
      MC=0
      DO 350 M=1,IZZ
      MM=M-1
  350 MC=MC+MM
      MNC=NOA-IXX+IYY-MC
      IX(MNO)=IXX
      IY(MNO)=IYY
      CD(I,MNO)=(BAYD/CD)*100.0
      WRITE(6,111) IX(MNO),IY(MNO),DD,BAYD,CD(I,MNO)
      IF(CD(I,MNO).GT.BMAX) BMAX=CD(I,MNO)
      IF(CD(I,MNO).LT.BMIN) BMIN=CD(I,MNO)
      IST=IP+NIT
      DO 318 KB=1,10
      IF(MNO.EQ.NBAY(KB)) GO TO 319
  318 CONTINUE
      KB=KBNEW
      II(KB)=1
  319 IF(KB.GT.10) GO TO 320
      II(KB)=II(KB)+1
      BTIME(KB,II(KB))=C(1,I)
      BST(KB,II(KB))=CD(I,MNO)
      NBAY(KB)=MNC
      NBAY1(KB)=IXX
      NBAY2(KB)=IYY
      IF(KB.GE.KBMAX) KBMAX=KB
      KBNEW=KBMAX+1
  320 CONTINUE
  499 CONTINUE
  500 CONTINUE
      IF(((KPLOT(6).EQ.1).OR.(KPLOT(17).EQ.1)).AND.(KPLOT(5).EQ.0))
     1GO TO 321
      IF(KPLOT(5).EQ.1) GO TO 501
      RETURN
  501 LX=11
      LY=31
      CALL AXES(MSC,BMIN,BMAX,LX,LY,JTYPE,HM,DEP,DAYMAX,XS,YS,5)
      EXC=IEXC
      DO 2010 K=1,55
      CALL EPLOT(1,EXC,0.0)
      IF(CD(1,K).EQ.0.0) GO TO 2020
      CALL EPLOT(2,C(1,1),CD(1,K))
      CALL PCYNT(1)
      IF(CD(2,K).EQ.0.0) GO TO 2050
 2020 DO 2030 I=2,NNN
      IF(CD(I,K).EQ.0.0) GO TO 2030
      J=I-1
      IF(CD(J,K).EQ.0.0) GO TO 2040
      CALL EPLOT(2,C(1,I),CD(I,K))
 2040 CALL EPLOT(1,C(1,I),CD(I,K))
      CALL PCYNT(1)
      J=I+1
      J2=I+2
      IF((I.EQ.NNN).OR.((CD(J,K).EQ.0.0).AND.(CD(J2,K).EQ.0.0)))
     1GO TO 2050
 2030 CONTINUE
      GO TO 2010
 2050 CALL PLTNUM(IX(K),'I2,'' -'',0.8,0.0)
      CALL PLTNUM(IY(K),'I2',0.8,0.0)
 2010 CONTINUE
```

```
      CALL ENDPIC
  111 FORMAT(4X,I2,1H-,I2,10X,E10.3,10X,E10.3,10X,E10.3)
      IF((KPLOT(6).EQ.1).OR.(KPLOT(17).EQ.1)) GO TO 321
      RETURN
  321 CONTINUE
      CALL READ2(HM,KBMAX,NBAY1,NBAY2,BTIME,BST,DEP,II,MSC,JTYPE,KPLOT,
     1IEXC,RDAY,RSTR,RSSTR,DAYMAX,STRMIN,STRMAX,SSTRMN,SSTRMX,KOUNT2,
     2RST,SSTMIN,SSTMAX,RSST)
      NO=KBMAX
      NUNIT=0
      CALL PLOT(HM,KPLOT,DEP,RDAY,RSTR,RSTR,RSTR,RSSTR,DAYMAX,NUNIT,
     1JPLOT,NO,NC,NC,NC,NO,STRMIN,STRMAX,SSTRMN,SSTRMX,IEXC,JTYPE,KOUNT2
     2,PLNO,MSC,NBAY1,NBAY2,RT,SSTMIN,SSTMAX,RSST)
      IF((KPLOT(11).EQ.1).OR.(KPLOT(12).EQ.1).OR.(KPLOT(13).EQ.1))
     1GO TO 800
      RETURN
  800 DAYMAX=0.0
      STMAX=0.0
      STMIN=0.0
      STRMAX=0.0
      STRMIN=0.0
      SSTRMX=0.0
      SSTRMN=0.0
      DO 805 M=1,10
      KOUNT2(M)=0
      DO 805 MN=1,150
      RDEP(M,MN)=0.0
      RSTD(M,MN)=0.0
      RSTRD(M,MN)=0.0
  805 RSSTRD(M,MN)=0.0
C
C        IF KPLOT HAS BEEN SPECIFIED AS 11, 12 OR 13, THEN UP TO
C        10 TIME VALUES CAN BE INPUT HERE FOR PLOTS OF BAY STRAIN ETC.,
C        AGAINST BOREHOLE DEPTH.
C                                                                (10F8.3)
      READ(5,810) (RT(I),I=1,10)
  810 FORMAT(10F8.3)
      DO 820 K=1,10
      LL=1
      DO 820 L=1,NO
      DO 820 I=1,150
      IF(RT(K).EQ.0.0) GO TO 821
      IF(RDAY(L,I).NE.RT(K)) GO TO 820
      LL=LL+1
      RSTD(K,LL)=RST(L,I)
      RSTRD(K,LL)=RSTR(L,I)
      RSSTRD(K,LL)=RSSTR(L,I)
      KOUNT2(K)=LL
      DO 815 LI=1,10
      IF(DEP(LI).EQ.0.0) GO TO 816
  815 CONTINUE
  816 LI=LI-1
      IDEP1=LI+1-NBAY1(L)
      IDEP2=LI+1-NBAY2(L)
      IF(NBAY1(L).EQ.0) GO TO 819
      RDEP(K,LL)=(DEP(IDEP2)+DEP(IDEP1))/2.0
      GO TO 820
  819 RDEP(K,LL)=(DEP(IDEP2))/2.0
  820 CONTINUE
  821 CONTINUE
```

```
                NU=K-1
                DO 825 K=1,10
                DO 825 L=1,150
                RDAY(K,L)=RDEF(K,L)
                RST(K,L)=RSTD(K,L)
                RSTR(K,L)=RSTRD(K,L)
                RSSTR(K,L)=RSSTRD(K,L)
                IF(RDAY(K,L).GT.DAYMAX) DAYMAX=RDAY(K,L)
                IF(RST(K,L).LT.STMIN) STMIN=RST(K,L)
                IF(RST(K,L).GT.STMAX) STMAX=RST(K,L)
                IF(RSTR(K,L).LT.STRMIN) STRMIN=RSTR(K,L)
                IF(RSTR(K,L).GT.STRMAX) STRMAX=RSTR(K,L)
                IF(RSSTR(K,L).LT.SSTRMN) SSTRMN=RSSTR(K,L)
                IF(RSSTR(K,L).GT.SSTRMX) SSTRMX=RSSTR(K,L)
            825 CONTINUE
                CALL PLOT(HM,KPLOT,DEP,RDAY,RSTR,RST,RSTR,RSSTR,DAYMAX,
               1NUNIT,JPLOT,NC,NO,STMIN,STMAX,STRMIN,STRMAX,SSTRMN,SSTRMX,
               2IEXC,JTYPE,KOUNT2,PLNO,MSC,NBAY1,NBAY2,RT,SSTMIN,SSTMAX,RSST)
                RETURN
                END


      C
      C*****
                SUBROUTINE PLOT(HM,KPLOT,DEP,RDAY,RDEF,RST,RSTR,RSSTR,
     1DAYMAX,NUNIT,JPLOT,NO,DEFMIN,DEFMAX,STMIN,STMAX,STRMIN,
     2STRMAX,SSTRMN,SSTRMX,IEXC,JTYPE,KOUNT2,PLNO,MSC,NBAY1,NBAY2,RT,
     3SSTMIN,SSTMAX,RSST)
                DIMENSION HM(17),KPLOT(17),DEP(10),RDAY(10,150),RDEF(10,150)
                DIMENSION RST(10,150),PLNO(10),RSTR(10,150),RSSTR(10,150),RT(10)
                DIMENSION XAX(10,150),YAX(10,150),KOUNT2(10),NBAY1(10),NBAY2(10)
                DIMENSION LLCG(10,150),RSST(10,150)
                REAL*8 RDAY,RDEF,RST,RSTR,RSSTR,XAX,YAX,RT,RSST
      C
                NPLOT=0
                REWIND 12
                DO 9000 JPL=1,17
                DO 8 J=1,NO
                DO 8 K=1,150
                XAX(J,K)=0.0
            8   YAX(J,K)=0.0
                IF(KPLOT(JPL).EQ.0) GO TO 9000
                IF((NBAY2(1).EQ.0).AND.((JPL.EQ.6).OR.(JPL.EQ.7).OR.(JPL.EQ.17)))
               1GO TO 9000
                IF((NBAY2(1).NE.0).AND.((JPL.NE.6).AND.(JPL.NE.7).AND.(JPL.NE.17))
               1.AND.(RT(1).EQ.0.0)) GO TO 9000
                IF((RT(1).EQ.0.0).AND.((JPL.EQ.11).OR.(JPL.EQ.12).OR.(JPL.EQ.13)))
               1 GO TO 9000
                IF((RT(1).NE.0.0).AND.(JPL.NE.11).AND.(JPL.NE.12).AND.(JPL.NE.13))
               1 GO TO 9000
                KLCG=0
                DO 7 J=1,NO
                DO 7 K=1,150
                LLCG(J,K)=0
                XAX(J,K)=RDAY(J,K)
                IF(JPL.NE.15) GO TO 96
                IF((J.GT.1).OR.(K.GT.KOUNT2(J))) GO TO 94
      C
      C         THIS IS FOR PLOTTING RESULTS, TO PLOT STRAIN AGAINST
      C         DRILLING DISTANCE. THE FIRST DISTANCE MUST BE ZERO AND ONE/SCAN.
```

```
C                                                                    (F6.2)
      READ(12,90) XAX(1,K)
   90 FORMAT(F6.2)
      WRITE(6,91)
   91 FORMAT(4X,9H SCAN NO.,5X,12H TIME (MINS),5X,13H DISTANCE(CM))
      WRITE(6,92) K,RDAY(J,K),XAX(J,K)
   92 FORMAT(8X,I3,8X,F9.4,12X,F7.2,/)
   94 XAX(J,K)=XAX(1,K)
   96 CONTINUE
      GO TO(1,2,3,4,9000,3,4,1,81,82,2,3,4,83,84,85,85),JPL
    1 BMIN=DEFMIN
      BMAX=DEFMAX
      YAX(J,K)=RDEF(J,K)
      LY=1
      IF(NUNIT.NE.0) LY=6
      LX=11
      GO TO 11
    2 BMIN=STMIN
      BMAX=STMAX
      YAX(J,K)=RST(J,K)
      LY=16
      LX=11
      IF(JPL.EQ.11) LX=36
      GO TO 11
    3 YAX(J,K)=RSTR(J,K)
      IF(KLOG.EQ.1) GO TO 41
      BMIN=(STRMIN)
      BMAX=(STRMAX)
   41 CONTINUE
      IF((YAX(J,K).LE.0.0).AND.(JPL.NE.12)) LLOG(J,K)=1
      IF(LLOG(J,K).EQ.1) GO TO 11
      LY=21
      LX=11
      IF(JPL.EQ.12) LX=36
      IF(JPL.EQ.12) GO TO 11
      BMIN=ALOG(STRMIN)
      BMAX=ALOG(STRMAX)
      IF(BMAX.LT.0.0000) BMAX=0.0
      KLOG=1
      YAX(J,K)=DLOG(YAX(J,K))
      LY=66
      GO TO 11
    4 YAX(J,K)=RSSTR(J,K)
      IF(KLOG.EQ.1) GO TO 42
      BMIN=(SSTRMN)
      BMAX=(SSTRMX)
   42 CONTINUE
      IF((YAX(J,K).LE.0.0).AND.(JPL.NE.13)) LLOG(J,K)=1
      IF(LLOG(J,K).EQ.1) GO TO 11
      LY=26
      LX=11
      IF(JPL.EQ.12) LX=36
      IF(JPL.EQ.12) GO TO 11
      BMIN=ALOG(SSTRMN)
      BMAX=ALOG(SSTRMX)
      IF(BMAX.LT.0.0000) BMAX=0.0
      KLOG=1
      YAX(J,K)=DLOG(YAX(J,K))
      LY=71
      GO TO 11
```

```
      81 YAX(J,K)=RSTR(J,K)
         IF(YAX(J,K).LE.0.0) LLOG(J,K)=1
         IF(YAX(J,K).LE.0.0) GO TO 11
         BMIN=ALOG(STRMIN)
         BMAX=ALOG(STRMAX)
         IF(BMAX.LT.C.CCOC) BMAX=0.0
         YAX(J,K)=DLOG(YAX(J,K))
         LY=76
         LX=11
         GO TO 11
      82 YAX(J,K)=RSSTR(J,K)
         IF(YAX(J,K).LE.0.0) LLCG(J,K)=1
         IF(YAX(J,K).LE.0.0) GO TO 11
         BMIN=ALOG(SSTRMN)
         BMAX=ALOG(SSTRMX)
         IF(BMAX.LT.C.CCOO) BMAX=0.0
         YAX(J,K)=DLOG(YAX(J,K))
         LY=81
         LX=11
         GO TO 11
      83 BMIN=STMIN
         BMAX=STMAX
         YAX(J,K)=RST(J,K)
         LY=51
         LX=11
         GO TO 11
      84 BMIN=STMIN
         BMAX=STMAX
         YAX(J,K)=RST(J,K)
         LY=16
         LX=56
         DAYMAX=XAX(NC,KCUNT2(NO))
         GO TO 11
      85 BMIN=SSTMIN
         BMAX=SSTMAX
         YAX(J,K)=RSST(J,K)
         LY=86
         LX=11
      11 CONTINUE
       7 CONTINUE
         IF((JTYPE.EQ.6).AND.(JPL.NE.15)) LX=61
         GO TO 12
      12 CONTINUE
         CALL AXES(MSC,BMIN,BMAX,LX,LY,JTYPE,HM,DEP,DAYMAX,XS,YS,JPL)
C
         ILOG=2
         DO 70 ID=1,NO
         EXC=IEXC
         IF((JPL.NE.1).AND.(JPL.NE.2).AND.(JPL.NE.5).AND.(JPL.NE.8)
        1.AND.(JPL.NE.14).AND.(JPL.NE.15)
        3.AND.(JPL.NE.16).AND.(JPL.NE.10)
        2.AND.(JPL.NE.4).AND.(JPL.NE.7)) GO TO 55
         CALL EPLOT(1,XAX(ID,1),YAX(ID,1))
         IF(LLOG(ID,1).EQ.1) GO TO 55
         GO TO 60
      55 CALL EPLOT(1,XAX(ID,2),YAX(ID,2))
         IF(LLOG(ID,2).EQ.1) GO TO 86
      60 CALL FCYNT(1)
         GO TO 89
      86 DO 87 I=3,150
```

```
      IF(LLOG(IC,I).EQ.0) GO TO 88
   87 CONTINUE
   88 CALL EPLOT(1,XAX(IC,I),YAX(IC,I))
      CALL EOYNT(1)
      ILOG=1
   89 CONTINUE
      DO 65 I=2,150
      IF(I.EQ.2) I=ILOG
      IF(I.GT.KCLNT2(IC)) GO TO 66
      IF(LLOG(IC,I).EQ.1) GO TO 65
      IZ=I
      CALL EPLOT(2,XAX(IC,I),YAX(IC,I))
   65 CALL EOYNT(1)
   66 X=XAX(IC,IZ)+0.25/XS
      Y=YAX(IC,IZ)
      CALL EPLOT(1,X,Y)
      GO TO (73,73,73,72,74,74),JTYPE
   74 CALL PLTNUM(IC,'I2*',0.8,0.0)
      GO TO 70
   73 N1=0
      N2=NO-IC+1
      IF((JPL.EQ.11).OR.(JPL.EQ.12).OR.(JPL.EQ.13)) GO TO 75
      IF((JPL.EQ.6).OR.(JPL.EQ.7).OR.(JPL.EQ.17)) N1=NBAY1(IC)
      IF((JPL.EQ.6).OR.(JPL.EQ.7).OR.(JPL.EQ.17)) N2=NBAY2(IC)
      CALL PLTNUM(N1,'I1*',0.8,0.0)
      CALL PLTNUM(N2,''' - ''',I2*',0.8,0.0)
      GO TO 70
   75 CALL PLTNUM(RT(IC),'WF4.1,'' DAYS''*',0.8,0.0)
      GO TO 70
   72 CALL PLTEXT(FLNO(IC),4,0.8,0.0)
   70 CONTINUE
      CALL ENDPIC
      NPLOT=NPLOT+1
 5000 CONTINUE
      RETURN
      END
C
C*****
      SUBROUTINE AXES(NSC,BMIN,BMAX,LX,LY,JTYPE,HM,DEP,DAYMAX,XS,YS,JPL)
      DIMENSION TITLE2(45)
      DIMENSION TITLE(90),HM(17),DEP(10)
      DATA TITLE/'DEFO','RMAT','ION ','(M) ','    ',
     1           'DEFO','RMAT','ION ','(IN)','    ',
     2           'TIME',' (DA','YS) ','.   ','    ',
     3           'STRA','IN (','PER ','CENT',')   ',
     4           'STRA','IN R','ATE ','(PC/','DAY)',
     5           'SMCO','THED',' STR','AIN ','RATE',
     6           'BAY ','STRA','IN(P','ER C','ENT)',
     7           'BORE','HOLE',' DEP','TH (','M)  ',
     8           'CONV','. RA','TE (','M/DA','Y)  '/
      DATA TITLE2/'SMCO','THED',' CON','V. R','ATE ',
     1            'STRE','SS (','X10,','000 ','KPA)',
     2            'DIST','ANCE',' (CM',')   ','    ',
     3            'TIME',' (MI','NS)  ','    ','    ',
     4            'LOG ','STRA','IN R','ATE ','    ',
     5            'LOG ','SMCO','TH S','TR. ','RATE',
     6            'LOG ','CONV','. RA','TE M','/DAY',
     7            'LOG ','SMCO','TH C','ONV ','RATE',
     8            'SMCO','TH  ','STRA','IN (','PCT)'/
      EQUIVALENCE(TITLE(1),TITLE2(1))
```

```
      C
            CALL SCALEM(1.0,1.0,0.0,-2.0)
            CALL EPLOT(1,1.0,0.0)
            CALL EPLOT(2,0.0,0.0)
            CALL EPLOT(2,0.0,1.0)
            CALL EPLOT(1,28.7,0.0)
            CALL EPLOT(2,29.7,0.0)
            CALL EPLOT(2,29.7,1.0)
            CALL EPLOT(1,29.7,20.0)
            CALL EPLOT(2,29.7,21.0)
            CALL EPLOT(2,28.7,21.0)
            CALL EPLOT(1,1.0,21.0)
            CALL EPLOT(2,0.0,21.0)
            CALL EPLOT(2,0.0,20.0)
            CALL EPLOT(1,1.0,1.0)
            CALL EPLOT(2,28.7,1.0)
            CALL EPLOT(2,28.7,19.7)
            CALL EPLOT(2,1.0,19.7)
            CALL EPLOT(2,1.0,1.0)
            IF(MSC.NE.0) GO TO 91
            AA=1.0
            A=(BMAX-BMIN)/6.0
            NEG=0
          5 CONTINUE
            IF((A.GE.1.0).AND.(A.LT.10.0)) GO TO 10
            IF(A.LT.1.0) GO TO 15
            IF(A.GE.10.0) A=A/10.0
            AA=10*AA
            GO TO 5
         15 A=A*10.0
            AA=AA/10.0
            NEG=1
            GO TO 5
         10 CONTINUE
            INCY=A+1
         60 CONTINUE
            YINC=INCY*AA
            GO TO 92
      C
      C        IF MSC HAS SPECIFIED AS 1 ON CARD 2, THE PLOT SCALES ARE INPUT HERE FOR
      C        EACH OF THE IN1 SETS OF DATA. FOR EACH SET THERE MUST BE A SCALE CARD
      C        FOR EVERY PICTURE WITHIN THE SET. THERE ARE ALWAYS 6 INTERVALS ON THE
      C        Y AXIS AND 10 ON THE X. HERE THE INTERVAL SIZE IS SPECIFIED FOR EACH
      C        AXIS AS XINC, YINC AND IB=NO. OF INTERVALS REQ'D IN THE -VE Y DIRECTION
      C                                                              (2F9.4,I2)
         91 READ(5,99) XINC,YINC,IB
         99 FORMAT(2F9.4,I2)
         92 YS=15.0/(6.0*YINC)
            IF(MSC.NE.0) GO TO 93
            BB=-BMIN/YINC
            IB4=0
            IF((BB.GT.0.0).AND.(BB.LE.0.25)) IB4=-1
            IB=BB
            BIB=IB
            IF((BIB.LT.BB).AND.(IB4.GE.0)) IB=IB+1
            YPOS=(6-IB)*YINC
            IF(YPOS.GT.BMAX) GO TO 92
            INCY=INCY+1
            GO TO 60
         93 YJ=(1.5/YS)+IB*YINC
```

```
      IF(MSC.NE.C) GC TO 94
      DA=1.0
      C=CAYMAX/1C.C
   20 CONTINUE
      IF((D.GE.1.0).ANC.(D.LT.10.0)) GO TO 30
      IF(D.LT.1.0) GC TO 25
      IF(D.GE.10.0) C=C/10.0
      DA=10*DA
      GO T. 20
   25 D=D*10.0
      DA=DA/10.0
      GO TO 20
   30 CONTINUE
      INCX=D+1
      XINC=INCX*DA
   31 CONTINUE
   94 XS=25.0/(10.C*XINC)
      XO=-1.5/XS
      CALL SCALEM(XS,YS,XO,-YO)
      CALL EGRIC(C,0.0,0.0,XINC,10)
      YMIN=0.0-(IB*YINC)
      CALL EGRIC(1,0.0,YMIN,YINC,6)
      DO 35 J=1,7
      YNUM=YMIN+(J-1)*YINC
      X=-0.2/XS
      Y=YNUM-(1.1/YS)
      CALL EPLOT(1,X,Y)
   35 CALL PLTNUM(YNUM,'WF3.4=',0.8,90.0)
      X=-0.8/XS
      Y=YMIN+(5.5/YS)
      CALL EPLOT(1,X,Y)
      CALL PLTEXT(TITLE(LY),20,1.4,90.0)
      DO 40 J=),11
      XNUM=(J-1)*XINC
      X=XNUM-(1.25/XS)
      Y=C.5/YS
      CALL EPLOT(1,X,-Y)
   40 CALL PLTNUM(XNUM,'WF4.3','',0.8,0.0)
      X=10.7/XS
      Y=1.3/YS
      CALL EPLOT(1,X,-Y)
      CALL PLTEXT(TITLE(LX),20,1.4,0.0)
      IF((JTYPE.EQ.4).OR.(JTYPE.EQ.5).OR.(JTYPE.EQ.6)) GO TO 45
      X=2.0/XS
      Y=YMIN+16.5/YS
      CALL EPLOT(1,X,Y)
      CALL PLTEXT(HM(1),16,1.4,0.0)
      Y=YMIN+15.5/YS
      CALL EPLOT(1,X,Y)
      CALL PLTEXT(HM(5),20,1.4,0.0)
      IF((JPL.EC.3).OR.(JPL.EQ.4).OR.(JPL.EQ.6).OR.(JPL.EQ.7)) GO TO 50
      Y=YMIN+14.5/YS
      CALL EPLOT(1,X,Y)
      CALL PLTEXT(HM(13),4,1.4,C.0)
      CALL PLTEXT(' HOLE ',6,1.4,C.0)
      CALL PLTNUM(DEP(1),'WF3.2,''M DEP''',1.4,J.0)
      GO TO 50
   45 X=2.0/XS
      Y=YMIN+16.5/YS
      CALL EPLOT(1,X,Y)
```

```
      IF(JTYPE.EQ.4) GO TO 46
      CALL PLTEXT(HM(1),16,1.4,C.0)
      Y=YMIN+15.5/YS
      CALL EPLOT(1,X,Y)
      CALL PLTEXT(HM(5),16,1.4,C.0)
      Y=YMIN+14.5/YS
      CALL EPLOT(1,X,Y)
      CALL PLTEXT(HM(9),28,1.4,C.0)
      GO TO 50
   46 CALL PLTEXT(HM(1),32,1.4,C.0)
      Y=YMIN+15.5/YS
      CALL EPLOT(1,X,Y)
      CALL PLTEXT(HM(11),12,1.4,C.0)
   50 CONTINUE
      RETURN
      END
END OF FILE


$SIG
```

APPENDIX B

TABLE B1 - Extensometer Anchor Depths.

DIAGRAMS

B 1 - B 4 Shaft Pillar Site Layouts

B 5 - B21 Shaft Pillar Site Geology

B22 - B36 Extensometer Results

B37 - B54 Convergence, Roof Sag, Floor Heave Results

TABLE B1 BOREHOLE EXTENSOMETER ANCHOR DEPTHS

Site	Borehole No. and Type (*)	Anchor Depths (m)			
		1	2	3	4
NU01	2(W)	0.9	2.4	5.3	
	3(R)	1.1	3.4	4.3	
NU02	4(R)	0.9	1.8	2.9	
	5(R)	0.9	1.8	2.9	
NU03	6(R)	1.1	2.6	6.1	
	7(R)	1.1	2.6	4.6	
NU05	11(W)	1.5	3.0	4.7	
	12(W)	2.0	4.0	6.0	
	13(R)	2.0	4.0	5.2	
	14(R)	2.0	4.0	5.5	
	15(R)	1.5	3.0		
	16(F)	2.0	4.0	5.1	
NU06	17(R)	2.0	4.0	6.0	
	18(R)	1.5	4.0	6.0	
	19(R)	1.5	4.0	6.0	
	20(W)	1.5	3.0		
	21(W)	1.5	3.0		
NU07	22(R)	2.0	4.0	6.0	
	23(R)	2.0	4.0	6.0	
	24(R)	1.8	3.7		
NU08	25(R)	2.0	4.0	5.0	
	26(R)	1.0	2.0	3.6	
	27(R)	2.0	4.0	4.5	
NU09	28(W)	1.0	4.0	6.0	
	29(W)	1.0	4.0	6.0	
NU10	30(R)	1.8	3.6	5.8	
	31(R)	1.9	3.8	5.5	
	32(R)	2.0	3.8	6.5	
NU11	33(R)	1.0	4.0	6.0	
	34(R)	2.0	4.0	6.0	
NU12	39(R)	2.0	4.0	6.0	

TABLE B1 cont. BOREHOLE EXTENSOMETER ANCHOR DEPTHS

Site	Borehole No. and Type (*)	Anchor Depths (m)			
		1	2	3	4
	40(R)	2.0	4.0	6.0	
	44(R)	1.0	4.0	6.0	
NU13	35(R)	1.0	3.5	5.8	
	41(R)	2.0	3.5	4.5	
	42(R)	1.5	3.8	5.2	
NU14	36(R)	1.5	6.0		
	37(R)	1.8	3.5	5.2	
	43(R)	2.0	4.0	5.7	
NU15	38(R)	2.0	4.0	6.0	
NU16	45(R)	1.0	3.0	4.3	
1P1	1(R)	1.8	3.8	5.5	
	2(R)	1.8	3.8	5.6	
	3(R)	1.8	3.8	5.8	9.2
	4(R)	2.0	4.0	5.5	
	5(R)	1.8	3.8	5.5	
	6(R)	2.0	4.0	5.2	
	7(R)	2.0	4.0	6.0	8.7
	8(R)	1.8	3.8	5.6	
1P2	10(R)	2.0	4.0	5.6	
	11(R)	2.0	4.0	5.6	
	13(R)	5.6			
1P4	22(R)	2.0	4.0		
	23(W)	2.0	4.0	7.0	9.0
	23(cont'd)	19.0	21.0	25.0	
	26(W)	2.0	4.0	7.0	9.0
	27(W)	2.0	4.0	7.0	9.0
	28(R)	2.0	4.0	5.0	
	29(W)	2.0	3.3	9.0	
	30(W)	2.0	4.0	7.0	9.0
	32(W)	2.0			
	33(W)	2.0			
1P7	34(W)	3.0	7.0	14.0	17.0

TABLE B1 cont. BOREHOLE EXTENSOMETER ANCHOR DEPTHS

Site	Borehole No. and Type (*)	Anchor Depths (m)			
		1	2	3	4
	35(W)	3.0	7.0	14.0	17.0
	36(W)	2.5			
	37(W)	2.0			
	38(W)	3.0	7.0	14.0	17.0
1P8	39(W)	2.5	6.0	9.5	
	40(W)	2.5	6.0	9.5	
	42(W)	2.5	6.0	9.5	
	43(W)	2.5	6.0	9.5	
	44(W)	2.5	6.0	9.5	
1P9	45(W)	2.0	4.0	6.0	
	46(W)	2.0	4.0	6.0	
	47(W)	2.0	4.0	6.0	
	48(W)	2.0	4.0	6.0	
	49(W)	2.0	4.0	6.0	
SD1	1(W)	3.0	7.0	12.0	17.0
	2(W)	3.0			
SD2	3(W)	3.0	7.0		
	4(W)	3.0	7.0	12.0	17.0
SD3	5(W)	3.0	6.0	12.0	20.0
	6(W)	3.0	7.0	12.0	20.0
SD4	7(W)	3.0	7.0	12.0	20.0
	8(W)	3.0	7.0	12.0	20.0
SD6	11(W)	3.0	7.0	12.0	17.0
	12(W)	3.0	7.0	12.0	17.0
SD7	13(W)	3.0	7.0	12.0	17.0
	14(W)	3.0	7.0	12.0	17.0
2P1	1(W)	1.0	2.2	3.4	4.5
	2(R)	2.0	4.0	5.8	
	3(W)	1.5	3.0	5.0	6.5
2P2	4(W)	1.5	3.0	5.0	
	5(W)	1.5	3.0	4.2	

TABLE B1 cont. BOREHOLE EXTENSOMETER ANCHOR DEPTHS

Site	Borehole No. and Type (*)	Anchor Depths (m)			
		1	2	3	4
EP1	1(W)	2.0	4.0	6.0	
	2(R)	2.0	4.0	6.0	
	3(W)	2.0	5.0	8.0	12.5
EP4	10(W)	2.0	5.0	8.0	12.5
	11(R)	2.0	4.0	6.0	
	12(W)	2.0	5.0	8.0	12.5
EP7	19(W)	2.0			
	20(R)	2.0	4.0	6.0	
	21(W)	2.0	2.8		

* Borehole types: R - roof borehole
W - wall borehole
F - floor borehole

B1

Rock Mechanics Sites
Borehole Locations

SITE | PLAN VIEW (↑N) | CROSS-SECTION VIEW

N.U.01 (6m wide roads)

Borehole	Excav'n Date	Instr'n Date	Final Date
2	5-10-73	7-10-73	
3	5-10-73	7-10-73	24-10-74

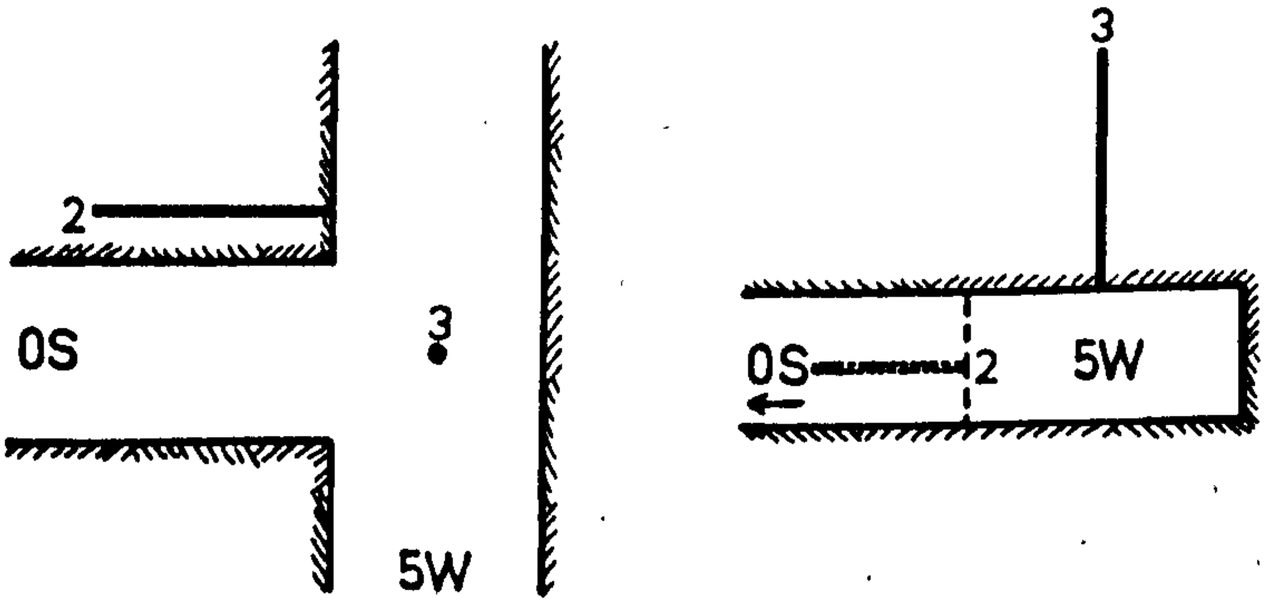

N.U.02 (6m wide roads)

Borehole	Excav'n Date	Instr'n Date	Final Date
4	30-10-73	1-11-73	
5	30-10-73	1-11-73	

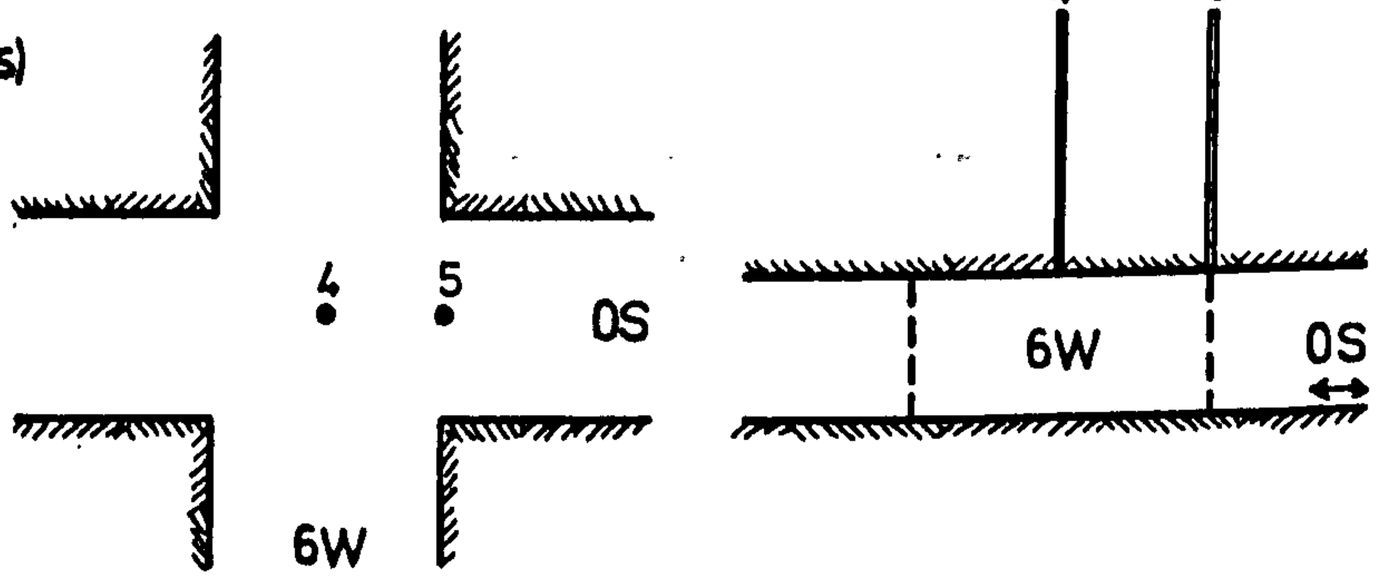

N.U.03 (6m wide roads)

Borehole	Excav'n Date	Instr'n Date	Final Date
6	22-1-74	25-1-74	28-3-74
7	22-1-74	25-1-74	16-5-74
8	22-1-74	25-1-74	11-7-74

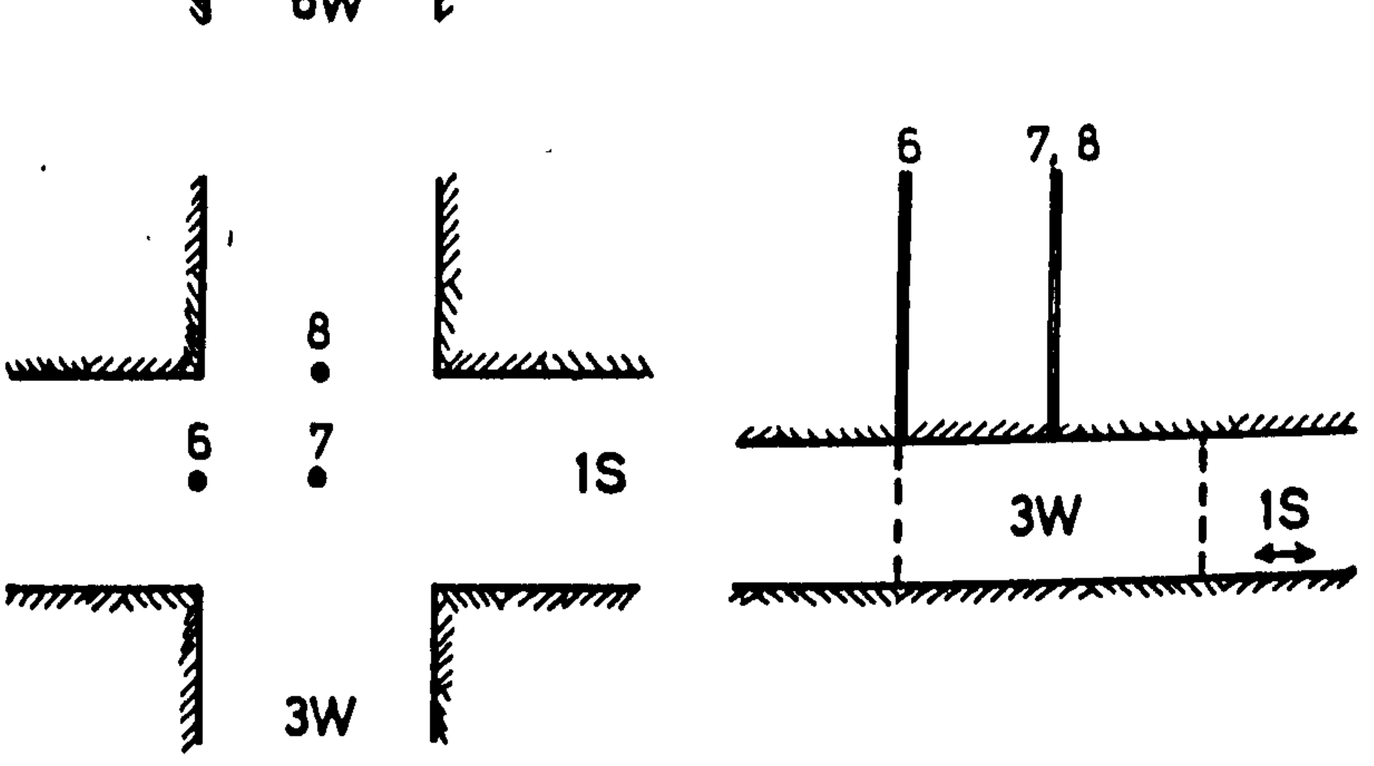

N.U.04 (6m wide road)

Convergence Station	Excav'n Date	Instr'n Date	Final Date
C1 - C4	25-2-74	1-3-74	1-76

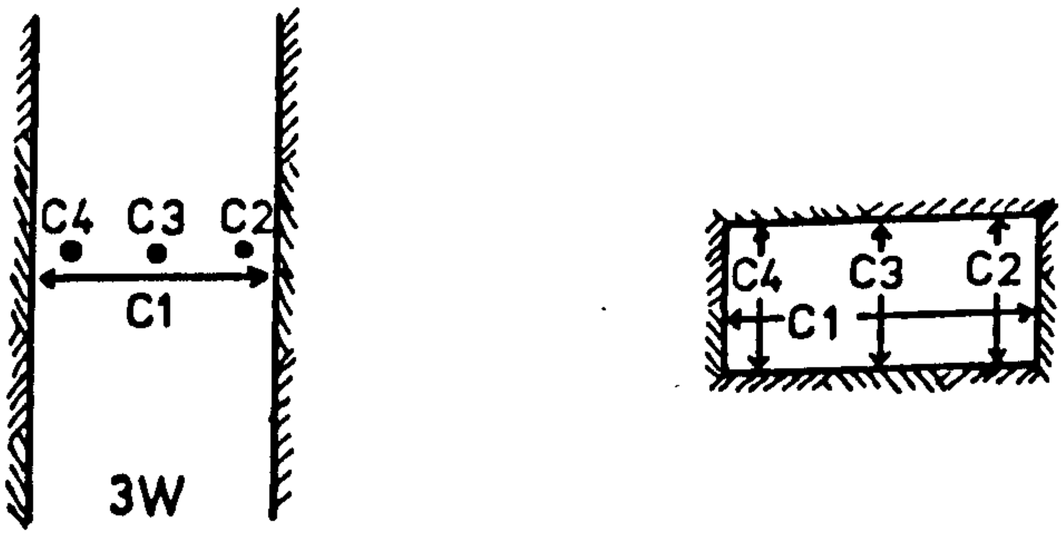

B2

Rock Mechanics Sites
Borehole Locations

SITE | PLAN VIEW (↑N) | CROSS-SECTION VIEW

NU05 (8m wide road)

Borehole	Excav'n Date	Instr'n Date	Final Date
11	11-3-74	12-3-74	27-2-75
12	11-3-74	12-3-74	13-6-74
13	11-3-74	12-3-74	22-8-74
14	11-3-74	12-3-74	27-2-75
15	11-3-74	12-3-74	27-2-75
16	11-3-74	12-3-74	16-5-74

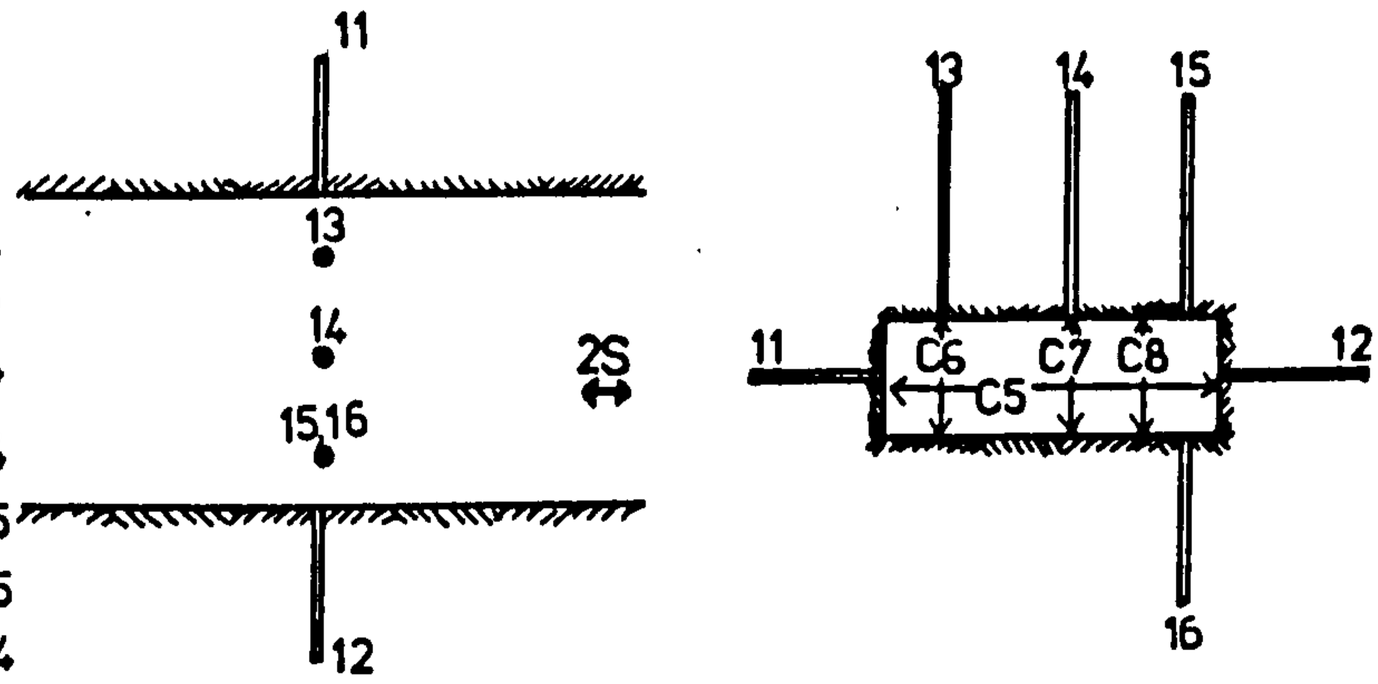

NU06 (6m wide road)

Borehole	Excav'n Date	Instr'n Date	Final Date
17	30-8-74	16-9-74	1-76
18	30-8-74	16-9-74	
19	30-8-74	16-9-74	
20	30-8-74	16-9-74	
21	30-8-74	16-9-74	

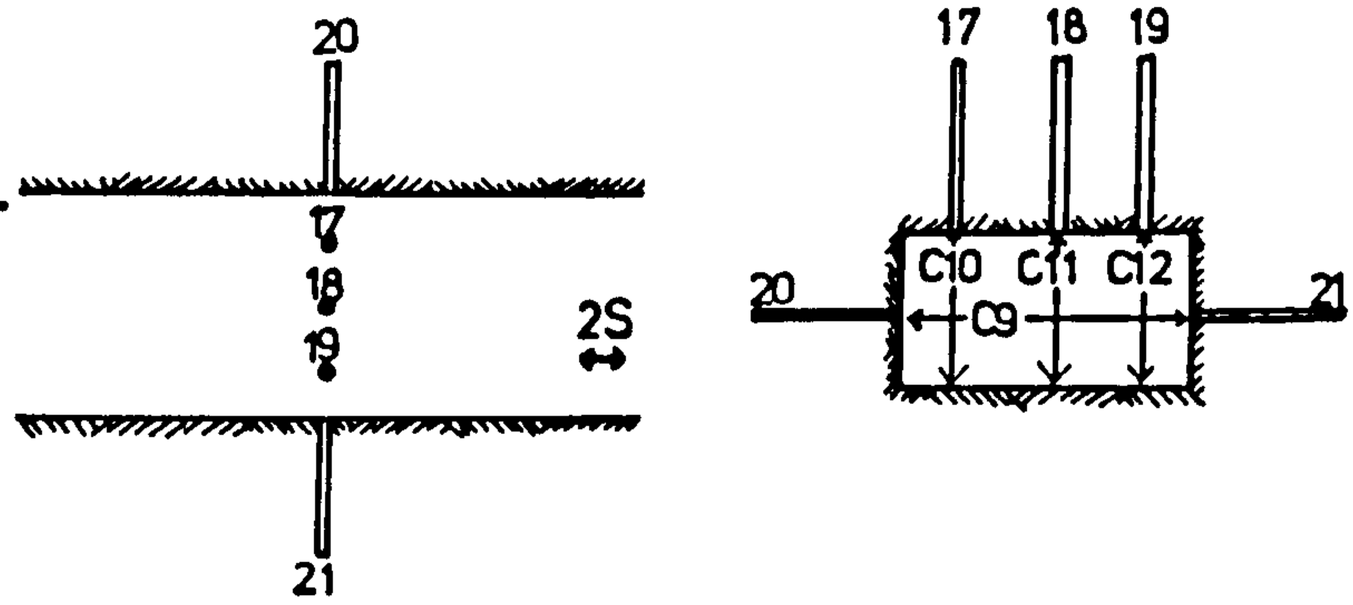

NU07 (6m wide road)

Borehole	Excav'n Date	Instr'n Date	Final Date
22	6-10-74	17-10-74	
23	11-10-74	17-10-74	
24	16-10-74	23-10-74	

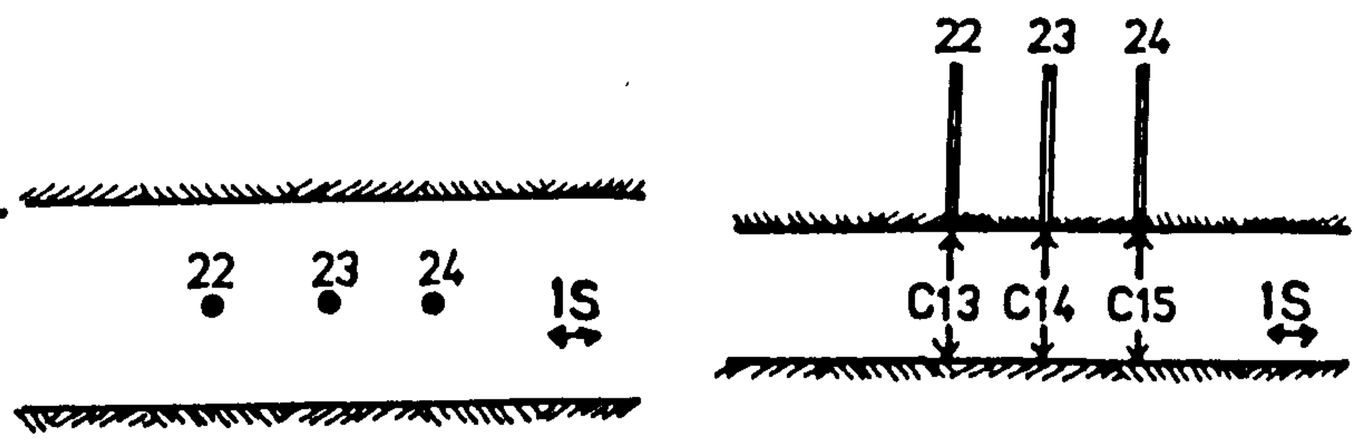

NU08 (6m wide road)

Borehole	Excav'n Date	Instr'n Date	Final Date
25	21-10-74	23-10-74	10-75
26	25-10-74	7-11-74	
27	1-11-74	7-11-74	

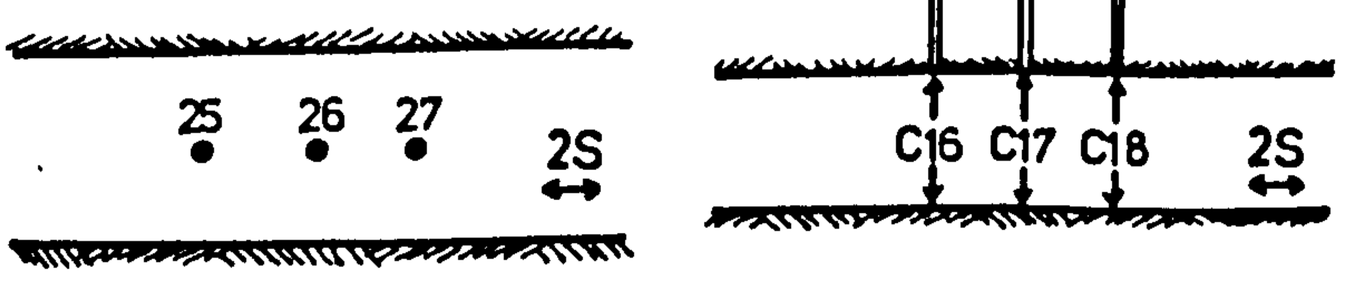

B3 Rock Mechanics Sites Borehole Locations

SITE | PLAN VIEW (↑N) | CROSS-SECTION VIEW

NU09 (6m wide road)

Borehole	Excav'n Date	Instr'n Date	Final Date
28	18-10-74	7-11-74	
29	18-10-74	7-11-74	

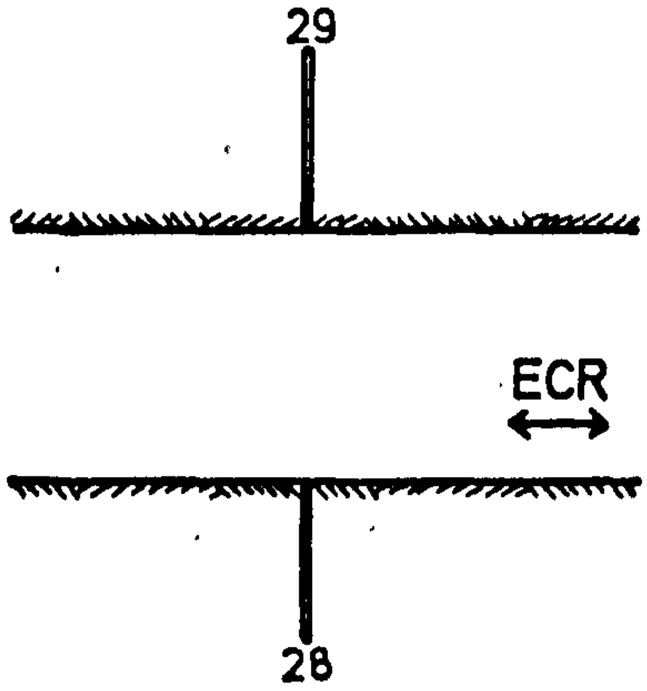

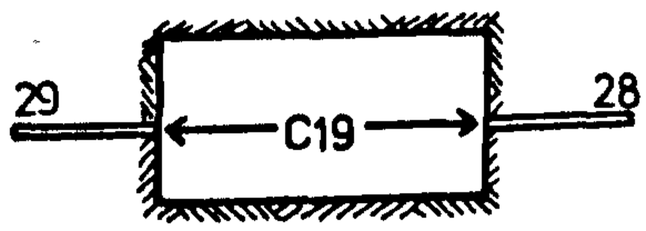

NU10 (5m wide road)

Borehole	Excav'n Date	Instr'n Date	Final Date
30	2-11-74	12-11-74	
31	8-11-74	12-11-74	
32	11-11-74	27-11-74	

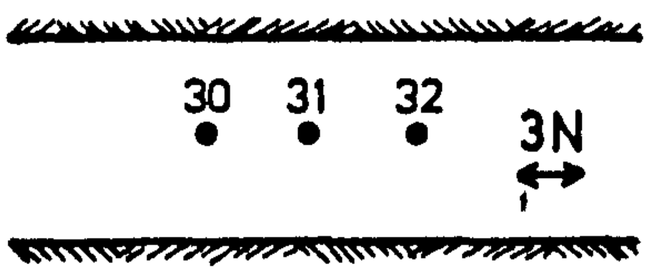

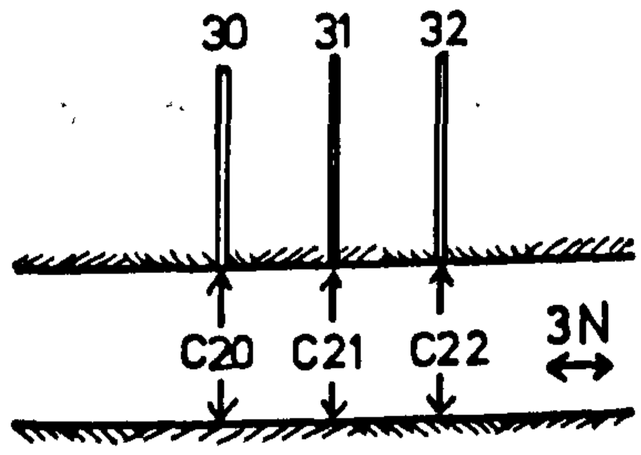

NU11 (6m wide road)

Borehole	Excav'n Date	Instr'n Date	Final Date
33	10-11-74	27-11-74	17-12-74
34	17-11-74	27-11-74	1-76

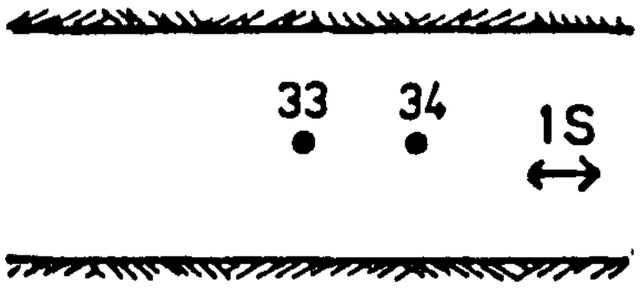

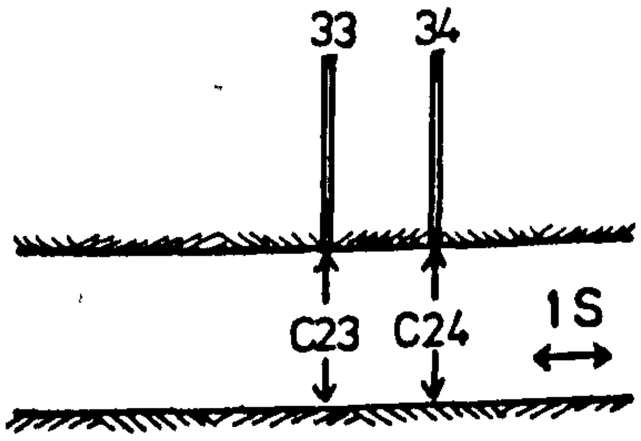

NU12 (6m wide road)

Borehole	Excav'n Date	Instr'n Date	Final Date
39	18-11-74	27-11-74	
40	1-12-74	17-12-74	
44	9 12 74	17- 4-75	

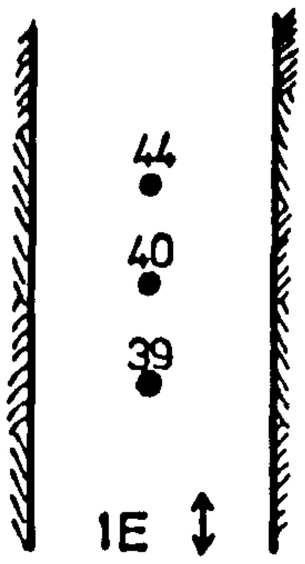

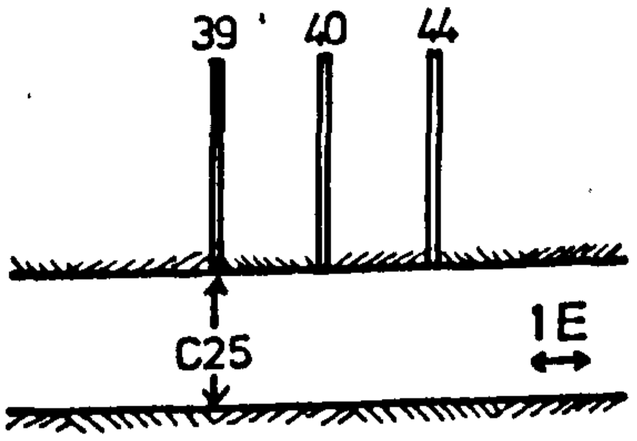

B4

Rock Mechanics Sites
Borehole Locations

SITE | PLAN VIEW (↑N) | CROSS-SECTION VIEW

NU13 (6m wide road)

Borehole	Excav'n Date	Instr'n Date	Final Date
35	13-12-74	17-12-74	
41	3-1-75	17-1-75	
42	8-1-75	17-1-75	

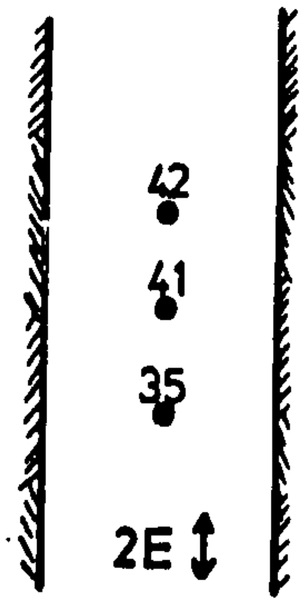

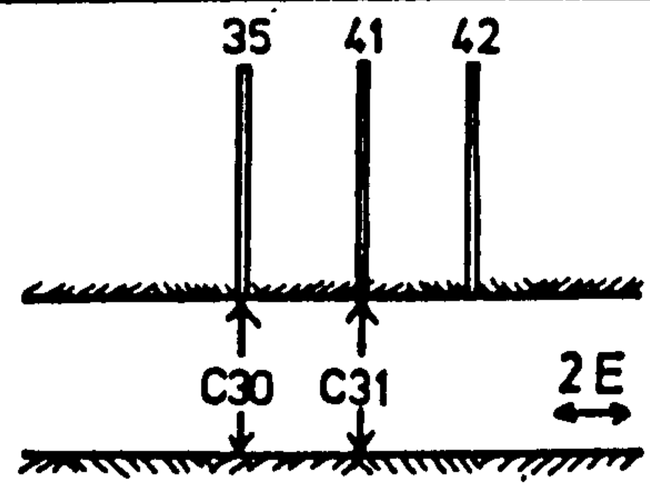

NU14 (6m wide road)

Borehole	Excav'n Date	Instr'n Date	Final Date
36	24-11-74	17-12-74	1-76
37	3-12-74	18-2-75	1-76
43	8-1-75	17-4-75	1-76

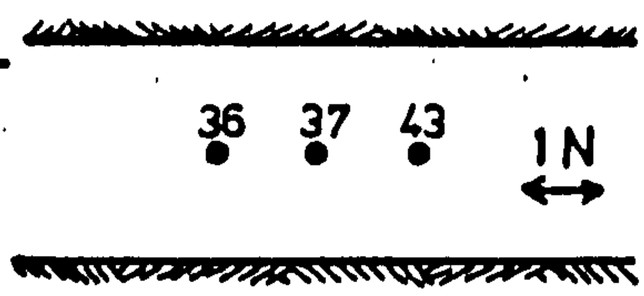

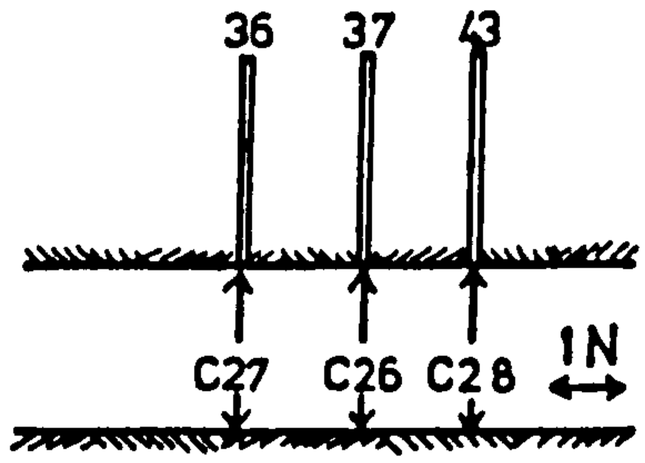

NU15 (6m wide road)

Borehole	Excav'n Date	Instr'n Date	Final Date
38	25-11-74	17-12-74	

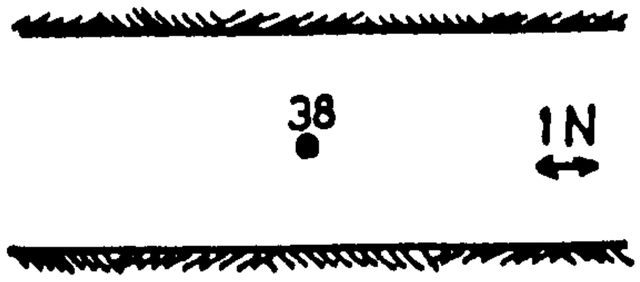

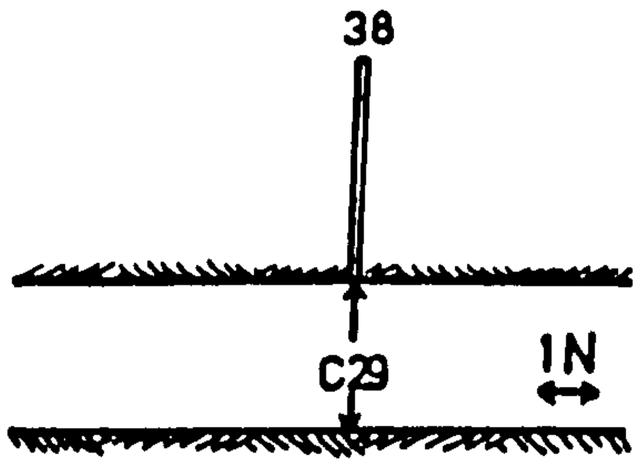

NU16 (5m wide road)

Borehole	Excav'n Date	Instr'n Date	Final Date
45	24-1-75	22-4-75	

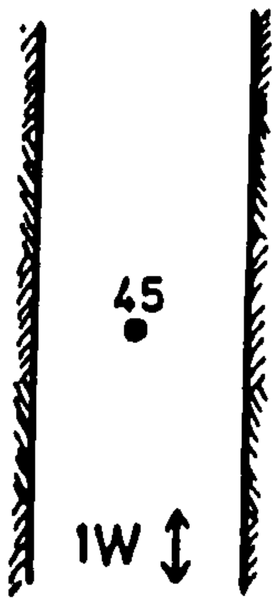

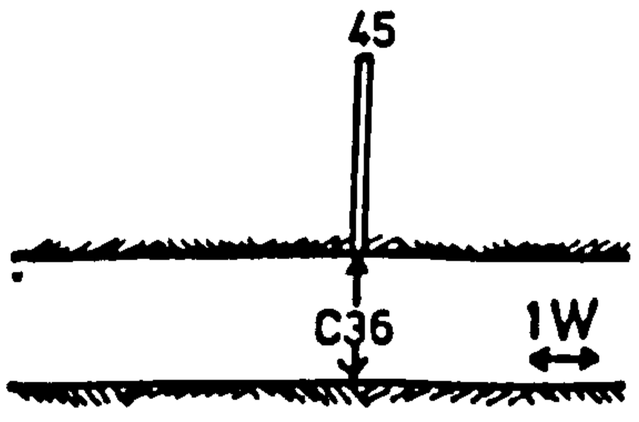

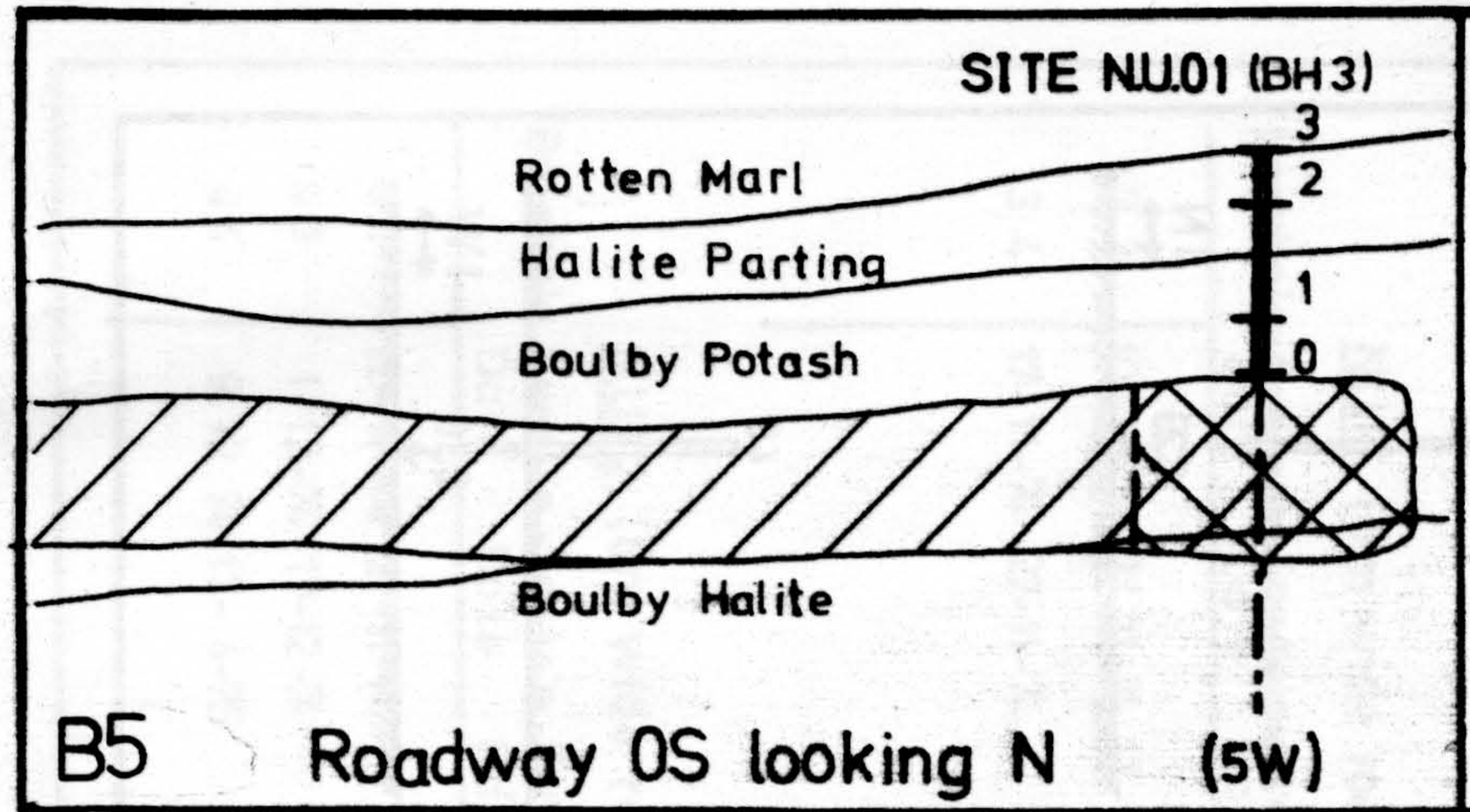

B5 Roadway 0S looking N

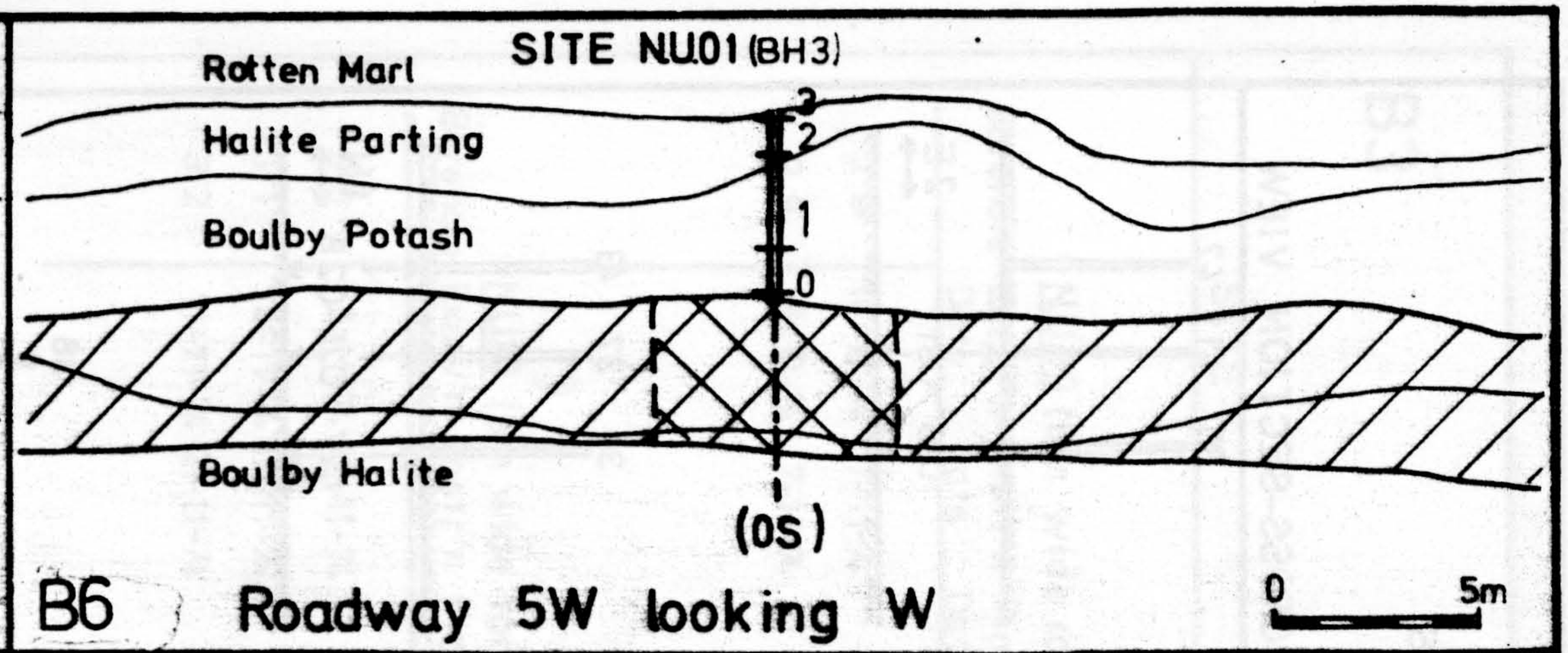

B6 Roadway 5W looking W

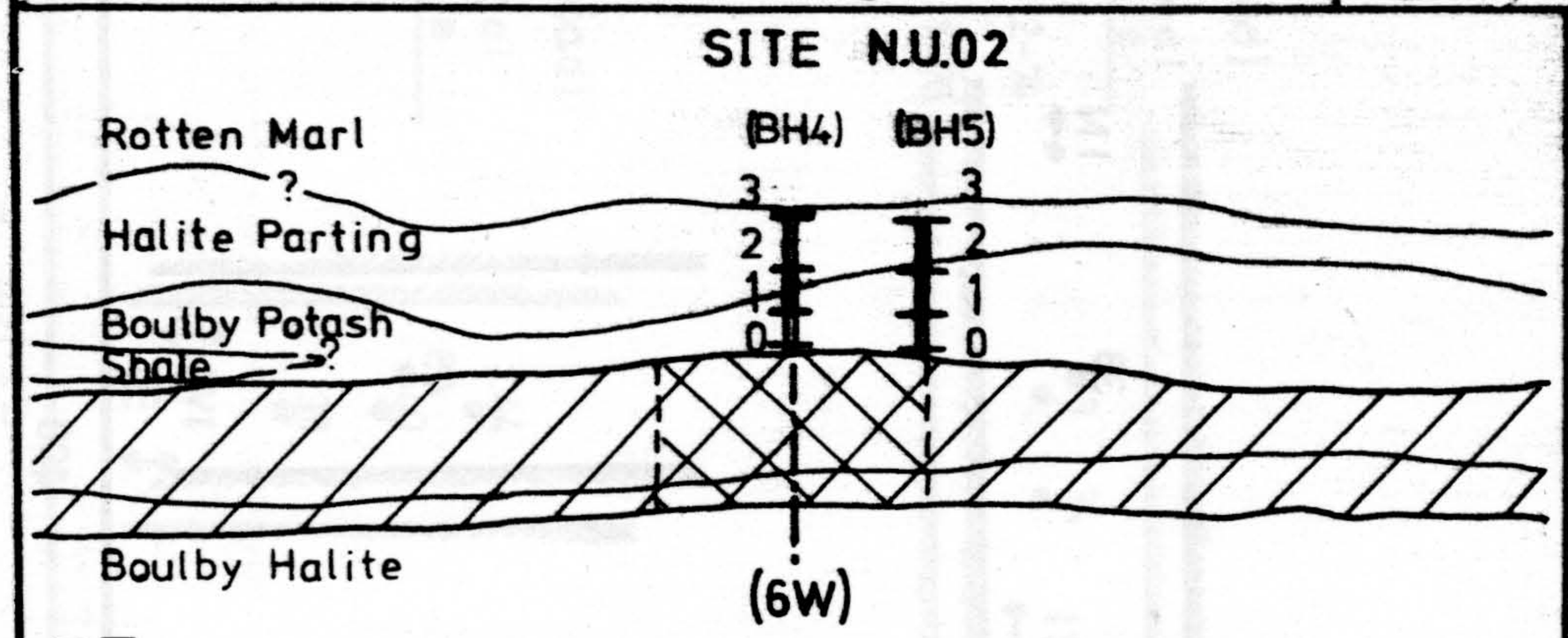

B7 Roadway 0S looking N

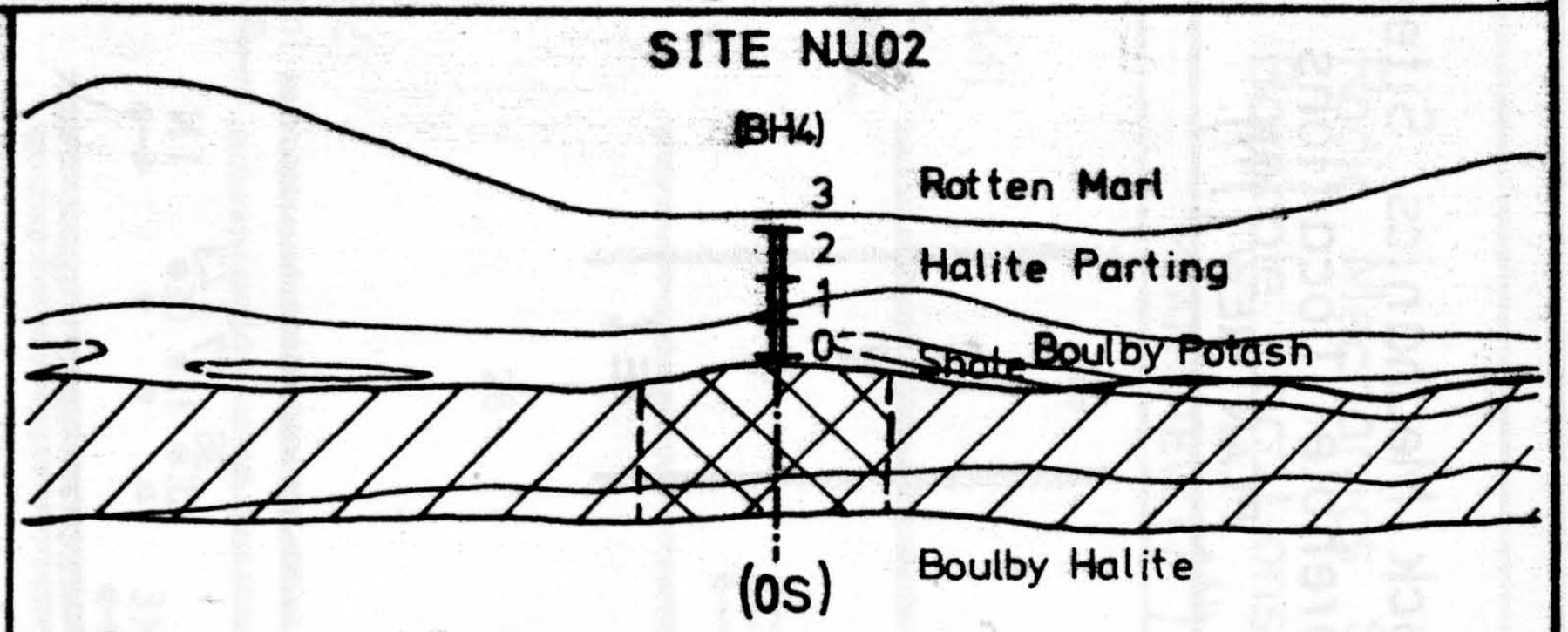

B8 Roadway 6W looking W

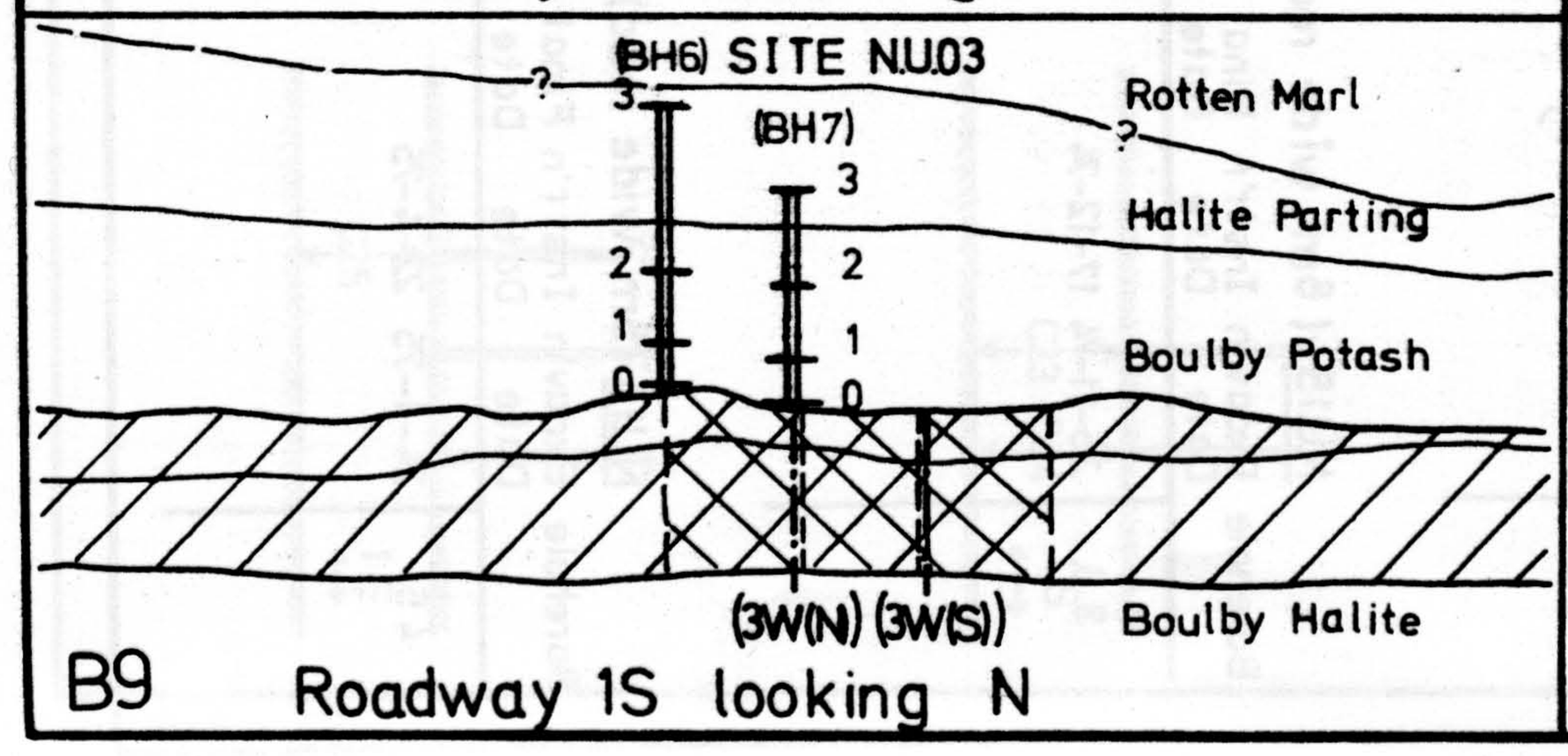

B9 Roadway 1S looking N

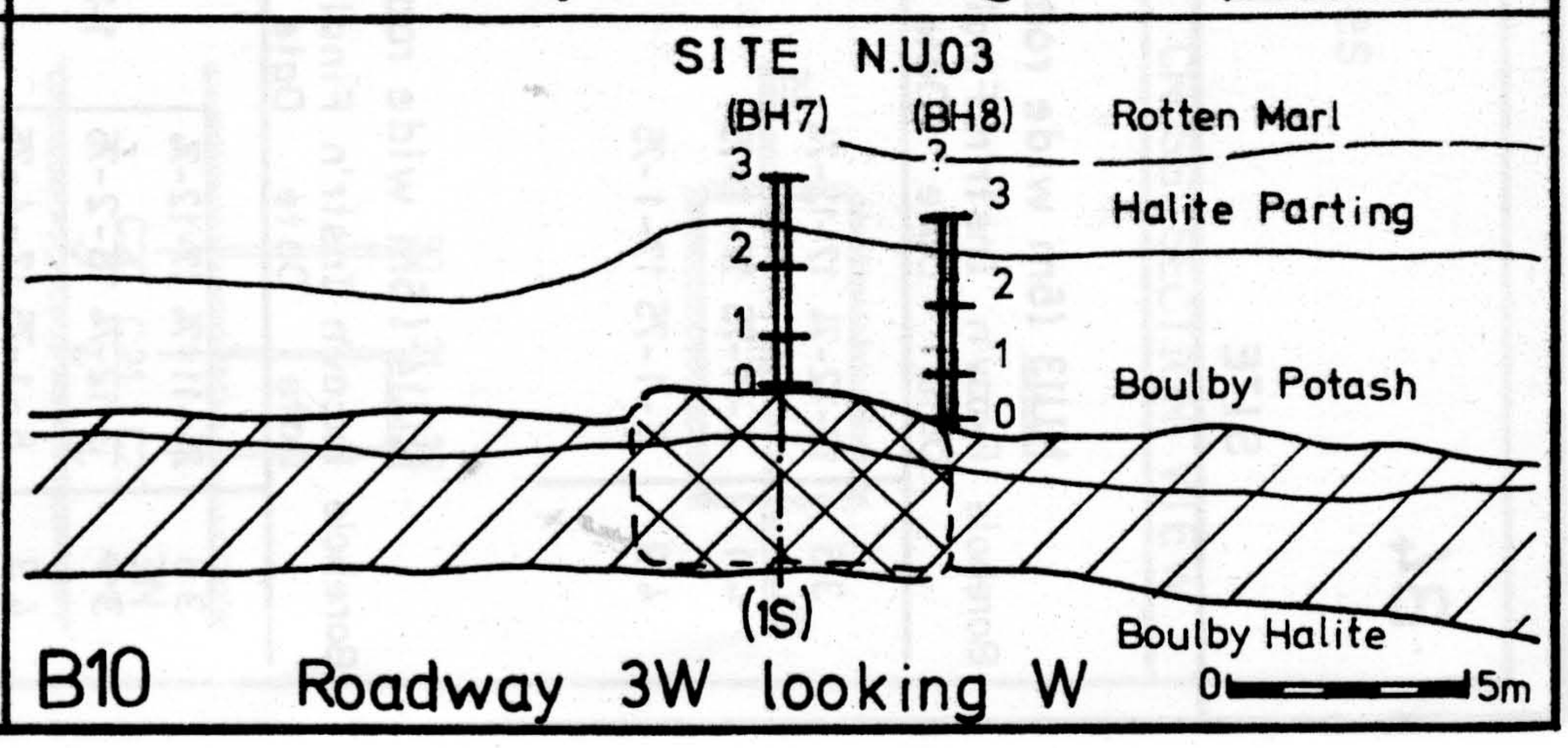

B10 Roadway 3W looking W

Rotten Marl

Shale

Halite Parting

SITE NU.04

(Conv site only)

Boulby Potash

Boulby Halite

(2S)

(1S)

0 5m 10m

B11 Roadway 3W looking W

SITE NU.05

(BH5,13,14) (BH15)

Rotten Marl

Shale with marl

Halite Parting

Boulby Potash

Boulby Halite

(BH16)

(2W)

(3W)

0 5m 10m

B12 Roadway 2S looking N

SITE NU.06 (BH17) (BH18,19)

Rotten Marl

Halite Parting

Shale + Sylvinite

Boulby Potash

Boulby Halite

(SCR)

(1E)

0 5m 10m

B13 Roadway 2S looking N

SITE N.U.01 (BH3)

Rotten Marl

SITE N.U.01 (BH3)

SITE N.U.07

(BH22) (BH23) (BH24)

Halite Parting

Boulby Potash

Shale and Sylvinite

Boulby Potash

Boulby Halite

(1E) B14 Roadway 1S looking N (2E)

0 5m 10m

SITE N.U.08

(BH25) (BH26) (BH27)

Shale and Sylvinite

Halite Parting

Shale

Boulby Potash

Rotten Marl

Shale

Boulby Halite

(1E) B15 Roadway 2S looking N (2E)

0 5m 10m

SITE N.U.10

(BH30) (BH31) (BH32)

Rotten Marl

Halite Parting

Boulby Potash

Boulby Halite

(2W) B16 Roadway 3N looking N (1W)

0 5m 10m

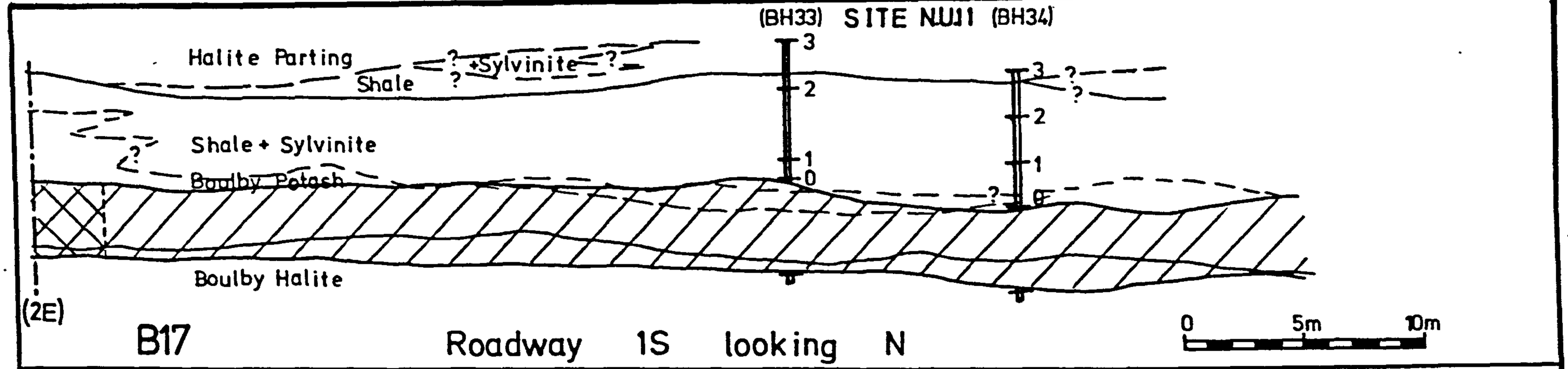

B17 Roadway 1S looking N

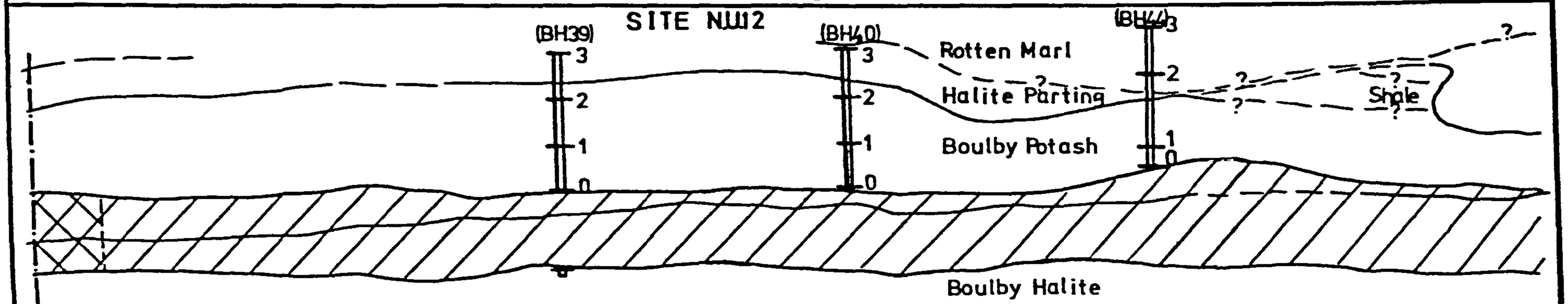

B18 Roadway 1E looking W

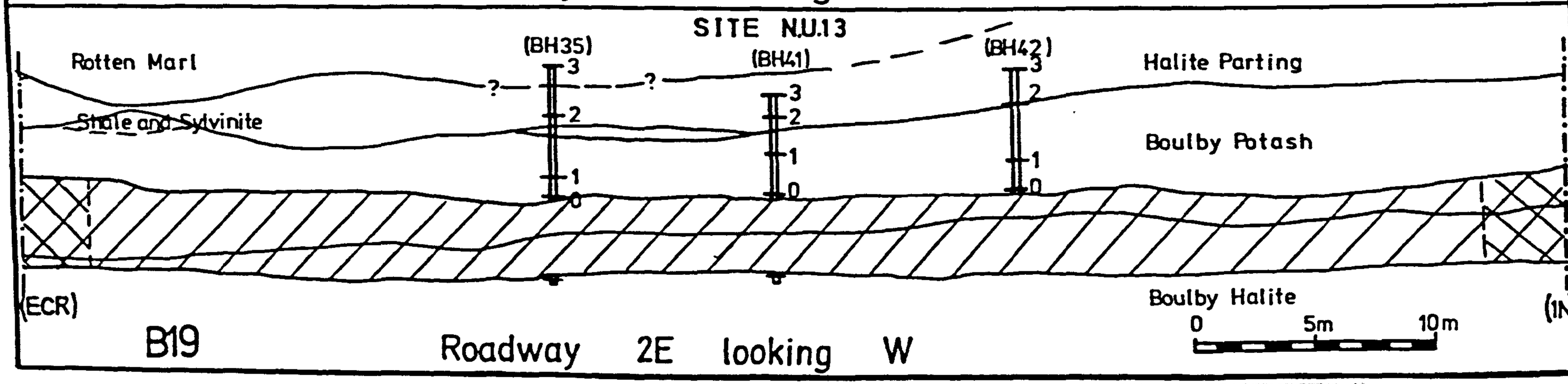

B19 Roadway 2E looking W

SITE NU.14

Rotten Marl

(BH36) (BH37) (BH43)

Halite Parting

Boulby Potash

Boulby Halite

(1E) B20 Roadway 1N looking N 0 5m 10m (2E)

SITE NU.15

(BH38)

Halite ?Parting

Boulby Potash

Boulby Halite

(NCR) B21 Roadway 1N looking N 0 5m 10m (1E)

0 5m 10m

413

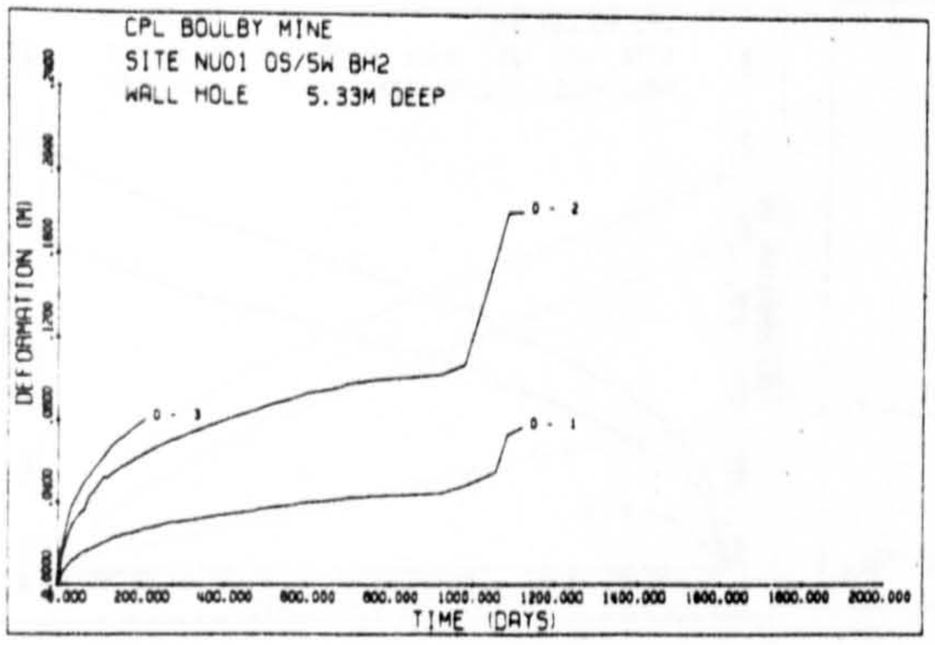
CPL BOULBY MINE
SITE NU01 OS/5W BH2
WALL HOLE 5.33M DEEP
DEFORMATION (M)
TIME (DAYS)
0 - 3
0 - 2
0 - 1

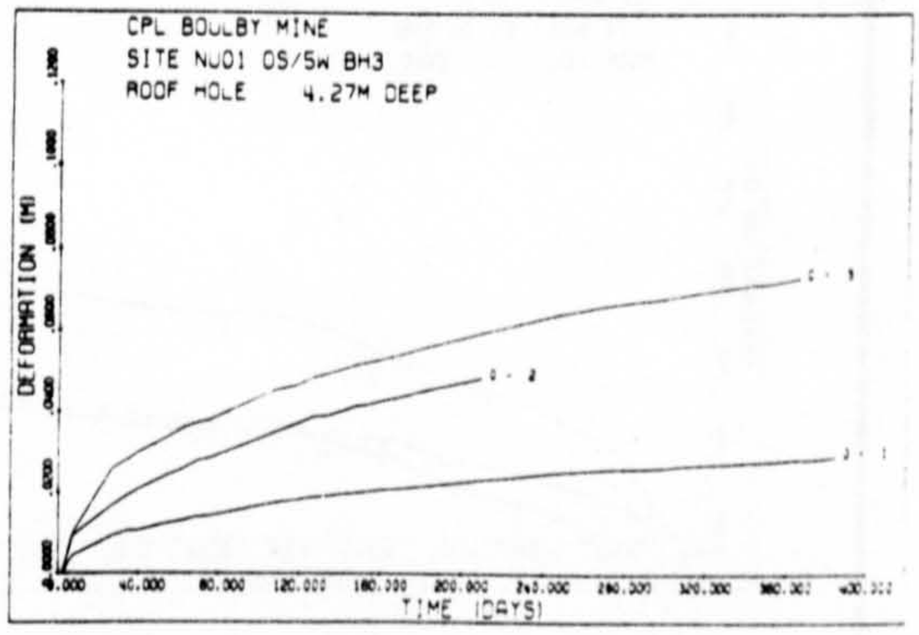
CPL BOULBY MINE
SITE NU01 OS/5W BH3
ROOF HOLE 4.27M DEEP
DEFORMATION (M)
TIME (DAYS)
0 - 3
0 - 2
0 - 1

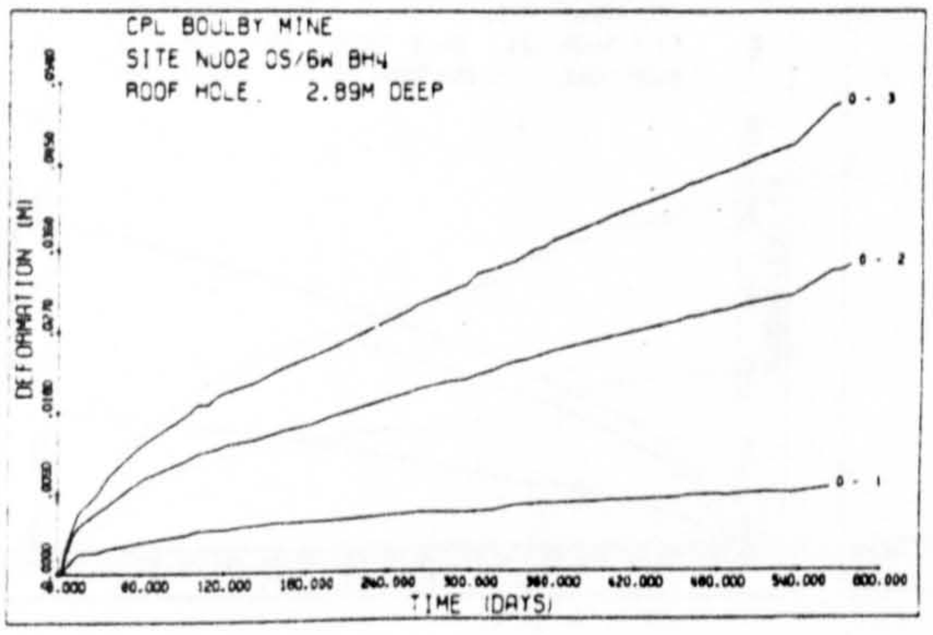
CPL BOULBY MINE
SITE NU02 OS/6W BH4
ROOF HOLE 2.89M DEEP
DEFORMATION (M)
TIME (DAYS)
0 - 3
0 - 2
0 - 1

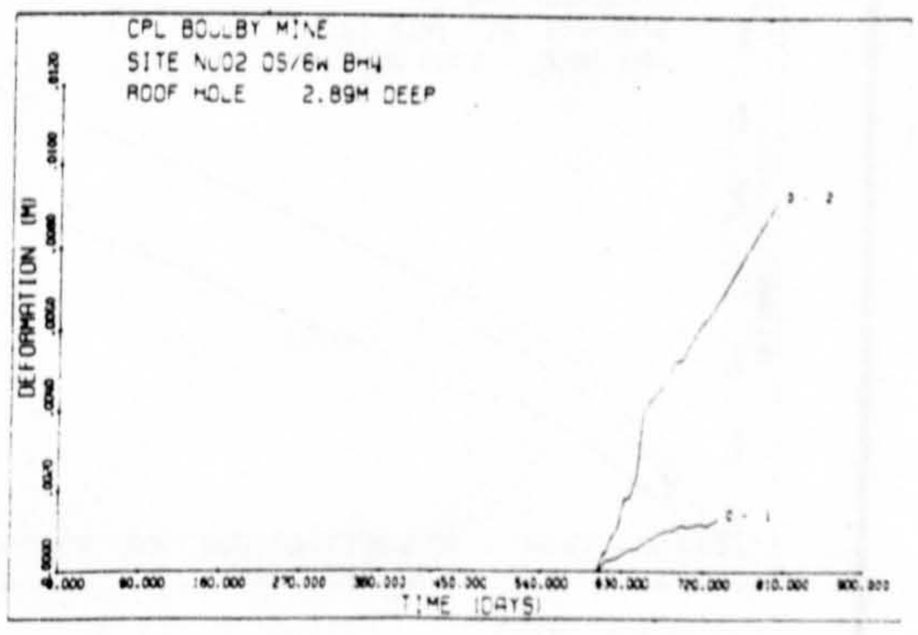
CPL BOULBY MINE
SITE NU02 OS/6W BH4
ROOF HOLE 2.89M DEEP
DEFORMATION (M)
TIME (DAYS)
0 - 2
0 - 1

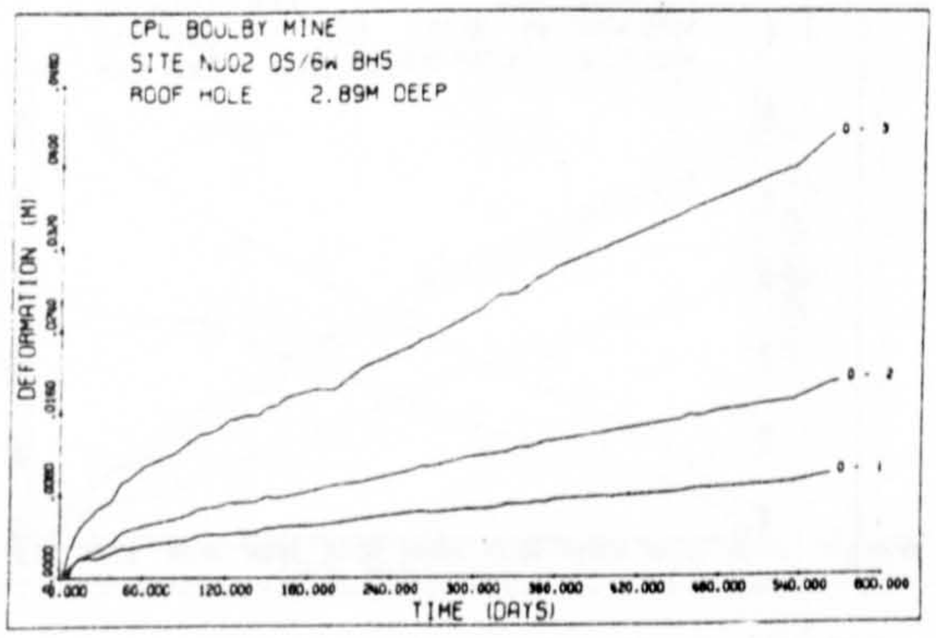
CPL BOULBY MINE
SITE NU02 OS/6W BH5
ROOF HOLE 2.89M DEEP
DEFORMATION (M)
TIME (DAYS)
0 - 3
0 - 2
0 - 1

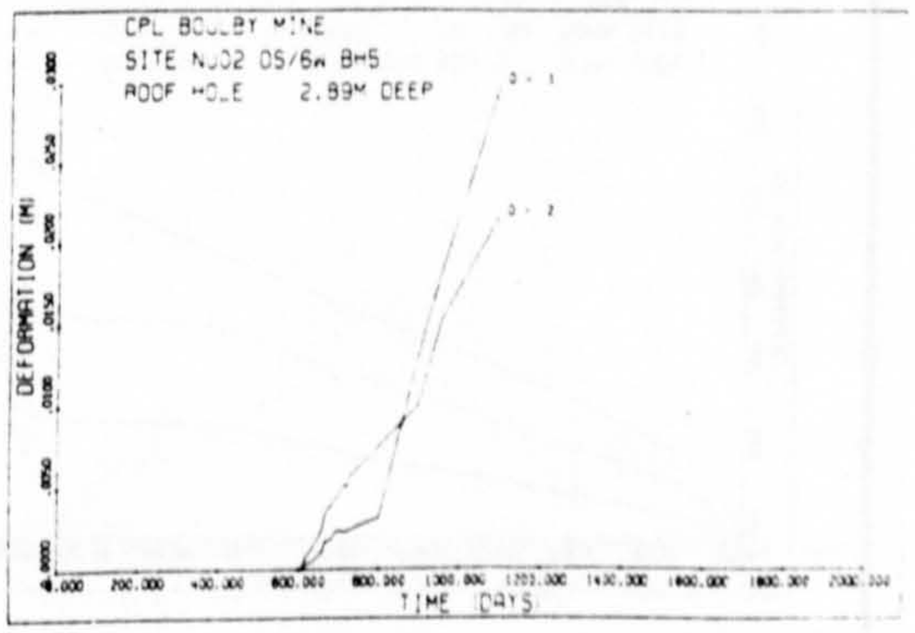
CPL BOULBY MINE
SITE NU02 OS/6W BH5
ROOF HOLE 2.89M DEEP
DEFORMATION (M)
TIME (DAYS)
0 - 1
0 - 2

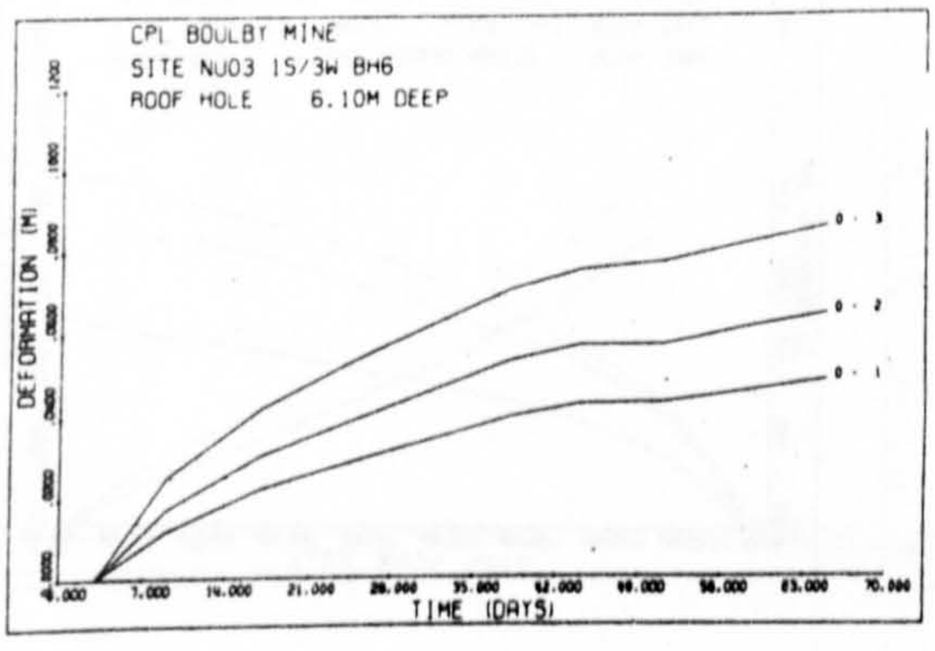
CPL BOULBY MINE
SITE NU03 IS/3W BH6
ROOF HOLE 6.10M DEEP
DEFORMATION (M)
TIME (DAYS)
0 - 3
0 - 2
0 - 1

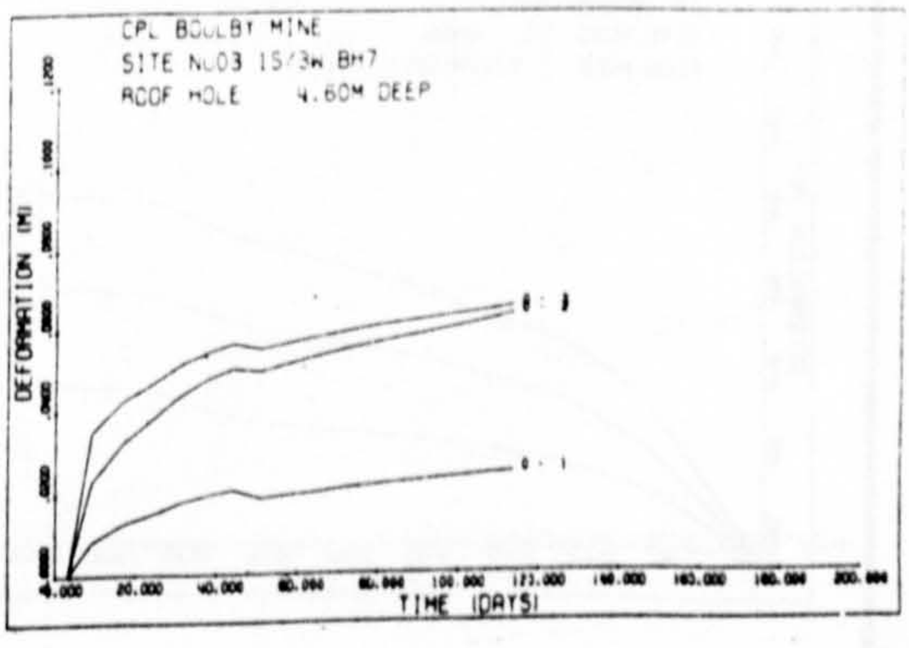
CPL BOULBY MINE
SITE NU03 IS/3W BH7
ROOF HOLE 4.60M DEEP
DEFORMATION (M)
TIME (DAYS)
0 - 3
0 - 1

B22

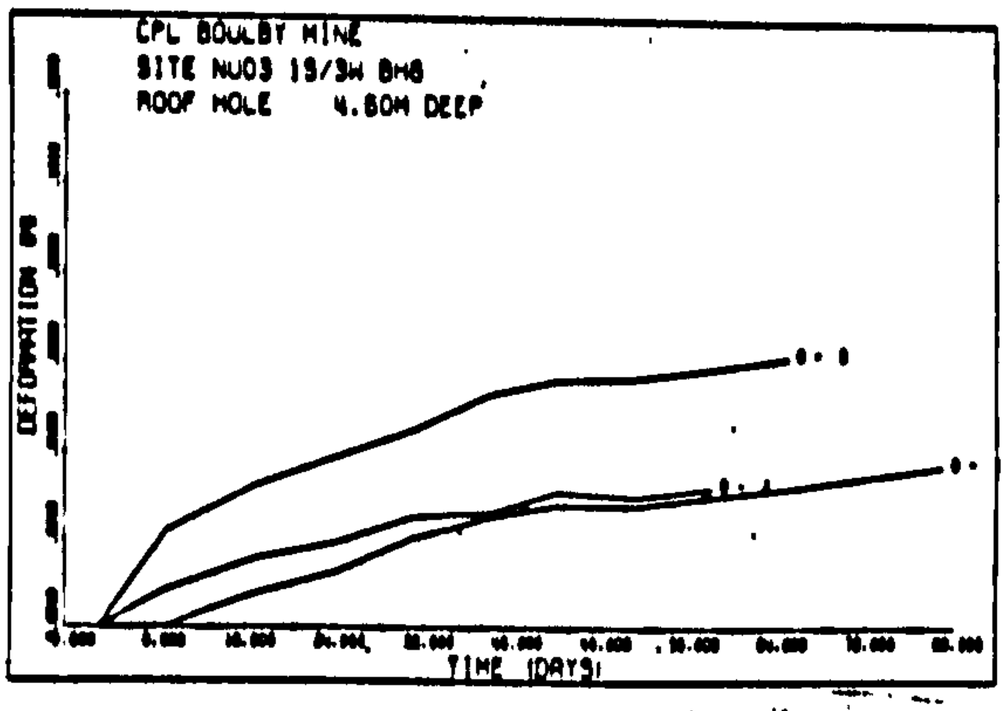
CPL BOULBY MINE
SITE NUO3 19/3W BH8
ROOF HOLE 4.80M DEEP
TIME (DAYS)

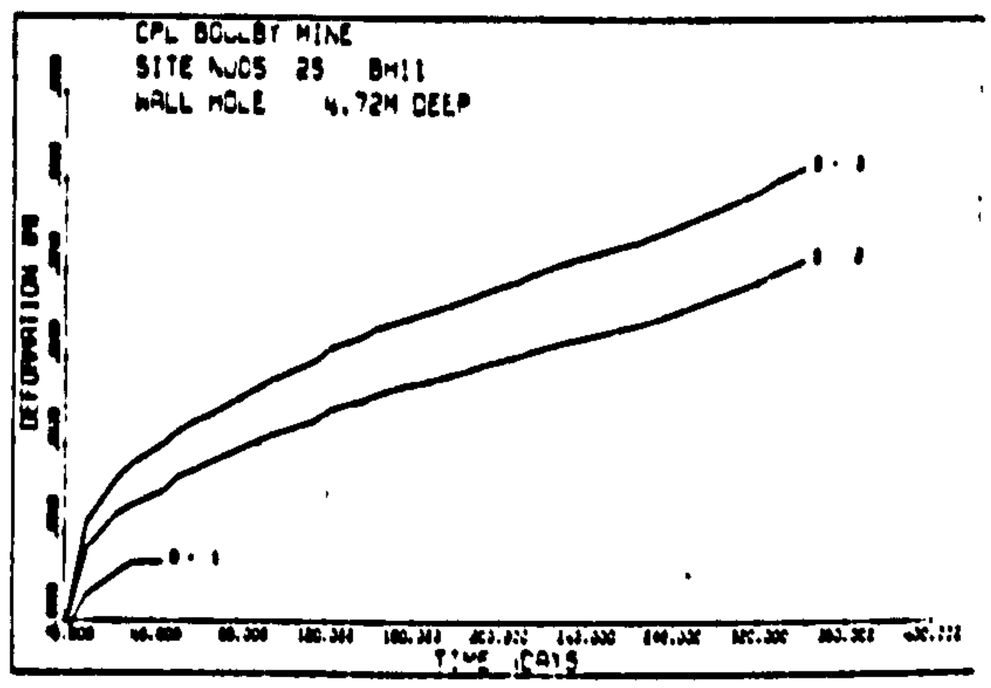
CPL BOULBY MINE
SITE NUO5 25 BH11
WALL HOLE 4.72M DEEP

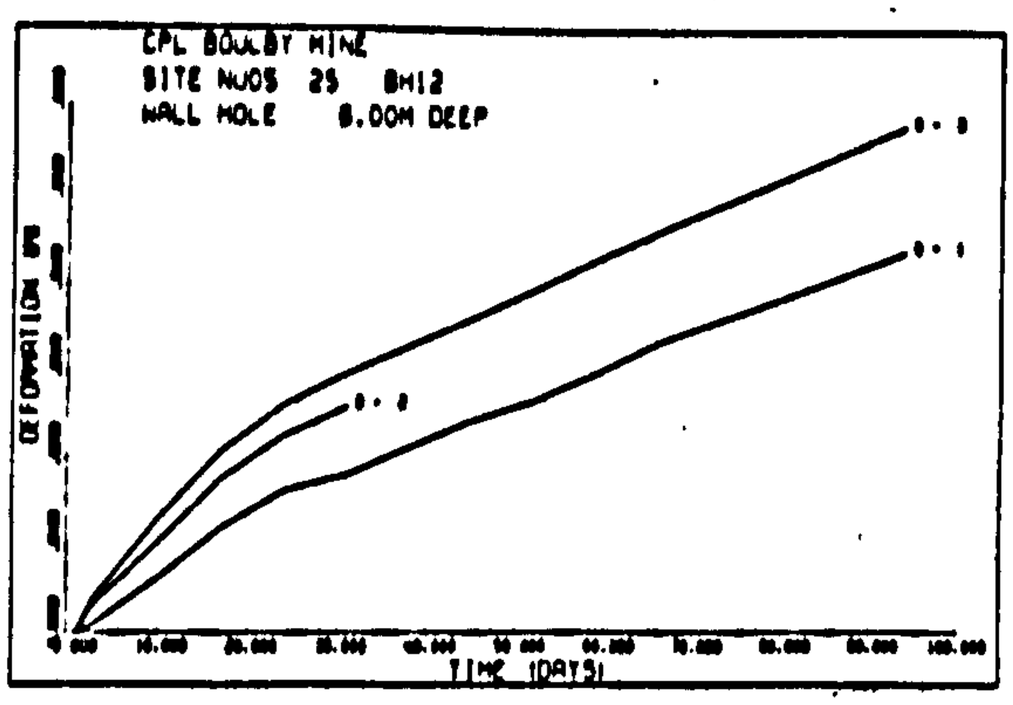
CPL BOULBY MINE
SITE NUO5 25 BH12
WALL HOLE 8.00M DEEP
TIME (DAYS)

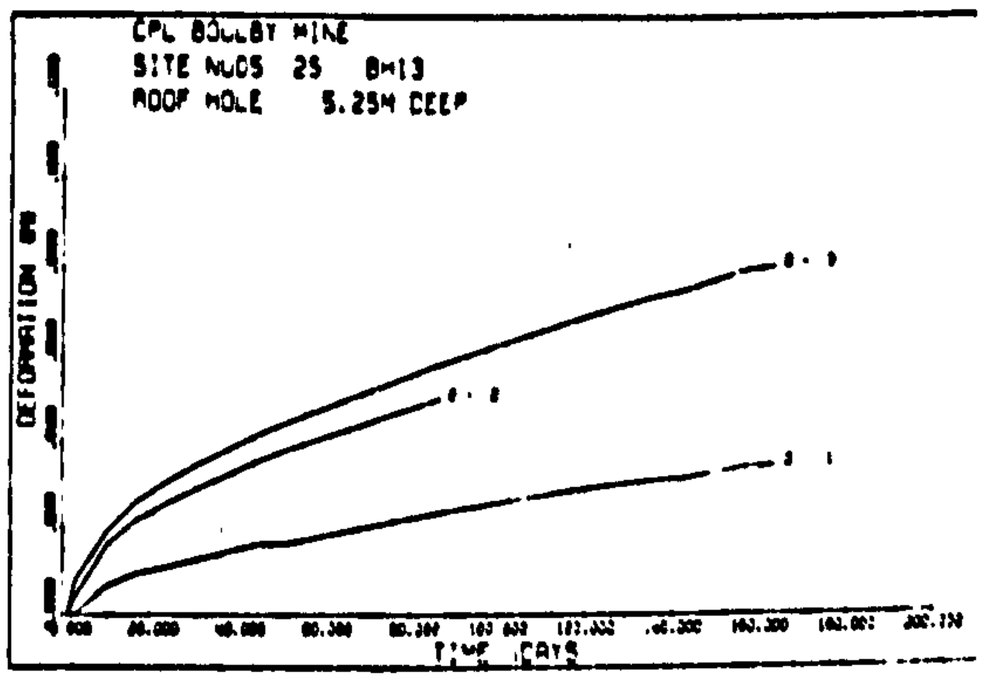
CPL BOULBY MINE
SITE NUO5 25 BH13
ROOF HOLE 5.25M DEEP

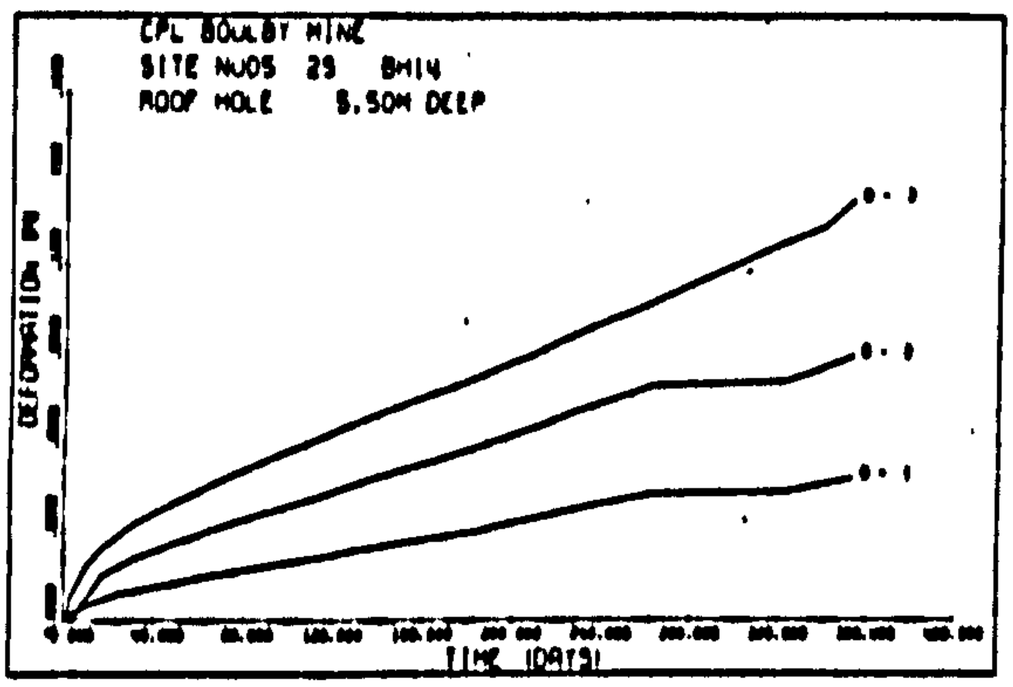
CPL BOULBY MINE
SITE NUO5 25 BH14
ROOF HOLE 8.50M DEEP
TIME (DAYS)

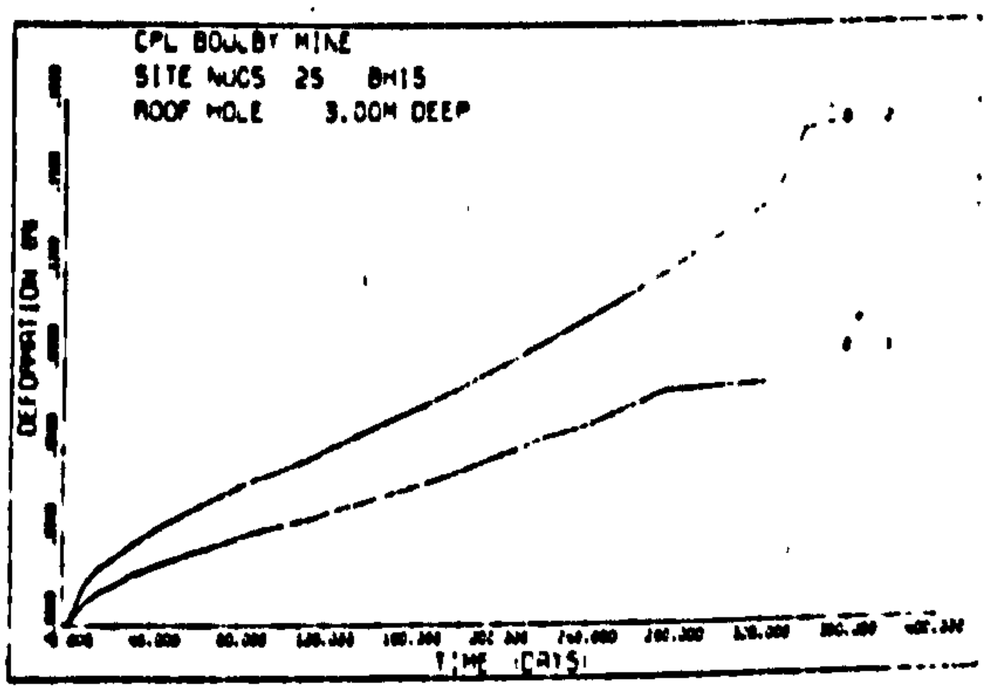
CPL BOULBY MINE
SITE NUO5 25 BH15
ROOF HOLE 3.00M DEEP

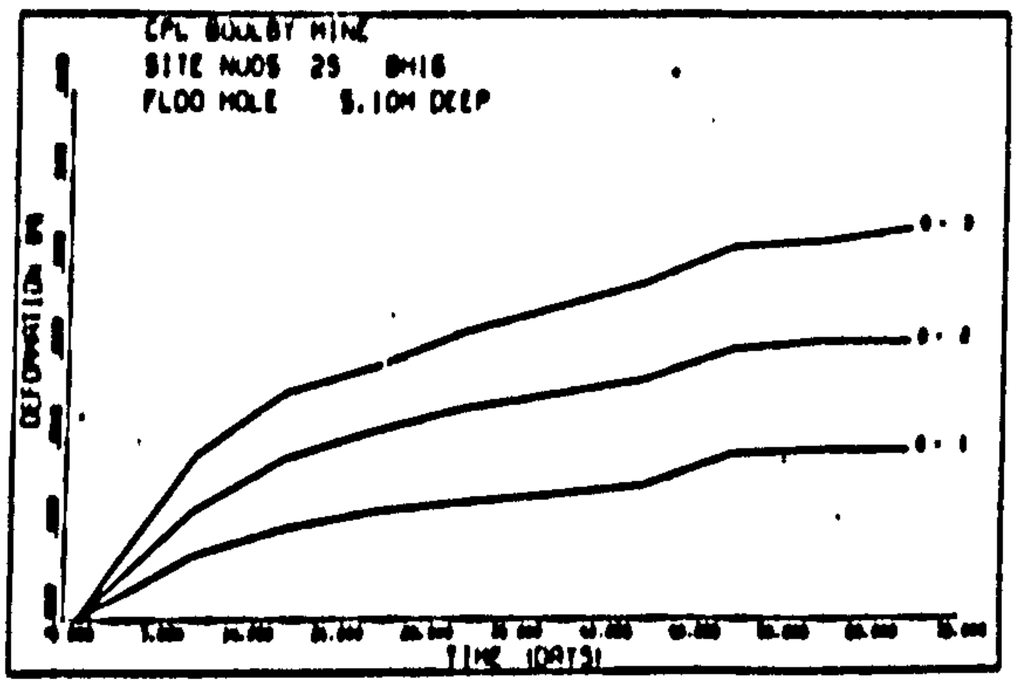
CPL BOULBY MINE
SITE NUO5 25 BH16
FLOO HOLE 5.10M DEEP
TIME (DAYS)

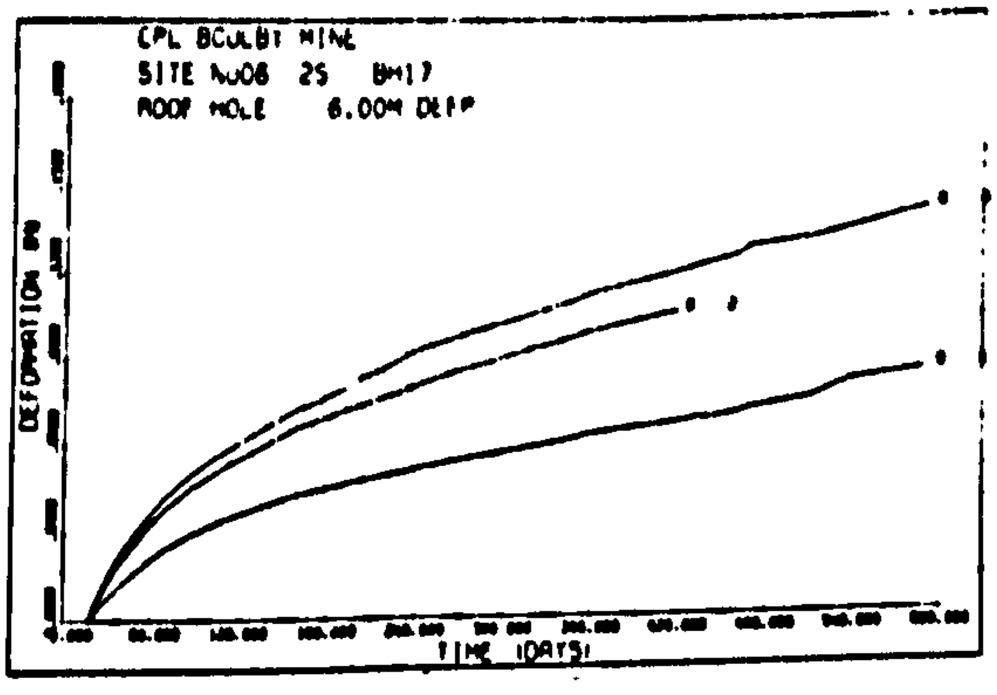
CPL BOULBY MINE
SITE NUO6 25 BH17
ROOF HOLE 6.00M DEEP
TIME (DAYS)

B23

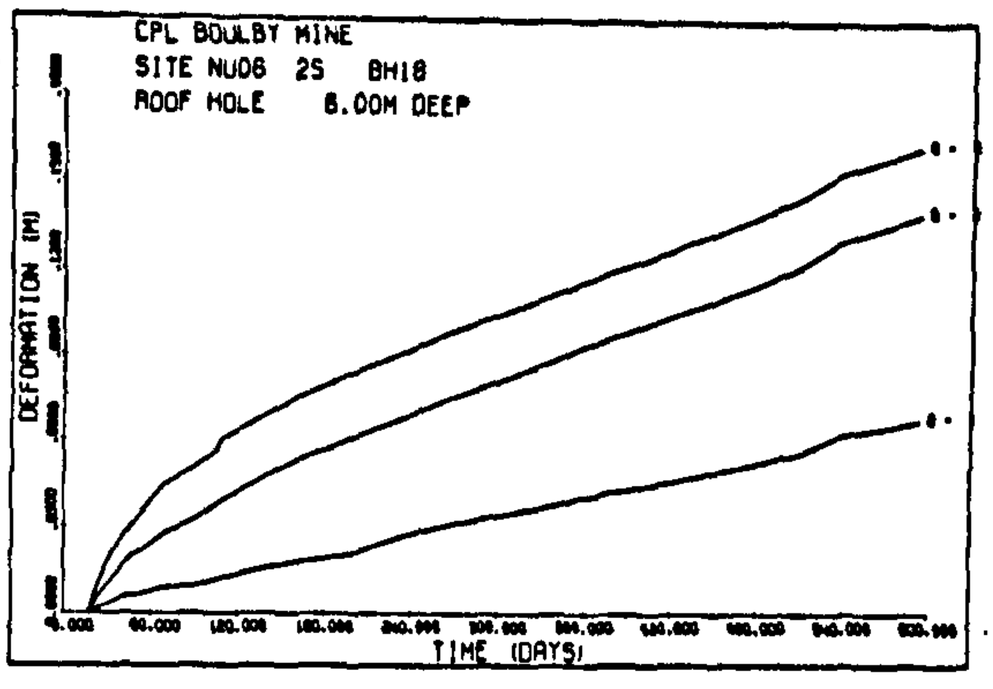
CPL BOULBY MINE
SITE NU06 2S BH18
ROOF HOLE 6.00M DEEP
DEFORMATION (M)
TIME (DAYS)

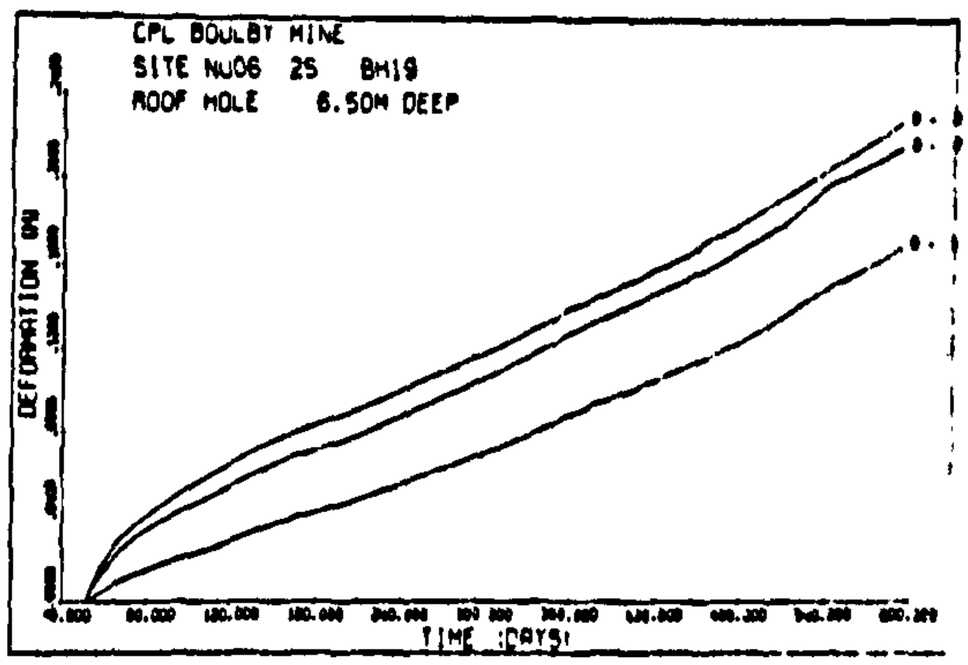
CPL BOULBY MINE
SITE NU06 2S BH19
ROOF HOLE 6.50M DEEP
DEFORMATION (M)
TIME (DAYS)

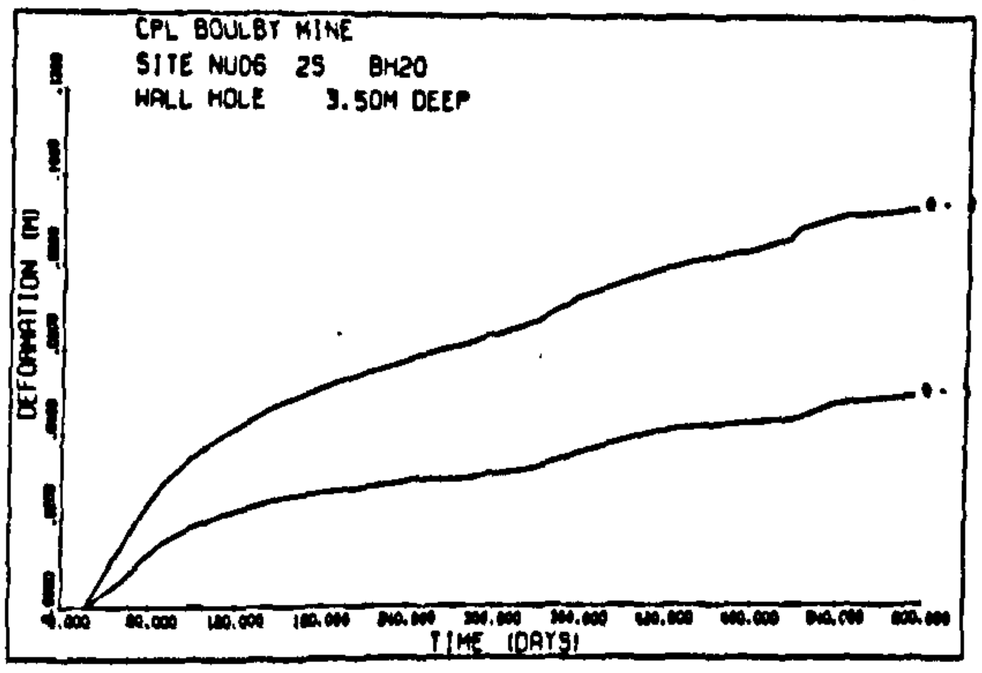
CPL BOULBY MINE
SITE NU06 2S BH20
WALL HOLE 3.50M DEEP
DEFORMATION (M)
TIME (DAYS)

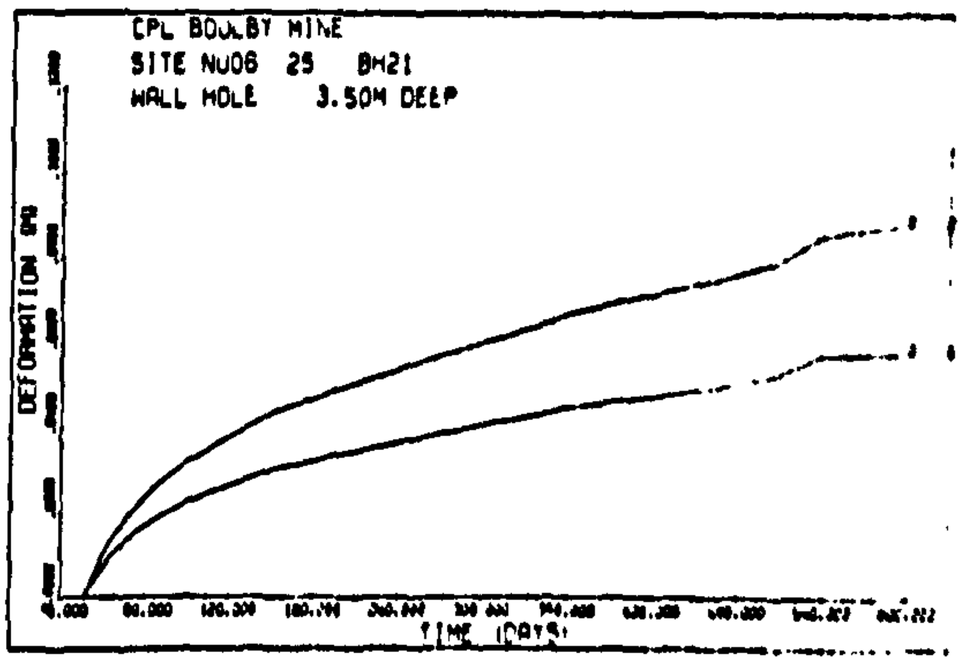
CPL BOULBY MINE
SITE NU06 2S BH21
WALL HOLE 3.50M DEEP
DEFORMATION (M)
TIME (DAYS)

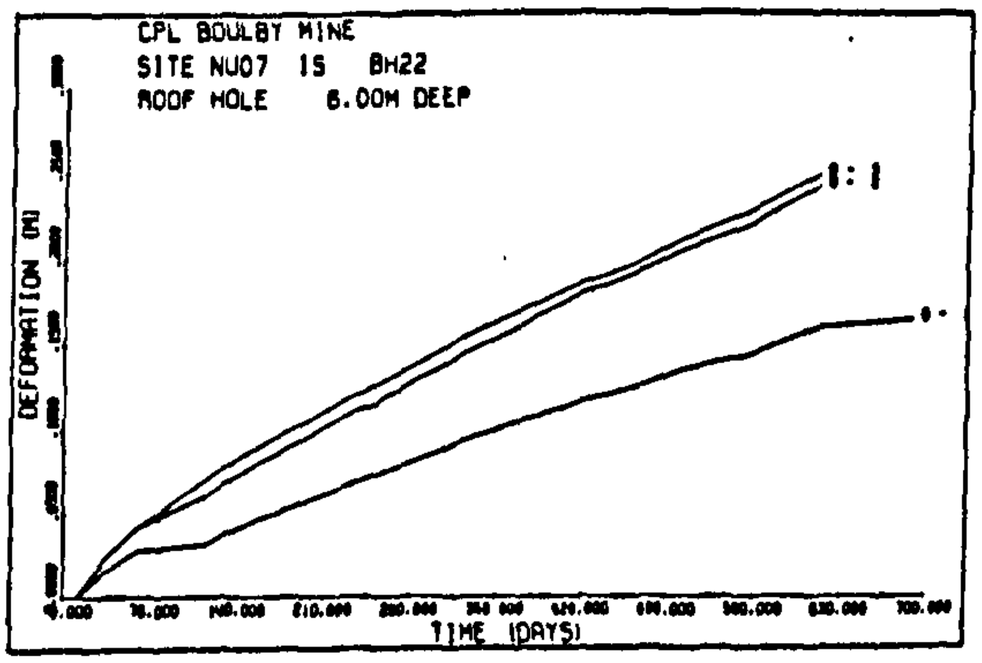
CPL BOULBY MINE
SITE NU07 1S BH22
ROOF HOLE 6.00M DEEP
DEFORMATION (M)
TIME (DAYS)

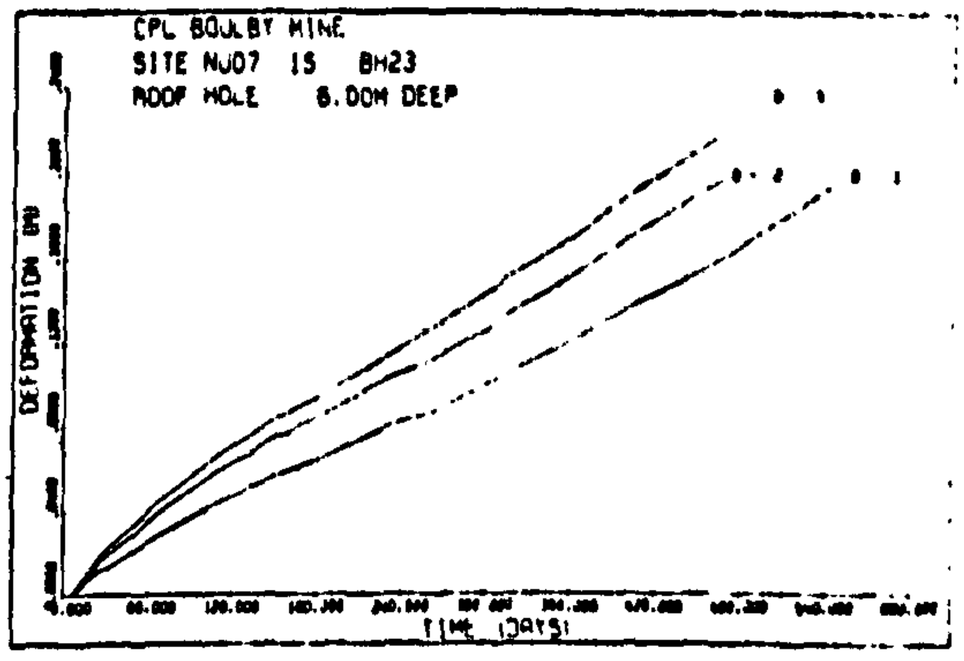
CPL BOULBY MINE
SITE NU07 1S BH23
ROOF HOLE 6.00M DEEP
DEFORMATION (M)
TIME (DAYS)

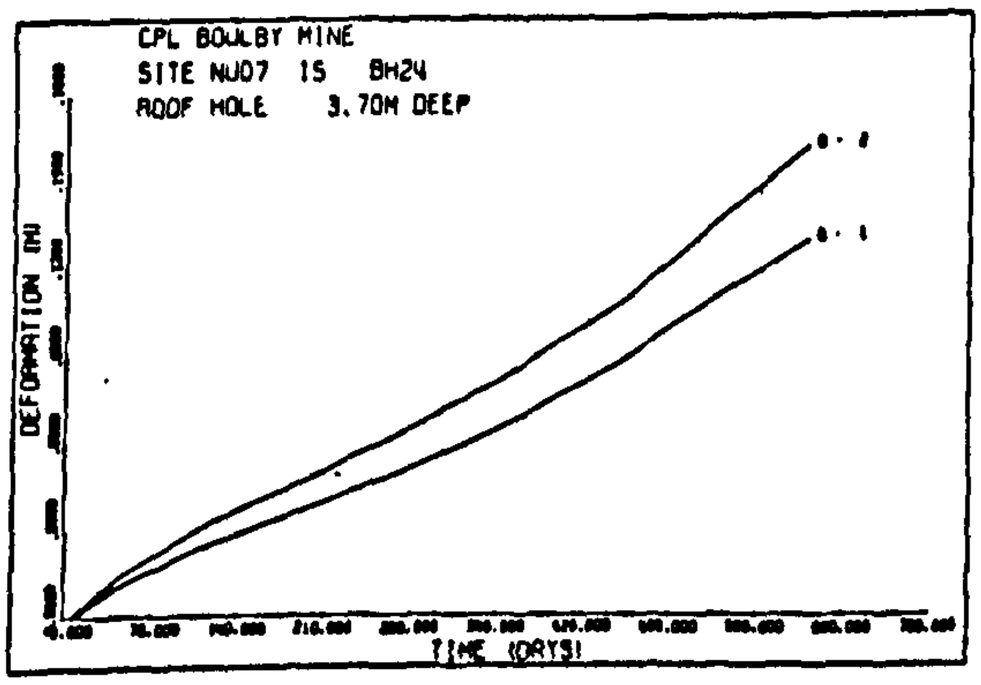
CPL BOULBY MINE
SITE NU07 1S BH24
ROOF HOLE 3.70M DEEP
DEFORMATION (M)
TIME (DAYS)

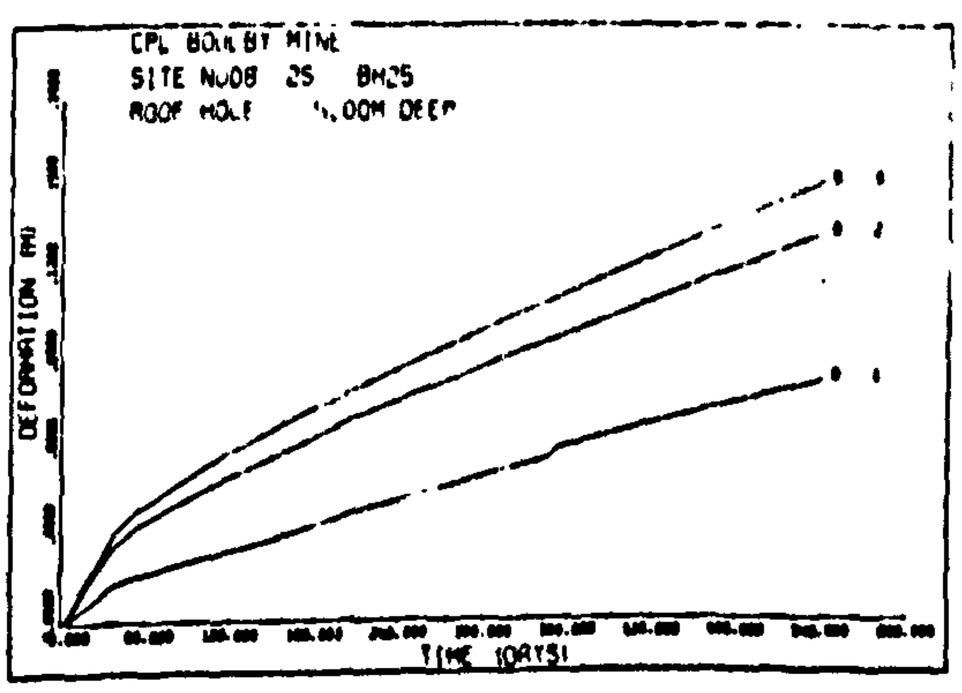
CPL BOULBY MINE
SITE NU08 2S BH25
ROOF HOLE 4.00M DEEP
DEFORMATION (M)
TIME (DAYS)

B24

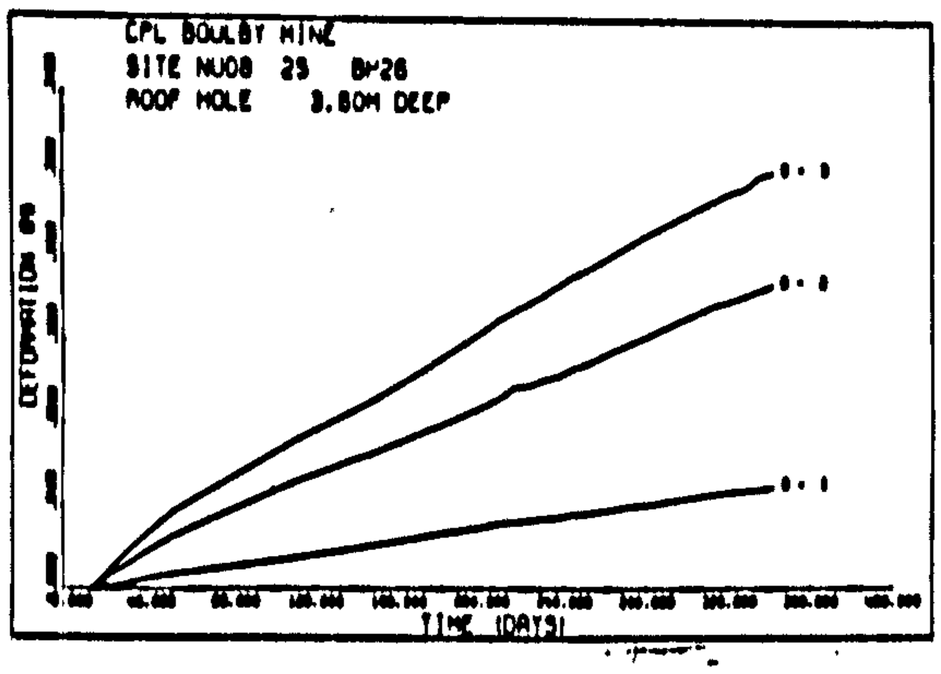
CPL BOULBY MINE
SITE NUOB 2S BH26
ROOF HOLE 3.80M DEEP
TIME (DAYS)

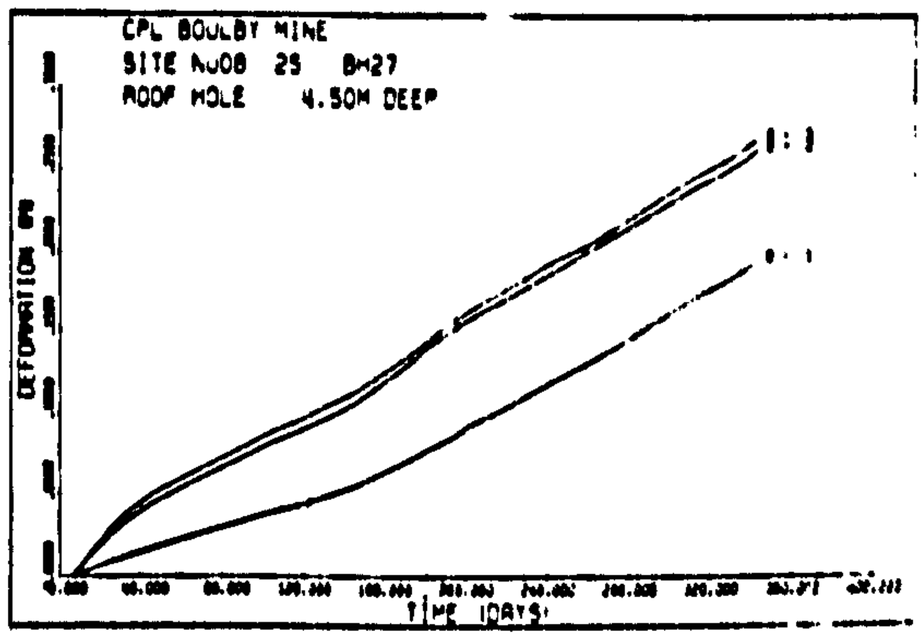
CPL BOULBY MINE
SITE NUOB 2S BH27
ROOF HOLE 4.50M DEEP
TIME (DAYS)

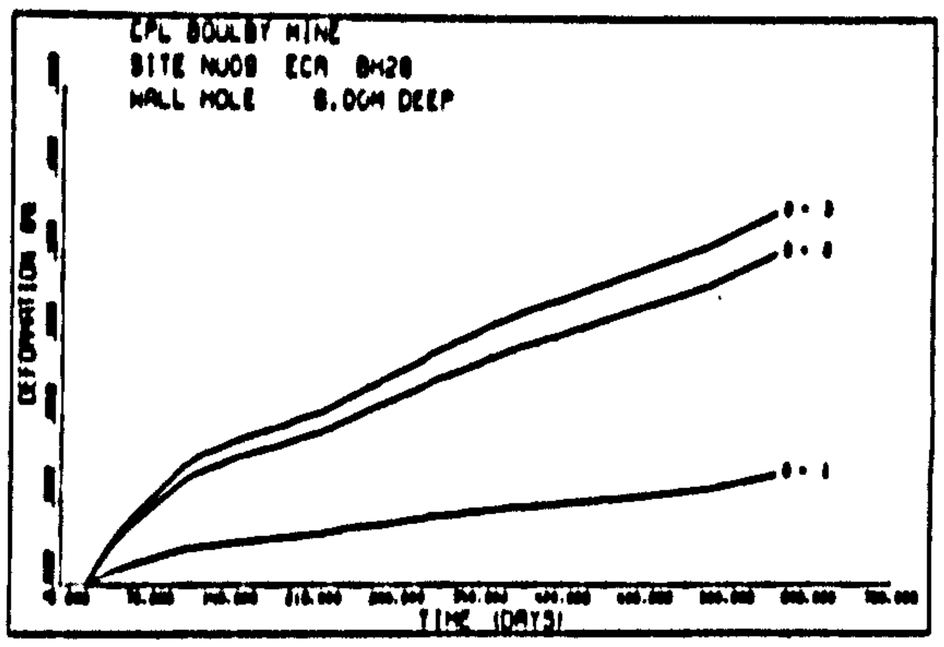
CPL BOULBY MINE
SITE NUOB ECA BH28
WALL HOLE 8.00M DEEP
TIME (DAYS)

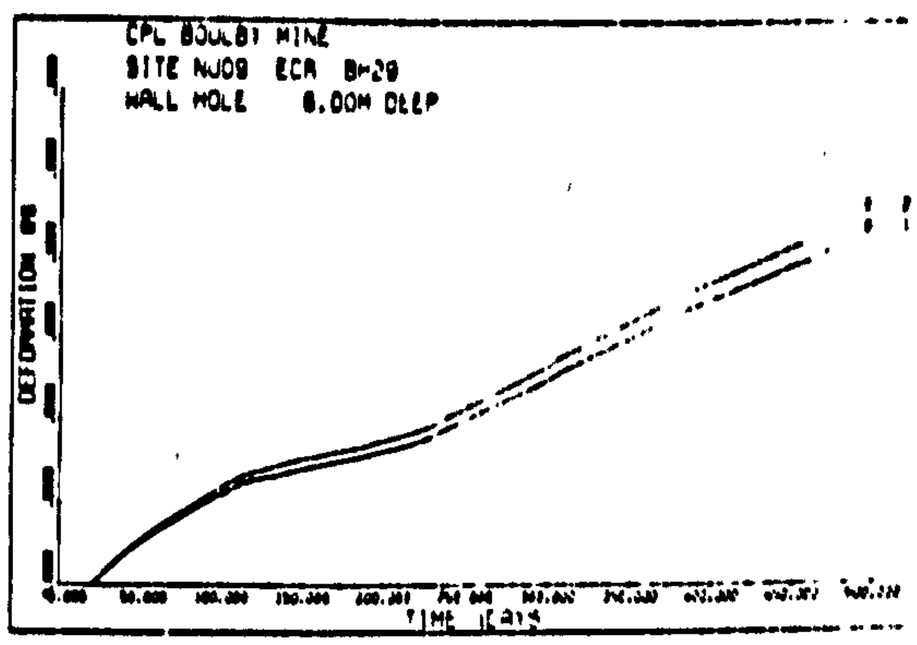
CPL BOULBY MINE
SITE NUOB ECA BH29
WALL HOLE 8.00M DEEP

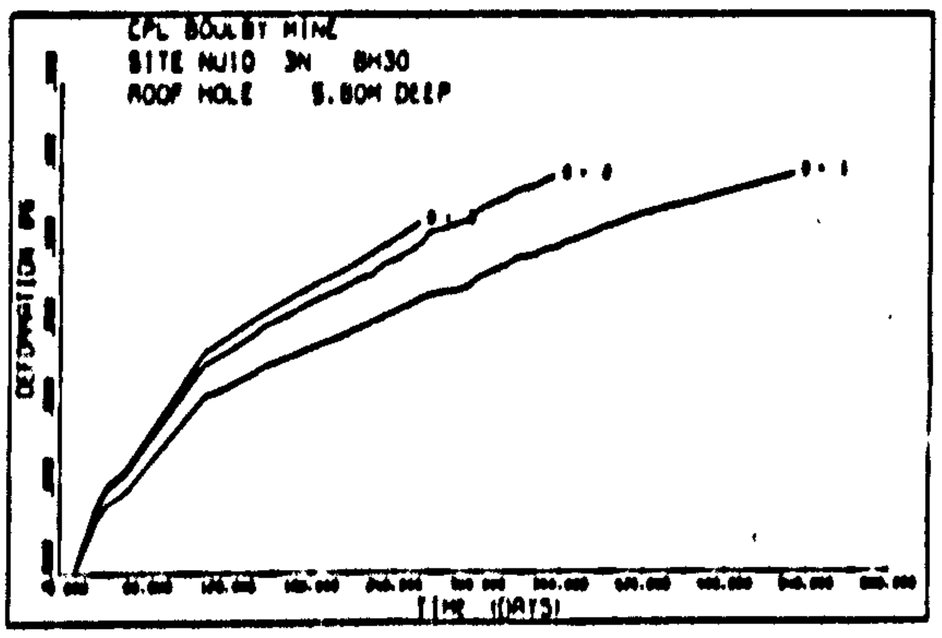
CPL BOULBY MINE
SITE NU10 3N BH30
ROOF HOLE 5.80M DEEP
TIME (DAYS)

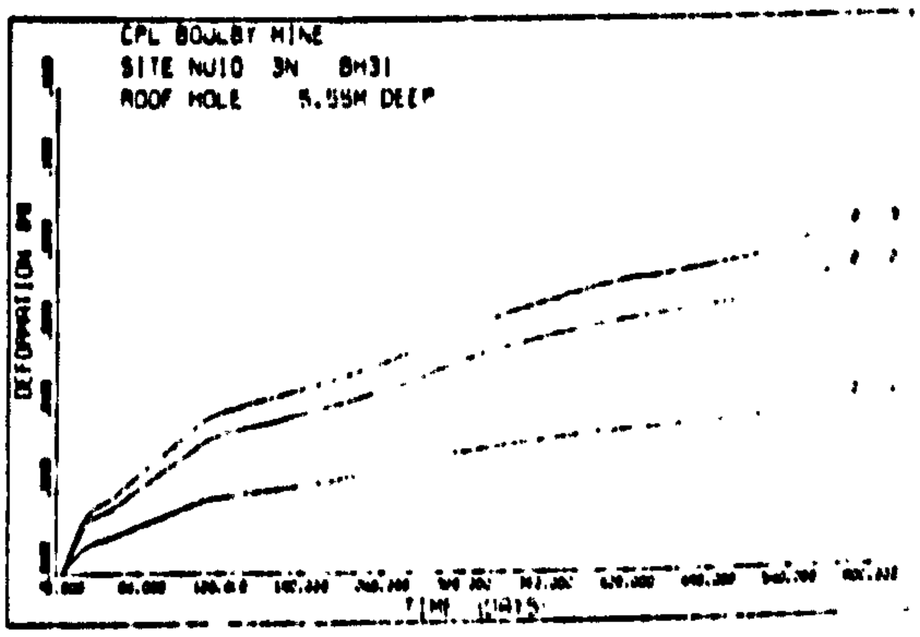
CPL BOULBY MINE
SITE NU10 3N BH31
ROOF HOLE 5.55M DEEP

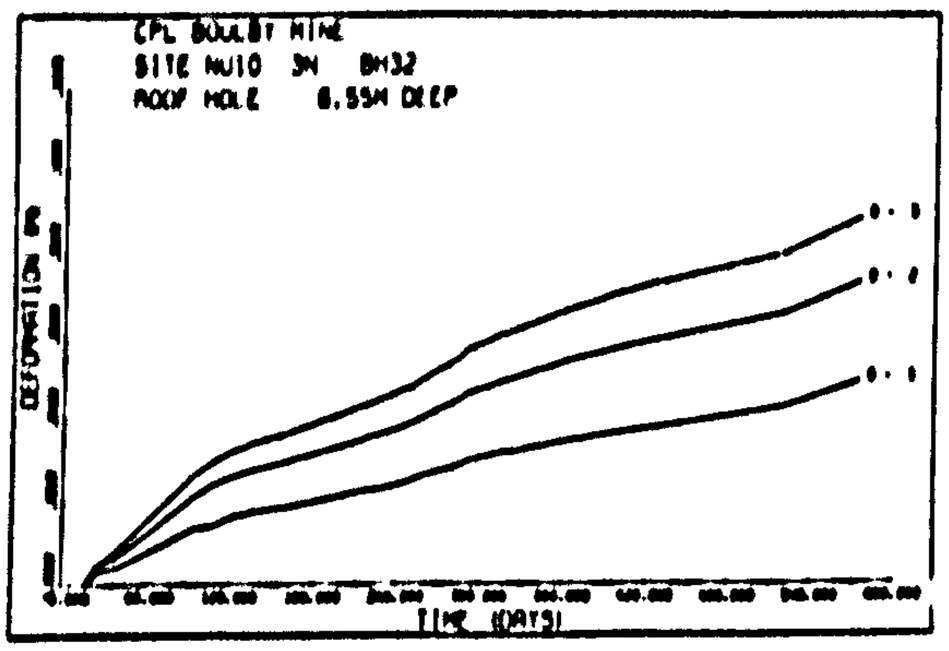
CPL BOULBY MINE
SITE NU10 3N BH32
ROOF HOLE 8.55M DEEP
TIME (DAYS)

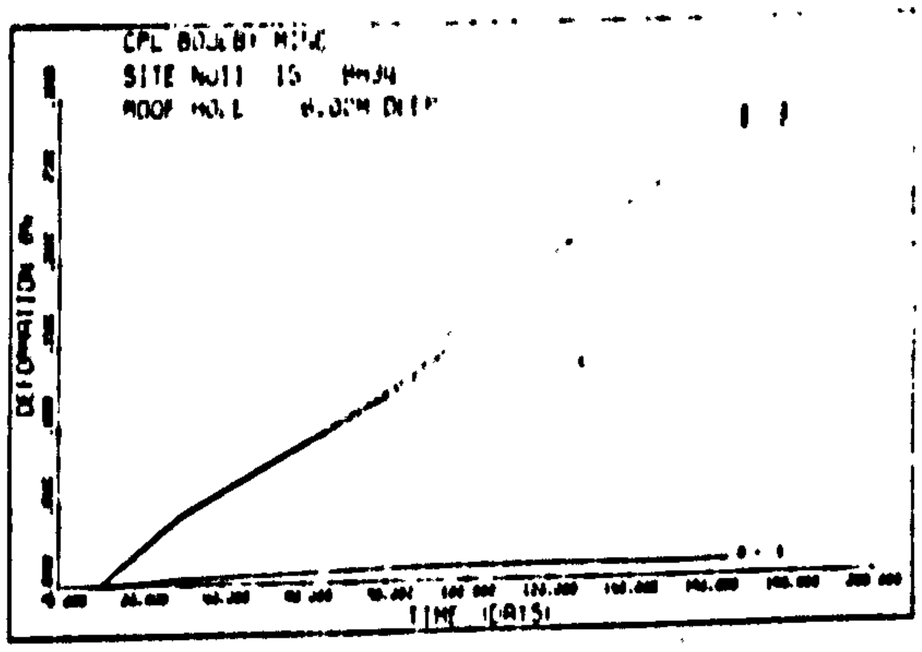
CPL BOULBY MINE
SITE NU11 1S BH34

B25

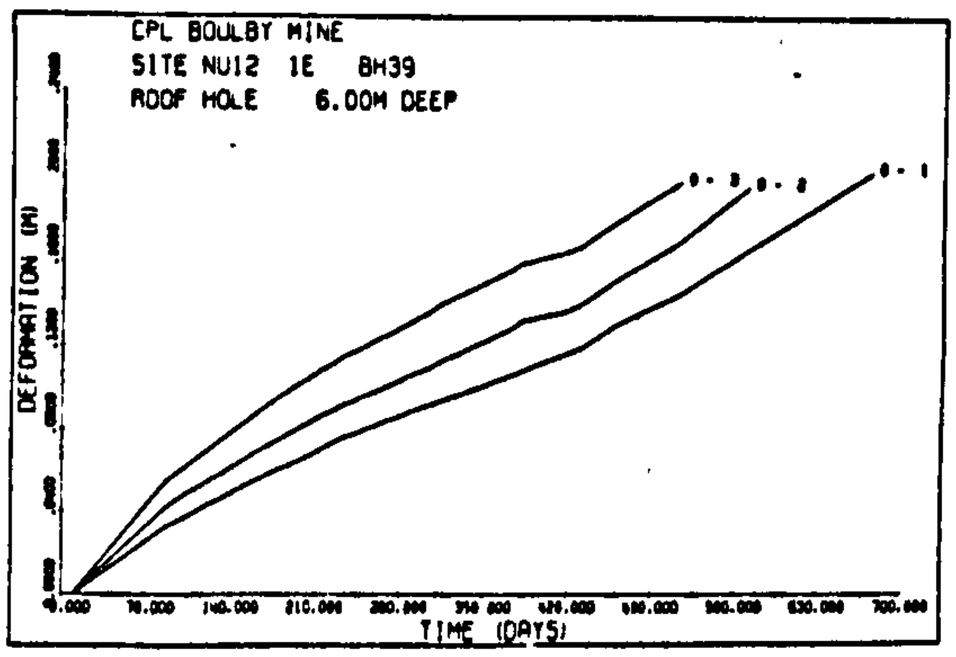
CPL BOULBY MINE
SITE NU12 1E BH39
ROOF HOLE 6.00M DEEP
DEFORMATION (M)
TIME (DAYS)

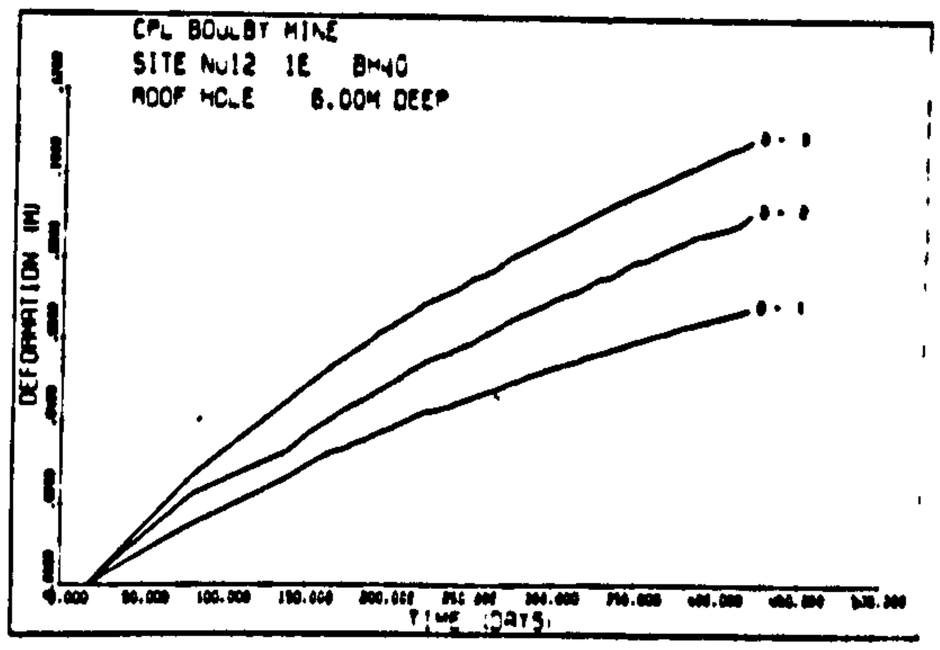
CPL BOULBY MINE
SITE NU12 1E BH40
ROOF HOLE 6.00M DEEP
DEFORMATION (M)
TIME (DAYS)

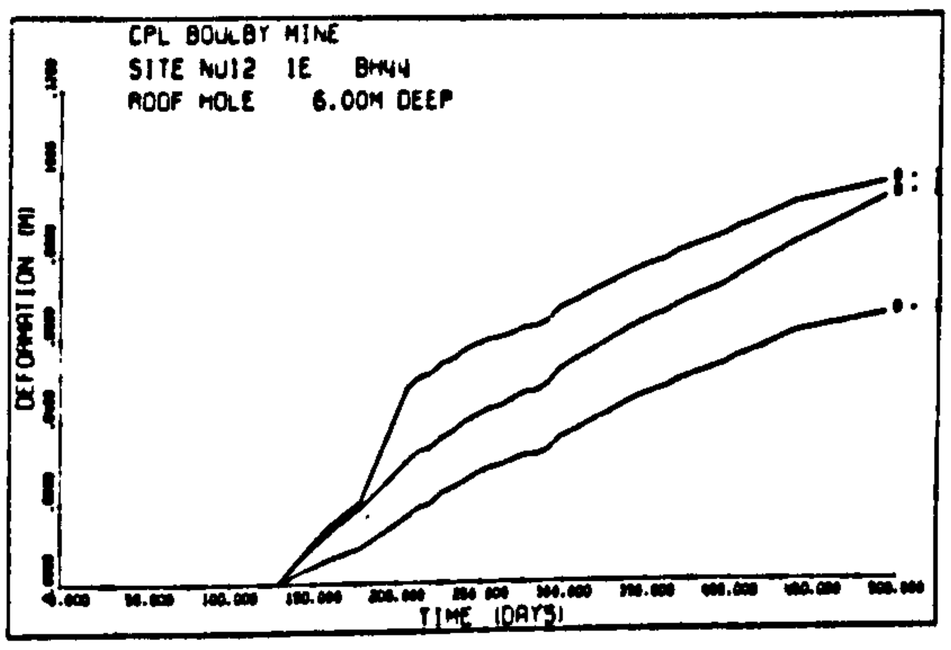
CPL BOULBY MINE
SITE NU12 1E BH44
ROOF HOLE 6.00M DEEP
DEFORMATION (M)
TIME (DAYS)

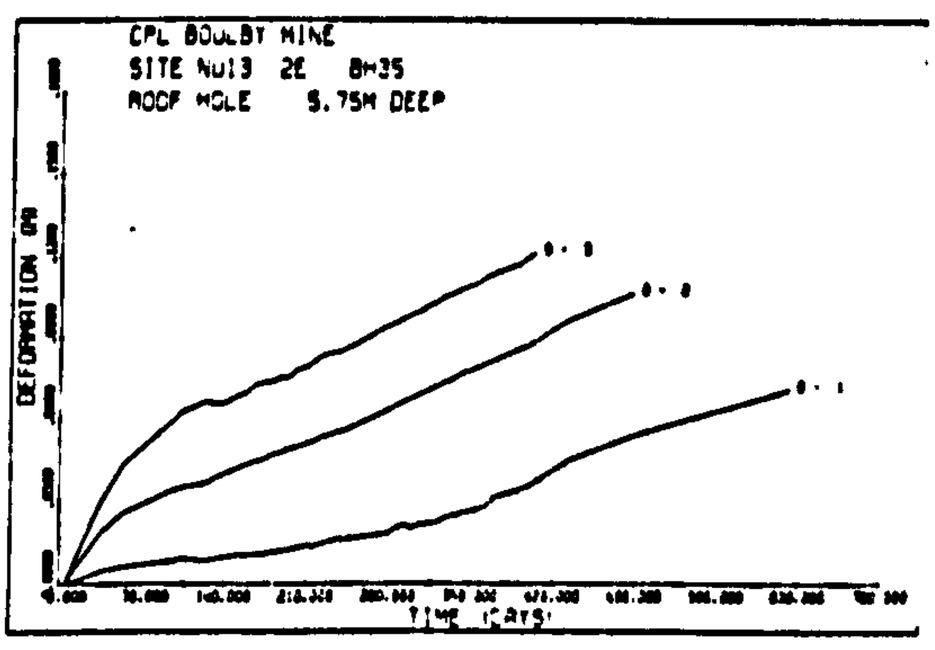
CPL BOULBY MINE
SITE NU13 2E BH35
ROOF HOLE 5.75M DEEP
DEFORMATION (M)
TIME (DAYS)

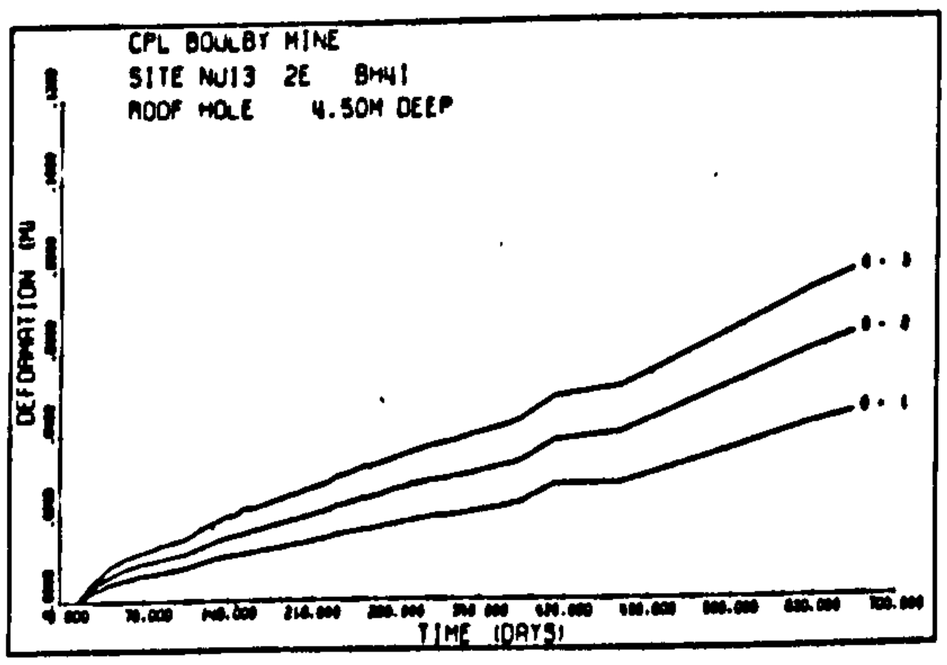
CPL BOULBY MINE
SITE NU13 2E BH41
ROOF HOLE 4.50M DEEP
DEFORMATION (M)
TIME (DAYS)

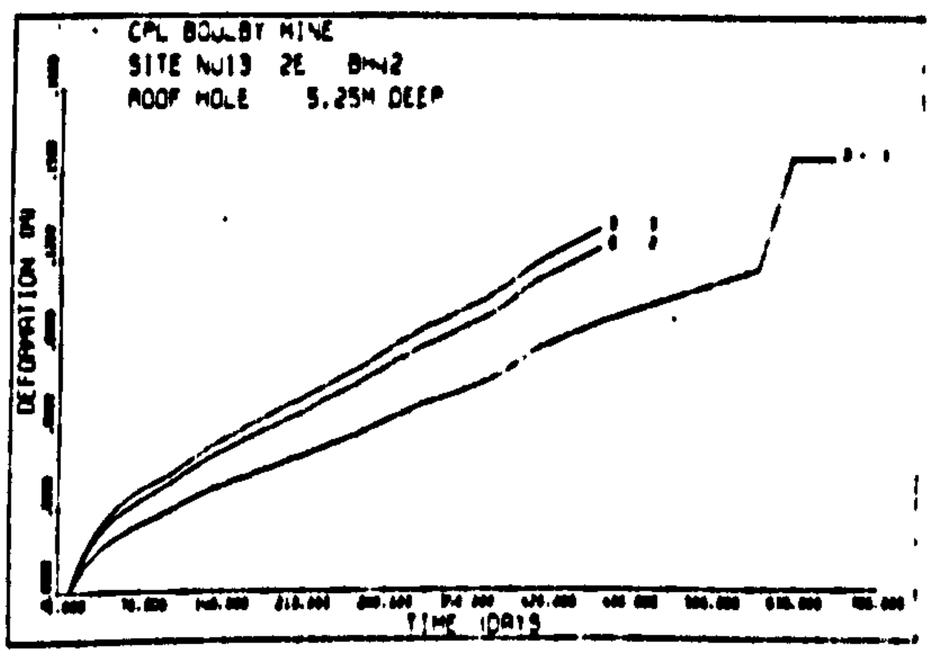
CPL BOULBY MINE
SITE NU13 2E BH42
ROOF HOLE 5.25M DEEP
DEFORMATION (M)
TIME (DAYS)

B26

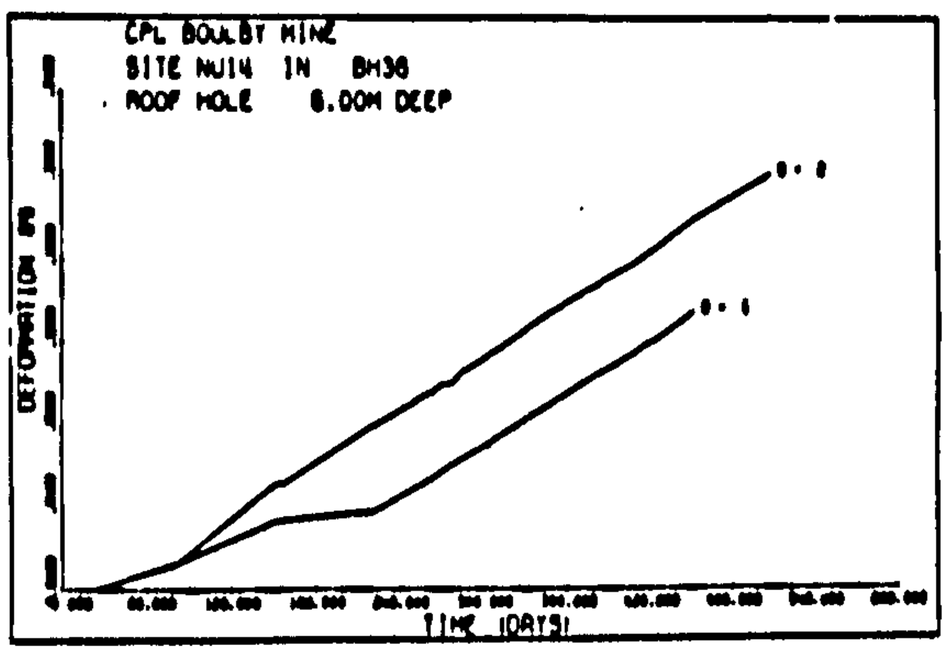
CPL BOULBY MINE
SITE NU14 IN BH36
ROOF HOLE 6.00M DEEP
DEFORMATION MM
TIME (DAYS)

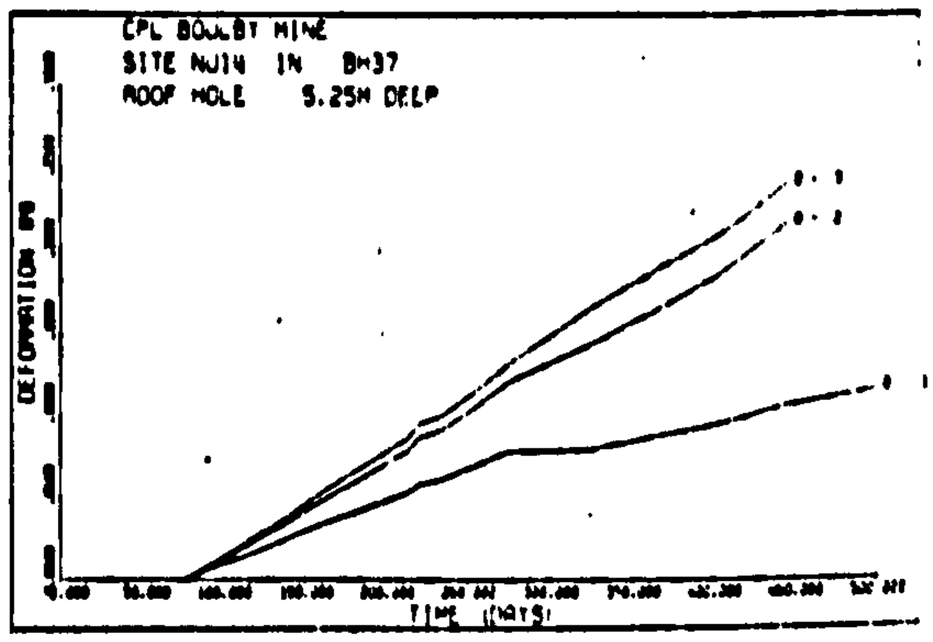
CPL BOULBY MINE
SITE NU14 IN BH37
ROOF HOLE 5.25M DEEP
DEFORMATION MM
TIME (DAYS)

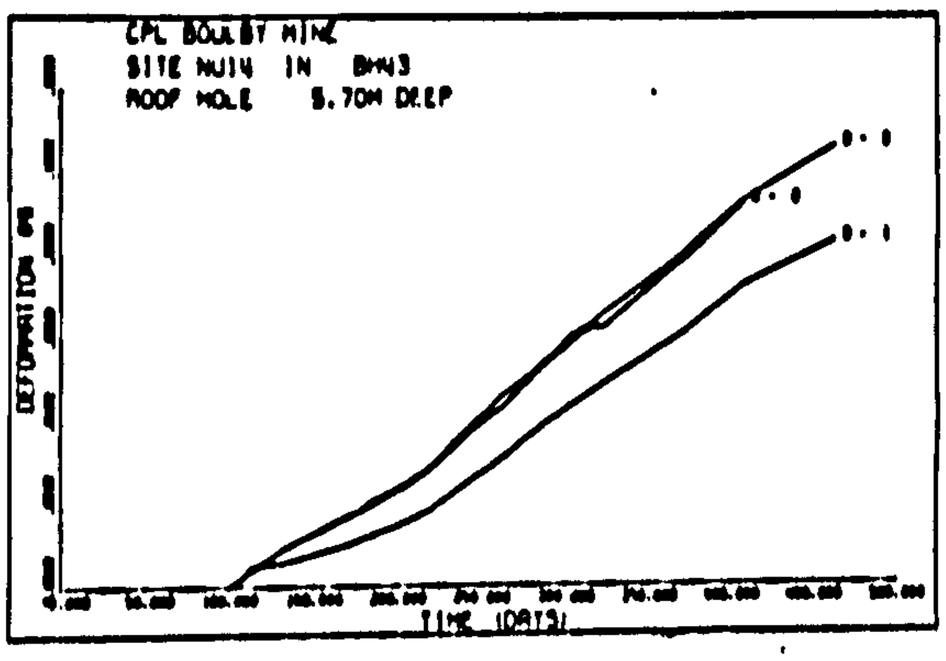
CPL BOULBY MINE
SITE NU14 IN BH43
ROOF HOLE 5.70M DEEP
DEFORMATION MM
TIME (DAYS)

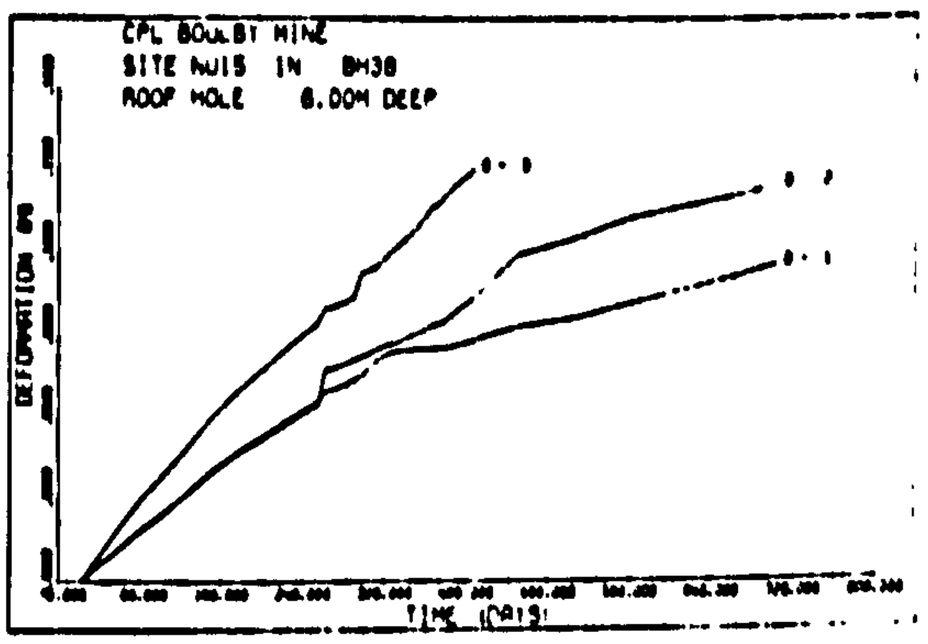
CPL BOULBY MINE
SITE NU15 IN BH38
ROOF HOLE 6.00M DEEP
DEFORMATION MM
TIME (DAYS)

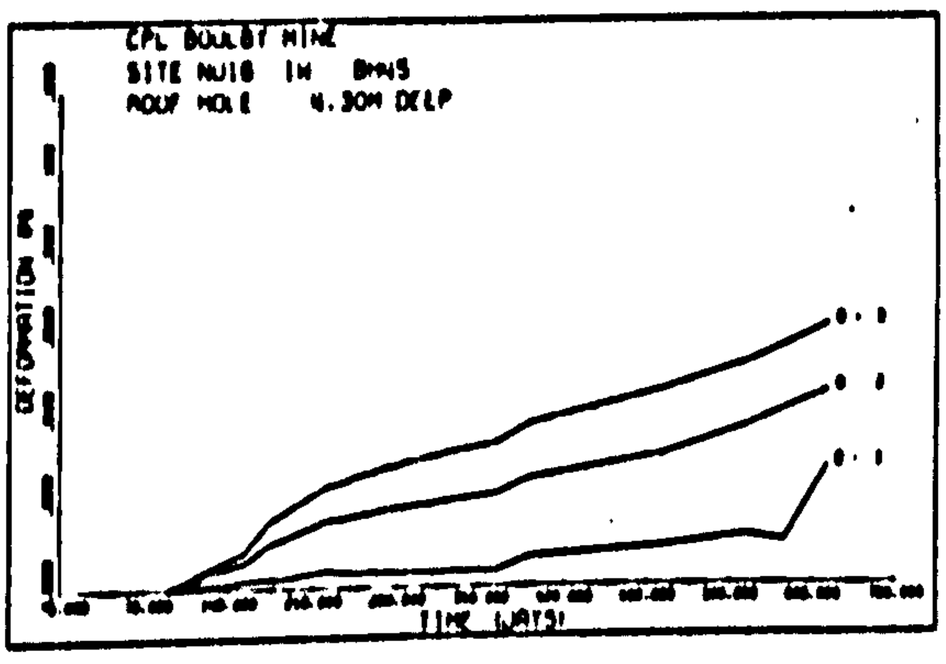
CPL BOULBY MINE
SITE NU16 IN BH45
ROOF HOLE 4.30M DEEP
DEFORMATION MM
TIME (DAYS)

B27

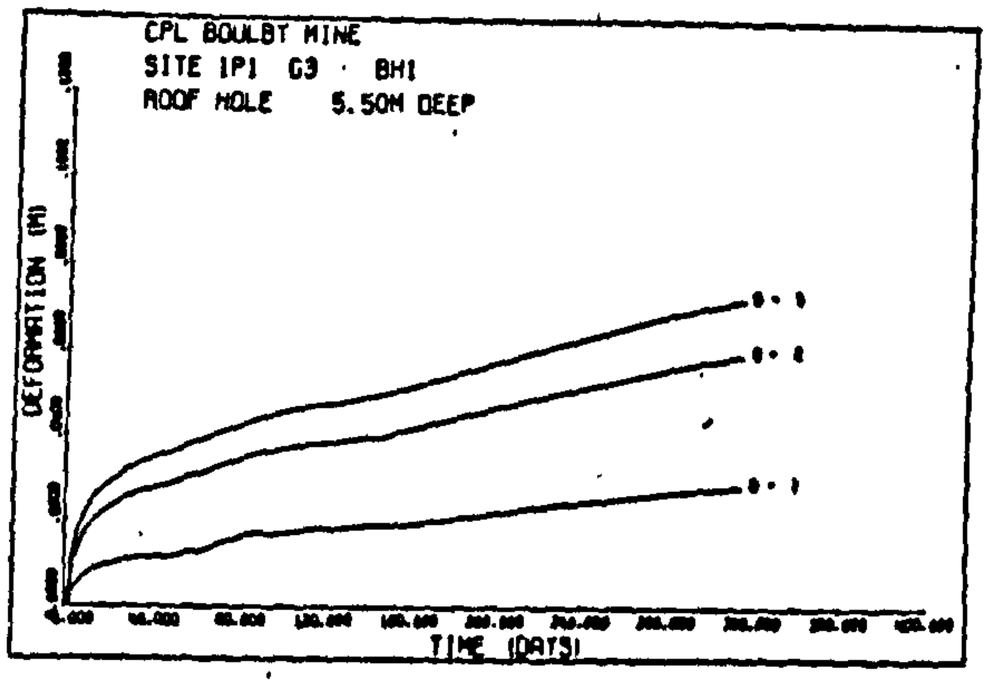
CPL BOULBY MINE
SITE IP1 G3 - BH1
ROOF HOLE 5.50M DEEP
DEFORMATION (MM)
TIME (DAYS)

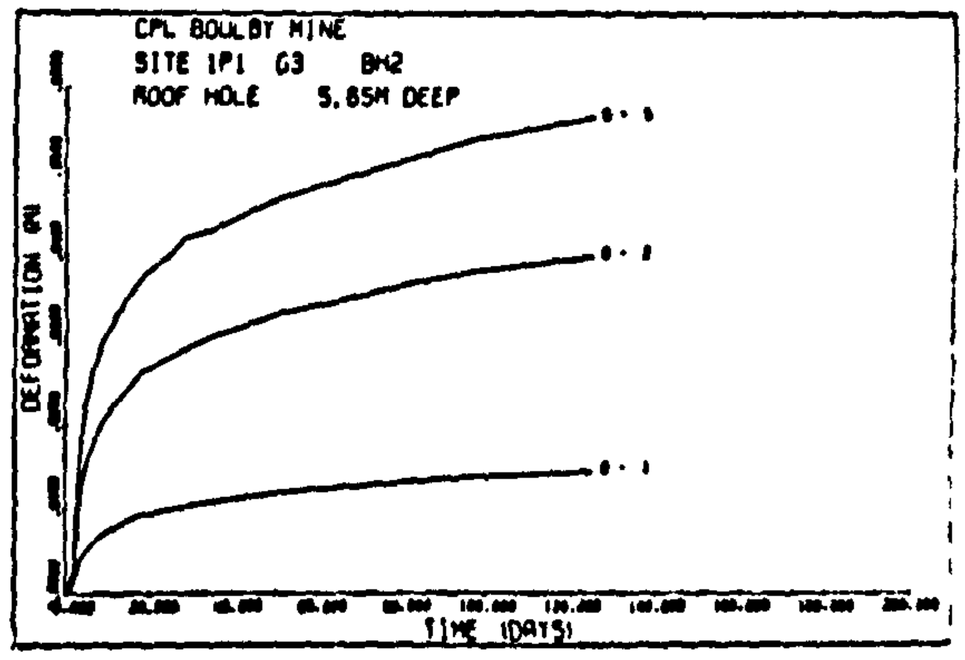
CPL BOULBY MINE
SITE IP1 G3 BH2
ROOF HOLE 5.85M DEEP
TIME (DAYS)

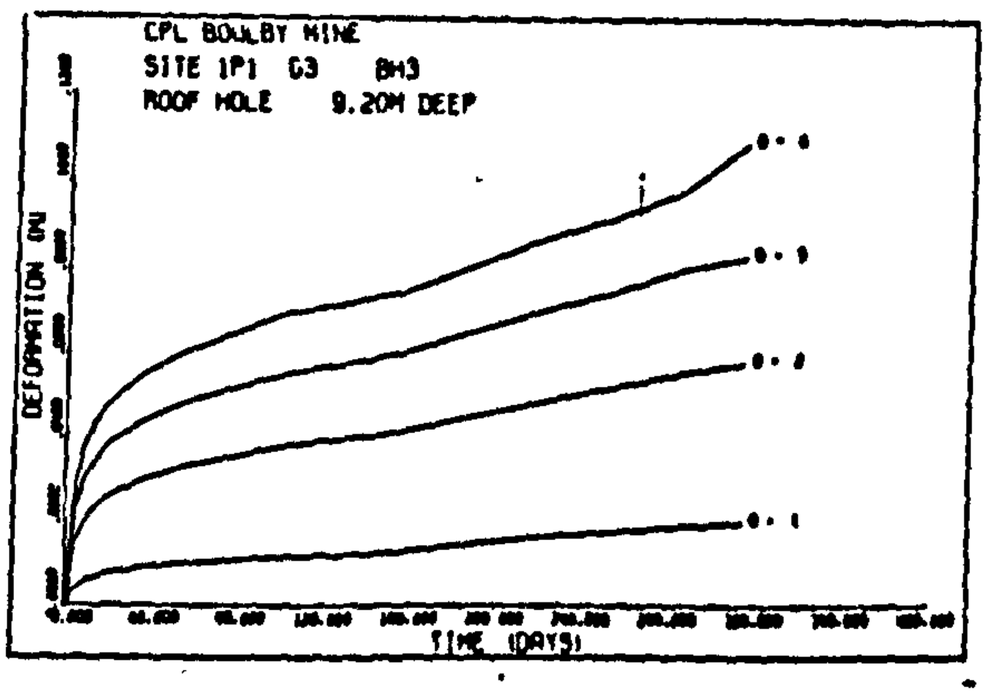
CPL BOULBY MINE
SITE IP1 G3 BH3
ROOF HOLE 9.20M DEEP
TIME (DAYS)

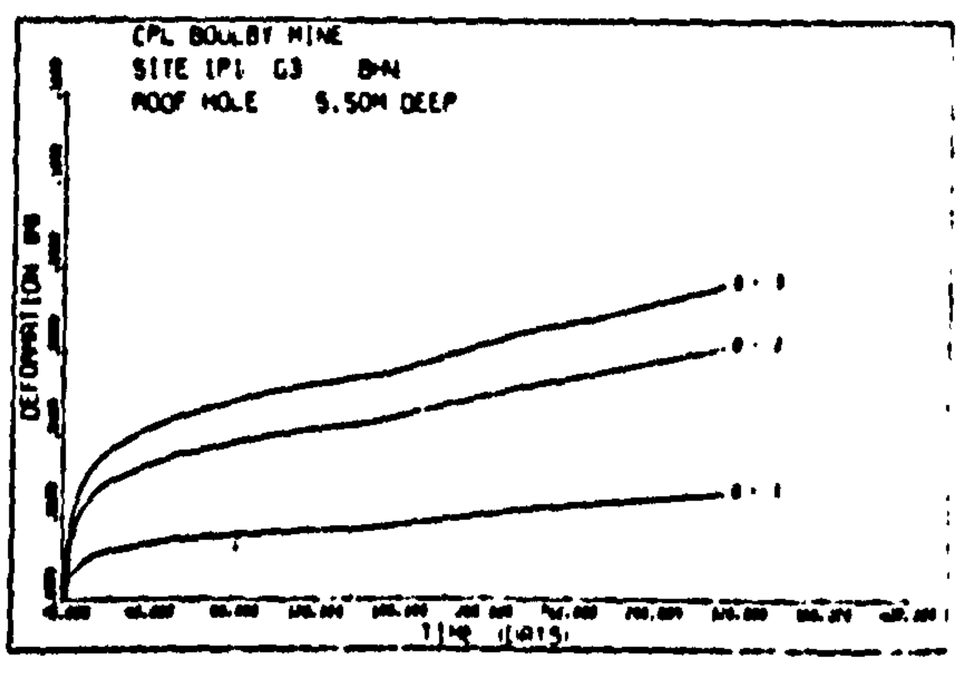
CPL BOULBY MINE
SITE IP1 G3 BH4
ROOF HOLE 5.50M DEEP
TIME (DAYS)

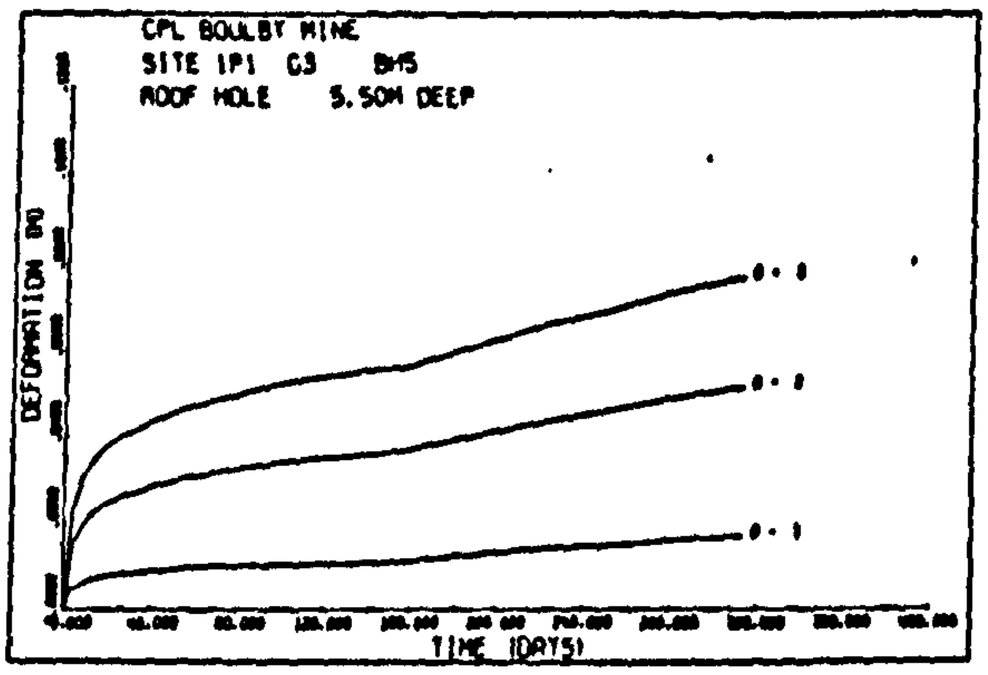
CPL BOULBY MINE
SITE IP1 G3 BH5
ROOF HOLE 5.50M DEEP
TIME (DAYS)

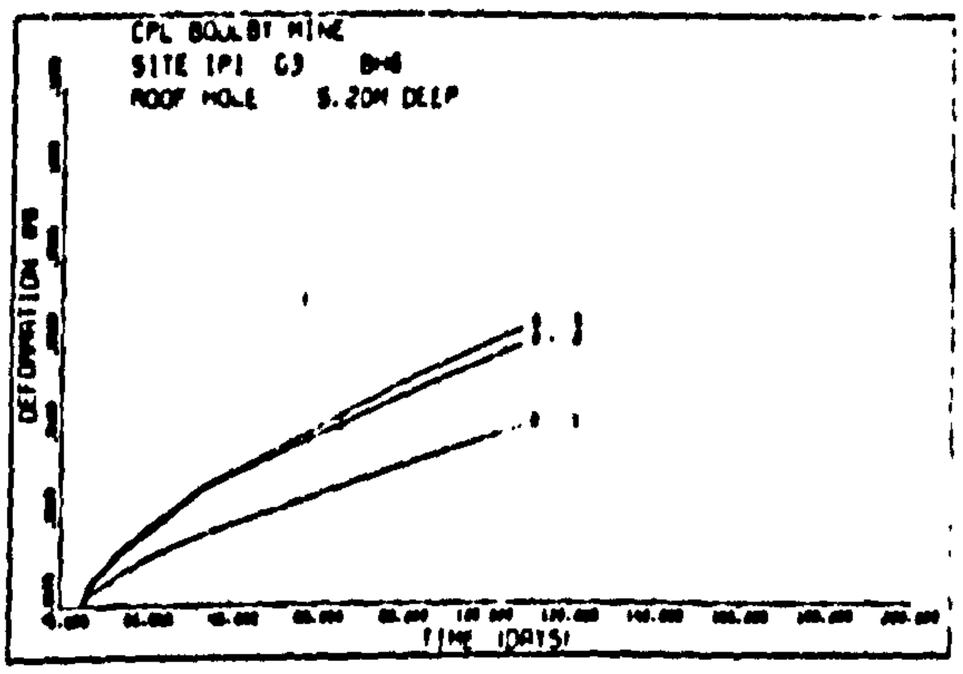
CPL BOULBY MINE
SITE IP1 G3 BH6
ROOF HOLE 5.20M DEEP
TIME (DAYS)

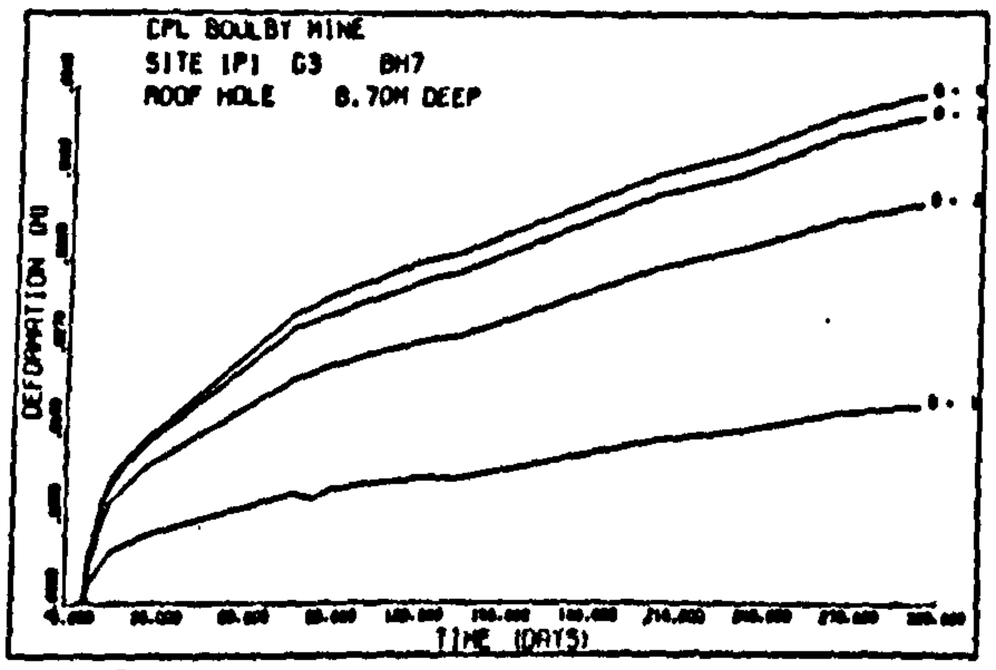
CPL BOULBY MINE
SITE IP1 G3 BH7
ROOF HOLE 8.70M DEEP
TIME (DAYS)

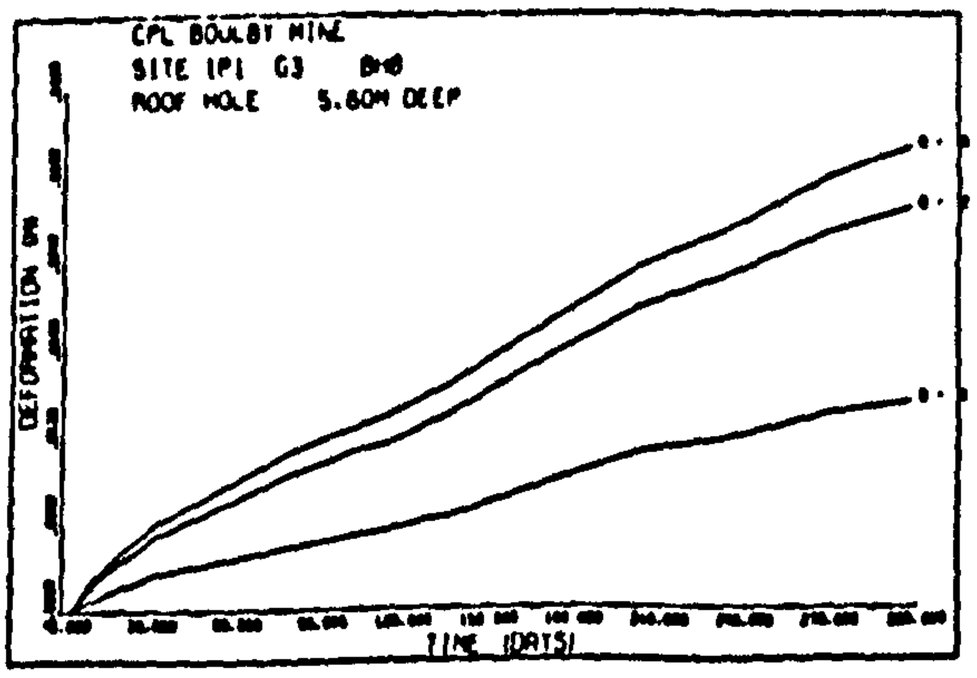
CPL BOULBY MINE
SITE IP1 G3 BH8
ROOF HOLE 5.80M DEEP
TIME (DAYS)

B 28

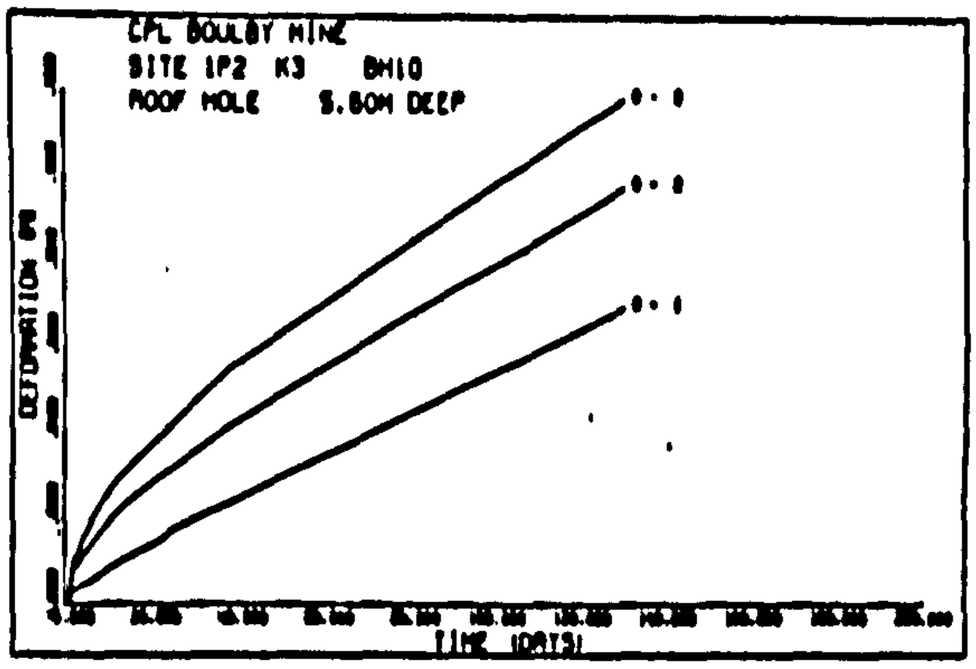
CPL BOULBY MINE
SITE IP2 K3 BH10
ROOF HOLE 5.80M DEEP
TIME (DAYS)

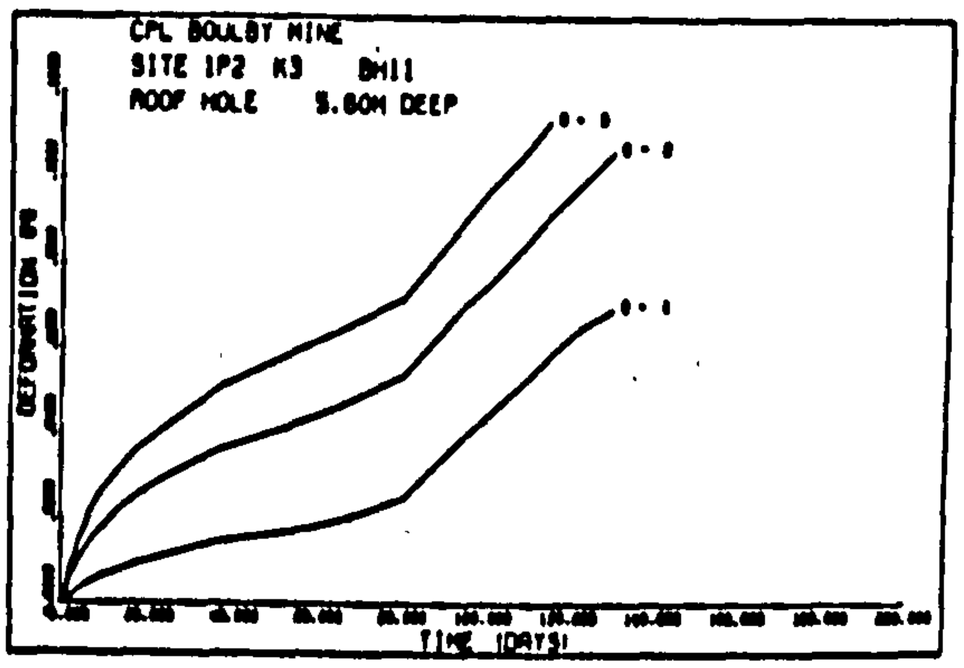
CPL BOULBY MINE
SITE IP2 K3 BH11
ROOF HOLE 5.80M DEEP
TIME (DAYS)

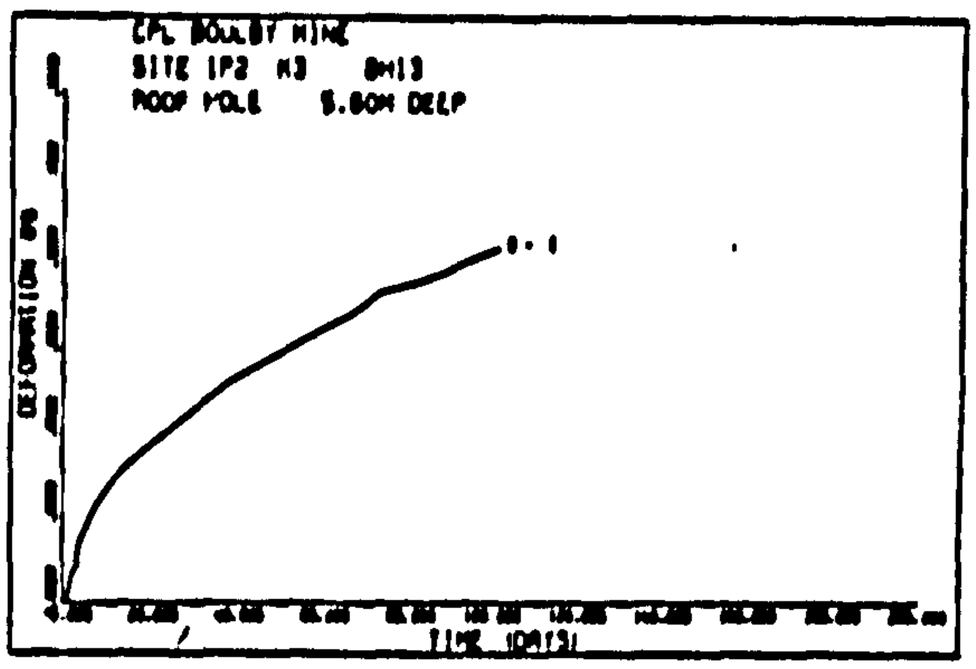
CPL BOULBY MINE
SITE IP2 K3 BH13
ROOF HOLE 5.80M DEEP
TIME (DAYS)

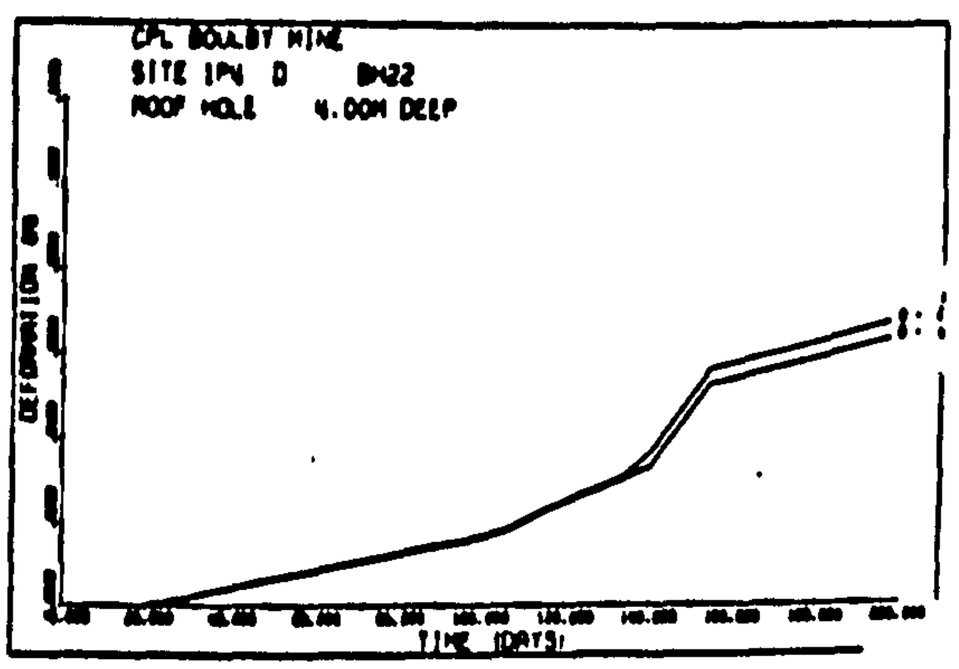
CPL BOULBY MINE
SITE IP4 D BH22
ROOF HOLE 4.00M DEEP
TIME (DAYS)

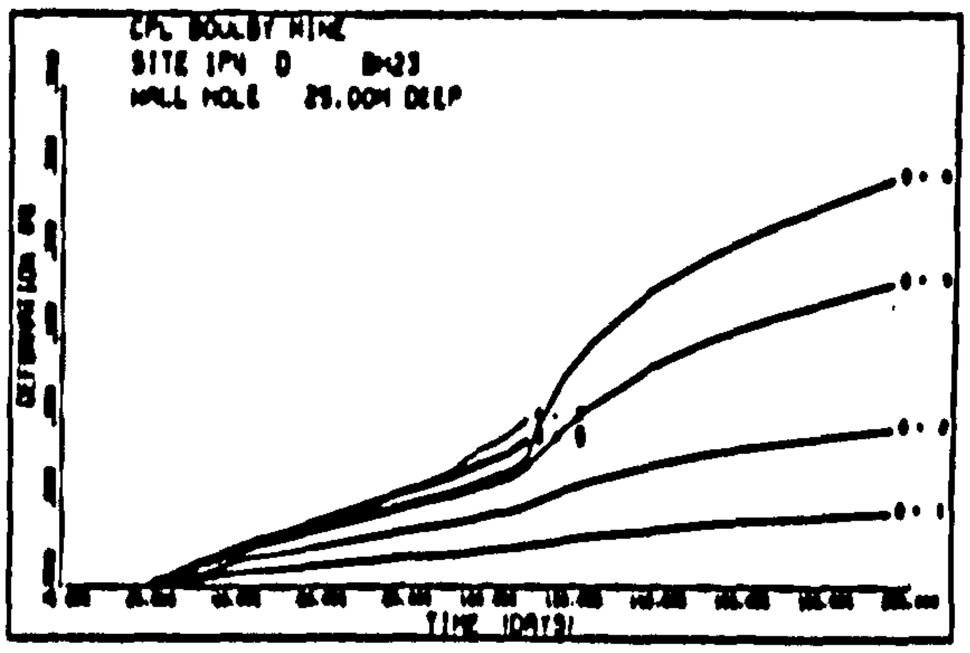
CPL BOULBY MINE
SITE IP4 D BH23
WALL HOLE 25.00M DEEP
TIME (DAYS)

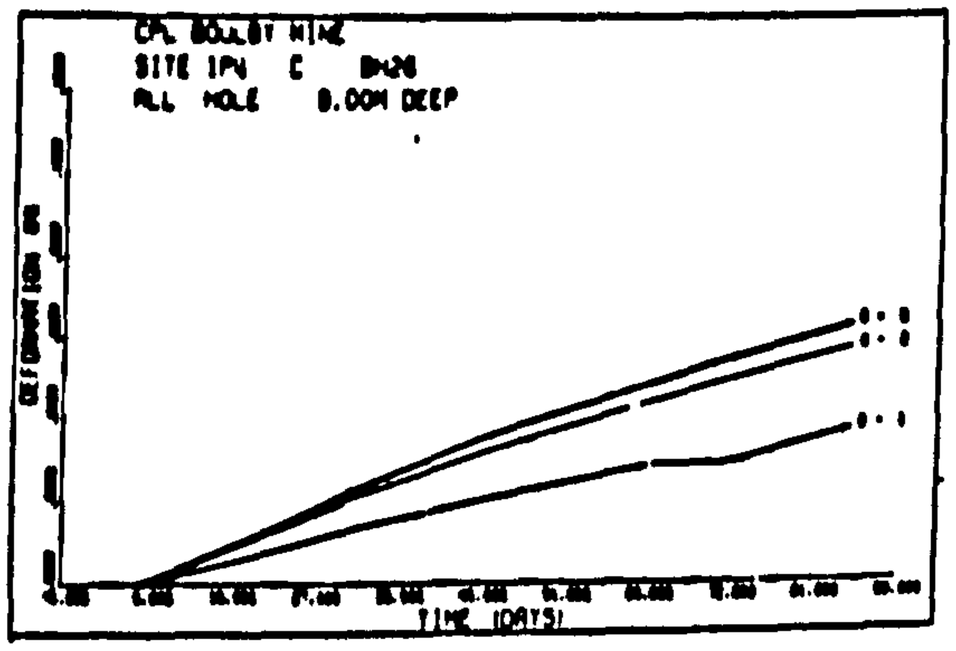
CPL BOULBY MINE
SITE IP4 C BH26
ALL HOLE 8.00M DEEP
TIME (DAYS)

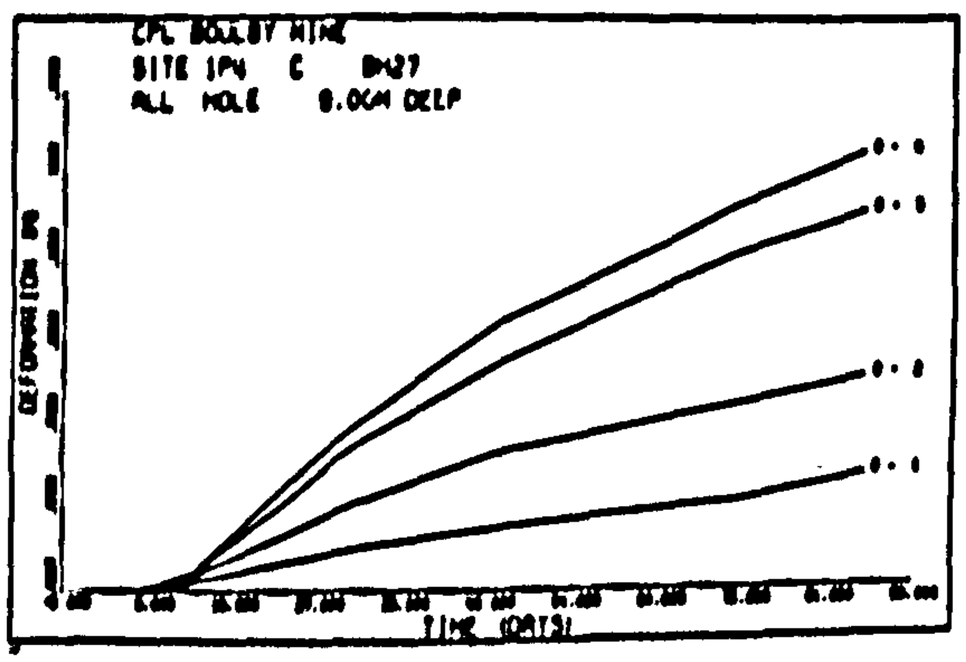
CPL BOULBY MINE
SITE IP4 C BH27
ALL HOLE 8.00M DEEP
TIME (DAYS)

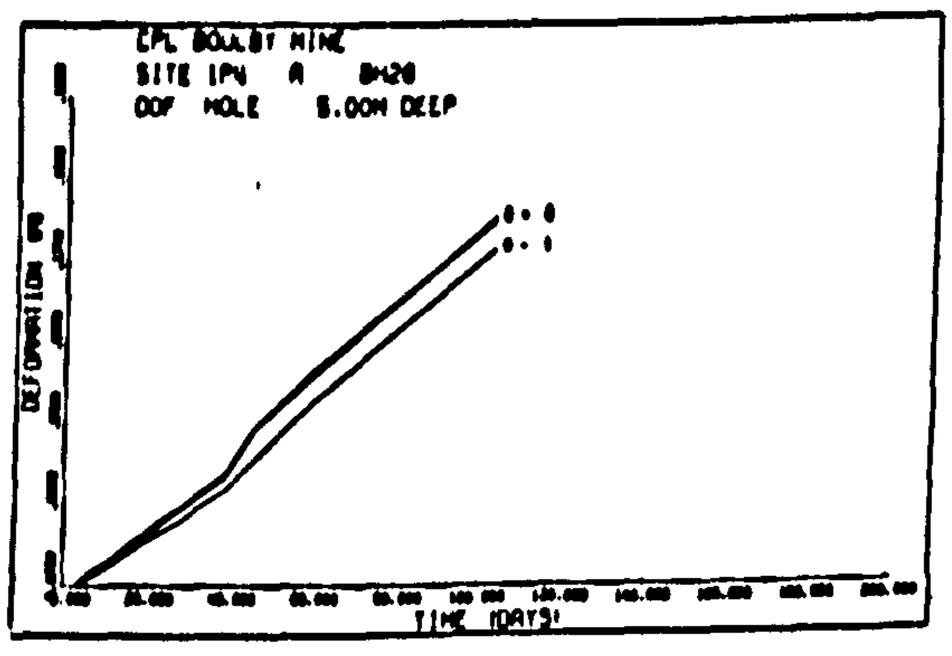
CPL BOULBY MINE
SITE IP4 A BH28
ROOF HOLE 5.00M DEEP
TIME (DAYS)

B29

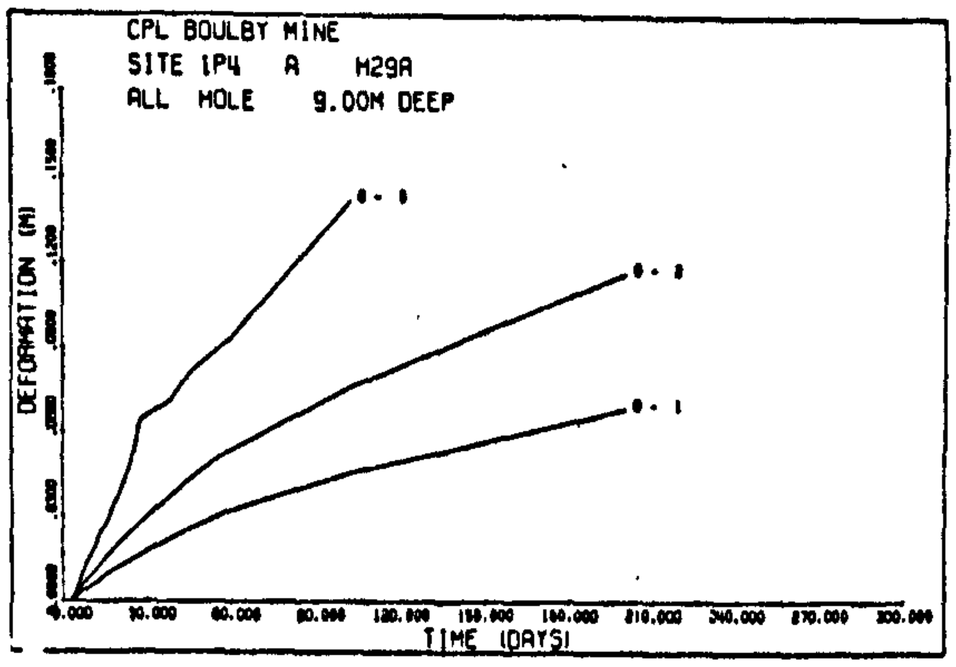
CPL BOULBY MINE
SITE 1P4 A H29A
ALL HOLE 9.00M DEEP
DEFORMATION (M)
TIME (DAYS)

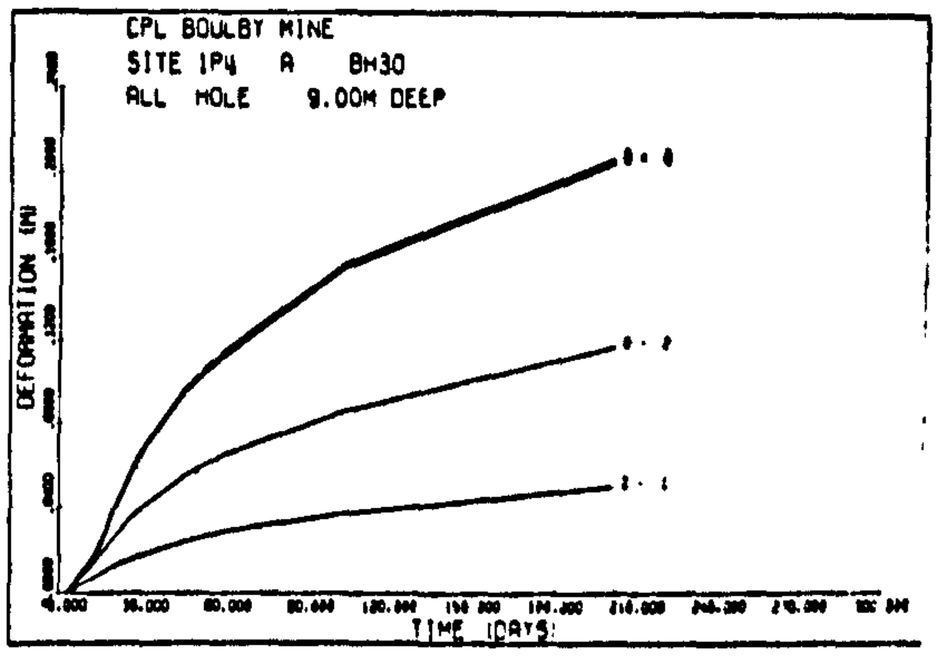
CPL BOULBY MINE
SITE 1P4 A BH30
ALL HOLE 9.00M DEEP
DEFORMATION (M)
TIME (DAYS)

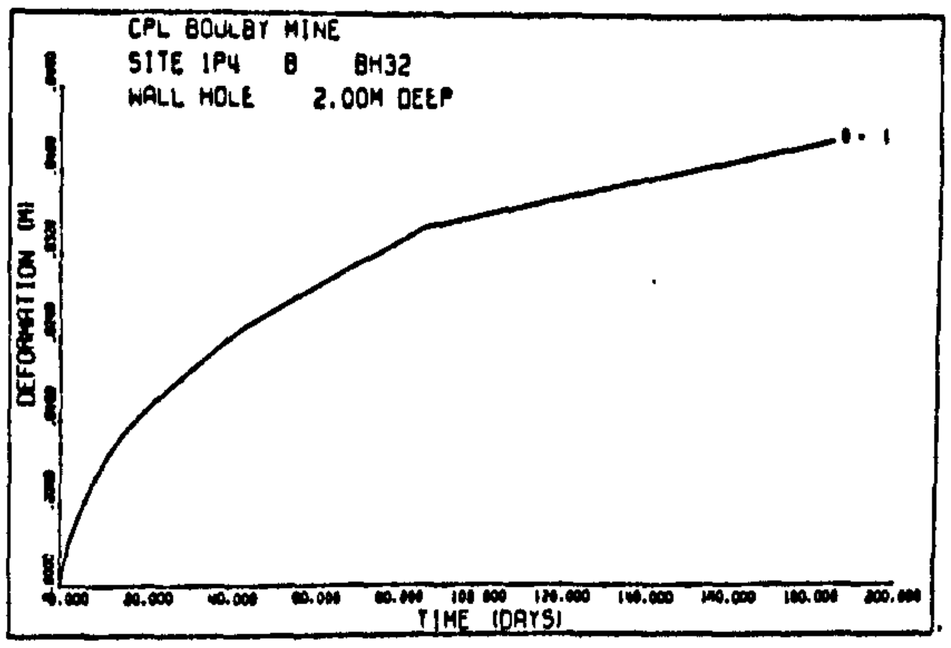
CPL BOULBY MINE
SITE 1P4 B BH32
WALL HOLE 2.00M DEEP
DEFORMATION (M)
TIME (DAYS)

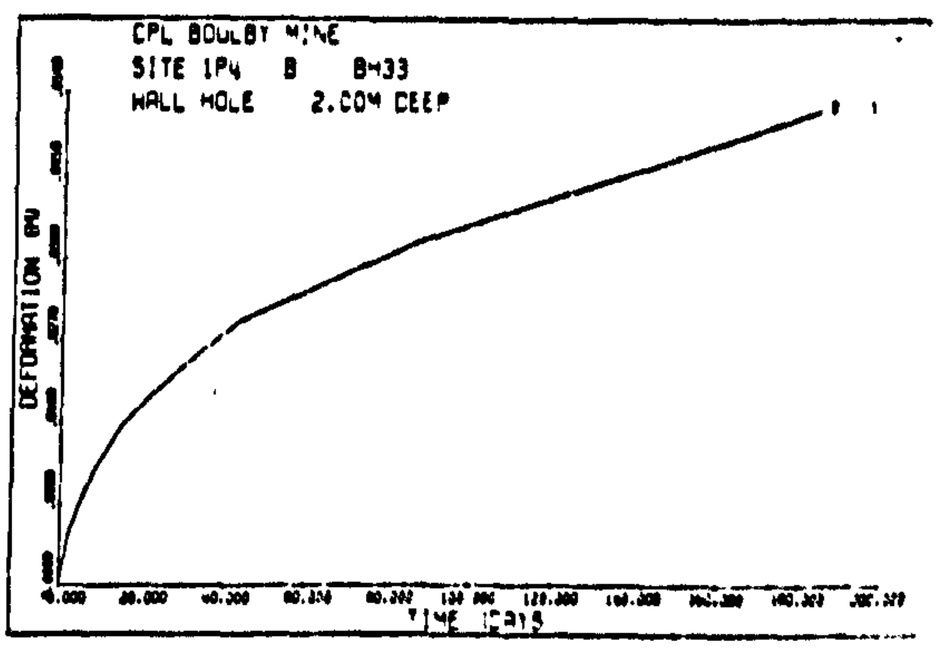
CPL BOULBY MINE
SITE 1P4 B BH33
WALL HOLE 2.00M DEEP
DEFORMATION (M)

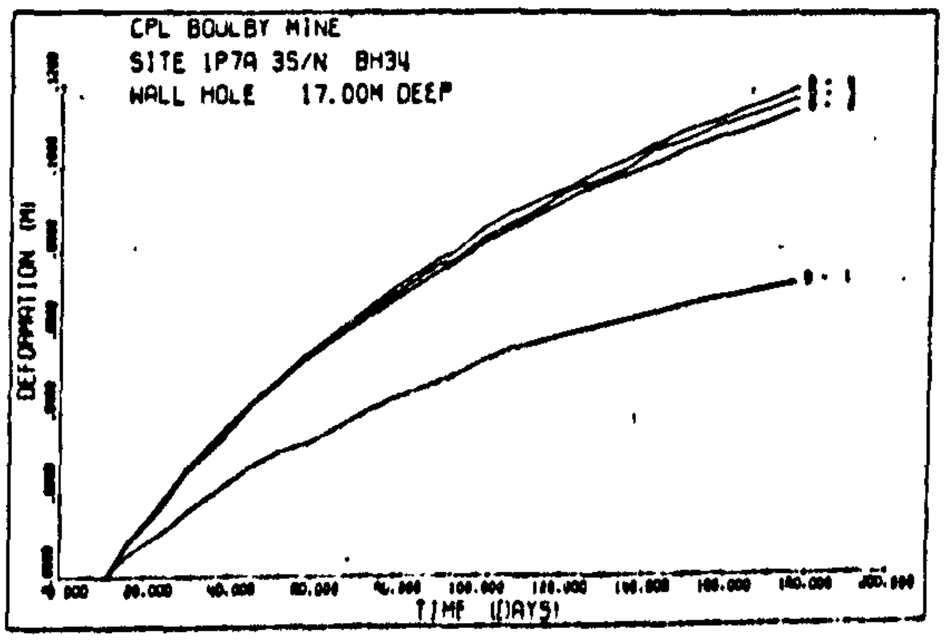
CPL BOULBY MINE
SITE 1P7A 35/N BH34
WALL HOLE 17.00M DEEP
DEFORMATION (M)
TIME (DAYS)

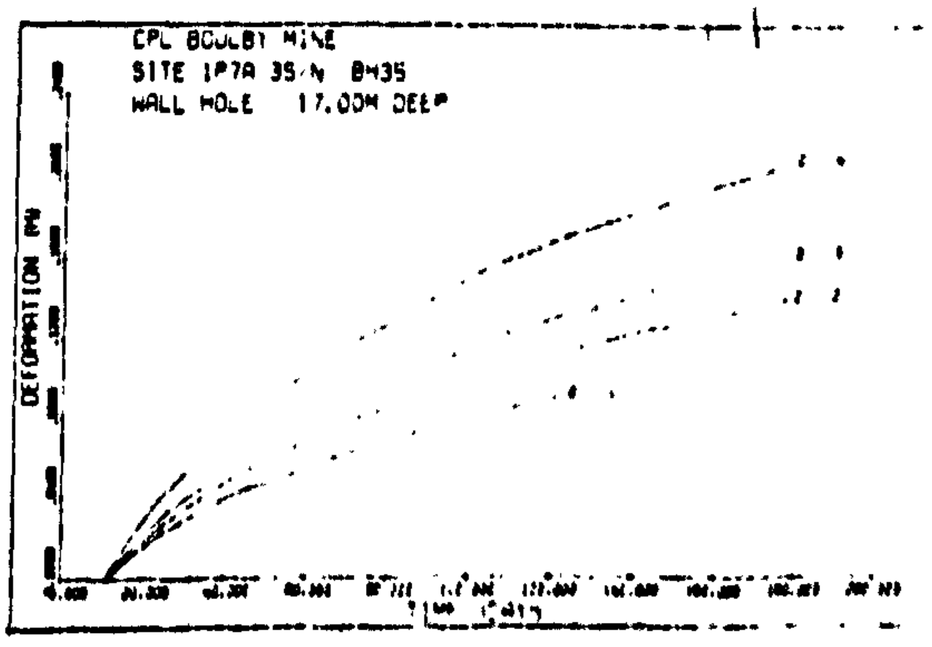
CPL BOULBY MINE
SITE 1P7A 35/N BH35
WALL HOLE 17.00M DEEP
DEFORMATION (M)

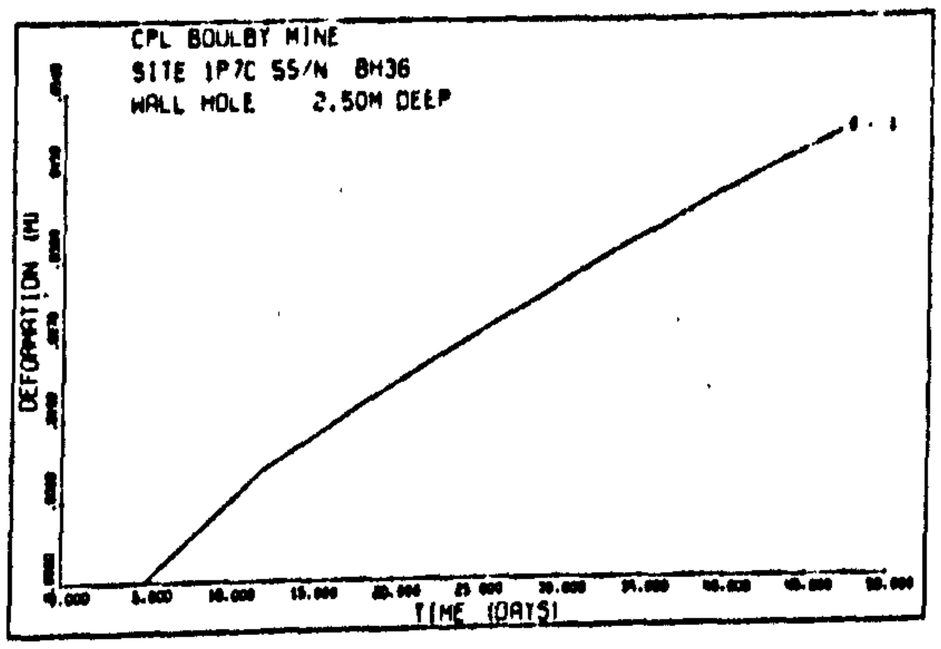
CPL BOULBY MINE
SITE 1P7C 55/N BH36
WALL HOLE 2.50M DEEP
DEFORMATION (M)
TIME (DAYS)

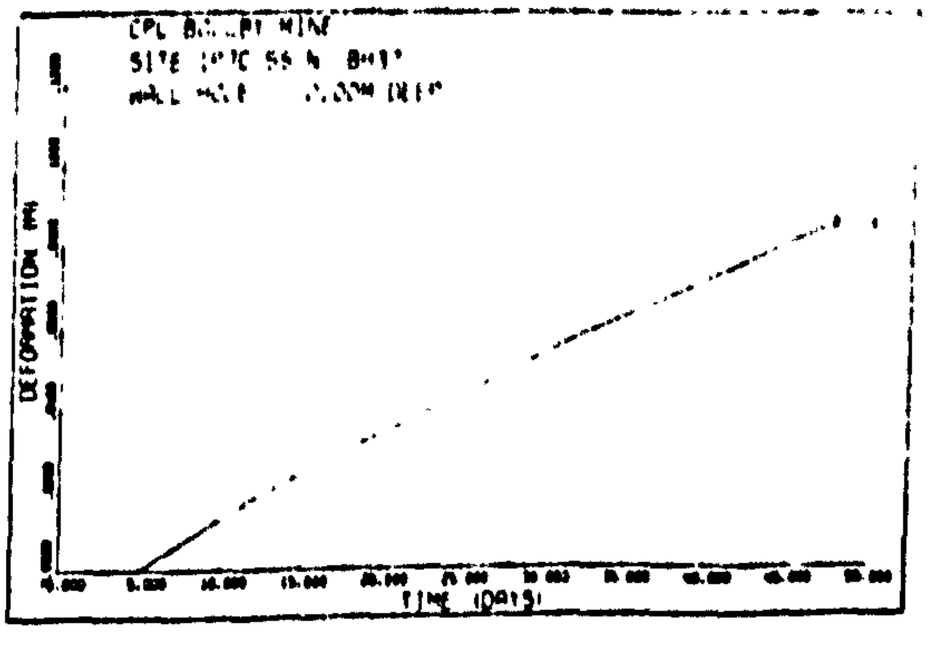
DEFORMATION (M)
TIME (DAYS)

B30

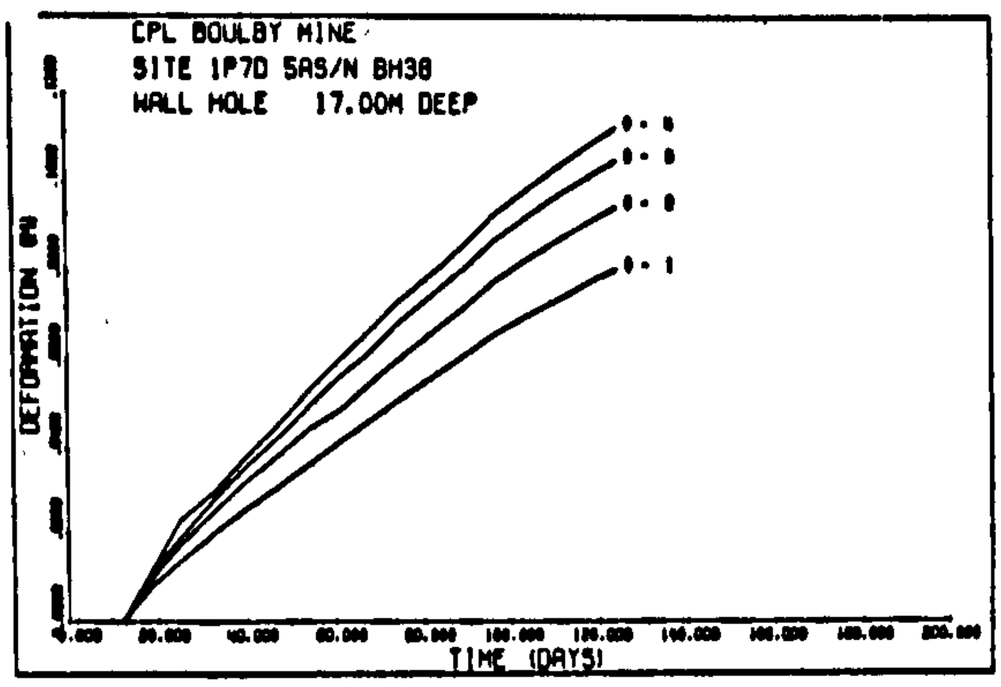
CPL BOULBY MINE
SITE 1P7D SAS/N BH38
WALL HOLE 17.00M DEEP
DEFORMATION MM
TIME (DAYS)

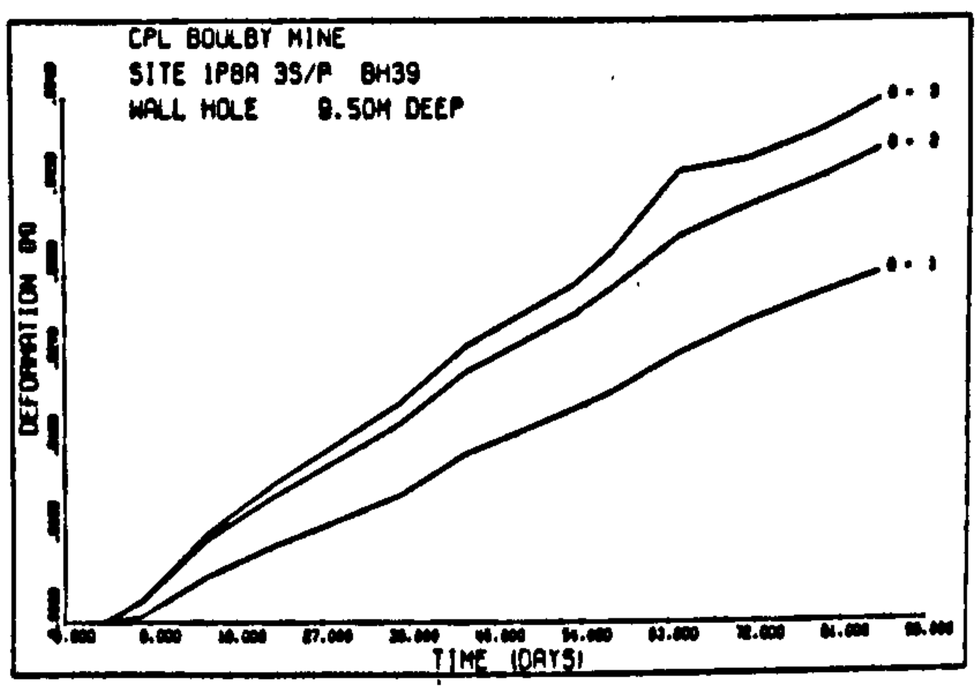
CPL BOULBY MINE
SITE 1P8A 3S/P BH39
WALL HOLE 8.50M DEEP
DEFORMATION MM
TIME (DAYS)

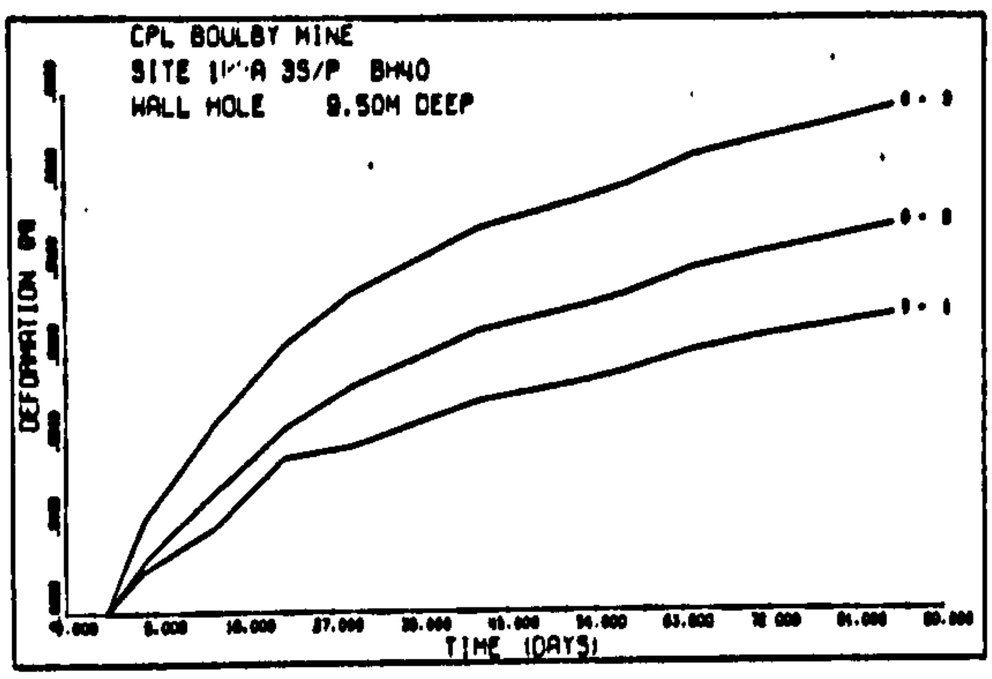
CPL BOULBY MINE
SITE 1P8A 3S/P BH40
WALL HOLE 8.50M DEEP
DEFORMATION MM
TIME (DAYS)

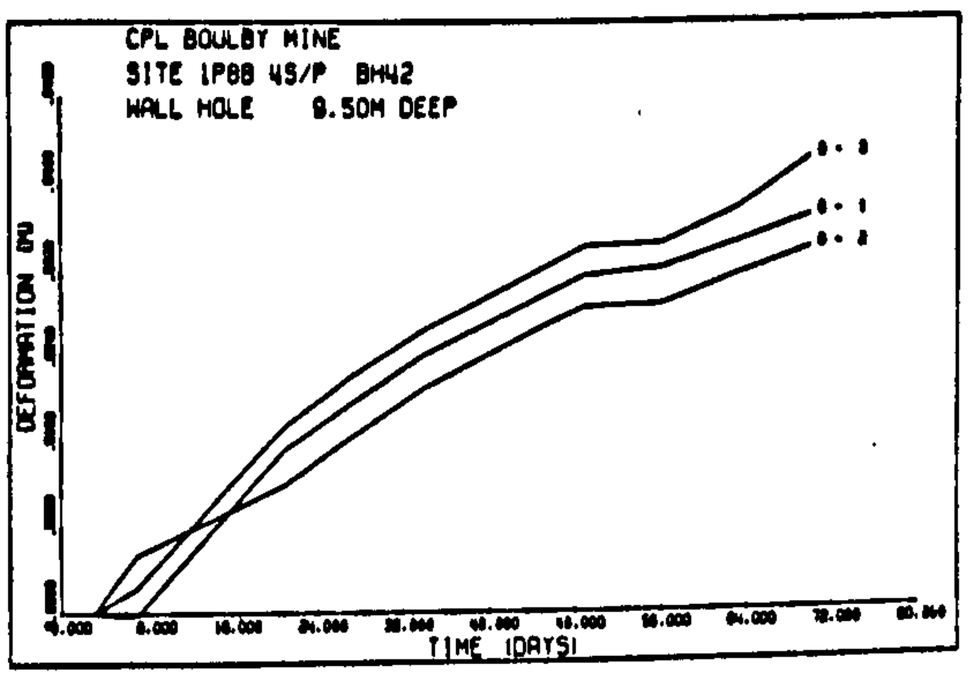
CPL BOULBY MINE
SITE 1P8B 4S/P BH42
WALL HOLE 8.50M DEEP
DEFORMATION MM
TIME (DAYS)

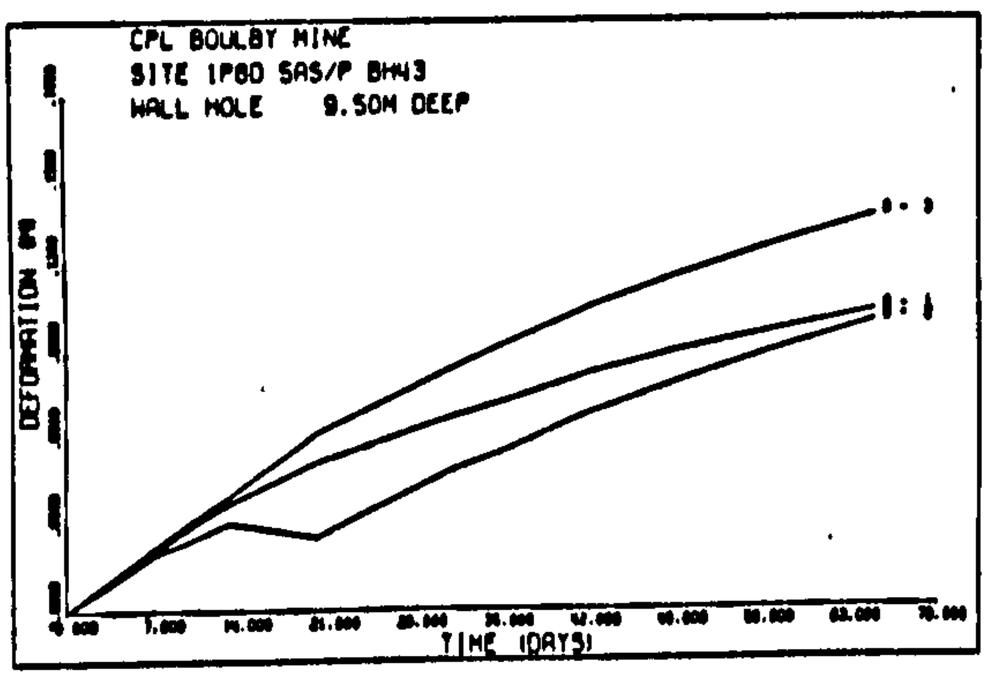
CPL BOULBY MINE
SITE 1P8D 5AS/P BH43
WALL HOLE 8.50M DEEP
DEFORMATION MM
TIME (DAYS)

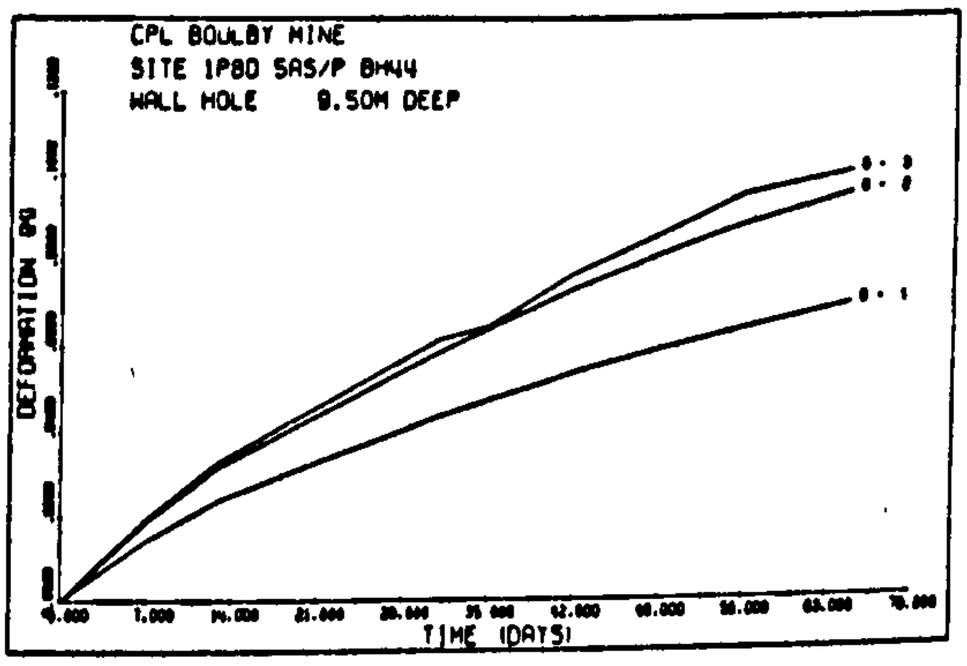
CPL BOULBY MINE
SITE 1P8D 5AS/P BH44
WALL HOLE 8.50M DEEP
DEFORMATION MM
TIME (DAYS)

B31

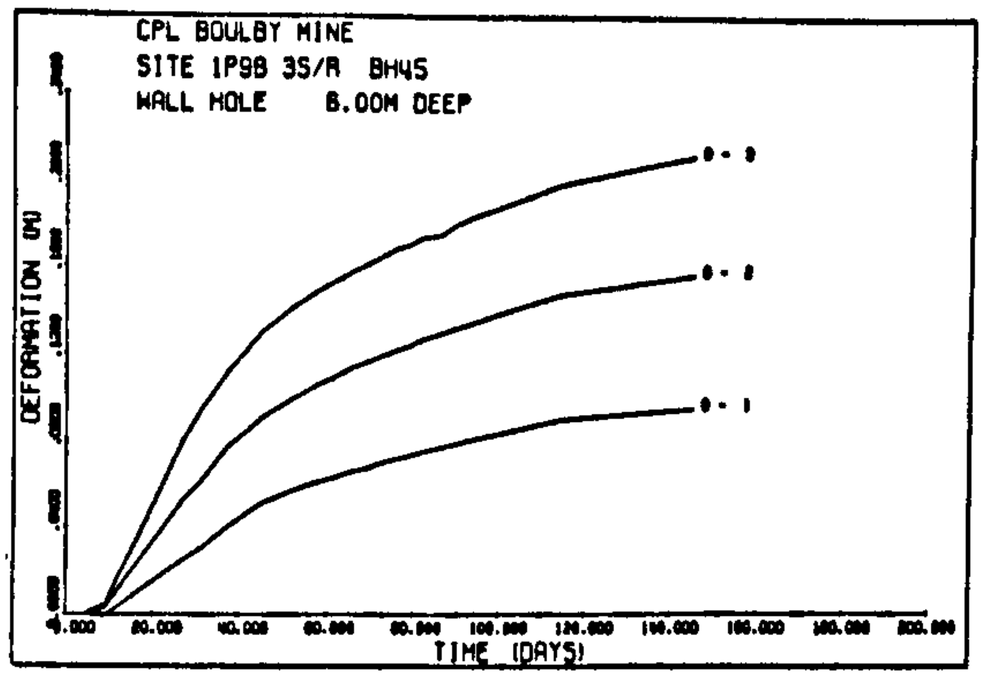
CPL BOULBY MINE
SITE 1P9B 3S/R BH45
WALL HOLE 6.00M DEEP
DEFORMATION (M)
TIME (DAYS)

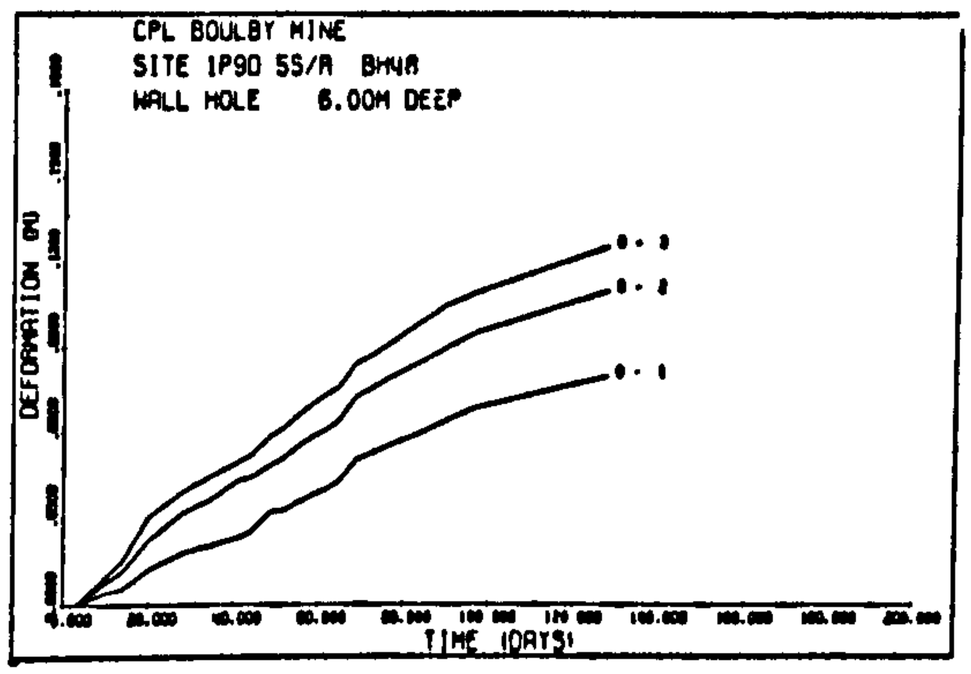
CPL BOULBY MINE
SITE 1P9D 5S/R BH4R
WALL HOLE 6.00M DEEP
DEFORMATION (M)
TIME (DAYS)

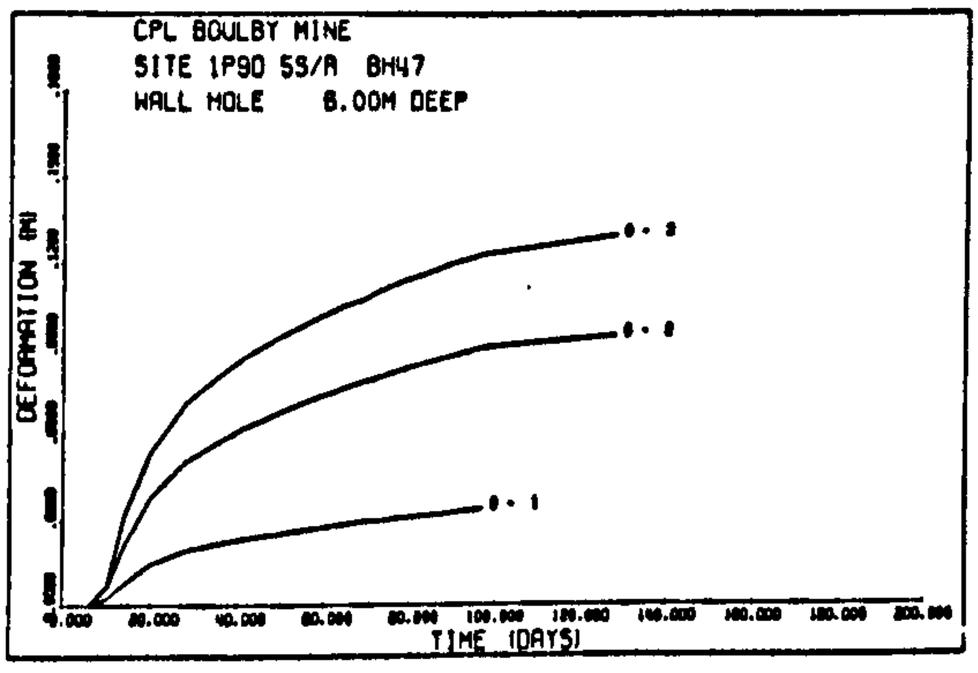
CPL BOULBY MINE
SITE 1P9D 5S/R BH47
WALL HOLE 6.00M DEEP
DEFORMATION (M)
TIME (DAYS)

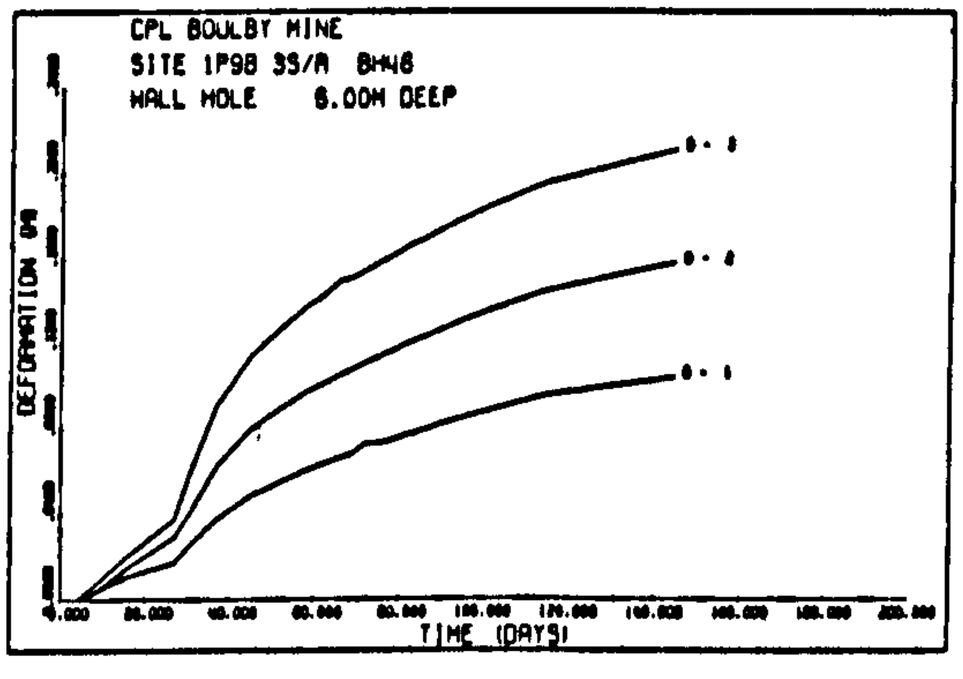
CPL BOULBY MINE
SITE 1P9B 3S/R BH46
WALL HOLE 6.00M DEEP
DEFORMATION (M)
TIME (DAYS)

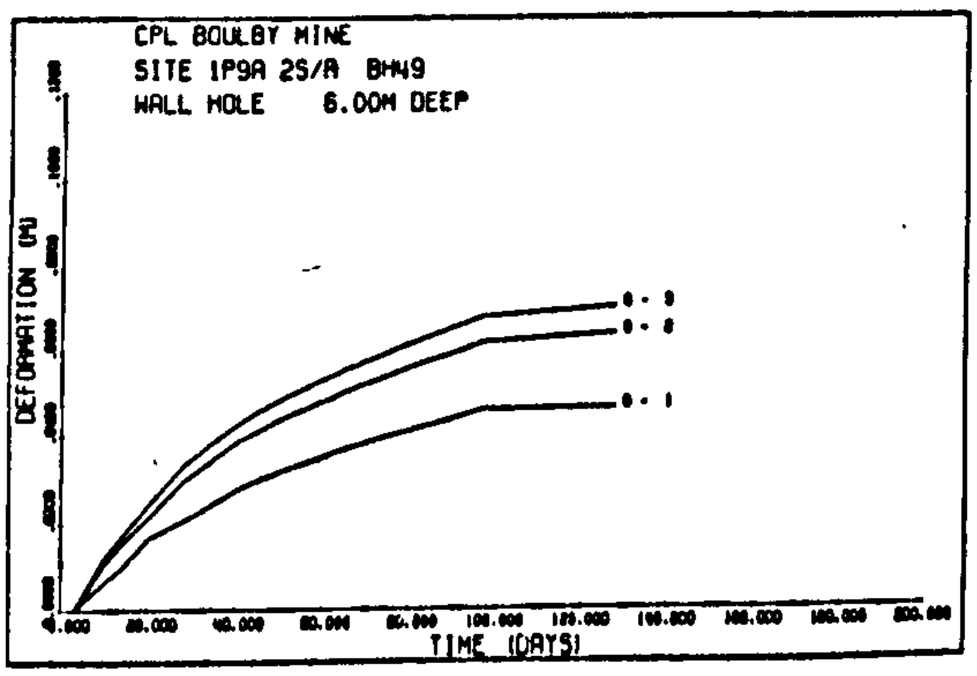
CPL BOULBY MINE
SITE 1P9A 2S/R BH49
WALL HOLE 6.00M DEEP
DEFORMATION (M)
TIME (DAYS)

B32

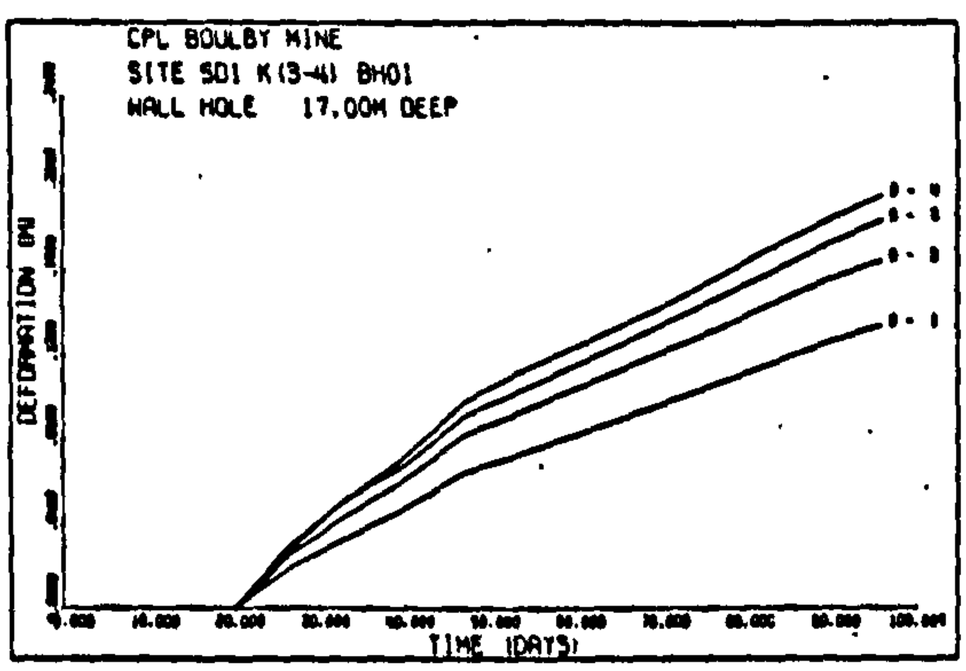
CPL BOULBY MINE
SITE SD1 K(3-4) BH01
WALL HOLE 17.00M DEEP
DEFORMATION (M)
TIME (DAYS)

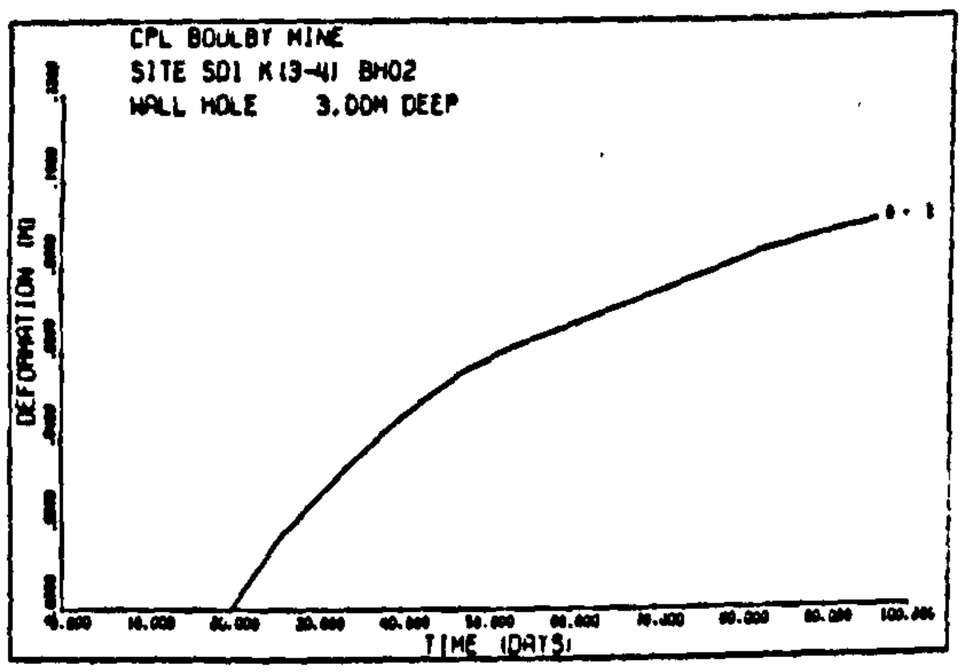
CPL BOULBY MINE
SITE SD1 K(3-4) BH02
WALL HOLE 3.00M DEEP
DEFORMATION (M)
TIME (DAYS)

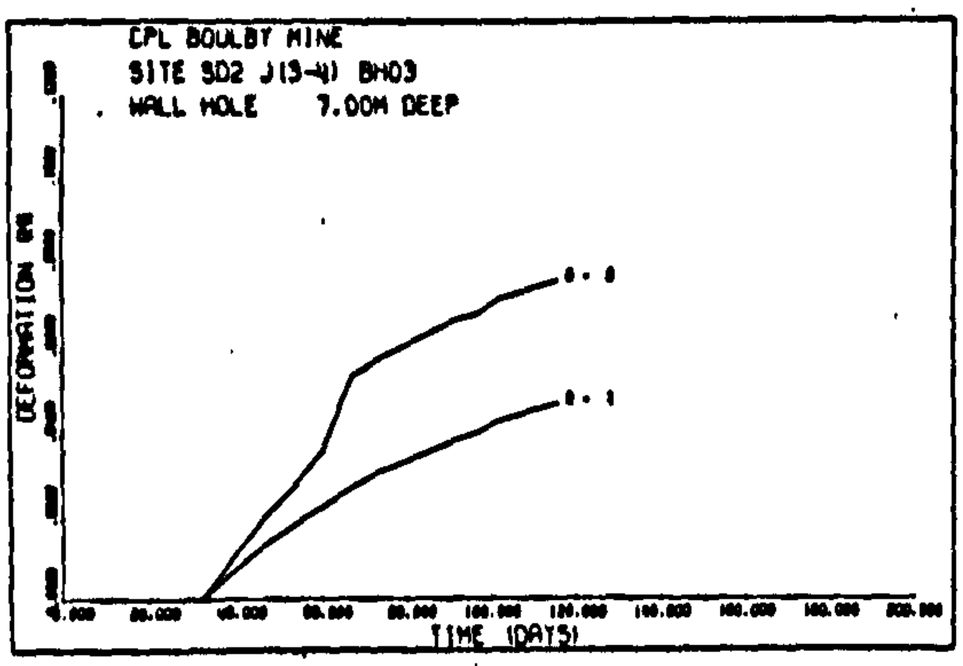
CPL BOULBY MINE
SITE SD2 J(3-4) BH03
WALL HOLE 7.00M DEEP
TIME (DAYS)

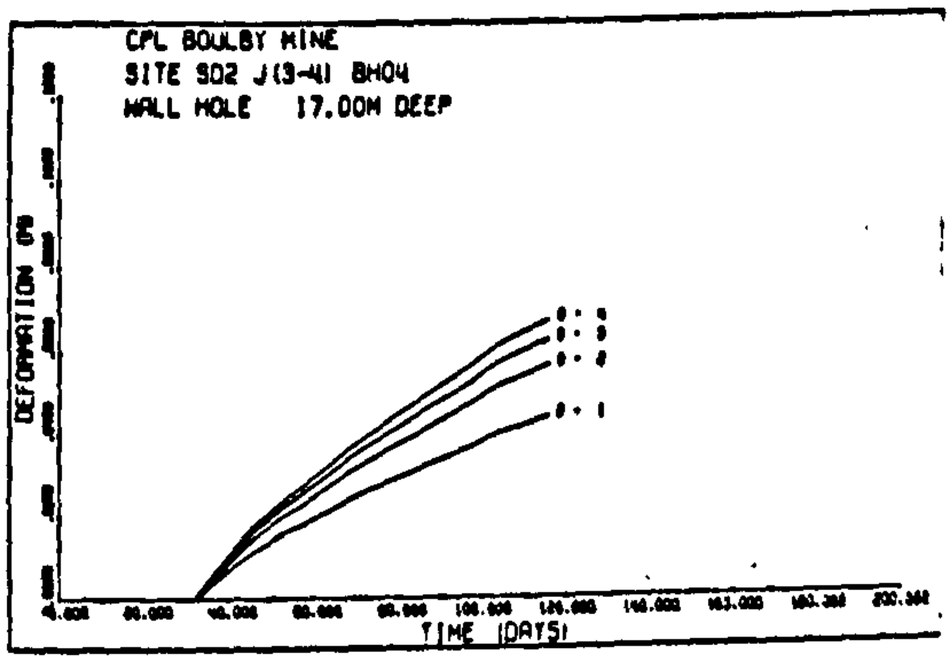
CPL BOULBY MINE
SITE SD2 J(3-4) BH04
WALL HOLE 17.00M DEEP
TIME (DAYS)

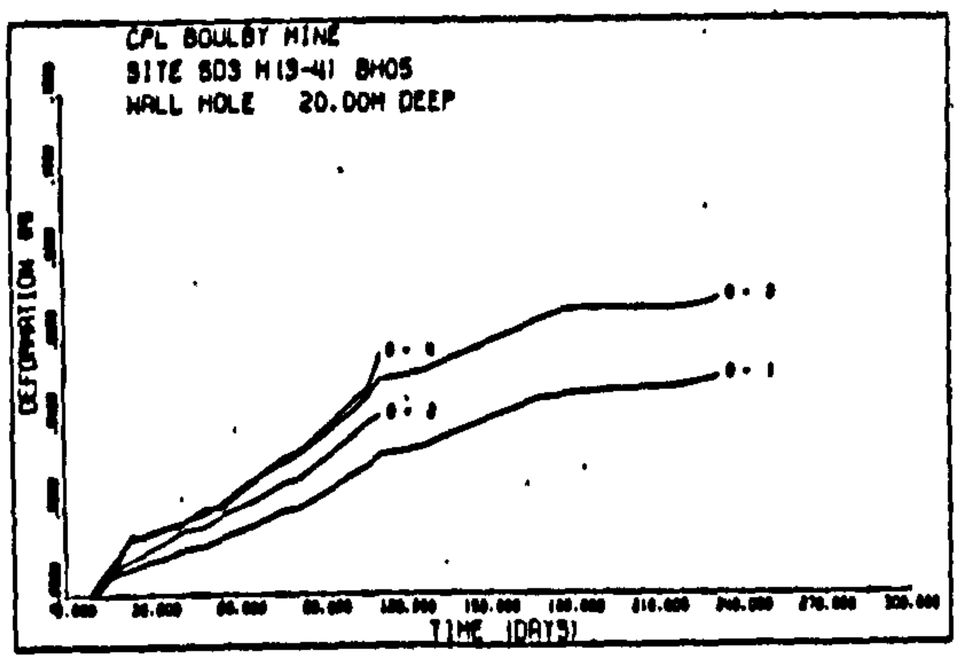
CPL BOULBY MINE
SITE SD3 H(3-4) BH05
WALL HOLE 20.00M DEEP
TIME (DAYS)

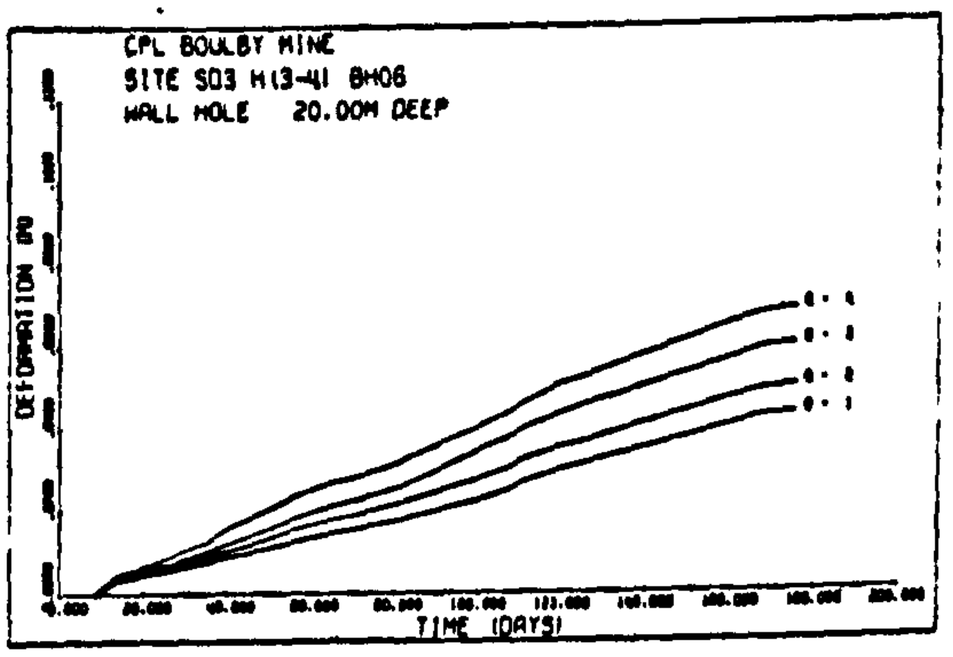
CPL BOULBY MINE
SITE SD3 H(3-4) BH06
WALL HOLE 20.00M DEEP
TIME (DAYS)

B33

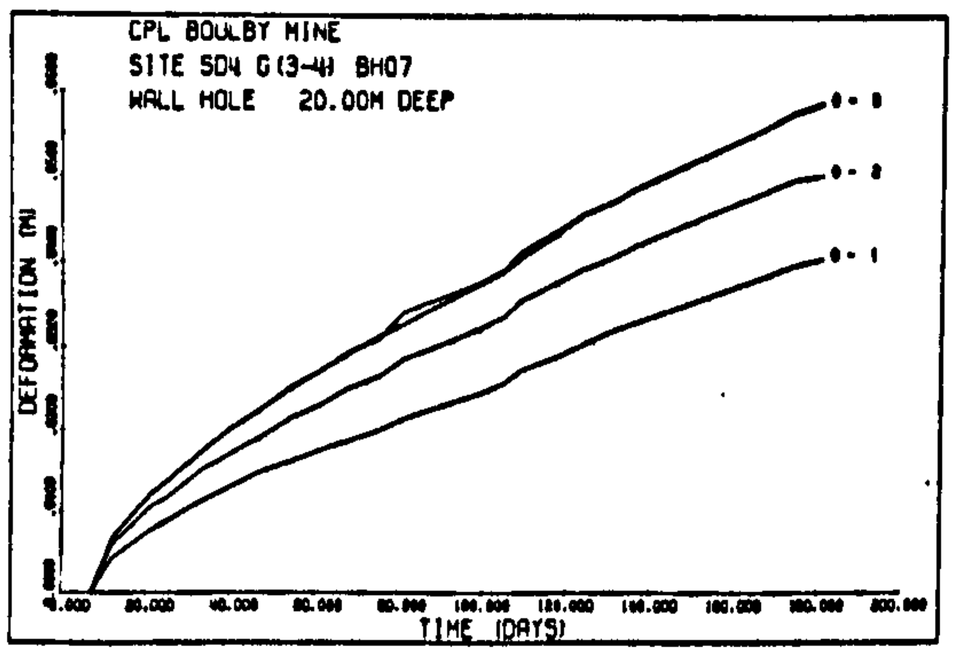
CPL BOULBY MINE
SITE SD4 G(3-4) BH07
WALL HOLE 20.00M DEEP
DEFORMATION (M)
TIME (DAYS)

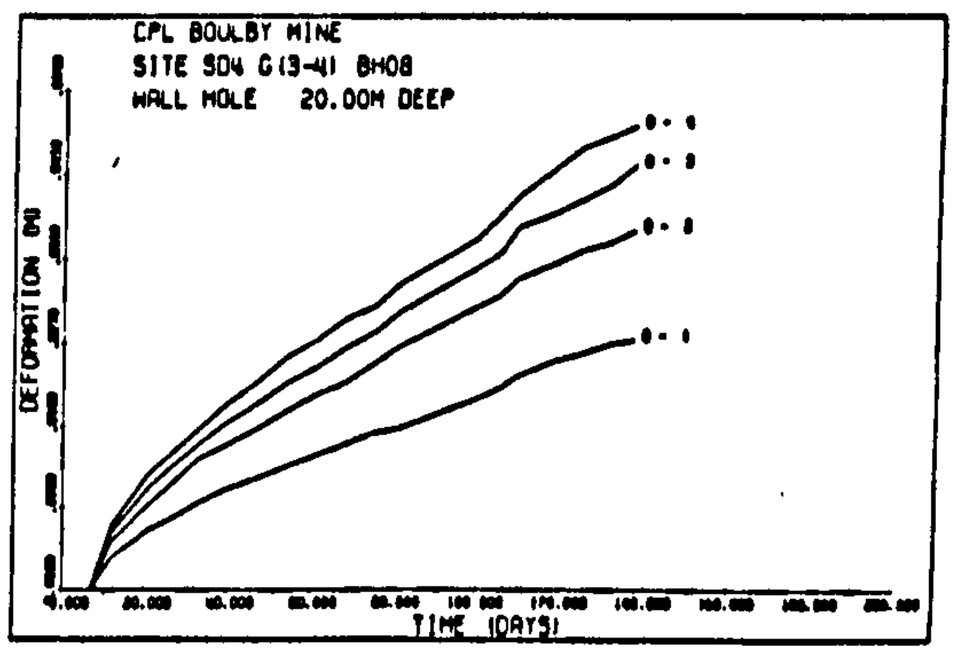
CPL BOULBY MINE
SITE SD4 G(3-4) BH08
WALL HOLE 20.00M DEEP
DEFORMATION (M)
TIME (DAYS)

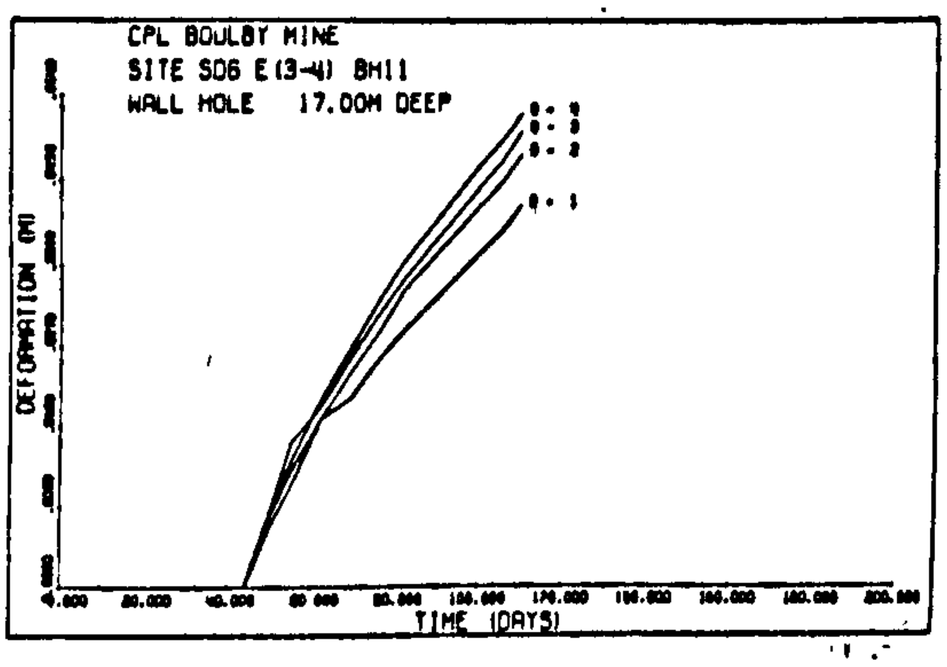
CPL BOULBY MINE
SITE SD6 E(3-4) BH11
WALL HOLE 17.00M DEEP
DEFORMATION (M)
TIME (DAYS)

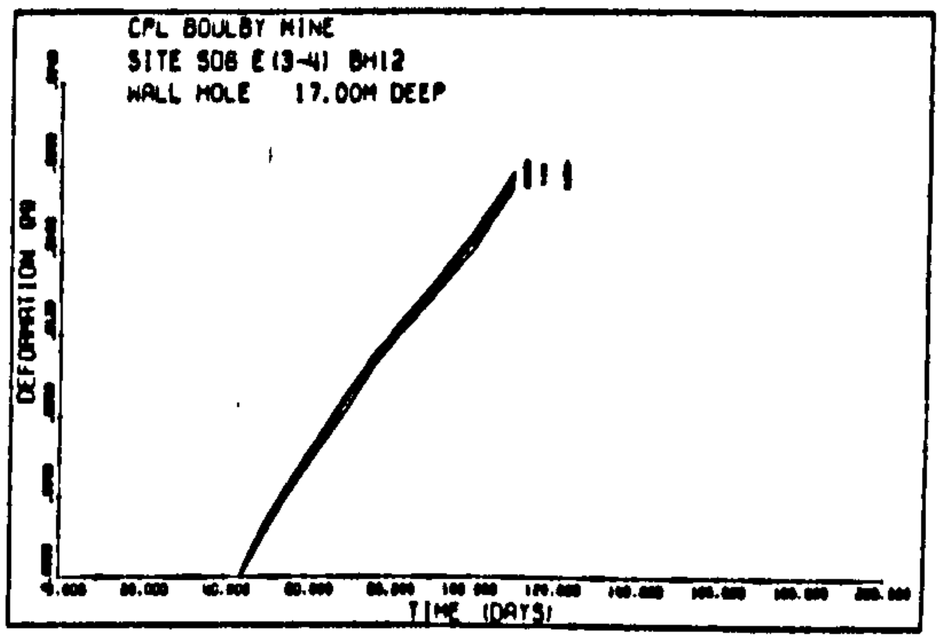
CPL BOULBY MINE
SITE SD6 E(3-4) BH12
WALL HOLE 17.00M DEEP
DEFORMATION (M)
TIME (DAYS)

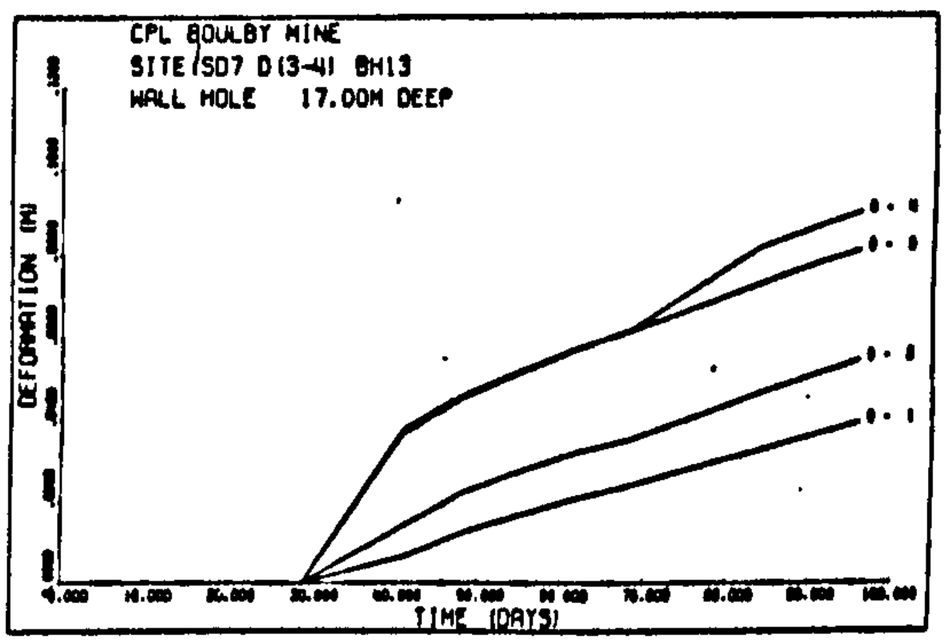
CPL BOULBY MINE
SITE SD7 D(3-4) BH13
WALL HOLE 17.00M DEEP
DEFORMATION (M)
TIME (DAYS)

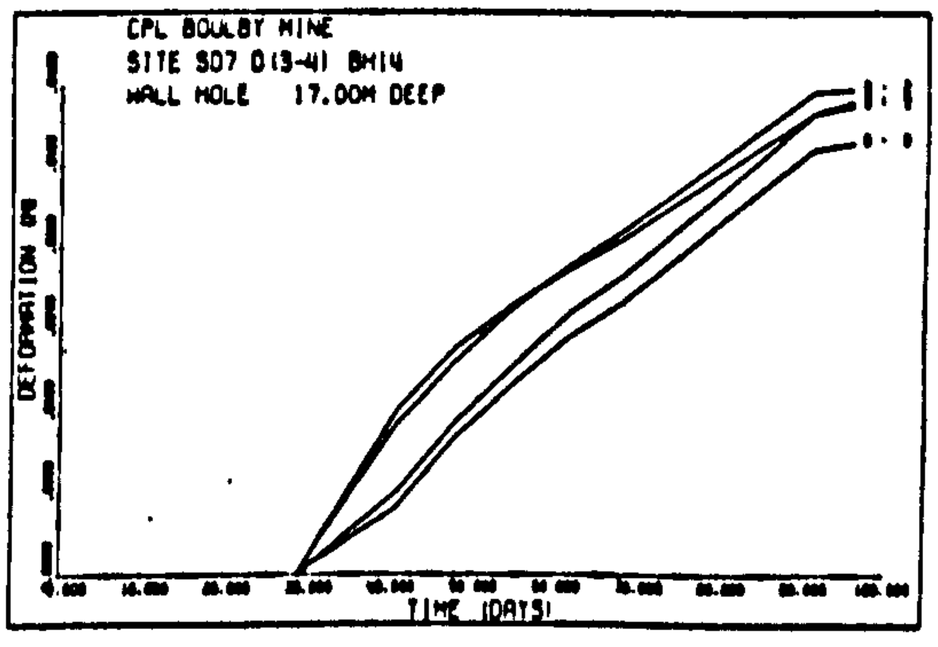
CPL BOULBY MINE
SITE SD7 D(3-4) BH14
WALL HOLE 17.00M DEEP
DEFORMATION (M)
TIME (DAYS)

B34

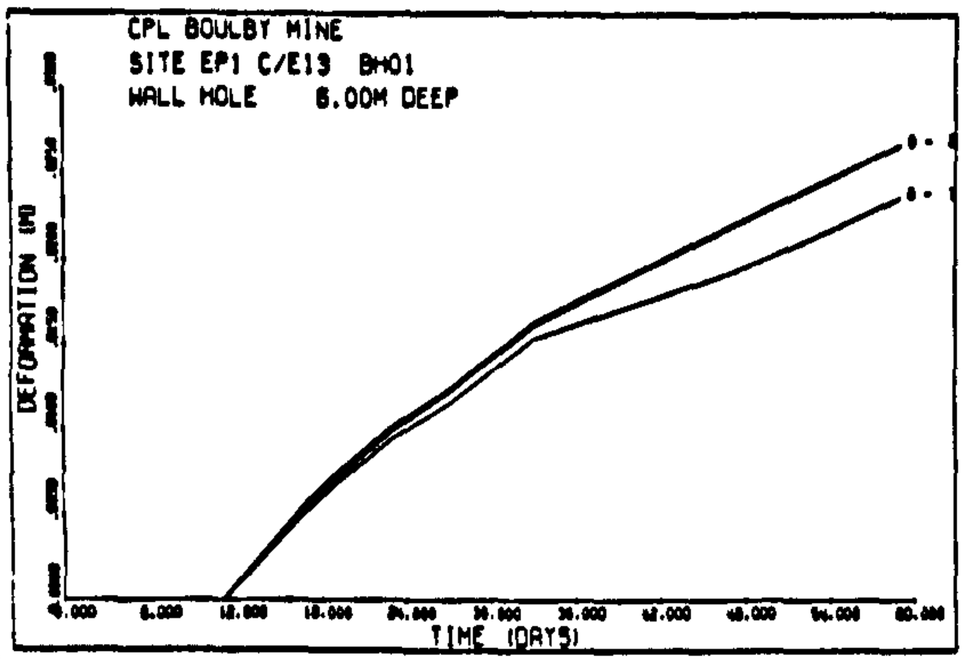
CPL BOULBY MINE
SITE EP1 C/E13 BH01
WALL HOLE 6.00M DEEP
DEFORMATION (M)
TIME (DAYS)

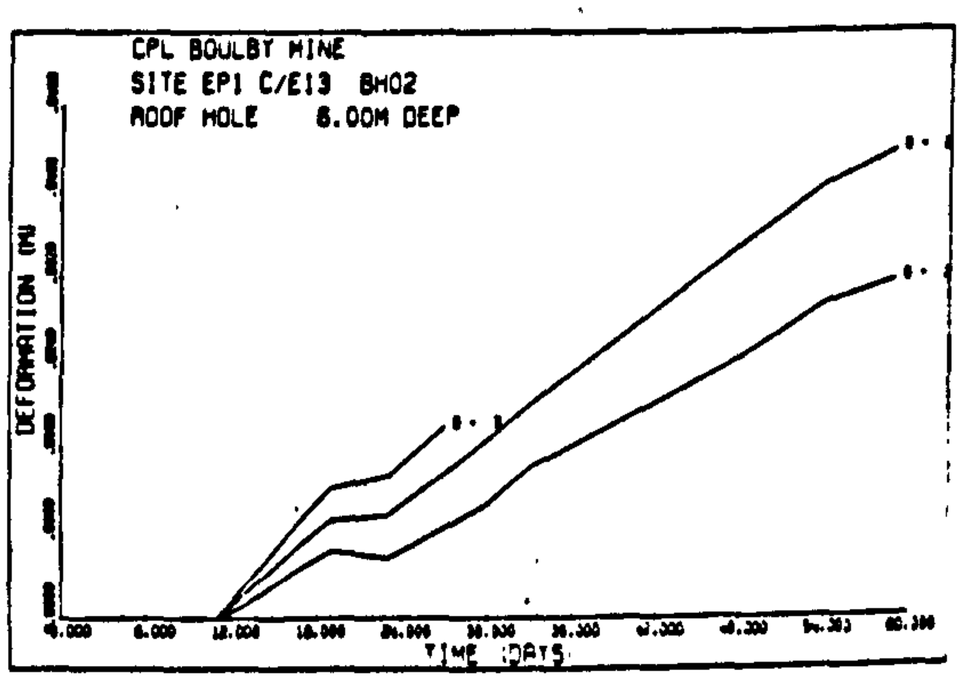
CPL BOULBY MINE
SITE EP1 C/E13 BH02
ROOF HOLE 6.00M DEEP
DEFORMATION (M)
TIME (DAYS)

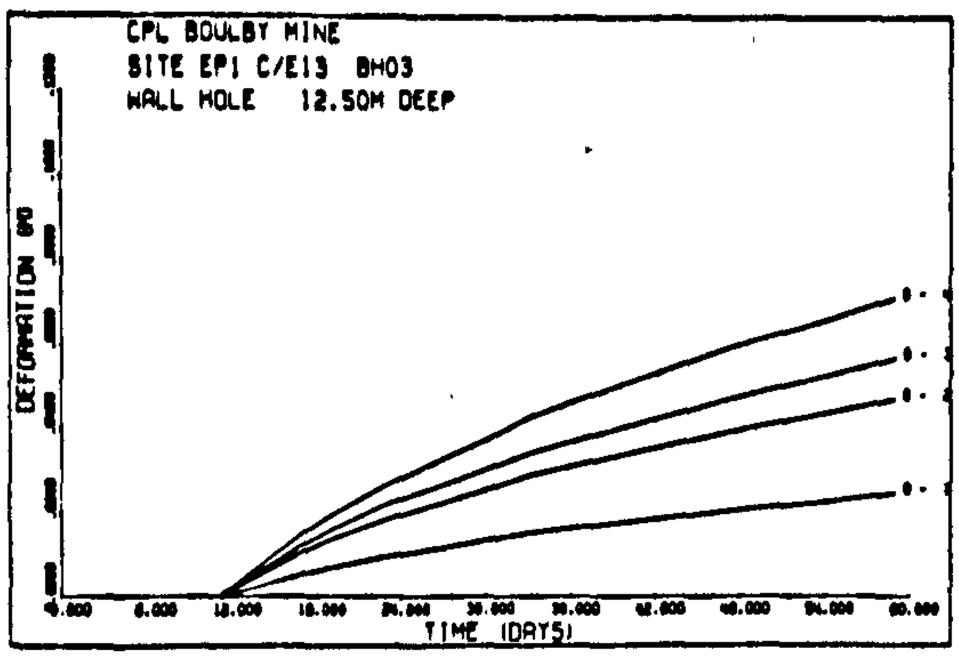
CPL BOULBY MINE
SITE EP1 C/E13 BH03
WALL HOLE 12.50M DEEP
DEFORMATION (M)
TIME (DAYS)

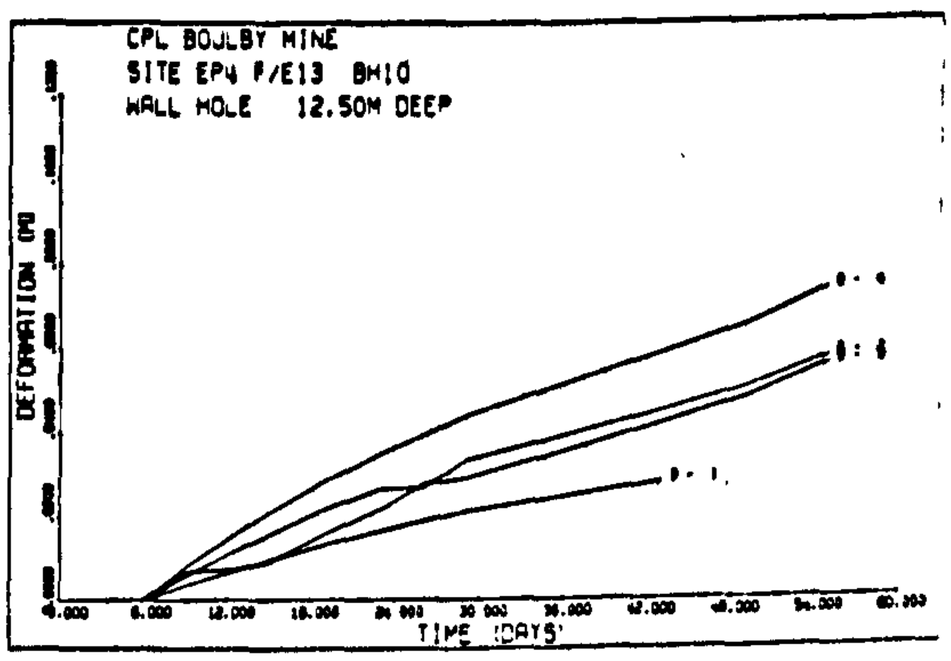
CPL BOULBY MINE
SITE EP4 F/E13 BH10
WALL HOLE 12.50M DEEP
DEFORMATION (M)
TIME (DAYS)

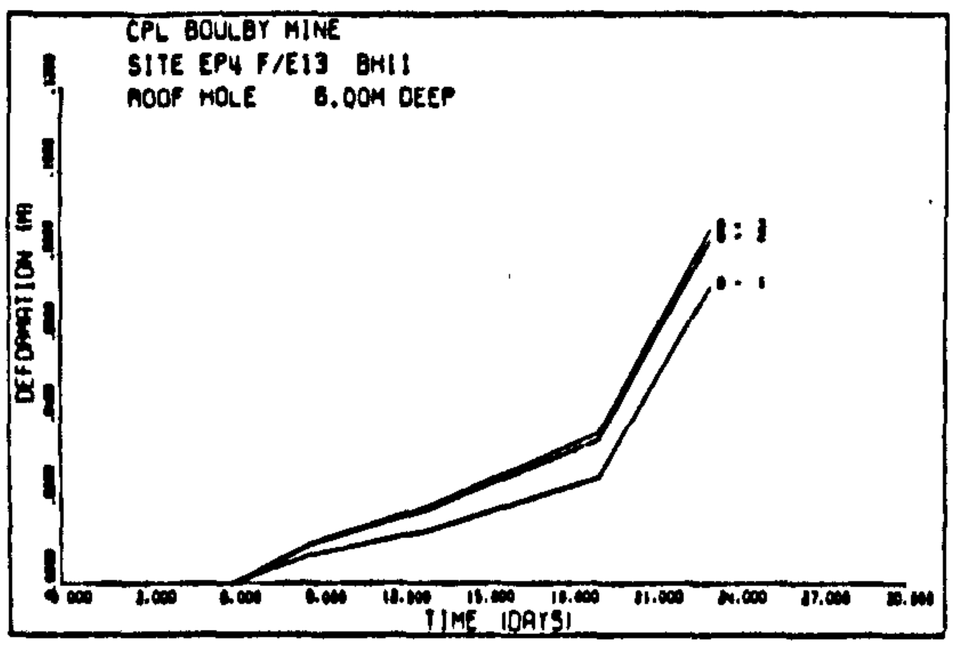
CPL BOULBY MINE
SITE EP4 F/E13 BH11
ROOF HOLE 6.00M DEEP
DEFORMATION (M)
TIME (DAYS)

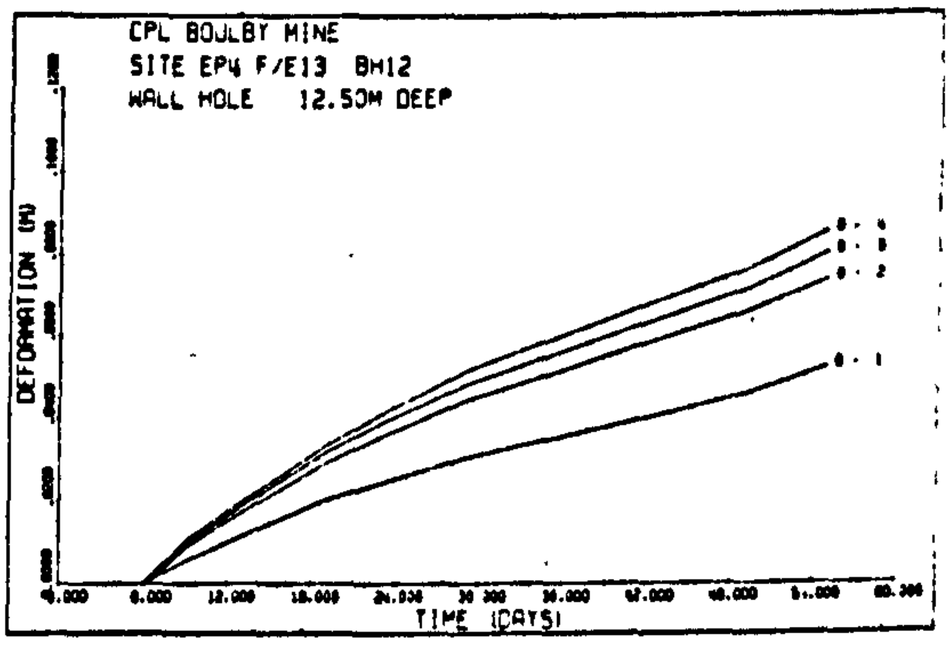
CPL BOULBY MINE
SITE EP4 F/E13 BH12
WALL HOLE 12.50M DEEP
DEFORMATION (M)
TIME (DAYS)

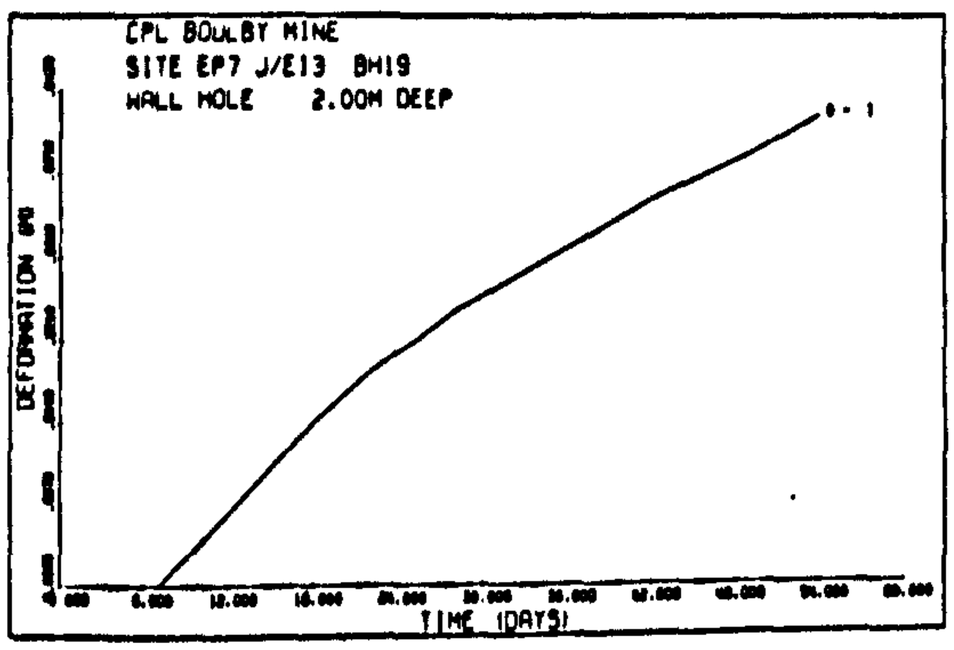
CPL BOULBY MINE
SITE EP7 J/E13 BH19
WALL HOLE 2.00M DEEP
DEFORMATION (M)
TIME (DAYS)

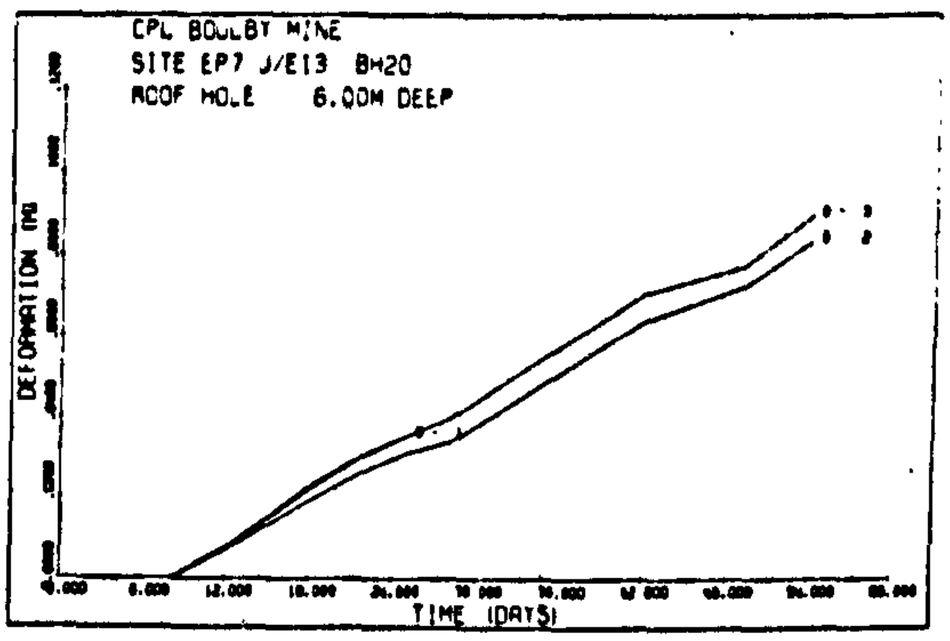
CPL BOULBY MINE
SITE EP7 J/E13 BH20
ROOF HOLE 6.00M DEEP
DEFORMATION (M)
TIME (DAYS)

B35

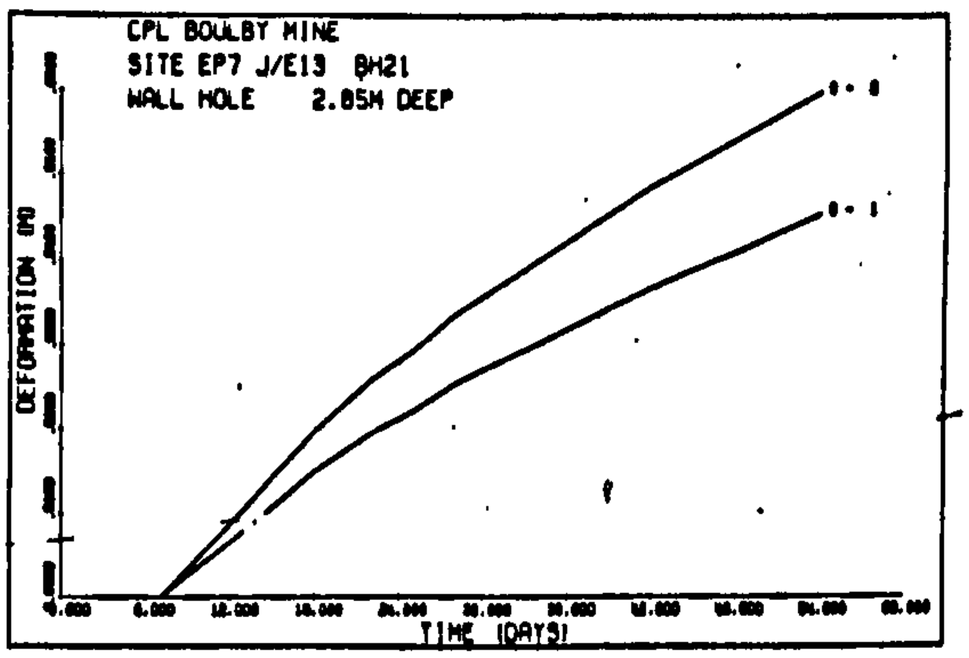
CPL BOULBY MINE
SITE EP7 J/E13 BH21
WALL HOLE 2.85M DEEP
DEFORMATION (M)
TIME (DAYS)

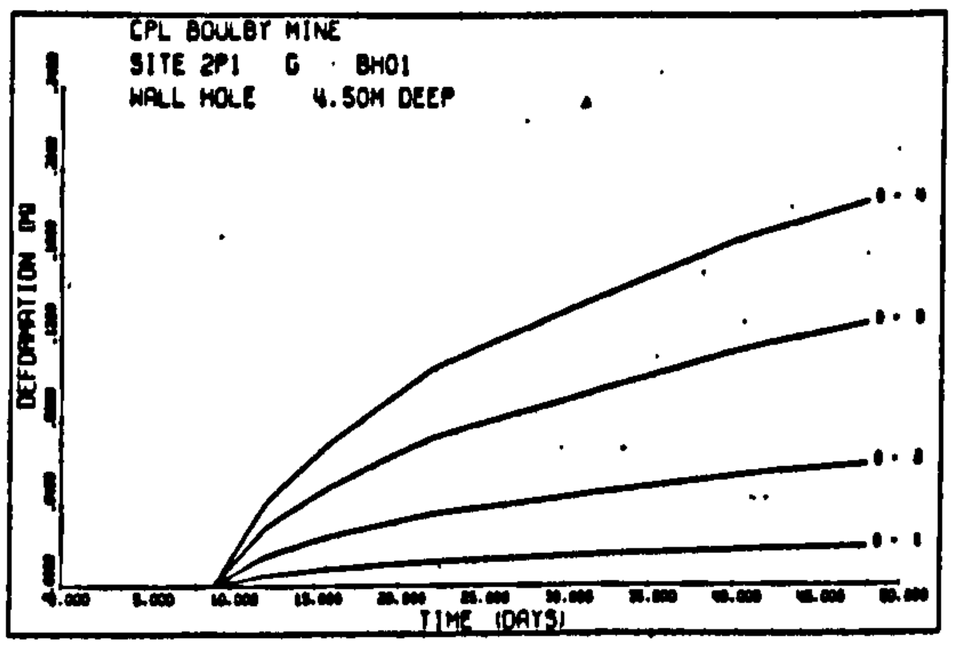
CPL BOULBY MINE
SITE 2P1 G - BH01
WALL HOLE 4.50M DEEP
DEFORMATION (M)
TIME (DAYS)

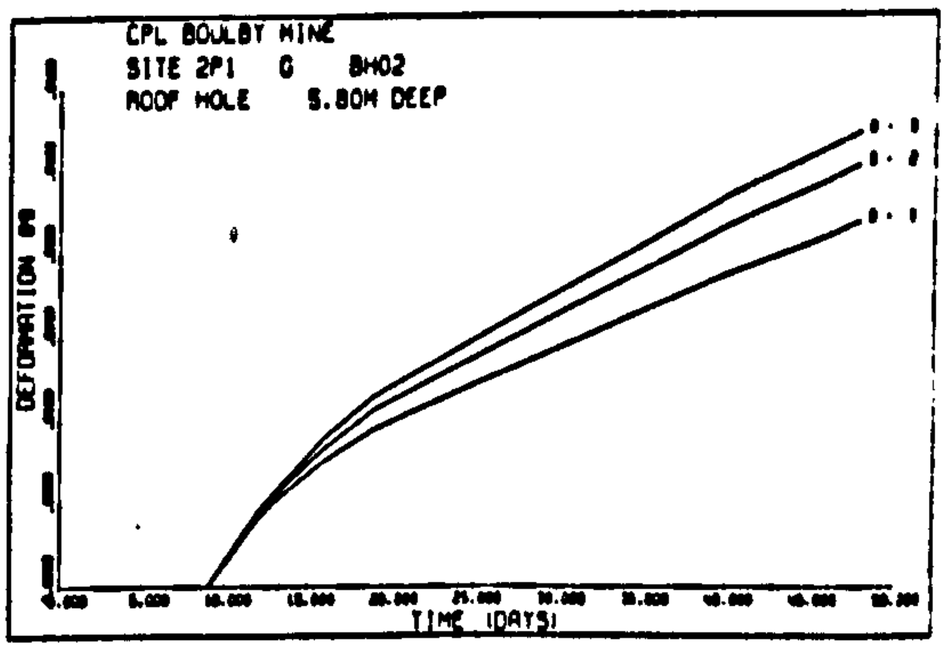
CPL BOULBY MINE
SITE 2P1 G BH02
ROOF HOLE 5.80M DEEP
DEFORMATION (M)
TIME (DAYS)

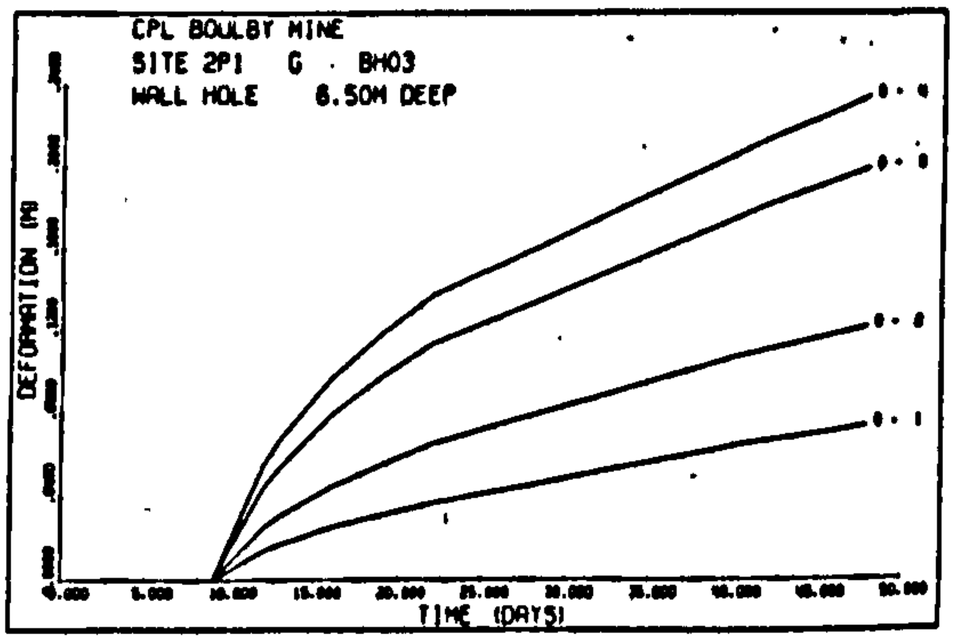
CPL BOULBY MINE
SITE 2P1 G - BH03
WALL HOLE 8.50M DEEP
DEFORMATION (M)
TIME (DAYS)

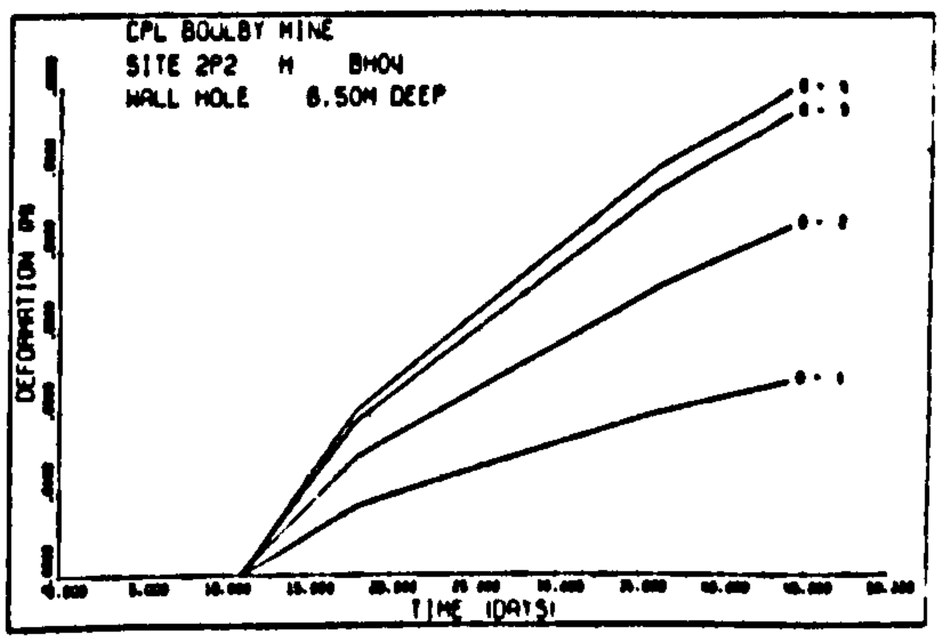
CPL BOULBY MINE
SITE 2P2 H BH04
WALL HOLE 8.50M DEEP
DEFORMATION (M)
TIME (DAYS)

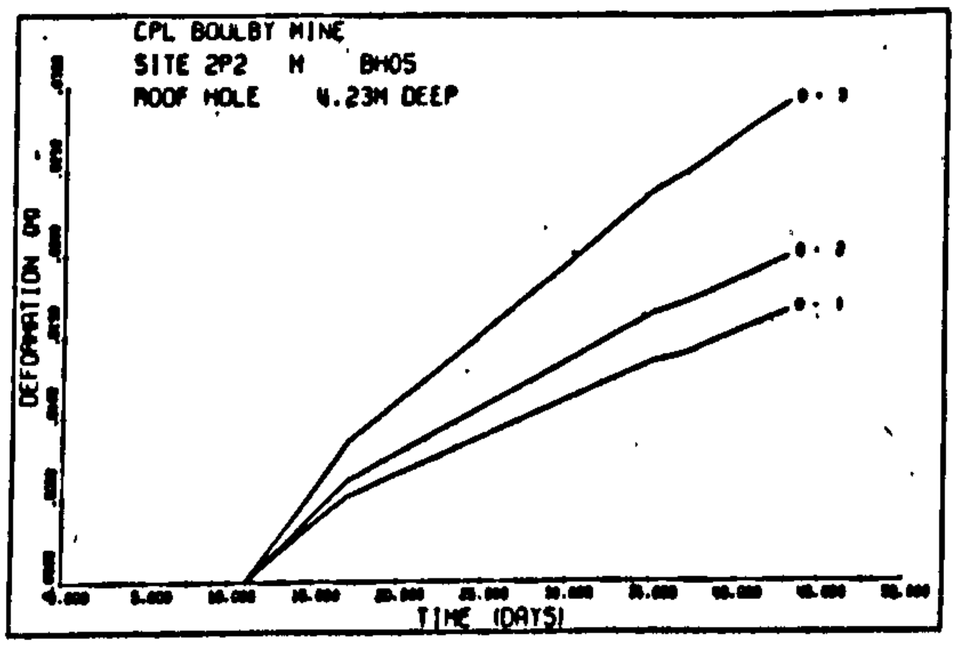
CPL BOULBY MINE
SITE 2P2 H BH05
ROOF HOLE 4.23M DEEP
DEFORMATION (M)
TIME (DAYS)

B36

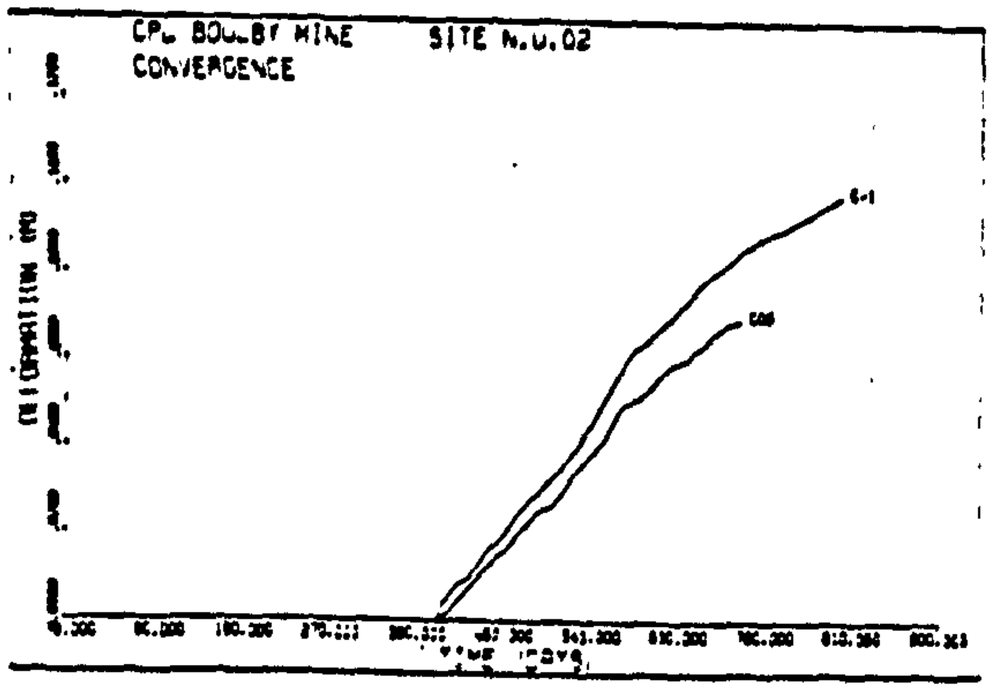
CPL BOULBY MINE SITE N.U.02
CONVERGENCE

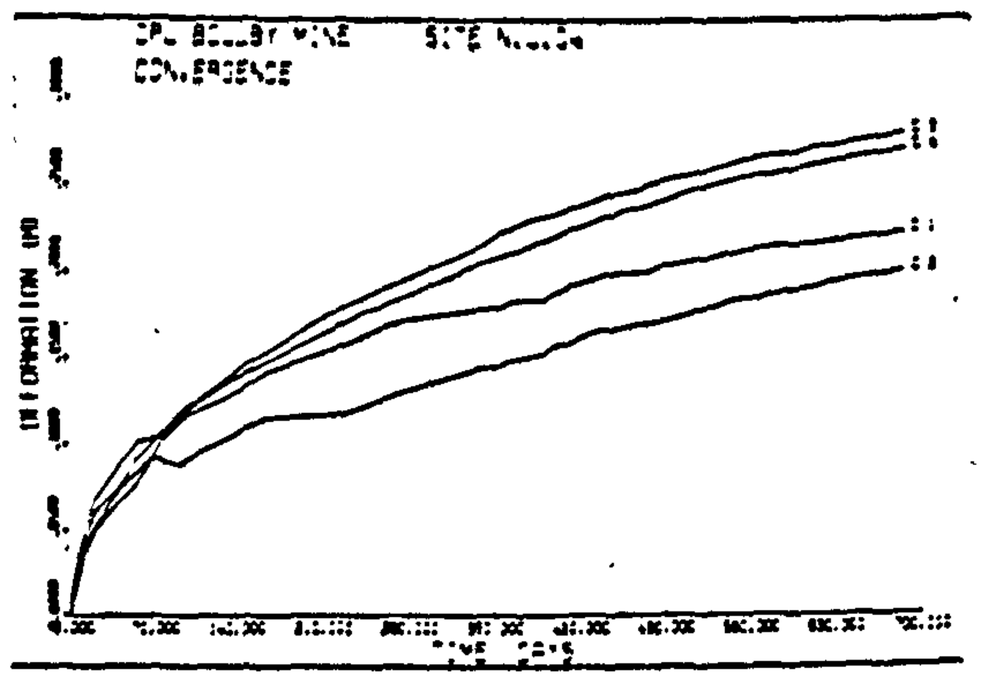
CPL BOULBY MINE
CONVERGENCE

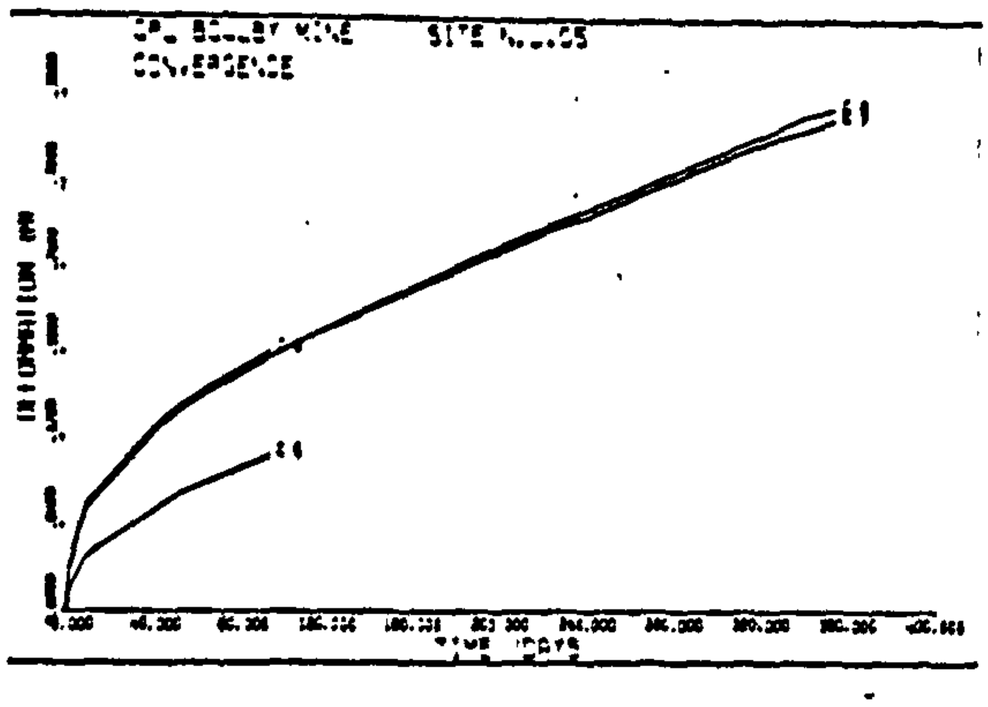
CONVERGENCE

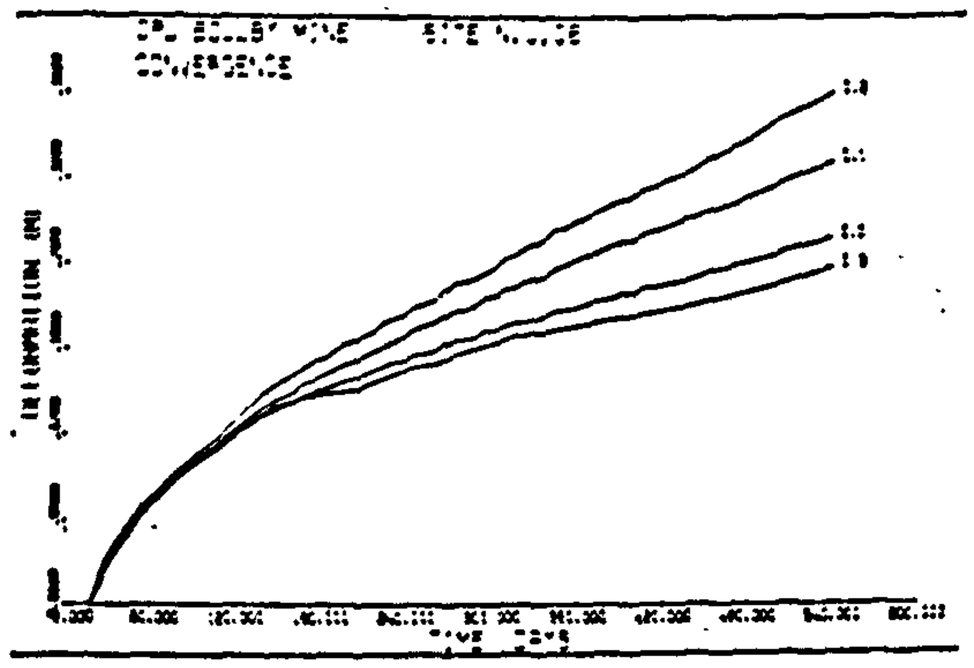
CONVERGENCE

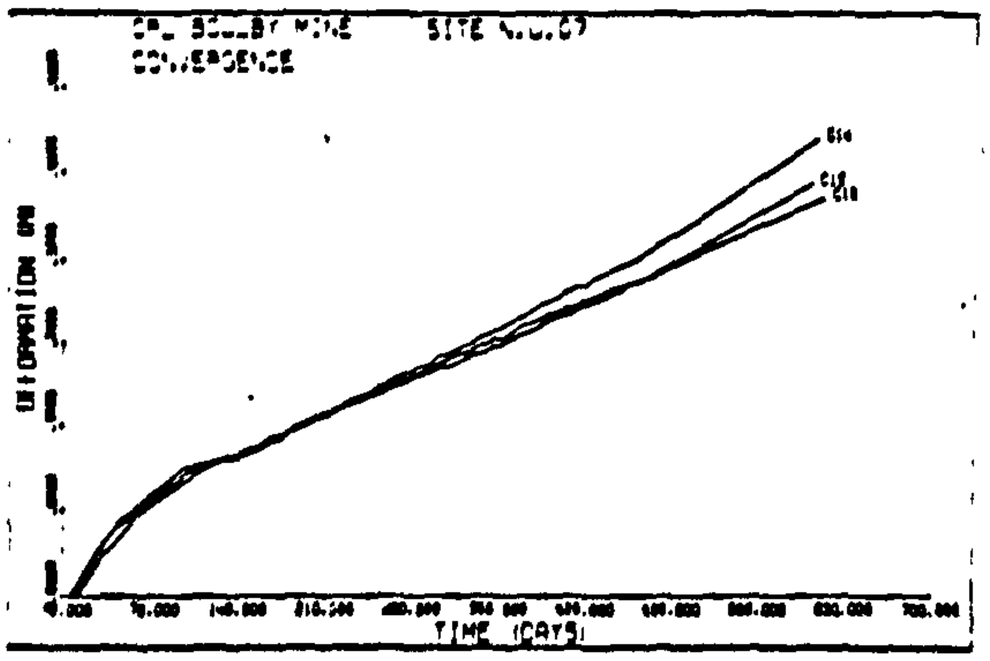
CONVERGENCE
TIME (DAYS)

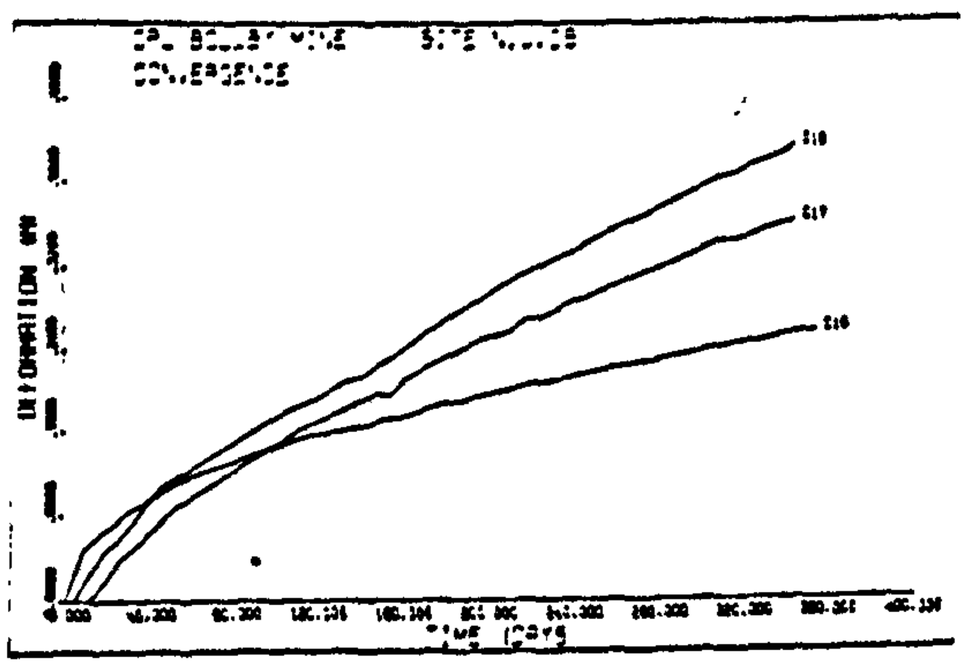
CONVERGENCE

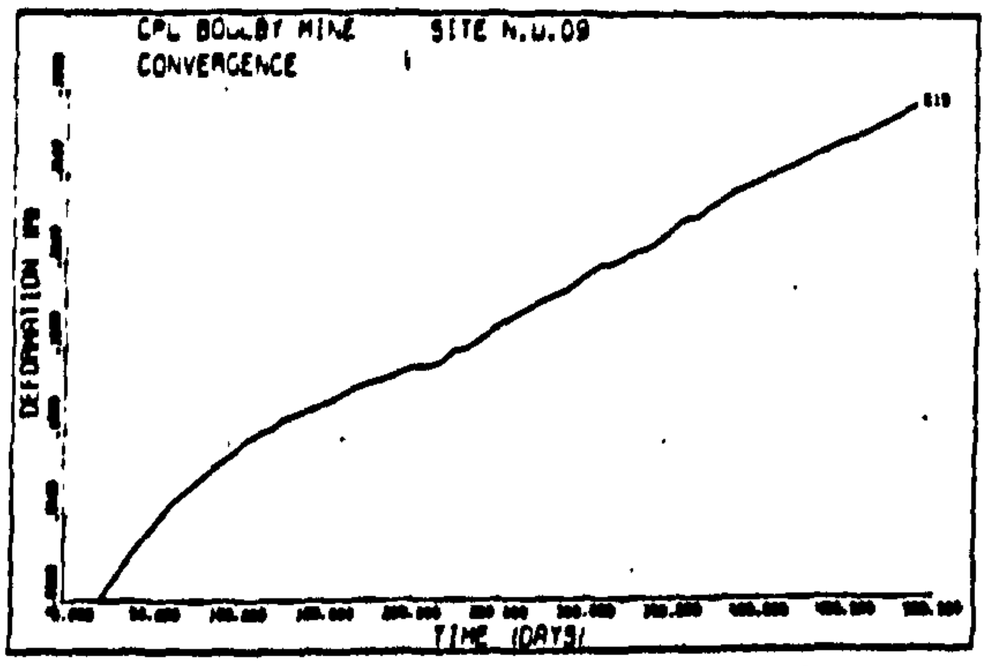
CPL BOULBY MINE SITE N.U.09
CONVERGENCE
TIME (DAYS)

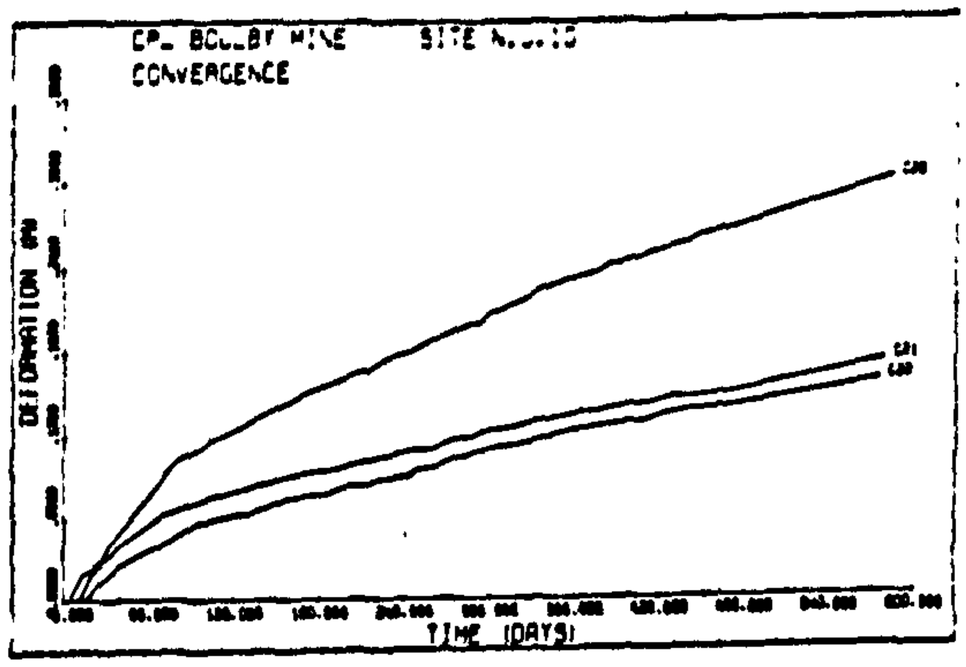
CONVERGENCE
TIME (DAYS)

B37

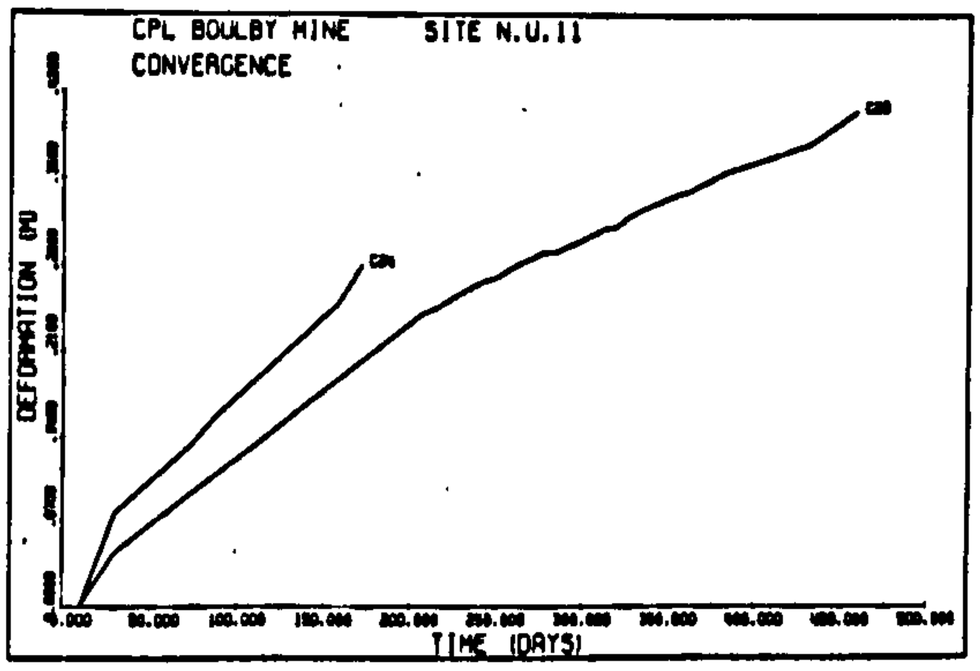
CPL BOULBY MINE SITE N.U.11
CONVERGENCE
DEFORMATION (M)
TIME (DAYS)

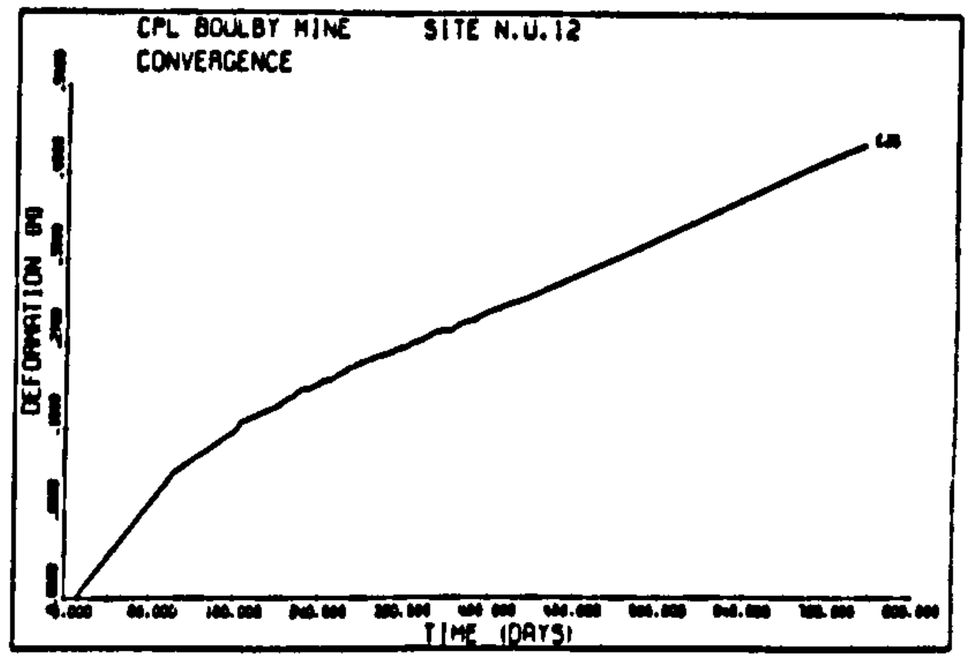
CPL BOULBY MINE SITE N.U.12
CONVERGENCE
DEFORMATION (M)
TIME (DAYS)

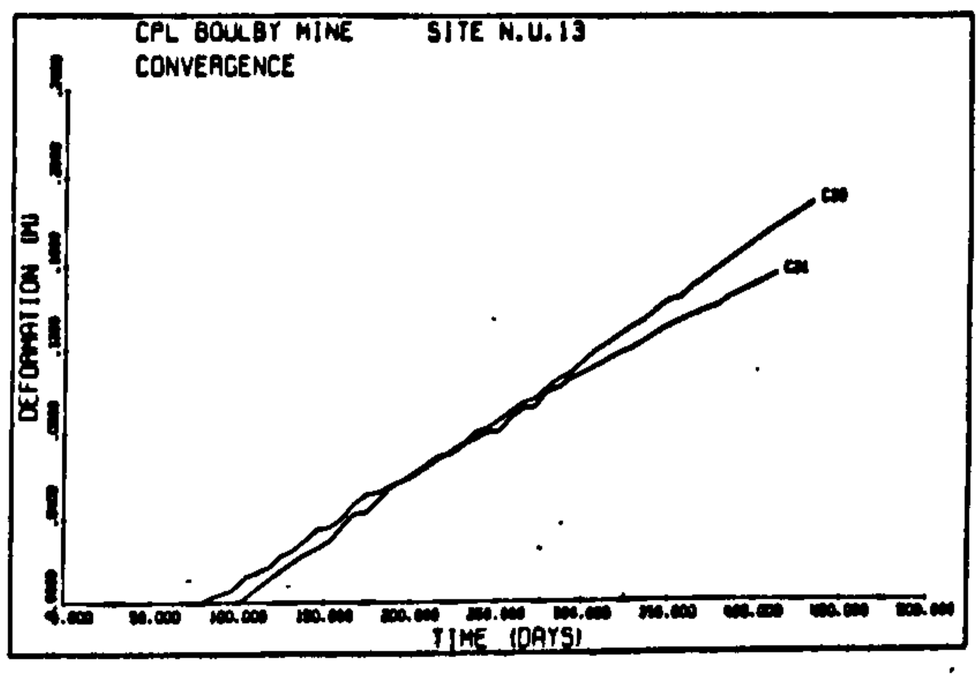
CPL BOULBY MINE SITE N.U.13
CONVERGENCE
DEFORMATION (M)
TIME (DAYS)

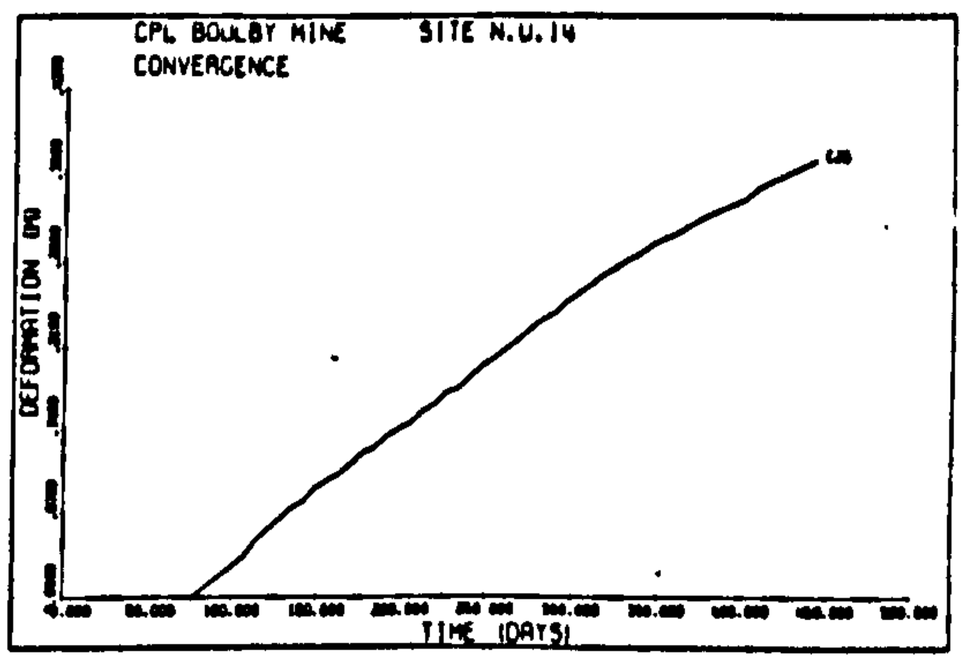
CPL BOULBY MINE SITE N.U.14
CONVERGENCE
DEFORMATION (M)
TIME (DAYS)

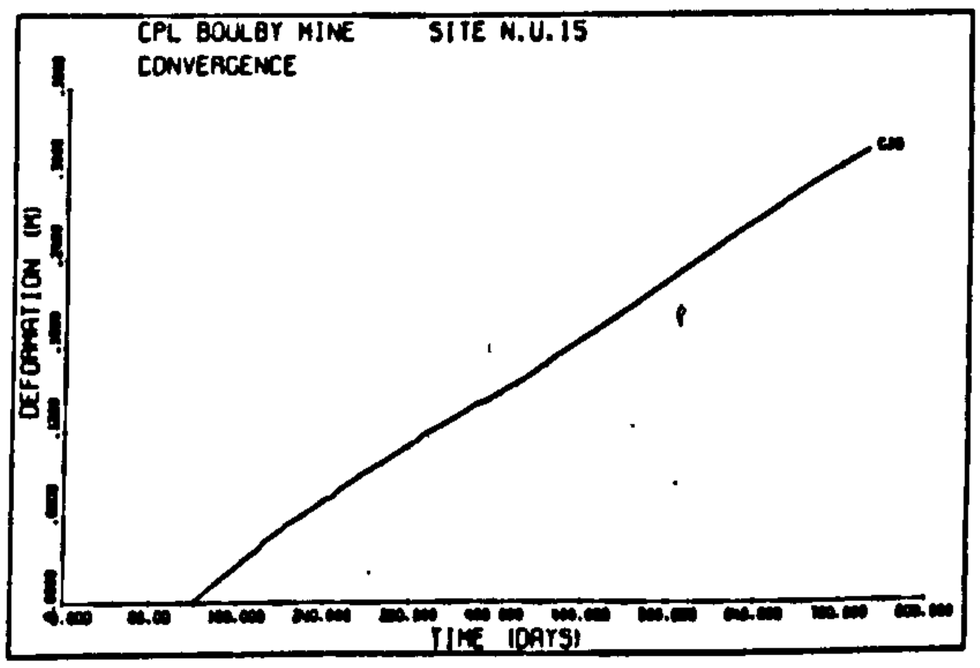
CPL BOULBY MINE SITE N.U.15
CONVERGENCE
DEFORMATION (M)
TIME (DAYS)

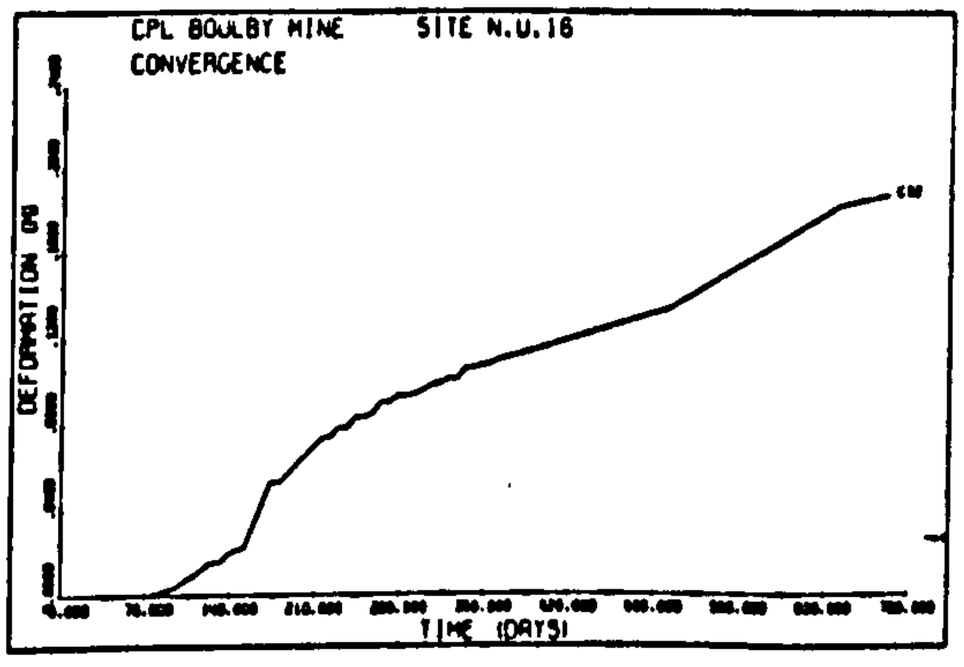
CPL BOULBY MINE SITE N.U.16
CONVERGENCE
DEFORMATION (M)
TIME (DAYS)

B38

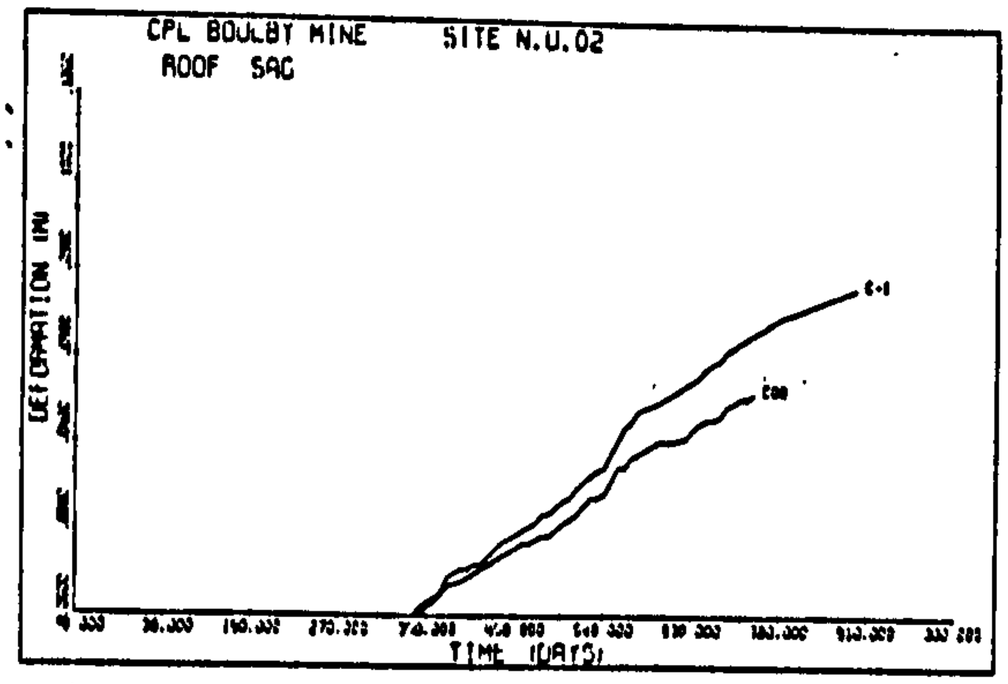
CPL BOULBY MINE SITE N.U.02
ROOF SAG
DEFORMATION (M)
TIME (DAYS)

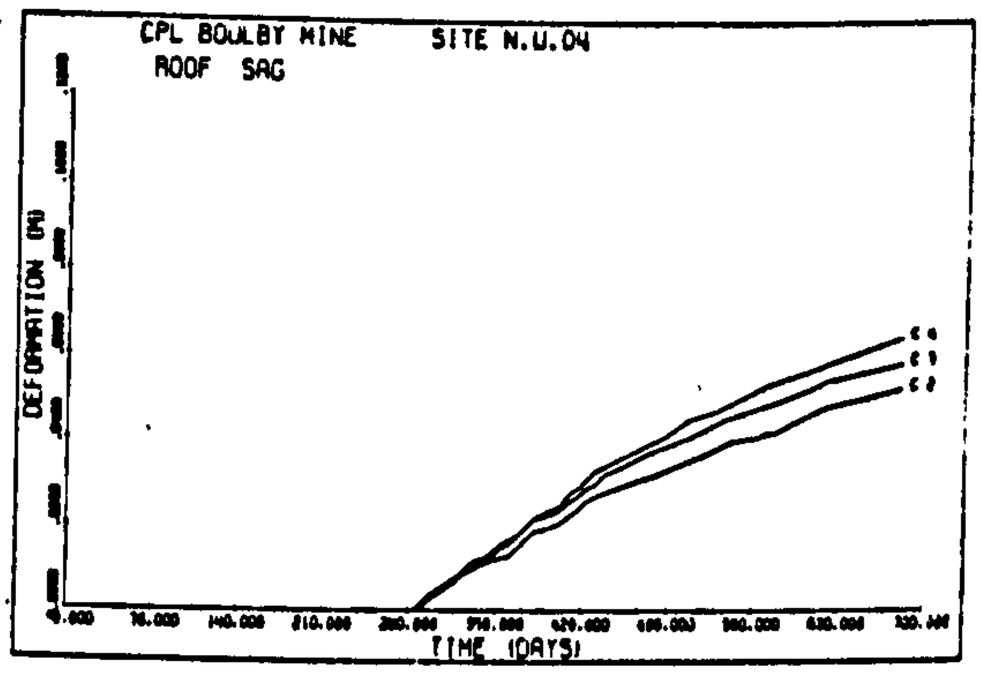
CPL BOULBY MINE SITE N.U.04
ROOF SAG
DEFORMATION (M)
TIME (DAYS)

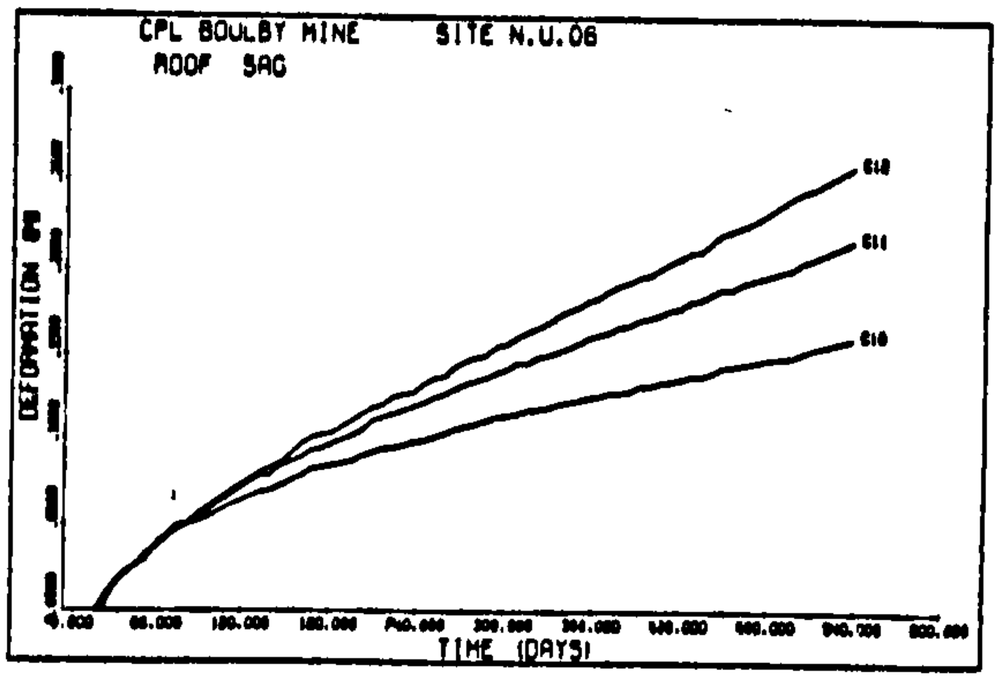
CPL BOULBY MINE SITE N.U.06
ROOF SAG
DEFORMATION (M)
TIME (DAYS)

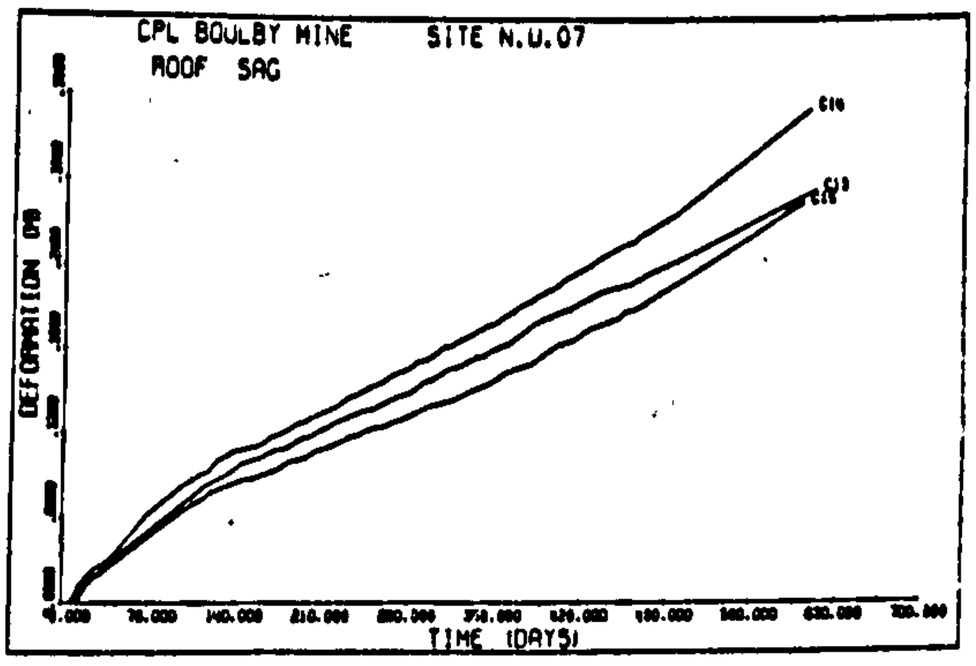
CPL BOULBY MINE SITE N.U.07
ROOF SAG
DEFORMATION (M)
TIME (DAYS)

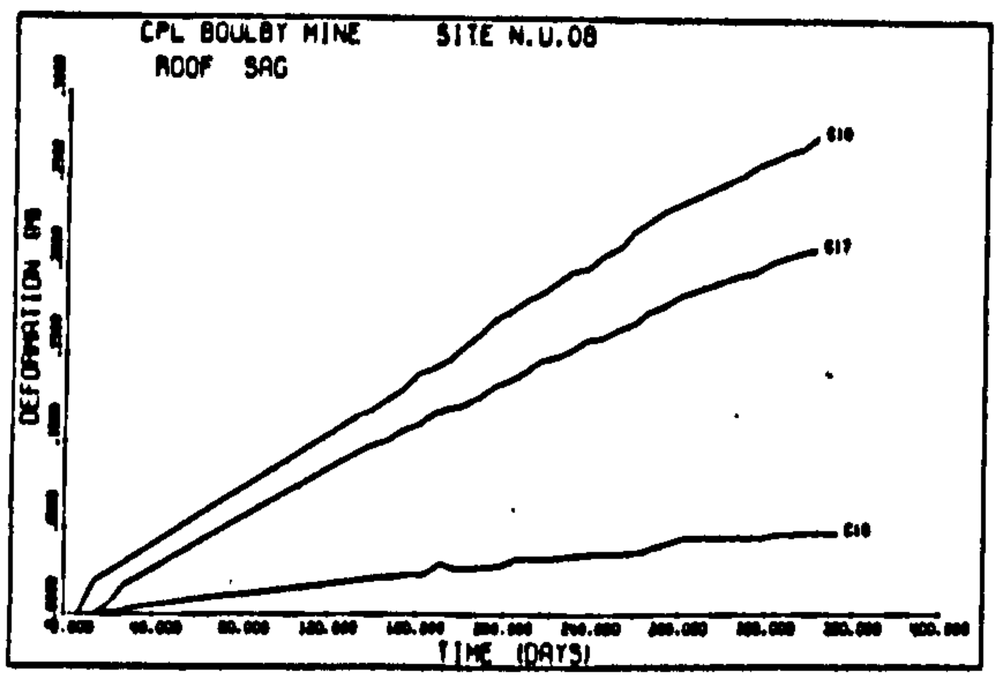
CPL BOULBY MINE SITE N.U.08
ROOF SAG
DEFORMATION (M)
TIME (DAYS)

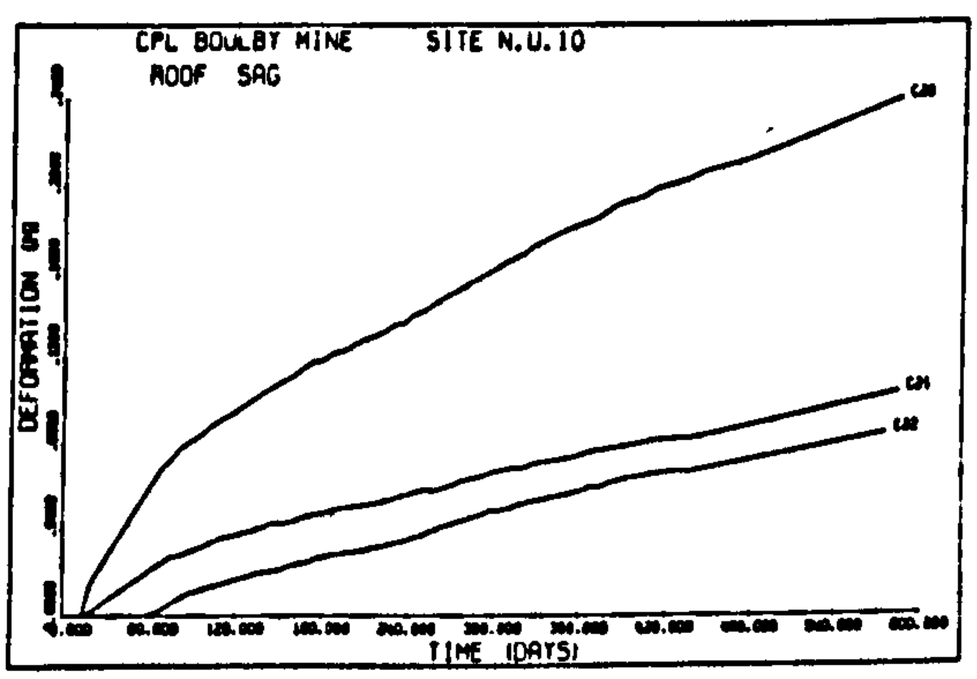
CPL BOULBY MINE SITE N.U.10
ROOF SAG
DEFORMATION (M)
TIME (DAYS)

B39

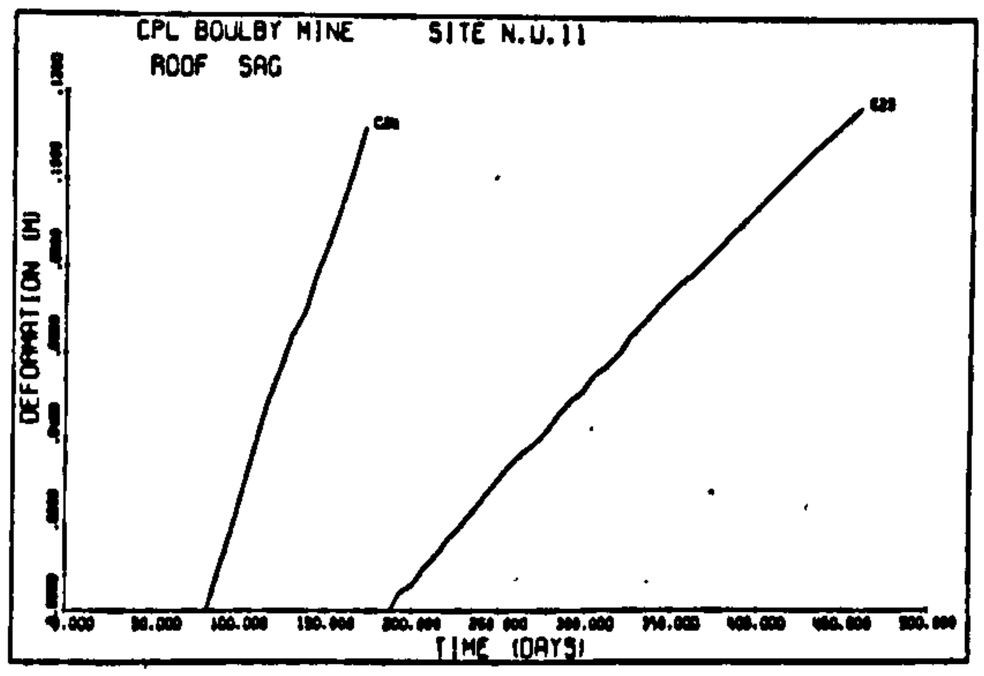
CPL BOULBY MINE SITE N.U.11
ROOF SAG
DEFORMATION (M)
TIME (DAYS)

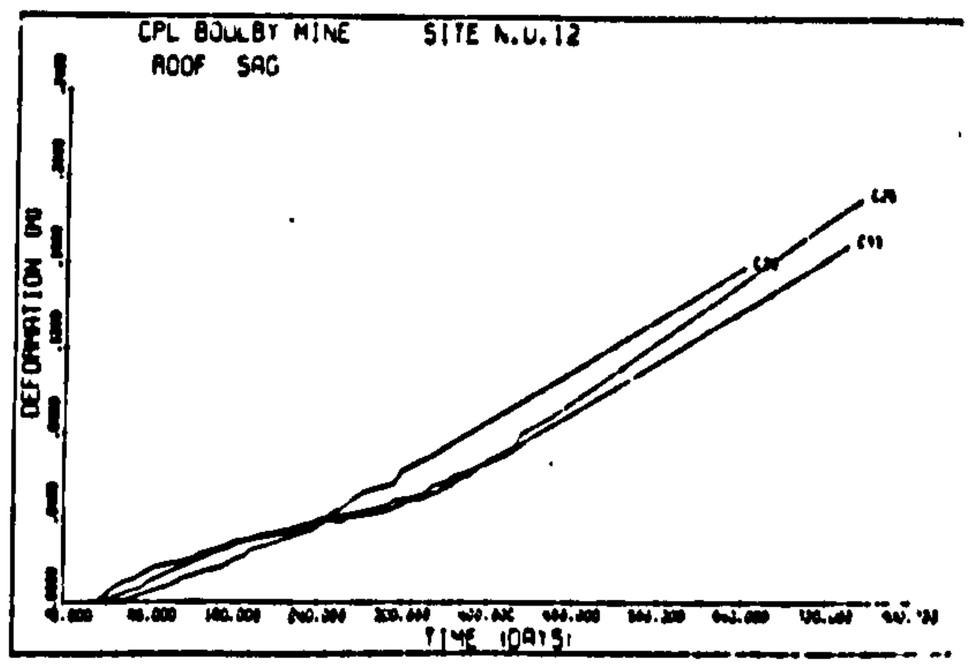
CPL BOULBY MINE SITE N.U.12
ROOF SAG
DEFORMATION (M)
TIME (DAYS)

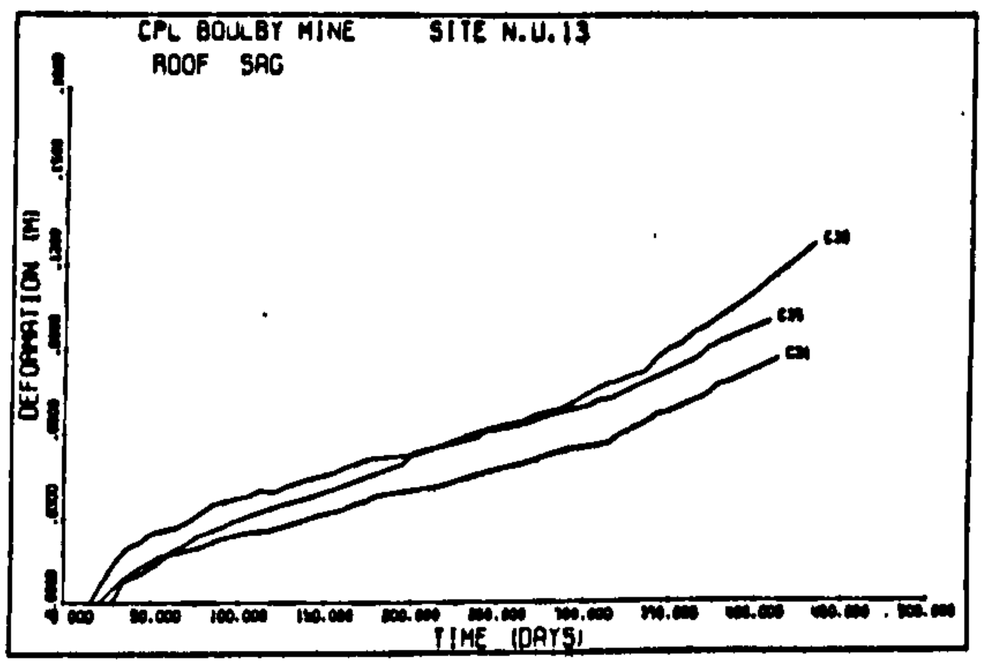
CPL BOULBY MINE SITE N.U.13
ROOF SAG
DEFORMATION (M)
TIME (DAYS)

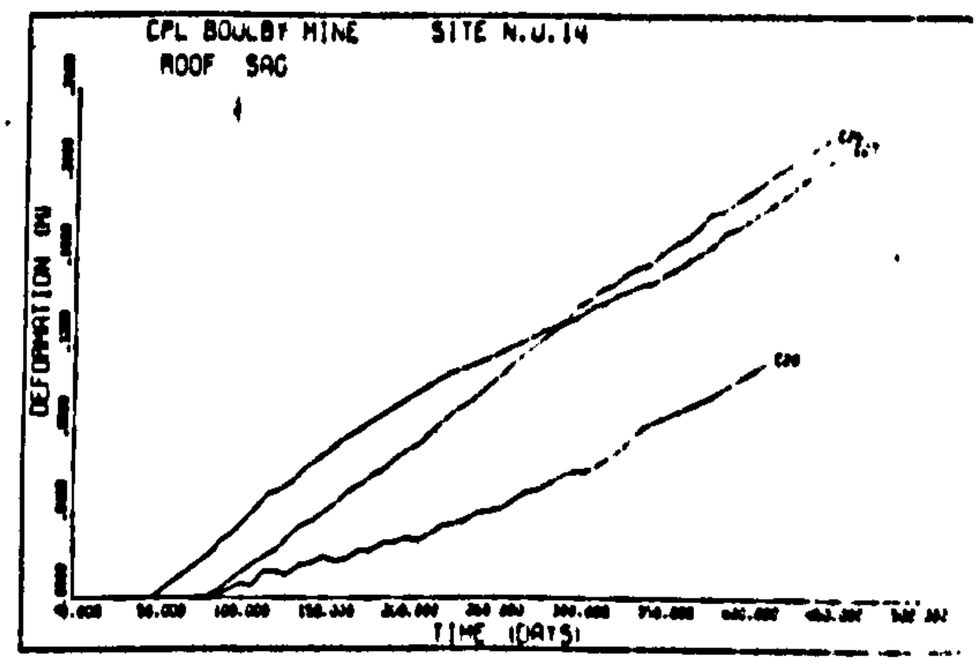
CPL BOULBY MINE SITE N.U.14
ROOF SAG
DEFORMATION (M)
TIME (DAYS)

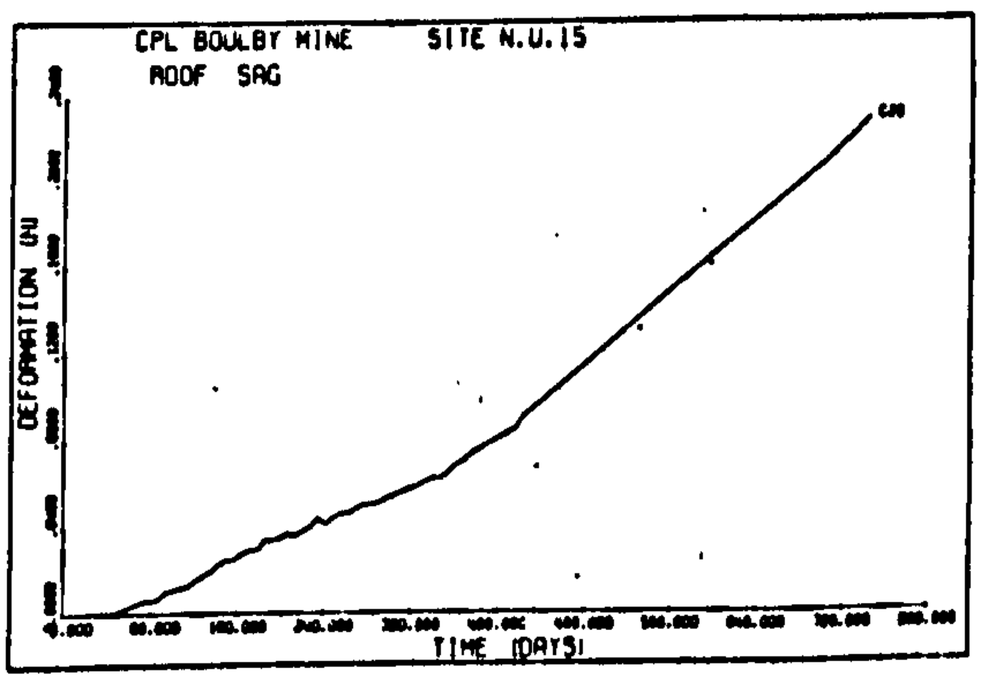
CPL BOULBY MINE SITE N.U.15
ROOF SAG
DEFORMATION (M)
TIME (DAYS)

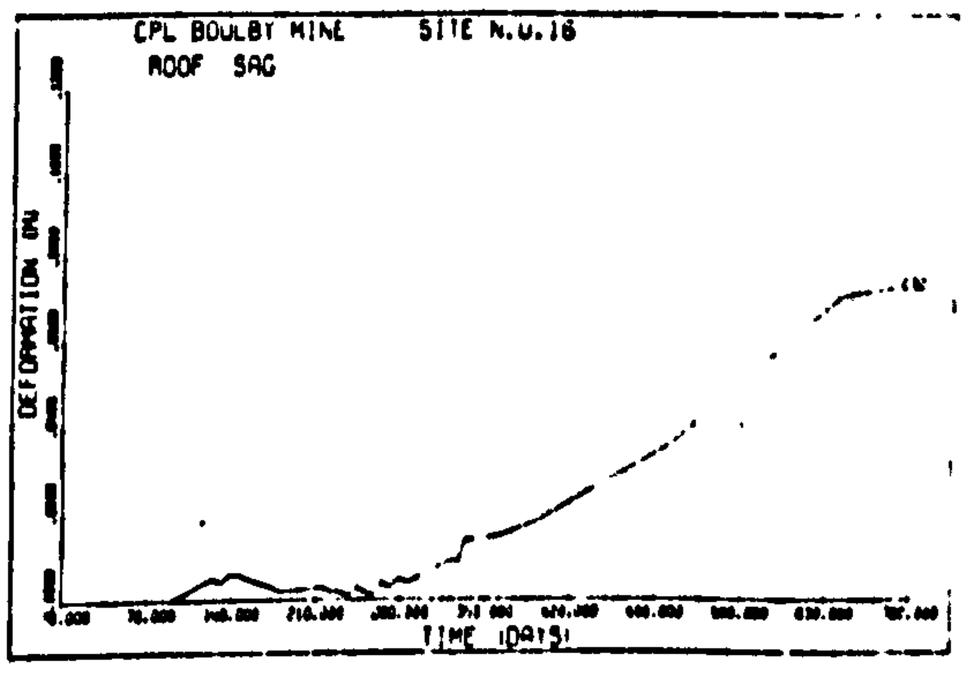
CPL BOULBY MINE SITE N.U.16
ROOF SAG
DEFORMATION (M)
TIME (DAYS)

B40

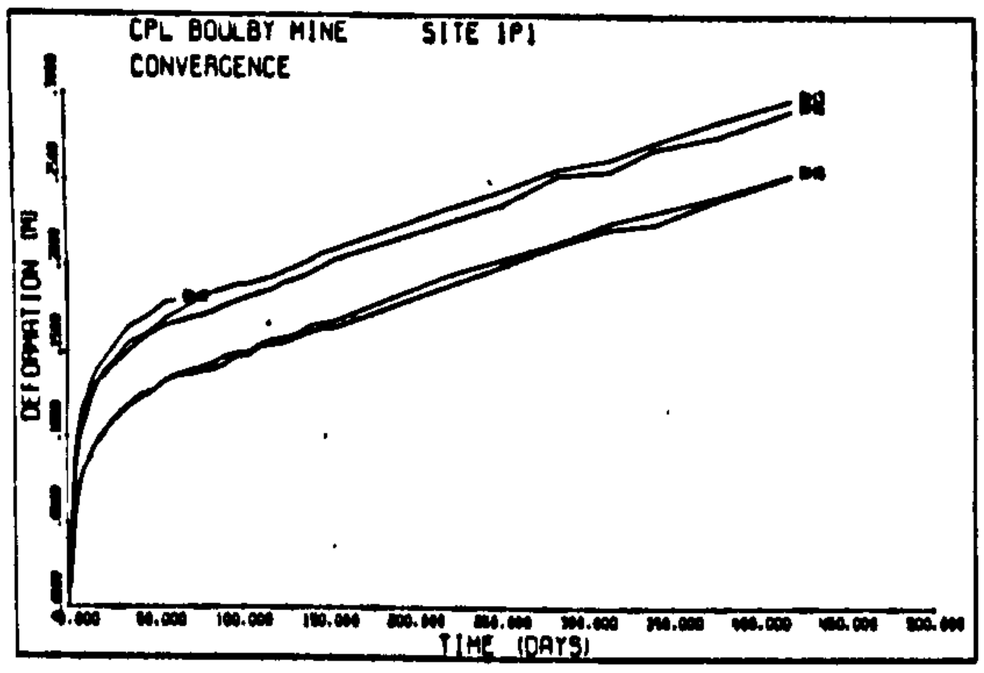
CPL BOULBY MINE SITE IP1
CONVERGENCE
DEFORMATION (MM)
TIME (DAYS)

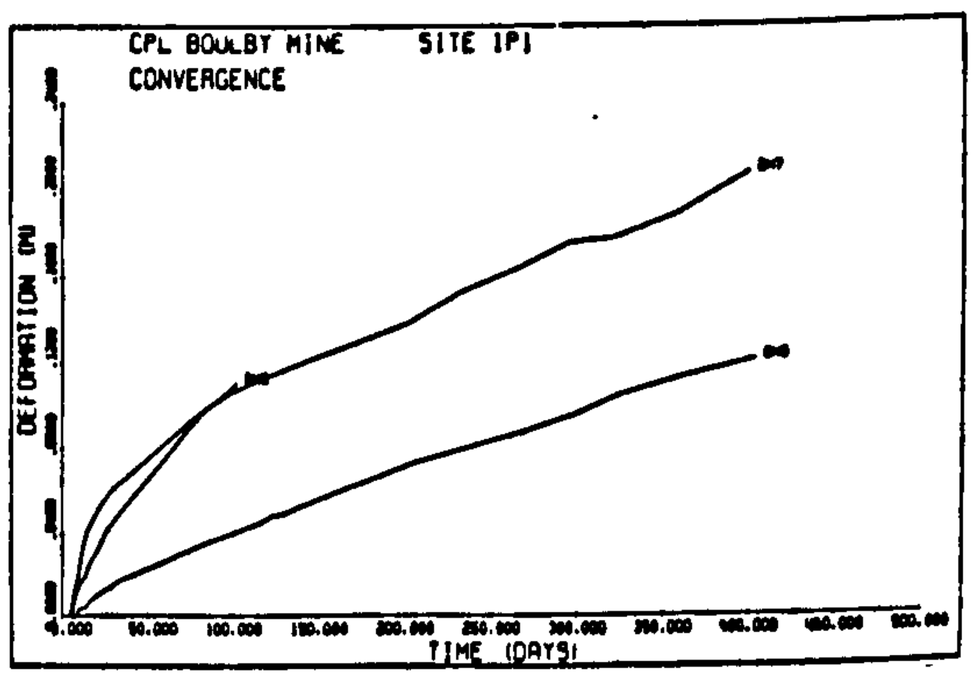
CPL BOULBY MINE SITE IP1
CONVERGENCE
DEFORMATION (MM)
TIME (DAYS)

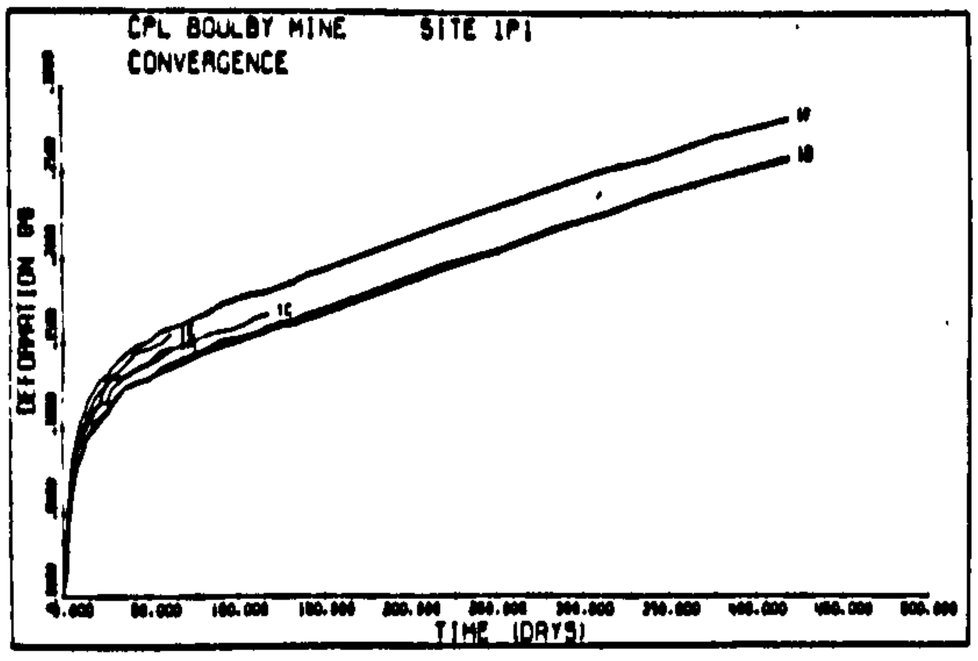
CPL BOULBY MINE SITE IP1
CONVERGENCE
DEFORMATION (MM)
TIME (DAYS)

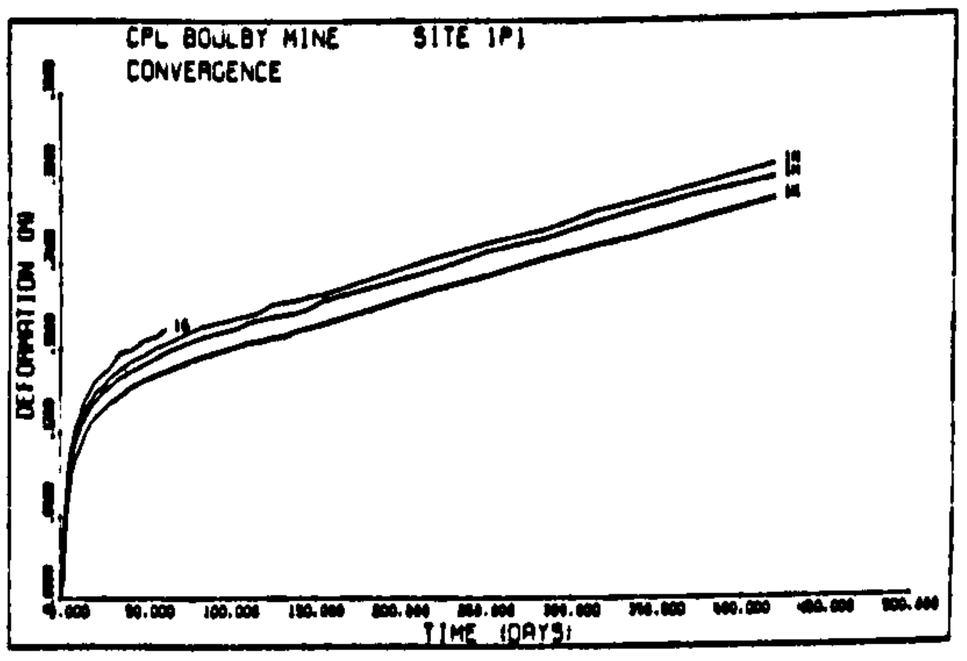
CPL BOULBY MINE SITE IP1
CONVERGENCE
DEFORMATION (MM)
TIME (DAYS)

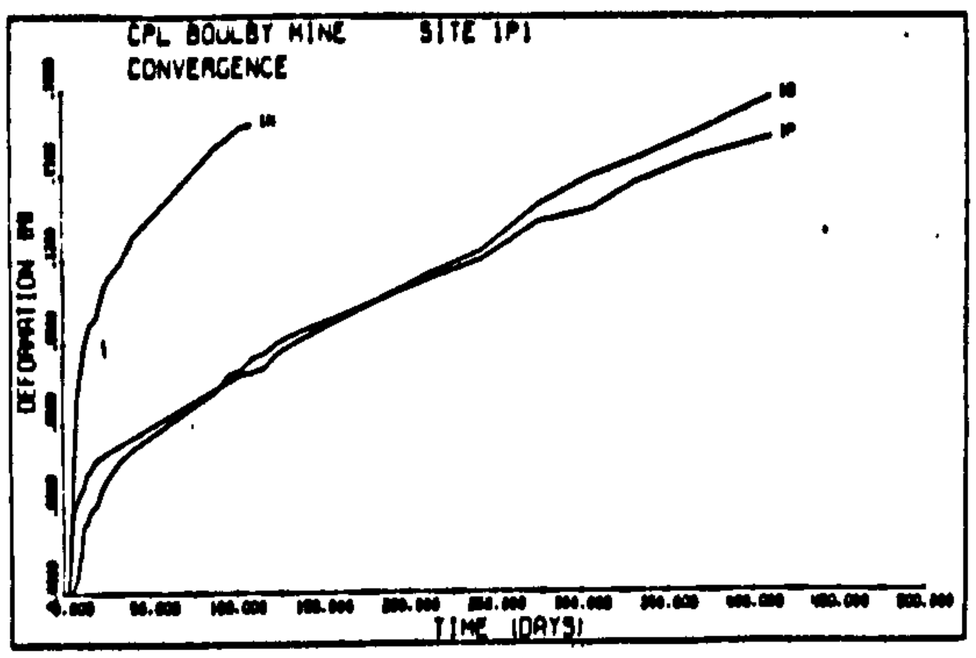
CPL BOULBY MINE SITE IP1
CONVERGENCE
DEFORMATION (MM)
TIME (DAYS)

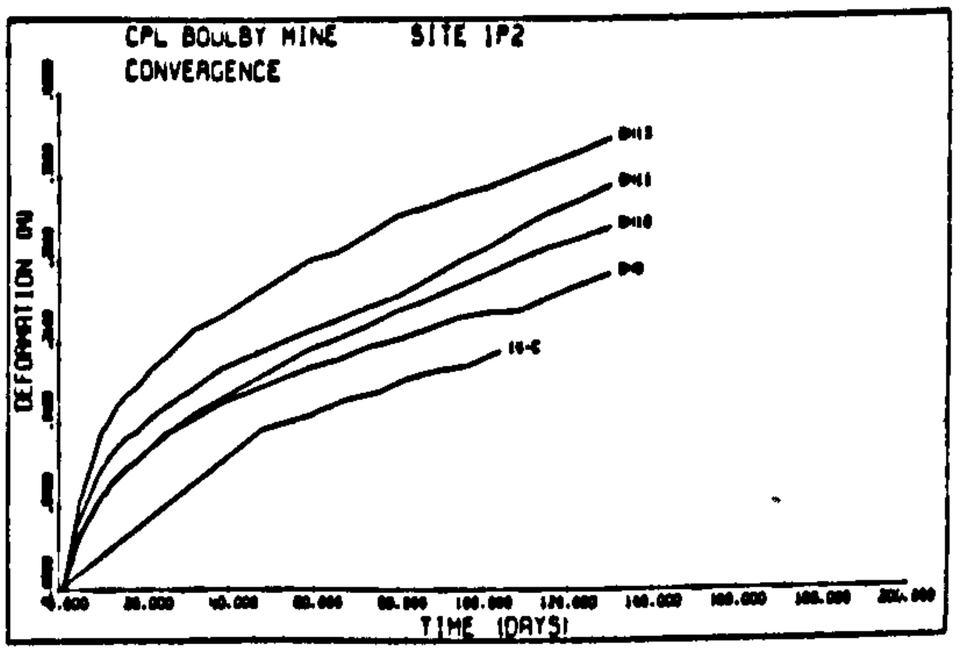
CPL BOULBY MINE SITE IP2
CONVERGENCE
DEFORMATION (MM)
TIME (DAYS)

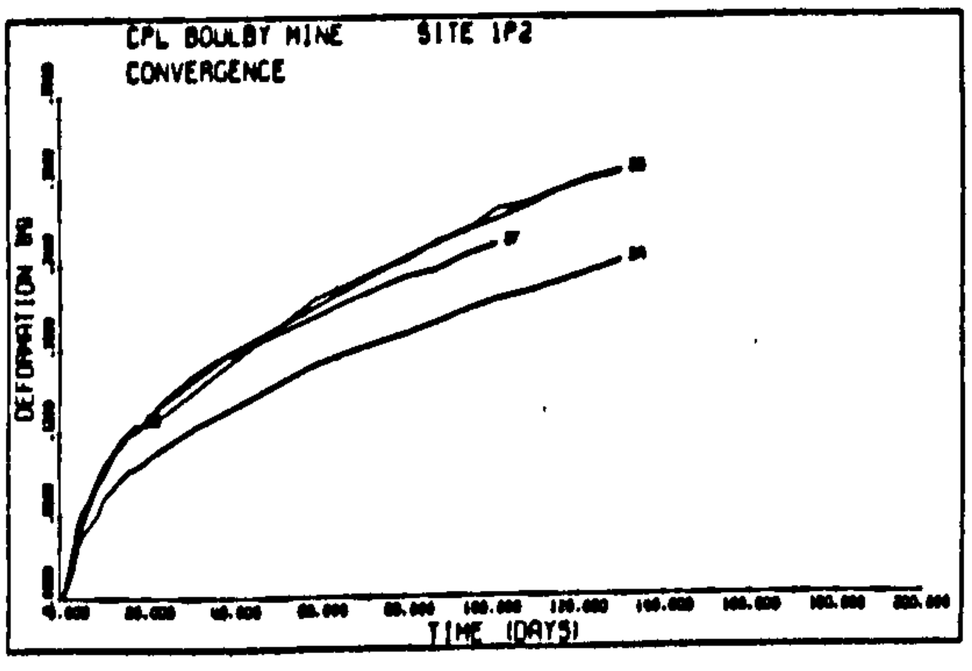
CPL BOULBY MINE SITE IP2
CONVERGENCE
DEFORMATION (MM)
TIME (DAYS)

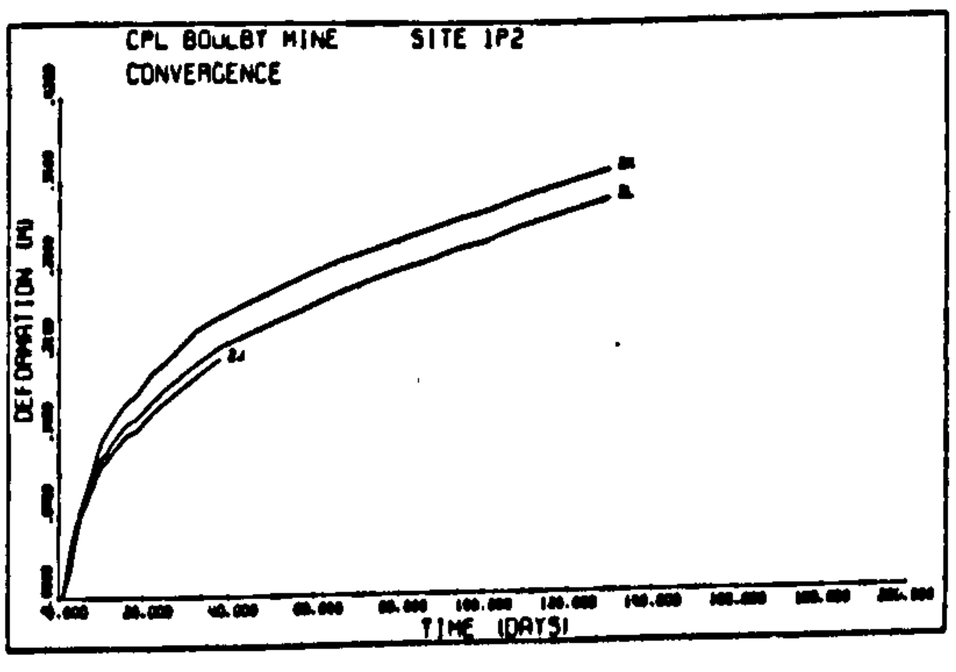
CPL BOULBY MINE SITE IP2
CONVERGENCE
DEFORMATION (MM)
TIME (DAYS)

B41

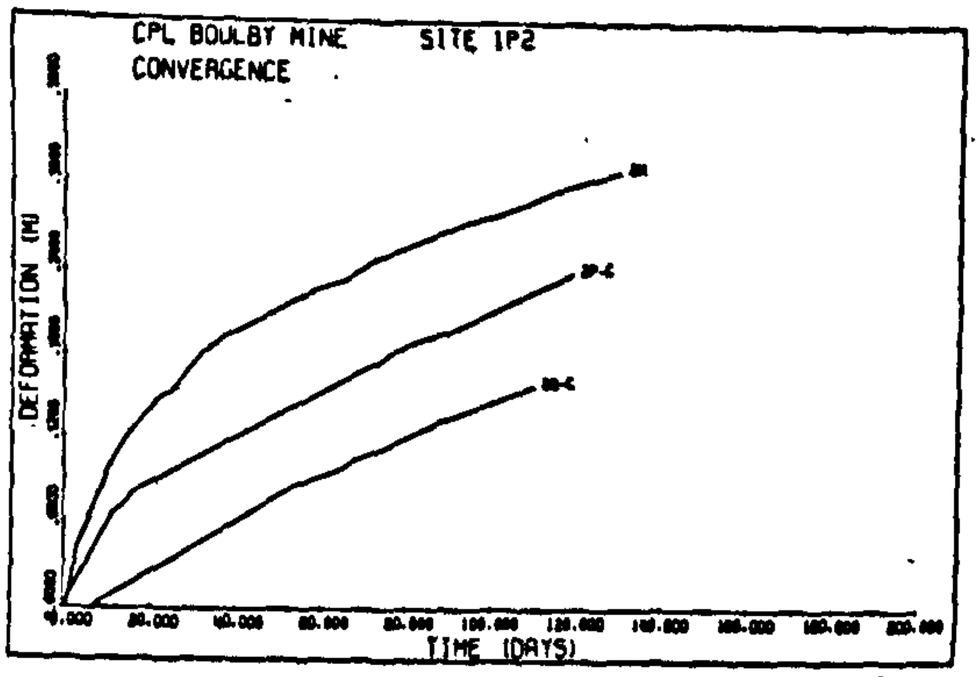
CPL BOULBY MINE SITE IP2
CONVERGENCE
DEFORMATION (M)
TIME (DAYS)

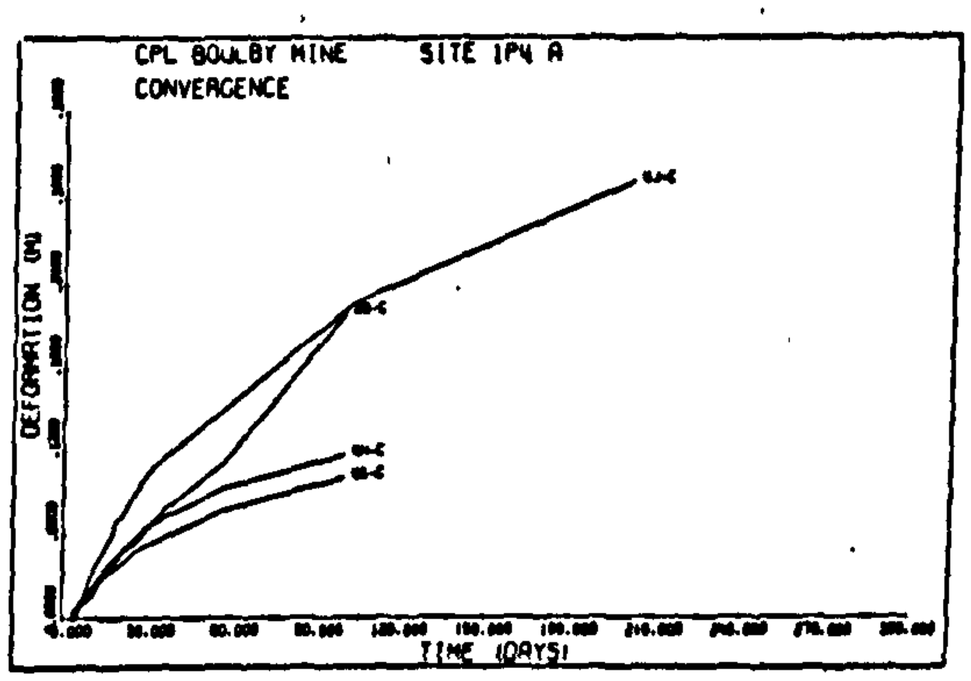
CPL BOULBY MINE SITE IP4 A
CONVERGENCE
DEFORMATION (M)
TIME (DAYS)

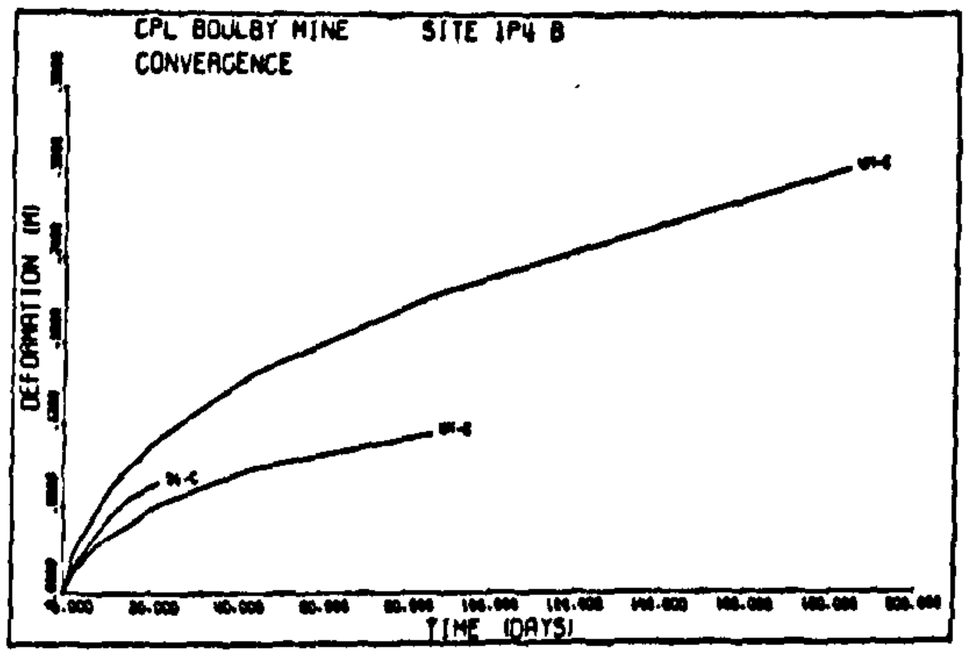
CPL BOULBY MINE SITE IP4 B
CONVERGENCE
DEFORMATION (M)
TIME (DAYS)

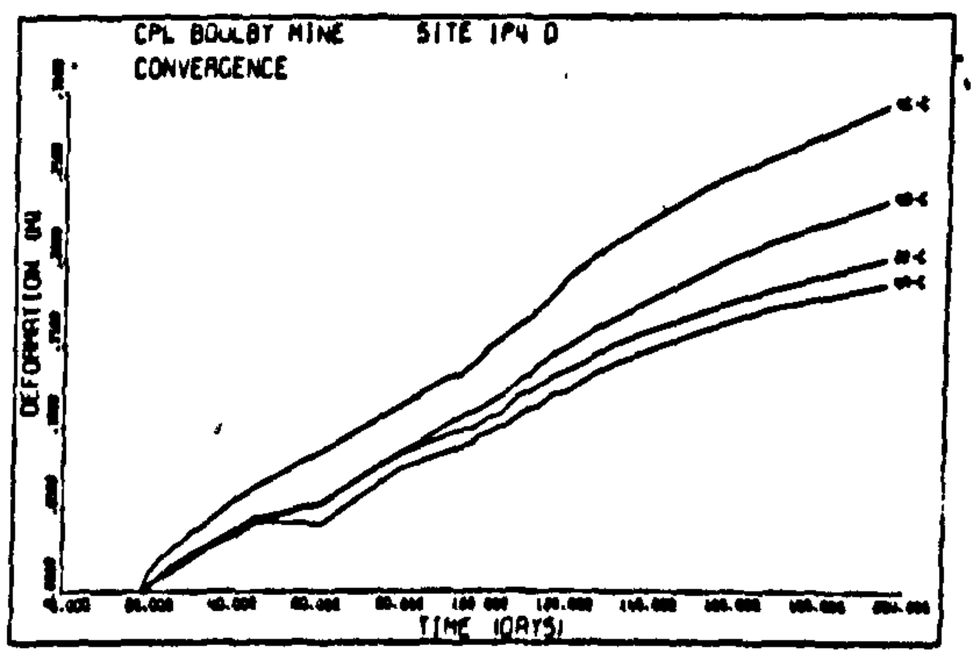
CPL BOULBY MINE SITE IP4 D
CONVERGENCE
DEFORMATION (M)
TIME (DAYS)

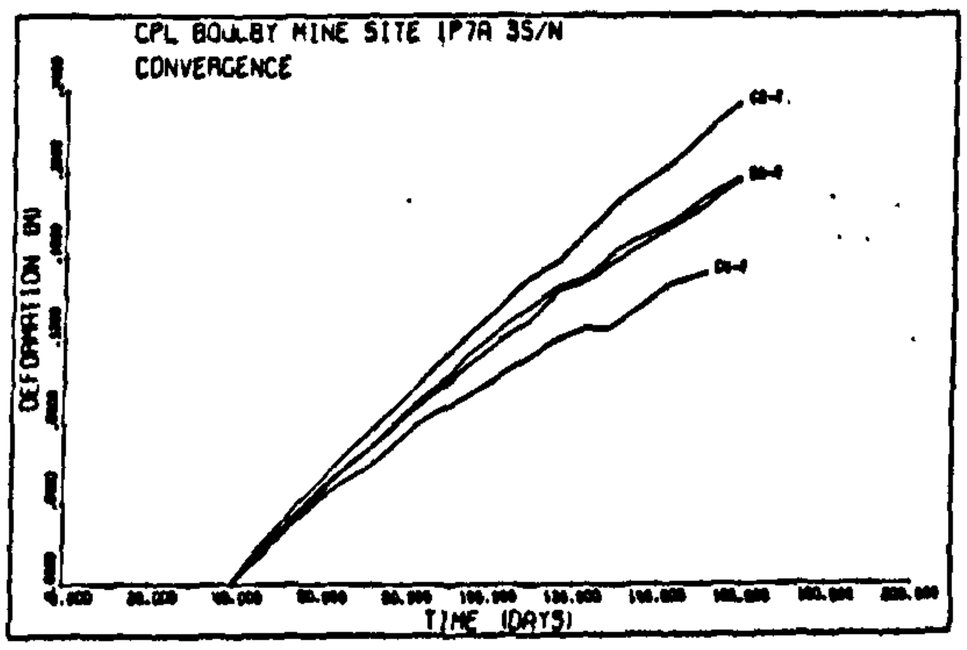
CPL BOULBY MINE SITE IP7A 3S/N
CONVERGENCE
DEFORMATION (M)
TIME (DAYS)

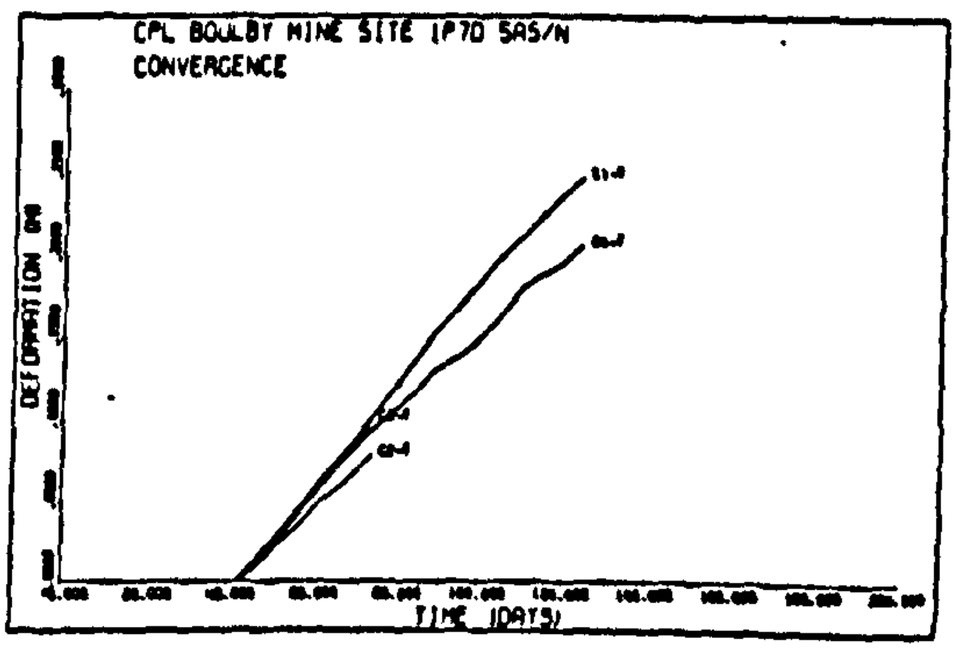
CPL BOULBY MINE SITE IP7D 5AS/N
CONVERGENCE
DEFORMATION (M)
TIME (DAYS)

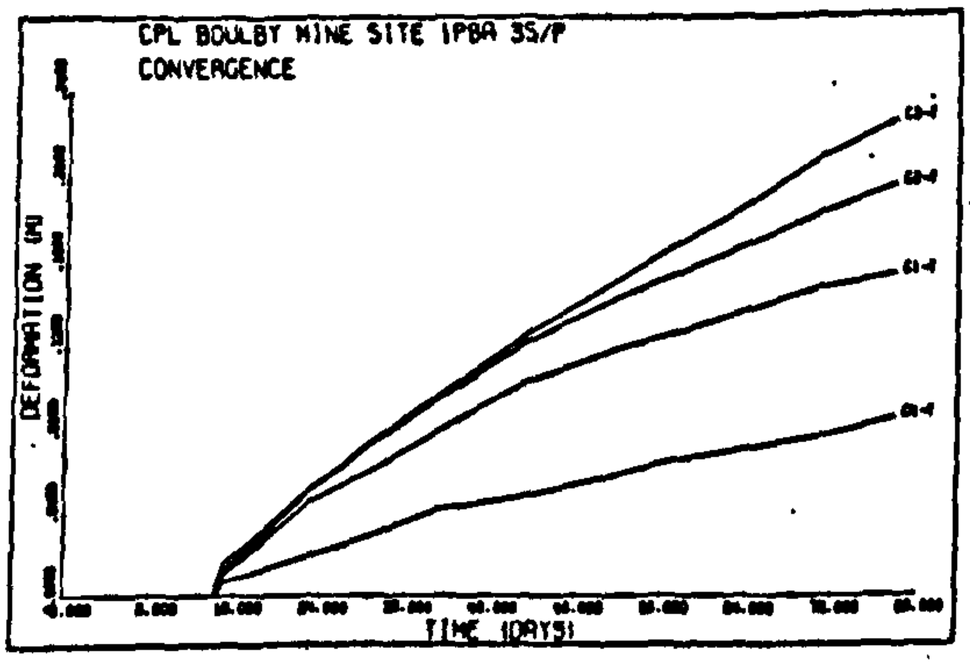
CPL BOULBY MINE SITE IP8A 3S/P
CONVERGENCE
DEFORMATION (M)
TIME (DAYS)

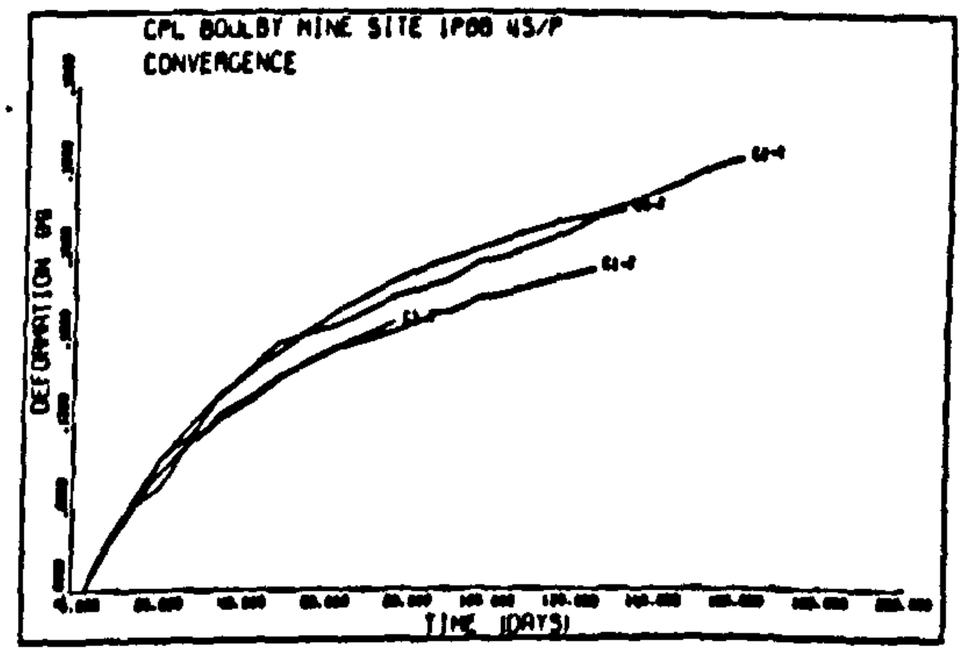
CPL BOULBY MINE SITE IP8B 4S/P
CONVERGENCE
DEFORMATION (M)
TIME (DAYS)

B42

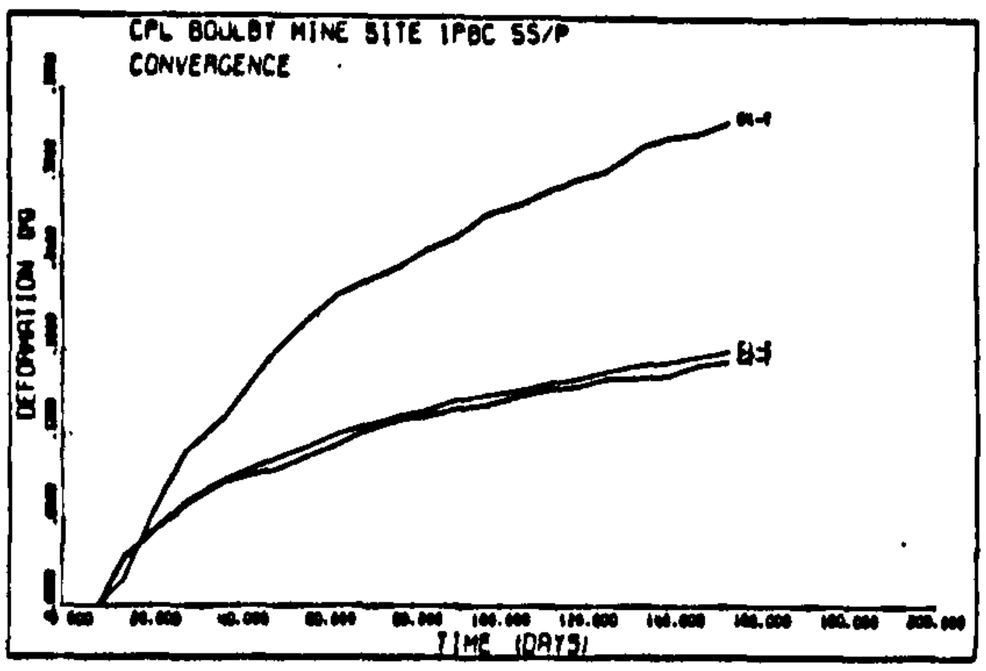
CPL BOULBY MINE SITE IPBC 5S/P
CONVERGENCE
DEFORMATION (MM)
TIME (DAYS)

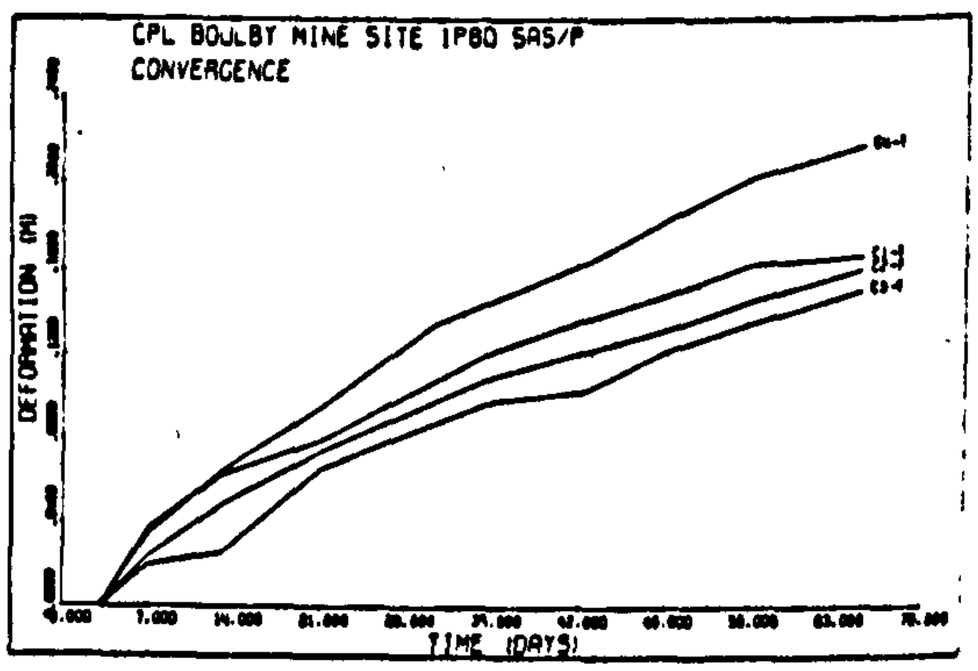
CPL BOULBY MINE SITE IPBD 5AS/P
CONVERGENCE
DEFORMATION (MM)
TIME (DAYS)

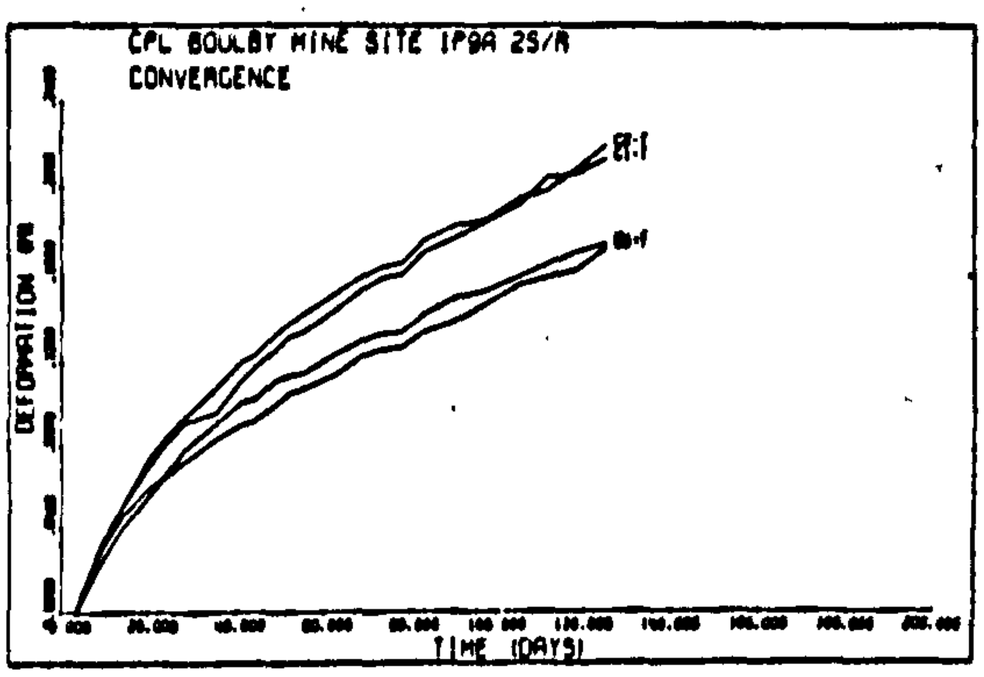
CPL BOULBY MINE SITE IP9A 2S/R
CONVERGENCE
DEFORMATION (MM)
TIME (DAYS)

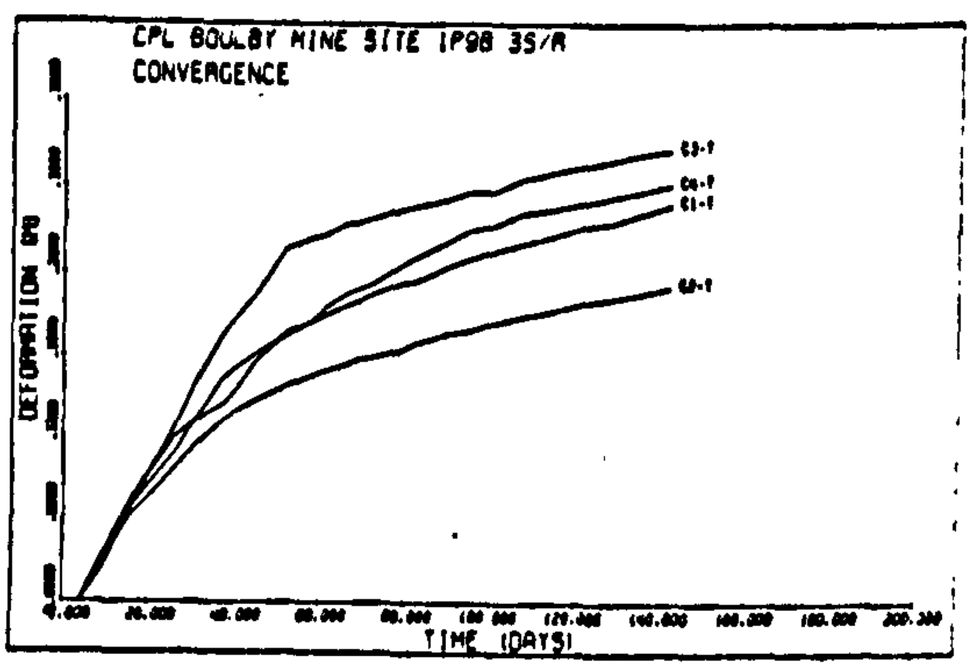
CPL BOULBY MINE SITE IP9B 3S/R
CONVERGENCE
DEFORMATION (MM)
TIME (DAYS)

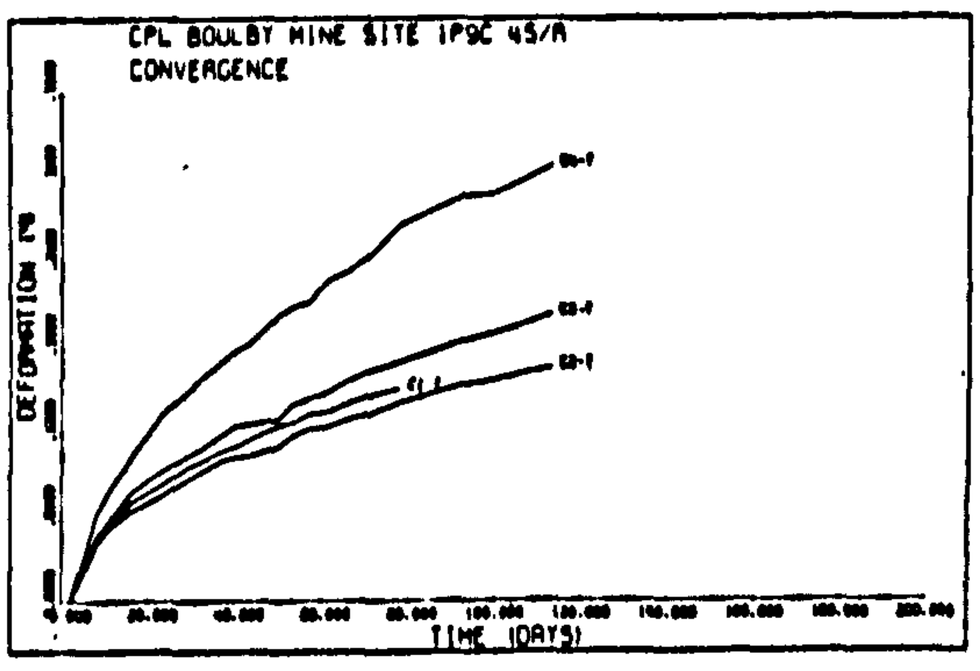
CPL BOULBY MINE SITE IP9C 4S/R
CONVERGENCE
DEFORMATION (MM)
TIME (DAYS)

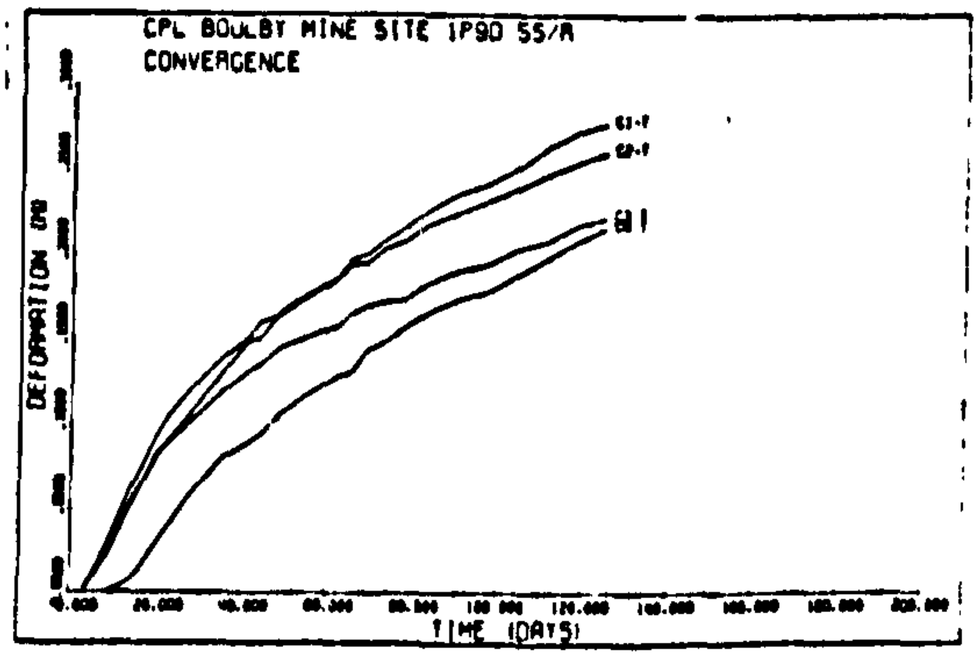
CPL BOULBY MINE SITE IP9D 5S/R
CONVERGENCE
DEFORMATION (MM)
TIME (DAYS)

B43

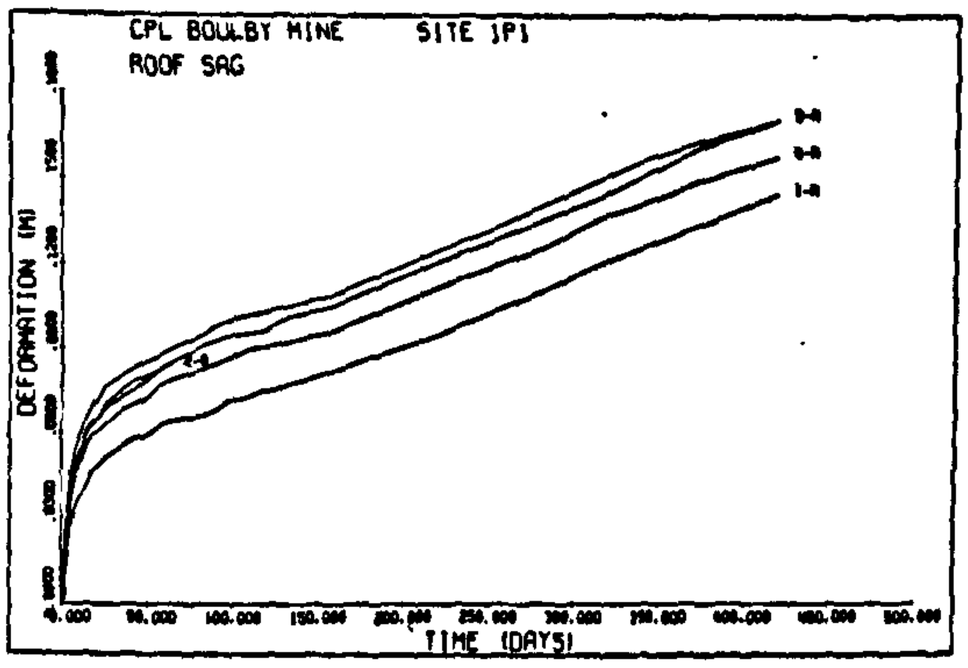
CPL BOULBY MINE SITE IP1
ROOF SAG
DEFORMATION (M)
TIME (DAYS)

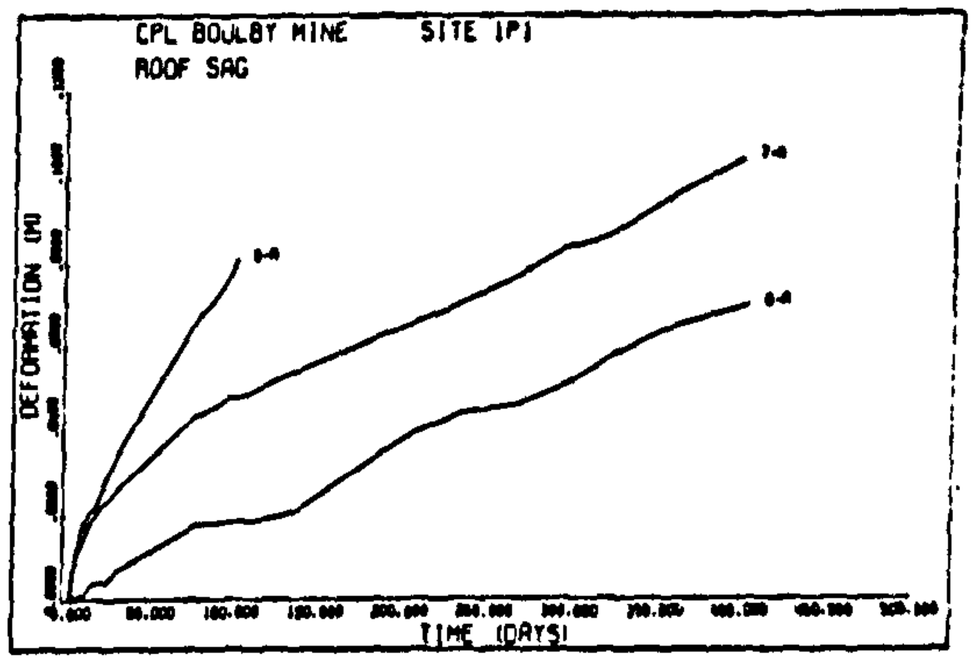
CPL BOULBY MINE SITE IP1
ROOF SAG
DEFORMATION (M)
TIME (DAYS)

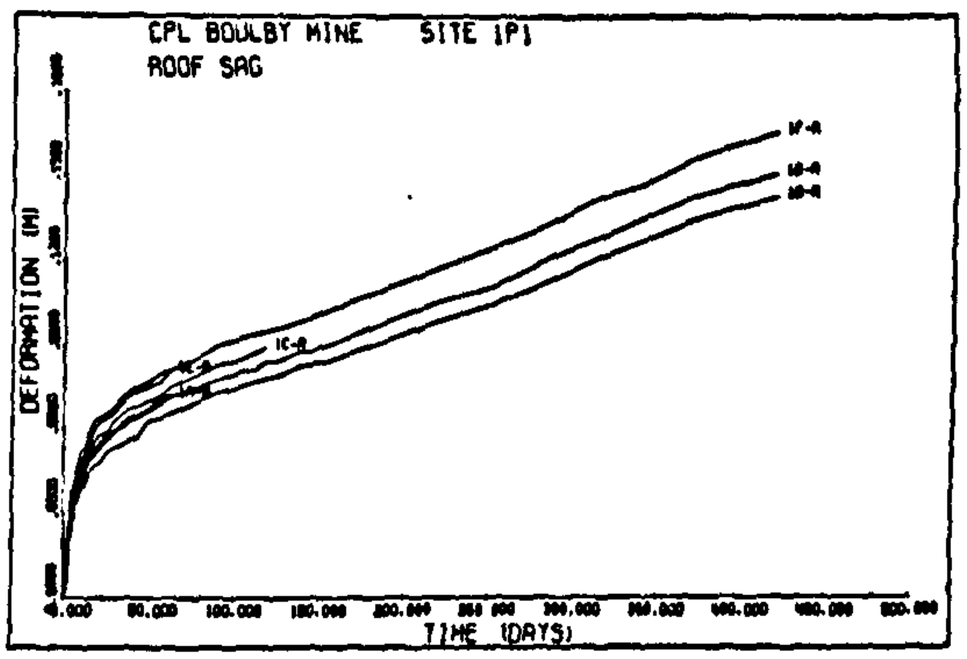
CPL BOULBY MINE SITE IP1
ROOF SAG
DEFORMATION (M)
TIME (DAYS)

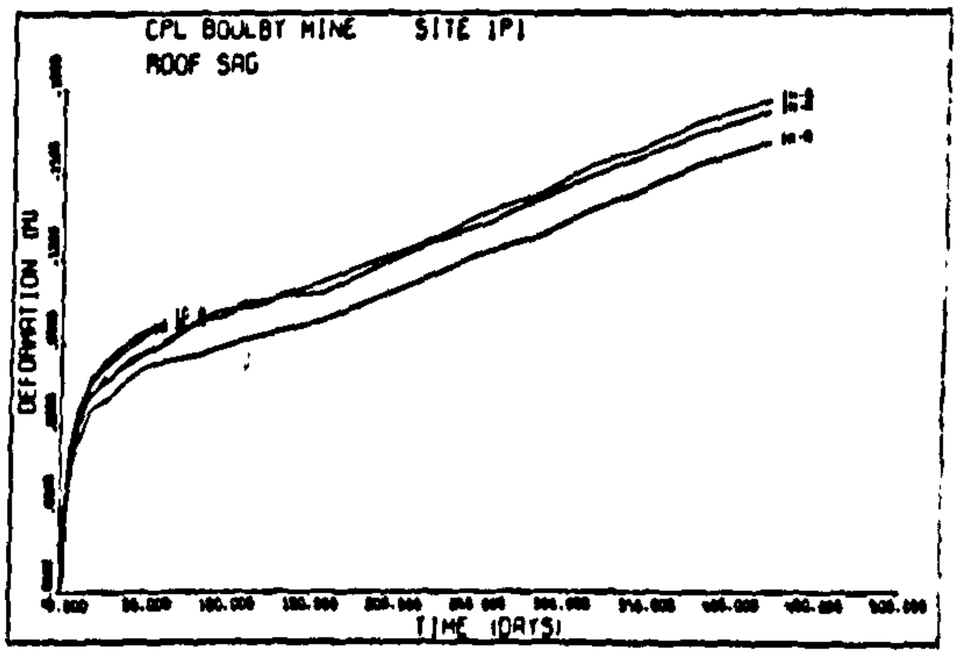
CPL BOULBY MINE SITE IP1
ROOF SAG
DEFORMATION (M)
TIME (DAYS)

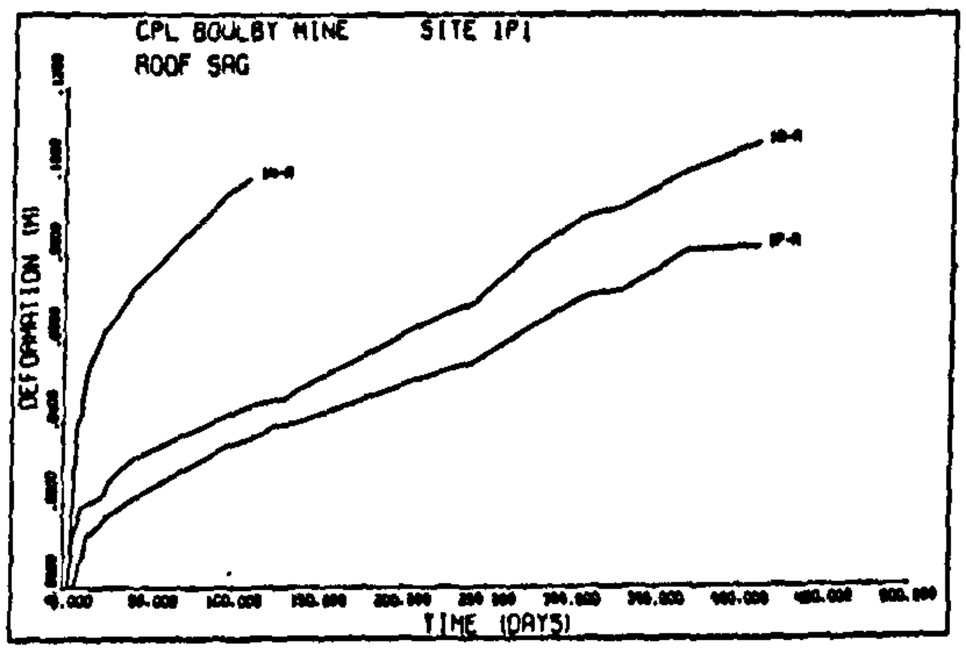
CPL BOULBY MINE SITE IP1
ROOF SAG
DEFORMATION (M)
TIME (DAYS)

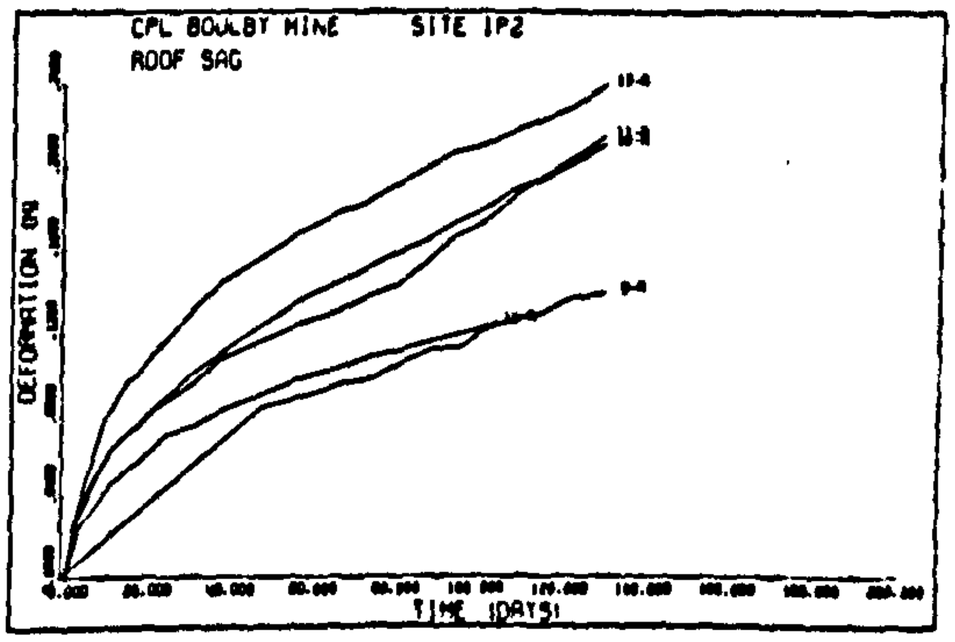
CPL BOULBY MINE SITE IP2
ROOF SAG
DEFORMATION (M)
TIME (DAYS)

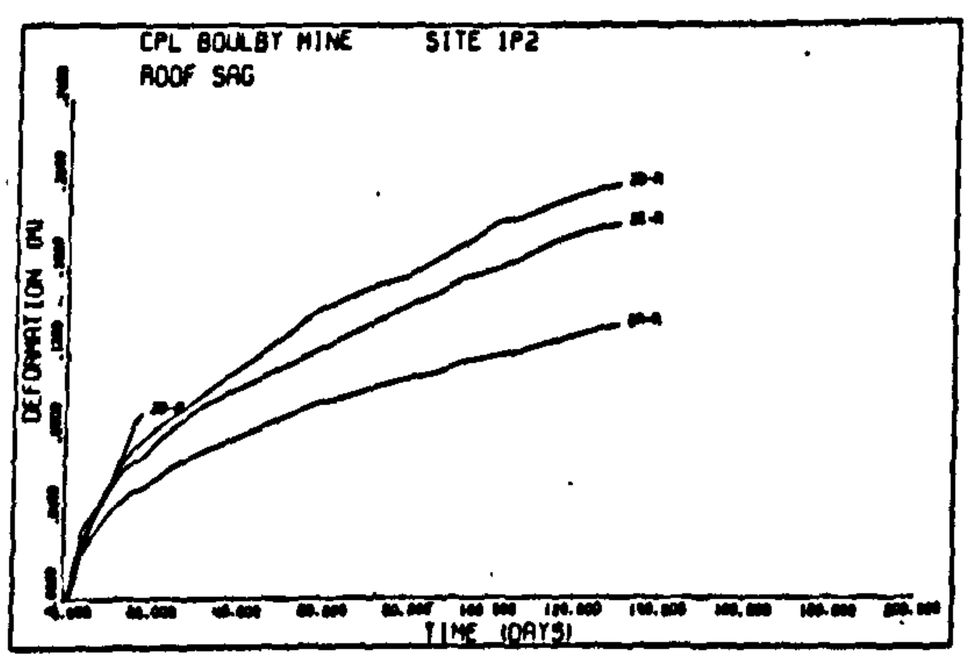
CPL BOULBY MINE SITE IP2
ROOF SAG
DEFORMATION (M)
TIME (DAYS)

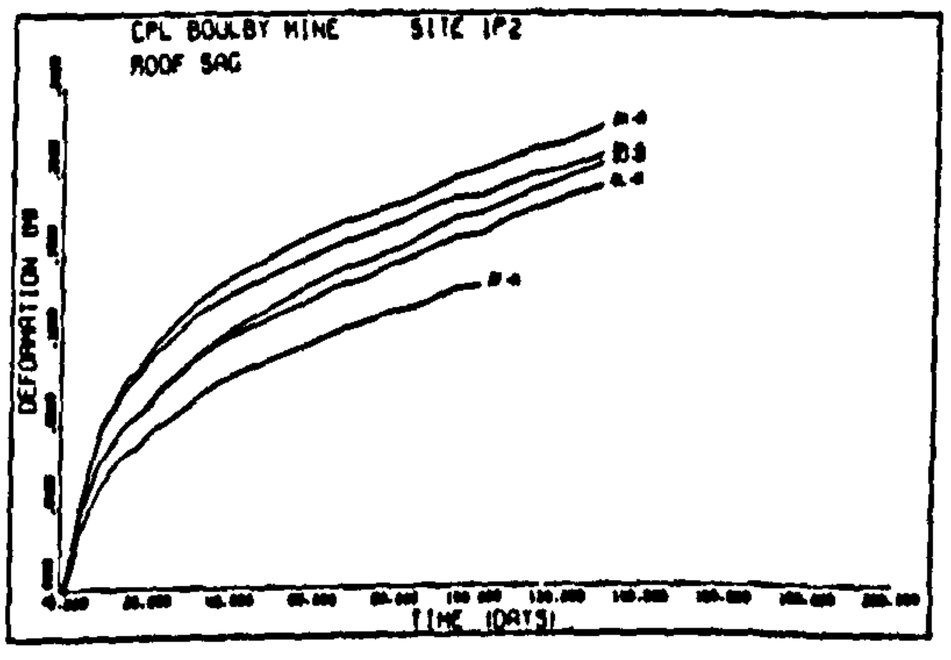
CPL BOULBY MINE SITE IP2
ROOF SAG
DEFORMATION (M)
TIME (DAYS)

B44

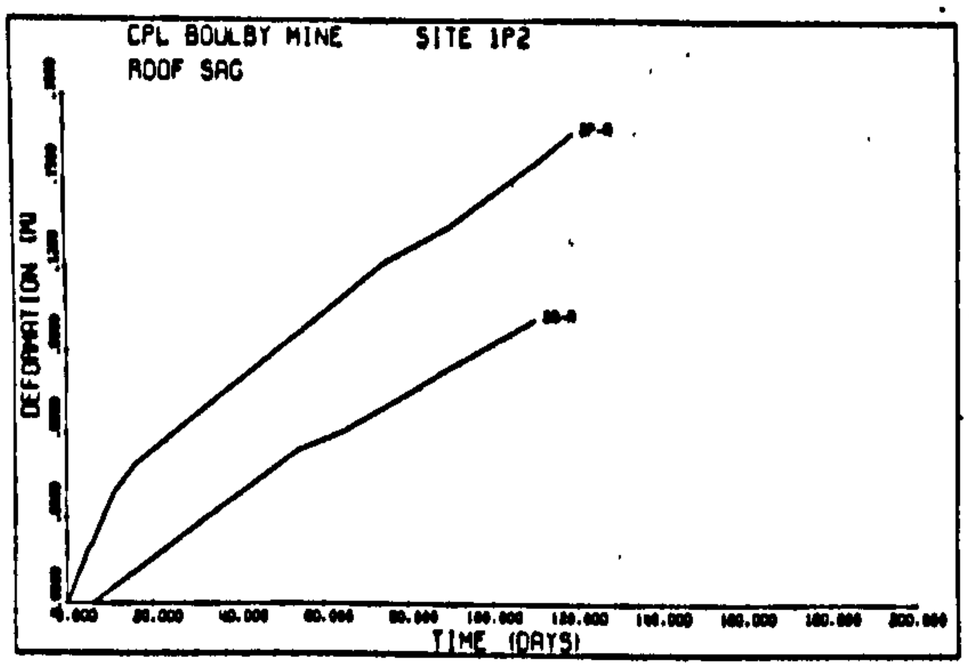
CPL BOULBY MINE SITE 1P2
ROOF SAG
DEFORMATION (MM)
TIME (DAYS)

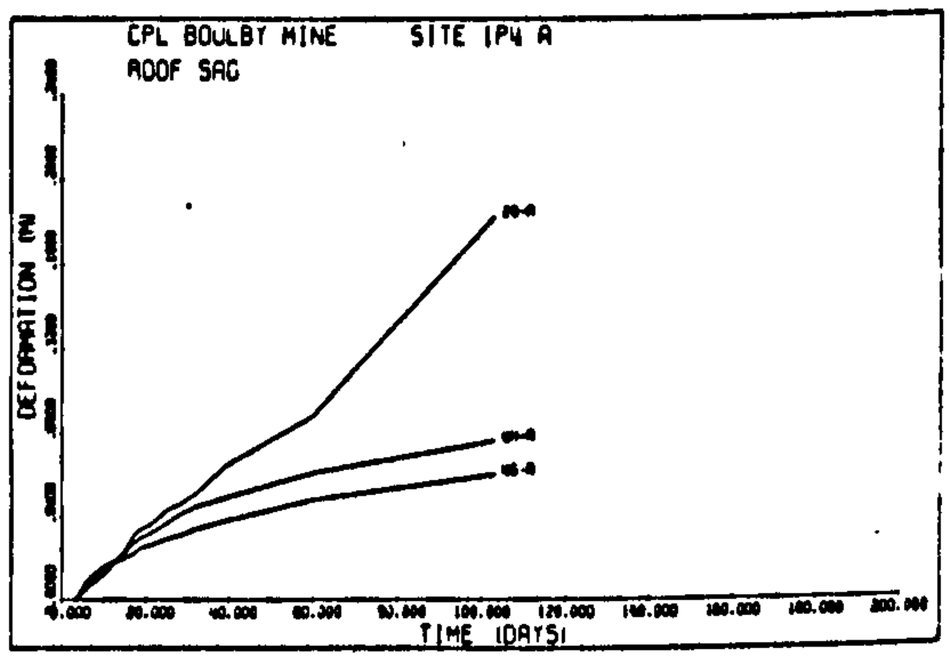
CPL BOULBY MINE SITE 1P4 A
ROOF SAG
DEFORMATION (MM)
TIME (DAYS)

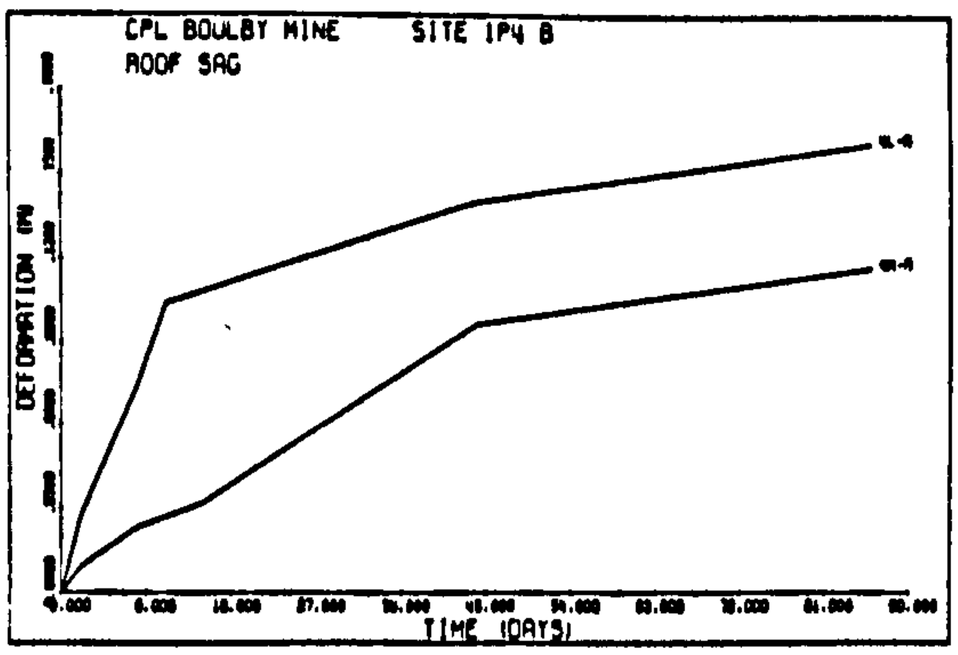
CPL BOULBY MINE SITE 1P4 B
ROOF SAG
DEFORMATION (MM)
TIME (DAYS)

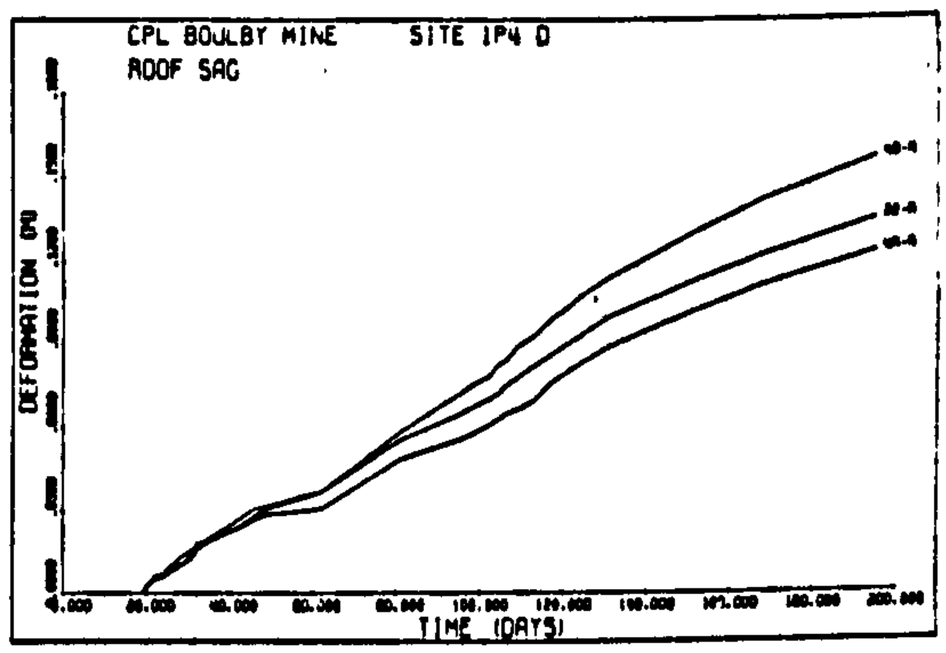
CPL BOULBY MINE SITE 1P4 D
ROOF SAG
DEFORMATION (MM)
TIME (DAYS)

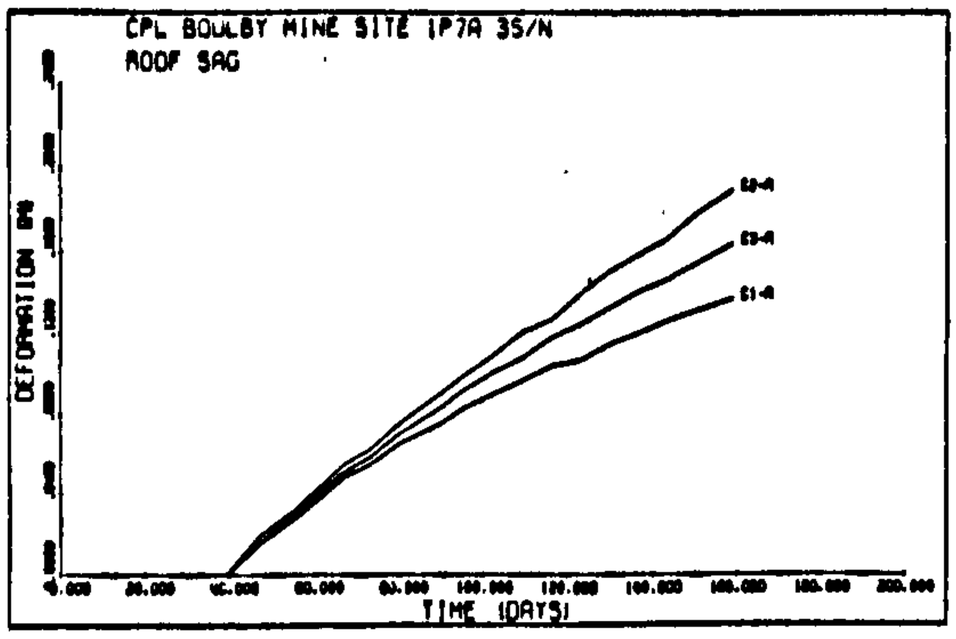
CPL BOULBY MINE SITE 1P7A 35/N
ROOF SAG
DEFORMATION (MM)
TIME (DAYS)

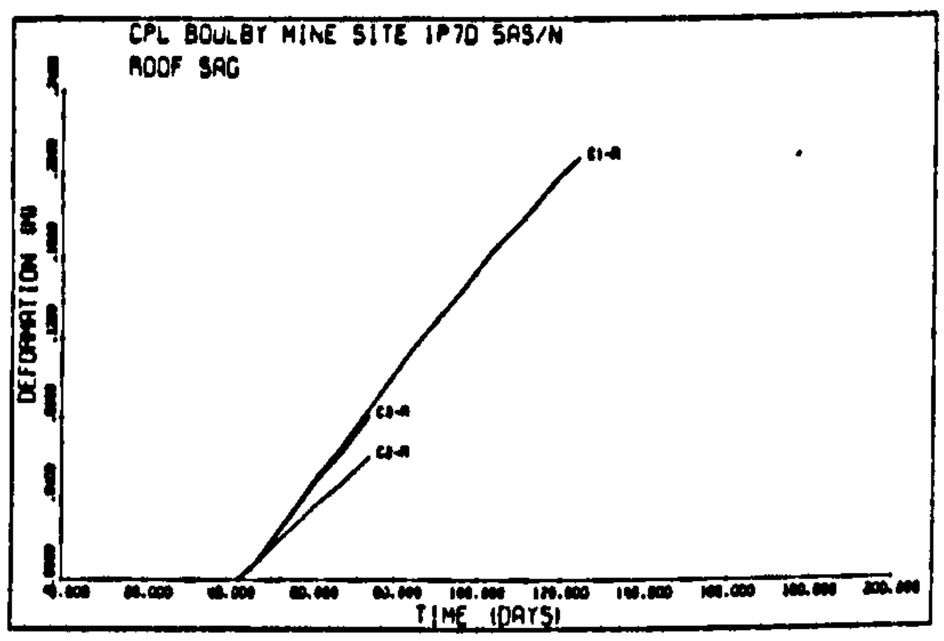
CPL BOULBY MINE SITE 1P7D 585/N
ROOF SAG
DEFORMATION (MM)
TIME (DAYS)

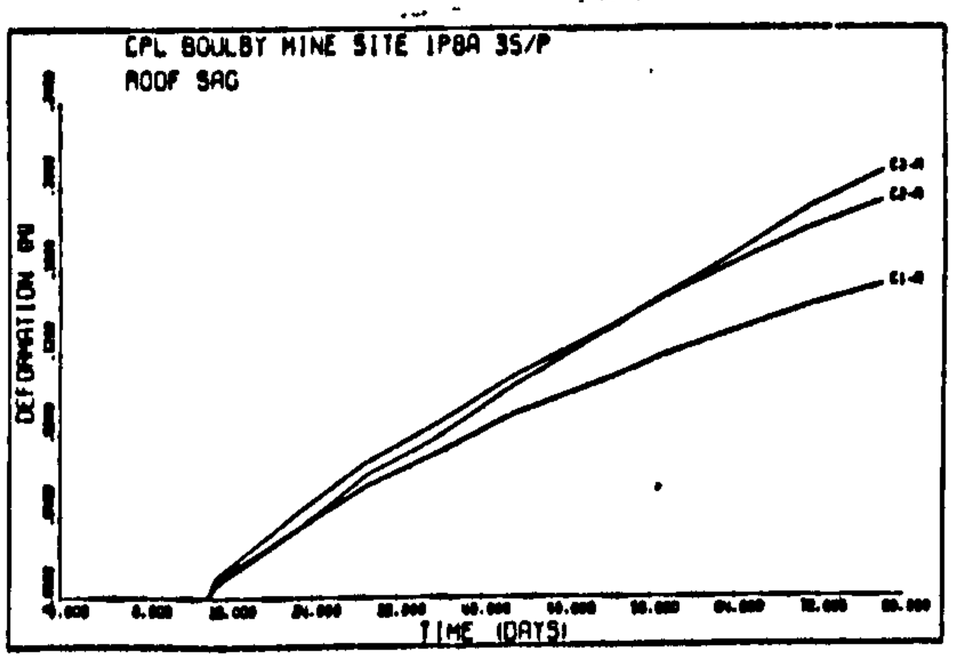
CPL BOULBY MINE SITE 1P8A 35/P
ROOF SAG
DEFORMATION (MM)
TIME (DAYS)

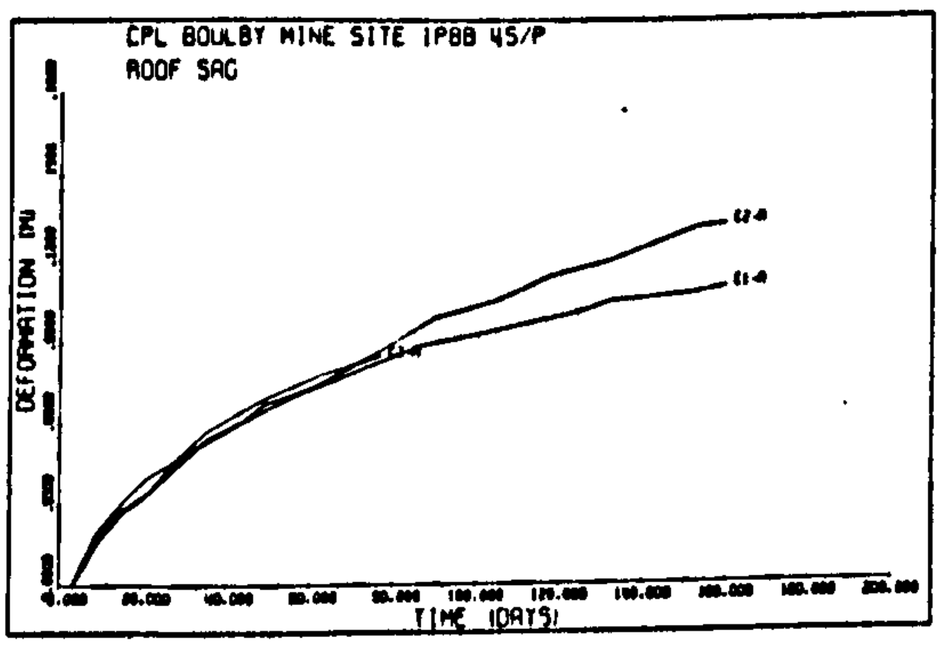
CPL BOULBY MINE SITE 1P8B 45/P
ROOF SAG
DEFORMATION (MM)
TIME (DAYS)

B45

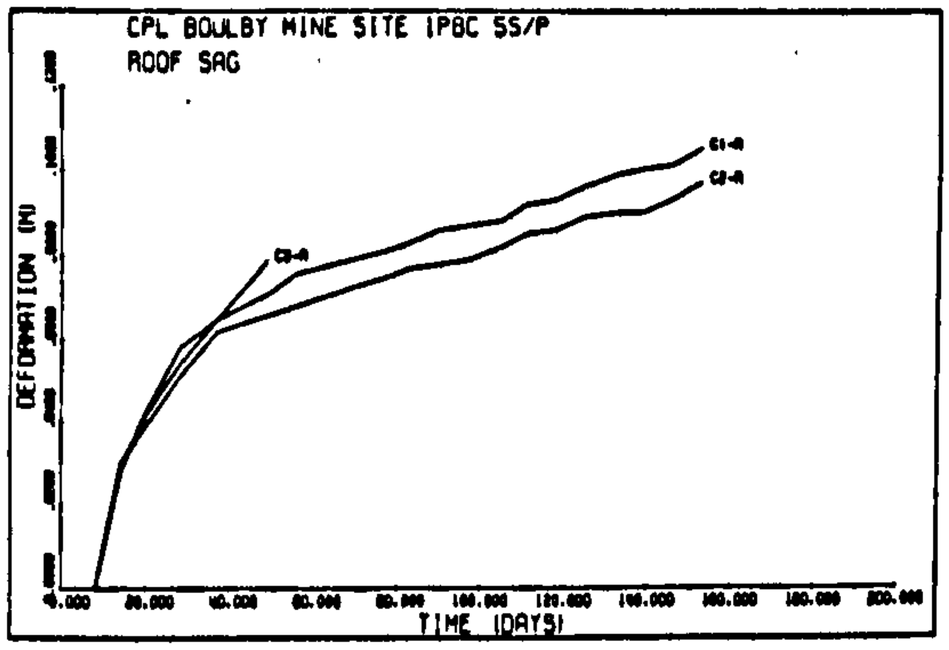
CPL BOULBY MINE SITE IP8C 5S/P
ROOF SAG
DEFORMATION (M)
TIME (DAYS)

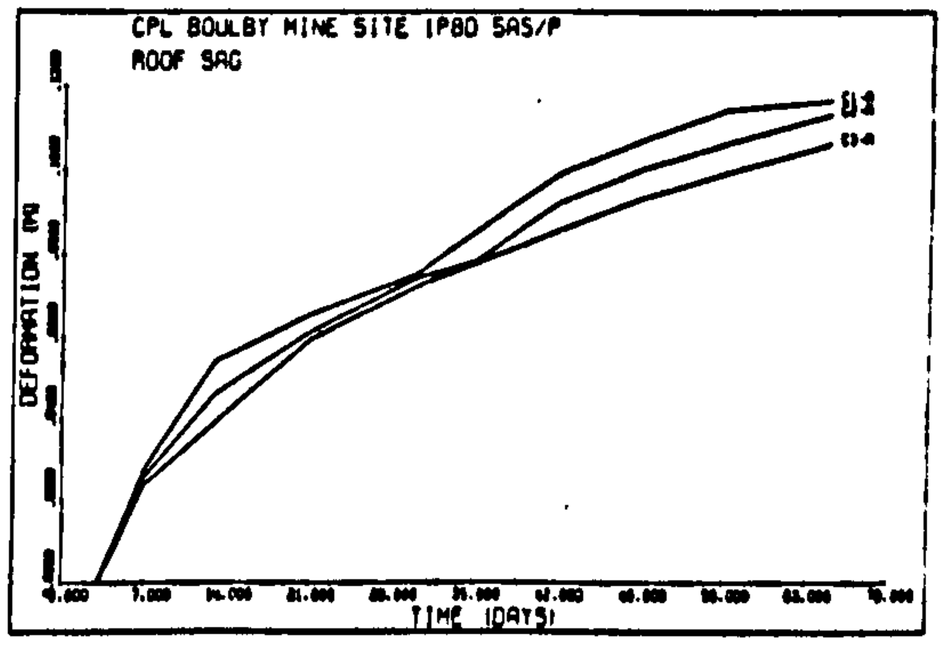
CPL BOULBY MINE SITE IP8D 5AS/P
ROOF SAG
DEFORMATION (M)
TIME (DAYS)

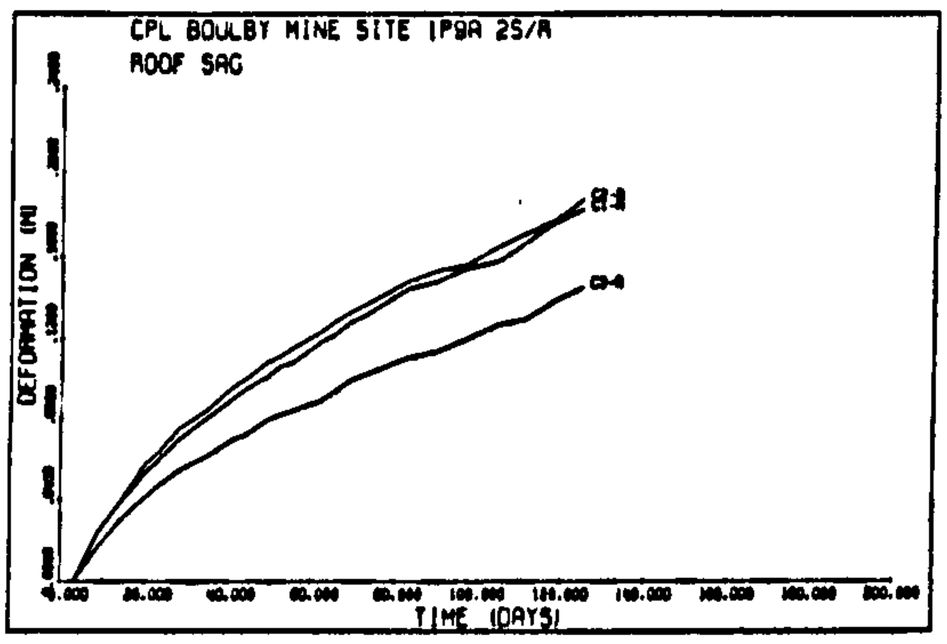
CPL BOULBY MINE SITE IP8A 2S/A
ROOF SAG
DEFORMATION (M)
TIME (DAYS)

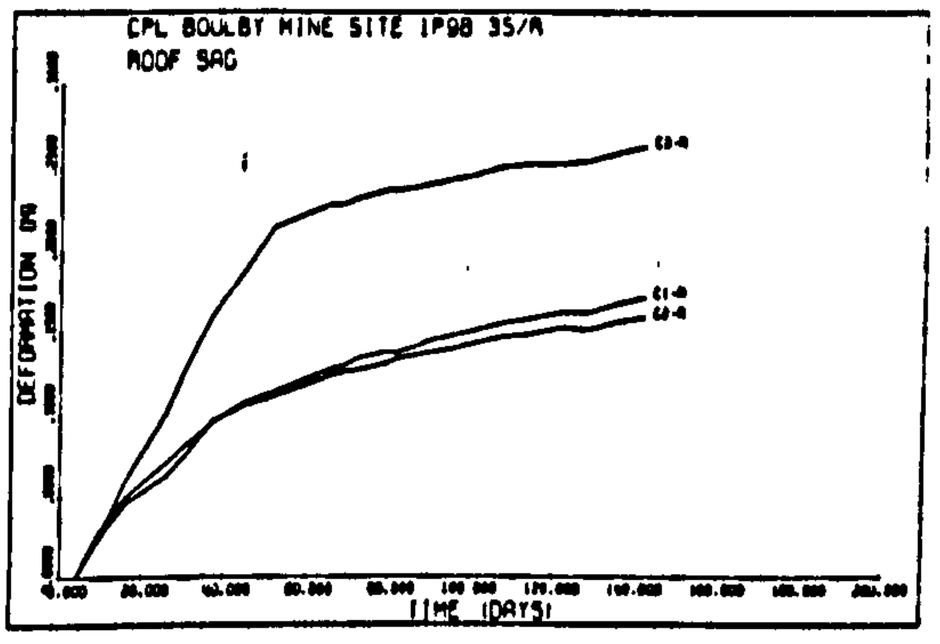
CPL BOULBY MINE SITE IP8B 3S/A
ROOF SAG
DEFORMATION (M)
TIME (DAYS)

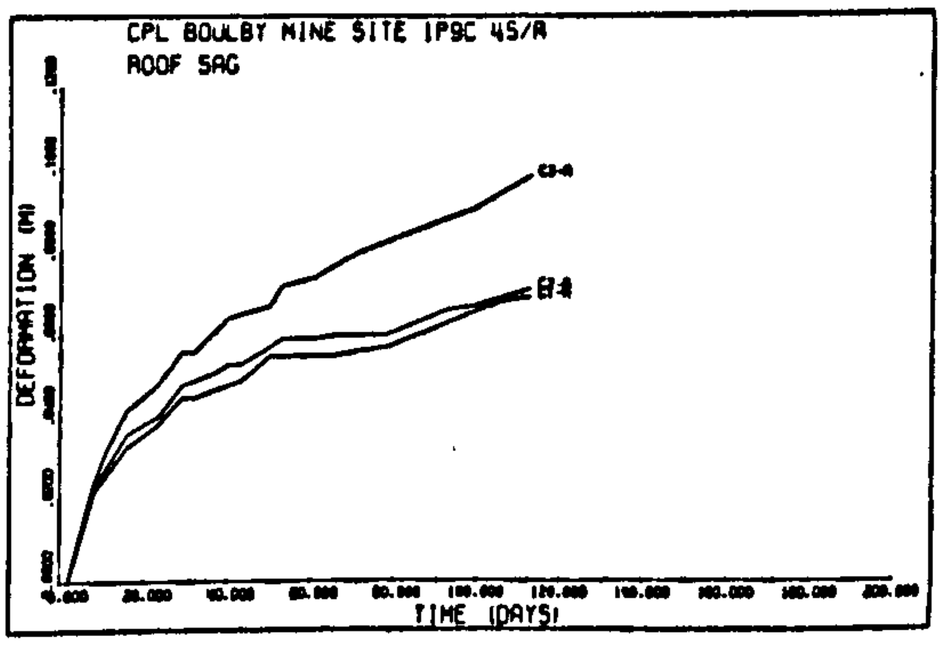
CPL BOULBY MINE SITE IP8C 4S/A
ROOF SAG
DEFORMATION (M)
TIME (DAYS)

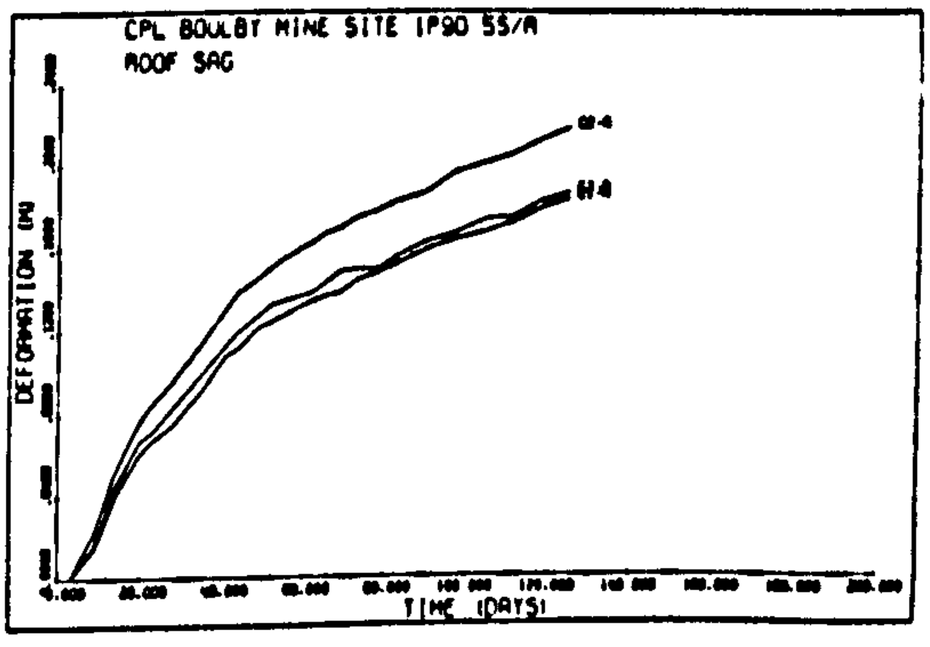
CPL BOULBY MINE SITE IP8D 5S/A
ROOF SAG
DEFORMATION (M)
TIME (DAYS)

B46

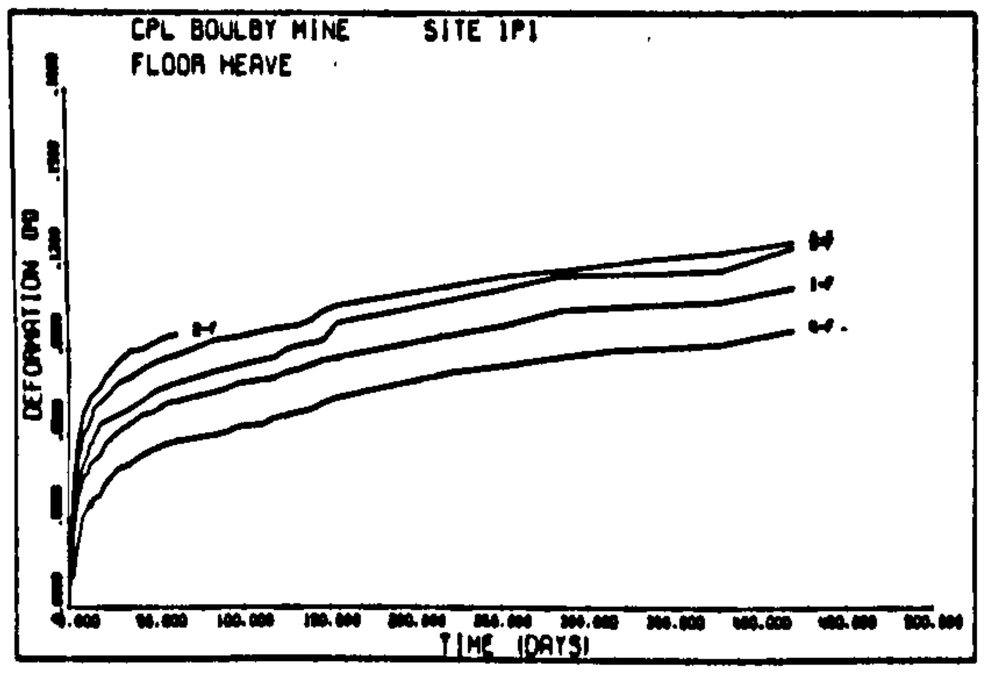
CPL BOULBY MINE SITE IP1
FLOOR HEAVE
DEFORMATION (M)
TIME (DAYS)

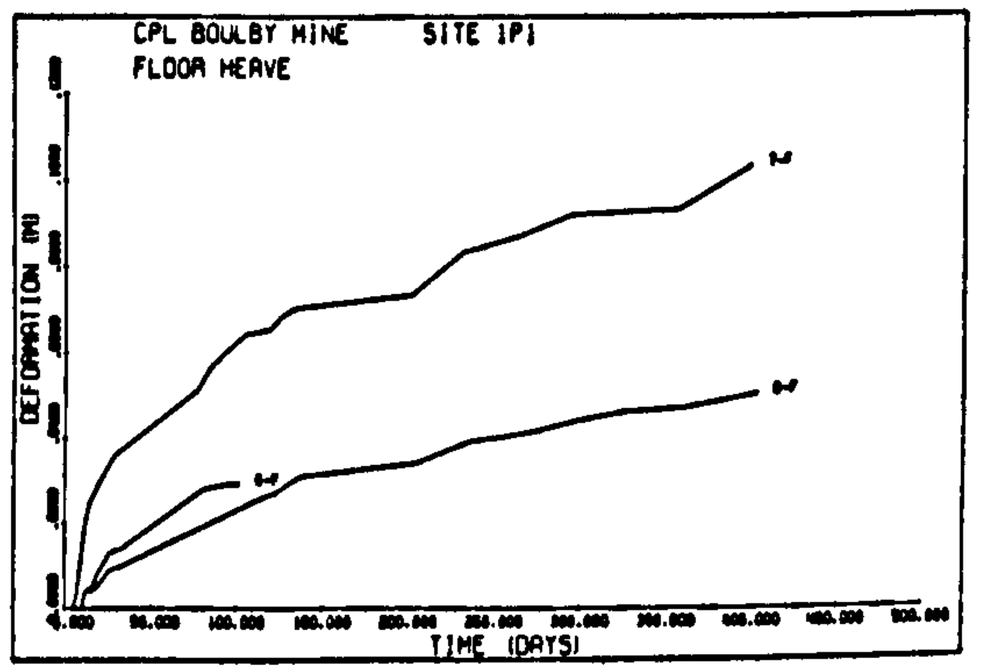
CPL BOULBY MINE SITE IP1
FLOOR HEAVE
DEFORMATION (M)
TIME (DAYS)

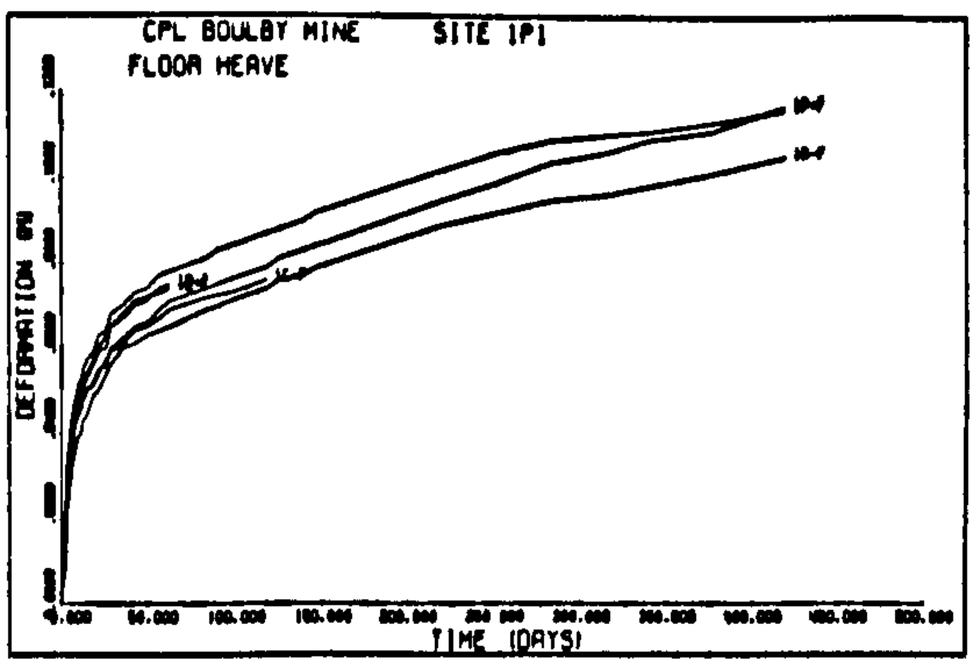
CPL BOULBY MINE SITE IP1
FLOOR HEAVE
DEFORMATION (M)
TIME (DAYS)

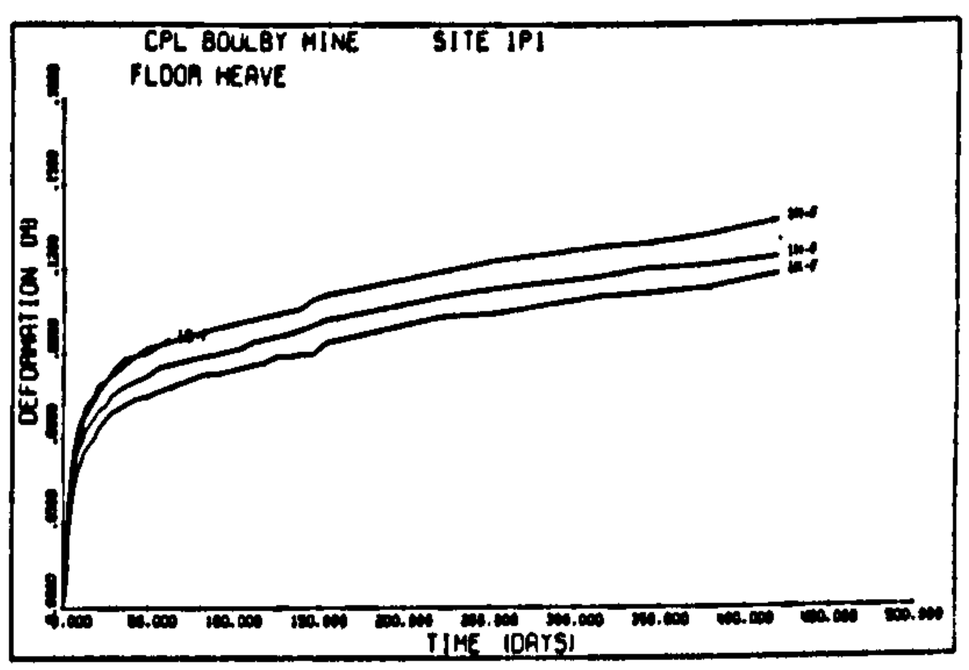
CPL BOULBY MINE SITE IP1
FLOOR HEAVE
DEFORMATION (M)
TIME (DAYS)

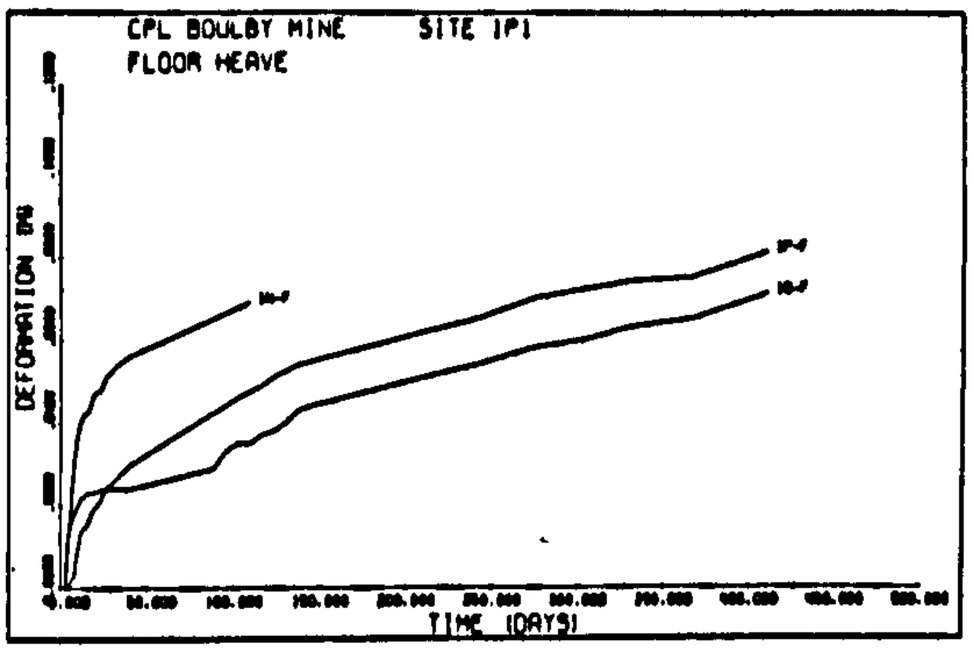
CPL BOULBY MINE SITE IP1
FLOOR HEAVE
DEFORMATION (M)
TIME (DAYS)

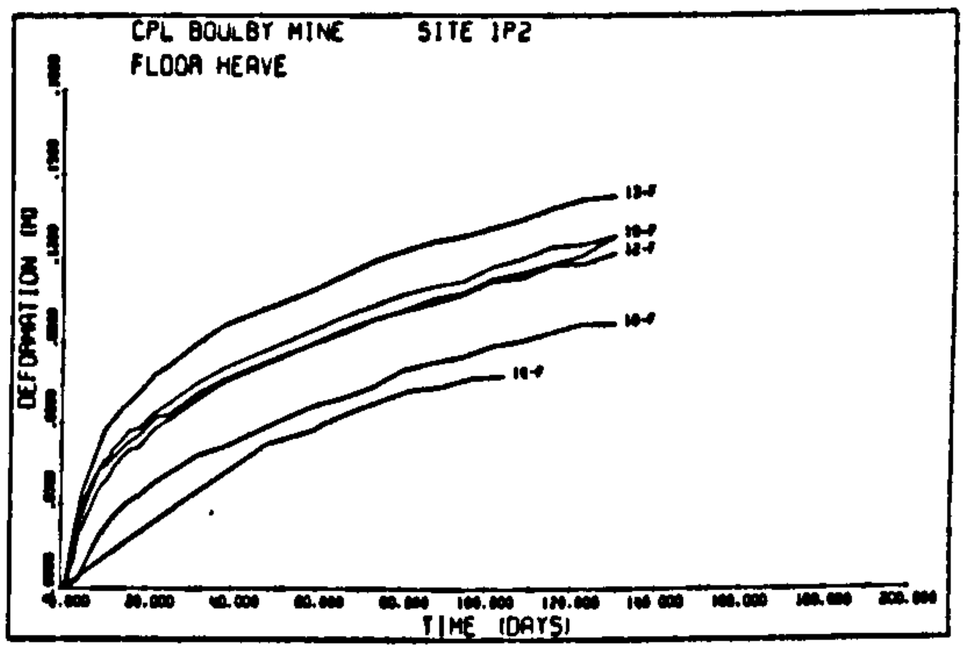
CPL BOULBY MINE SITE IP2
FLOOR HEAVE
DEFORMATION (M)
TIME (DAYS)

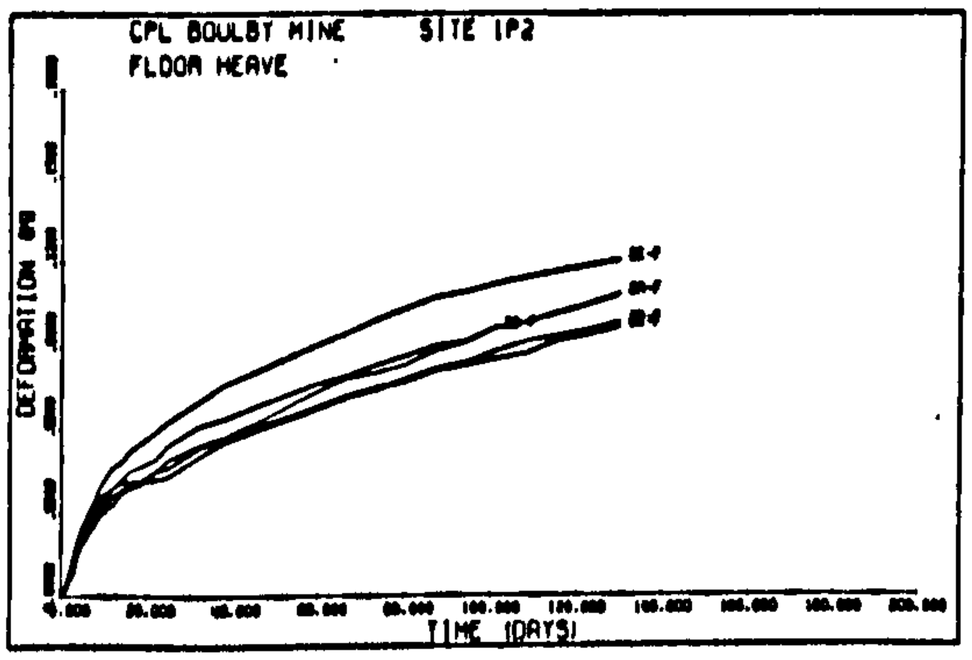
CPL BOULBY MINE SITE IP2
FLOOR HEAVE
DEFORMATION (M)
TIME (DAYS)

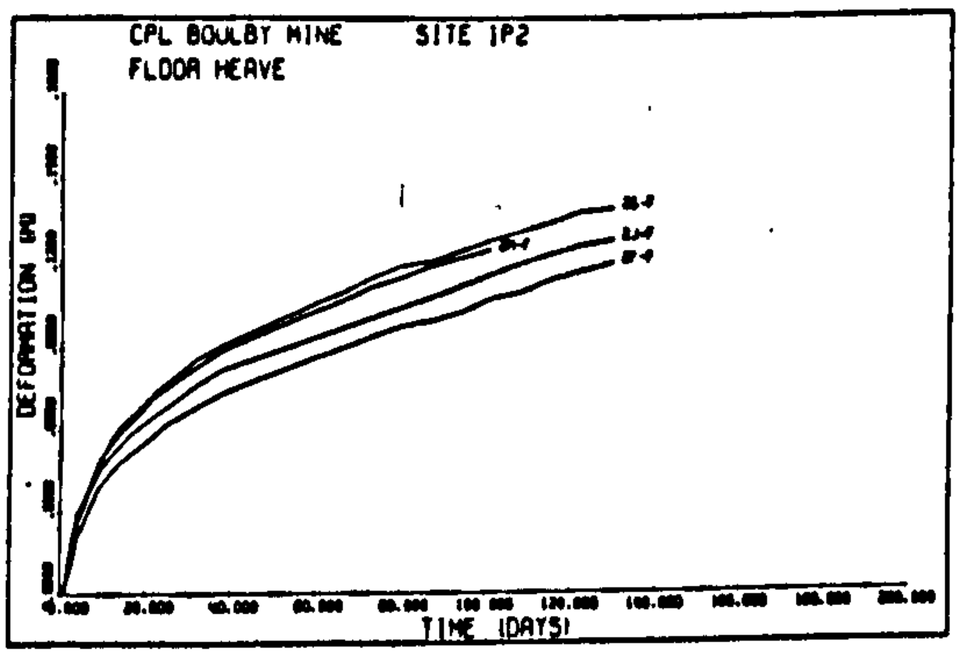
CPL BOULBY MINE SITE IP2
FLOOR HEAVE
DEFORMATION (M)
TIME (DAYS)

B47

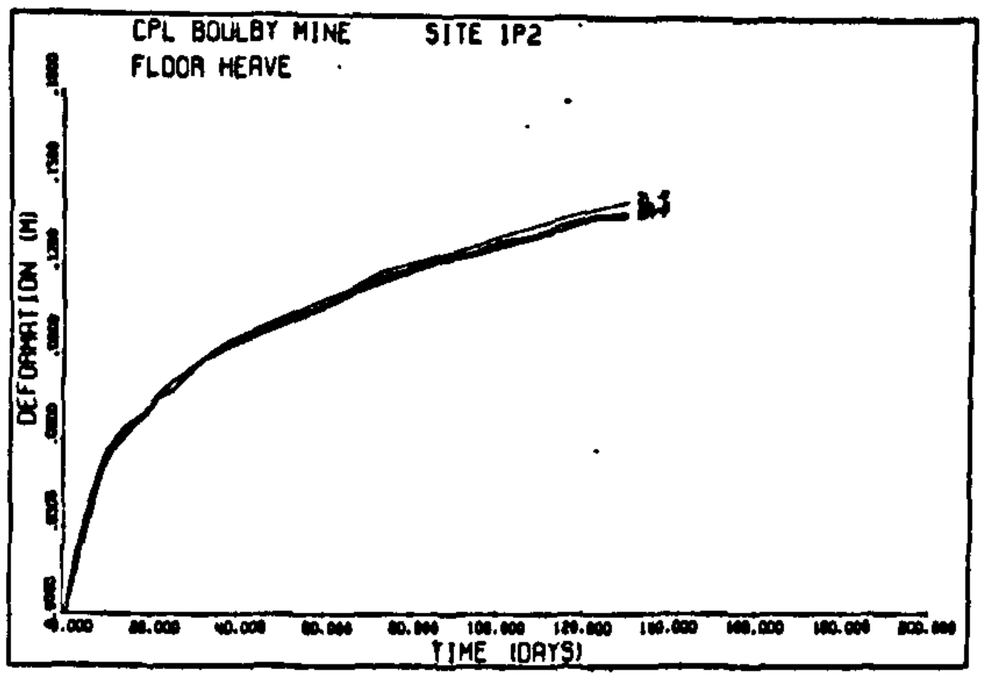
CPL BOULBY MINE SITE IP2
FLOOR HEAVE
DEFORMATION (M)
TIME (DAYS)

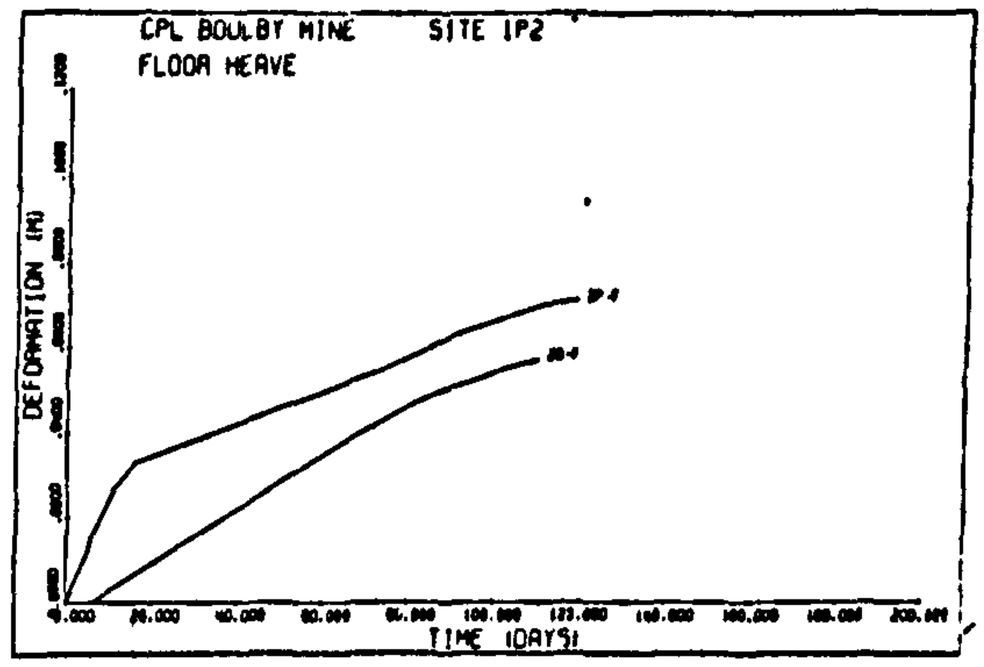
CPL BOULBY MINE SITE IP2
FLOOR HEAVE
DEFORMATION (M)
TIME (DAYS)

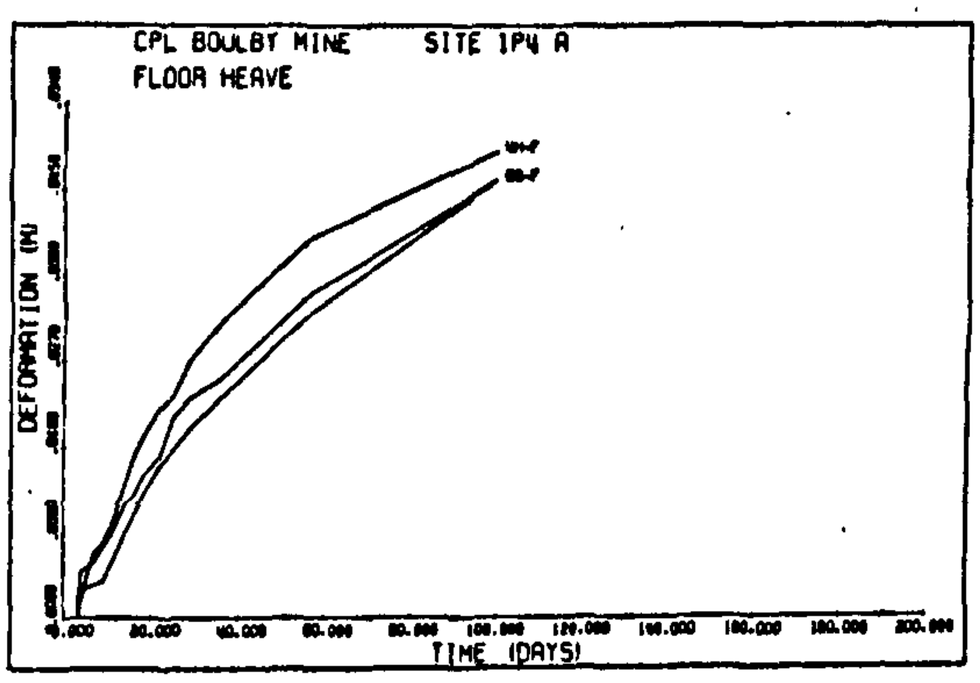
CPL BOULBY MINE SITE IP4 A
FLOOR HEAVE
DEFORMATION (M)
TIME (DAYS)

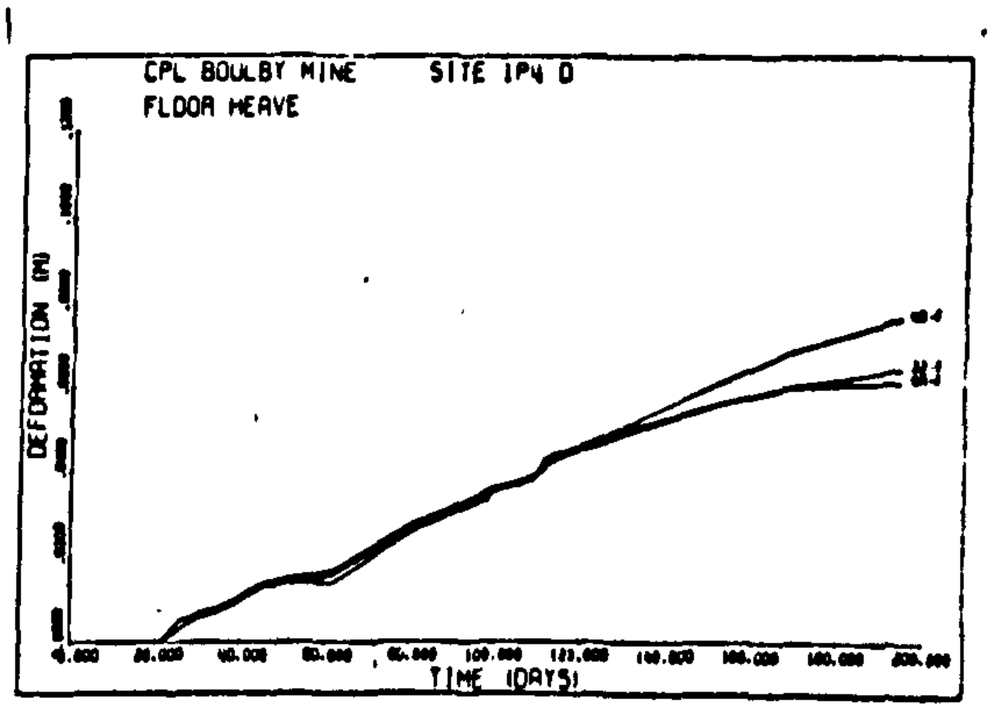
CPL BOULBY MINE SITE IP4 D
FLOOR HEAVE
DEFORMATION (M)
TIME (DAYS)

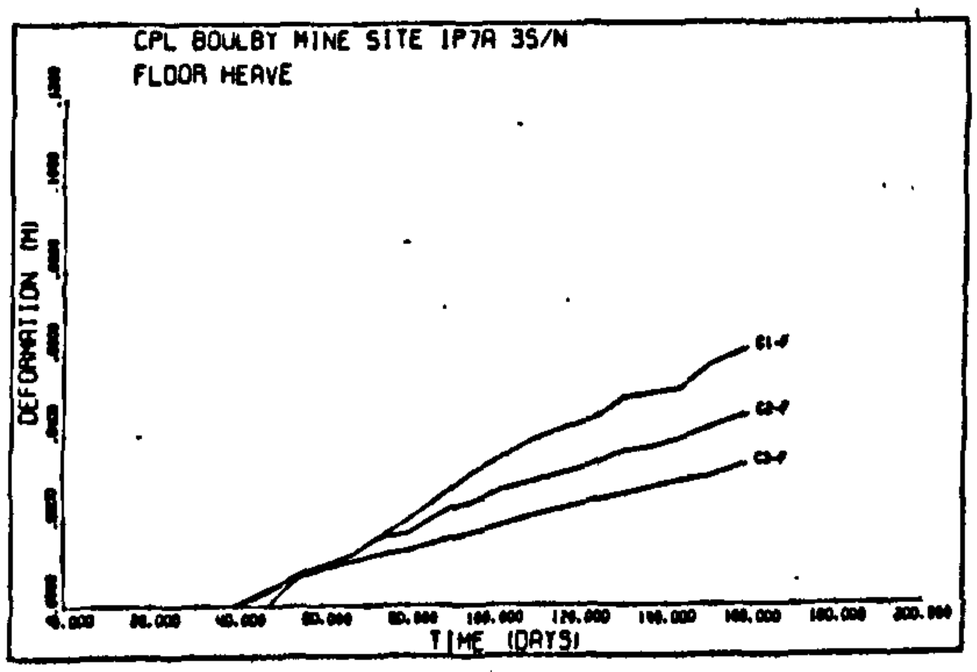
CPL BOULBY MINE SITE IP7A 3S/N
FLOOR HEAVE
DEFORMATION (M)
TIME (DAYS)

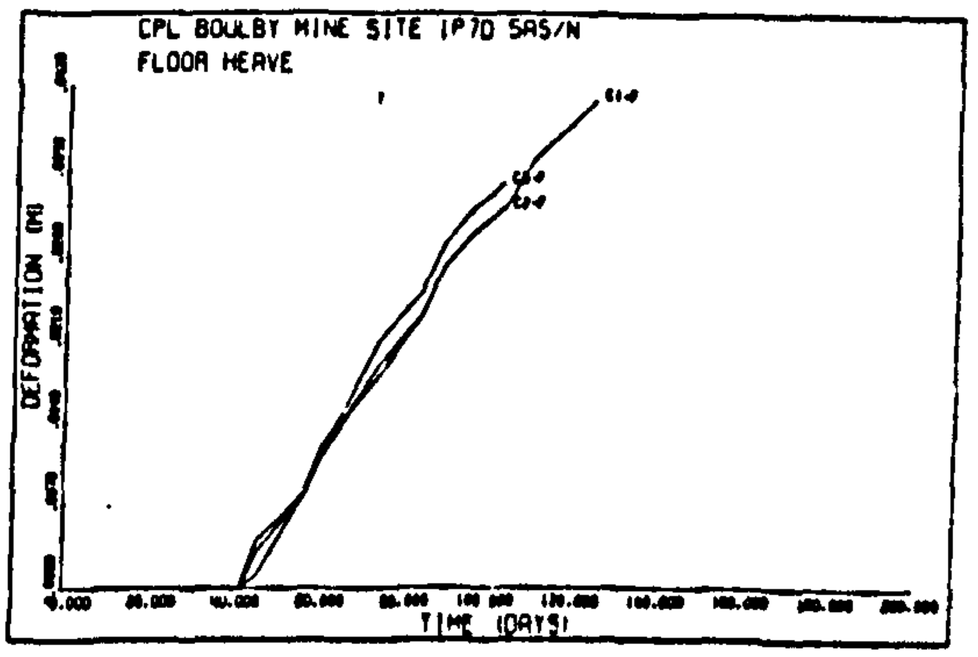
CPL BOULBY MINE SITE IP7D 5AS/N
FLOOR HEAVE
DEFORMATION (M)
TIME (DAYS)

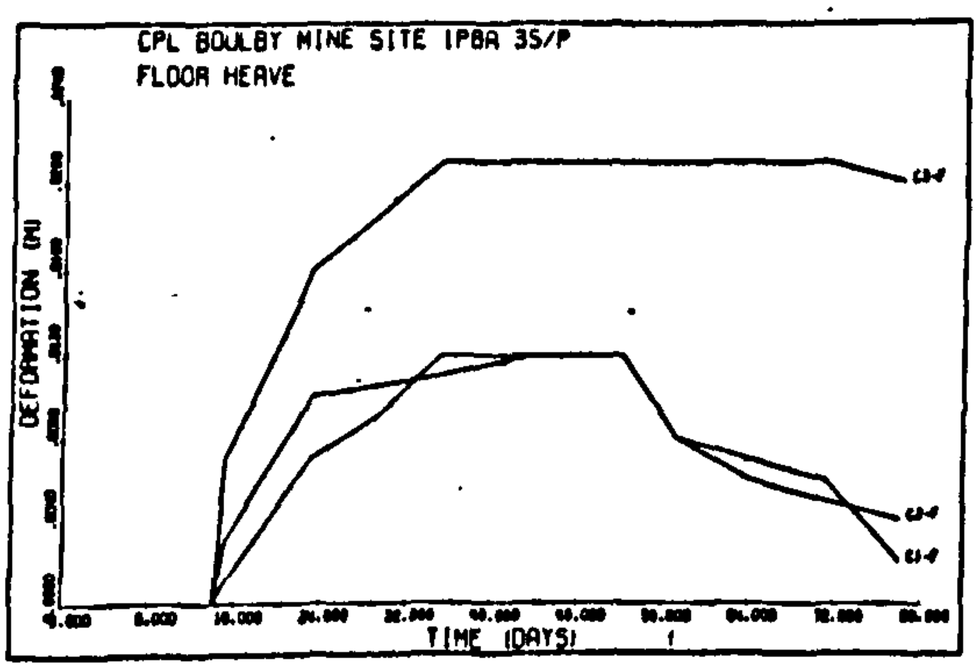
CPL BOULBY MINE SITE IP8A 3S/P
FLOOR HEAVE
DEFORMATION (M)
TIME (DAYS)

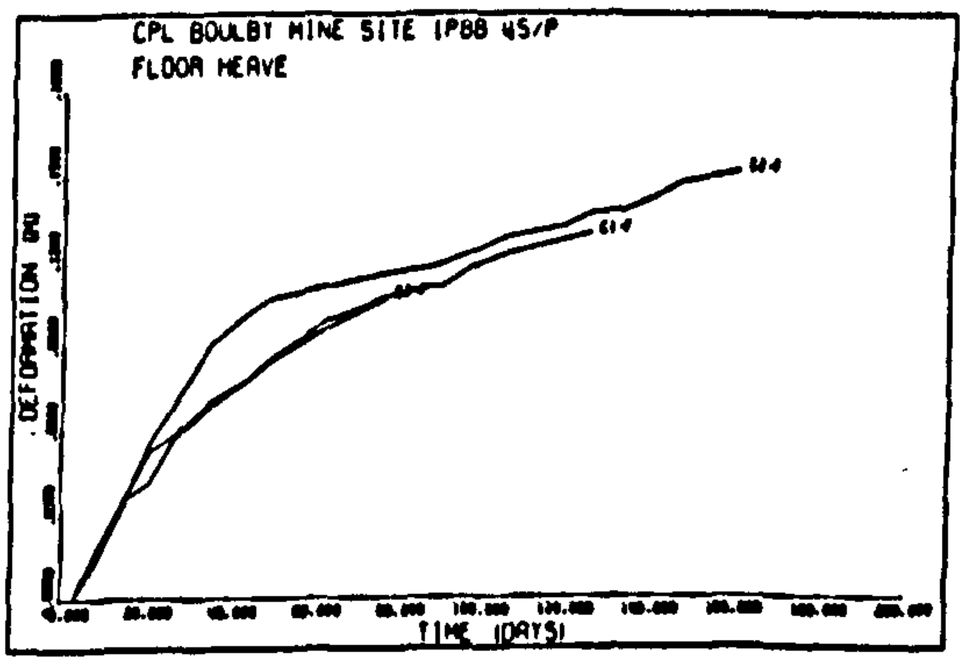
CPL BOULBY MINE SITE IP8B 4S/P
FLOOR HEAVE
DEFORMATION (M)
TIME (DAYS)

B48

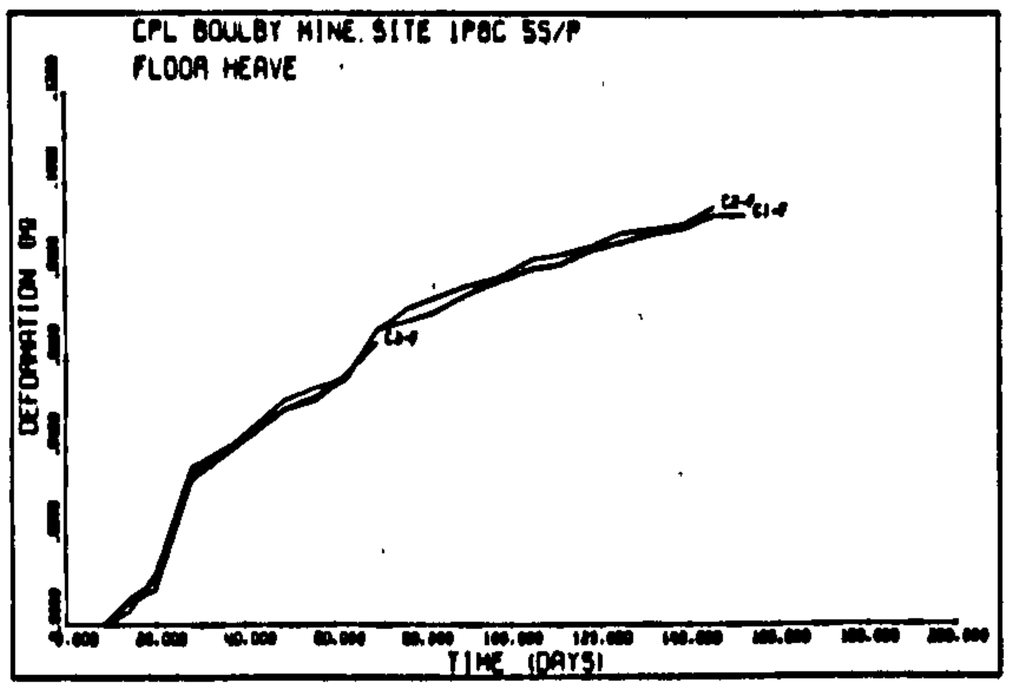
CPL BOULBY MINE SITE IP8C 5S/P
FLOOR HEAVE
DEFORMATION (M)
TIME (DAYS)

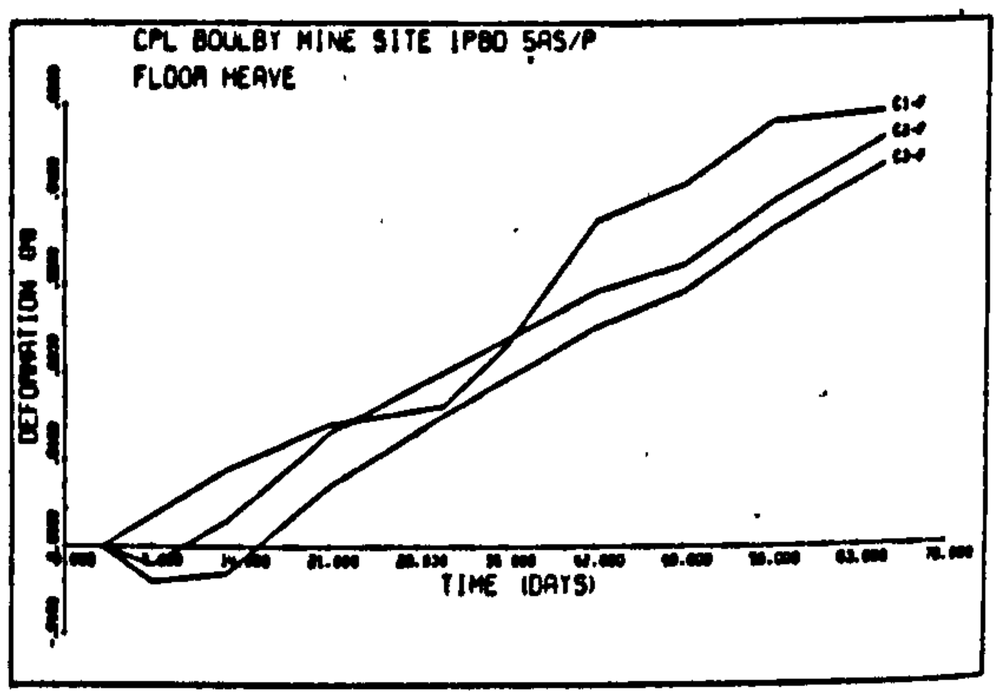
CPL BOULBY MINE SITE IP8D 5AS/P
FLOOR HEAVE
DEFORMATION (M)
TIME (DAYS)

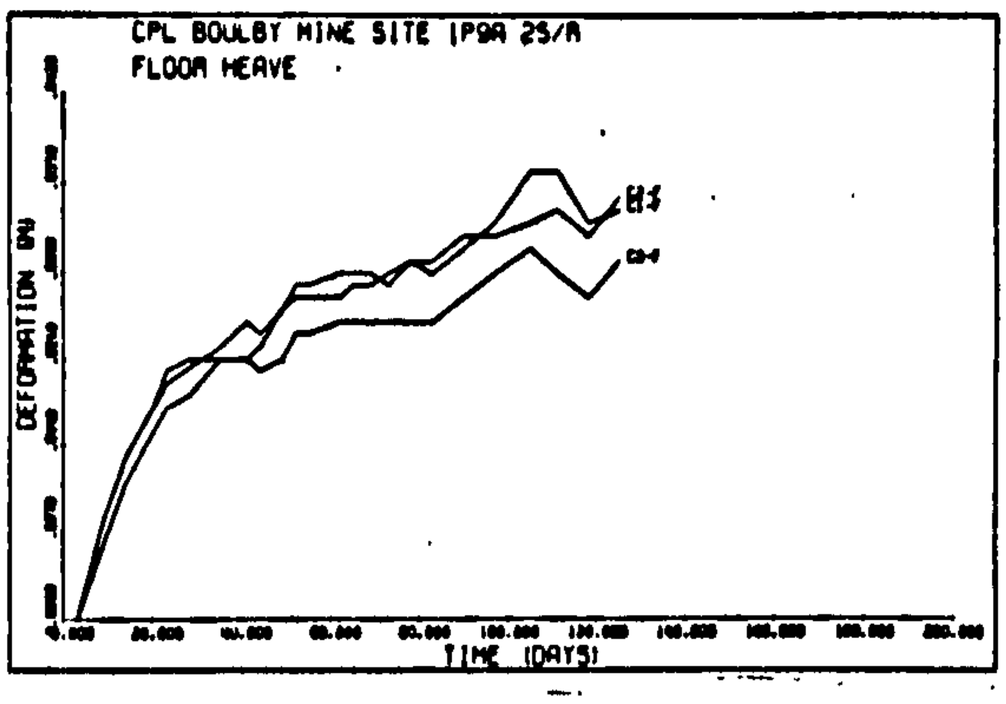
CPL BOULBY MINE SITE IP9A 2S/A
FLOOR HEAVE
DEFORMATION (M)
TIME (DAYS)

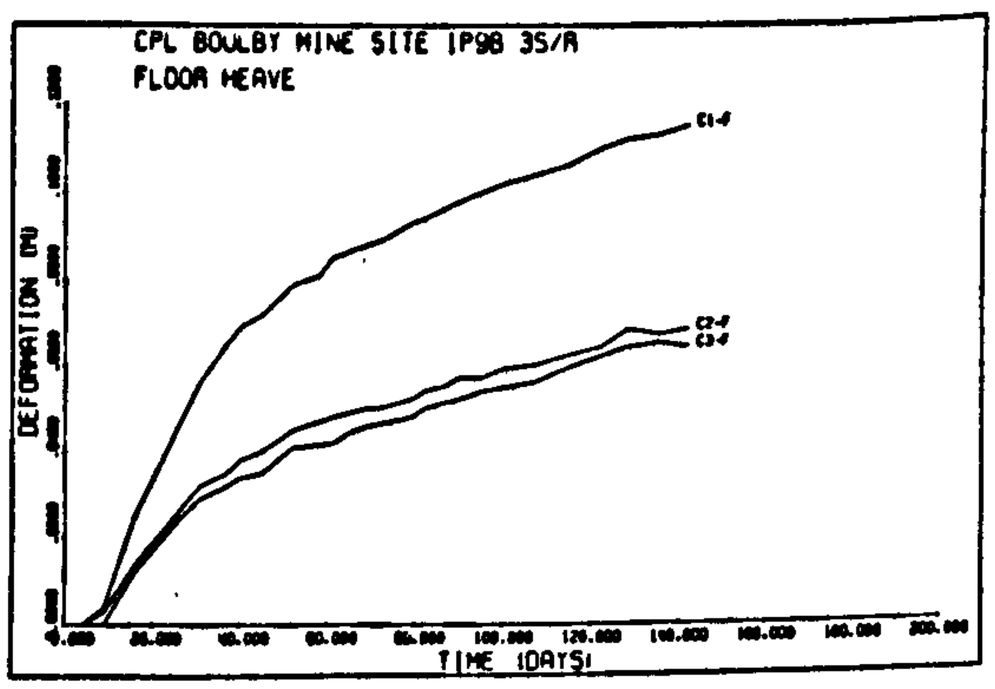
CPL BOULBY MINE SITE IP9B 3S/A
FLOOR HEAVE
DEFORMATION (M)
TIME (DAYS)

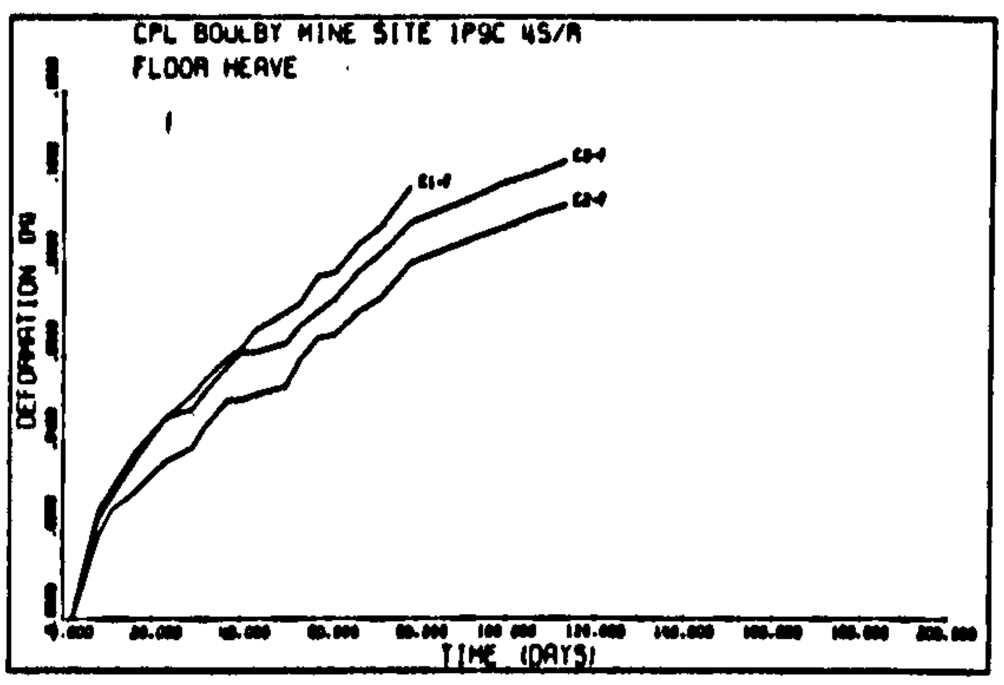
CPL BOULBY MINE SITE IP9C 4S/A
FLOOR HEAVE
DEFORMATION (M)
TIME (DAYS)

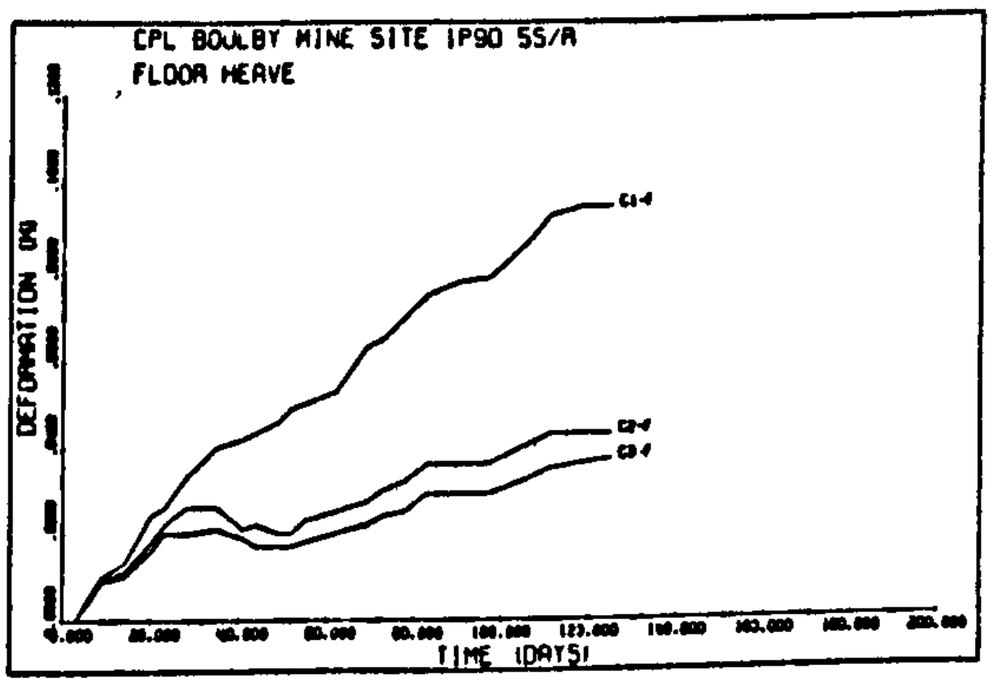
CPL BOULBY MINE SITE IP9D 5S/A
FLOOR HEAVE
DEFORMATION (M)
TIME (DAYS)

B49

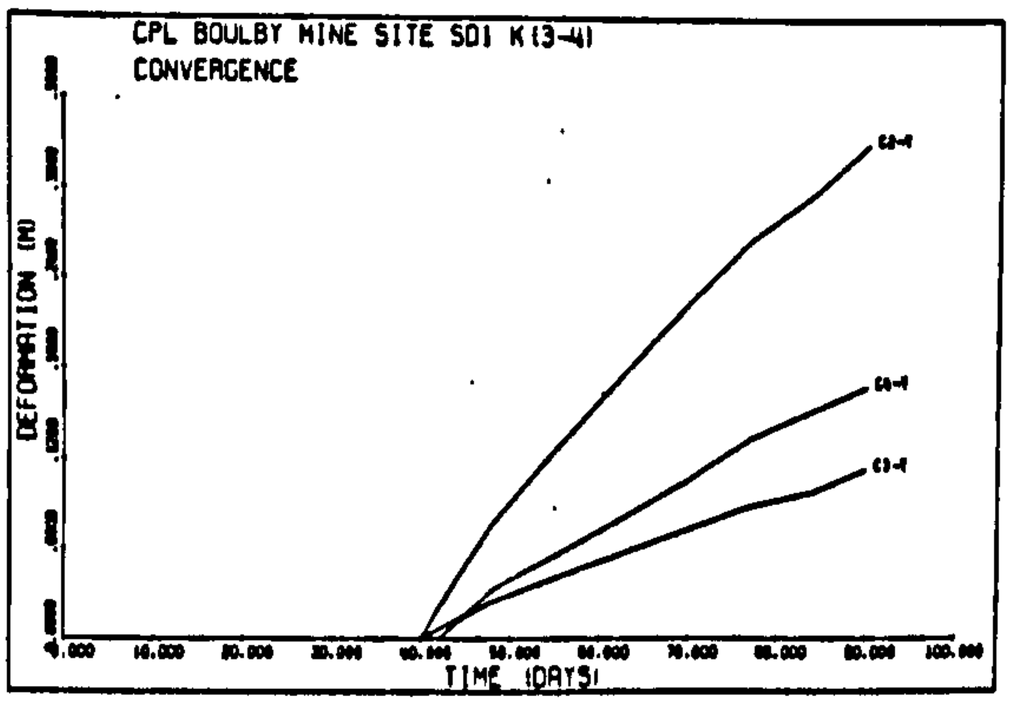
CPL BOULBY MINE SITE SD1 K(3-4)
CONVERGENCE
DEFORMATION (M)
TIME (DAYS)

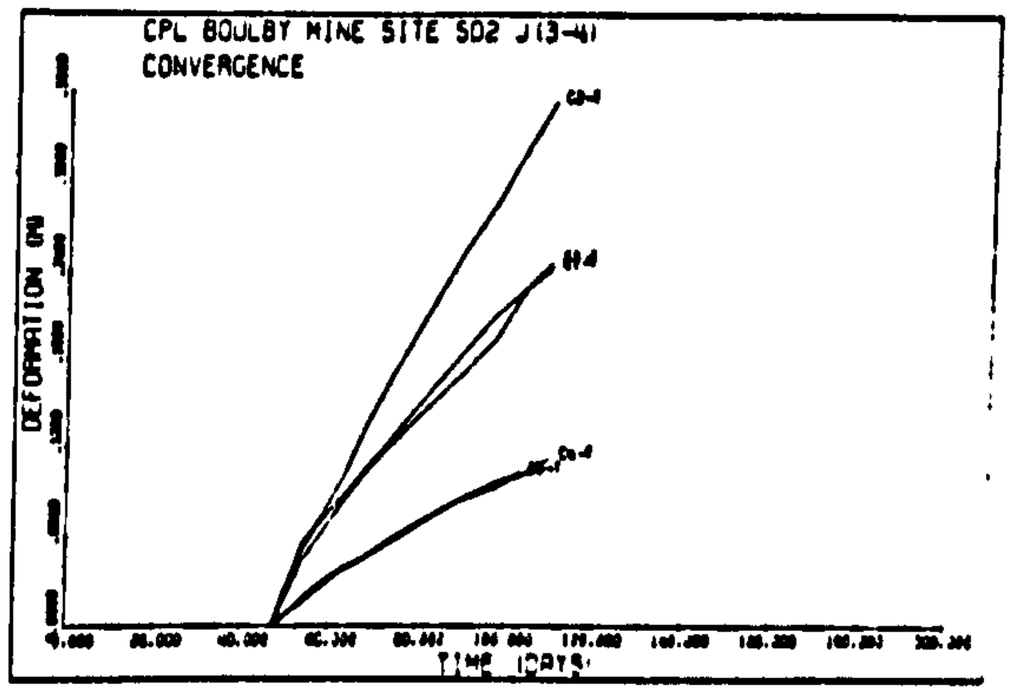
CPL BOULBY MINE SITE SD2 J(3-4)
CONVERGENCE
DEFORMATION (M)
TIME (DAYS)

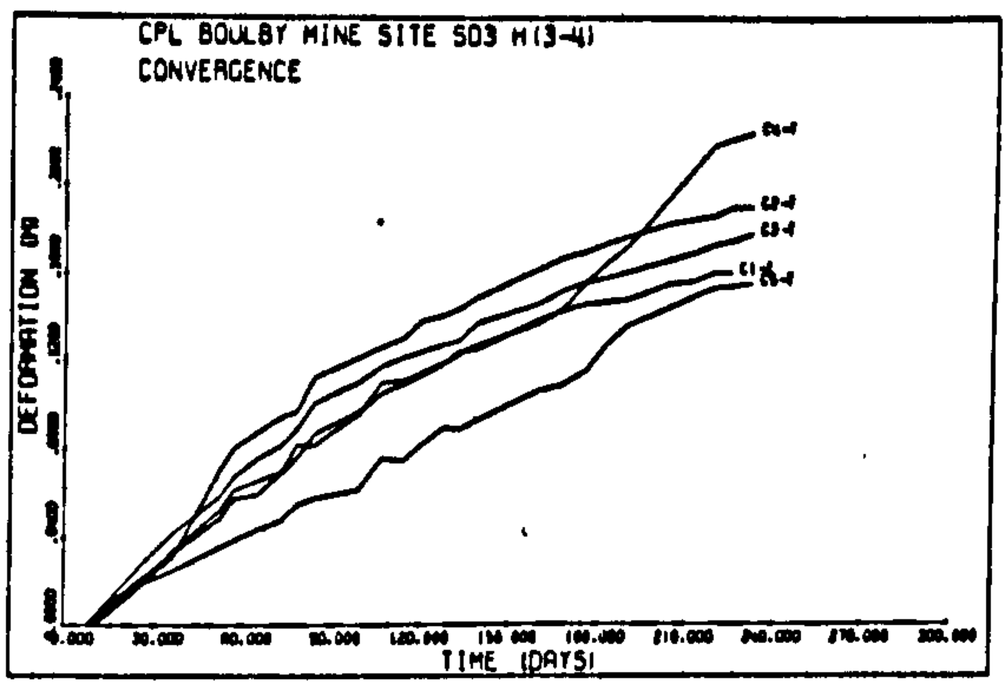
CPL BOULBY MINE SITE SD3 H(3-4)
CONVERGENCE
DEFORMATION (M)
TIME (DAYS)

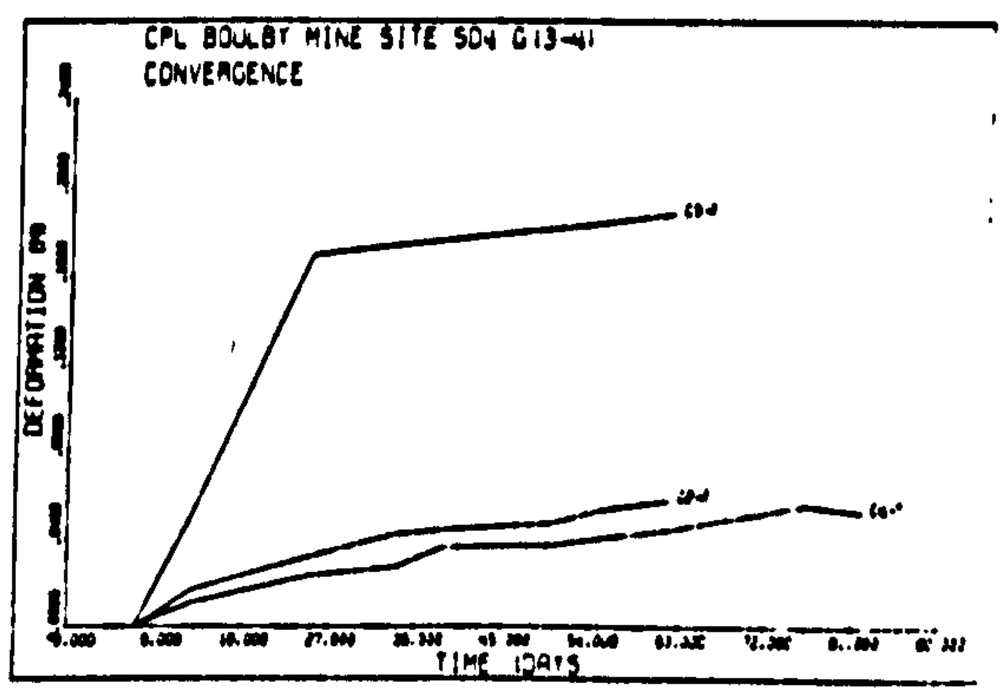
CPL BOULBY MINE SITE SD4 G(3-4)
CONVERGENCE
DEFORMATION (M)
TIME (DAYS)

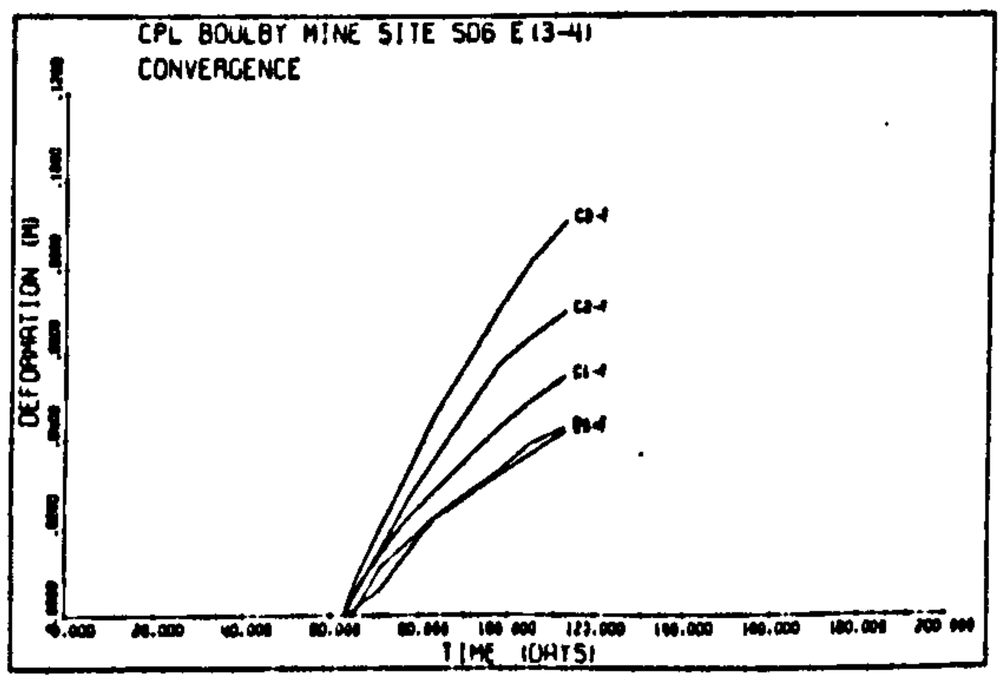
CPL BOULBY MINE SITE SD6 E(3-4)
CONVERGENCE
DEFORMATION (M)
TIME (DAYS)

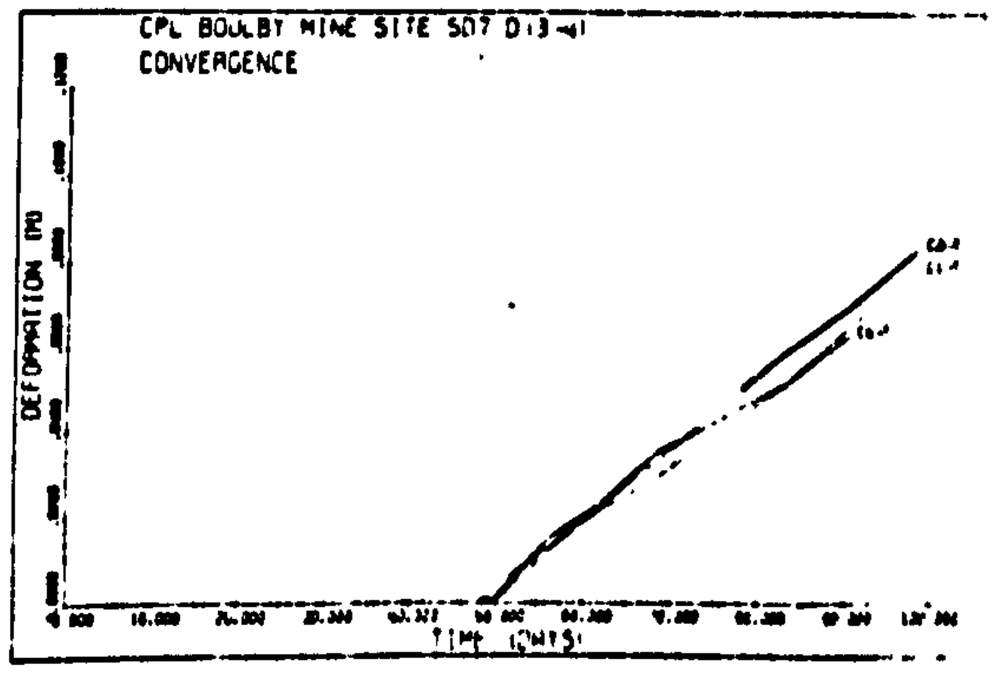
CPL BOULBY MINE SITE SD7 D(3-4)
CONVERGENCE
DEFORMATION (M)
TIME (DAYS)

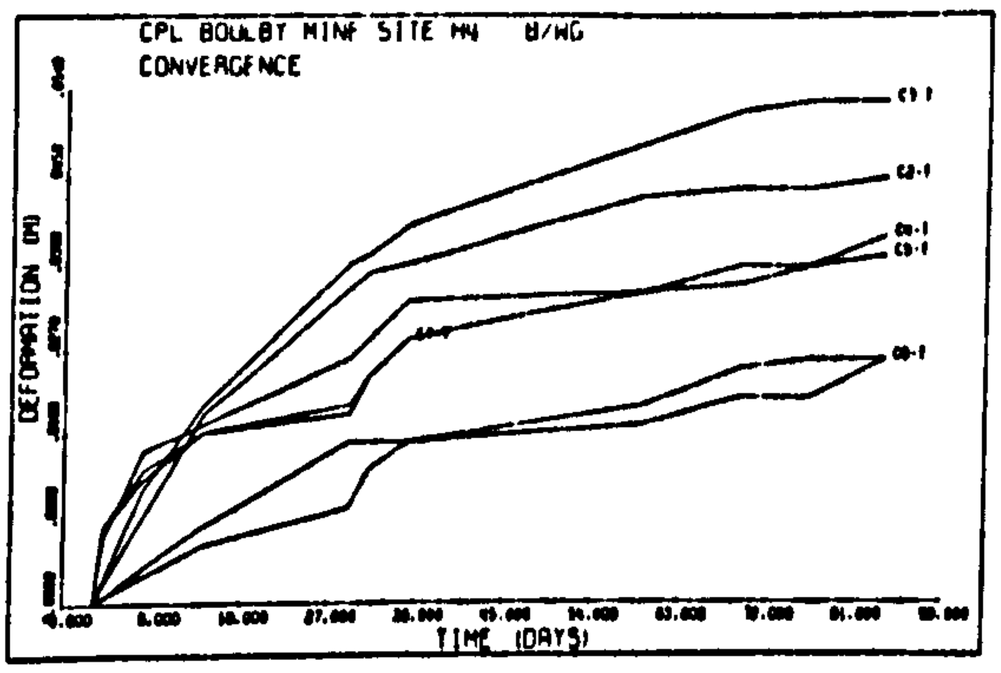
CONVERGENCE
DEFORMATION (M)
TIME (DAYS)

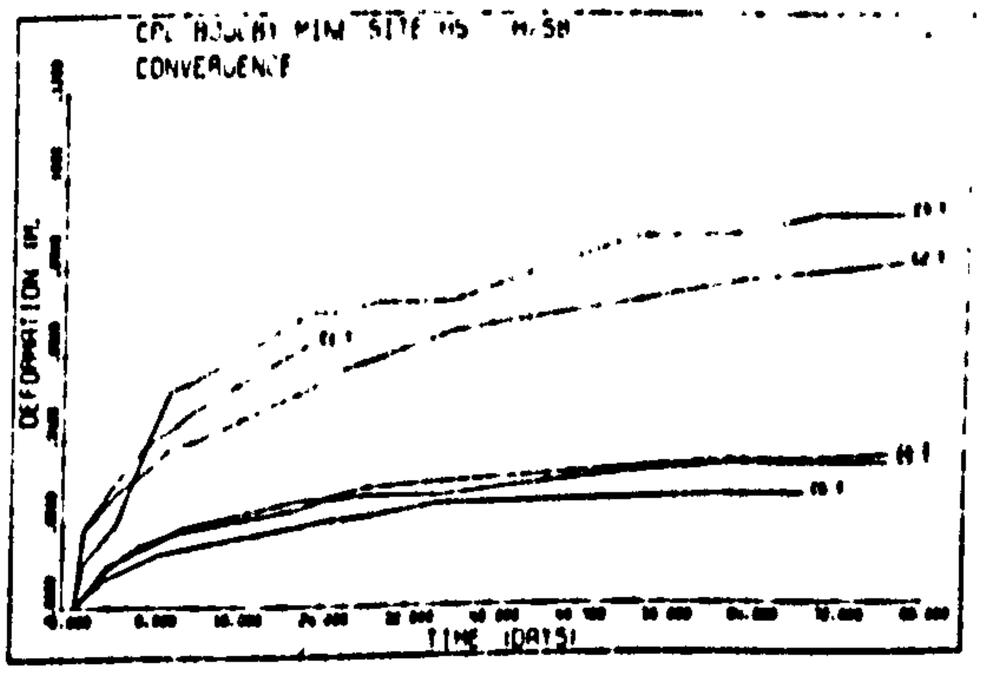
CONVERGENCE
DEFORMATION (M)
TIME (DAYS)

B50

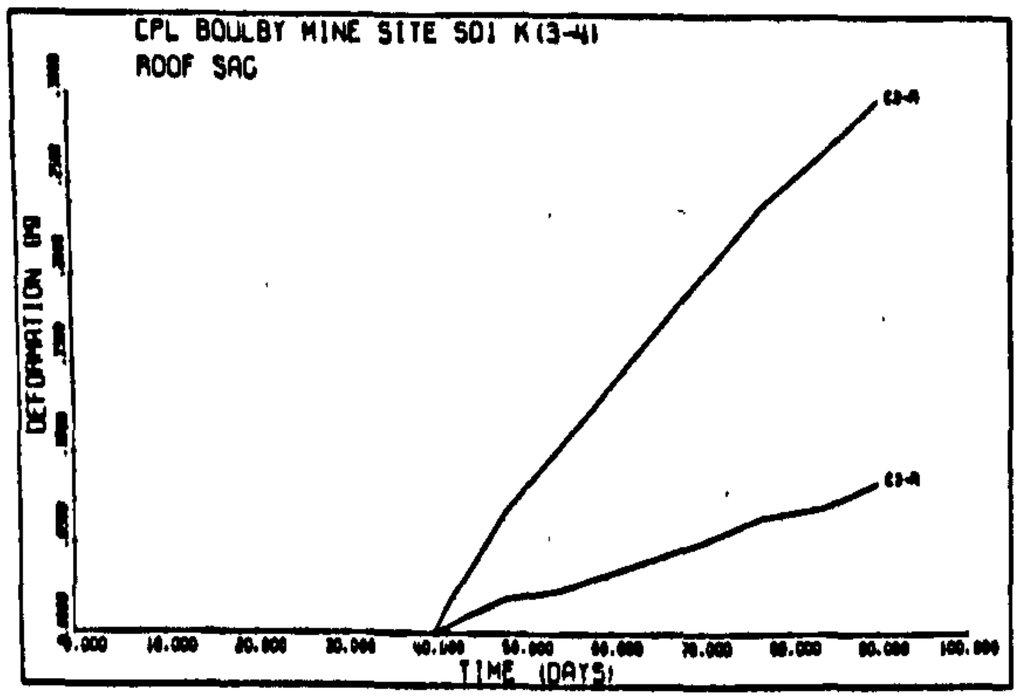
CPL BOULBY MINE SITE SD1 K(3-4)
ROOF SAG
DEFORMATION (MM)
TIME (DAYS)

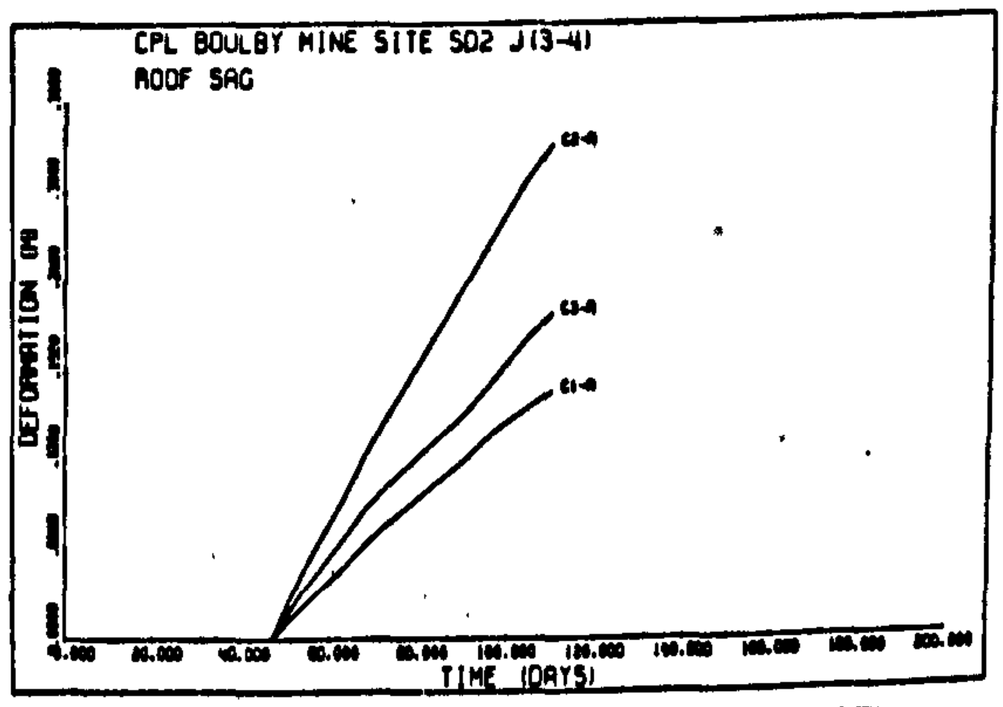
CPL BOULBY MINE SITE SD2 J(3-4)
ROOF SAG
DEFORMATION (MM)
TIME (DAYS)

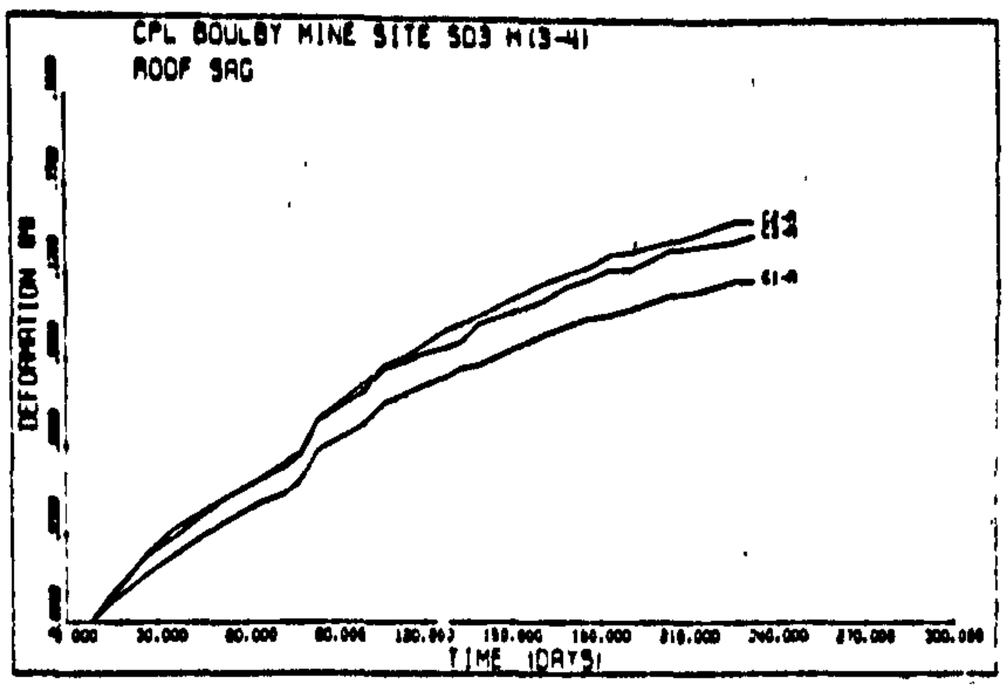
CPL BOULBY MINE SITE SD3 H(3-4)
ROOF SAG
DEFORMATION (MM)
TIME (DAYS)

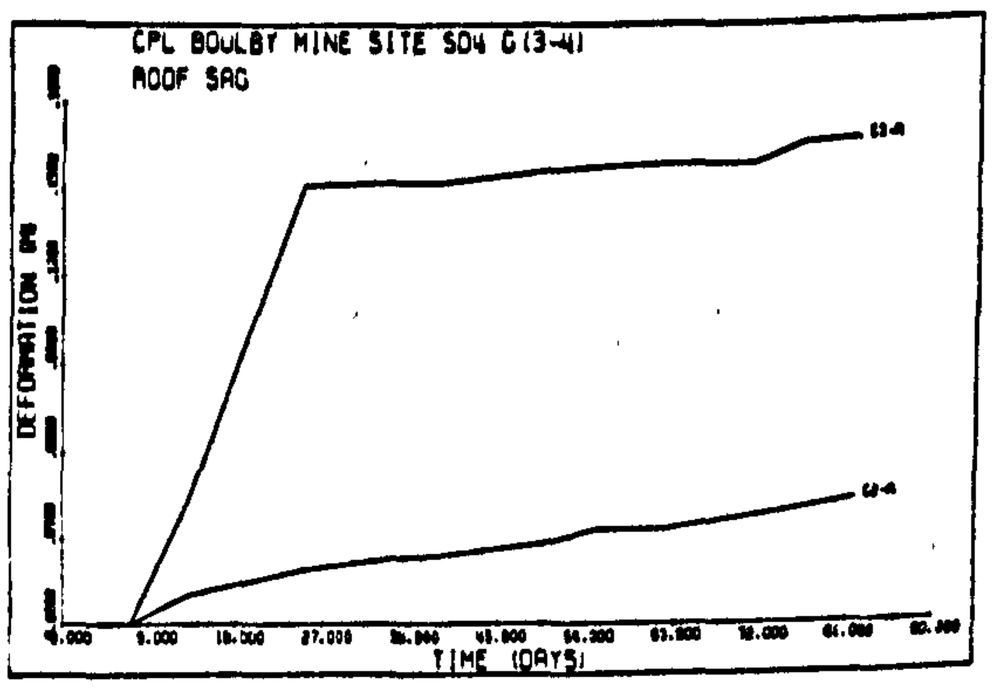
CPL BOULBY MINE SITE SD4 G(3-4)
ROOF SAG
DEFORMATION (MM)
TIME (DAYS)

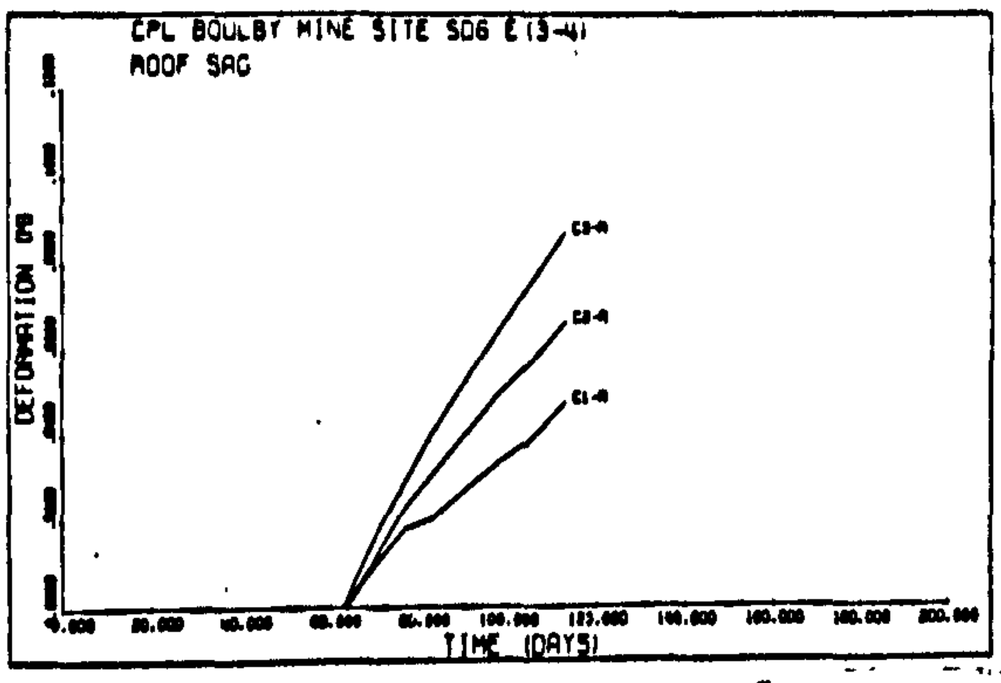
CPL BOULBY MINE SITE SD6 E(3-4)
ROOF SAG
DEFORMATION (MM)
TIME (DAYS)

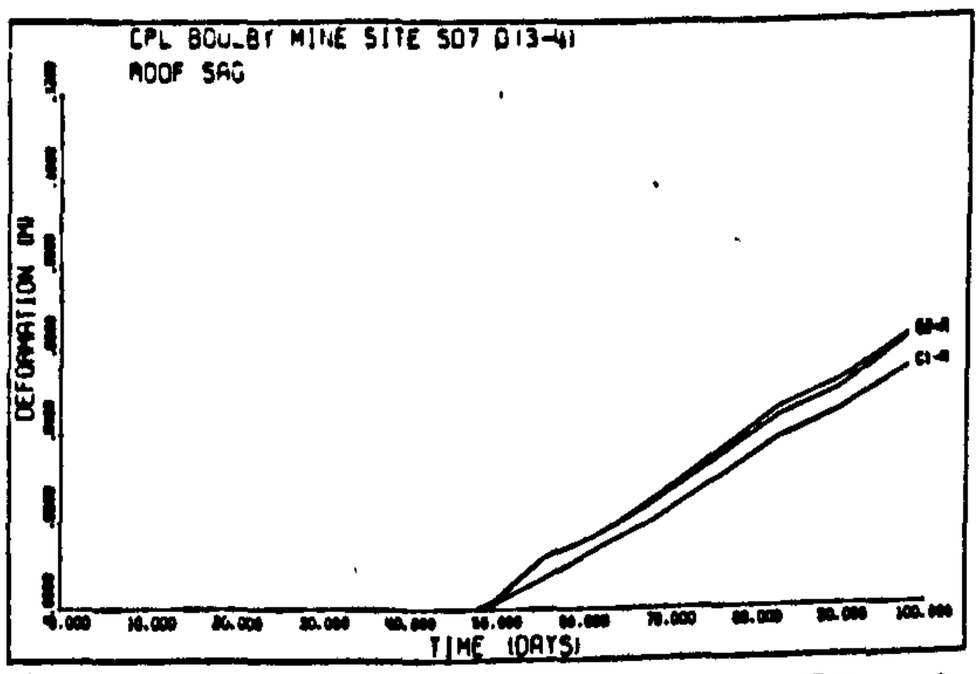
CPL BOULBY MINE SITE SD7 D(3-4)
ROOF SAG
DEFORMATION (MM)
TIME (DAYS)

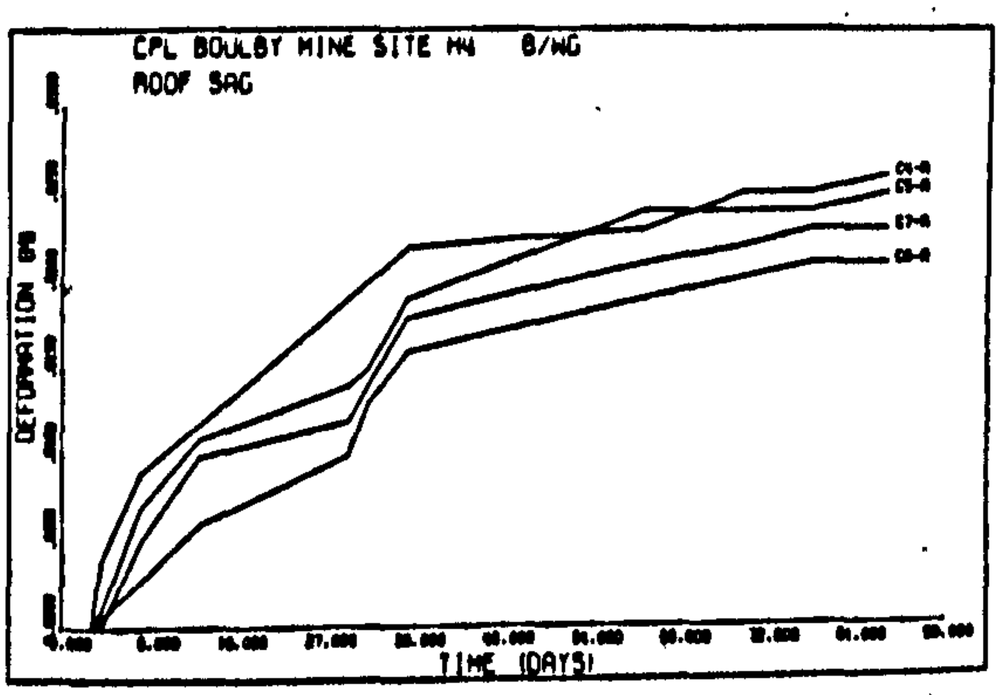
CPL BOULBY MINE SITE H4 B/WG
ROOF SAG
DEFORMATION (MM)
TIME (DAYS)

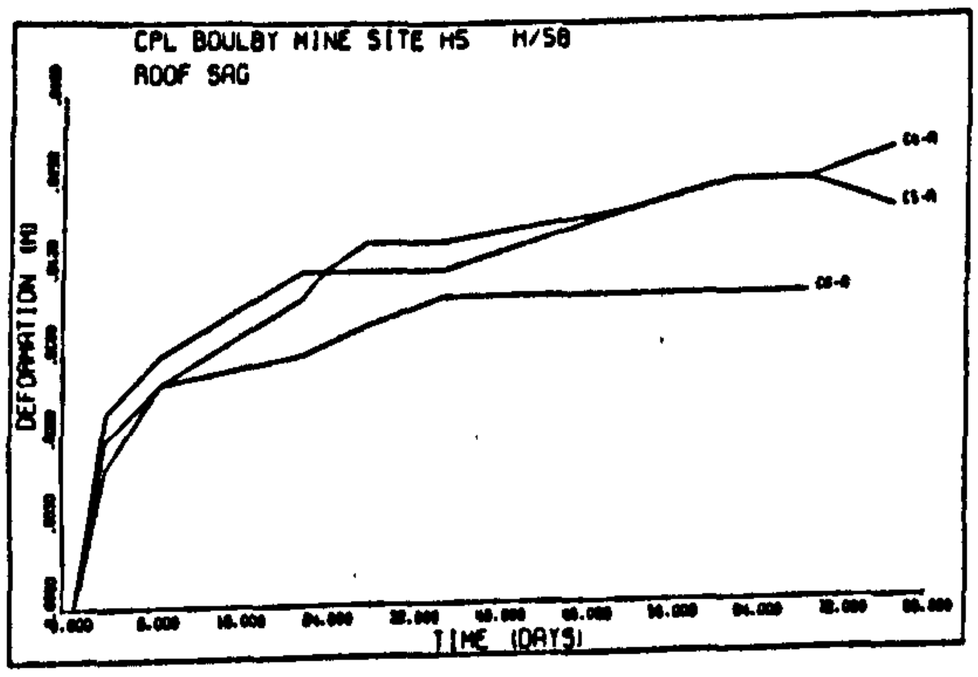
CPL BOULBY MINE SITE H5 H/SB
ROOF SAG
DEFORMATION (MM)
TIME (DAYS)

B51

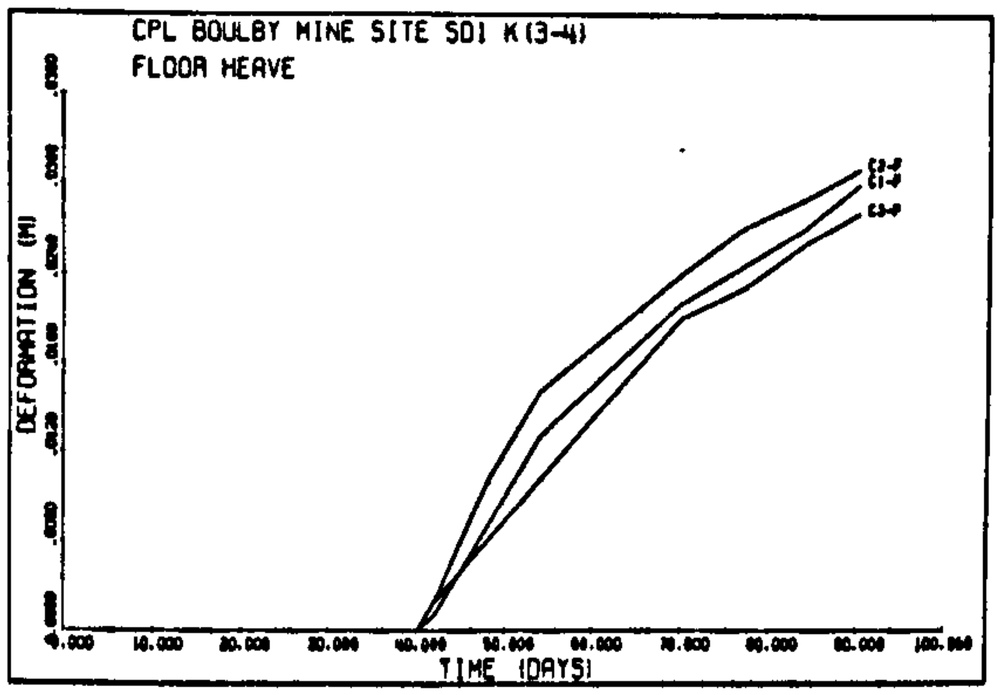
CPL BOULBY MINE SITE SD1 K(3-4)
FLOOR HEAVE
DEFORMATION (M)
TIME (DAYS)

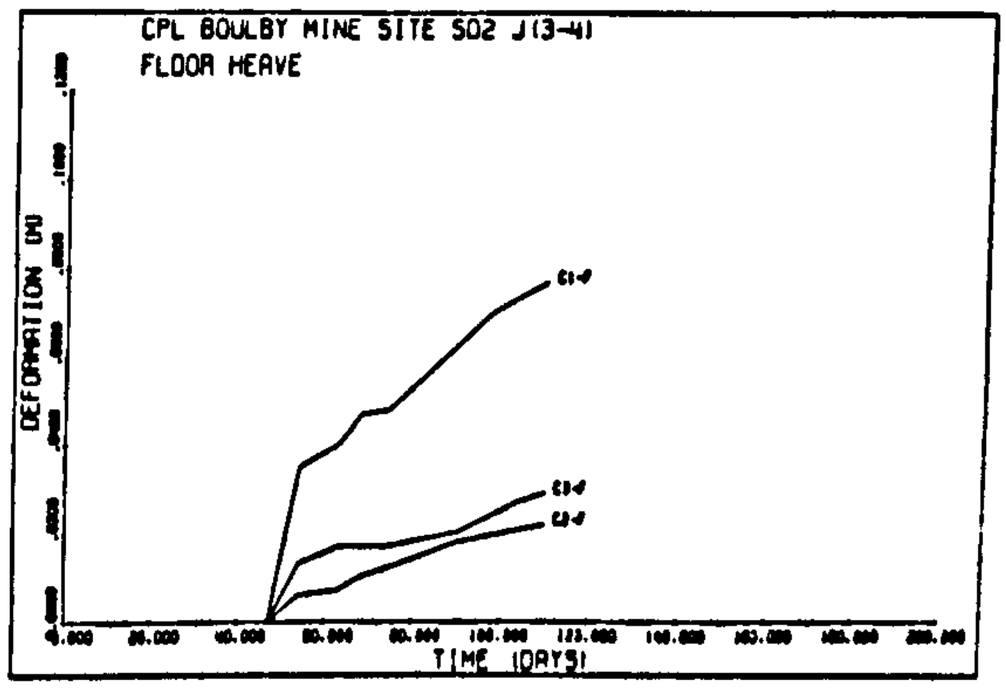
CPL BOULBY MINE SITE SD2 J(3-4)
FLOOR HEAVE
DEFORMATION (M)
TIME (DAYS)

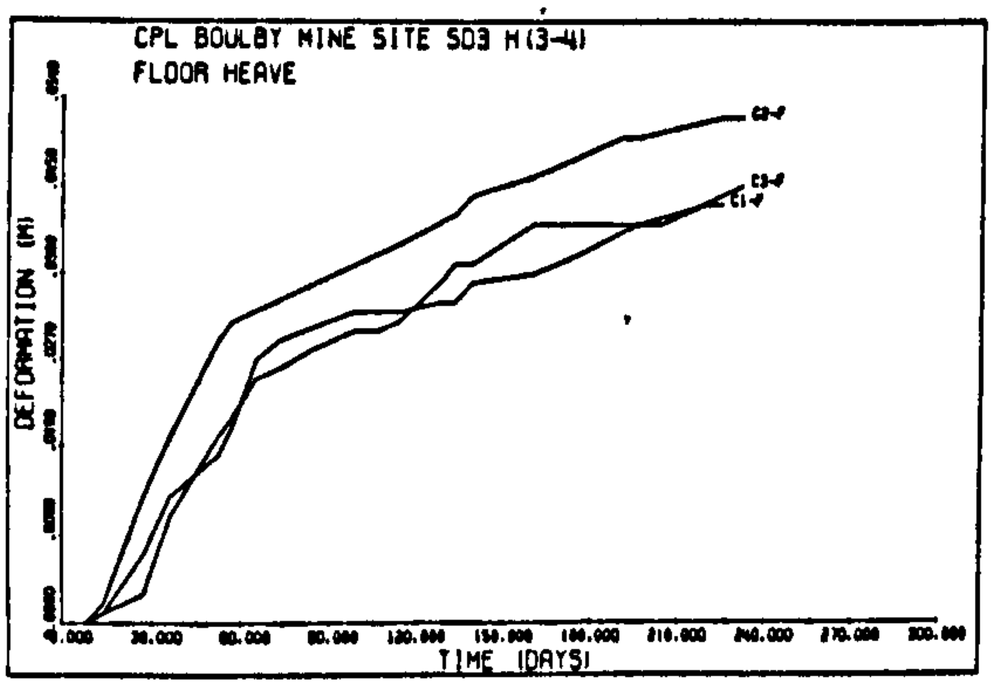
CPL BOULBY MINE SITE SD3 H(3-4)
FLOOR HEAVE
DEFORMATION (M)
TIME (DAYS)

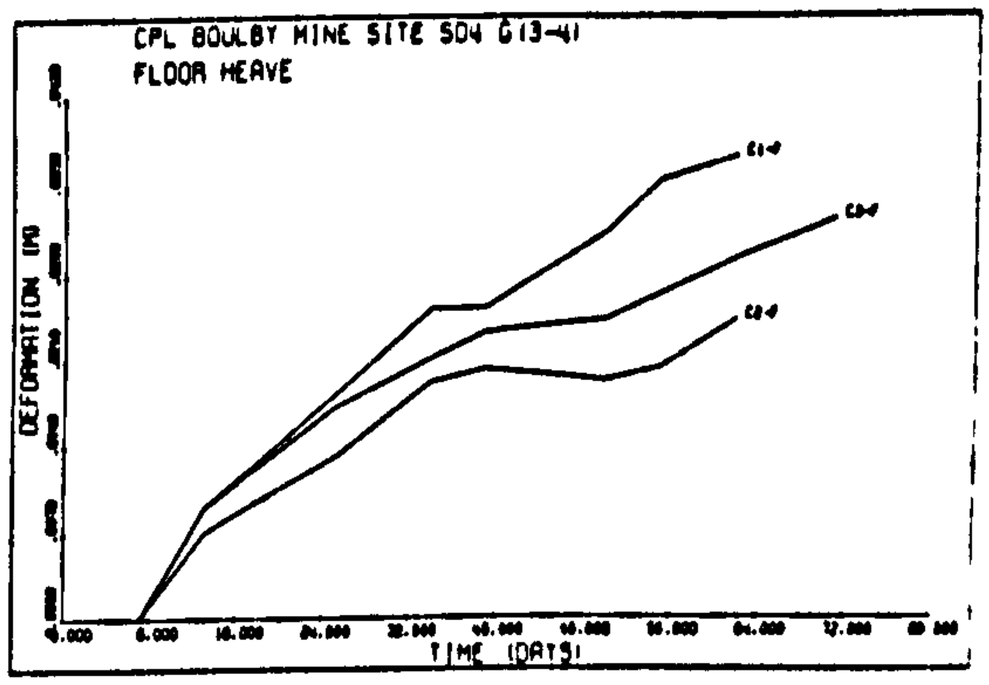
CPL BOULBY MINE SITE SD4 G(3-4)
FLOOR HEAVE
DEFORMATION (M)
TIME (DAYS)

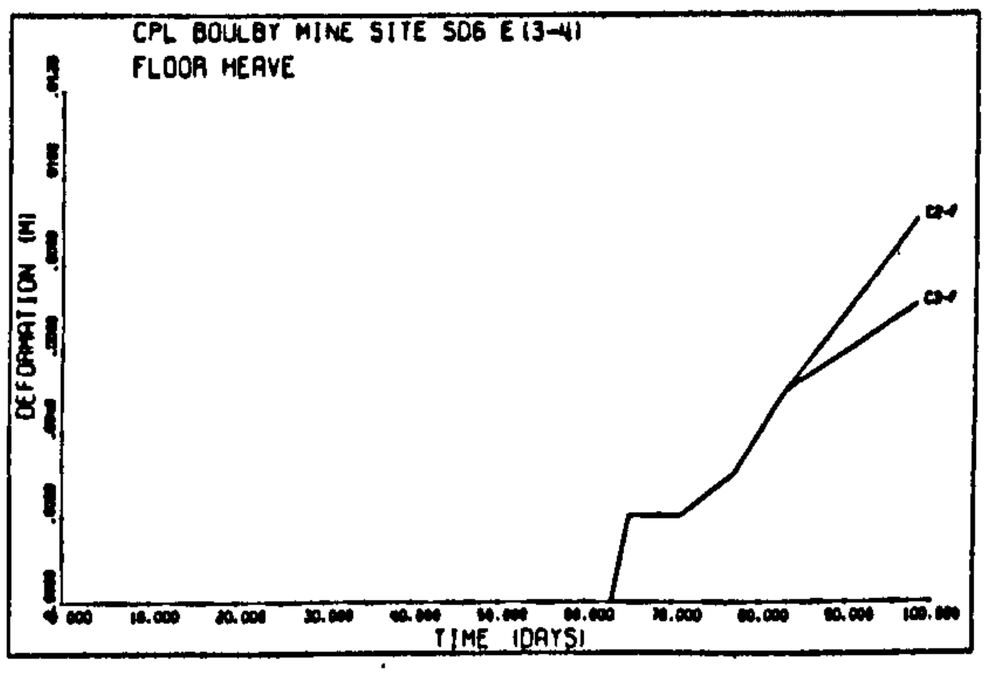
CPL BOULBY MINE SITE SD6 E(3-4)
FLOOR HEAVE
DEFORMATION (M)
TIME (DAYS)

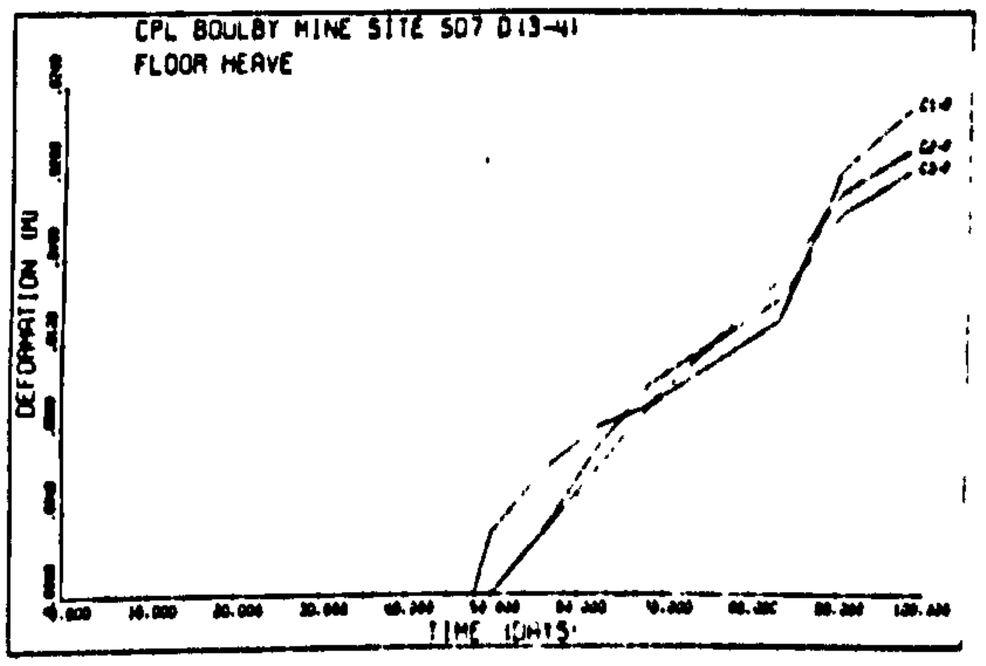
CPL BOULBY MINE SITE SD7 D(3-4)
FLOOR HEAVE
DEFORMATION (M)
TIME (DAYS)

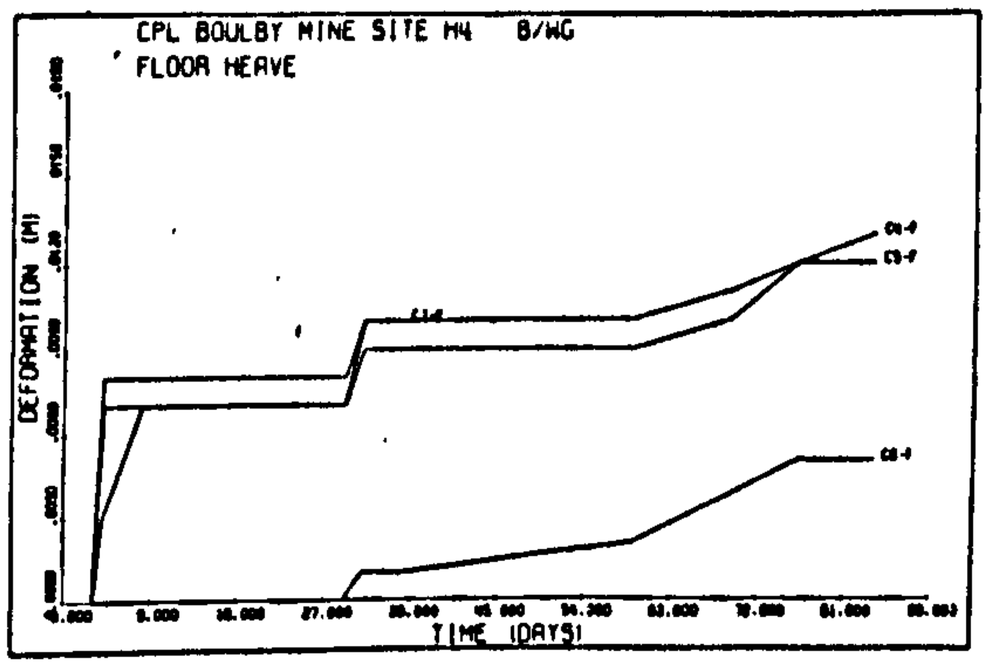
CPL BOULBY MINE SITE M4 B/WG
FLOOR HEAVE
DEFORMATION (M)
TIME (DAYS)

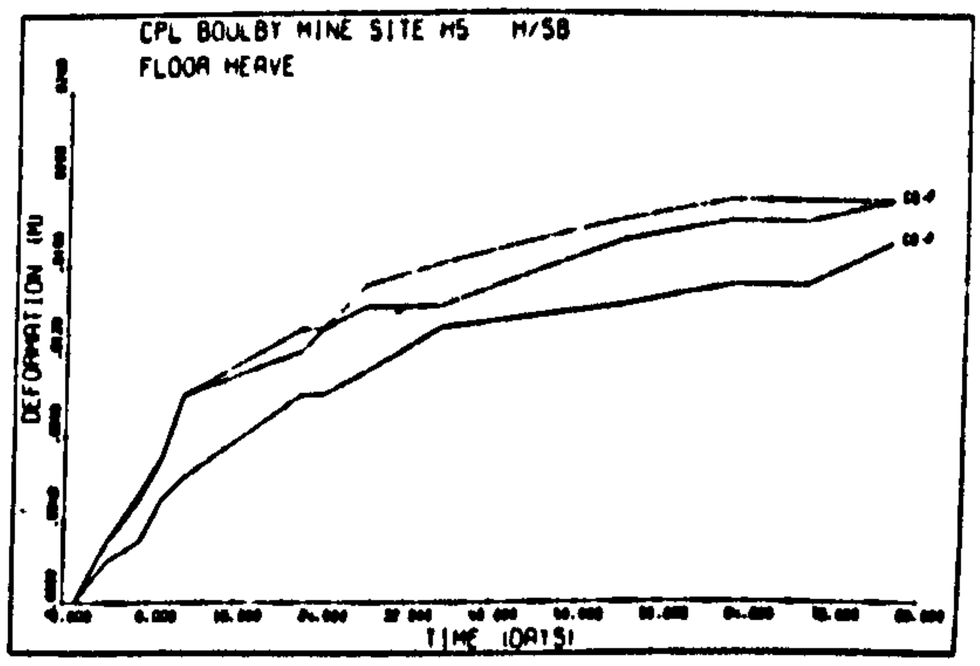
CPL BOULBY MINE SITE M5 M/SB
FLOOR HEAVE
DEFORMATION (M)
TIME (DAYS)

B52

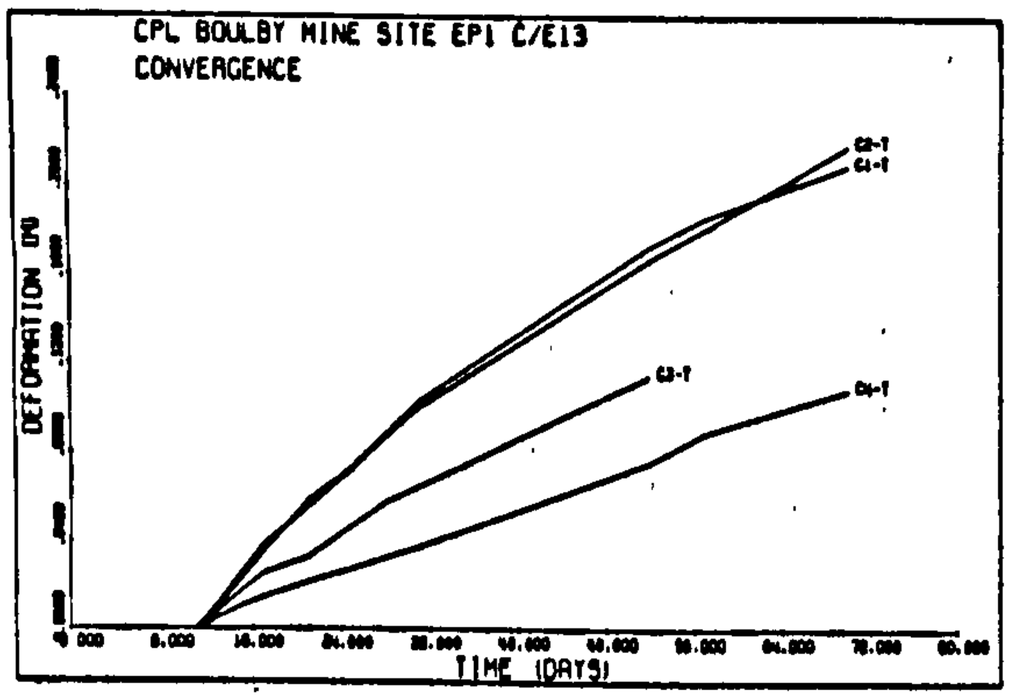
CPL BOULBY MINE SITE EP1 C/E13
CONVERGENCE
DEFORMATION (M)
TIME (DAYS)

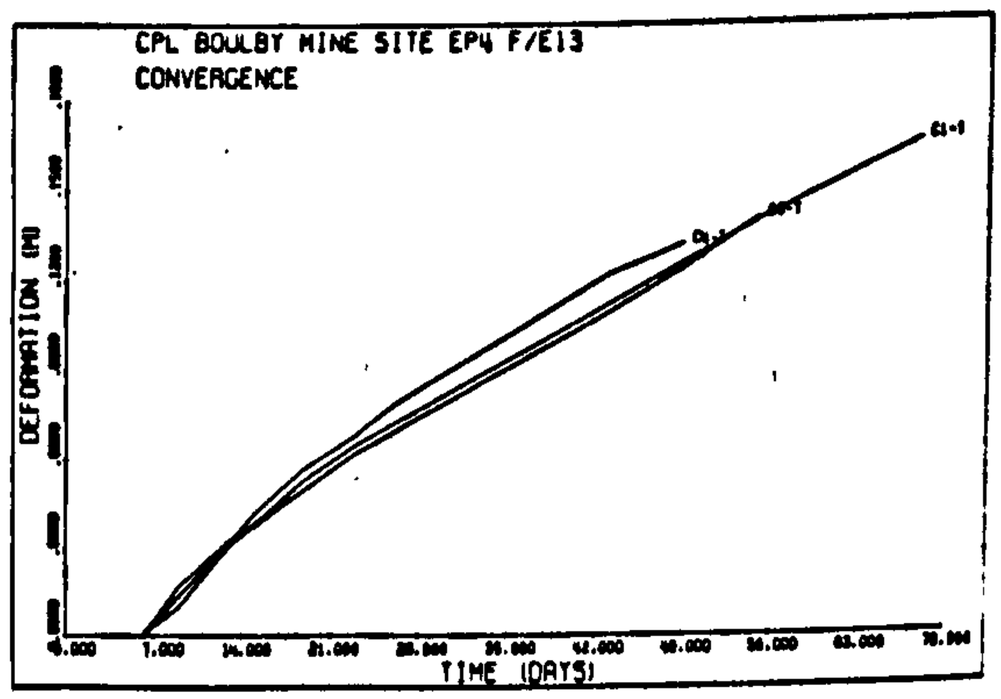
CPL BOULBY MINE SITE EP4 F/E13
CONVERGENCE
DEFORMATION (M)
TIME (DAYS)

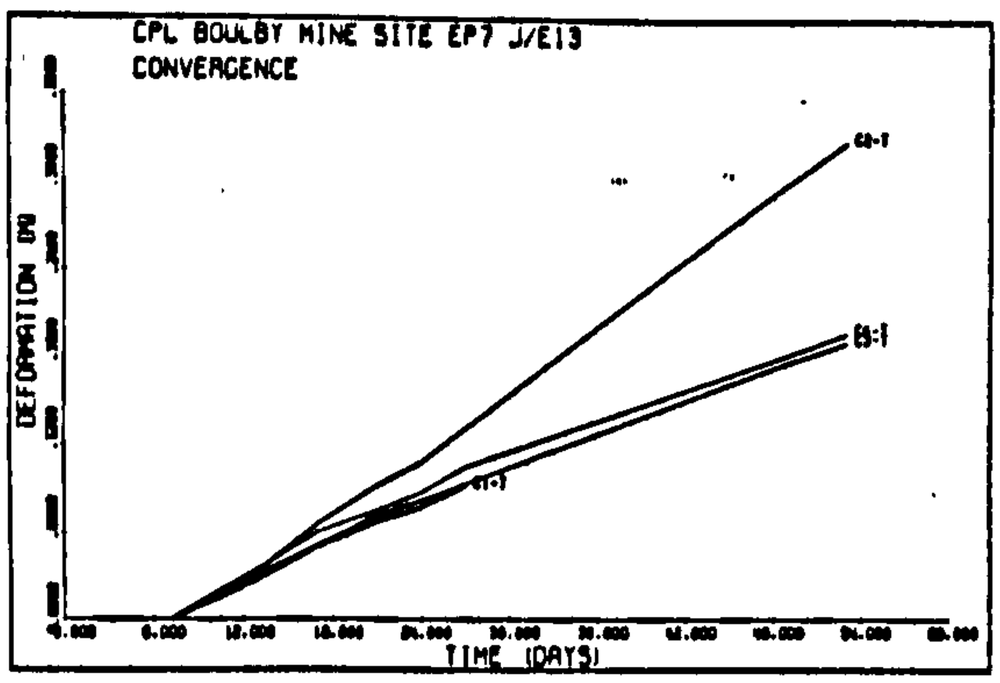
CPL BOULBY MINE SITE EP7 J/E13
CONVERGENCE
DEFORMATION (M)
TIME (DAYS)

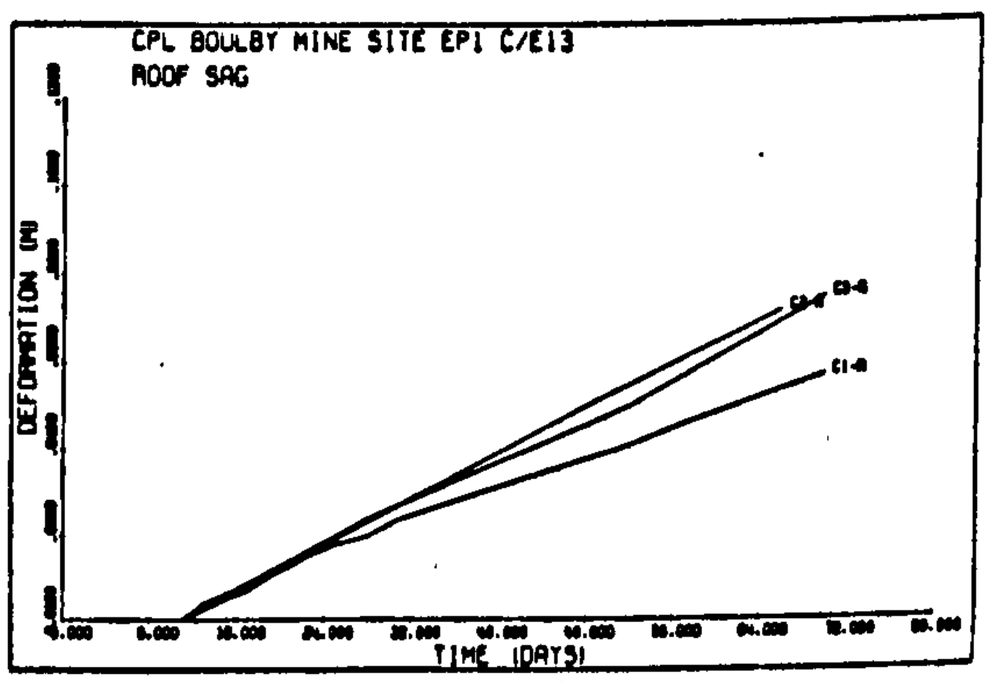
CPL BOULBY MINE SITE EP1 C/E13
ROOF SAG
DEFORMATION (M)
TIME (DAYS)

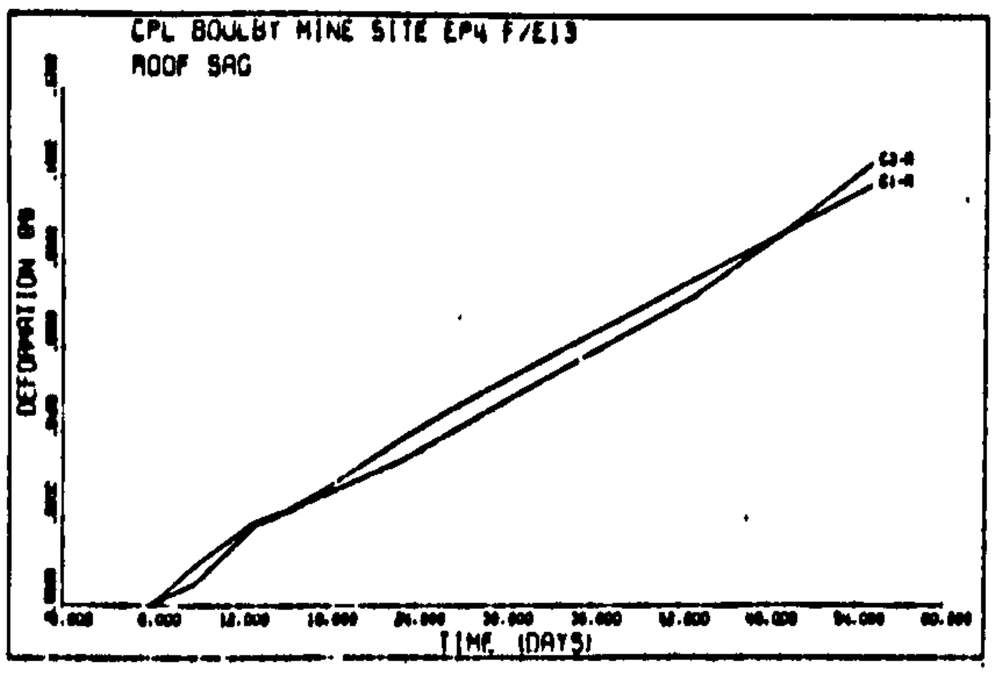
CPL BOULBY MINE SITE EP4 F/E13
ROOF SAG
DEFORMATION (M)
TIME (DAYS)

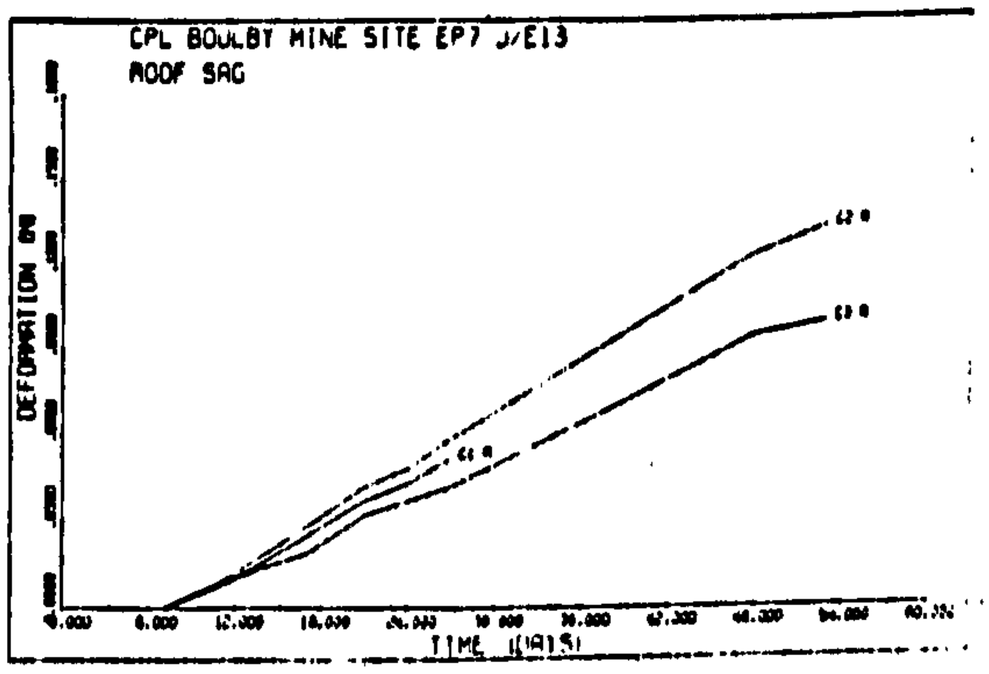
CPL BOULBY MINE SITE EP7 J/E13
ROOF SAG
DEFORMATION (M)
TIME (DAYS)

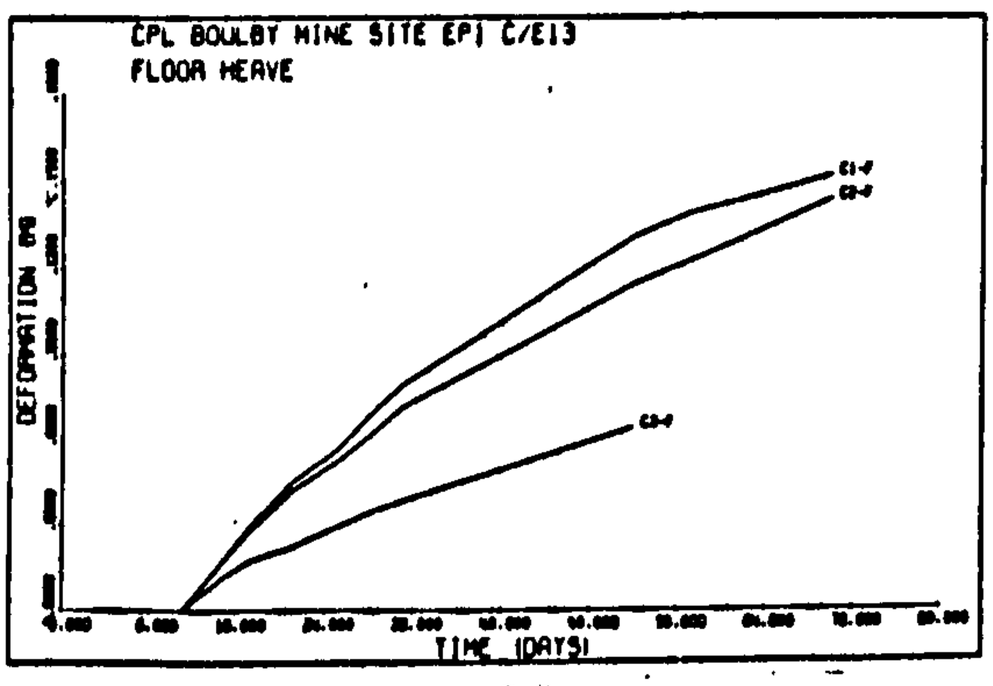
CPL BOULBY MINE SITE EP1 C/E13
FLOOR HEAVE
DEFORMATION (M)
TIME (DAYS)

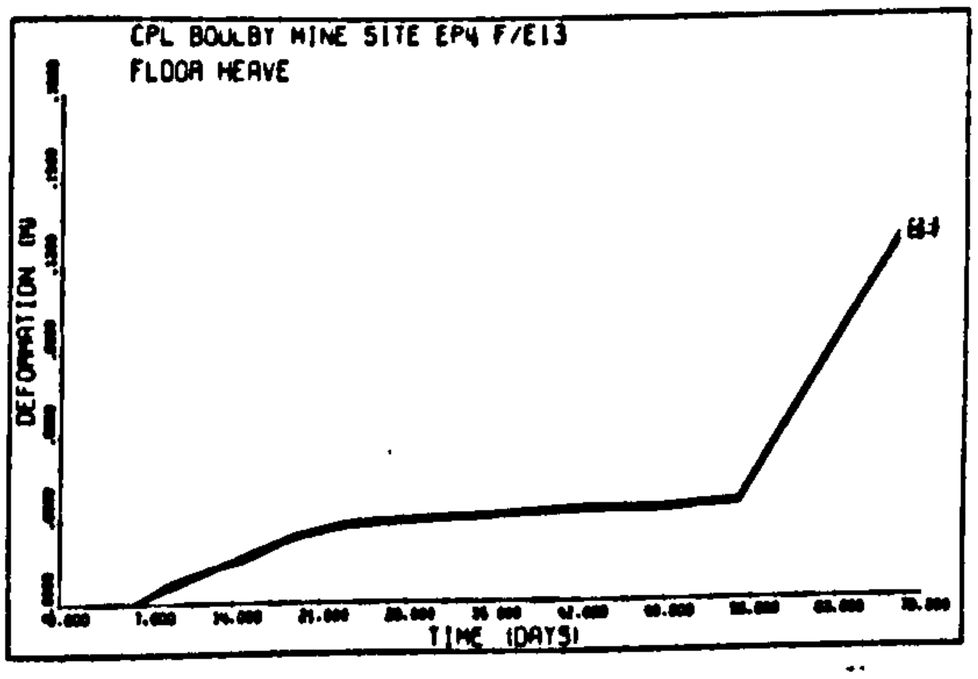
CPL BOULBY MINE SITE EP4 F/E13
FLOOR HEAVE
DEFORMATION (M)
TIME (DAYS)

B53

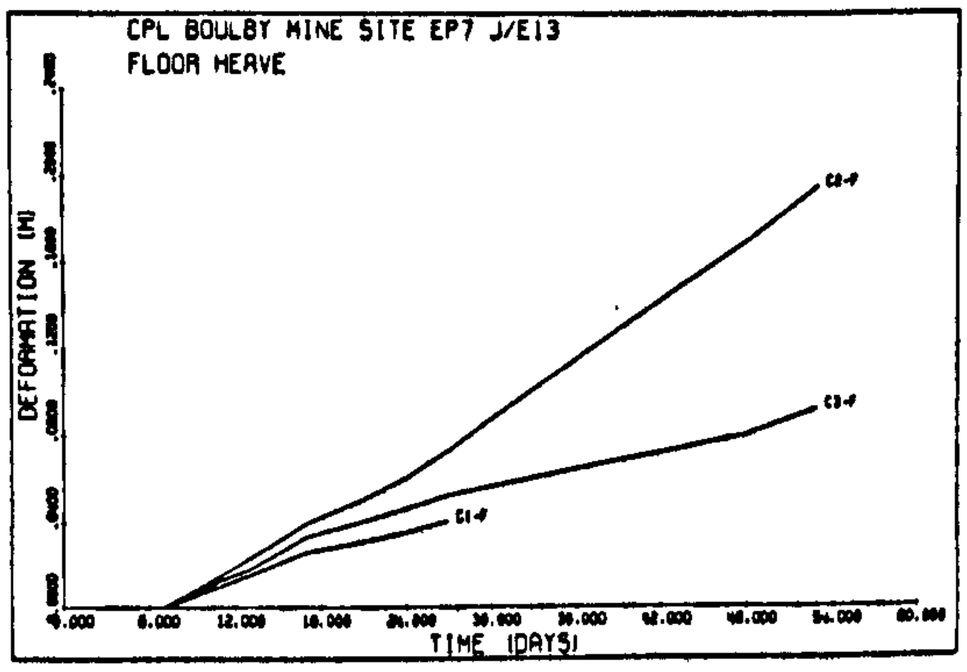
CPL BOULBY MINE SITE EP7 J/E13
FLOOR HEAVE
DEFORMATION (M)
TIME (DAYS)

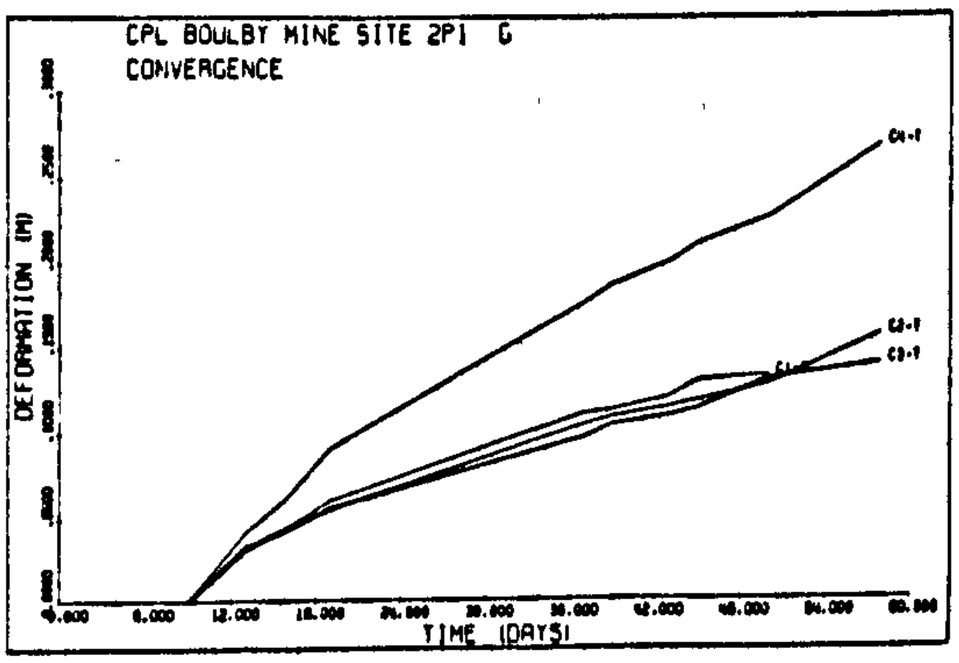
CPL BOULBY MINE SITE 2P1 G
CONVERGENCE
DEFORMATION (M)
TIME (DAYS)

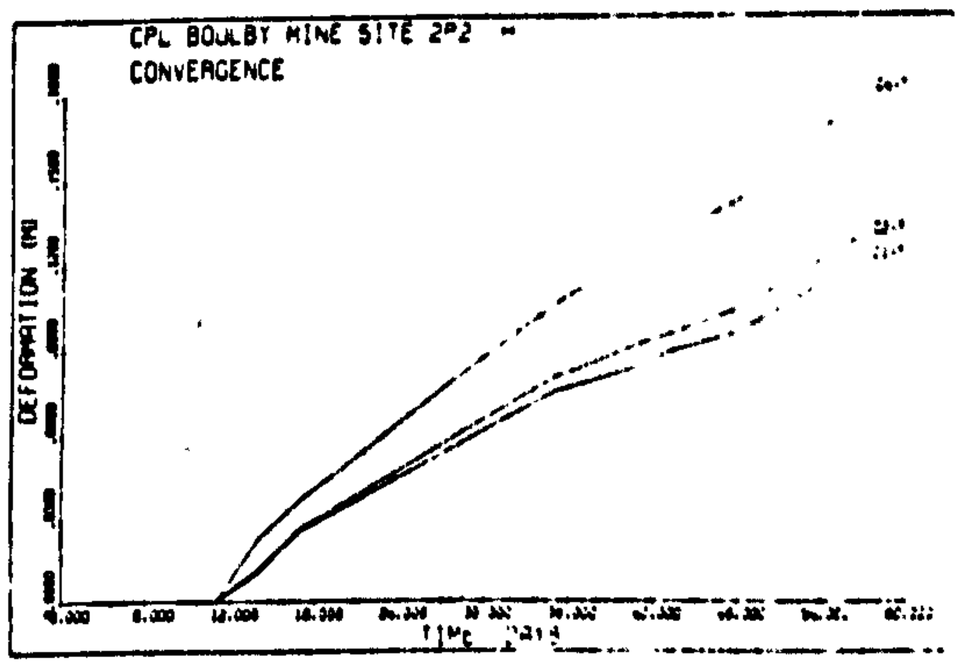
CPL BOULBY MINE SITE 2P2
CONVERGENCE
DEFORMATION (M)

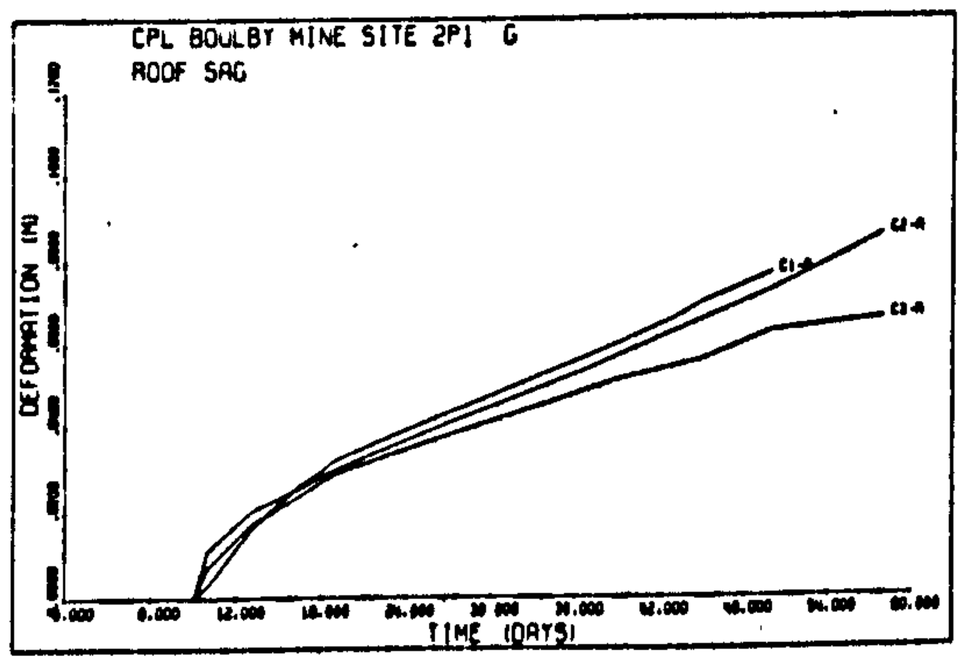
CPL BOULBY MINE SITE 2P1 G
ROOF SAG
DEFORMATION (M)
TIME (DAYS)

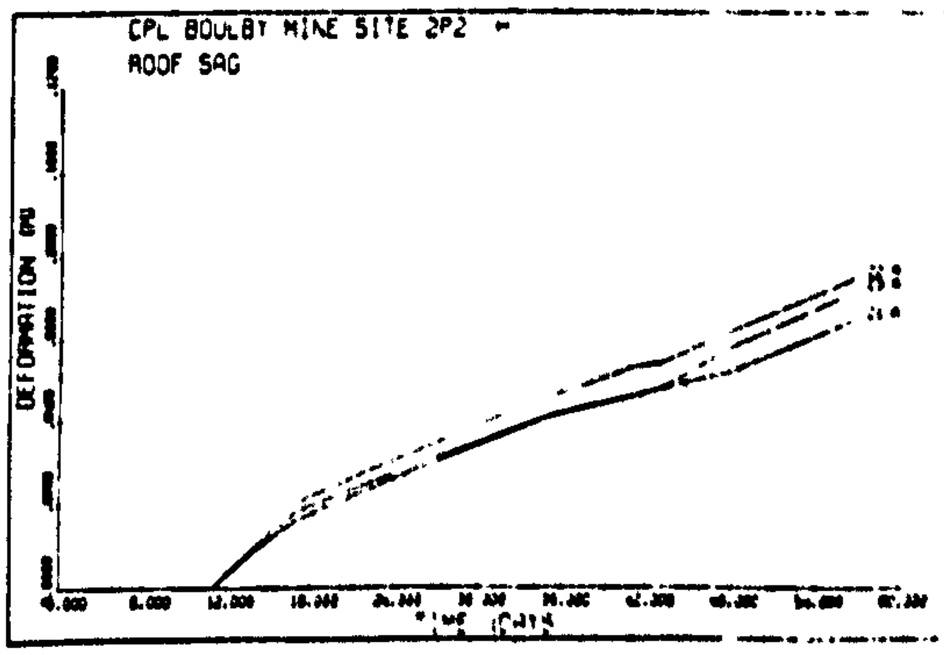
CPL BOULBY MINE SITE 2P2
ROOF SAG
DEFORMATION (M)

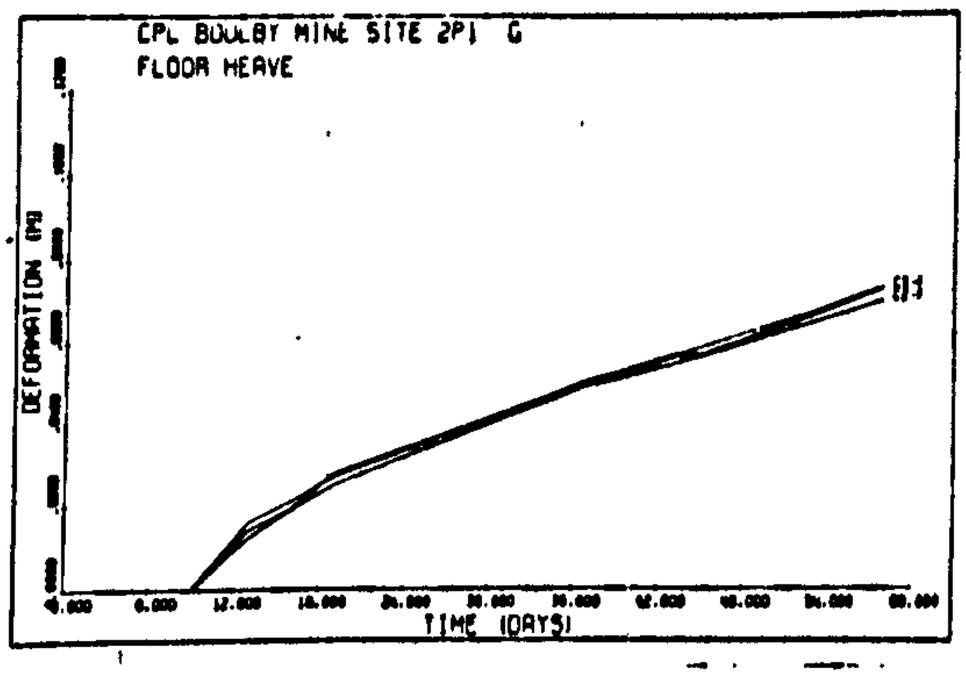
CPL BOULBY MINE SITE 2P1 G
FLOOR HEAVE
DEFORMATION (M)
TIME (DAYS)

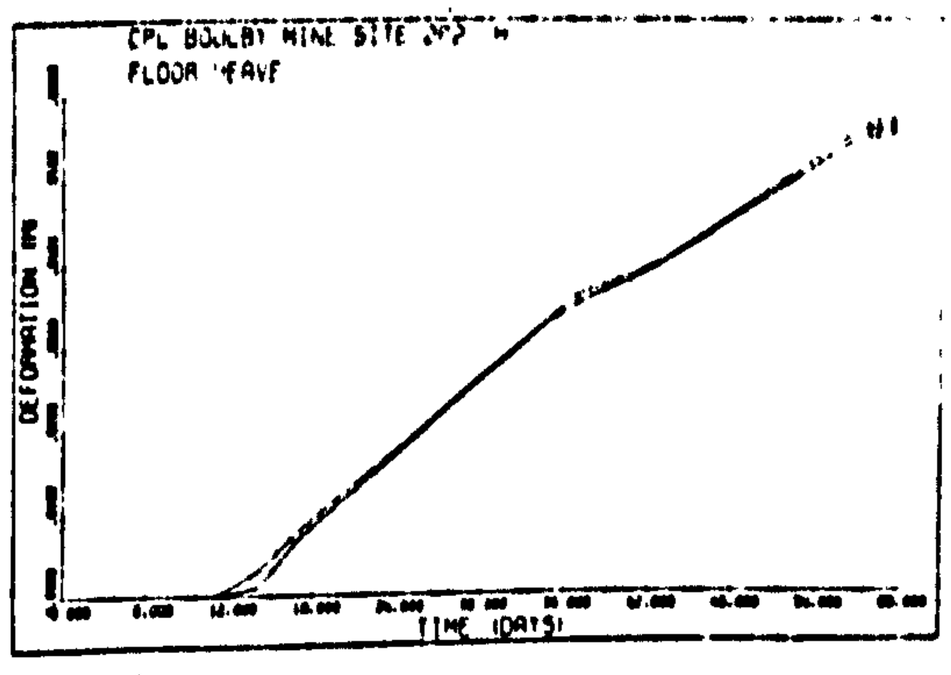
DEFORMATION (M)
TIME (DAYS)

B54

APPENDIX C

No. 2 SHAFT EXTENSOMETER RESULTS

A set of four radial borehole extensometers was installed by Cook (8) around the circumference of the 7.6m diameter No. 2 shaft at a level of 1056m in the Upper Halite. Each extensometer consisted of four anchors at depths of 0.6m, 1.5m, 3.0m and 4.5m into the rock mass.

Cook had modelled this configuration in laboratory tests for design purposes, and initial in-situ analysis showed that deformation of the rock mass on the horizontal plane towards the excavation was uniform in all directions, i.e. axisymmetric.

After readings had been taken for almost three years, sufficient data had been obtained to analyse the creep rates at each anchor depth, and an extremely good fit was obtained using a power law function.

Due to the axisymmetry of the situation, a simple analytical model was established by the author on the assumption that the time-dependent behaviour of this material was a result of zero volumetric strain. Consequently, deformations, though minimal, occur even at great distances from the excavation boundary. Deformations calculated from this 'equal area sector analysis', in conjunction with one of the measured deformations, were compared with those of the other three anchors. Close agreement of these values validated the method of analysis. Similar work in a shaft in Canada was reported by Barron and Toews (75). This analysis has been fully described in a paper by Hebblewhite et al. (76). The fundamental equation of the method is

$$u_{R2} = R_2 - \sqrt{(R_2^2 - R_1^2 + (R_1 - u_{R1})^2)} \qquad (11.1)$$

where u_{R1} is a known radial deformation at a radius of R_1,

u_{R2} is the unknown radial deformation at a radius of R_2.

Fig. C1 shows the radial deformations from the shaft station which were used in this analysis.

C1

RADIAL CLOSURE AROUND NC. 2 SHAFT AT 1,056m.

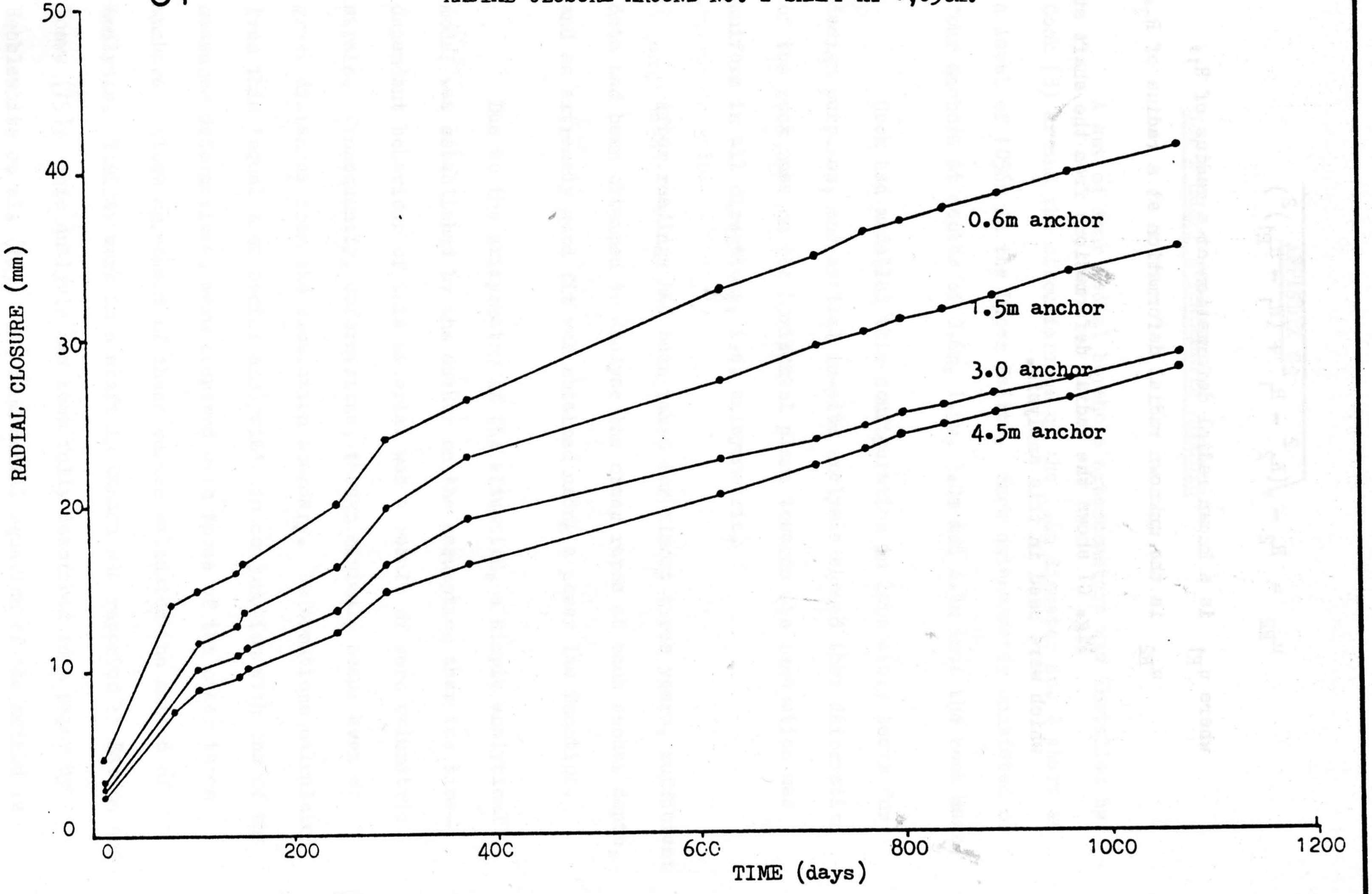

REFERENCES

1 Bryan, Sir Andrew — Planning permission and the place of the Public Inquiry in the development on mined resources in Britain. Trans. I.M.M., 1971.

2 Anon. — Potash in Saskatchewan. Department of Mineral Resources, Province of Saskatchewan, 1973.

3 McClain, W.C. — A study of the Strata Movement in the Partial Extraction of Potash. Ph.D. thesis, Univ. Newcastle upon Tyne, 1963.

4 Ramirez, P. — A Study of Longwall Mining of Potash. M.Sc. thesis, Univ. Newcastle upon Tyne, 1966.

5 Freeman, M.R. — Mining Journal, Annual Review, 1977.

6 Woods, P.J.E. — Potash exploration in Yorkshire: Boulby mine pilot borehole. Trans. I.M.M., Part B, 1973.

7 Patchet, S.J. — Rock Mechanics Studies Associated with the Development of a Deep Potash Mine. Ph.D. thesis, Univ. Newcastle upon Tyne, 1970.

8 Cook, R.F. — Rock Mechanics Investigations Associated with Shaft Excavations in a Deep Evaporite Deposit. Ph.D. thesis, Univ. Newcastle upon Tyne, 1974.

9 Wiggett, C.H. Rock Mechanics Investigation Associated with Roof Support and Rock Properties at Boulby Mine. M.Sc. thesis, Univ. Newcastle upon Tyne, 1976.

10 Pearse, G.E. The selection of mining equipment and the initial operations at Boulby Potash Mine, Cleveland Potash Limited. Mining Engineer, 1975.

11 Buzdar, S.A.R.K. A Laboratory Investigation into the Mechanical Properties of some Sedimentary Rocks with Special Reference to Potash, Ph.D. thesis, Univ. Newcastle upon Tyne, 1968.

12 Dunham, R.K. Behaviour of Resin-Anchored Bolts for Strata Reinforcement, Ph.D. thesis, Univ. Newcastle upon Tyne, 1975.

13 Tonkin, R. An Investigation into the Stress Distribution Along a Full Column Anchored Rock Bolt and Some Aspects of their Uses as Strata Reinforcement in Evaporites. M.Sc. thesis, Univ. Newcastle upon Tyne, 1975.

14 Crouch, S.L. Fairhurst, C. The mechanism of coal mine bumps and the interaction between coal pillars, mine roof and floor. University of Minnesota, U.S.B.M. Contract Report (H0101778), 1973.

15 McClain, W.C., Starfield, A.M. Analysis of combined effects. In: A Demonstration of the Disposal of High-Activity Solidified Wastes in Underground Salt Mines, ORNL-4555, 1971.

16 Deist, F.H., Georgiadis, E., Morris, J.P.E. Computer applications in rock mechanics. J. S. Afr. Inst. Min. Metall., 1972.

17 Oravecz, K.I. Loading of Coal Pillars in Bord and Pillar Workings, Ph.D. thesis, Univ. of the Witwatersrand, 1973.

18 Oravecz, K.I. Analogue modelling of stresses and displacements in bord and pillar workings of coal mines. Int. J. Rock Mech. Min. Sci., Vol. 14, 1977.

19 Thompson, M. The Face Element Method: The Numerical Solution of Elastostatic Problems by the Use of Harmonic Functions. Ph.D. thesis, Univ. Newcastle upon Tyne, 1975.

20 Salamon, M.D.G. Elastic analysis of displacements and stresses induced by mining seam or reef deposits. Part 1. J. S. Afr. Inst. Min. Metall., 1963.

21 Zienkiewicz, O.C. The Finite Element Method in Engineering Science, 2nd. ed. McGraw-Hill, London, 1971.

22 Hebblewhite, B.K. Progress report on Ph.D. research in rock mechanics. Internal report to Univ. of N.S.W., Aust., 1974.

23 Deist, F.H., Oraveoz, K.I. The finite element method and its application to problems in rock mechanics. Research Report 60/68(C.R.L.) to Chamber of Mines of S. Africa, 1968.

24 Salamon, M.D.G. Stiffness of strata surrounding pillar layouts. Research Report 60/69(C.R.L.) to Chamber of Mines of S. Africa, 1969.

25 Anon. Subsidence Engineers' Handbook, N.C.B., Mining Department, 1975.

26 Dejean, M.J.P., Martin, F. Amplitude of subsidence of underground openings subject to the influence of mining adjacent and below. Proc. of 4th. Symp., Illawarra Branch, Aus. I.M.M., 1973.

27 Maconochie, D.J. Geotechnical Studies for the Channel Tunnel. Ph.D. thesis, Univ. Newcastle upon Tyne, (in preparation).

30 Holland, C.T. Factors in the design of barrier pillars in coal mines. Proc. West Virginian Coal Mining Inst., 1965.

31 Wilson, A.H. Research into the determination of pillar size, Trans. I.M.E., Vol. 131, 1972.

32 Alder, H., Potts, E.L.J., Walker, A. — Yield-pillar technique in deep coal mining, Engineering, 1949.

33 Serata, S. — Stress control technique - An alternative to roof bolting. Mining Engineering, S.M.E. of A.I.M.E., Vol. 28, 1976.

34 Obert, L. et al. — Standardized tests for determining the physical properties of mine rock. U.S.B.M. R.I. 3891, 1946.

35 Vutukuri, S. — Internal Report, Department of Mining Engineering, Newcastle University, 1976.

36 Hudson, J.A., Crouch, S.L., Fairhurst, C. — Soft, stiff and servo controlled testing machines. A review with reference to rock failure. Engineering Geology, 1972.

37 Forster, J. — Stability Investigations Applied to the Mining of Evaporites, Ph.D. thesis, Univ. Newcastle upon Tyne, 1967.

38 Bieniawski, Z.T. — Time-dependent behaviour of fractural rock. Rock Mechanics, Vol. 2/3, 1970.

39 Brown, E.T. — Strength - size effects in rock material. Mineral Resources Research Center, Univ. of Minnesota, Progress Report No. 24, 1971.

40 Hudson, J.A. Studying time dependent effects in failed rock, Mineral Resources Research Center, Univ. of Minnesota, Progress Report No. 24, 1971.

41 Starfield, A.M., Fairhurst, C. How high-speed computers advance design of practical mine pillar systems. Engineering, Mining Journal, 169, 1968.

42 Salamon, M.D.G. Stability, instability and design of pillar workings, Int. J. Rock Mech. Min. Sci., Vol. 7, 1970.

43 Obert, L. Design and Stability of Excavations. S.M.E. Mining Engineering Handbook, Vol. 1, Section 7. ed. Cummins, Given., New York, 1973.

44 Rowley, N. In Situ Stress Determinations Carried Out in the Experimental Tunnel at Sangatte - France - Report to Mott, Hay and Anderson from Univ. Newcastle upon Tyne, 1974.

45 Miller, H.D.S., Potts, E.L.J., Szeki, A., Talbott, A.C. Development of a borehole strain cell for 'in situ' stress determination in rock - Part I. Brit. Geotech. Soc. Conf. on Rock Eng., Newcastle upon Tyne, 1977.

46 Merrill, R.H., Williamson, J.V., Ropchan, D.M., Kruse, G.H. — Stress determinations by flatjack and borehole - deformation methods. U.S.B.M. R.I. 6400, 1964.

47 Potts, E.L.J., Tomlin, N. — Investigation into the measurement of rock pressures in the mine and in the laboratory. Rept. D-4, Int. Conf. on Strata Control, 1960.

48 Wilson, A.H. — A laboratory investigation of a high modulus borehole plug gage for the measurement of rock stress. Proc. 4th. Symp. Rock Mech., 1961.

49 Roberts, A., Hawkes, I., Williams, F.T., Dhir, R.K. — A laboratory study of the photoelastic stressmeter. Int. J. Rock Mech. Min. Sci., Vol. 1, No. 3, 1964.

50 Leeman, E.R. — Experience throughout the world with the C.S.I.R. Doorstopper Rock Stress Measuring Equipment. Proc. 2nd. Cong. Int. Soc. Rock Mech., 1970.

51 Leeman, E.R. — The measurement of stress in rock. J. S. Afr. Inst. Min. Metall. 65, 1964.

52 Leeman, E.R., Hayes, D.J. — A technique for determining the complete state of stress in rock using a single borehole. Proc. of 1st. Int. Cong. of the Int. Soc. Rock Mech., Lisbon, Vol. 2, 1966.

53 Hiramatsu, Y., Oka, Y. — Stress around a shaft or level excavated in ground with a three-dimensional stress state. Mem. Faculty of Eng., Kyoto Univ., 1962.

54 Gumperayarmnont, N. — The Measurement of Stress in Rock by the Stress-Relief Techniques, M.Sc. thesis, Univ. Newcastle upon Tyne, 1971.

55 Hebblewhite, B.K., Miller, H.D.S. — Initial report on installation and overcoring of strain cells in the potash and marl strata at Boulby mine. Internal Report No. 47-0476 to Cleveland Potash Ltd. from Univ. Newcastle upon Tyne, 1976.

56 Hooker, V.E., Aggson, J.R., Bickel, D.L. — Improvements in the three-component bore-hole deformation gauge and overcoring techniques. U.S.B.M. R.I. 7895.

57 Potts, E.L.J., Hebblewhite, B.K. — Potash mines in Saskatchewan, Canada. Internal Report No. 52-1076 to Cleveland Potash Ltd. from Univ. Newcastle upon Tyne, 1976.

58 Potts, E.L.J. An investigation into the design of room and pillar workings in rock salt. The Mining Engineer, No 49, 1964.

59 Potts, E.L.J., Potts, W.H., Szeki, A. Development of ground control techniques and mining design parameters in rock salt mining. 5th Int. Strata Control Conf., 1972.

60 McClain, W.C. The effect of non-elastic behaviour of rocks. Proc. 8th Symp. on Rock Mechanics, 1967.

61 Hedley, D.G.F. An evaluation of roof stability at a Canadian salt mine, 5th Int. Strata Control Conf., 1972.

62 McClain, W.C. Time-dependent behaviour of pillars in the Alsace potash mines, Proc. 6th Symp. on Rock Mechanics, 1964.

63 Höfer, K.H., Menzel, W. Comparative study of pillar loads in potash mines established by calculation and by measurements below ground. Int. J. Rock Mech. Min. Sci., Vo. 1, 1964.

64 Höfer, K.H., Knoll, P. Investigations into the mechanism of creep deformation in Carnallite, and practical applications. Int. J. Rock Mech. Min. Sci., vol. 8, 1971.

65 Menzel, W., Eckart, D., Bruckner, G., Thoma, K. Pillar and roof span dimensioning methods in potash mining, as developed by the Mines Safety Institute in Leipzig. 5th Int. Strata Control Conf., 1972.

66 Gimm, W.A.R., Pforr, H. Breaking behaviour of salt rock under rockbursts and gas outbursts. 4th Int. Conf. Rock Mech., 1964.

67 Serata, S. Application of continuum mechanics to design of deep potash mines in Canada. Int. J. Rock Mech. Min. Sci., Vol. 5, 1968.

68 Baar, C.A. Applied rock mechanics in deep pctash mines. Internal report to Saskatchewan Research Council, E 71-2, 1971.

69 Baar, C.A. Dangerous application of laboratory parameters to the design of deep potash mines. Internal report to Saskatchewan Research Council, E 72-6, 1972.

70 King, M.S. Creep in model pillars of Saskatchewan potash. Int. J. Rock Mech. Min. Sci., Vol. 10, 1973.

71 Zahary, G. Rock mechanics at International Minerals and Chemical Corporation (Canada) Limited. Proc. 3rd Canadian Rock Mech. Symp., 1965.

72 Serata, S., Schultz, W.G. Application of stress control in deep potash mines. Mining Congress Journal, 1972.

73 McKinlay, D.W. Practical rock mechanics at Allan Potash Mine. Western C.I.M. Meeting, Saskatchewan, 1972.

74 Mackintosh, A.D. Applied rock mechanics. The development of safe travelways at the Cominco potash mine. Preprint Report.

75 Barron, K., Toews, N.A. Deformation around a mine shaft in salt. 2nd Canadian Rock Mech. Symp., 1963.

76 Hebblewhite, B.K., Miller, H.D.S., Potts, E.L.J. A method for predicting time-dependent deformations in evaporites around a vertical shaft. Brit. Geotech. Soc. Conf. on Rock Eng., Newcastle upon Tyne, 1977.